

UNIVERSITY OF NEW SOUTH WALES

**The Aerodynamic Interaction of a Rotating Wheel
and a Downforce Producing Wing in Ground Effect**

By

Sammy Diasinos

Submitted for the Degree of Doctor of Philosophy

School of Mechanical and Manufacturing Engineering

March, 2009

ORIGINALITY STATEMENT

'I hereby declare that this submission is my own work and to the best of my knowledge it contains no materials previously published or written by another person, or substantial proportions of material which have been accepted for the award of any other degree or diploma at UNSW or any other educational institution, except where due acknowledgement is made in the thesis. Any contribution made to the research by others, with whom I have worked at UNSW or elsewhere, is explicitly acknowledged in the thesis. I also declare that the intellectual content of this thesis is the product of my own work, except to the extent that assistance from others in the project's design and conception or in style, presentation and linguistic expression is acknowledged.'

Signed

Date

Acknowledgements

During the course of this research project, I have been fortunate enough to have received the assistance of many people that have been instrumental in the completion of this project. For this reason, these acknowledgements may seem long, but definitely necessary given that this is the only formal way that I can express my gratitude to all the people that have helped me along this journey.

I would like to commence by thanking my supervisor, Dr Tracie Barber and co-supervisor Professor Eddie Leonardi who have provided me with all the resources, advice and opportunity required to commence and complete this PhD. I appreciate that there were times that I was not a model student and therefore would also like to thank them both for the patience and tolerance during the course of this work. Prior to commencing this project, I had no prior experience of using CFD and I have learnt a lot from both about this very powerful tool during the course of this PhD. Sadly, Professor Leonardi passed away prior to the completion of this thesis and I am very disappointed that I was not able to present it to him prior to these tragic circumstances unfolding.

I would also like to give additional thanks to Dr Tracie Barber who together with Professor Mark Wainwright undertook to secure for me a scholarship that allowed me to take on this project.

Another person who has been with me every step of the way is Dr Alvin Gatto. Thanks Alvin for all your help and advice that allowed me to design and commission the wind tunnel, moving ground and LDA system and not forgetting me despite being located in England for the best part of this research project. Your advice over the phone and the constant discussions regarding this work has been a great assistance and I doubt I could have completed this project without your help. Definitely I would not have had any LDA data without your advice, so thanks once again.

I have also been fortunate enough to take this journey with a number of other PhD students which definitely made this project much more enjoyable. I would like to thank Chris Beves, Yonah Azriel and Graham Doig for all the great laughs in our office (505), the

hallway Frisbee, chocolate time and triple challengers! Thanks Chris for all your help in manufacturing the experimental apparatus, Yonah for all your IT assistance and advice and Graham for keeping me sane during all those late hours either spent in the Laser Lab or in our office, introducing me to hallway Frisbee and all the great football games at the village green. I look forward to the near future when we can all sit down together and not have the burden of completing a PhD distract us from talking about Formula One and the Daily Show.

The construction of all the experimental apparatus was a mammoth task and I was very fortunate to have the support of the school's workshop which manufactured all of the experimental apparatus that I used. I would like to pay special thanks particularly to Ian Cassapi who manufactured the majority of the apparatus required for this project as well as Rahda Kottieth Pullambil and Vince Carnevale. I definitely learnt a lot about manufacturing through this process and enjoyed every moment spent in the workshop.

Being mostly a computational investigation, this project would not have been possible without the large amount of IT support that I received from Vladimir Kuperman, Sam Lor and once I moved to Germany, Lorenzo Toniutti (Toyota F1). All at some stage were instrumental in providing me with working equipment that allowed me to undertake and complete this project. Thanks must also be given to Le Han Tan and Jason Middleburg who answered numerous computing and CFD related questions during countless hours spent in the CFD lab and also taught me how to use the cluster at AC3.

A great deal of motivation for this research project came from desire to work for a Formula One team, and one person who was instrumental in making this dream a reality for me was Jean-Paul (JP) Ballard (BMW Sauber). JP also found a unique way to motivate me to complete my PhD after I started working at Toyota F1 which required him to sacrifice a much loved snowboard. Now that I have finally finished this thesis, I look forward to using this snowboard during the next European winter. Thanks JP for your help, motivation and understanding during this time.

While this project has not been officially supported by an industrial partner, I have also been fortunate since commencing work at Toyota F1 to have had the support of many of my superiors and colleagues to complete this thesis. I would like to thank Dr Jonathon Ralph

Hardman and Simon Dodman for their encouragement, support and understanding during the last two years while I completed this project. I would also like to acknowledge the assistance provided to me by Giuseppe Azzollini and Ehab Fares as well as the time that they took to read portions of this thesis. I would also like to thank Mark Gillan, Jason Somerville and Christos Pashias who all willingly read this thesis in its entirety and provided me with valuable feedback that undoubtedly increased the quality of this thesis.

I would also like to thank my parents, sisters and brother in laws who have helped me greatly during the course of this project. I greatly appreciate the support that you all provided me during this period of my life and the interest that you shared in this project. Coming home to a family dinner and hearing about everybody else's day was a welcome relief from the PhD and was also extremely valuable in helping me complete this project.

Finally, I would like to thank Theodora Konstantinou who for the last 15 months has patiently waited for me to complete writing this PhD. During this period she has shared my stress, listened to my complaints, helped me focus when necessary and distracted me when appropriate. Thankyou for your patience and understanding during this time and I look forward to not having to share my time away from work between my studies and you in the future.

Ευχαριστο μορο μου για ολοι την βοηθια σου. Χερομε καθε στιγμι που ειμαι μαζι σου, σα' γαπαο!

Abstract

The performance and safety of current open wheeler race cars depend heavily on the effectiveness of the aerodynamic package. The front wing and front wheels make a significant contribution and therefore must be well understood. Previous investigations have focused on the aerodynamic characteristics of either an isolated downforce generating wing in ground effect or a rotating wheel in isolation. Investigations that have considered both bodies working in unison conflictingly claim that the addition of a wheel downstream of a wing can aid or hinder the performance of the wing, and the wheel's aerodynamic performance has not been reported. In order to obtain a more thorough understanding of the interaction of a wing and wheel, experimental results were used to conduct an extensive validation of a computational model, after an equally rigorous verification study had been conducted. A number of investigations were then conducted of a wing and wheel working in unison as well as each in isolation using the computational model.

The combined wing and wheel investigation demonstrated that three main interactions can occur, depending on the selection of wing span, angle of attack and height used, while the wheel width and track were found to be less sensitive parameters. The three interacting states differ in the path that the main and secondary wing vortices take around the wheel and the subsequent variation in the combined wake structure. In general, the wing in the presence of the wheel reduced the wing's ability to generate downforce by up to 45%. This is due to the high pressure regions generated forward of the wheel, which reduce the suction that can be achieved by the bottom surface. This was also found to alleviate the adverse pressure gradients experienced by the wing, and also reduce the drag by up to 70%. For this reason, the downforce loss phenomenon was observed to occur at a height 0.08c to 0.32c lower in comparison to the same wing in isolation, dependant on the wing span. Wheel lift and drag values were also observed to reduce in the presence of a wing by up to 65% and 38% respectively. The upwash and vortices generated by the wing were found to assist in reducing the separation from the contact patch and increasing the separation from the upper wheel tread; a phenomenon also observed during an isolated wheel investigation which was found to reduce the wheel's lift and drag. As a result, it was shown that the combined wing and wheel downforce and drag optima differed by up to 75% and 25% respectively to those which would be estimated if the two bodies were

investigated individually and the results summed. This highlights the importance of investigating these two bodies in unison.

Contents

Acknowledgements	i
Abstract	iv
List of Figures	xii
List of Tables	xx
Nomenclature	xxi
Chapter 1: Introduction	1
1.1 Literature review	2
1.1.1 Flow features and aerodynamic characteristics of an isolated downforce producing wing in ground effect	2
1.1.2 Flow features and aerodynamic performance characteristics of an isolated wheel	11
1.1.3 Combined wing and wheel studies	24
1.1.4 Summary of Previously Conducted Relevant Investigations	29
1.2 Thesis Aim and Outline	32
Chapter 2: Experimental Apparatus	36
2.1 Wind tunnel and Moving Ground	36
2.1.1 Description of UNSW 225x340mm open circuit wind tunnel	36

2.1.2 Description of the moving ground	38
2.2 Wind Tunnel models	41
2.2.1 Wing and wing support system	43
2.2.2 Wheel and wheel sting	45
2.3 Laser Doppler Anemometry	49
2.3.1 Hardware, software and setup specifications	52
2.3.2 Alignment technique	54
2.3.3 Seeding system	56
2.3.4 LDA System Measurement Errors	60
2.4 Summary	62
Chapter 3: Computational Method and Model Description	64
3.1 Theory and Methodology	64
3.1.1 Governing Equations of Fluid Flow	65
3.1.2 Reynolds Averaged Navier Stokes Equations and Turbulence Modelling	68
3.1.2.1 Spalart-Allmaras Turbulence Model	70
3.1.2.2 Standard k - ϵ Turbulence Model	70
3.1.2.3 RNG k - ϵ Turbulence Model	71
3.1.2.4 Realizable k - ϵ Turbulence Model	72
3.1.2.5 Standard k - ω Turbulence Model	72
3.1.2.6 Shear Stress Transport k - ω Turbulence Model	73
3.1.2.7 Reynolds Stress Turbulence Model	74

3.1.2.8 Boundary Layer Modelling and y^+ Values	74
3.1.3 Numerical Procedure	76
3.1.3.1 Finite Volume Method	76
3.1.3.2 Discretization Technique	77
3.1.3.3 Solution Process	77
3.1.3.4 Velocity-Pressure Coupling	79
3.1.3.5 Flow Initialisation and convergence criteria	79
3.1.4 Validation and Verification Requirements	80
3.1.4.1 Verification Process	80
3.1.4.2 Validation Process	81
3.2 Description of Computational Model Geometries	81
3.2.1 Full-scale computational model	82
3.2.1.1 Full-scale Computational Model Boundaries	83
3.2.1.2 Mesh structure description and verification	84
3.2.1.3 Inlet, Outlet, Top and Side Boundary Positions	88
3.2.2 Scaled computational model	90
3.2.2.1 Mesh structure description and verification	91
3.3 Summary	93
Chapter 4: Validation of Computational Model	95
4.1 Selection of Turbulence Model	95
4.1.1 Turbulence Model comparisons of x-velocity and x-plane velocity vectors	96

4.1.2 Comparisons to LDA Results of turbulence intensity	104
4.2 Isolated Wing in Ground Effect Validation	109
4.3 Isolated Wheel Validation	119
4.3.1 Comparison to Experimental Study Conducted by Fackrell	119
4.3.2 Comparison to Numerical Study Conducted by McManus	127
4.4 Combined Wing and Wheel Validation	131
4.4.1 Comparisons to LDA Results for wing with span $S/c=0.97$	131
4.4.2 Comparisons to LDA Results for wing with span $S/c=1.6$	137
4.5 Summary	142
Chapter 5: Independent Wheel or Wing Investigations	144
5.1 Independent Wheel Investigations	144
5.1.1 Lift, drag and wake structure dependency on wheel rotation	144
5.1.2 Variations due to size of the contact patch	155
5.1.3 Effects of geometry simplification to wheel characteristics	164
5.1.4 Variations in characteristics for adjacent wheel pair relative to isolated wheel	176
5.2 Isolated Wing Investigations	190
5.3 Summary	198
Chapter 6: Combined Wing and Wheel Investigations	201
6.1 Main Interacting States of Wing and Wheel Vortices	202

6.1.1 Causes and consequences of both wing vortices travelling outboard of wheel	206
6.1.2 Causes and consequences of main wing vortex travelling inboard while secondary vortex travels outboard of wheel	212
6.1.3 Causes and consequences of both wing vortices travelling inboard of wheel	218
6.2 Variations in Interaction due to Wing Angle of Attack	223
6.2.1 Adjustments in angle of attack causing transition from interaction “a” to “b”	229
6.2.2 Adjustments to angle of attack causing variations for interaction “c”	238
6.3 Variations in Interaction due to Wing Span	245
6.3.1 Variations caused by changes of span for a wing with 0° angle of attack	252
6.3.2 Main and secondary wing vortex variations for adjustments of wing span and angle of attack	255
6.3.3 Main and secondary wing vortex variations for adjustments of wing span and angle of attack	263
6.4 Wing Downforce loss Phenomenon in the Presence of a Wheel and Other Effects Due to Variations in Wing Height	270
6.4.1 Lift loss phenomenon for $S/c=0.97$ wing in the presence of a wheel	276
6.4.2 Lift loss phenomenon for $S/c=1.6$ wing in the presence of a wheel	282
6.5 Variations in Performance due to Wheel Width and Track	289
6.5.1 Force variations for a reduction in wheel width to $W/c=0.54$	289
6.5.2 Force variations for an increased wheel track value of 1.78c	294
6.6 Summary	299

Chapter 7: Conclusions and Future Work	303
7.1 Summary of Conclusions	303
7.2 Recommendations for Future Work	310
List of Publications	313
List of References	314
Appendix A: Detailed drawings of experimental models	321
Appendix B: Verification comparisons of flow field	359
Appendix C: Further comparisons of LDA and computational results	370

List of Figures

- Figure 1.1 Downforce generating components of an open wheel racing car
- Figure 1.2 Downforce results obtained by Zerihan and Zhang (2000a)
- Figure 1.3 On surface flow visualisation conducted by Zerihan and Zhang (2000a)
- Figure 1.4 Schematic of the flow structures described by Zerihan *et al.* (2002) about an isolated downforce producing wing in ground effect
- Figure 1.5 Static pressure measurements obtained about the central circumference of a stationary and rotating wheel (Fackrell *et al.* 1972)
- Figure 1.6 Expected flow structures as described by Fackrell (1975)
- Figure 1.7 Wheel shoulder profiles tested by Fackrell et al. (1973)
- Figure 1.8 Schematic of the flow structures obtained by McManus and Zhang (2006)
- Figure 1.9 Conceptual wing and wheel geometry that will be used during this investigation
-
- Figure 2.1 Figure 2.1 Schematic of the UNSW 225x340mm open circuit wind tunnel and moving ground
- Figure 2.2 Schematic of the moving ground used in the UNSW 225x340mm wind tunnel
- Figure 2.3 Mechanisms used to control the tracking and the vinyl strip used to seal the leading edge fairing to the belt surface
- Figure 2.4 Velocity profile of an empty test section 150mm upstream of wheel centre
- Figure 2.5 Wind tunnel models used during experimental investigations
- Figure 2.6 Wing support system used allowing span, height and angle of attack to be varied
- Figure 2.7 Jig used to ensure the correct positioning of the endplate
- Figure 2.8 Schematic of wheel and wheel sting assembly
- Figure 2.9 Normalised x-velocity and in plane velocity vectors comparisons of CFD undertaken of experimental apparatus with and without wheel sting
- Figure 2.10 Normalised x-velocity and in plane velocity vectors comparisons of CFD undertaken of experimental apparatus with and without wheel sting
- Figure 2.11 Schematic of the crossed beams and the receiver location for an LDA system
- Figure 2.12 Schematic of the components associated with a typical 3D LDA system
- Figure 2.13 Arrangement of the 2D and 1D probe used to obtain LDA measurements

- Figure 2.14 CCD tool used for the alignment of the LDA system
- Figure 2.15 Schematic of Laskin type atomiser
- Figure 2.16 Lorenz-Mie Scatter Diagram for spherical particles, note light intensity is shown on logarithmic scale (Dantec, 2006)
- Figure 2.17 Forces acting on a particle travelling with a fluid flow
-
- Figure 3.1 Schematic of Conservation of Mass
- Figure 3.2 Schematic of Conservation of Momentum
- Figure 3.3 Flowchart describing Pressure Based Segregated Solver
- Figure 3.4 Computational domain and boundaries of the full-scale computational model
- Figure 3.5 Surface mesh indicating grid structure of full-scale computational model
- Figure 3.6 Variation in wing and wheel, lift and drag due to off surface mesh density
- Figure 3.7 Variation in wing and wheel, lift and drag due to number of control volumes in boundary layer height
- Figure 3.8 Variation in wing and wheel, lift and drag due to boundary positions
- Figure 3.9 Computational domain and boundaries of the scaled computational model
- Figure 3.10 Surface mesh indicating grid structure of scaled computational model
- Figure 3.11 Variation in wing and wheel, lift and drag due to number of control volumes in boundary layer height for the scaled computational model
-
- Figure 4.1 Planes on which comparisons are conducted on
- Figure 4.2 Normalised x-velocity and in plane comparisons to LDA results on $X/c=-0.63$ plane
- Figure 4.3 Normalised x-velocity and in plane comparisons to LDA results on $X/c=0.75$ plane
- Figure 4.4 Normalised x-velocity and in plane comparisons to LDA results on $X/c=1.5$ plane
- Figure 4.5 Turbulence intensity comparisons to LDA results on $X/c=-0.63$ plane
- Figure 4.6 Turbulence intensity comparisons to LDA results on $X/c=0.75$ plane
- Figure 4.7 Turbulence intensity comparisons to LDA results on $X/c=1.5$ plane
- Figure 4.8 Computational domain and boundaries for comparisons to Zerihan's (2001) experimental results
- Figure 4.9 Comparison of the lift coefficients for Zerihan's wing at various heights for an AOA of 1°

- Figure 4.10 Comparison of the pressure coefficients obtained at the centre of the wing
- Figure 4.11 Comparison of span wise pressure coefficients obtained along the quarter chord
- Figure 4.12 Comparison of x-vorticity obtained with computational model (contour lines) to those measured by Zerihan, 2001 (flooded contours) at; a) $h=0.091c$, b) $h=0.134c$ c) $h=0.224c$
- Figure 4.13 Comparison of Zerihan's (2001) wing wake at; a) $h=0.091c$, b) $h=0.134c$ c) $h=0.224c$
- Figure 4.14 Comparison of the drag coefficients for Zerihan's wing at various heights
- Figure 4.15 Computational domain and boundaries for comparisons to Fackrell's (1975) experimental results
- Figure 4.16 Geometry of Fackrell's (1975) wheels (shown to closest millimetre)
- Figure 4.17 Force comparisons for Fackrell's (1975) rotating and stationary B2 wheel
- Figure 4.18 Centre pressure coefficient comparisons for B2 stationary and rotating wheels
- Figure 4.19 Total pressure comparison for Fackrell's B2 rotating wheel
- Figure 4.20 Force comparisons for Fackrell's A2 and B2 rotating wheels
- Figure 4.21 Schematic comparison to McManus and Zhang's results for Fackrell's A2 wheel
- Figure 4.22 Wake comparison to McManus' time averaged results for Fackrell's A2 wheel
- Figure 4.23 Comparisons to LDA for 0° and 12° angles of attack for span $S/c=0.97$ at $X/c=-0.63$
- Figure 4.24 Comparisons to LDA for 0° and 12° angles of attack for span $S/c=0.97$ at $X/c=0.75$
- Figure 4.25 Comparisons to LDA for 0° and 12° angles of attack for span $S/c=0.97$ at $X/c=1.5$
- Figure 4.26 Comparisons to LDA for 0° and 12° angles of attack for span $S/c=1.6$ at $X/c=-0.63$
- Figure 4.27 Comparisons to LDA for 0° and 12° angles of attack for span $S/c=1.6$ at $X/c=0.75$
- Figure 4.28 Comparisons to LDA for 0° and 12° angles of attack for span $S/c=1.6$ at $X/c=1.5$

- Figure 5.1 Comparison of wheel wake structure and forces obtained with slip ground condition
- Figure 5.2 Separated Top and Bottom wheel regions for Fackrell's A2 wheel
- Figure 5.3 Streamlines indicating separation for tested boundary conditions
- Figure 5.4 Central pressure coefficients obtained for wheels with separated boundaries
- Figure 5.5 Wheel wake structures obtained with wheels with different boundaries
- Figure 5.6 Flow structures obtained with attempted "gurney" trip
- Figure 5.7 Comparison of wheel wake structure obtained when varying the separation
- Figure 5.8 Force coefficients obtained for wheels with separated boundaries
- Figure 5.9 Contact made by solid wheel and geometry used for computational model
- Figure 5.10 Variations in contact patch step height tested with Fackrell's A2 wheel
- Figure 5.11 Variations in wheel wake obtained when increasing the step height
- Figure 5.12 Wheel tread separation due to the variation in the contact patch step height
- Figure 5.13 Force coefficients obtained for variations in the contact patch step height
- Figure 5.14 Central pressure coefficients obtained for variations in the step height
- Figure 5.15 Simplified wheel geometries tested (measurements shown to closest millimetre)
- Figure 5.16 Force comparisons for simplifying Fackrell's A2 wheel geometry
- Figure 5.17 Centre pressure coefficients for simplified rotating wheel geometries
- Figure 5.18 Flow structures associated with Fackrell's A2 wheel with and without the hubs
- Figure 5.19 Wake comparisons of Fackrell's A2 wheel with and without the hubs
- Figure 5.20 Static pressure comparisons of A2 wheel without hubs and W1 wheel
- Figure 5.21 Centre pressure coefficients for simplified rotating wheel geometries
- Figure 5.22 Entrainment into wheel wake for Fackrell's A2 wheel with and without hubs
- Figure 5.23 Flow structures associated with simplified wheel geometries
- Figure 5.24 Lift and drag forces experienced by both wheels side by side and in isolation
- Figure 5.25 Side forces obtained for both wheels when side by side
- Figure 5.26 Pressure coefficients on W1 wheel at $z/d=0.107$, $z/d=0.239d$ and $z/d=0.503$
- Figure 5.27 Pressure coefficients and cross component velocity at $x=-0.63d$ for W1 wheel
- Figure 5.28 Pressure coefficients on W2 wheel at $z/d=0.107$, $z/d=0.239d$ and $z/d=0.503$
- Figure 5.29 Pressure coefficients and cross component velocity at $x/d=-0.63$ for W2 wheel

- Figure 5.30 Pressure coefficients on W1 and W2 wheels at $z/d=0.0015$ (contact patch)
- Figure 5.31 Variations in W1 wheel wake obtained when varying the wheel track
- Figure 5.32 Variations in W2 wheel wake obtained when varying the wheel track
- Figure 5.33 Lift coefficient obtained for variations in span of Zerihan's wing
- Figure 5.34 Comparison of Zerihan's on surface flow visualisation to shear stress values
- Figure 5.35 Shear stress and spanwise pressure for Zerihan wing with varied spans
- Figure 5.36 X-Vorticity on a plane located at $X=1.5c$
- Figure 5.37 Centre chord pressure coefficients for Zerihan's wing with varied span at $h=0.134c$
- Figure 5.38 Centre chord pressure coefficients for Zerihan's wing with varied span at the respective maximum downforce heights
- Figure 5.39 Drag coefficient obtained for variations in span of Zerihan's wing
- Figure 6.1 Flow chart outlining investigations undertaken of a combined wing and wheel pair
- Figure 6.2 The three wing and wheel vortex interactions; a) both outer, b) main inner and secondary outer, and c) both inner
- Figure 6.3 Force variation experienced by wing in the three interacting states
- Figure 6.4 Force variation experienced by wheel in the three interacting states
- Figure 6.5 Vectors and Vorticity on x-planes for a wing and/or wheel with $W/c=0.63$, $T/c=1.6$, $h/c=0.13$, $S/c=1.6c$ and $AOA=0^\circ$
- Figure 6.6 Pressure coefficients around endplate on z-planes for a wing and/or wheel with $W/c=0.63$, $T/c=1.6$, $h/c=0.13$, $S/c=1.6c$ and $AOA=0^\circ$
- Figure 6.7 Vectors and Total Pressure on x-planes for a wing and/or wheel with $W/c=0.63$, $T/c=1.6$, $h/c=0.13$, $S/c=1.6c$ and $AOA=0^\circ$
- Figure 6.8 Vectors and Vorticity on x-planes for a wing and/or wheel with $W/c=0.63$, $T/c=1.6$, $h/c=0.13$, $S/c=1.6c$ and $AOA=12^\circ$,
- Figure 6.9 Pressure coefficients around endplate on z-planes for a wing and/or wheel with $W/c=0.63$, $T/c=1.6$, $h/c=0.13$, $S/c=1.6c$ and $AOA=0^\circ$
- Figure 6.10 Vectors and Vorticity on x-planes for a wing and/or wheel with $W/c=0.63$, $T/c=1.6$, $h/c=0.13$, $S/c=1.6c$ and $AOA=12^\circ$,
- Figure 6.11 Vectors and Vorticity on x-planes for a wing and/or wheel with $W/c=0.63$, $T/c=1.6$, $h/c=0.13$, $S/c=0.97c$ and $AOA=12^\circ$,
- Figure 6.12 Pressure coefficients around endplate on z-planes for a wing and/or wheel

with $W/c=0.63$, $T/c=1.6$, $h/c=0.13$, $S/c=1.6c$ and $AOA=0^\circ$

- Figure 6.13 Vectors and Vorticity on x-planes for a wing and/or wheel with $W/c=0.63$, $T/c=1.6$, $h/c=0.13$, $S/c=0.97c$ and $AOA=12^\circ$;
- Figure 6.14 Wing lift results for variations in angle of attack for an isolated wing ($h/c=0.13$) and also in the presence of a wheel pair ($W/c=0.63$, $T/c=1.6$)
- Figure 6.15 Wing drag results for variations in angle of attack for an isolated wing ($h/c=0.13$) and also in the presence of a wheel pair ($W/c=0.63$, $T/c=1.6$)
- Figure 6.16 Wheel lift and drag results for an isolated wheel pair ($W/c=0.63$, $T/c=1.6$) and also in the presence of a wing ($h/c=0.13$) with varied angle of attack
- Figure 6.17 Wheel side force results for an isolated wheel pair ($W/c=0.63$, $T/c=1.6$) and also in the presence of a wing ($h/c=0.13$) with varied angle of attack
- Figure 6.18 Vectors and Vorticity on x-planes for a wing with varied AOA and with a wheel
- Figure 6.19 Wall shear stress and spanwise pressure distribution for variations in AOA
- Figure 6.20 Streamlines indicating upwash variation due to changes in wing angle of attack
- Figure 6.21 Central pressure coefficients obtained for wheel with varied wing angle of attack
- Figure 6.22 Vectors and Total Pressure on x-planes for a wing and wheel with varied angle of attack
- Figure 6.23 Pressure coefficients on wheel at $z/d=0.107$, $z/d=0.239d$ and $z/d=0.503$ in isolation and in the presence of a wing with 0° angle of attack
- Figure 6.24 Pressure coefficients on wheel at $z/d=0.107$, $z/d=0.239$ and $z/d=0.503$ in isolation and in the presence of a wing with 12° angle of attack
- Figure 6.25 Vectors and Vorticity on x-planes for a wing with varied AOA and with a wheel
- Figure 6.26 Wall shear stress and spanwise pressure distribution for variations in AOA
- Figure 6.27 Central pressure coefficients obtained for wheel with varied wing angle of attack
- Figure 6.28 Vectors and Total Pressure on x-planes for a wing and wheel with varied angle of attack
- Figure 6.29 Pressure coefficients on wheel at $z/d=0.107$, $z/d=0.239$ and $z/d=0.503$ in isolation and in the presence of a wing with 0° angle of attack

- Figure 6.30 Pressure coefficients on wheel at $z/d=0.107$, $z/d=0.239$ and $z/d=0.503$ in isolation and in the presence of a wing with 12° angle of attack
- Figure 6.31 Wing lift results for variations in span and angle of attack for an isolated wing ($h/c=0.13$) and also in the presence of a wheel pair ($W/c=0.63$, $T/c=1.6$)
- Figure 6.32 Wing drag results for variations in span and angle of attack for an isolated wing ($h/c=0.13$) and also in the presence of a wheel pair ($W/c=0.63$, $T/c=1.6$)
- Figure 6.33 Wheel lift and drag (a) and side force (b) results for an isolated wheel pair ($W/c=0.63$, $T/c=1.6$) and also in the presence of a wing ($h/c=0.13$) with varied span and AOA
- Figure 6.34 Wheel side force results for an isolated wheel pair ($W/c=0.63$, $T/c=1.6$) and also in the presence of a wing ($h/c=0.13$) with varied span and AOA
- Figure 6.35 Total lift results for variations in span and angle of attack for an isolated wing ($h/c=0.13$) and also in the presence of a wheel pair ($W/c=0.63$, $T/c=1.6$)
- Figure 6.36 Total drag results for variations in span and angle of attack for an isolated wing ($h/c=0.13$) and also in the presence of a wheel pair ($W/c=0.63$, $T/c=1.6$)
- Figure 6.37 Vectors and Vorticity on the $x/c=-0.63$ plane for a wing in isolation and in the presence of a wheel with varied span, $AOA=0^\circ$, $h/c=0.13$ and wheel with $W/c=0.63$, $T/c=1.6$
- Figure 6.38 Vectors and Vorticity on the $x/c=-0.63$ plane for a wing in isolation and in the presence of a wheel with varied span, $AOA=0^\circ$, $h/c=0.13$ and wheel with $W/c=0.63$, $T/c=1.6$
- Figure 6.39 Vectors and Vorticity on the $x/c=-0.63$ plane for a wing in isolation and in the presence of a wheel with varied span, $AOA=12^\circ$, $h/c=0.13$ and wheel with $W/c=0.63$, $T/c=1.6$
- Figure 6.40 Vectors and Vorticity on the $x/c=-0.63$ plane for a wing in isolation and in the presence of a wheel with varied span, $AOA=12^\circ$, $h/c=0.13$ and wheel with $W/c=0.63$, $T/c=1.6$
- Figure 6.41 Pressure coefficients around endplate on z-planes for a wing and wheel with $W/c=0.63$, $T/c=1.6$, $h/c=0.13$, $AOA=0^\circ$ and varied span
- Figure 6.42 Central pressure coefficients obtained for wheel with varied wing span and 12° angle of attack
- Figure 6.43 Vectors and Total Pressure on $x/c=0.75$ for a wing and wheel with varied span
- Figure 6.44 Pressure coefficients on wheel at $z/d=0.239$ in isolation and in the presence

of a wing with 12° angle of attack and varied span

- Figure 6.45 Main wing vortex core y (a) and z (b) position for $AOA=0^\circ$ wings in isolation and in the presence of a wheel pair
- Figure 6.46 Main wing vortex core y (a) and z (b) position for $AOA=4^\circ$ wings in isolation and in the presence of a wheel pair
- Figure 6.47 Main wing vortex core y (a) and z (b) position for $AOA=0^\circ$ wings in isolation and in the presence of a wheel pair
- Figure 6.48 Main wing vortex core y (a) and z (b) position for $AOA=0^\circ$ wings in isolation and in the presence of a wheel pair
- Figure 6.49 Secondary wing vortex strength for wings in isolation and in the presence of a wheel a pair
- Figure 6.50 Wing lift results for variations in height for wings of two different spans in isolation and also in the presence of a wheel pair ($W/c=0.63$, $T/c=1.6$)
- Figure 6.51 Wing drag results for variations in height for wings of two different spans in isolation and also in the presence of a wheel pair ($W/c=0.63$, $T/c=1.6$)
- Figure 6.52 Wheel lift and drag results for variations in wing height for two different spans in isolation and also in the presence of a wheel pair ($W/c=0.63$, $T/c=1.6$)
- Figure 6.53 Side force results for variations in wing height for two different spans in isolation and also in the presence of a wheel pair ($W/c=0.63$, $T/c=1.6$)
- Figure 6.54 Wall shear stress and spanwise pressure distribution for variations in height for a wing with span $S/c=0.97$
- Figure 6.55 Vectors and Vorticity on x-planes for a wing wheel with $W/c=0.63$, $T/c=1.6$, $S/c=0.97c$ and $AOA=4^\circ$
- Figure 6.56 Vectors and Vorticity on x-planes for a wing wheel with $W/c=0.63$, $T/c=1.6$, $S/c=0.97c$ and $AOA=4^\circ$
- Figure 6.57 Vectors and Total Pressure on x-planes for a wing and wheel with $W/c=0.63$, $T/c=1.6$, $S/c=0.97c$ and $AOA=4^\circ$
- Figure 6.58 Wall shear stress and spanwise pressure distribution for variations in height for a wing with span $S/c=1.6$
- Figure 6.59 Streamlines indicating vortex path variation due to changes in wing height
- Figure 6.60 Vectors and Vorticity on x-planes for a wing and wheel with $W/c=0.63$, $T/c=1.6$, $S/c=1.6c$ and $AOA=4^\circ$,
- Figure 6.61 Y-plane velocity between the wing and wheel for variations in wing height

- Figure 6.62 Vectors and Total Pressure on x-planes for a wing and wheel with $W/c=0.63$, $T/c=1.6$, $S/c=1.6c$ and $AOA=4^\circ$
- Figure 6.63 Wing lift (a) and drag (b) results for variations in span and angle of attack for a wing ($h/c=0.13$) in isolation and also in the presence of a wheel pair ($W/c=0.63$, $T/c=1.78$)
- Figure 6.64 Wheel lift and drag results for an isolated wheel pair ($W/c=0.54$, $T/c=1.6$) and also in the presence of a wing ($h/c=0.13$) with varied span and AOA
- Figure 6.65 Wheel side force results for an isolated wheel pair ($W/c=0.54$, $T/c=1.6$) and also in the presence of a wing ($h/c=0.13$) with varied span and AOA
- Figure 6.66 Total lift (a) and drag (b) results for variations in span and angle of attack for a wing ($h/c=0.13$) in isolation and also in the presence of a wheel pair ($W/c=0.63$, $T/c=1.78$)
- Figure 6.67 Wing lift (a) and drag (b) results for variations in span and angle of attack for a wing ($h/c=0.13$) in isolation and also in the presence of a wheel pair ($W/c=0.63$, $T/c=1.78$)
- Figure 6.68 Wheel lift and drag (a) and side force (b) results for an isolated wheel pair ($W/c=0.63$, $T/c=1.78$) and also in the presence of a wing ($h/c=0.13$) with varied span and AOA
- Figure 6.69 Wheel side force results for an isolated wheel pair ($W/c=0.63$, $T/c=1.78$) and also in the presence of a wing ($h/c=0.13$) with varied span and AOA
- Figure 6.70 Total lift (a) and drag (b) results for variations in span and angle of attack for a wing ($h/c=0.13$) in isolation and also in the presence of a wheel pair ($W/c=0.63$, $T/c=1.78$)

List of Tables

- Table 2.1 Statistical variance assumptions (Benedict and Gould, 2006)
- Table 3.1 GCI calculated for grid with characteristic length of $h=0.0266c$
- Table 4.1 Lift and drag coefficients obtained by Fackrell based on frontal area

Table 6.1	Interaction types obtained for a wheel pair configuration of $W/c=0.63$, $T/c=1.6$
Table 6.2	Interaction types obtained for a wheel pair configuration of $W/c=0.54$, $T/c=1.6$
Table 6.3	Interaction types obtained for a wheel pair configuration of $W/c=0.63$, $T/c=1.78$

Nomenclature

AOA	wing angle of attack
c	wing chord
C_D	drag coefficient
C_{DA}	drag coefficient not normalised with a reference area (m ²)
C_L	lift coefficient
C_{LA}	lift coefficient not normalised with a reference area (m ²)
C_p	static pressure coefficient
C_S	side force coefficient
C_{SA}	side force coefficient not normalised with a reference area (m ²)
d	wheel diameter
d_p	diameter of seeding particles
d_P	seeding particle diameter
f_c	critical frequency for which particle follows oscillations in flow
f_{coarse}	result obtained with the coarse mesh that the grid convergence index will be calculated for
F_D	drag force experienced by a particle of seeding
f_{Err}	doppler frequency error
f_{fine}	result obtained with the fine mesh that the grid convergence index will be calculated in comparison to
F_L	lift force experienced by a particle of seeding
F_S	factor of safety for used for the calculation of the grid convergence index
h	height of wing measured from the point closest to the ground
h_{grid}	grid characteristic length
h_{coarse}	grid characteristic length of the coarse grid that the grid convergence index will be calculated for
h_{fine}	grid characteristic length of the fine grid that the grid convergence index will

	be calculated in comparison to
h_{LDA}	constant dependant on confidence level of LDA measurements
h_{ref}	reference height for calculation of turbulence length scale
I	turbulence intensity
k	kinetic energy
l	turbulent length scale
l_R	ratio between aperture of a Guassian beam and the beam waist
N	number of samples
p	factor describing the order of convergence used for the calculation of the grid convergence index
p'	fluctuating pressure component
\bar{P}	mean pressure component
r	ratio of coarse to fine grid characteristic lengths for the calculation of the grid convergence index
S	wing span (measured from center to tip)
s	particle of seeding slip velocity
T	wheel track
t_i	transit time of the i'th particle crossing the measurement volume
\vec{u}	velocity magnitude
u', v', w'	fluctuating velocity component
$\bar{U}, \bar{V}, \bar{W}$	mean velocity component
u, v, w	velocities in the x,y,z directions respectively
u_1, u_2, u_3	velocity measured by the green blue and violet LDA channels respectively
u_F	fluid seeding is traveling in velocity
u_i	velocity of the i'th particle crossing the measurement volume
u_∞	freestream velocities
$u_{rms}, v_{rms}, w_{rms}$	rms velocities in the x,y,z directions respectively
u_t	friction velocity
v_F	fluid seeding is traveling in velocity
v_P	particle of seeding velocity
v_S	particle of seeding slip velocity
W	wheel width
\bar{X}	mean value of variable that the error will be calculated for

x,y,z	orthogonal directions
x_D	beam waist
x_{IFS}	distance of inlet boundary from wheel center
x_{OFS}	distance of outlet boundary from wheel center
y^+	y plus value
y_{FS}	distance of side boundary from symmetry plane
y_p	distance from the boundary to the center of the adjacent control volume used to calculate the y^+ value
z_D	length of measurement volume
z_{FS}	distance of top boundary from ground

Greek Symbols

α	angle of 2D LDA probe
β	angle of 1D LDA probe
ε	turbulent dissipation rate
ε	percentage variation of coarse and fine variable for the calculation of the grid convergence index
Φ	variable for which the error is required to be calculated
ϕ	angle about a circumference of the wheel parallel to the ground measured from the central, upstream point
η	non dimensionalised span measured from wing tip (0) to wing center (1)
η_i	non-uniform weighting factor for correcting velocity bias
λ	volumetric deformation
λ_{LDA}	wavelength of laser beam
μ	dynamic viscosity
μ_F	fluid seeding is traveling in viscosity
μ_t	turbulent viscosity
ν	kinematic viscosity
θ	angle around the central circumference of a wheel measured from the most upstream point
θ_{LDA}	beam separation angle
ρ	density of fluid
ρ_p	seeding particle density

- τ shear stress acting on a volume of fluid
- τ_0 time required to make slip velocity zero
- ω specific dissipation rate
- ω_c critical frequency for which slip can be tolerated
- ζ equation dependant on the variable that measurement error will be calculated for

Glossary

- CCD Charged Couple Device
- DNS Direct Numerical Simulation
- F1 Formula One
- GCI Grid Convergence Index
- LDA Laser Doppler Anemometer
- LES Large Eddy Simulation
- PIV Particle Image Velocimetry
- RANS Reynolds Averaging Navier Stokes
- RNG Renormalization Group theory
- RSM Reynolds Stress Modeling
- SIMPLE Semi-Implicit Method for Pressure Linked Equations
- SIMPLEC SIMPLE Consistent
- SST Shear Stress Transport
- UNSW University of New South Wales

Chapter 1: Introduction

The performance of current open wheel race cars depends heavily on the effectiveness of the aerodynamic package. Numerous components including wings, floor, diffuser, barge boards and splitter plate are all currently used to generate downforce (Figure 1.1). The ultimate goal is to optimise the shape of these appendages within the scope of a given set of regulations in order to extract the maximum possible downforce while also improving the vehicle's aerodynamic efficiency. Downforce allows the normal load experienced by each tire to be increased and subsequently each tire can generate greater longitudinal and transverse loads enhancing the vehicle's acceleration, braking and cornering ability (Katz, 1995). The addition of such devices can also increase the drag of the vehicle resulting in a reduction in the maximum speed that the vehicle can obtain and as a result, a compromise between downforce and drag is required. Assuming that all other vehicle parameters remain constant, a 10% increase in downforce has been estimated to reduce the time required to complete a lap from between 0.7 seconds (Agathangelou and Gascoyne, 1998) and 1 second (Dominy and Dominy, 1984) depending on the configuration of the circuit.

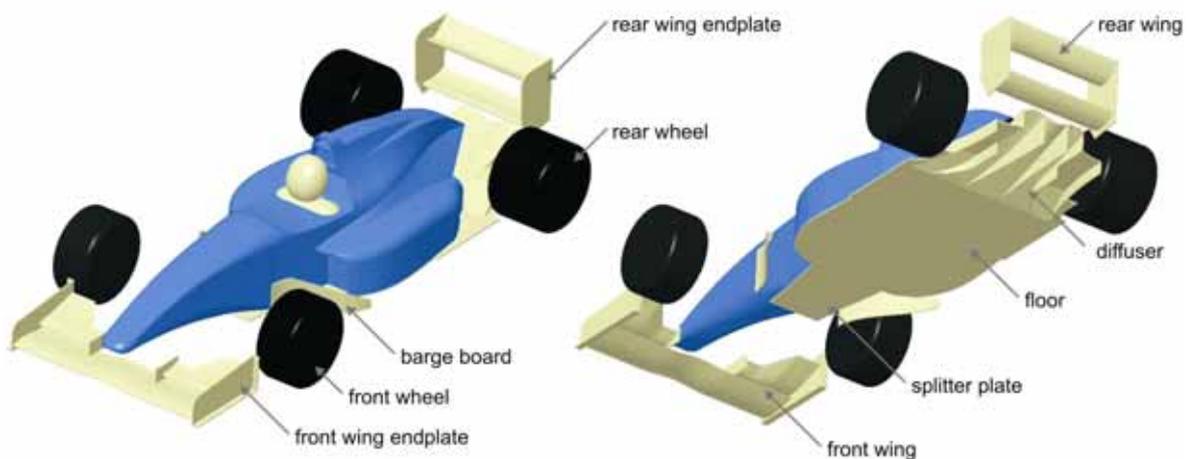


Figure 1.1 Downforce generating components of an open wheel racing car

On modern open wheel racing cars, approximately 30% of the total downforce originates from the front wing (Metz, 1987; Dominy, 1992) and the wake of the front wing is likely to influence the performance of aerodynamic components located downstream (Zhang and

Zerihan, 2003). Due to the requirements of the regulations, the wheels are exposed and therefore can contribute up to 40% of the vehicles total drag (Agathangelou and Gascoyne, 1998). However, the close proximity of the front wheels to the front wing is expected to have an adverse effect on the performance of the front wing. Despite this, the physics associated with the interaction of these two components remains poorly understood (Katz, 2006).

While little research has been conducted considering the interaction of a downforce producing wing and wheel operating together, there is however a number of investigations concerned specifically with these two bodies in isolation.

1.1. Literature review

1.1.1. Flow features and aerodynamic characteristics of an isolated downforce producing wing in ground effect

The most significant variation for a downforce producing wing used for motor sport applications in comparison to that used for a conventional aircraft is the direction in which the lift force is created. In order to produce downforce, or negative lift, the aerofoil profile of the wing is required to be inverted such that the suction side of the wing is facing downward. Additionally, while aircraft wings typically have little camber and a large aspect ratio, restrictions placed on the design of bodywork related to motor sport vehicles forces the wings to have a comparatively short span, multiple elements and profiles that are highly cambered (Katz, 1995).

The first report of a downforce producing wing in ground effect was made inadvertently by Zahm and Bear (1921) who were conducting an experimental investigation of a lifting wing in ground effect and for “completeness” also undertook a series of experiments where the ground plane was placed above, as opposed to below, the wing. They reported that in this configuration, the lift and drag of the wing increased significantly as the proximity to the ground was reduced for angles of attack between 0° and 14°.

Despite the wide use of these aerodynamic devices in motor racing since the late 1960's, little published research then appears until the early 90's. Ranzenbach and Barlow (1994) undertook an experimental investigation on a symmetrical NACA 0015 aerofoil at an angle of attack of 0° and with a Reynolds number of 1.5×10^6 utilising an elevated ground representation technique. While Abbott and Von Doenhoff (1959) demonstrated that this aerofoil produces zero lift in free stream conditions, Ranzenbach and Barlow (1994) demonstrated that at heights of $0.9c$ and less, the NACA 0015 aerofoil would generate downforce. This was determined to be caused by the flow between the ground and the aerofoil's lower surface being accelerated further than that experienced by the flow over the upper surface. Similarly, the drag generated by the aerofoil also increased due to a rise in the shear stress experienced by the accelerated flow beneath the aerofoil.

As the height was reduced the downforce produced by the NACA 0015 aerofoil increased up to a height of $0.0324c$ where a minimum lift coefficient of -0.35 was achieved. At further reduced heights the downforce produced by the aerofoil reduced and the authors believed that this phenomenon, which they referred to as the "force reversal phenomenon", was being influenced by the experimental ground representation technique that they had employed. They believed that this phenomenon could be attributed to the boundary layer that formed over the ground board and the aerofoil's bottom surface merging and subsequently restricting the flow beneath the aerofoil, preventing it from being accelerated. In an attempt to prove the proposed hypothesis, the experimental results were used to validate a two dimensional computational model that mimicked their experimental setup that would later be used to determine the effect that replacing the stationary ground with a moving ground would have. Comparisons of the experimental and numerical results indicated that the "force reversal phenomenon" was predicted at a lower height and that the downforce was slightly over predicted at the lower heights by the computational model. Despite this, the computational model was determined to be capable of reproducing the results obtained experimentally. By re-solving the computational model after incorporating a moving ground plane, Ranzenbach and Barlow (1994) came to the conclusion that the stationary ground utilised during the experiments was increasing the height at which the maximum downforce condition would be expected to occur. Additionally, the computational model was used to visualise the thickness of the boundary layer using contours of vorticity magnitude at the height at which the "force reversal phenomenon" had occurred which supported their proposed explanation.

Simultaneously, a two dimensional experimental investigation was undertaken by Knowles *et al.* (1994) utilising a the NASA LS(1)-0417 aerofoil and a moving ground at a Reynolds number of 4.3×10^5 . Experimental results were obtained at angles of attack varying from -9° to 15° and at heights from $0.12c$ to $1c$. Knowles *et al.* demonstrated that as the height of the aerofoil is reduced, the angle at which stall occurred at was also reduced. Like Ranzenbach and Barlow, Knowles *et al.* explained the increase in downforce with reductions in height was also attributed to the flow between the wing and the ground being further accelerated, but the heights that were tested did not allow the “force reversal phenomenon” to be observed.

In a later study, Ranzenbach and Barlow (1995) repeated their previous experimental investigation with a NACA 4412 aerofoil to determine what effect camber would have on the “force reversal phenomenon”. Using the same experimental setup it was demonstrated that the cambered aerofoil also experienced increased levels of downforce and drag as it approached the ground up to the height at which the “force reversal phenomenon” occurs. This was achieved at a height of $0.097c$ for the NACA4412 aerofoil which was approximately three times greater than the height previously reported for the symmetrical aerofoil. This led to the conclusion that increasing the camber of the aerofoil was responsible for increasing the height at which the “force reversal phenomenon” occurred.

Ranzenbach and Barlow (1996) also repeated the NACA4412 experiments using a numerical model with both a stationary and moving ground. Despite the aerofoil in the presence of the moving ground experiencing the “force reversal phenomenon” at a larger height than the aerofoil in the presence of the stationary case, Ranzenbach and Barlow still conclude that the merging of boundary layers is the cause for the “force reversal phenomenon”. The results presented by them during this study also demonstrate a 10% variation between the downforce generated with a stationary ground and moving ground at the greatest height tested ($0.903c$) highlighting the importance of the ground representation technique for a downforce producing wing in ground effect study.

The first two dimensional multi-element downforce producing aerofoil in ground effect investigations were conducted by Ranzenbach *et al.* (1997) using identical techniques to that used for the previous investigations by Ranzenbach and Barlow. They utilised a

NACA 63₂-215 Mod B airfoil with a 30% chord flap and determined that this profile experienced a lift loss phenomenon at a height of 0.25c, confirming their previous finding linking the camber to this performance characteristic of an aerofoil. Vorticity contour plots presented indicated that the boundary layer over the ground and the bottom surface of the aerofoil remained apart at heights less than 0.25c, yet it was still believed that the boundary layers were responsible for the “force reversal phenomenon”.

A three dimensional downforce producing wing in ground effect study was conducted by Jasinski and Selig (1998) using a two element profile wing with two interchangeable side profile endplates and with aspect ratio of 2.8. Their experimental apparatus consisted of a half span wing mounted to a balance in line with the floor of the test section that acted as a symmetry plane while the ground plane was simulated using the elevated ground technique by placing a board parallel to the side wall of the test section facing the suction surface of the wing. The ground representation technique limited the height at which they could conduct their experiments, as heights less than 0.2c were observed to have caused the boundary layer over the elevated ground to separate once again indicating the importance of a moving ground for such studies. As a result the experiments were conducted at a constant height of 0.3c. During this study, it was determined that increases in the side area of the endplates improves the performance of the wing and measurements made in the wake of the wing (using a seven hole probe) indicated that two vortices rotating in the same direction form from the upper and lower edges of the endplates. A 10° increase in the flap angle was also shown to alter the position of the lower vortex by increasing the height by 0.4c and shifting it towards the symmetry plane by the same amount on a plane located one chord length aft of the wing's trailing edge. The speed was also varied such that downforce and drag results were obtained within a Reynolds number range of 0.7×10^6 to 1.3×10^6 and this resulted in the lift and drag coefficients not varying by more than 5%.

Endplates located on the ends of the wing improve the efficiency of the wing by providing a physical barrier between the low pressure regions beneath the wing and the higher pressure regions either side or above the wing. The addition of endplates allows the low pressure region beneath the wing to be lower than that which would be obtained had the tip been exposed. This results in an increase in the downforce that the wing can produce by up to 30% (McBeath, 1998).

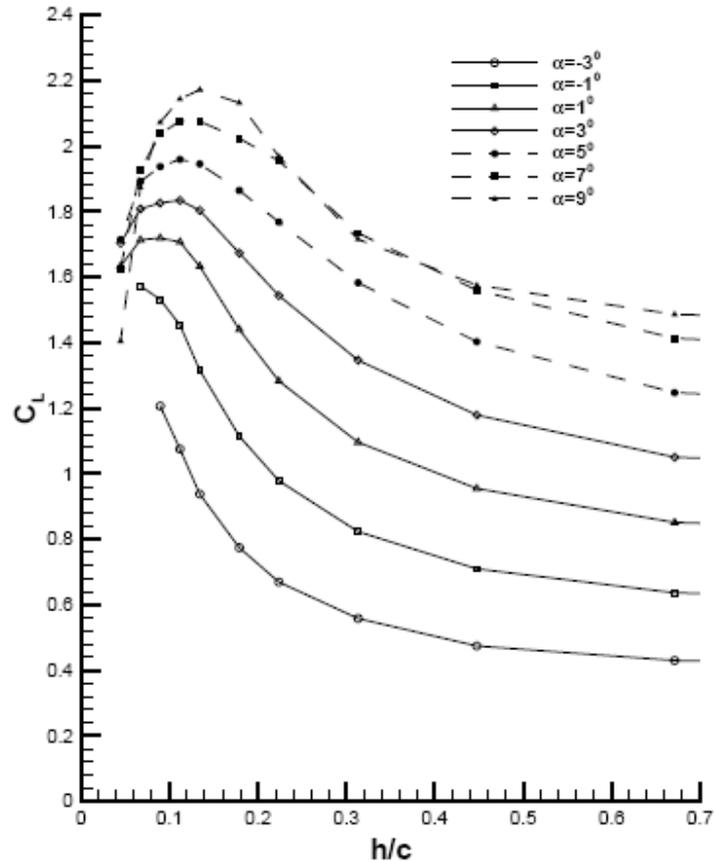


Figure 1.2 Downforce results obtained by Zerihan and Zhang (2000a)

A subsequent three dimensional study was also undertaken by Zerihan and Zhang (2000a) for a single element downforce producing wing with aspect ratio of 2.46. The aerofoil profile was provided by the Tyrrell formula one (F1) team which was designed by modifying the NASA LS(1)-0417 aerofoil previously used by Knowles *et al* (1994). Experiments were conducted at a Reynolds number of 2.0×10^6 and also utilised a moving ground. Lift and drag results were obtained for heights in the range of $0.045c$ to $1.007c$ and angles of attack between -10° and 25° . Zerihan and Zhang successfully reproduced the trends described by Ranzenbach and Barlow, and Knowles *et al.* previous investigations and additionally determined that as the angle of attack is increased, the height at which the “force reversal phenomenon” occurs also increases (Figure 1.2). Zerihan and Zhang found it more appropriate to rename this feature of a downforce producing wing as the “lift loss phenomenon”.

While being able to reproduce the “lift loss phenomenon” previously reported by Ranzenbach and Barlow, Zerihan and Zhang’s explanation for the cause of this phenomenon differed. They believed that the downforce loss is attributed to excessive levels of separation that occur over the bottom rear portion of the wing due to the adverse pressure gradient that the flow experiences in this region. Due to the increase in separation, the extent that the flow can be accelerated and the suction that can be generated beneath the wing, is reduced by further reductions in height. This explanation is consistent with how a conventional wing stalls when operating in freestream conditions and the angle of attack is increased and also agrees with the observations made by Knowles *et al.* (1994) linking the wing height to the stall angle. To verify this hypothesis, Zerihan and Zhang undertook surface flow visualisation at a constant angle of attack of 1° and demonstrated that the amount of separation that occurs over the bottom surface of the wing is affected by the ground clearance. These results were further supported by results obtained with pressure tappings at the wing’s centre chord. Zerihan and Zhang also took lift and drag measurements of a transition fixed case for the same wing at the same angle of attack. This reduced the maximum downforce coefficient that the wing could produce from 1.72 to 1.15 and moved the height at which it occurred at up from $0.08c$ to $0.14c$. This result further validated Zerihan and Zhang’s theory that the downforce loss phenomenon is due to separation and not the merging of the boundary layers as originally proposed by Ranzenbach and Barlow. The sensitivity of an aerofoil’s stall position due to the location of the boundary layer transition has previously been demonstrated by Smith (1975) for a lifting wing operating in free stream conditions.



Figure 1.3 On surface flow visualisation conducted by Zerihan and Zhang (2000a)

The surface flow visualisation also demonstrated that the separation experienced by the lower surface of the wing was fairly constant across the wing span with the exception of the wing tips. Close to the wing edges, or endplates, there was no separation evident and this was attributed to the tip vortex inducing a local downwash which reduced the incidence of the flow at the tip and subsequently allowed the boundary layer to remain attached (Figure 1.3).

In a separate study, Zerihan and Zhang (2000b) also investigated the effect that adding gurneys¹ have on a downforce producing wing in ground effect. This resulted in the wing downforce increasing and the downforce variations due to changes in height being more sensitive, particularly within the region of the “lift loss phenomenon”. Measurements made with pressure tappings indicate that the increase in downforce obtained by adding a gurney can be attributed to an increase in the suction generated on the bottom surface of the wing. An additional Laser Doppler Anemometry survey conducted by Zerihan and Zhang (2001a) also indicated that the height of the wake is increased by the addition of the gurney flap and that this is a contributing cause for the increase in drag obtained for the wing.

To investigate the cause of the “lift loss phenomenon” further, Zerihan and Zhang (2001b) also created a two-dimensional computational model representative of the central plane of their experimental model. Results obtained using the Spalart-Allmaras and $k-\omega$ standard turbulence models were compared to those obtained experimentally which included both on surface pressure measurements and off wake measurements using Laser Doppler Anemometry (LDA). From this comparison Zerihan and Zhang came to the conclusion that the Spalart-Allmaras model was the more effective as the $k-\omega$ turbulence model over predicted the velocity deficit and the thickness of the wake. They then used the computational model to demonstrate that the separation point on the bottom surface of the aerofoil moves further forward as the height is reduced further confirming their theory for cause of the “lift loss phenomenon” and, like Ranzenbach and Barlow, demonstrated that

¹ A small, thin extension mounted at the trailing edge of a wing typically, perpendicular to the high pressure surface, first tested for a motor sport application by Dan Gurney in 1971.

a computational model is capable of reproducing this feature of a downforce producing wing.

A three-dimensional experimental investigation was also undertaken by Zhang *et al.* (2002) to determine what role the tip vortex would have for the “lift loss phenomenon”. Using the same experimental apparatus used by the numerous previous investigations undertaken by Zerihan and Zhang, LDA measurements made on a plane located 0.2c downstream of the wing’s trailing edge indicated that the tip vortex formation varies depending on the rate of change of the wing’s total downforce. For the Tyrrell profiled wing at the reference angle of attack, reducing the height up to a value of 0.179c resulted in the downforce increasing at an increasing rate and the vortex strength also reacting in a similar manner. Further reductions in height resulted in increases in downforce at a reduced rate up to the height where the “lift loss phenomenon” was observed (0.134c). During this phase, the main wing vortex was observed to drastically increase in size and begin to breakdown. At the height at which the lift loss phenomenon occurs, the tip vortex was observed to have completely broken down or “burst” by the measurement plane. By comparing results obtained with pressure tappings located at the centre chord and at the tip, Zhang *et al.* determined that the rate of change of the wing’s total downforce closely resembles the variation of the contribution made by the tip of the wing and therefore came to the conclusion that the formation of the tip vortex contributed to the wing’s ability to generate downforce. This would suggest that the height at which the “lift loss phenomenon” would be expected to occur should also vary with the aspect ratio of the wing but this was not investigated.

Zhang *et al.* continued to explain that the tip vortex is susceptible to bursting as the core has a low stream wise velocity component due to the vortex being formed by a separation from the bottom edge of the endplate. A second vortex was also observed to form over the top edge of the endplate in a similar manner to the tip vortex (Figure 1.4), but this flow structure appears to have little influence on the performance of the wing.

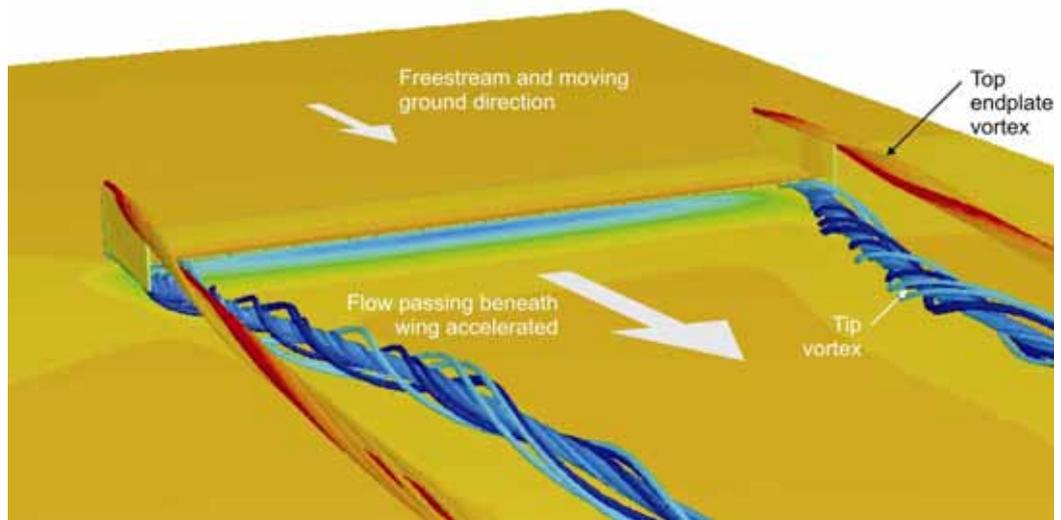


Figure 1.4 Schematic of the flow structures described by Zerihan *et al.* (2002) about an isolated downforce producing wing in ground effect

During the same study, Zhang *et al.* were able to demonstrate that the tip vortex could be translated inboard and further away from the ground relative to the endplate bottom edge with reductions in height as it travels downstream. Jasinski and Selig (1998) had also previously observed the same vortex position variation for increases in flap angle of attack. Given that both increasing the flap angle of attack and reducing the height of the wing resulted in an increase in the downforce produced by the wing, it is expected that any variation that causes an increase in downforce should result in a similar variation in the position of the wing tip vortex as it propagates downstream.

A number of additional experimental studies were also undertaken by Zhang and Zerihan (2002, 2003 and 2004) investigating the same features as those described above for a three dimensional two element wing. While these investigations demonstrated that a two element wing can produce increased levels of downforce the trends observed during the single element wing study were reproduced. Variations in the downforce produced by the wing with variations in height and the relationship with the separation experienced by the wing causing it to stall where once again repeated. Additionally, the wing tip vortex also reacted in a similar manner demonstrating that the tip vortex had burst when the height at which the “lift loss phenomenon” was achieved, but additional measurements taken on a plane closer to the trailing edge of the wing demonstrate that the tip vortex does form and only bursts further downstream of the wing.

More recently, a numerical study undertaken by Doig *et al.* (2007) discussed the compressibility effects related to a downforce producing wing using a two-dimensional model. The same aerofoil profile tested by Zerihan and Zhang (2000a) was used during this numerical investigation allowing a valid comparison to be made against the pressure measurements obtained during this experimental investigation. While most open wheel race cars are capable of reaching speeds in excess of 90ms^{-1} (approximately Mach 0.25 or 325km/h) generally it is considered that the flow about these vehicles is incompressible. Doig *et al.* investigated the validity of this assumption on the basis that the flow around the wings of these vehicles is accelerated to be greater than twice the freestream velocity particularly in the region between the wing's bottom surface and the ground. This was undertaken by obtaining compressible and incompressible computational results for a range of Mach numbers between 0.088 to 0.4 (30ms^{-1} to 136ms^{-1}) at heights of 0.067c, 0.134c, 0.313c and 1c. As Doig *et al.* had postulated, the influence of compressibility increased as the aerofoil approached the ground and the speed obtained between the aerofoil and ground increased. As a result, lift was underestimated by 16.6% and drag overestimated by 14% at a freestream velocity of mach 0.3 and at the lowest height tested by the incompressible results. This asymptotically reduced to a variation of less than 1% at the slowest speed tested of Mach 0.088 (or 30ms^{-1}) for the lowest height tested.

1.1.2. Flow features and aerodynamic performance characteristics of an isolated wheel

Aerodynamic investigations of an isolated wheel applicable to open wheel racing cars commenced with a three dimensional experimental study undertaken by Morelli (1969, 1970) to determine what effect adding fairings above the wheel would have on the lift and drag of the wheel. This investigation utilised an actual F1 wheel used during the 1960's by the Ferrari team (Dunlop racing 6.00 L-13) which had a diameter of 630mm and a width to diameter ratio of 0.34. The ground was represented by a stationary ground board which included a 15mm (0.024 diameters) recess for the wheel to rotate within such that its tangential velocity was always equal to the free stream velocity and never in contact with the ground board. One reason for using the recess was to more accurately portray the tyre deformation due to the static force applied on it by the weight of the vehicle when in contact with the ground, and also to allow for the wheel's lift and drag to be measured with a balance without being influenced by the loads applied to the wheel by any contact with

the stationary ground. Drag and lift coefficient results, calculated using the frontal area of the exposed wheel as a reference, were determined to be approximately 0.5 and -0.1 respectively indicating that the wheel produced downforce. These results had been obtained at a Reynolds number of 1.3×10^6 based on the wheel diameter, but additional measurements taken to determine the variation of the lift and drag coefficient within the Reynolds number range of 6.0×10^5 and 1.3×10^6 indicated that these values could vary by up to 50% and 20% respectively. The results investigating the effects of adding a fairing above the wheel are expected to be irrelevant to an investigation concerning an exposed wheel and are therefore not discussed here. Morelli also tested an additional configuration that added flat plates to the side of the wheel effectively reducing the volume of the wheel hubs exposed to the airflow around the wheel. The addition of the side walls was determined to reduce the drag of the wheel by 22% at a Reynolds number of 1.3×10^6 , but results presented by Morelli should be viewed with some caution given that he measured that the wheel produced downforce instead of the more widely reported lift.

Stapleford and Carr (1970) undertook an investigation to determine an appropriate method of modelling wheels for automobiles during wind tunnel tests. They manufactured a wind tunnel model that consisted of four wheels attached to a cylindrical body. The body was used to house a motor and drive system that rotated all four wheels and also an encoder that measured the speed of wheel rotation. This body also allowed for the wheels to be interchanged so that different width wheels could be tested and was used to mount the model to a force balance using a sting. To obtain the lift and drag of the wheels, the lift and drag of the body and sting was measured without the wheels and then deducted from the value obtained with the wheels. Wind tunnel tests were carried out in two different tunnels, one with a moving ground and one with a ground board to determine the effect the ground representation technique might have. A freestream velocity of 46mph (20.6ms^{-1}) was maintained throughout the tests as when the moving ground was used, the belt was observed to lift at greater velocities. During this study, Stapleford and Carr determined that rotating wheels not in contact with the ground would generate downforce consistent with Morelli's results and experimental setup. This was tested at heights of $0.0625d$, $0.125d$, $0.25d$, $0.5d$ as well as the wheels in contact with the ground. When the wheels were in contact with the ground a lift force was measured but this force was greater when the wheels were not spun. The drag of the wheels was found to increase by both rotation and proximity to the ground. Results comparing a moving ground to that of a stationary ground

indicated that it is more crucial to have the wheels in contact with the ground when using a moving ground in comparison to when using a stationary ground. Stapleford and Carr suggest that adequate lift and drag results can be obtained for automobile wheels in wind tunnel tests using stationary wheels not in contact with the ground, as long as the gap between the wheels and the ground is less than 5% of the wheel diameter and that the wheel is partially enclosed.

Fackrell *et al.* (1972, 1973 and 1975) undertook a number of experimental investigations that would become the benchmark for later research undertaken on exposed wheels. The lift and drag of the wheel was investigated using three different wheel widths ($A=0.46d$, $B=0.61d$ and $C=0.81d$) and two different wheel shoulder shapes (called 1 and 2) which all shared a common diameter of 416mm. Prior to commencing these studies, Fackrell *et al.* identified that in order to correctly model the flow structures experienced by an exposed racing car wheel, it is necessary to replicate the conditions experienced by these wheels. A typical racing car wheel operates within a Reynolds number range between 5×10^5 and 2.5×10^6 based on the wheel diameter which completely lies within the supercritical range for boundary layers forming over circular cylinders and therefore all results were obtained at a Reynolds number within this range (5.3×10^5) to ensure that this condition was maintained during the experiments. Unlike previous investigations which utilised force balances to measure the load on the wheel that prevented the wheel from being in contact with the ground representation technique, Fackrell *et al.* integrated the static pressure measurements obtained using tappings located on a horizontal profile as the wheel rotated. While this technique does not allow the viscous forces acting on the wheel to be measured, this was still considered to be a valid method to use given that the wheel can be considered to be a bluff body and that the viscous forces acting on a bluff body should be negligible. Additionally, the previous study conducted by Stapleford and Carr (1970) demonstrated that the forces experienced by the wheel are sensitive to the gap between the wheel and the ground. Therefore, an additional benefit of using this technique was that the wheel could always be in contact with the moving ground, replicating the conditions experienced in reality by a wheel belonging to a vehicle.

By integrating the pressure coefficients over the surface of the B2 wheel, Fackrell *et al.* were able to determine the lift and drag of a rotating wheel on a moving ground to be approximately 42% and 25% lower respectively than that experienced by a stationary

wheel in contact with a stationary ground. For the rotating wheel, a lift and drag coefficient of 0.44 and 0.76 respectively were obtained confirming that an isolated wheel experiences lift and not downforce as Morelli had previously reported. While the wheel rotation was also found to reduce the lift by Stapleford and Carr, the drag variation reported due to the wheel rotation differed between the results presented by Stapleford and Carr and Fackrell *et al.*

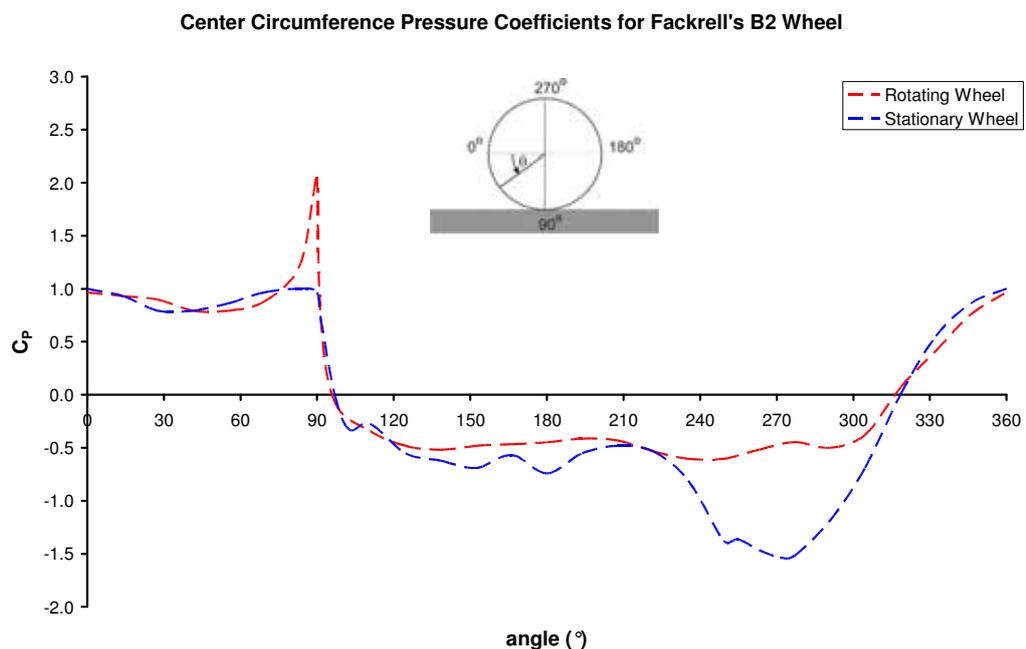


Figure 1.5 Static pressure measurements obtained about the central circumference of a stationary and rotating wheel (Fackrell *et al.* 1972)

Comparing the pressure distribution obtained over the central circumference of a rotating wheel with that of a stationary wheel, Fackrell *et al.* found key differences between these two configurations. As Figure 1.5 indicates, the wheel rotation moves the stagnation point located at the most upstream location on the wheel approximately 15° towards the front contact patch. A positive pressure gradient is then experienced up until the pressure rise obtained forward of the contact patch, which for the rotating wheel, values greater than two were obtained, while the stationary wheel experienced a peak value of one.

While it is uncommon for subsonic flows to experience stagnation pressures greater than one, Fackrell *et al.* explain that this is a result of viscous forces associated with the rotating

wheel and moving ground surfaces that are converging. The moving boundaries transmit energy into the flow through the shear stresses created by the boundary layers that form over the two converging surfaces. As a result they expected that an upstream moving jet, as depicted in Figure 1.6, will form between the two boundary layers. This increase in pressure achieved at the wheel centre by the wheel rotation is expected to cause the jetting action at either side of the front contact patch to increase and to encourage the formation of two stronger vortices from each side of the wheel. Unfortunately Fackrell *et al.* were not able to obtain qualitative results to prove that these flow structures existed.

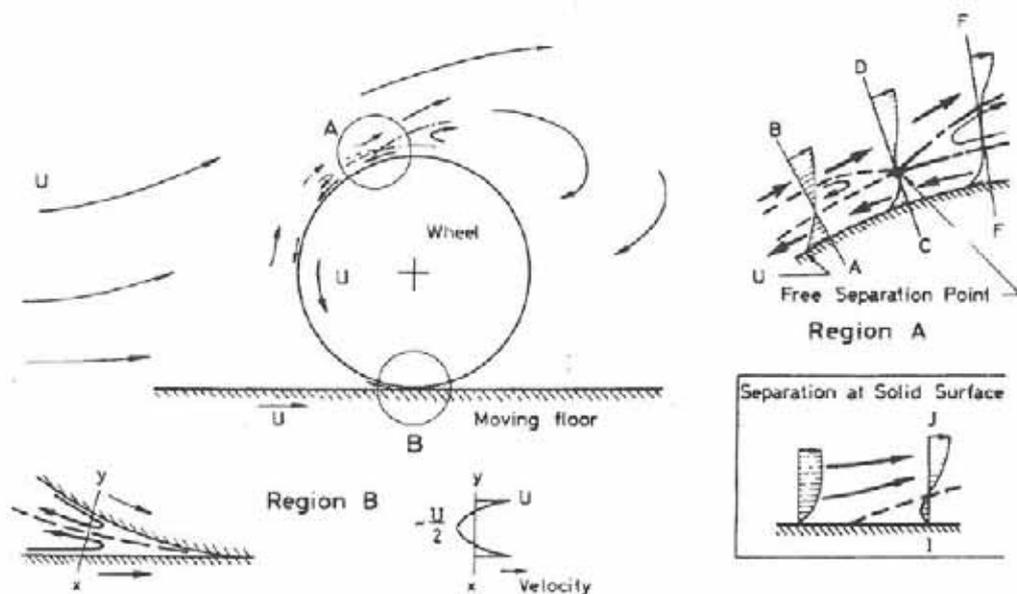


Figure 1.6 Expected flow structures as described by Fackrell (1975)

The central diameter pressure coefficient plot (Figure 1.5) also indicates that the stationary wheel develops a lower static pressure region over the top of the wheel in comparison to the rotating wheel. This provides some indication why the lift generated by the stationary wheel is more than that of a rotating wheel. Smoke visualisation conducted by Fackrell *et al.* indicated that boundary layer separation occurs forward of the top for the rotating wheel as opposed to rear of the top for the stationary wheel despite the favourable pressure gradient that exists in this region in both cases. Fackrell *et al.* believe that because the wheel surface is moving in the opposite direction to that of the flow passing over the wheel for the rotating case, the separation occurs above the surface of the wheel in a manner depicted by Figure 1.6. They also report that the wheel rotation carries a turbulent

boundary layer that is formed in the wake of the rotating wheel and for this reason higher turbulence values were measured in the boundary layer close to the stagnation point in comparison to that which was measured for the stationary wheel.

Variations in pressure measurements attributed to the wheel rotation were not only confined to the central circumference of the wheel, but also on the remaining wheel tread, shoulder and hubs indicating that the wake structures behind a rotating and stationary wheel should be significantly different. Total pressure measurements made in the wake of the two different configurations indicated that the wheel rotation caused the wake to be generally taller and narrower at the base. The variation in height obtained is consistent with the central circumference pressure coefficients indicating that the rotating wheel separated earlier, but the narrower lower wheel wake experienced by the rotating wheel seems to contradict the additional jetting action that was expected due to the higher pressure obtained forward of the contact patch. Fackrell *et al.* therefore postulated that this was because the boundary layer over the stationary ground forward of the stationary wheel would separate allowing two vortices to form forward of the wheel and therefore increase the width of the lower wheel wake, however, no evidence of such flow structures were obtained.

The experimental investigation also continued considering the effect that the width has only for rotating wheels. The A2 (narrower) wheel was reported to experience a 12% and 36% reduction in lift and drag coefficients respectively in comparison to the B2 wheel while C2 (wider) was reported to have 21% larger drag coefficient and a 2% smaller lift coefficient. It should be noted that Fackrell *et al.* raised some doubts regarding the rotating B2 wheel results but time constraints prevented him from repeating the results and this may explain why the lift coefficient did not vary in the same manner as the drag coefficient. When the same variation was repeated with alternative shoulder wheel, the lift and drag coefficients did increase with increases in wheel width as were expected. Regardless, it should be noted that the lift and drag coefficient presented by Fackrell *et al.* were calculated using the frontal area of each wheel and therefore despite the variation obtained for the coefficients, the magnitude of the lift and drag forces also increased with increases in the wheel width. The layout of the pressure tapings also allowed for the force contribution made by the hubs to be calculated and they were found to make a negligible

contribution to the lift and a less than 5% contribution to the drag which also seems to contradict the 22% drag reduction reported by Morelli when the side fairings were added.

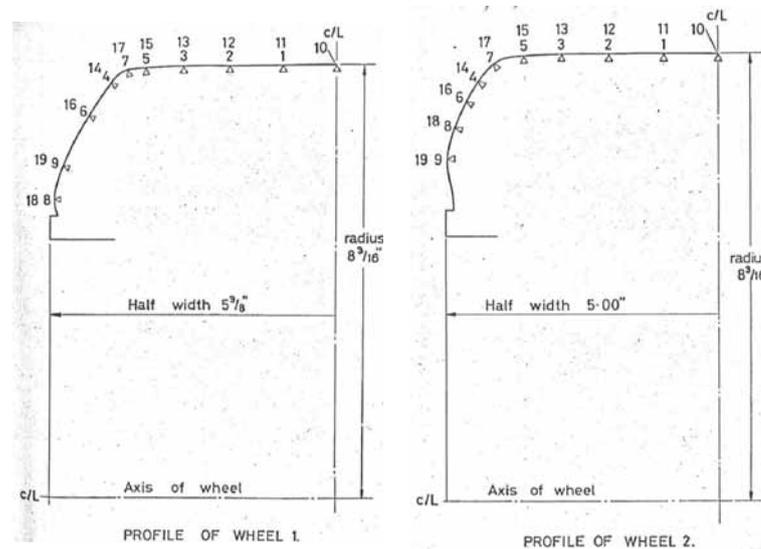


Figure 1.7 Wheel shoulder profiles tested by Fackrell et al. (1973)

As has already been mentioned, two alternative wheel shoulders were also investigated by Fackrell *et al.* and are shown in Figure 1.7. It should be noted that changing the wheel shoulder from option 2 to option 1 resulted in the wheel width also being reduced by approximately 5%, but the width of the wheel tread was maintained. Small variations in pressure were obtained over the central circumference of the wheel indicating that the wheel shoulder also has an effect on the wake and the flow over the wheel. Despite this, both wheel shoulders demonstrated similar trends as those discussed previously for a rotating wheel. It was found that based on the wheel's frontal area the B1 wheel had a 23% smaller drag coefficient and a 7% larger lift coefficient in comparison to the B2 wheel, while the shoulder comparison at the alternative wheel widths showed no variation in the lift or drag coefficients for the same change. This once again raised doubts about the rotating B2 wheel results that Fackrell *et al.* had presented.

While it has been demonstrated that the results obtained with a wheel in contact with the ground are significantly different to those obtained with a gap between the wheel and the ground, the cause for this variation was first investigated by Cogotti (1983). This was undertaken experimentally by varying the height while recording the static pressure along

the central circumference of the wheel and measuring the lift and drag of the wheel. The experimental apparatus used by Cogotti utilised a stationary floor and the contact condition for the rotating wheels was simulated by placing a piece of foam between the ground and the wheel in the shape of the wheels contact patch. The wheel, drive shafts and motor assembly were mounted on the force balance and exposed to the freestream which Cogotti acknowledges adversely influenced his measurements. Despite this, the static pressure measurements made by Cogotti indicated that when a gap was left between the wheel and the ground, the flow is accelerated between the surfaces of these two bodies causing the bottom of the wheel to generate suction. As the ground clearance is reduced, this effect was enhanced and subsequently the downforce of the wheel would increase until the gap was small enough to choke the flow beneath the wheel. From this point onwards, the spinning wheel would generate lift. Further reducing the gap would continue to increase the lift until no gap exists. This demonstrated how critical it was for the wheel to be in contact with the ground and also explains why previous investigations into rotating wheels which have used various heights between the wheel and the ground representation technique have provided conflicting results regarding the direction of the lift force experienced by a rotating wheel. The height at which the flow beneath the wheel is choked was not accurately indicated, but Cogotti's results suggest that this occurred at a height less than 1% of the wheel diameter which is significantly less than the original 5% recommendation made by Stapleford and Carr (1970). Therefore, based on the results that Cogotti and Fackrell *et al.* have presented, the only way of making certain that the flow features reproduced during an experiment are representative of that of a wheel belonging to an open wheeler racing car, is to have a rotating wheel in contact with a moving ground.

Using the same experimental apparatus as Fackrell *et al.*, Bearman *et al.* (1998) used a nine-hole pressure probe to conduct a wake survey behind both a rotating and stationary wheel. The experimental results were obtained at a Reynolds number of 5.5×10^5 . Contour plots presented of these results demonstrated that two main vortices are clearly defined in the wake structure in both the stationary and rotating wheel cases that travel downstream along the ground as Fackrell (1975) had originally postulated. The vortices produced by the stationary wheel were found to travel further downstream from the wheel, further apart closer to the ground and have a greater intensity than those produced by the rotating wheel. The rotating wheel also produced a narrower and taller wake.

Experimental studies have also been undertaken by Imaizumi and Yoshida (1991) to determine the effect that the wheel rotation has on the total vehicle lift and drag and how this varies depending on the type of vehicle that is being wind tunnel tested. Two different generic bodies had been considered which simulated an open wheel racing car and a sedan type car. The main variation between these two bodies being that the sedan model had the wheels enclosed within the bodywork of the vehicle while the open wheeler's wheels were completely exposed. Experiments were conducted with the wheel always in contact with the ground and when the wheels were rotated, a moving ground was also employed. Imaizumi and Yoshida concluded that the variation due to the rotation is similar but larger for the open wheel racing car body in comparison to the sedan type vehicle. This would suggest that previous studies conducted on rotating wheels within a wheel housing (Oswald and Brone, 1981 as well as Mercker *et al.* 1991 for example) would have little relevance to the flow around an isolated wheel.

A more recent study of an isolated wheel was undertaken by Hinson (1999) to commission a pressure measurement system that would allow the lift and drag of the wheel to be measured on behalf of the BAR F1 team similar to that used by Fackrell (1975). Unlike the previous investigations, Hinson's wheel geometry incorporated grooves in the wheel tread as used in F1 since 1997, instead of the customary slick tyre. This variation in geometry was expected to reduce the lift that the wheel would generate due to the wheel not being able to make a complete seal with the ground over the entire contact patch and therefore reduce the positive pressure experienced forward of the contact patch. Experiments were conducted for both a stationary and rotating configuration and were also undertaken within a range of Reynolds numbers between 3.5×10^5 and 9.6×10^5 . The drag was found to vary by approximately 10% within the range of Reynolds numbers tested such that the greatest drag was achieved at a value of 7.6×10^5 while the lift variation included no specific trend with Reynolds number but did not vary by more than 5%. As was expected, comparing the lift results obtained at a similar Reynolds number to that obtained by Fackrell (1975), Hinson's wheel geometry produced less lift. While it was expected that the grooves in the tread surface would contribute to this variation, it is unclear what other variations in the wheel geometry exist as a drawing of the wheel was not included in the report made for this investigation. This may be due to the wheel geometry being provided by the BAR F1 team and as a result being of a sensitive nature. Therefore, it would be difficult to use the data collated during this investigation for validation of a computational model and such an

exercise would have to be conducted using the data collated by Fackrell (1975). The measurements made by Hinson qualitatively agreed well with those made previously by Fackrell *et al.* and included the additional information of error bars to indicate the extent of the variation of the measurements obtained. Most significantly, these indicated that the variation of the peak pressure measured forward of the contact patch of a rotating wheel was in the order of approximately ± 1.5 .

The experimental apparatus commissioned by Hinson was also later used in a subsequent study by Whitbread (2000). Several improvements were made to the experimental apparatus prior to investigating the effect that yaw would have on a wheel to simulate a steered condition. It was determined that while the static pressures measured along the central circumference of the wheel did not vary in comparison to those measured for a wheel with no yaw, the drag of the wheel was found to increase by 20% approximately for steer angle of 10° . The drag variations obtained in yaw were also found to be dependant on the direction of the yaw angle and this was attributed to the asymmetric hubs and the sting that supported the wheel from only one side. No variations in lift were presented for this investigation.

As of 1998, investigations conducted concerning the flow around a wheel began to utilise computational models. The first to do so was Axon *et al.* and Skea *et al.* who both concurrently investigated the flow within a wheel well but also included in their studies investigations concerning an isolated wheel for comparison. In a series of studies undertaken by Axon (1998) and Axon *et al.* (1998, 1999) a steady state computational analysis of an exposed wheel was developed using a commercial CFD code (FLUENT). The wheel geometry utilised by Axon *et al.* shared a common wheel width to diameter ratio as that used by Fackrell (1975) but was simplified such that the wheel hubs were removed and the wheel shoulder was replaced with a constant radius. In this body of work, comparisons of static pressure plots obtained over different regions of the wheel tread and the 0.9 total head contour on x-planes located downstream of the wheel were compared to those obtained by Fackrell (1975) in order to validate the computational model. Both the $k-\epsilon$ standard and $k-\epsilon$ RNG turbulence models were tested with the $k-\epsilon$ RNG turbulence model found to be more suitable of the two. In agreement with the results of Fackrell, Axon's computational model also indicated that the rotating wheel produced C_p values greater than 2 in the region forward of the contact patch and confirm Fackrell's hypothesis that the

jetting action forward of the wheel assists the formation of the vortical structures emanating from either side of the wheel which were measured within the wheel wake by Bearman *et al* (1998).

Skea *et al.* (1998, 2000) also undertook a series of computational studies of an isolated wheel in order to investigate the flow associated with a wheel within a wheel well using a commercially available code (Star-CD 3.1). The isolated wheel used during these investigations was a further simplification of the wheel geometry that had no shoulder radius and a greater width to diameter ratio (0.5) in comparison to that used by Axon (1998) and Fackrell (1975). Skea *et al.* (1999) initial study validated the computational model by comparing pressure coefficients obtained over the central circumference of the wheel to those obtained by Fackrell for different turbulence models despite the significant variations in the geometry modelled and the Reynolds number (6.9×10^5) used for the computational model. Based on these comparisons, they concluded that the RNG $k-\epsilon$ turbulence model best reproduced the experimental results obtained by Fackrell (1975). Despite this being the best performing turbulence model, the peak pressure calculated forward of the wheel was significantly less than that measured by Fackrell (approximately 1.15). A subsequent study conducted by Skea *et al.* (2000) also included an experimental investigation where pressure measurements were obtained about the circumference of the wheel using an identical wheel geometry and Reynolds number as that used for the computational model. This provided better agreement with the computational model than the previous comparisons to Fackrell's experimental results provided, particularly the peak pressure value obtained forward of the contact patch, indicating that the geometry of the wheel could influence this flow feature, but this was not investigated further.

The first non-intrusive wake measurements of an isolated wheel were made by Knowles *et al.* (2002) using Laser Doppler Anemometry. Wind tunnel experiments were conducted with a wheel rotated by the contact made with a moving ground at a Reynolds number of 3.69×10^5 based on a wheel diameter of 0.263m. The aim of this study was to take measurements in the wake of an isolated wheel and also one with camber. In the process, it was attempted to confirm Cogotti's proposed wake structure containing six vortices. The Laser Doppler Anemometry results indicate that only four vortex structures could be found in the wake of the wheel, two counter rotating vortices forming at the base of the wheel wake adjacent to the floor as previously measured by Bearman *et al.* (1998), and two

additional counter rotating vortices at the top of the wheel wake. The measurements made here were the first to indicate the formation of the upper wheel vortices and additionally, Knowles *et al.* concluded that these smaller vortex structures had a larger vorticity value in comparison to the lower vortex structures.

Experimental results obtained by Fackrell (1975) were also used to validate a numerical investigation undertaken by Wray (2003). The numerical model was created using a commercial code (FLUENT 6.0) and used to study the changes in the flow when an isolated wheel is yawed. Wray (2003) investigated the flow around an exposed rotating wheel using a similar simplified geometry as that of Axon (1998) at a Reynolds number of 5.3×10^5 . Axon (1998) was also the first to highlight the difficulty associated with creating a mesh around the contact patch of the wheel. By meshing the acute junction between the ground and the wheel surfaces, a large number of skewed² control volumes were introduced and subsequently it was decided to avoid this problem by introducing a small step around the perimeter of the contact patch. Unfortunately the effect that this simplification might have on the flow structures was not investigated. Only the $k-\epsilon$ realizable turbulence model was tested by Axon (1998) during the validation of his computational model and in the process he demonstrated that the drag of the wheel is predicted within 2% of that measured by Fackrell (1975), but the lift was 70% less. The large variation in the lift could not be improved by Axon (1998) before he proceeded to investigate the flow structures associated with a rotating wheel. For a wheel with no yaw, the flow structures closely resembled that described by Knowles *et al* (2002) with both pairs of counter rotating vortices being displayed when streamlines were released within the wheel wake. In contradiction with the results presented by Whitbread (2000), Wray's computational model suggested that up to a yaw angle of 10° , the drag of the wheel does not vary significantly before increasing by 5% at the maximum yaw angle tested of 30° . Wray also indicated that the lift and side force increase almost linearly with increasing angle of attack such that at the maximum yaw angle tested, they increased to 0.26 and 0.28 respectively.

McManus and Zhang (2006) also conducted a computational analysis of an isolated wheel, but this computational study was unique in that it employed an unsteady approach.

² Control volumes or cells that have internal angles between edges that are close to zero.

The geometry used by McManus and Zhang was also the most accurate representation of Fackrell's (1975) wheel in comparison to the previous computational studies with both the wheel hubs and shoulders being identical to Fackrell's A2 wheel. McManus and Zhang computed both a stationary and rotating variations of this wheel and made comparisons to Fackrell's A2 rotating wheel and B2 stationary wheel given. While the B2 wheel is wider than the A2 wheel, this was necessary as Fackrell (1975) only collated stationary results with the B2 wheel. The comparisons were conducted using both the Spalart-Allmaras and $k-\varepsilon$ realizable turbulence models. Despite the two turbulence models obtaining very similar results in comparisons to Fackrell's central circumference static pressure measurements, McManus and Zhang concluded that the $k-\varepsilon$ realizable turbulence model was most suitable for calculating the flow over an isolated wheel. Compared to Fackrell's results, the lift and drag were underestimated by approximately 43% and 14% respectively.

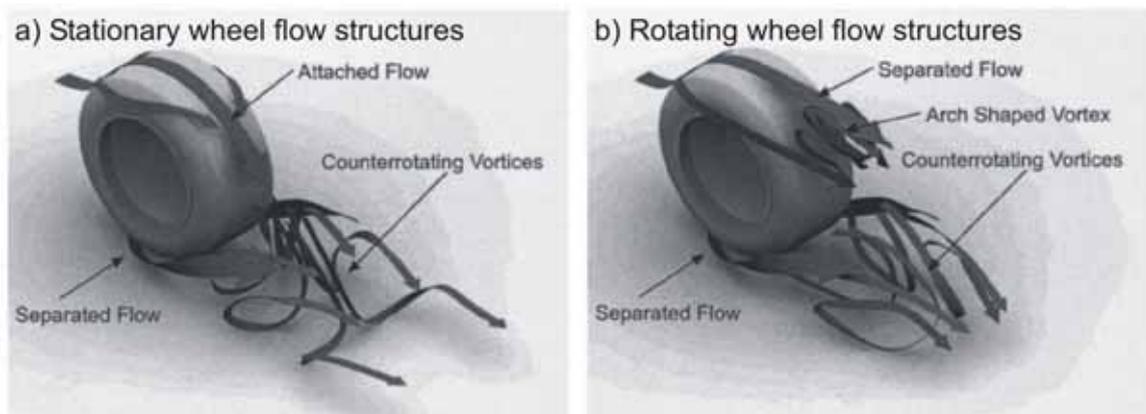


Figure 1.8 Schematic of the flow structures obtained by McManus and Zhang (2006)

Mean flow structures were also presented (Figure 1.8) demonstrating the upper and lower rotating vortices previously described by both Knowles *et al.* (2000) and Wray (2003) were reproduced by the computational model. As was indicated by Fackrell previously, the pair of counter rotating vortices located adjacent to the ground were found to form further apart than the same flow structures associated with the rotating wheel. While Fackrell hypothesised that this was due to the formation of two additional vortices forward of the wheel that generate due to boundary layer over the stationary floor separating, McManus and Zhang found no evidence of such a flow structure forward of the stationary wheel. They instead suggested that the cause for the wider wheel wake that is associated with a stationary wheel is due to the jetting action from either side of the front contact patch being

deflected by the oncoming flow by a smaller amount due to the formation of the boundary layer over the stationary ground. No attempt was made to prove this hypothesis. Other variations observed also included a reduction in strength and size of the upper vortices and the flow remaining attached over the top of the wheel tread which creates a downwash in the centre of the wheel wake for the stationary wheel.

1.1.3. Combined wing and wheel studies

The first specific investigation published concerning the interaction of a front wing and wheel was undertaken by Taylor (1992) using an experimental approach. A one-third scale model of a Jordan 192 F1 car, which did not include a rear wing, was supported by a central strut and used to mount a two element front wing from the nose of the model. While no drawings and dimensions are provided of the wing geometry, images of the experimental apparatus indicate that the wing spanned up to the inner face of the wheel such that none of the wing overlapped the wheel. A single front wheel was used on the model's left side which was held in position by a second strut allowing the drag forces of the wheel to be measured directly. No indication was given of the possible consequences of establishing such an asymmetric flow which included the wheel blockage only on one side of the wing and model. The wheel was rotated by the contact made with a moving ground which was operated at the same speed as the freestream velocity, of 27.5ms^{-1} , achieving a Reynolds number of 3.9×10^5 using the wheel diameter as a reference. The lift and drag of the wing was determined by integrating the results obtained from pressure tappings located along the chord at two different span positions on both elements of the wing.

Simultaneous results obtained from the pressure tappings located on the left and right sides of the wing were used to determine the effect that the presence of the wheel had on the front wing performance. These indicated that the presence of the wheel enhanced the downforce produced by the wing and this effect was further increased when the second elements angle of attack was increased. While Taylor indicated that this result was unexpected, it was hypothesised that the high pressure region forward of the wheel causes "more air to flow under the endplate, thus accelerating the flow beneath the wing". No attempt was made to prove this theory. Additionally, smoke flow visualisation

conducted indicated that the wing vortex travels downstream of the wing adjacent to the inner shoulder of the wheel.

While maintaining a constant wing span, several subtly different endplate geometries were tested during Taylor's investigation which showed little variation in the wings performance and influence due to the presence of the wheel. It should also be noted that while the wheel drag could be measured, no indication was given on the likely variation of this parameter due to the presence of the wing, the different endplates tested and the angle of attack of the wing's second element.

Agathangelou and Gascoyne (1998) also indicated that the performance of the front wing of an open wheel racing car is influenced by the interaction of the rotating wheel located immediately behind it. Due to the complexity of the three dimensional flow structures generated by both a wing and a wheel, Agathangelou and Gascoyne believe that experimental techniques alone would not be sufficient to obtain an understanding of the flow structures generated by such an interaction. They instead suggest that this type of study would also require the aid of computational models.

As Agathangelou and Gascoyne (1998) had suggested, Kellar *et al.* (1999, 2000) also undertook a number of studies that included both experimental and numerical investigations of a combined wing and wheel interaction. Like Taylor previously, Kellar *et al.* provided no detail information of the wing and wheel geometry used during these investigations, but from figures presented indicating the pressure coefficients over the surface of the wing and wheel, it appears that the span is such that approximately a quarter of the wheel is overlapped by the wing.

The experimental apparatus used by Kellar *et al.* was a 40% scale model which included the front right hand quarter of a generic early nineties F1 car mounted to a rigid board that represented the symmetry plane. A two element wing was used that also attached to the symmetry plane board which allowed for multiple endplates to be interchanged without altering the span of the wing. A single wheel was mounted using suspension members from the nose of the model in a similar manner to that found typically on an open wheel racing car which were strain gauged such that the drag force of the wheels could be measured directly. All drag measurements were conducted at a Reynolds number of

6.5×10^5 based on the wheel diameter. The ground was represented by a raised board with a cut out which the wheel dropped into allowing it to be driven by a mechanism below the board to achieve the required wheel rotation. It should be noted that such a ground representation technique has been demonstrated to adversely influence the results of investigations concerning both isolated downforce producing wings (Ranzenbach and Barlow, 1997) and isolated wheels (Stapleford and Carr, 1970) in ground effect.

The results of the experiments conducted by Kellar *et al.* (1999) indicated that the removal of the front wing caused the wheel drag to increase by between 10% and 20% depending on the endplate geometry used. Smoke flow visualisation was also conducted (albeit at a much lower Reynolds number of 2.5×10^4) which indicated that the addition of the wing forward of the wheel caused the wheel wake to become asymmetric. This was expected to be caused by the wing tip vortex which was determined to shed from the bottom edge of the endplate, travel across the wheel tread and along the inner face of the wheel. The reduced drag was hypothesised to be caused by the increase in vorticity created by the front wing, but contradictory to this assumption, it was determined that the endplate which produced the weakest vortex provided the wheel with the greatest drag reduction. Unfortunately, no images of the flow visualisation conducted had been presented with only a schematic of streamlines indicating the described flow structures about a different geometry to that used during the experiments.

The computational model used by Kellar *et al.* (1999) initially consisted of only the wing and wheel geometry which did not include the wheel rotation or the ground moving, but in a subsequent study (Kellar *et al.* 2000), the geometry modelled much more closely resembled that used during the experiments. Closure was provided by the $k-\varepsilon$ model which also allowed for compressibility. This required that the computational model be solved with a freestream value of Mach 0.3 in order to achieve convergence, which is greater than the highest speeds typically obtained by an open wheel racing car. Multiple calculations were done for each of the different endplate geometries tested of which no force results were presented or comparisons made to the experimental results. Only qualitative results of on surface pressure contours have been presented by Kellar *et al.* that indicate that the stagnation point at the most upstream location of the wheel can be influenced by the endplate geometry. Similarly, the streamlines released from beneath the shedding edge of

the endplate also indicate that the wing vortex can be altered by the geometry of the front wing endplate.

Two independent and solely computational investigations considering a combined wing and wheel geometry were carried out by Cumming (2002) and Mortel (2002). Unfortunately neither of these computational studies included any validation to demonstrate that the computational model was providing reliable results. Additionally, neither obtained results of the wing or the wheel in isolation in order to determine how the lift and drag of the wing and wheel varied in isolation and in unison. Instead they both solely focused on investigating the effect that changing specific geometric characteristics of the front wing would have on the lift and drag of each wing and the flow structures associated with these bodies. Images of the geometry used of the wing in both studies indicate that the span allowed approximately a quarter of the wheel to be overlapped by the wing. Consistent with the path that the wing vortex takes described by Kellar *et al.* both Cumming and Mortel show that the wing vortex passes inboard of the wheel. Variations in the wing sweep (Cumming, 2002) and the endplate geometry (Mortel, 2002) were shown to alter the path that the wing vortex would take.

An experimental investigation of an open wheeler's aerodynamics was conducted by Katz (2002) that included the effect that increasing the front wing downforce would have on the total vehicle downforce. Lift and drag measurements were taken of an entire quarter scale model and a separate balance installed in the model was able to record the lift and drag of the front wing. An elevated ground was used to represent the ground and tests were conducted at a Reynolds number of 4.5×10^6 using the entire model length as the reference length. This study demonstrated that increasing the front wing downforce by increasing the angle of attack of the second element of the front wing consistently moved the centre of pressure of the vehicle forward. This change had a non linear relationship on the total car's downforce with initial changes in the flap angle of attack increasing the total downforce before a peak was reached and subsequent increases in flap angle of attack resulted in reductions in the total downforce achieved. Katz and Garcia believed that this demonstrated that increasing the downforce of the front wing adversely affected the performance of the remaining aerodynamic components further downstream and for this reason the total downforce reduced after a particular flap angle.

An additional computational investigation considering the design of the front wing endplate, which also included the front wheels, has been conducted by Thisse (2004). The geometry used for this investigation included a single element, NACA4412 profile wing geometry to represent the front wing, and a finite width cylinder with constant radius shoulders to represent the wheels. Like Cumming (2002) and Mortel (2002), no validation was presented for the computational investigation undertaken by Thisse (2004). Results presented by Thisse (2004) indicate that the separation point from the wheel tread is behind, as opposed to forward, of the highest point of the wheel. This was previously demonstrated by Fackrell (1975) during an experimental investigation to be a key variation of a rotating and stationary isolated wheel which suggests that the wheel rotation is not being modelled correctly and raises doubts regarding the accuracy of the computational model used by Thisse (2004). This investigation did include results of the wing operating in isolation as well as in the presence of the wheel which suggest that the wing would generate 36% less downforce in the presence of the wheels. This was thought to be due to the exposure of the wing to the high pressure region formed forward of the wheel's contact patch.

While specific investigations that consider the interaction of a front wing and wheel of an open wheel racing car are rare, numerous recent publications have acknowledged that the close proximity of the wing to the wheel causes some aerodynamic interaction to occur and that research into this topic is limited. For example, Doddegowda *et al.* (2006) claims that when designing a front wing for an open wheel vehicle, the wing should avoid the high pressure regions formed forward of the wheel as this is expected to increase the adverse pressure gradient experienced by the wing. Similarly, Wordley and Saunders (2006) state that the performance of the wing is affected by the blockage created behind the wing by the presence of the wheel but fail to indicate whether or not this is a benefit or a hindrance. It has also been reported by Katz (2006) that investigations have been carried out demonstrating that increasing the span of a front wing such that it overlaps the wheel reduces the total vehicle's aerodynamic performance, but these investigations have not been published. Additionally, a recent review of aerodynamic studies relevant to open wheel racing cars has been presented by Zhang *et al.* (2006) which solely focuses on studies conducted on isolated wings, isolated wheels and diffusers mounted to Ahmed bodies. No mention is made of any investigations concerning wing and wheel interactions and it is suggested by Zhang *et al.* that greater research is required on this specific topic.

1.1.4. Summary of Previously Conducted Relevant Investigations

Investigations undertaken considering downforce producing wings in ground effect have determined that a downforce producing wing within one chord length of the ground can be considered to be in ground effect. As a result, the flow between the wing's bottom surface and the ground has been observed to be accelerated further than that which would have been achieved for the same wing in freestream. This allows the wing when in ground effect to produce increased levels of downforce and also causes the wing drag to increase. Reducing the height of the wing continues to increase the downforce produced by the wing up until a point where the flow on the bottom surface of the wing excessively separates and the wing stalls. This phenomenon has been referred to previously with numerous names, but from this point forward will be referred to as the "downforce loss phenomenon". Previous studies have indicated that the height at which the downforce loss phenomenon is experienced at is increased with increases in camber and the angle of attack of the wing. The ground representation technique has also had an influence on the height at which the downforce loss phenomenon occurs at, and therefore it is important that a moving ground be used for either experimental or numerical investigations concerning downforce producing wings in ground effect. Due to the large accelerations obtained by a downforce wing in ground effect it has been demonstrated that the effects of compressibility significant at freestream velocities of 90ms^{-1} but are negligible at speeds of approximately 30ms^{-1} .

The front wing used for most open wheel racing cars generates approximately 30% of the total vehicles downforce and utilize endplates at each tip of the wing. The endplates have been determined to increase the downforce generated by a wing by up to 30% and are vital in determining the three dimensional flow structures associated with the wing. Beneath the bottom edge of the endplate, the flow is drawn from outboard towards the low pressure region beneath the wing and in the process a vortex forms from the lower endplate edge that will be referred to as the "main wing vortex". A second weaker and less significant vortex forms from the upper edge of the endplate in a similar manner which will be referred to as the "secondary wing vortex". As the main wing vortex propagates downstream, it moves away from the ground and towards the symmetry plane. The strength of this vortex has also been shown to be influenced by the downforce loss phenomenon and reduce the separation experienced at the tip of the wing. This would

suggest that the downforce loss phenomenon would also be dependant on the span of the wing, but no investigation has been carried out to indicate this.

Previous studies conducted on isolated wheels have indicated that two high pressure regions exist forward of the wheel (Fackrell *et al.* 1972). The first is located near the most upstream location of the wheel while the second is located directly in front and in the center of the contact patch. The peak pressure coefficient obtained forward of the contact patch has been measured to be a value of approximately 2.3 while the stationary wheel obtained a more conventional stagnation pressure coefficient value of 1. The cause for the greater than unity stagnation value for a rotating wheel is due to the viscous forces associated with the wheel tread and ground surfaces that are converging and that feed energy into the flow through the shear stress in the boundary layers. In order to reproduce this feature in either a computational or experimental model, a moving ground is vital.

This high pressure region also causes a jetting action on either side of the front contact patch which is more pronounced when the wheel is rotating. As the ejected flow from the front contact patch passes the side of the wheel, the flow separates and a pair of counter rotating vortices are created adjacent to the floor in the wake of the wheel. During the course of this investigation, these vortices will be referred to as the “primary wheel vortices”. While the rotating wheel produces a greater jetting action forward of the wheel, counter intuitively, the width of the lower wheel wake is less for a rotating wheel than that for a stationary wheel. While hypotheses have been proposed by Fackrell (1975) and McManus and Zhang (2006) for why this is the case, neither have been proven and therefore this phenomenon requires greater investigation.

An additional difference between a rotating and stationary wheel also exist in the upper wheel wake region where the rotating and stationary wheels experience a separation point upstream and downstream of the highest point of the wheel tread respectively. Due to the more upstream separation point experienced by the rotating wheel, a pair of additional, counter rotating vortices form in the upper wheel wake region which are smaller in size and strength than that of the primary wheel vortices. From this point forward, these vortices will be referred to as the “secondary wheel vortices”. The earlier separation point and the formation of the secondary vortices cause the wheel wake for a rotating wheel to

be taller than that of a stationary wheel. Additionally, the lift and drag of a rotating wheel is less than that of the same wheel when stationary.

While numerous computational investigations have been conducted for an isolated wheel that use Fackrell's experimental results for validation, these typically have not accurately reproduced the geometry of the wheel tested by Fackrell. In order to simplify the mesh required for the computational model the wheel shoulder and the hubs have been removed or modified. Similarly, some previous investigations indicate that a step has been included surrounding the contact patch to avoid introducing highly skewed cells into the mesh due to the acute angle made between the ground and the tangent wheel surface. Unfortunately, it has never been investigated what the consequences of these geometric variations are on the aerodynamic characteristics of an exposed wheel. Additionally, previous investigations have mostly considered a single wheel in isolation while all open wheel racing cars utilise a pair of adjacent wheels. Despite this being the case, no experimental or numerical investigations have been carried out in order to determine what influence a second wheel placed alongside the initial wheel would have.

When considering the knowledge obtained through these isolated wing and wheel studies, a number of questions are raised on how it may be applied to an open wheel racing car as was originally intended. For example, most open wheel racing cars have the front wing extending across a portion or the entire front wheel. It would be expected then that the main wing vortex cannot continue to travel along the path described during the isolated wing studies due to the presence of the rotating wheel. If the presence of the wheel changes the formation of the front wing vortex, then it would also be expected that front wing downforce will also be affected. If the wing vortices travel downstream past the wheel, they should also have some effect on the aerodynamic characteristics of the wheel since it is well documented that vortex structures can prevent or reduce the likelihood of separation occurring.

Understanding the flow downstream of the wing and wheel is also critical to optimizing the aerodynamic design of the rear of the vehicle. Other components such as barge boards, the rear wing, the floor and the diffuser all operate in the wake of the front wing and wheel (Zhang *et al*, 2006). Therefore having a solid understanding of the path that the wing and wheel flow structures take and how they vary for certain wing and wheel parameters is

critical to obtaining the greatest level of downforce possible in an efficient manner. Such a study is expected to be too complicated to undertake using solely experimental techniques and therefore, it has been suggested that computational models will be required (Agathangelou and Gascoyne, 1998).

Previous studies that have investigated wing and wheel interactions have neglected to vary key wing and wheel parameters and therefore these investigations are likely to be relevant only to specific vehicles (Cumming, 2002 and Mortel, 2003). Additionally, the computational models used during these studies have not been validated, raising doubts about the results presented. Despite this, they have indicated that the downforce generated by the wing may be reduced by approximately 36% due to the presence of the wheels (Thisse, 2004). Recently it has been acknowledged that further work is required to obtain a better understanding of the interaction of the front wing and wheel (Zhang *et al*, 2006 and Katz, 2006).

1.2. Thesis Aim and Outline

This study is intended to determine how the forces experienced by a wing and wheel individually vary in isolation relative to the same wing and wheel working in unison. This is expected to occur due to changes in the flow structures associated with these two bodies and therefore the cause of the change of the lift and drag will also be investigated. In order to achieve this, a computational model will be used that will allow the wing span, angle of attack and height to be adjusted as well as wheel width and track. The geometry that will be used to undertake this investigation is shown in Figure 1.9 and will consist of a single element wing utilizing an inverted NACA4412 profile and a rectangular endplate with a rounded leading edge and tapered trailing edge. The wheel geometry consist of a finite width cylinder with radiused shoulders that has a diameter approximately 1.17 times the chord length.

The computational investigation will be conducted at full scale to best replicate the flow field expected to be experienced by a wing and wheel of an open wheel racing car and therefore a wing chord and wheel diameter of 562.5mm and 660mm respectively will be used similar to that currently used in F1 (FIA, 2009). While greater speeds can be obtained by these vehicles a freestream velocity of 33.3ms^{-1} (or 120km/h) was chosen as this is a

typical speed at which an open wheel racing car would negotiate a corner at and it is during a cornering phase that the downforce generated by the wing is most required (Agathangelou and Gascoyne, 1998).

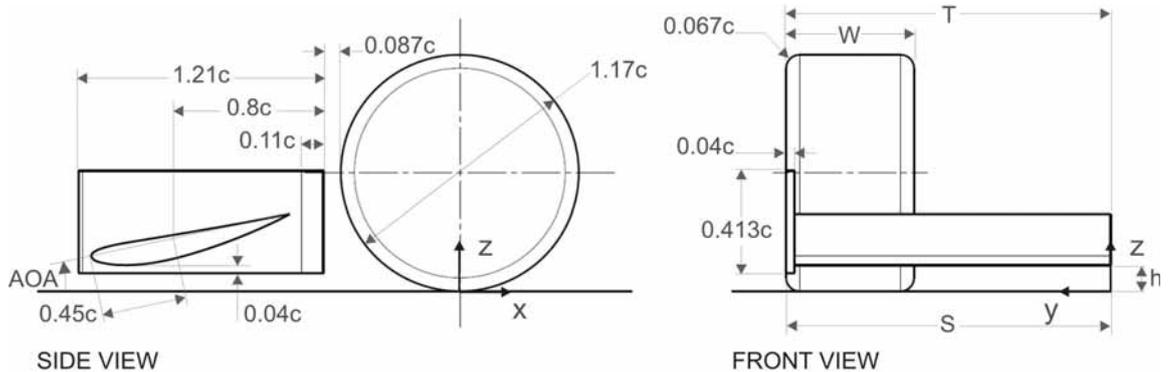


Figure 1.9 Conceptual wing and wheel geometry that will be used during this investigation

Prior to undertaking any computational investigations, it was required that the computational model be validated. In order to achieve this, it was necessary to collate experimental data of a combined wing and wheel. Given the lack of experimental data that exists for a combined wing and wheel in the current literature, this was undertaken during the course of this investigation. The open circuit wind tunnel, moving ground and Laser Doppler Anemometer (LDA) used to take the required measurements are outlined in Chapter Two as well as the expected errors associated with these measurements.

Chapter Three includes a description of the governing equations required to be solved in order to predict the flow associated with a combined wing and wheel using a computational model. A short discussion of the turbulence models used previously in computational investigations for either an isolated wing or wheel investigation will also be outlined as well as the solution procedure required to solve the computational model. A verification study has also been undertaken to ensure that the errors associated with the computational model are minimised and understood which are also presented in this chapter.

The validation procedure undertaken is outlined in Chapter Four with the intention of demonstrating that the computational model can reproduce the trends obtained

experimentally as recommended by the AIAA guide to validation and verification (1998). Initially, the previously used turbulence models described in Chapter Three will be compared to the LDA results obtained by the author in order to choose the most suitable turbulence model. The computational model will then be used to demonstrate that the lift and drag trends measured by Fackrell and Zerihan can be reproduced for an isolated wheel and wing respectively. Additionally, comparisons will be made to McManus's computational investigation to demonstrate that the flow structures predicted by an unsteady computational model can also be predicted by a steady state computational model. Finally, computational results obtained using four different combined wing and wheel geometries will be used to demonstrate that the computational model predicts similar variations in the flow structures as those measured experimentally by the author using the LDA system.

Prior to investigating the interaction of a combined wing and wheel, a number of investigations will be undertaken for an isolated wing or isolated wheel in Chapter Five that should assist with the combined wing and wheel investigation. For an isolated wheel, an explanation will be provided for the wake variations obtained between a stationary and rotating wheel including why the lower wheel wake width is greater for a stationary wheel. Additionally, the consequence of the contact patch simplification will be investigated prior to determining what effect removing the wheel hubs and simplifying the wheel shoulder has. The isolated wheel investigations will conclude by determining the effect of a second wheel placed alongside an initial wheel. For an isolated wing, an investigation will be undertaken showing that the wing's span is also a parameter that can alter the height at which the downforce loss phenomenon occurs at.

The combined wing and wheel investigations are outlined in Chapter Six. These commence with a description outlining the three different wing and wheel interactions that are defined by the path that the primary and secondary wheel vortices take about the wheel. Then the angle of attack is varied at two different spans which is followed by an investigation where additional increments of span are included. These two investigations demonstrate that different combinations of span and angle of attack can achieve any of the three interactions previously defined. The height of the wing is then altered to determine how the downforce loss phenomenon is affected by the presence of the wheel. This

chapter concludes by also considering how changes to the wheel width and track can also alter the wing and wheel interaction.

The thesis concludes with a summary of the findings obtained during the above investigations and a recommendation for future work for this topic in Chapter Seven.

Chapter 2: Experimental Apparatus

As noted in Chapter One, qualitative experimental results are not available in the literature for an interacting wing and wheel. Therefore, a series of experiments were undertaken in order to obtain data to validate a numerical model of these two bodies working in unison. This chapter describes the experimental setup used to achieve this.

2.1. Wind tunnel and Moving Ground

All experimental results for this investigation were obtained using the 225x340mm open circuit wind tunnel at the University of New South Wales (UNSW), which also incorporates a moving ground. A brief description of this experimental apparatus is given here, however, for a full discussion of the design, construction and commissioning of the wind tunnel and moving ground the reader is referred to Diasinos and Beves (2009).

2.1.1. Description of UNSW 225x340mm open circuit wind tunnel

As the name suggests, the inlet of the test section for the wind tunnel used during this investigation has a height and width of 225mm and 340mm respectively. The test section is 1500mm long (Figure 2.1) and expands with an angle of 0.15° to ensure that as the boundary layer grows over the test section walls, the effective test section size remains constant throughout its length (Barlow *et al.* 1999). When facing downstream, the left hand side test section wall was manufactured from a single sheet of polished acrylic so that unrestricted access could be provided to the LDA system, while the right test section wall was used to mount the wind tunnel model of the wing.

Upstream of the test section (Figure 2.1), the flow enters the wind tunnel through a bell mouth before passing through three turbulence screens each separated by a distance of 150mm. The diameter and spacing of the wire was selected such that the screen Reynolds number based on the wire diameter is no less than 30 and greater than 60. Assuming an inlet velocity of 1.3ms^{-1} the turbulence screens required a wire diameter of 0.3mm to allow any large scale eddies entering the bell mouth to be broken down and reduced in size

(Schubauer *et al.* 1950). After passing through the turbulence screens, the flow is accelerated in the contraction, with a ratio of 7.8:1, prior to entering the test section, allowing any small scale eddies that remain after the turbulence screens to be further reduced in size or eliminated prior to entering the test section (Motson and Archer, 1969).

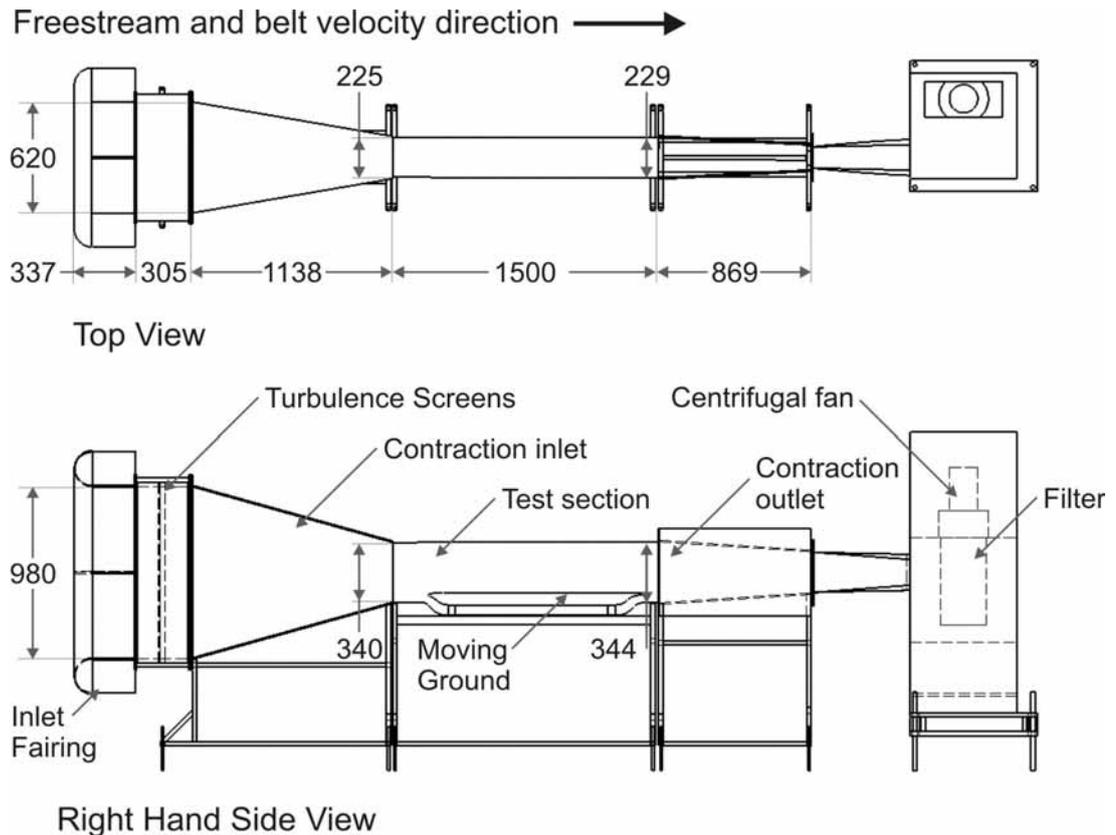


Figure 2.1 Schematic of the UNSW 225x340mm open circuit wind tunnel and moving ground

Due to the limitations of the wind tunnel used, all experiments were conducted at a freestream velocity value of 10ms^{-1} at which a nominal freestream turbulence intensity value of 0.15% was measured at the inlet of the test section. The reference freestream velocity was measured at a point 200mm downstream of the test section inlet and 50mm below the wind tunnel ceiling by a pitot static tube (KIMO TPL-3-100-T) that was mounted in the centre of the test section ceiling in conjunction with a digital micromanometer (Furness FCO510). The measured freestream value was displayed in the wind tunnel control software that also allowed the free stream velocity to be controlled with a resolution of 0.1ms^{-1} . The wind tunnel control software was specifically written for this wind tunnel using LAB view and allowed the freestream velocity to be maintained at a constant speed

within an accuracy of $\pm 0.05 \text{ ms}^{-1}$ of the desired value, using feedback from the measurements made with the pitot static tube.

The wind tunnel was driven by a TORIT VS1500 vacuum chamber that included a centrifugal fan, a 5Hp AC electric motor, variable frequency motor controller and air filter. By using this arrangement, the air filter allowed the LDA seeding to be captured before the flow exited the wind tunnel. As the amount of seeding collected by the air filter increased, the maximum freestream velocity that could be obtained in the tunnel was reduced. While a clean air filter would allow a maximum freestream velocity of 13ms^{-1} to be achieved in the test section, it was decided to conduct all experiments with a freestream velocity of 10ms^{-1} to ensure that all results were obtained at a constant freestream velocity independent of the age of the filter.

2.1.2. Description of the moving ground

Numerous techniques have previously been used to represent the ground during wind tunnel investigations of automotive related bodies in ground effect. These techniques attempt to mimic a boundary moving with the same velocity as the freestream velocity relative to the vehicle being wind tunnel tested. These techniques have included; a stationary ground (Beauvis 1968, Bearman *et al.* 1988 and Kim and Geropp 1988), boundary layer suction (Carr 1998 and Hucho and Sovran 1993), tangential blowing (Wickern and Dietz 2003) and the symmetry method (Sardou, 1986). Previous investigations for an isolated wing and isolated wheel have indicated wind tunnel testing of either body in ground effect requires the use of a moving ground in order to realistically reproduce the flow conditions experienced by these bodies (Ranzenbach and Barlow, 1995 and Cogotti, 1983). This was also expected to be the case for a combined wing and wheel and therefore a moving ground (Figure 2.2) was designed and constructed during the course of this research project to use during all the experiments undertaken.

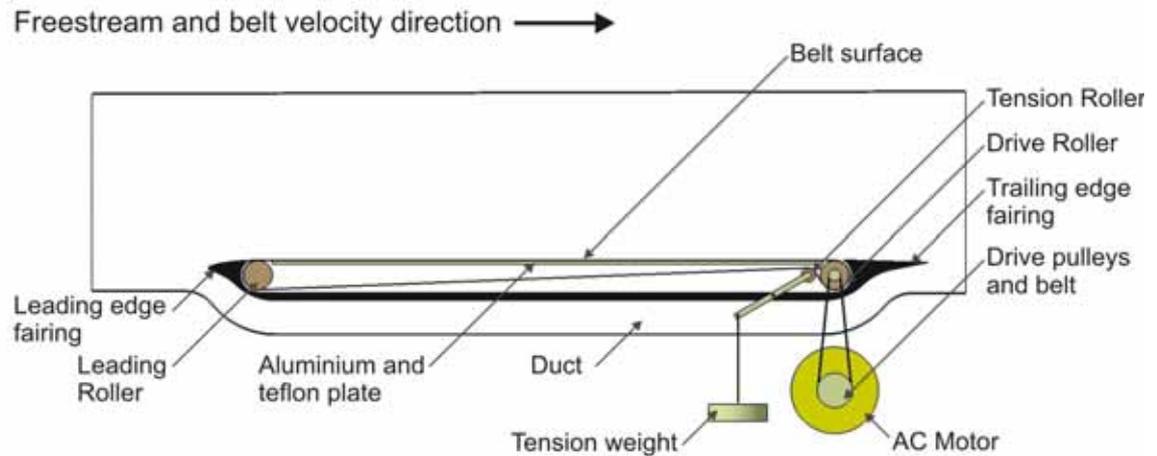


Figure 2.2 Schematic of the moving ground used in the UNSW 225x340mm wind tunnel

The belt of the moving ground, which has a smooth surface, has a width of 210mm (93% of the wind tunnel width) and a length of 990mm. The downstream roller was used to drive the belt by a CMG Electric, 3 phase, 415V, 1.1kW electric motor, via a timing belt, with power supplied by a Danfoss VLT6000 HVAC variable frequency speed controller. The speed of the moving ground was measured using an encoder disc (US Digital 800.736.0194) mounted on the drive roller, and optical encoder (US Digital HEDS-9000) which was displayed in the wind tunnel control software. This software was also used to set the velocity of the belt, in 0.1ms^{-1} increments, which could be independently controlled from the wind tunnel freestream velocity if desired. Measurements made with the encoder indicated that at no time did the velocity of the moving ground vary from the required velocity by more than a value of $\pm 0.01\text{ms}^{-1}$.

Tracking of the belt was provided by the most upstream roller which was mounted in a pair of spherical ball bearings that allowed the angle of the axis of the upstream roller relative to the drive roller to be adjusted. The mechanism that controlled the tracking was accessible externally of the test section and therefore adjustments could be made while the belt was being operated and the wind tunnel model installed. This was achieved by rotating the adjustment bolt that acted on a chamfered slide causing the left hand bearing housing to move forward or rearward (Figure 2.3). Once the belt was positioned at the

centre of the rollers, a second bolt was used to lock the tracking adjustment and no additional adjustments were then required.

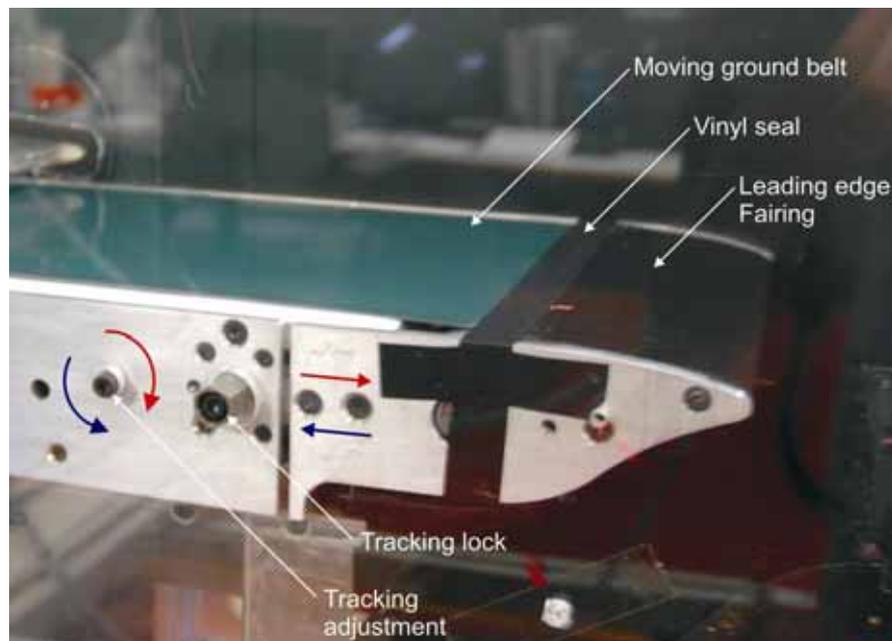


Figure 2.3 Mechanisms used to control the tracking and the vinyl strip used to seal the leading edge fairing to the belt surface

To ensure that the moving ground belt did not slip over the drive roller, tension was applied to the belt via a third roller located between the duct and the structure of the moving ground. The third roller was mounted on two arms that would rotate such that the tension could be applied to the belt by 40N of weight suspended below the wind tunnel test section (Figure 2.2). The tension applied to the belt also ensured that at all times during the experiments the belt was in contact with a flat horizontal surface parallel to the freestream velocity and would not rise due to the low pressure generated between the wind tunnel models and the belt surface. To reduce the friction and the subsequent heat that may occur with such an arrangement, the flat surface that the belt ran over was provided by a 1mm thick Teflon sheet mounted on a machined 6mm aluminium plate.

Ahead of the upstream roller and behind the downstream roller, leading and trailing edge fairings were mounted and connected such that a duct was created beneath the moving ground structure (Figure 2.2). This was to prevent the boundary layer that formed over the bottom surface of the wind tunnel's test section and contraction inlet from passing over the

moving ground's belt surface. The leading edge fairing was designed to provide a positive pressure gradient that minimised the boundary layer growth over this component and allowed a constant velocity profile to form over the surface of the moving ground's belt (Diasinos *et al.* 2005a). Sealing the gap between the belt surface and the front fairing has also been demonstrated to be vital for ensuring that a constant velocity profile is obtained (Diasinos *et al.* 2005a). The required seal was achieved by placing a 0.2mm thick strip of vinyl that spanned across the rear of the leading edge fairing and attached at either side of the moving ground structure (Figure 2.3).

Prior to conducting any experimental results, the LDA system (refer to Section 2.3) was used to measure the velocity profile over the belt for an empty test section. This measurement indicated that at heights above 2mm from the belt surface, the velocity profile did not vary by more than 0.5% of the freestream velocity value (Figure 2.4).

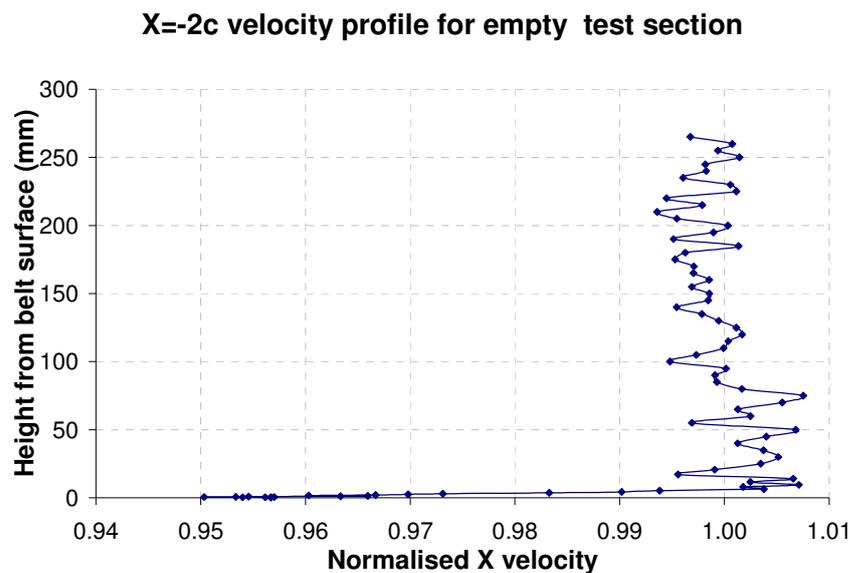


Figure 2.4 Velocity profile of an empty test section 150mm upstream of wheel centre

2.2. Wind Tunnel Models

The experimental results will be used to validate a numerical model and therefore the wind tunnel models (Figure 2.5) were designed to be an accurate representation of the intended simulated geometry shown in Figure 1.9. Additionally, it was necessary that the wind

tunnel models allowed adequate adjustability such that the wing span, angle of attack and height can be varied as well as the wheel width and track. Detailed drawings of the components making up this system can be found in Appendix A.

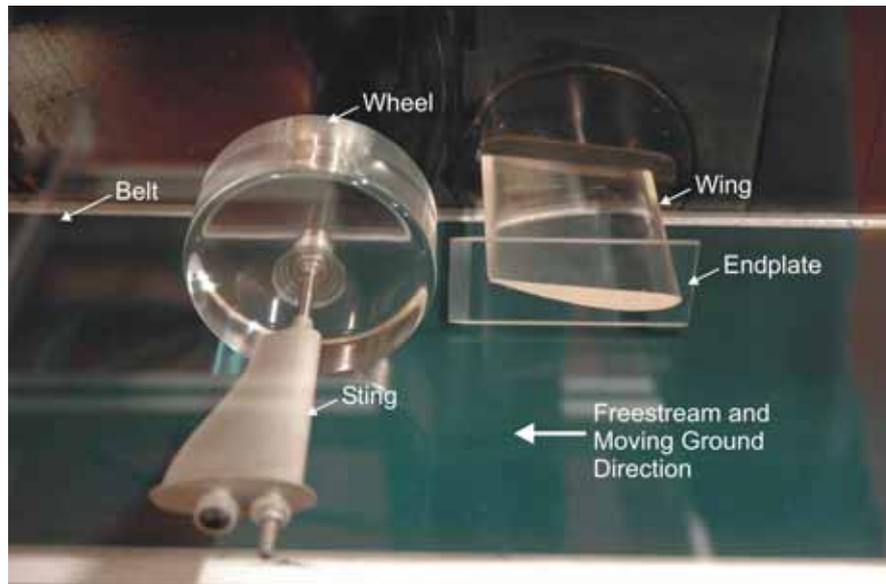


Figure 2.5 Wind tunnel models used during experimental investigations

When determining the appropriate scale for the wind tunnel models, it was necessary to obtain a compromise of the Reynolds number that could be achieved with the blockage that would be created in the test section. The best compromise was believed to have been achieved with wind tunnel models with a scale of approximately 1:7.5 which required a wing chord and wheel diameter of 75mm and 88mm respectively. The experiments would therefore be conducted at a Reynolds number of 5.11×10^4 using the wing chord as the reference length (or 5.98×10^4 based on the wheel diameter of 88mm). Because at this Reynolds number it is expected that the boundary layer over the models will be mostly laminar, the validation process will also include comparisons to previously published experimental results of an isolated wing or isolated wheel at higher Reynolds numbers that should be a better representation of the boundary layer being modelled by the computational model. Despite this, low Reynolds number experiments have been demonstrated in an unpublished investigation undertaken by a constructor of an open wheel racing car to not significantly alter the formation of the flow structures associated with such a vehicle. The large scale generally used by open wheel racing car constructors is purely required to increase the level of detail modelled experimentally (Gillan, 2009).

With this scale wind tunnel models, the maximum test section blockage was calculated to be approximately 9.5%. At this level, it is envisaged that blockage effects will cause a certain degree of constraint on the flow field such as, reduced vortex expansion and artificial delay of flow separation (Stapleford and Carr, 1986). It should be noted that the intention of collating these experimental results is solely to provide data for correlation, and as long as the computational model also replicates these experimental conditions, this is not expected to adversely affect the comparison between the experimental and numerical results.

2.2.1. Wing and wing support system

As mentioned previously, the left hand side of the test section comprised a single Perspex sheet so that the LDA system had unrestricted access to the wind tunnel test section. This required the wind tunnel model of the wing to be cantilevered from the right wall of the test section; the wing was supported by upper and lower clamps that were machined to have the inverse profile of the wing section. Sliding the wing section through the clamps allowed the portion of the wing located within the test section to be varied such that the desired wing span could be achieved.

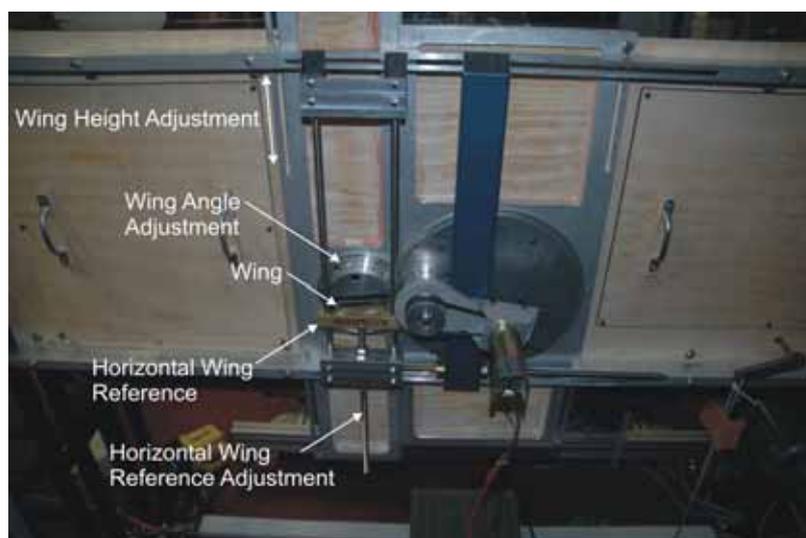


Figure 2.6 Wing support system used allowing span, height and angle of attack to be varied

The clamps supporting the wing were housed in a rotating device that allowed the angle of attack of the wing to be varied in increments of 1° , about an axis located 565mm (7.53c) downstream of the test section inlet and also 365mm (4.87c) downstream of the leading edge of the moving ground. The rotatable component was located within a vertical slide that allowed the height of the wing to be varied (Figure 2.5). The span and the height of the wing could be set within a tolerance of 0.1mm while the angle of attack could be set within an accuracy of 0.01° . The wing section was machined with a length of 300mm allowing this wing section to achieve all the required spans for this investigation and also to span the entire test section for a series of related two dimensional studies (Diasinos *et al.* 2005b and 2006). In all configurations, a portion of the wing would extend past the clamps allowing the height of the wing to be measured externally of the wind tunnel using a series of slides (Figure 2.6). The wing section was manufactured by a numerically controlled mill from acrylic and then polished to have a smooth and transparent finish.

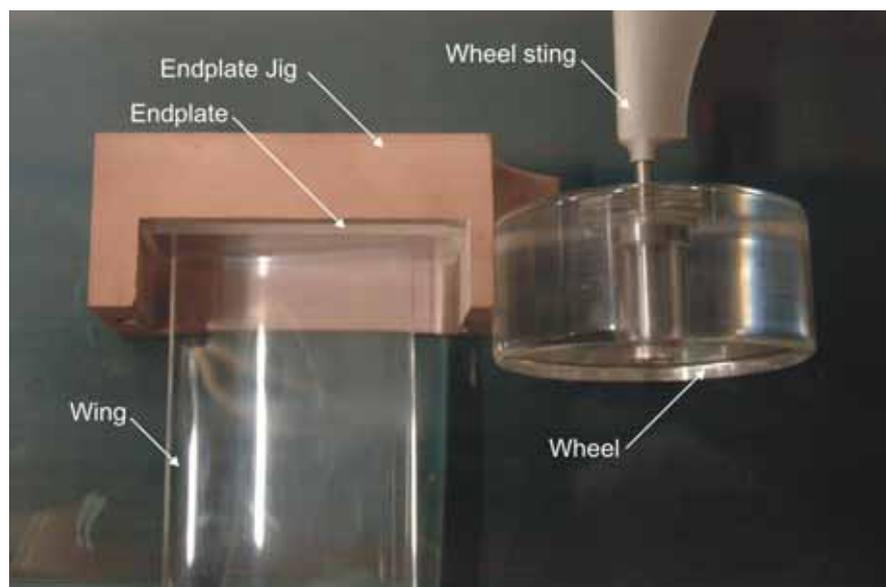


Figure 2.7 Jig used to ensure the correct positioning of the endplate

The wing geometry that is to be investigated also required that an endplate be manufactured. This was also machined from acrylic and polished to have a smooth and transparent surface. This was mounted at the wing tip using an adhesive with the aid of a jig to ensure that the relative position of the endplate to the wing and the wheel was always constant regardless of the wing angle of attack, span or height being tested (Figure 2.7).

2.2.2. Wheel and wheel sting

Two different wheel geometries were manufactured that have a wheel width of $0.462d$ (40.7mm) and $0.538d$ (47.3mm). Both were machined from a solid piece of acrylic and polished to have a smooth and transparent surface finish. Each wheel was mounted to a shaft using a pair of grooved ball bearings that allowed the wheel to spin freely by the contact made with the belt (Figure 2.8). Measurements taken using an encoder indicated that the wheel was rotating with an angular velocity of 227.3rads^{-1} such that the tangential velocity of the wheel is equal to the freestream velocity and that a zero slip condition is achieved with the moving belt surface. During the experiments, the wheel was supported by a faired sting that was attached to the left test section wall of the wind tunnel (Figure 2.5). The shaft that the wheel was mounted on could be interchanged with the wheel sting so that the two wheels could be independently used with the same wheel sting. Each wheel was mounted on its own shaft that extended past the test section wall and included a threaded section such that the horizontal position could be adjusted externally of the wind tunnel to obtain the required wheel track value and then locked once the desired wheel track position was obtained.

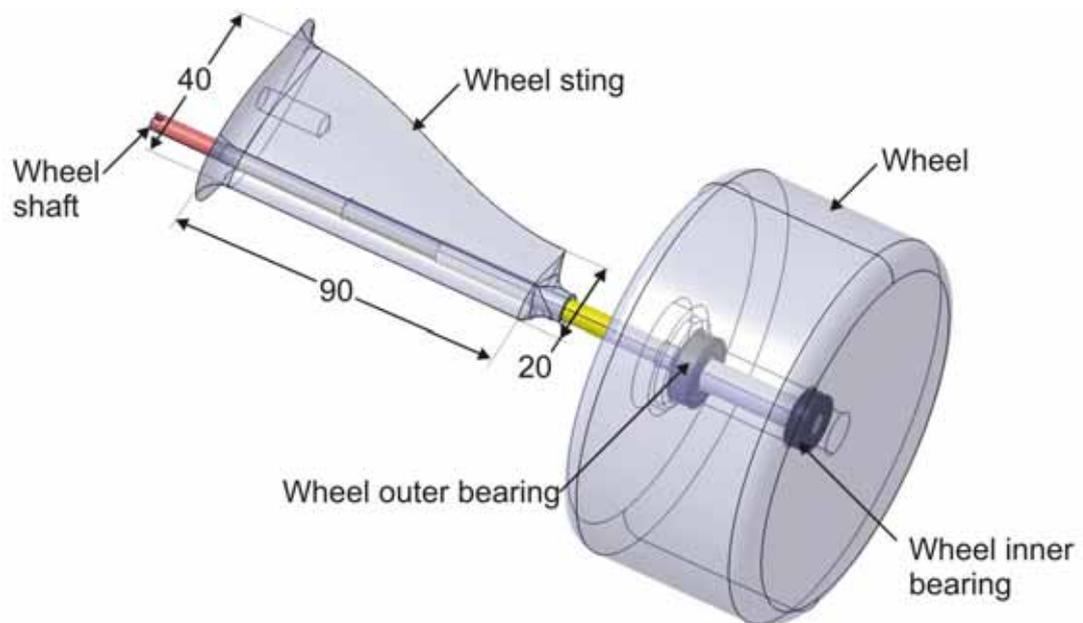


Figure 2.8 Schematic of wheel and wheel sting assembly

To assist with minimising the impact that the sting would have on the experimental results, the sting was profiled using a NACA 6 aerofoil and the chord length was reduced towards the sting's tip (Figure 2.8). It was mounted from the left wall of the test section as it was expected that mounting the sting from the right hand side (or directly behind the wing) would adversely affect the wake structure produced by the wing and as a result provide an unrealistic interaction with the wheel wake. The sting was machined from aluminium using a numerically controlled mill and incorporated a smooth surface finish.

In order to determine what influence the selected location and geometry of the wheel sting has on the flow structures associated with a combined wing and wheel, the numerical model that is intended to be used for comparison with the LDA results was used to determine what variations would occur if the wheel sting was removed. The comparisons have been conducted on four different planes located $x/c=-0.63$, $x/c=0.75$, $x/c=1.5$ and $x/c=3$ relative to the wheel's rotation axis (Figure 2.9 and Figure 2.10). Greater details regarding the scaled computational model used for this comparison will be provided in the proceeding chapter (see Section 3.2.2) and therefore only a brief description of the variation in flow predicted will be given here.

Comparing the $x/c=-0.63c$ plane located between the wing and the wheel for the computational results mimicking the experimental apparatus with (Figure 2.9b) and without (Figure 2.9a) the wheel sting present indicate that the stagnation point expected to occur at the most upstream location of the wheel ($y/c=1.3$, $z/c=0.6$) is unaffected by the presence of the wheel sting. Similarly, the velocity deficit expected to occur at the core of the wing vortex ($y/c=1.3$, $z/c=0.2$) and in the wing wake ($0 < y/c < 1$, $z/c=0.25$) also appear unaffected by the addition of the wheel sting. The only variation obtained on this plane due to the presence of the wheel sting can be observed above and below the wing wake where the flow is accelerated to a value approximately 1.2 times greater than that of the freestream velocity. This indicates that the presence of the wheel sting is providing an additional blockage in the test section outboard of the wheel that promotes an increase in flow to the inboard side of the wheel. An increase in the blockage in the test section should also cause an increase in the lift and drag experienced by the wing and wheel model. Reviewing the values obtained by the scaled computational model confirm this, but the increase in lift and drag obtained on these bodies due to the presence of the wheel sting is less than 1%.

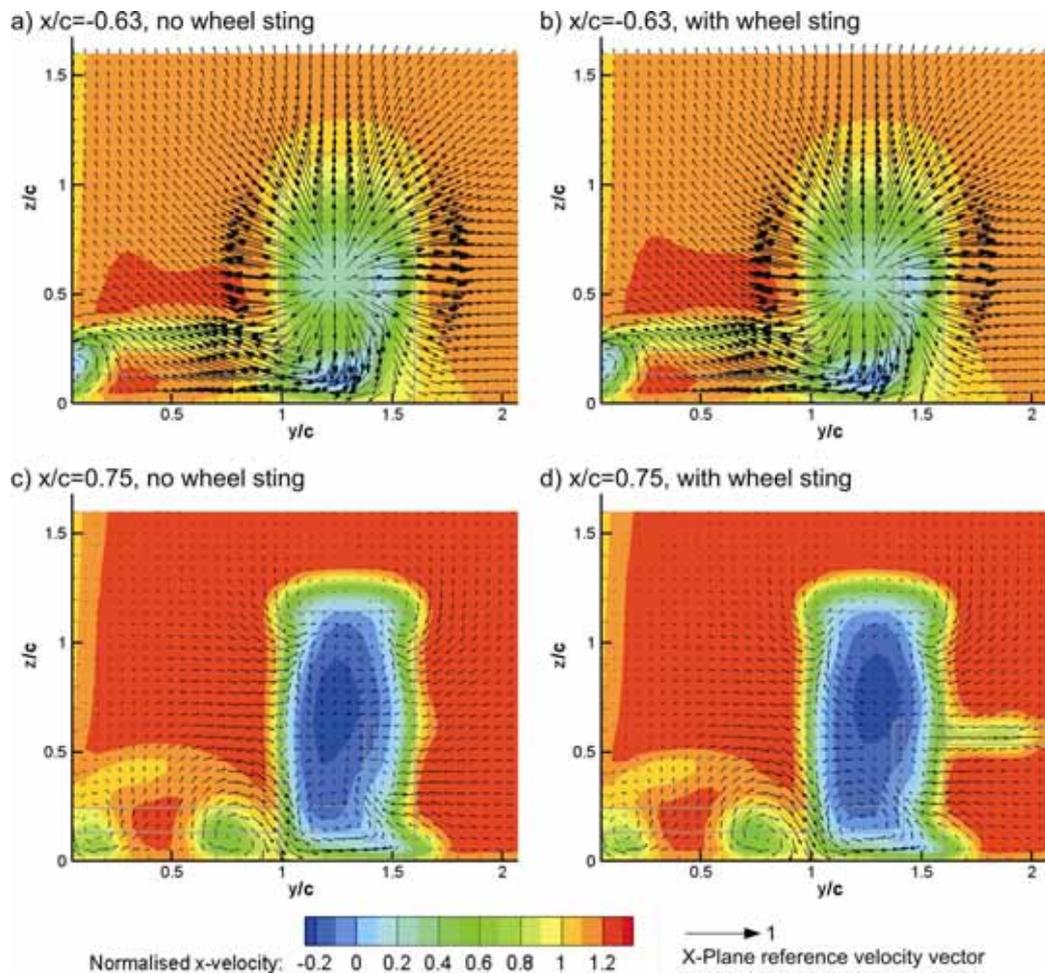


Figure 2.9 Normalised x-velocity and in plane velocity vectors comparisons of CFD undertaken of experimental apparatus with and without wheel sting

On the plane located immediately behind the wheel ($x/c=0.75$) comparing with (Figure 2.9d) and (Figure 2.9c) without the sting, the most noticeable variation obtained is the presence of the sting wake ($1.6 < y/c < 2.1$, $z/c=0.65$). The presence of the sting once again appears to have little influence on the position of the main wing vortex and the maximum extremity of the wheel wake, but variations have been obtained within the wheel wake with the peak velocity deficit being position more outboard within the wheel wake.

The effect that the presence of the wheel sting has is more pronounced further downstream as results obtained on the $x/c=1.5$ and $x/c=3$ planes with (Figure 2.10b,d) and without (Figure 2.10a,c) a wheel sting indicate. The presence of the sting, and its wake,

causes the centre of the wheel wake to be positioned further outboard. This is expected to occur due to the low pressure region generated by the wake of the sting drawing flow from within the wheel wake towards the sting wake. Evidence of this effect is provided by the inboard cross flow component that is obtained at the wheel wakes mid height on both the $x/c=1.5$ and $x/c=3$ planes. When the wheel sting is not present, an inboard velocity component is obtained (Figure 2.10a,c), but with the addition of the wheel sting, this effect is reduced (Figure 2.10b) or reversed (Figure 2.10d). This also affects the path that the main wing vortex takes ($y/c=0.8, z/c=0.2$) with the addition of the wheel sting causing the main wing vortex to be positioned approximately $0.1c$ more outboard in comparison to no sting present on the $x/c=1.5$ plane. Similarly, the wing wake also varies with a lower and wider shape obtained with the inclusion of the wheel sting.

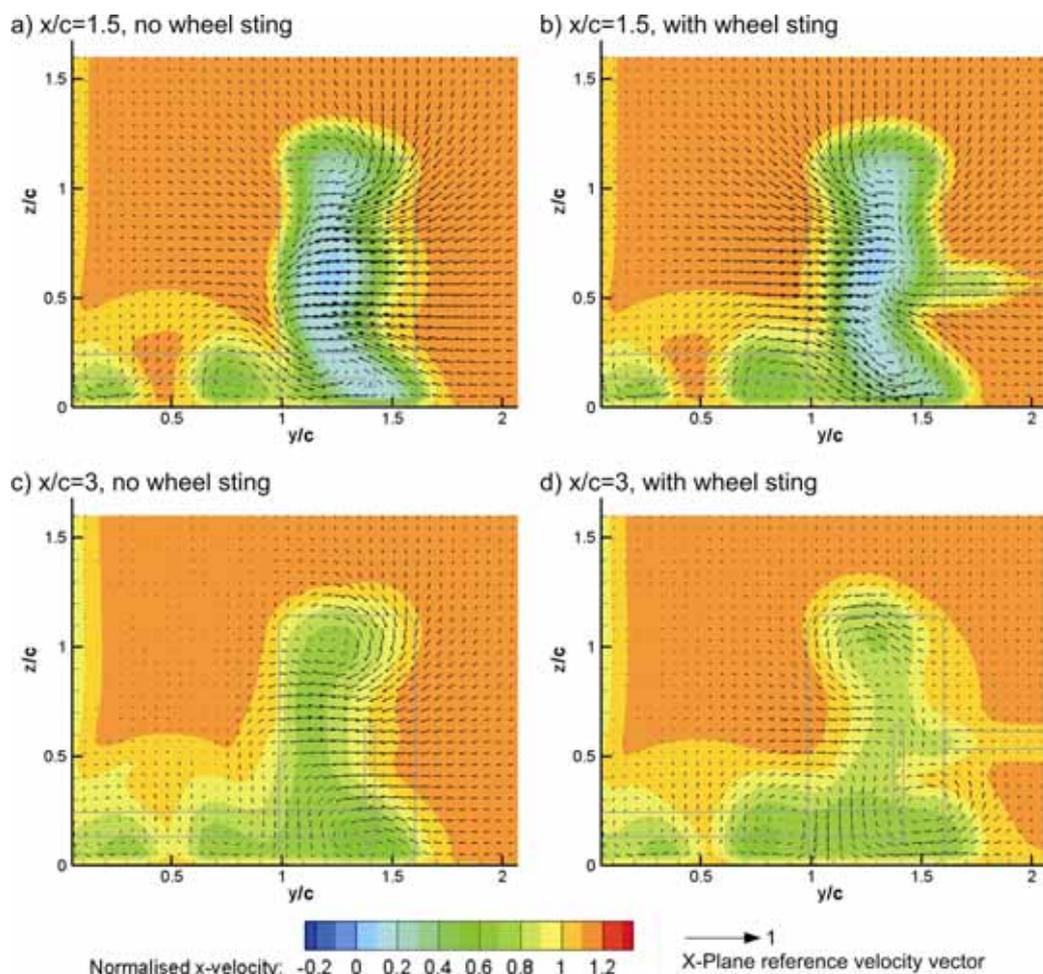


Figure 2.10 Normalised x-velocity and in plane velocity vectors comparisons of CFD undertaken of experimental apparatus with and without wheel sting

From the results presented here, it is evident that the inclusion of a wheel sting to support the wheel during an experimental investigation can alter the interaction observed between a wing and wheel. While it is necessary to include a wheel sting during experimental investigations that include a wheel, a wheel sting is not necessary for a computational model and therefore it may be possible to more accurately replicate the flow structures associated with a wing and wheel of an open wheeler using a computational model as opposed to an experimental model. This further adds weight to Agathangelou and Gascoyne's (1998) suggestion that such an investigation would be better suited to a computational investigation rather than an experimental investigation. Regardless, it is necessary to obtain some experimental results of a wing and wheel for the purpose of validation and therefore this will still be undertaken during the course of this research project. It is vital that all computational results obtained with the sole purpose of conducting comparisons with the experimental results obtained using the apparatus described in this chapter include the wheel sting for a fair and valid comparison.

2.3. Laser Doppler Anemometry

Laser Doppler Anemometry (LDA) is a single point optical measuring technique which enables the velocity of seeded particles travelling with a fluid to be measured in a non-intrusive manner. This is achieved by focussing a pair of laser beams with a known frequency offset onto a selected point, called the measurement volume. While the velocity of a particle can be determined by utilising the Doppler Effect with a single laser beam, this does not allow a particle with zero velocity to be measured or the direction of the velocity to be determined. For this reason an LDA system requires a pair of beams that have a frequency offset that when are superimposed at the measurement volume, create a series of light and dark fringes that are moving with their own frequency (Figure 2.11). As a particle travels through the measurement volume, the reflection created by the particle produces a shift in the frequency that can be used to determine the velocity and direction of the particle. If a reflection is obtained from a particle with equal frequency as that of the fringe frequency, then the system can still determine that there is a particle in the measurement volume that is stationary.

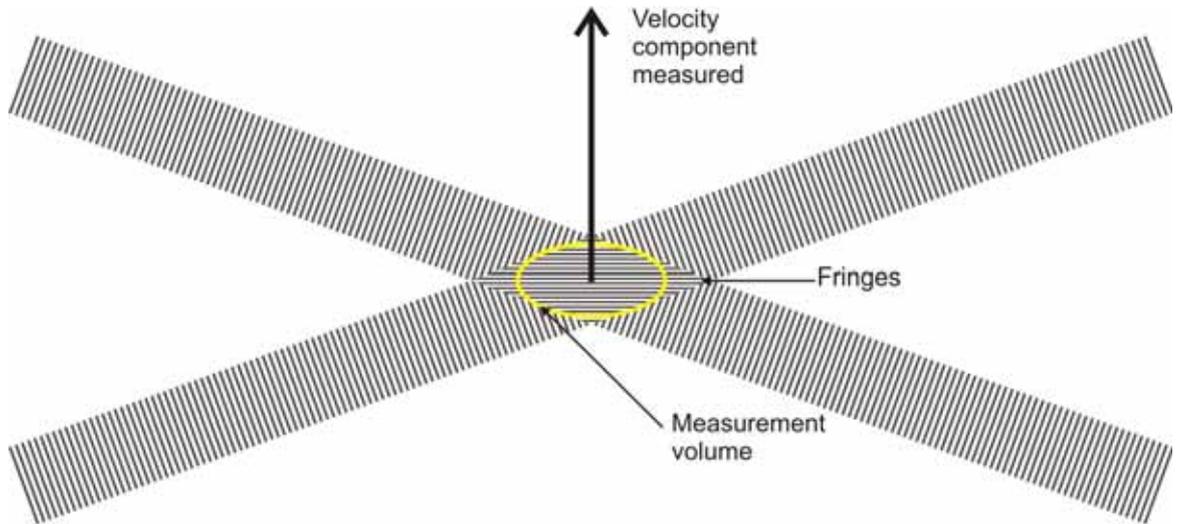


Figure 2.11 Schematic of the crossed beams and the receiver location for an LDA system

Two different techniques can be used in order to collect the light scattered by the particles travelling through the measurement volume which is dependant on the location of the receiving optics relative to the measurement volume. When the receiving optics are located on the opposite side of the measurement volume relative to the location at which the laser beams are delivered from, this is known as forward scattering. The receiving optics can also be located on the same side of the measurement volume relative to the location in which the beams are delivered from and this is referred to as backward scattering. Usually systems that employ backward scattering have the receiving optics built into a probe that also encompass the required lenses to focus and cross each beam belonging to a pair onto the measurement volume. Once collated, the scattered light is transferred via optic cables to a photon multiplier that converts the light source into an electrical signal. This signal is then amplified and filtered prior to being analysed so that the velocity measurement may be made.

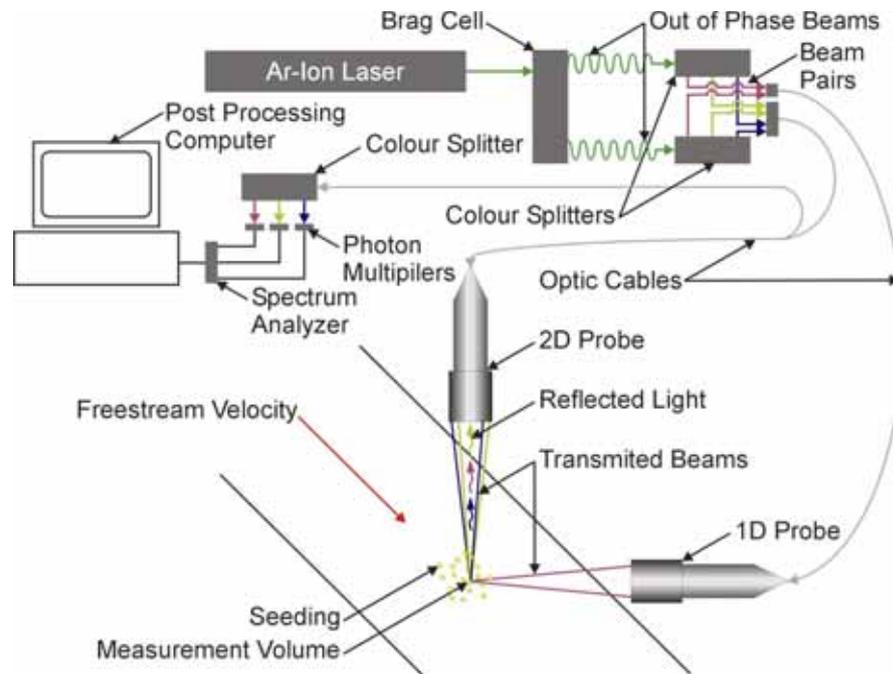


Figure 2.12 Schematic of the components associated with a typical 3D LDA system

A single pair of beams allows the velocity component in plane with the intersecting lasers and normal to their bisecting angle to be measured and therefore, three pairs of laser beams are required in order to obtain all three components. These are delivered by two different probes, the first delivering two pairs of beams, and the second probe delivering the third pair. In order for the scattered light associated with the three velocity components to be distinguishable, three laser pairs of different wavelengths (or colours) are used and collected by the single receiving optics. These are created by a colour splitter that is located after the laser source and the Bragg cell allowing three different colour pairs of laser beams to be delivered to the probes. Not only does this system allow for three velocity components to be measured, but also for many velocity samples to be taken in a short period of time such that statistical analysis can be conducted in order to determine the turbulent quantities associated with each of the velocity measurements. In order to obtain the turbulent quantities of the flow, it is necessary that all three velocity components be measured using common particles travelling through the measurement volume which is referred to as being a “coincident” measurement.

2.3.1. Hardware, software and setup specifications

A Dantec 3D LDA system was used that comprised a 5W Argon-Ion laser that provided the primary laser source. This was delivered to a silver mirror that was used to create two equal strength laser beams of which one passed through a Bragg cell allowing the laser beam to obtain a frequency shift of 40Hz such that the fringe velocity at the measurement volume was approximately 2000ms^{-1} . In order to obtain the three velocity components, the two out of phase laser beams were each split into three different colour pairs with wavelengths of 514.5nm (green), 488nm (blue) and 476.5nm (purple). The blue and green beam pairs were delivered to the measurement volume by a single probe while the purple beam pair was delivered by a second probe. From this point forward these two probes will be referred to as the 2D probe and 1D probe respectively. Both probes utilised 500mm focal length lenses which produced a beam waist of $148\mu\text{m}$, $141\mu\text{m}$ and $137\mu\text{m}$ for the green blue and violet beam pairs respectively. The 2D probe also housed the receiving optics such that the LDA system operated in backscatter mode. The required seeding was provided by oil droplets that were introduced at the bell mouth of the wind tunnel (see Section 2.3.3).

In order to obtain measurements over a range of points in various planes, the 2D and 1D probes were both mounted to a DANTEC 41T333 electronically controlled, motorised three axis traverse system (Figure 2.13). This system allowed for 1010mm range in all three axes and could be repositioned within an accuracy of 0.01mm. This system was controlled by an Isel model C142-4 motor controller via the BSA flow software where a series of points that defined the measurement grid were entered by the operator. Once the measurements commenced, the traverse automatically moved the probes after 3000 coincident samples had been collected or after 30s had elapsed at each point in the predefined grid. Once moving to the new measurement position and prior to taking the subsequent measurements, a settling time of 0.5s was used to allow any vibrations induced by the traverse movement to be damped out.

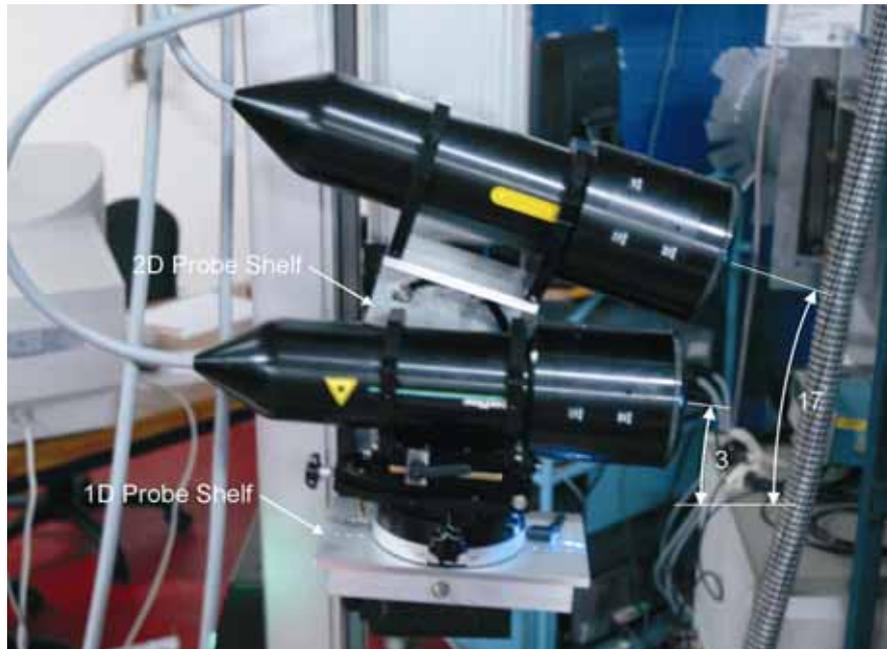


Figure 2.13 Arrangement of the 2D and 1D probe used to obtain LDA measurements

So that measurements could be obtained in close proximity to the moving ground's belt surface the 2D and 1D probe were mounted to the traverse in a vertical plane such that they subtended angles of 17° and 3° to the horizontal respectively (Figure 2.13). Increasing the angle of the 2D probe further than 17° would result in a limitation in the height of the measurement planes as the wind tunnel structure would block either the blue or green laser beams from accessing the measurement volume. By positioning the probes above each other as opposed to alongside each other measurements could be made on planes perpendicular to the freestream between the wing and wheel model and as well as in the wake of both bodies using a single, common configuration. In order to achieve this configuration, aluminium shelves were manufactured allowing the required angle of each probe to be set.

While both probes were mounted to the motorised traverse, the 1D probe was also mounted on its own mechanical traverse system that allowed for manual adjustments in the longitudinal position, pitch and yaw angles to facilitate with the necessary adjustments required to align all three laser pairs with the measurement volume. Once the necessary adjustments were made, the mechanical traverse could be locked so that the 1D probe position would not change relative to the 2D probe while the two were translated by the

motorised traverse. Details of the method used to achieve the necessary alignment of the three beam pairs and the measurement volume will be discussed in Section 2.3.2.

Given the selected arrangement of the LDA probes, it was not possible to directly measure the three orthogonal velocity components of the flow and therefore a transformation matrix was required in order for them to be calculated. Equation 2. 1 describes the transformation matrix as a function of the 2D and 1D probe angles required (α and β respectively) while Equation 2. 2 displays the actual coefficients used to determine the three orthogonal velocities (Dantec, 2006).

$$\begin{bmatrix} u \\ v \\ w \end{bmatrix} = \begin{bmatrix} 1 & 0 & 0 \\ 0 & -\frac{\sin \beta}{\sin(\alpha - \beta)} & \frac{\sin \alpha}{\sin(\alpha - \beta)} \\ 0 & \frac{\cos \beta}{\sin(\alpha - \beta)} & \frac{\cos \alpha}{\sin(\alpha - \beta)} \end{bmatrix} \cdot \begin{bmatrix} u_1 \\ u_2 \\ u_3 \end{bmatrix} \quad \text{Equation 2. 1}$$

$$\begin{bmatrix} u \\ v \\ w \end{bmatrix} = \begin{bmatrix} 1 & 0 & 0 \\ 0 & 0.1530 & 0.8548 \\ 0 & 2.9198 & 2.7961 \end{bmatrix} \cdot \begin{bmatrix} u_1 \\ u_2 \\ u_3 \end{bmatrix} \quad \text{Equation 2. 2}$$

BSA Flow software provided by Dantec was used to analyse the data. This software also displayed the rate at which the data was collected, the number of samples collected, the confidence level of the measurements, the mean and rms velocity of each component and the measurement errors associated with these quantities in real time. It was also used to calculate the turbulence intensity using the following equation:

$$I = \frac{\sqrt{\frac{1}{3}(u_{rms}^2 + v_{rms}^2 + w_{rms}^2)}}{u_{\infty}} \quad \text{Equation 2. 3}$$

2.3.2. Alignment technique

In order for 3D coincident results to be taken, a procedure was required that allowed the measurement volume to be aligned with the waist of the three different colour beams accurately and in a repeatable manner. Several methods had been attempted which

utilised a pin hole, a pin hole meter (Swales *et al.* 1993) and a CCD (charged couple device) chip (Gatto, 2004) of which the method utilising the CCD chip proved to be most reliable. This method utilised a CCD chip from a Logitech “QuickCam Express” web camera mounted onto a mechanical traverse after the case and the focussing lens had been removed. The traverse was then mounted in such a way that the CCD chip subtended an equal angle to the two LDA probes (Figure 2.14). The CCD chip was then connected to a computer where the webcam software was used to display the image obtained by the CCD chip magnified such that 12 pixels displayed by the software represented an approximate distance of 50 μ m.



Figure 2.14 CCD tool used for the alignment of the LDA system

In order to align the measurement volume with the waist of the three beam pairs, it was necessary to first view the measurement volume. This was achieved by transmitting a light source through the receiver which was then used to align the focal point of the measurement volume with the CCD chip by adjusting the mechanical traverse that it was mounted on. A marker was then used to define the centre of the measurement volume in the CCD software and then the blue and green beam pairs were individually aligned with the mark left on the computer screen using the vertical and horizontal positions adjustments built into the 2D probe for each individual beam (Figure 2.14). So that the

CCD chip would not be completely flooded with light, it was necessary to attenuate the laser beams by partially opening the gate for each of the beams at the colour splitters. While the receiver located in the 2D probe was used to collect the backscattered light during all experiments, the 1D probe also had a receiver built into it that could be used if required. This was only used during the alignment process to position the focal point of the 1D receiver with the focal point of the 2D receiver and was achieved by transmitting a light source through its receiver and then adjusting the mechanical traverse that the 1D probe was mounted on until the focal point of the 1D probe was aligned with the mark made in the software. The two violet beams were then also aligned using the vertical and horizontal adjustments in the 1D probe until they were aligned with the mark made on the screen.

While the alternative, pin hole methods were also attempted, it was determined that both required that a suitable size hole be selected according to the beam waist of the laser beams which were not able to be supplied by the LDA manufacturer for the focal length lenses provided. An additional advantage of the CCD method was that the alignment apparatus required was independent of the beam waist diameter and therefore could be used to align any combination of beam expanders and focal length lenses if required. After aligning the LDA probes using the CCD alignment technique described here, it was possible to achieve consistent data rates of between 1500 to 3000 samples per second.

2.3.3. Seeding system

Given that the LDA system operates on the basis of light being reflected from particles travelling with the fluid flow, it was necessary to introduce some seeding particles that were adequately small and light to follow the trajectory of the flow yet large enough to produce the adequate reflections required by the LDA system (Dantec, 2006). A homogeneous distribution of particles is also required with a density that never allows more than a single particle to cross the measurement volume at any one time and therefore the density of the seeding places a limit on the data rate that can be obtained.

A previous study conducted at UNSW demonstrated that the most effective, non-solid particle to use as seeding for a Particle Image Velocimetry system (PIV) would be a vegetable oil aerosol (Coray, 2005). A Laskin type seeding generator manufactured by PivTec was used to create 1 μ m spherical oil droplets that were introduced at the inlet of

the tunnel. The particles were created by using pressurised air that was released from five nozzles with 1mm diameter holes submerged in vegetable oil (Figure 2.15). The pressure difference generated by the air supply caused the air introduced into the vegetable oil to rise and create spherical droplets that would then leave the atomiser and could be varied by a series of valves in order to control the density. An impactor plate located within the atomiser also ensured that no particles greater than 1µm in diameter were able to leave the atomiser. Given the similar requirements of an LDA and PIV systems, the same seeding system was considered to use in conjunction with the LDA system.

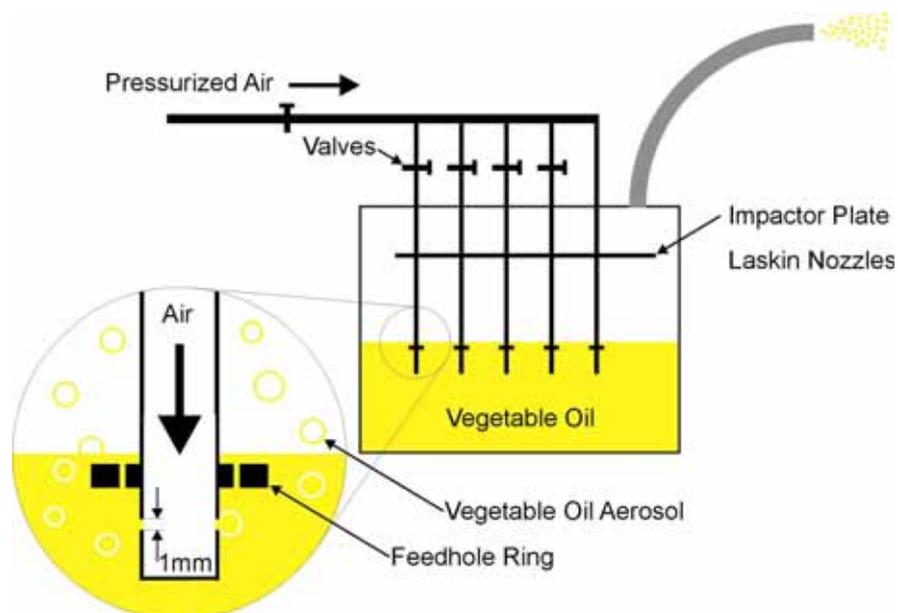


Figure 2.15 Schematic of Laskin type atomiser

For particles that are between 0.1 and 50µm, the Lorenz-Mie light scattering theory can be applied when the particle size is comparable to the wavelength of the light source and spherical in shape to determine the ratio of the refractive index as a function of the light incidence angle (Kahler, 2004). While larger particles scatter more light, the distribution of the scattered light is more even for smaller particles as indicated by Figure 2.16. Of particular importance is the increase in ratio of forward to backward scattered light, which can be in the order of 10^2 to 10^3 for the larger particles in this range (Dantec, 2006). Given that the LDA system that will be used for this investigation will be working in backscatter mode, particles closer to the smaller end of the range specified above will be considered more suitable which is consistent with the diameter of the vegetable oil aerosol that is

produced by the atomiser ($1\mu\text{m}$ or $d_p=0.51\lambda$, 0.49λ and 0.48λ for the green blue and violet beams respectively). It should also be noted that larger particles would be expected to create more background noise by reflections created by particles not passing through the measurement volume (Dantec, 2006).

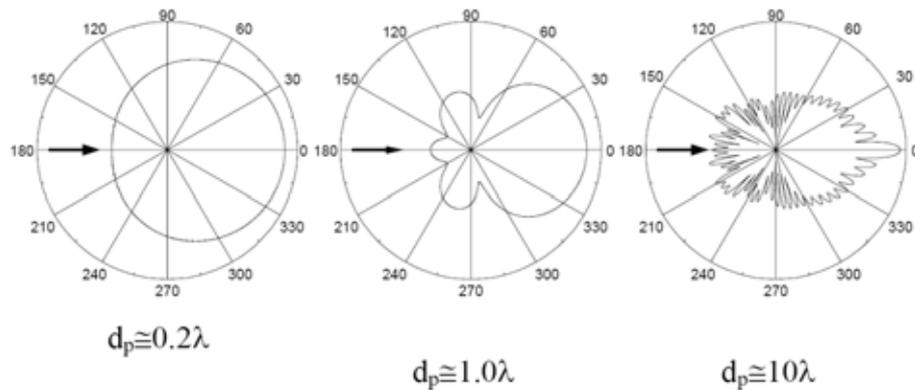


Figure 2.16 Lorenz-Mie Scatter Diagram for spherical particles, note light intensity is shown on logarithmic scale (Dantec, 2006)

Given that the LDA system measures the velocity of the seeding as opposed to the flow itself, it is vital that the seeding travels with the flow. Figure 2.17 indicates the lift and drag forces acting on a particle (F_L and F_D) travelling in a fluid flow of velocity (v_F), while the particle has its own velocity (v_P). The relative difference of the fluid and the particle velocity is the slip velocity (v_S).

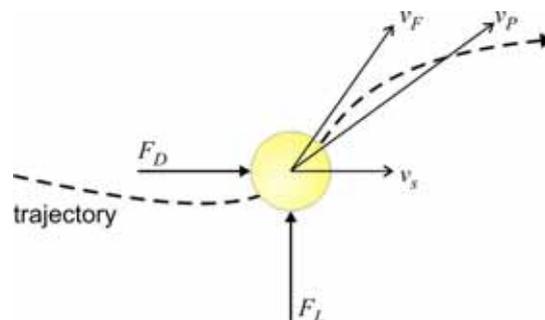


Figure 2.17 Forces acting on a particle travelling with a fluid flow

The acceleration time, or the time that it takes for the lift and drag forces to bring the slip velocity of the particle in the fluid to be zero is known as the relaxation time (τ_o) and can be evaluated using Equation 2. 4 (Albrecht, 2003):

$$\tau_o = \frac{\rho_p d_p}{18\mu_f} \quad \text{Equation 2. 4}$$

- where d_p is the particle diameter (1 μ m), ρ_p is the particle density (894kg/m³) and μ_f is the fluid viscosity (1.8x10⁻⁵). Using Equation 2. 4 a relaxation time of 2.759x10⁻⁶ has been determined. This is required to calculate the velocity slip ratio described by Equation 2. 5, where v_p and u_f are the velocity of the particle and the fluid respectively and provides an indication of the lag of the particle in the fluid flow which should be minimised.

$$s = \frac{u_f - v_p}{u_f} \quad \text{Equation 2. 5}$$

By using the Basset-Boussinesq-Ossen equation, Albrecht (2003) gave a closed solution by neglecting the body force terms and the Bassert term which is a valid assumption for high particle to fluid density ratios ($\rho_p/\rho_f \gg 1$). Therefore, by applying a sinusoidal velocity fluctuation in a one dimensional flow field, Equation 2. 6 can be derived:

$$1 - s = \frac{v_p}{u_f} = \frac{1}{\sqrt{1 + \omega_c^2 \tau_o^2}}, \quad \omega_c = 2\pi f_c \quad \text{Equation 2. 6}$$

- where ω_c is the critical frequency for which a given slip value can be tolerated. Equation 2. 6 also states the relationship between the critical frequency, f_c , where the particles still follow the oscillations in the velocity (Albrecht, 2003) and therefore, for a 1% slip, $f_c = 0.0227 \tau_o$. These equations indicate that the particle size and density limit the particles ability to follow the oscillations in the flow and therefore may limit the ability of the LDA system to measure the turbulence characteristics of the fluid flow. In order to ensure that a particle of diameter d_p , does not suffer from this limitation, it must satisfy equation Equation 2. 7 (Albrecht, 2003):

$$d_p < \sqrt{\frac{18\mu_f}{\rho_p f_c} \frac{1}{2\pi} \sqrt{\frac{1}{(1-s)^2} - 1}} \quad \text{Equation 2. 7}$$

- therefore, if a 1% slip velocity ratio is tolerated, the vegetable oil droplet, can have a diameter of up to 2.5 μ m. Given that the laskin type atomiser produces oil droplets no greater than 1 μ m in diameter, Equation 2. 7, indicates that the actual slip velocity ratio of

the oil droplets created by the atomiser approaches 0. Therefore, it would be expected that any error that may be introduced by the particles not following the trajectory of the flow using the above described setup will be negligible.

Based on the light scattering properties and the ability of the oil droplets to follow the trajectory of the flow, it can be concluded that the seeding system selected to use in conjunction with the LDA system has suitable optical and physical characteristics for their desired application.

2.3.4. LDA System Measurement Errors

Errors that may be introduced into the measurements obtained using an LDA system can be attributed to; uncertainty of the values being measured by the LDA system, inconsistent fringe separation from misalignment of the beam pairs and velocity bias favouring particles travelling through the measurement volume with higher velocities. Of these three sources of error, it is possible to quantify the error introduced by the first two, while the later requires a correction to be applied to the measurement taken.

In order to prevent the measurement obtained to be unfairly biased by the particles travelling through the measurement volume with a higher velocity, a correction is required. Particles with higher velocities are expected to pass through the measurement volume with a greater flow rate and subsequently, a larger number of samples will be collected with a higher velocity (Albrecht, 2003). To correct this velocity-bias, a non-uniform weighting factor η_i has been employed which is described by the equation below:

$$\bar{u} = \sum_{i=0}^{N-1} \eta_i u_i \quad , \quad \eta_i = t_i \left(\sum_{j=0}^{N-1} t_j \right)^{-1} \quad \text{Equation 2. 8}$$

- where N is the number of samples, u_i and t_i is the velocity and the transit time of the i 'th particle crossing the measurement volume respectively (Dantec, 2006).

Errors can also be introduced into the LDA measurements by having laser beam pairs that do not intersect at the beam waist causing the wavefronts to be curved instead of planer. As a result, the fringe spacing will be inconsistent throughout the measurement volume causing the measured Doppler frequency to be dependant on the location at which a

seeding particle crosses the measurement volume and therefore not directly proportional to the particle's velocity (Dantec, 2006). This is significant for highly concentrated beams where the beams have a strong divergence in the beam waist and strong wave front curvature (Albrecht, 2003) as is the case for the beams used by an LDA system. While it is unexpected that it would be possible to obtain measurements with poorly aligned beams (Dantec, 2006), the maximum error introduced due to the non-planar fringe separation and the subsequent error due to the Doppler frequency (f_{Err}) can be quantified using the following equation:

$$f_{Err} \approx \frac{1}{2 \tan \frac{\theta}{2}} \left(\frac{x_{D1} z_{D1}}{z_{D1}^2 + l_{R1}^2} - \frac{x_{D2} z_{D2}}{z_{D2}^2 + l_{R2}^2} \right) \quad \text{Equation 2.9}$$

- where x_D is the beam waist, z_D is the length of the measurement volume along the beam axis as a consequence of the misalignment, θ is the beam separation angle and l_R is the ratio between the aperture of a Gaussian beam at the beam waist to the wavelength of the beam. Given that the alignment technique described above allowed an alignment within an accuracy of $50\mu\text{m}$, the frequency shift that may be introduced due to the beams not being aligned at the beam waist was considered to be negligible.

Variable; \bar{X}	Value for ζ
\bar{U}	$\overline{u'^2}$
$\left(\overline{u'^2}\right)^{\frac{1}{2}}$	$\frac{\overline{u'^2}}{2}$
$\overline{u'^2}$	$2\left(\overline{u'^2}\right)^2$
$\overline{u'v'}$	$\left(1 + R_{uv}^2\right)\left(\overline{u'^2}\right)\left(\overline{v'^2}\right)$
R_{uv}	$\left(1 - R_{uv}^2\right)^2$

$$\text{Where: } R_{UV} = \frac{\overline{u'v'}}{\left(\overline{u'^2}\right)^{\frac{1}{2}}\left(\overline{v'^2}\right)^{\frac{1}{2}}}$$

Table 2. 1 Statistical variance assumptions (Benedict and Gould, 2006)

Benedict and Gould (1996) have outlined methods to estimate the uncertainty of turbulence measurements made using LDA systems on a fluid flow with a normal

distribution assumption. These are listed above and have also been employed by the BSA flow software (Dantec, 2006) in order to calculate the uncertainty associated with each of the measured quantities. For a property being measured “ Φ ”, with variable “ x ”, the uncertainty is determined over a number “ N ” samples by Equation 2. 10, where “ h ” is a constant dependant on the confidence level of the measurement taken. This method allows the uncertainty of each of the three velocity components to be calculated by replacing u with either v or w :

$$\Phi = \bar{X} \pm h \left(\frac{\zeta}{N} \right)^{\frac{1}{2}} \quad \text{Equation 2. 10}$$

Using the above method to calculate the errors associated with the three velocity components and the turbulence intensity allows an error to be determined at each of the measurement points. Contour plots of the errors over the planes at which measurements have been taken indicate that at no time did the uncertainty of the measurement exceed $\pm 0.1 \text{ms}^{-1}$ for the x, y or z velocity components and $\pm 0.004\%$ of the turbulence intensity.

2.4. Summary

This chapter outlines the specifications of the UNSW 225x340mm open circuit wind tunnel and moving ground that has been used to collate the experimental results of a combined wing and wheel for the purpose of validating a numerical model. The variation in the freestream velocity and the moving ground velocity observed during the course of the experiments has been outlined as well as the freestream turbulence intensity at the inlet of the test section. Measurements undertaken of an empty wind tunnel test section with the moving ground installed and operating indicate that a constant velocity profile has been obtained over the surface of the belt that is representative of the conditions that a wing and wheel operating on an open wheel racing car would experience. Wind tunnel models have been designed that allow the wing angle of attack, height and span to be adjusted as well as the wheel width and track. In order to support the wheel during the experiments, a wheel sting was designed and computational results have indicated that the wheel sting alters the combined wing and wheel wake and therefore should be included in the computational model that will be compared to the experimental results. The experimental

results have been collected with a Laser Doppler Anemometer system of which the function and the errors of this system have been outlined.

Chapter 3: Computational Method and Model Description

This chapter describes the governing equations that are required to be solved in order to develop a computational model and the techniques employed to solve them. Once these have been established, a description of the computational model is provided as well as a summary of the procedure undertaken to ensure that the errors associated with computational model have been minimised.

3.1. Theory and Methodology

In order to reduce the complexity of the computational model, some simplifications can be made to the governing equations of fluid flow. For example, given that the freestream velocity for this investigation has been chosen to be 33.3ms^{-1} , an investigation undertaken by Doig *et al.* (2008) has indicated that the flow about a downforce producing wing is expected to be largely incompressible at this speed despite the accelerations experienced beneath the wing. Since a wing produces a greater pressure drop than that experienced by an isolated wheel, it would also be expected that the same assumption can be made for the flow about a wheel. Therefore, it can be safely assumed for a combined wing and wheel, the density of the fluid will remain constant throughout the domain.

While the flow structures associated with a wheel are expected to vary over time, steady state solvers are commonly used during the development of open wheel racing cars to reduce the required computational resources (Akanni, 1995). Given that this investigation is relevant to the development of open wheel racing cars, it has been decided to employ a steady state solver during this investigation. To ensure that the mean flow structures have not been compromised as a result of this assumption, a comparison will be conducted to a previous unsteady numerical investigation conducted by McManus and Zhang (2006) of an isolated wheel during the following chapter.

Therefore, based on the two assumptions stated above, a series of governing equations are required that can describe a viscous, steady state and incompressible flow.

3.1.1. Governing Equations of Fluid Flow

The governing equations of fluid motion utilized by computational models ensure that the mass, momentum and the energy of the fluid are conserved for each discretised volume within the computational domain. Given that the flow associated with an interacting wing and wheel is expected to be incompressible and that no thermal effects will be considered for the investigation of a combined wing and wheel, only the equations that ensure that the mass and momentum is conserved will be required (Versteeg and Malalasekera, 1998), and are discussed here.

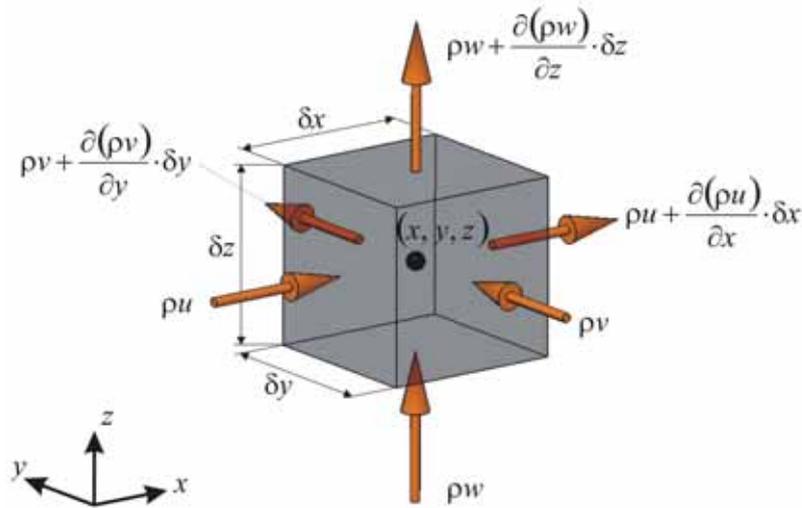


Figure 3.1 Schematic of Conservation of Mass

The conservation of mass equates the variation in the mass of a fluid volume to the rate of fluid flowing into the volume (Figure 3.1) and can be written as:

$$\frac{\partial \rho}{\partial t} + \nabla(\rho \vec{u}) = \frac{\partial \rho}{\partial t} + \frac{\partial(\rho u)}{\partial x} + \frac{\partial(\rho v)}{\partial y} + \frac{\partial(\rho w)}{\partial z} = 0 \quad \text{Equation 3. 1}$$

- where ρ is the density of the fluid and u , v and w are the velocity components in the x , y and z directions respectively. Given that the flow is expected to be incompressible, the mass of the fluid volume will remain constant and therefore the variation in the mass of the fluid volume will always be zero. Therefore, Equation 3. 1 can be simplified to be:

$$\frac{\partial u}{\partial x} + \frac{\partial v}{\partial y} + \frac{\partial w}{\partial z} = 0 \quad \text{Equation 3. 2}$$

When applying Newton's second law of motion to the fluid within a specified volume, it is possible to equate the forces applied to the fluid volume to the change in velocity that the fluid passing through this volume experiences. The forces acting on the volume can be described as either surface forces, which include the pressure and viscous forces, or the body forces that may include the effects of gravity, centripetal, coriolis and electromagnetic effects. For the investigation of the wing and wheel, the effects of the various body forces are expected to be negligible or irrelevant and therefore only the surface forces are expected to contribute to the momentum variation. Those that are expected to contribute to the variation of the fluid's momentum in the x direction are depicted in Figure 3.2 where the viscous forces are acting parallel to the volume's surface (τ_{yx} and τ_{zx}) while the pressure forces are acting normal to the volume's surface (p and τ_{xx}).

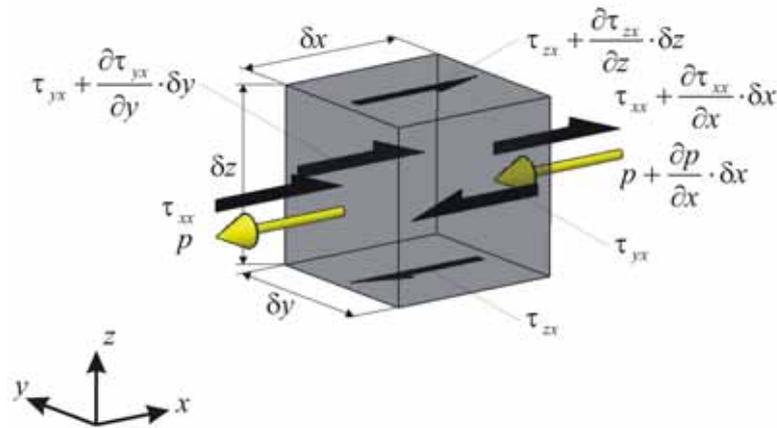


Figure 3.2 Schematic of Conservation of Momentum

Equating all the forces in the x-direction and making this equal to the rate of change of the x momentum yields the following conservation of momentum equation for the x direction:

$$\rho \frac{Du}{Dt} = \frac{\partial(-p + \tau_{xx})}{\partial x} + \frac{\partial \tau_{yx}}{\partial y} + \frac{\partial \tau_{zx}}{\partial z} \quad \text{Equation 3. 3}$$

Following a similar procedure, it is possible to derive the conservation of momentum equations in the y and z directions respectively which are:

$$\rho \frac{Dv}{Dt} = \frac{\partial \tau_{xy}}{\partial x} + \frac{\partial(-p + \tau_{yy})}{\partial y} + \frac{\partial \tau_{zy}}{\partial z} \quad \text{Equation 3. 4}$$

$$\rho \frac{Du}{Dt} = \frac{\partial \tau_{xz}}{\partial x} + \frac{\partial \tau_{yz}}{\partial y} + \frac{\partial(-p + \tau_{zz})}{\partial z} \quad \text{Equation 3. 5}$$

In a Newtonian fluid, the viscous stresses are proportional to the rates of deformation which consists of the linear deformation rate and the volumetric deformation rate. Newton's law of viscosity can be used to evaluate the viscous stresses where, the dynamic viscosity μ , relates the linear stresses to linear deformations, while the second constant λ relates stresses to volumetric deformation. As a result, nine stress components can be evaluated, but since an isotropic incompressible fluid is being used for this investigation, this reduces to six and λ is equal to zero (Versteeg and Malalasekera, 1998):

$$\tau_{xx} = 2\mu \frac{\partial u}{\partial x} + \lambda \text{div} \bar{u} \quad \tau_{yy} = 2\mu \frac{\partial v}{\partial y} + \lambda \text{div} \bar{u} \quad \tau_{zz} = 2\mu \frac{\partial w}{\partial z} + \lambda \text{div} \bar{u}$$

$$\tau_{xy} = \tau_{yx} = \mu \left(\frac{\partial u}{\partial x} + \frac{\partial v}{\partial y} \right) \quad \tau_{xz} = \tau_{zx} = \mu \left(\frac{\partial u}{\partial x} + \frac{\partial w}{\partial z} \right) \quad \text{Equation 3. 6}$$

$$\tau_{yz} = \tau_{zy} = \mu \left(\frac{\partial v}{\partial y} + \frac{\partial w}{\partial z} \right)$$

By substituting the equations describing the shear stresses into the three previous momentum equations, the following form of the momentum equations can be obtained which together with the continuity equation (Equation 3. 1) are known as the Navier Stokes equations:

$$\frac{\partial(\rho u)}{\partial t} + \text{div}(\rho u \bar{u}) = -\frac{\partial p}{\partial x} + \text{div}(\mu \text{grad } u) \quad \text{Equation 3. 7}$$

$$\frac{\partial(\rho v)}{\partial t} + \text{div}(\rho v \bar{u}) = -\frac{\partial p}{\partial y} + \text{div}(\mu \text{grad } v) \quad \text{Equation 3. 8}$$

$$\frac{\partial(\rho w)}{\partial t} + \text{div}(\rho w \bar{u}) = -\frac{\partial p}{\partial z} + \text{div}(\mu \text{grad } w) \quad \text{Equation 3. 9}$$

3.1.2. Reynolds Averaged Navier Stokes Equations and Turbulence Modelling

Turbulent flow structures are expected to be generated at the Reynolds number at which this investigation will be conducted. Therefore, a method is required that will allow the governing equations to model turbulence with a reasonable level of computing power. Several different techniques exist for achieving this which include; Direct Numerical Simulation (DNS), Large Eddy Simulation (LES), or Reynolds Averaging. Of the three described here, Reynolds averaging is the most computationally efficient as DNS and LES resolve all or the larger turbulence structures respectively, requiring significantly finer grids and a time dependant approach to be taken. As a result, both DNS and LES require vastly increased computational resources in comparison to Reynolds Averaging (Wilcox, 2000) and for this reason have not been considered for this study. Additionally, previous computational investigations considering either an independent wing (Zerihan, 2001) or wheel (Axon, 1998) have successfully utilised Reynolds Averaging and therefore this turbulence modelling technique has been selected to be used for all the numerical results presented during the course of this thesis.

Reynolds averaging accounts for turbulence by replacing the velocity terms in the Navier Stokes equations with a mean (\bar{U}) and fluctuating (u') component for each velocity component:

$$u = \bar{U} + u', \quad v = \bar{V} + v' \quad \text{and} \quad w = \bar{W} + w' \quad \text{Equation 3. 10}$$

Similarly, the scalar quantities are also replaced by mean and variable components. For an incompressible flow, this is only required for the pressure:

$$p = \bar{P} + p' \quad \text{Equation 3. 11}$$

Replacing the velocity and pressure terms in the Navier-Stokes equations with the terms described in Equation 3. 10 and Equation 3. 11 and then averaging them with respect to time allows the Reynolds-averaged Navier-Stokes (RANS) equations to be derived which are shown below:

$$\frac{\partial \bar{U}}{\partial x} + \frac{\partial \bar{V}}{\partial y} + \frac{\partial \bar{W}}{\partial z} = 0 \quad \text{Equation 3.12}$$

$$\frac{\partial(\rho u)}{\partial t} + \text{div}(\rho \bar{U} \bar{U}) = -\frac{\partial \bar{P}}{\partial x} + \text{div}(\mu \text{grad} \bar{U}) + \left[-\frac{\partial(\rho \overline{u'^2})}{\partial x} - \frac{\partial(\rho \overline{u'v'})}{\partial y} - \frac{\partial(\rho \overline{u'w'})}{\partial y} \right] \quad \text{Equation 3.13}$$

$$\frac{\partial(\rho u)}{\partial t} + \text{div}(\rho \bar{V} \bar{U}) = -\frac{\partial \bar{P}}{\partial x} + \text{div}(\mu \text{grad} \bar{V}) + \left[-\frac{\partial(\rho \overline{u'v'})}{\partial x} - \frac{\partial(\rho \overline{v'^2})}{\partial y} - \frac{\partial(\rho \overline{v'w'})}{\partial y} \right] \quad \text{Equation 3.14}$$

$$\frac{\partial(\rho u)}{\partial t} + \text{div}(\rho \bar{W} \bar{U}) = -\frac{\partial \bar{P}}{\partial x} + \text{div}(\mu \text{grad} \bar{W}) + \left[-\frac{\partial(\rho \overline{u'w'})}{\partial x} - \frac{\partial(\rho \overline{v'w'})}{\partial y} - \frac{\partial(\rho \overline{w'^2})}{\partial y} \right] \quad \text{Equation 3.15}$$

Doing so introduces six additional quantities, called the Reynolds stresses, without any additional transport equations and as a result, the RANS equations can not be solved on their own. A commonly used technique to provide closure for the RANS equations was first proposed by Boussinesq (1877) which relates the Reynolds stresses to the mean velocity gradients (Hinze, 1975):

$$-\rho \overline{u'_i u'_j} = \mu_t \left(\frac{\partial u_i}{\partial x_j} + \frac{\partial u_j}{\partial x_i} \right) - \frac{2}{3} \left(\rho k + \mu_t \frac{\partial u_k}{\partial x_k} \right) \delta_{ij} \quad \text{Equation 3.16}$$

This technique is used by several turbulence models including the Spalart-Allmaras, $k-\varepsilon$ and $k-\omega$ turbulence models. For the Spalart-Allmaras turbulence model, only a single additional transport equation is required to solve for the turbulent viscosity (μ_t) and as a result is also referred to as a one-equation turbulence model. The $k-\varepsilon$ and $k-\omega$ turbulence models are both two-equation turbulence models which solve two additional transport equations for the kinetic energy (k) and the turbulent dissipation rate (ε) or the specific dissipation rate (ω). The Reynolds Stress model offers an alternative method that does not utilise a Boussinesq approximation and instead requires that seven additional transport equations be solved for a three-dimensional flow. A short description of these turbulence models is given here focussing on those that have been previously used for computational investigations of either an isolated wing or wheel. Computational results obtained using the most appropriate of these turbulence models will be compared to LDA results in Chapter 4 to determine the most suitable to use for the study of a combined wing and wheel.

3.1.2.1. Spalart-Allmaras Turbulence Model

The original Spalart-Allmaras turbulence model was initially presented as an alternative turbulence model for predicting the flow over aerofoils in the transonic region (Spalart and Allmaras, 1992). The authors state that the advantage of this turbulence model over previous one equation turbulence models is that it is local and does not require information from surrounding elements to obtain a solution. Therefore, this turbulence model can be used on an unstructured grid. Spalart and Allmaras also indicate that this model is well suited to predicting flows that include; mixing layers, wakes and boundary layers including those located in adverse pressure gradient regions. Additionally, the original Spalart-Allmaras turbulence model is capable of modelling laminar to turbulent transition when the transition region is specified by the user. Further improvements for this model have allowed the transition region to be automatically predicted (Fluent, 2006). The Spalart-Allmaras turbulence model is written in terms of the eddy viscosity and uses eight closure coefficients and three closure functions (Wilcox, 2000).

Initially, the Spalart-Allmaras turbulence model was validated against a series of experiments undertaken of a transonic wing (Spalart and Allmaras, 1992), but since then it has been used for various incompressible and subsonic flows and has been described as the best one equation model despite its deficiency at predicting jetting flows (Wilcox, 2000). Such flow features are expected at either side of the front wheel contact patch, previous computational wheel studies conducted by McManus (2006) and Axon (1999) have successfully used this turbulence model to predict the surface pressure coefficients and wake profiles. Additionally, Zerihan (2001) has also demonstrated that the Spalart-Allmaras model can successfully predict the same parameters for an aerofoil in ground effect as well as the lift coefficient.

3.1.2.2. Standard $k-\epsilon$ Turbulence Model

The $k-\epsilon$ turbulence model is the most frequently used turbulence model for computational studies conducted on low speed incompressible flows due to its robustness and economy (Chung, 2002). It has been found to be effective for both free shear flows and wall bounded flows, when used in conjunction with a wall function or near wall model (see Section 3.1.2.8). This two equation model provides closure by using semi-empirical

formulae that determine the turbulent kinetic energy (k) and the dissipation energy (ϵ). This fully turbulent model was originally proposed by Chou (1945), but since then Launder and Spalding (1972) have presented an improved version which is now referred to as the standard k - ϵ model. The constants used with this turbulence model have been obtained by Launder and Sharma (1974) by conducting numerous experiments with air and water. These now form the basis of the most commonly used model (Wilcox, 2000). These values can be adjusted to further tune the turbulence model to a desired application if required (Chung, 2002).

Axon (1999) considered this turbulence model for his numerical study of an isolated wheel. While the geometry used for the computational wheel was simplified by using completely flat sides, pressure coefficients obtained by Fackrell (1975) were used to validate the numerical model. The standard k - ϵ model yielded results with significant variations where separation was expected to occur. This is consistent with the standard k - ϵ models deficiency in handling regions of adverse pressure gradients (Fluent, 2006). Despite this, this turbulence model did correctly predict that the lift and drag of a rotating wheel is less than that of a stationary one. Variations of the standard k - ϵ model that enhance the accuracy of this turbulence model are the RNG and Realizable k - ϵ turbulence models.

3.1.2.3. RNG k - ϵ Turbulence Model

The RNG k - ϵ model was originally proposed by Yakhot and Orszag (1986) who used the renormalization group theory to derive new coefficients for the k - ϵ turbulence model (Wilcox, 2000). These coefficients allow small scale motions to be systematically removed from the governing equations and be replaced by larger scale motions with a modified viscosity. One benefit of this turbulence model over the standard k - ϵ model is reported to be improved performance in regions of adverse pressure gradients (Fluent, 2006). Such regions are expected to form over the bottom surface of the wing and the top of the wheel in this study. Barber (2000) used the RNG k - ϵ model for a study on a lifting wing in ground effect and demonstrated that velocity and turbulent kinetic energy comparisons of the computational and experimental (PIV) results obtained for two different wing heights agreed qualitatively. Axon (1999) also demonstrated that this turbulence model is more effective at predicting the separation point and the pressure coefficients in comparison to

the standard $k-\varepsilon$ model. Other reported improvements include predicting of rapidly strained and swirling flows as well as low-Reynolds number effects for near wall regions (Fluent, 2006).

3.1.2.4. Realizable $k-\varepsilon$ Turbulence Model

The most recent improvement of the standard $k-\varepsilon$ model is the Realizable $k-\varepsilon$ model originally presented by Shih *et al.* (1995). This model differs from the standard $k-\varepsilon$ model by providing a new formulation for the turbulent viscosity and an improved transportation equation for the dissipation rate ε . The term realizable implies that the calculation of the Reynolds Stress complies with mathematical constraints that are consistent with those found in turbulent flows (Wilcox, 2000). This is expected to improve the turbulence model's ability to predict flows involving rotation, boundary layers under strong adverse pressure gradients, separation and recirculation. All features that are expected to dominate the flow around an interacting wing and rotating wheel.

McManus (2006) demonstrated the realizable $k-\varepsilon$ model's effectiveness during a computational study of Fackrell's experimental study (1975). Unlike Axon (1999), McManus modelled the geometry of the wheel and the wind tunnel to be identical to that used by Axon with the exception of the supporting struts used during the experiment. McManus managed to predict the separation point within 5 degrees to that measured by Fackrell and his pressure coefficients only varied significantly at the contact patch. While the previous mentioned studies were conducted using steady state solvers, an additional reason for McManus' improvement could be the use of an unsteady solver. Despite this investigation undertaken by McManus, it is not entirely clear if the realizable $k-\varepsilon$ model is most effective as results obtained by McManus using the Spalart-Allmaras model were also very similar.

3.1.2.5. Standard $k-\omega$ Turbulence Model

The $k-\omega$ turbulence model was the first two equation model initially proposed by Kolmogorov in 1942 who used the turbulence kinetic energy (k) and the dissipation per unit turbulence kinetic energy (ω) as the two parameters to determine turbulence (Wilcox,

2000). The parameter ω can also be used to describe the portion of turbulence associated with vorticity within the flow (Chung, 2002). Since 1942, the $k-\omega$ turbulence model has undergone numerous revisions with the most recent, and since, widely used version being derived by Wilcox (1998). Modifications implemented by Wilcox improved the $k-\omega$ turbulence model's ability to predict free shear flows such as those expected to form at the extremities of the wheel wake. One advantage it has over the $k-\varepsilon$ turbulence models is that it can be solved up to a boundary without requiring any modification but is also much more sensitive in the freestream than the $k-\varepsilon$ turbulence models (Wilcox, 2000).

Zerihan (2001) demonstrated that the $k-\omega$ turbulence model could more accurately predict the pressure coefficients over the central chord of his single element wing in comparison to the Spalart-Allmaras model. While the results were quite similar at ground clearances greater than 0.313c, at smaller clearances where separation was more prone, the comparison favoured the $k-\omega$ turbulence model. This trend was repeated when comparing the wake profiles created by the aerofoil. Despite being better than the Spalart-Allmaras model, the $k-\omega$ turbulence model over predicted the velocity wake deficit by approximately 20% of the freestream value.

3.1.2.6. Shear Stress Transport $k-\omega$ Turbulence Model

A more recent version of a $k-\omega$ turbulence model is the Shear-Stress Transport (SST) $k-\omega$ model proposed by Menter (1994). This differs from the standard $k-\omega$ model in that it gradually changes from the standard $k-\omega$ in the inner region of the boundary layer to a high Reynolds version of the $k-\varepsilon$ model in the far field. By doing so, it utilises the best features of both the $k-\varepsilon$ and $k-\omega$ turbulence models. A series of validation studies have been undertaken by Menter et al. (2003) demonstrating this turbulence model's ability to predict the separation point off an aircraft aerofoil and the velocity profiles within the wake of a ground mounted cube. Additionally, the authors highlight the SST $k-\omega$ turbulence models ability to be able to calculate the magnitude of both the lift and drag of an aircraft in comparison to that measured experimentally. This was considered as one of the advantages of the SST $k-\omega$ turbulence model in comparison to the more widely used $k-\varepsilon$ turbulence models. At this point in time, no computational study has been reported of either a downforce producing wing in ground effect or wheel study validating this

turbulence model, but this turbulence model will be considered during the validation investigation that will follow in the subsequent chapter.

3.1.2.7. Reynolds Stress Turbulence Model

The Reynolds Stress Turbulence Model (RSM) was originally proposed by Launder *et al.* (1975) and provides closure to the RANS equations by solving additional transport equations for each of the Reynolds stresses as well as the dissipation rate. As a result, this turbulence model requires that seven additional transport equations be solved when being applied to a three-dimensional flow field which in themselves are incomplete and require additional empirical models to provide closure. For this reason RSM is also known as a second-order or second-moment closure model (Versteeg and Malalasekera, 1998). RSM should theoretically improve the ability to predict streamline curvature, swirl and rapid changes in strain rate and therefore be superior at predicting cyclone flows, high swirling flows in combustors, rotating flow passages and stress induced secondary flow in ducts. Additionally, RSM should also prove beneficial in comparison to the $k-\varepsilon$ turbulence model when predicting flows with significant body forces.

Given that the RSM model is required to solve seven additional transport equations, to obtain convergence, this turbulence model is often found to be unstable or a greater number of iterations are required to obtain convergence. This further increases the computational resources required and therefore will not be considered for this study.

3.1.2.8. Boundary Layer Modelling and y^+ Values

The $k-\varepsilon$ and Reynolds Stress Turbulence models are better suited to predicting flows away from boundaries and as a result require a correction for the near wall regions when modelling wall bounded flows. The $k-\omega$ and Spalart-Allmaras turbulence models do not require a further correction as they have been formulated to be solved up to the boundary regions and therefore only require that the grid resolution adjacent to the boundary be adequately fine enough to do so. In order to achieve the required correction for the $k-\varepsilon$ and Reynold Stress models for regions near boundaries expected to provide a shear force to the flow, two different methods exist that utilise either a wall function or a near wall model.

The wall function, such as the one proposed by Launder and Spalding (1974), utilises an empirical formulation which assumes that the boundary layer takes a logarithmic profile while in reality this is not entirely correct for the complete turbulent boundary layer. The near wall model originally proposed by Jongen (1992) calculates both the linear, viscous sublayer and the logarithmic, turbulent upper layer which allows for a more representative turbulent boundary layer profile to be calculated. As a result, the near wall model requires a greater grid resolution adjacent to non zero shear boundaries which would otherwise not be required when the wall function has been employed making the wall function the more efficient of the two. While more computationally expensive, utilising the near wall models allows the turbulence models ability to predict separation points to be improved and therefore the ability to predict wall bounded flows to be enhanced. A numerical study conducted by Ramnefors *et al.* (1996) has also demonstrated that a near wall model is required to more accurately predict the drag of automotive bodies.

In order to obtain an initial indication whether a specific grid resolution adjacent to boundaries with a no slip condition is suitable for the chosen boundary layer technique, a y^+ value can be calculated using the following equation:

$$y^+ = \frac{\rho u_\tau y_p}{\mu} \quad \text{Equation 3. 17}$$

- where ρ is the density of the fluid, μ is the kinematic viscosity, y_p is the distance from the boundary to the centre of the adjacent control volume and u_τ is the friction velocity. It is recommended that when utilising a wall function y^+ values between 30 and 300 be employed while a near wall model requires that a y^+ value less than 3 be used.

Modelling the boundary layer accurately is expected to be a crucial requirement in predicting the flow features associated with both a wing and wheel given that both experience regions of adverse pressure gradients that lead to boundary layer separation. For this reason, all numerical results presented as part of this thesis that employ one of the $k-\varepsilon$ turbulence models, have been obtained utilising an enhanced wall model (Fluent, 2006). Similarly, given that the $k-\omega$ and Spalart-Allmaras turbulence models also require that the grid resolution is such that allows both the viscous sub layer and the turbulent

upper layer to be calculated, then it will be expected that a common grid can be used to compare the performance of the different turbulence models. While it is recommended that a y^+ value less than 3 and no less than 10 control volumes are used to capture the boundary layer profile when utilising a near wall model, a verification study has been undertaken to demonstrate that the wing and wheel forces are independent of these grid parameters and is reported on in Section 3.2.1.2.

3.1.3. Numerical Procedure

Now that the required equations to describe incompressible turbulent flow have been established, a method is required to solve them. Numerous commercially available Computational Fluid Dynamics (CFD) codes exist that can be used to achieve this. Fluent (2006) is one such CFD code that has frequently been used for related studies and is currently being used extensively in the motor sport industry on a wide range of problems (Akanni, 1995). Fluent utilises the finite volume method to solve the RANS equations and also offers the option of using the above mentioned turbulence and boundary layer models. Therefore, Fluent 6.1.18 (subsequently referred to as Fluent) was chosen to obtain all the computational results presented during this thesis and an outline is given here describing how Fluent solves the governing equations of fluid flow.

3.1.3.1. Finite Volume Method

The finite volume method was initially developed specifically to solve the equations of heat transfer and fluid flow and is now widely used in commercially available CFD codes. This technique is described in great detail by several texts including (Patanker, 1980 and Ferziger and Peric, 2002) and therefore only a brief description will be given here. The initial step of applying the finite volume method requires that the computational domain be divided into a discrete number of control volumes or cells. The strategy employed to achieve this for the wing and wheel computational model will be described later in this chapter during Section 3.2.1.2. Once this has been achieved, an integral form of the RANS equations can be applied to each control volume allowing the differential equations to take on an algebraic form such that each quantity ϕ can be calculated at the centre of the control volume.

3.1.3.2. Discretization Technique

The finite volume method requires that values be obtained at the finite volume's faces so that the values at the centre of the volume may be calculated. While this does not pose a problem for the control volumes faces that coincide with the domain's boundary, the remaining faces of the control volumes require a discretization technique to obtain this information from the control volume centre. Upwinding schemes were preferred over the central differencing schemes as they provide greater transportiveness and take into account the direction of the flow. Central differencing schemes are typically better suited to finer meshes where the velocities are extremely low and the effects of diffusion are dominant.

Fluent provides multiple upwinding discretization techniques of which the second-order upwinding scheme was chosen for all results presented in this thesis. While a first order upwinding scheme is more computationally efficient and stable, it assumes that the value at the centre of the control volume is equal to the values at the faces of the control volumes. The second-order upwinding scheme utilises a multidimensional linear reconstruction technique instead which considers values located at the centre of multiple surrounding control volumes by using a Taylor series expansion. This allows a higher degree of accuracy to be achieved particularly for meshes that are not strictly aligned with the flow, by reducing the truncation errors associated with a first order scheme which results in unrealistic numeric diffusion (Fluent, 2006). Given that the wheel and wing are expected to have significant regions of separation and it will therefore be difficult to align the mesh with the fluid flow particularly in the wake of these bodies, it was considered necessary to utilise a second order upwinding scheme for all the momentum and turbulence equations. Similarly, previous numerical investigations of either a wing (Zerihan, 2001) or a wheel (Axon, 1998) have successfully used this discretization technique.

3.1.3.3. Solution Process

Fluent allows for either a density based solver or a pressure based solver to be used of which the former is recommended for subsonic incompressible flows and was therefore used for all the computational results presented in this thesis. Two different pressure

based algorithms are also offered that allow the governing equations to be solved either sequentially or in a coupled manner. Of these two, a segregated algorithm was selected as this solves for u , v , w or P individually and therefore only requires that the discretised equations for a single variable be loaded in the memory at any one time. Alternatively, a coupled solution solves for all variables simultaneously requiring greater data to be stored in the memory and increasing the required computational resources. The segregated algorithm therefore requires that the three velocity components be initially solved sequentially prior to a correction being applied by a velocity-pressure coupling which is then followed by a re-calculation of the turbulence properties. This loop is then repeated until the required convergence has been obtained (Figure 3.3).

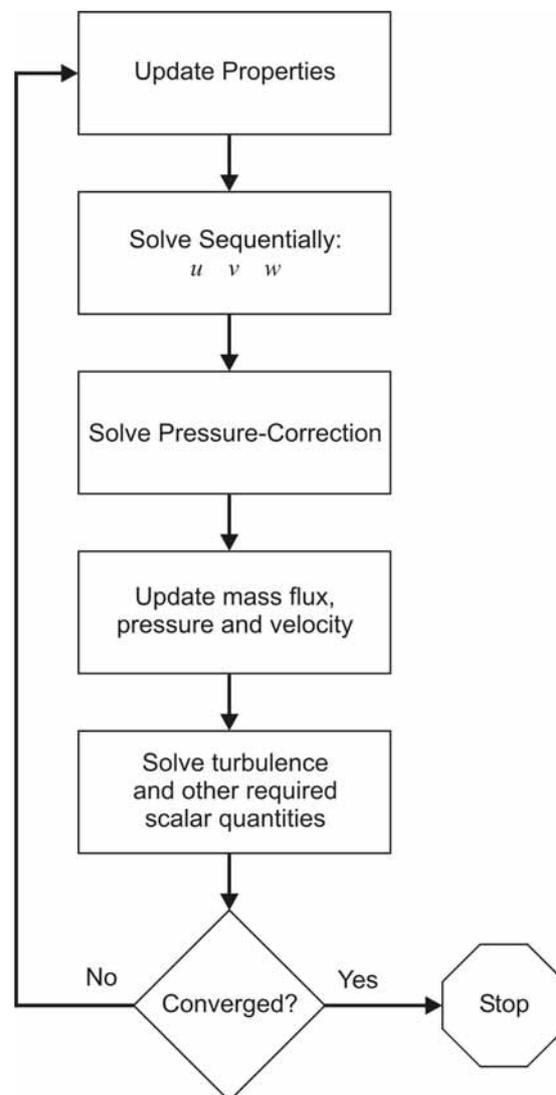


Figure 3.3 Flowchart describing Pressure Based Segregated Solver

In the process of determining each of the variables using the pressure based segregated algorithm, an implicit formulation has been used. This allows each of the unknown variables to be calculated using values which are both known from the previous iteration and unknown and belonging to the next iteration from the neighbouring control volumes using a series of simultaneous equations. While being more computationally expensive, this technique is considered to be more stable than the alternative explicit technique which solves for a given variable by only using the data which is known for the surrounding control volumes from the previous iteration. Advantages of using an implicit scheme rather than an explicit formulation include quicker convergence and a more stable solution (Shaw, 1992).

3.1.3.4. Velocity-Pressure Coupling

As mentioned previously, the pressure based segregated solver requires that each of the velocities be solved sequentially prior to a correction being applied to the pressure. This is referred to as pressure coupling and this was achieved by using a variation of the Semi-Implicit Method for Pressure Linked Equations (SIMPLE) called SIMPLE-Consistent (SIMPLEC) which was originally proposed by Van Doormal and Raithby (1984). The two methods differ only in the way that the face flux correction is calculated and is reported to be able to allow for convergence to be obtained in less iterations. This is because the use of the SIMPLEC velocity-pressure coupling allows for higher under relaxation factors to be used. The chosen velocity-pressure coupling has also been used during past computational investigations of a wheel by McManus and Zhang (2006)

3.1.3.5. Flow Initialisation and convergence criteria

In order to obtain a solution, values are required from the previous iteration in order to obtain a solution at the subsequent iteration. Therefore, prior to commencing the iteration process all the control volumes in the computational domain must all be initialised using specified values. For all the computational results presented in this thesis, the computational domain was always initialised using the inlet freestream conditions as this was determined to provide the quickest convergence as opposed to initialising the flow domain with zero values.

In order to determine when convergence had been established, all computational models were iterated until the lift and drag forces of the wing and wheel were determined to have not varied by more than 1% over the last 1000 iterations. The number of iterations required to reach this level of convergence varied amongst the different geometries tested to be between 6000 and 8000 iterations. In all cases a residual convergence of greater than 10^{-4} was obtained prior to the lift and drag values reaching their converged result.

3.1.4. Validation and Verification Requirements

The AIAA Guide to Validation and Verification (V&V), 1998 defines Verification as “the process of determining that a model implementation accurately represents the developer’s conceptual description of the model and the solution to be modelled”. Validation is defined as “the process of determining the degree to which a model is an accurate representation of the real world from the perspective of the intended uses of the model”. It is suggested that the computational model be validated against experimental results only after a verification study has been undertaken. Both procedures are vital but have no specific completion and this must be determined by the user considering the budgetary constraints and the intended use of the model (AIAA, 1998).

3.1.4.1. Verification Process

The AIAA Guide indicates that the first step to verifying the computational model requires that the parameters that can affect the accuracy of the model be defined. For this investigation, they have been determined to be;

- Grid density
- Height and number of control volumes adjacent to the non zero shear boundaries (or y^+ value)
- Iterative convergence, and
- Boundary positions relative to the wing and wheel

To determine if the computational result is independent of the parameters described above, the AIAA Guide recommends that they be systematically varied and compared to

an extreme solution. A way to quantify the errors for a desired variable associated with the grid density is outlined by Celik and Zhang (1995) that utilises Richardson's extrapolation technique to calculate a Grid Convergence Index (GCI). The forces acting on the wing and wheel have been selected as the variables to calculate the GCI for given that these will be a significant point of discussion during the wing and wheel investigations. Once the GCI has been determined for a grid resolution that is a suitable compromise between accuracy and computational expense, the remaining variables have also been investigated to ensure that the error introduced by these characteristic are all smaller than the specified GCI. The results of these investigations will be shown in Section 3.2.

3.1.4.2. Validation Process

Validation requires that results obtained using a numerical model be compared to those obtained experimentally. The AIAA (1998) indicates that a validation test is expected to demonstrate that the numerical model can reproduce trends obtained by an experiment and not necessarily obtain agreement with a high level of accuracy.

It is recommended by the AIAA that a "building-block" approach be taken to validating a computational model. Instead of using the computational model to simply demonstrate that it is capable of reproducing the flow features required of the final case, it is advised that it be broken down into a series of subsystems. Once it is demonstrated that the computational model is capable of predicting the flow associated with these simpler problems, the complete model can be validated. This approach has been taken for this study. While the final goal was to validate a numerical model of an interacting wing and wheel, in the process comparisons have also been made to results published of an isolated wing as well as that of an isolated wheel. The results of these comparisons are presented in the following chapter.

3.2. Description of Computational Model Geometries

A commercially available 3D CFD pre-processing package (Gambit 2.3.16) was used to discretise the computational domain for all the numerical models presented as part of this thesis. Two specific computational model geometries were created to investigate the

aerodynamic interaction of the wing and wheel. The first, hereafter referred to as the ‘full-scale’ computational model, was created to replicate the operating conditions, and scale, experienced by a generic full-scale open wheel racing car as originally outlined in Chapter One. The second, “scaled” model was developed to identically reproduce the experimental configuration and test conditions discussed in Chapter Two.

Given that the full-scale computational model would be used for the majority of the investigations presented as part of this thesis, the verification steps described here initially focused on this computational model. While a turbulence model comparison has been undertaken and is described in the following chapter, all the verification was undertaken with the $k-\varepsilon$ realizable model. Additionally, the wing height, span and angle of attack values during this study have been maintained at 0.13c, 1.42c and 8° respectively while the wheel width and track are set at 0.631c and 1.6c respectively.

3.2.1. Full-scale computational model

The full-scale computational model was created to reproduce numerically the conditions that would be expected to be experienced by a combined wing and wheel operating on a generic open wheel racing car. As a result, a full-scale wing and wheel (with chord and diameter of 562.5mm and 660mm respectively) were chosen with an inlet velocity of 33.3ms^{-1} as initially outlined in Chapter One. This equates to a Reynolds number of 1.28×10^6 based on the wing chord and 1.50×10^6 based on the wheel diameter.

The full-scale computational model (Figure 3.4) was developed to ensure that the wing and the wheel were modelled without any constraints from the surrounding boundaries. Therefore, a study was undertaken to ensure that both the top and side boundaries were located adequately far enough to ensure that this was the case. Similarly, the location of the model inlet and outlet was also varied too ensure that their location also had little influence on the final computational result. Prior to this, a grid refinement study was undertaken focussing on two key areas; the off body density of the cells making up the domain; as well as the height of the first cell and the number of cells located perpendicular to all boundaries expected to contribute a shear force to the flow within the domain.

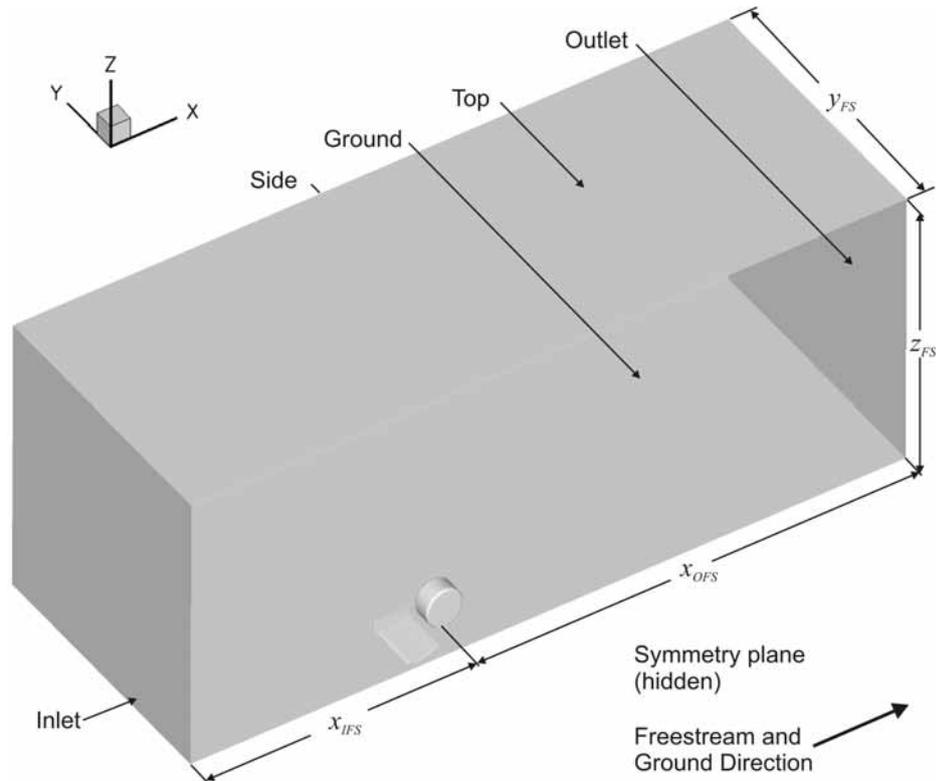


Figure 3.4 Computational domain and boundaries of the full-scale computational model

3.2.1.1. Full-scale Computational Model Boundaries

As Figure 3.4 demonstrates, the full-scale computational model consists of an inlet, outlet, symmetry, ground, upper and side boundaries. Both the upper and side boundaries have been modelled as walls with zero shear while the ground has been modelled as a smooth moving wall with a velocity equal to that of the freestream velocity. The process in which the location of these boundaries was determined will be reported on in Section 3.2.1.1. The wing and the wheel have also been modelled as smooth walls while an angular velocity of 100.9rads^{-1} has been applied to the wheel boundary about its own axis so that the wheel's tangential velocity at the circumference is equal to that of the freestream velocity and also produces a zero slip condition with the ground at the contact patch. In order to reduce the size of the computational model, a symmetry plane has also been used allowing half the wing and only a single wheel to be modelled as opposed to the complete wing and a pair of wheels. The outlet was modelled as a pressure outlet while the inlet was modelled as a velocity inlet which utilised a constant velocity, turbulence

intensity and length scale (l) of 33.3ms^{-1} , 0.15 and 0.327 respectively of which the latter was calculated using the following equation using the inlet height as the reference length (Versteeg and Malalasekera, 1998):

$$l = 0.07h_{ref} \quad \text{Equation 3. 18}$$

3.2.1.2. Mesh structure description and verification

The grid structure of the full-scale computational model can be described as consisting of two portions: the first being a volume created by offsetting the surface of the ground, wing and wheel surfaces, which from hereafter will be described as the “boundary layer mesh”, and the second region surrounding the boundary layer mesh and extending to the outer boundaries which shall be referred to as the “off surface mesh”. Portions of the boundary layer and off surface mesh can be visualised in the surface mesh at the junction of the symmetry plane and the wing surface (subset figure in Figure 3.5).

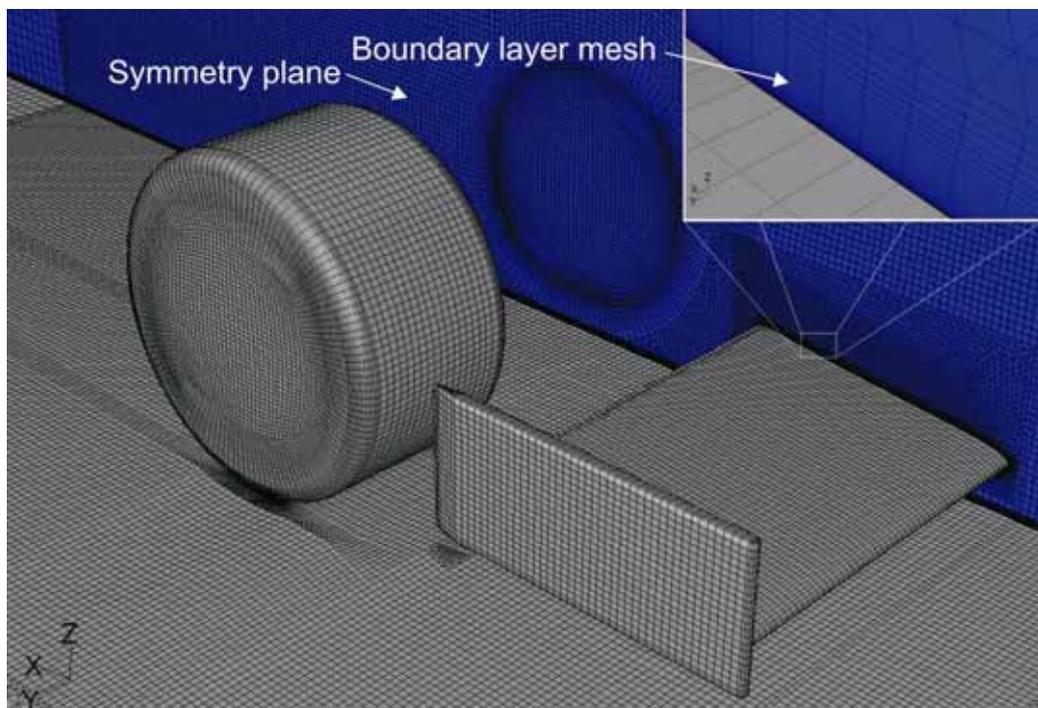


Figure 3.5 Surface mesh indicating grid structure of full-scale computational model

The off surface mesh consisted of four refinement regions which doubled in size for each successive region. The three most outer refinement zones consisted of structured controlled volumes arranged to be parallel with the orthogonal directions while the finest refinement region mostly consisted of a structured O-grid around the wheel (Figure 3.5). Due to the complexity of the combined wing and wheel geometry, and to allow for some automation in the grid generation, regions between the wing and the wheel and surrounding the wing between the endplate and the symmetry plane were meshed using triangular prisms.

The four different refinement regions were connected by three regions of unstructured cells as it was not possible to create hanging nodes with the pre-processing software that was used. This is a common technique used by other solvers that are incapable of handling hanging nodes and a comparison to a more conventional grid where the aspect ratio of the cells is increased towards the surrounding boundaries indicated that no variation in the flow structures were obtained using this technique despite being more computationally efficient.

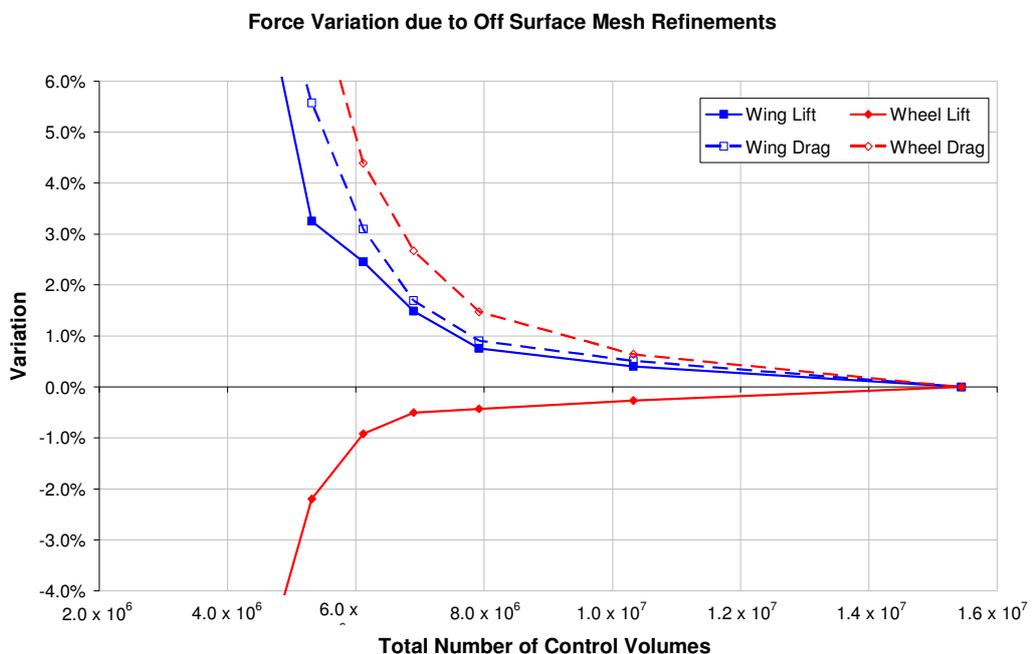


Figure 3.6 Variation in wing and wheel, lift and drag due to off surface mesh density

The first verification step undertaken was to determine the number of control volumes required to obtain a grid independent result. This was achieved by adjusting the reference length of the control volumes from values between 0.02c to 0.04c in increments of approximately 0.0033c. The characteristic length describes the spacing of the mesh around the circumference of the wheel which when adjusted altered the entire off surface mesh resolution in a proportional manner. This resulted in a series of models being created with a total number of control volumes ranging from 4.5×10^6 to 15.5×10^6 which were each iterated until the forces associated with the wing and wheel had converged as described previously. The variation in the lift and drag of the wing and wheel due to the mesh size was then calculated by comparing each result obtained to that obtained with the model with the smallest characteristic length and therefore the largest number of control volumes (Figure 3.6) as suggested by the AIAA (1998).

Doing so indicated that a model with approximately 8×10^6 control volumes did not alter the lift and drag of both the wing and the wheel by no more than 2% in comparison to a computational model with twice this number of control volumes. This was considered to be a suitable compromise between accuracy and the computational resources required to obtain a solution as the computational model with 8×10^6 control volumes required approximately 30 hours to converge on 10 nodes in parallel while the larger model required approximately 90 hours. The Grid Convergence Index (GCI) was also calculated for this grid density to obtain a better indication of the error associated with the lift and drag of both the wing and the wheel due to the grid dependency. The GCI utilises the Richardson extrapolation technique, to determine the error introduced for a specific parameter for a selected mesh density in comparison to a theoretical asymptotic value and is calculated using the following equation (Celik and Zhang, 1995):

$$GCI = \frac{F_s |\epsilon| r^p}{(r^p - 1)}, \quad \epsilon = \frac{f_{coarse} - f_{fine}}{f_{coarse}}, \quad r = \frac{h_{coarse}}{h_{fine}} \quad \text{Equation 3. 19}$$

- where F_s is the factor of safety employed dependant on the number of mesh intervals calculated, p is a factor describing the order of convergence and f_{coarse} and f_{fine} are the parameters for which the GCI is required to be determined for using the values calculated with two different grids with a characteristic length of h_{coarse} and h_{fine} . For instances that more than two grid resolutions have been tested and a second order calculation has been

undertaken, a factor of safety value of 1.25 and convergence factor of 2 are recommended (Celik and Zhang, 1995). The GCI calculated using the above constants for a grid with characteristic length of $0.0266c$ in comparison to the finest grid solved are shown in Table 3. 1 for the forces acting on the wing and wheel. These values will be used as an estimate of the error associated with the lift, drag and side forces and will be displayed as error bars in all figures that include these results from Chapter Four and onwards.

	Wheel	Wing
Lift	1.2%	2.2%
Drag	4.2%	2.6%
Side-Force	5.2%	Not Applicable

Table 3. 1 GCI calculated for grid with characteristic length of $h_{grid}=0.0266c$

Following the off surface dependency check, the boundary layer mesh was then investigated to determine the dependency of the wing and wheel lift and drag results on the number of the control volumes along the height of the boundary layer mesh. This was considered necessary given that the enhanced wall function was being utilised which required y^+ values over all boundaries providing a shear force to the flow to be less than 3 and that adequate resolution be provided so that both the viscous and turbulent layers of the boundary layer may be captured. Therefore, the number of control volumes in the height of the boundary layer mesh was adjusted such that the height of the control volume furthest from the boundary remain unchanged and the first cell height, which influences the y^+ value, is reduced as the number of control volumes is increased. The height of the boundary layer mesh (or the offset from the wing, wheel and ground surfaces) was maintained at $0.0333c$ or $0.0284d$ for all the computational results presented in this thesis. This investigation included eight different grids with the number of control volumes in the boundary layer height being varied from 34 to 48 in increments of two which were each solved until the previously mentioned convergence criteria had been met. The variation in the results were then determined by comparing each result to that obtained with the highest resolution in the boundary layer mesh (Figure 3.7).

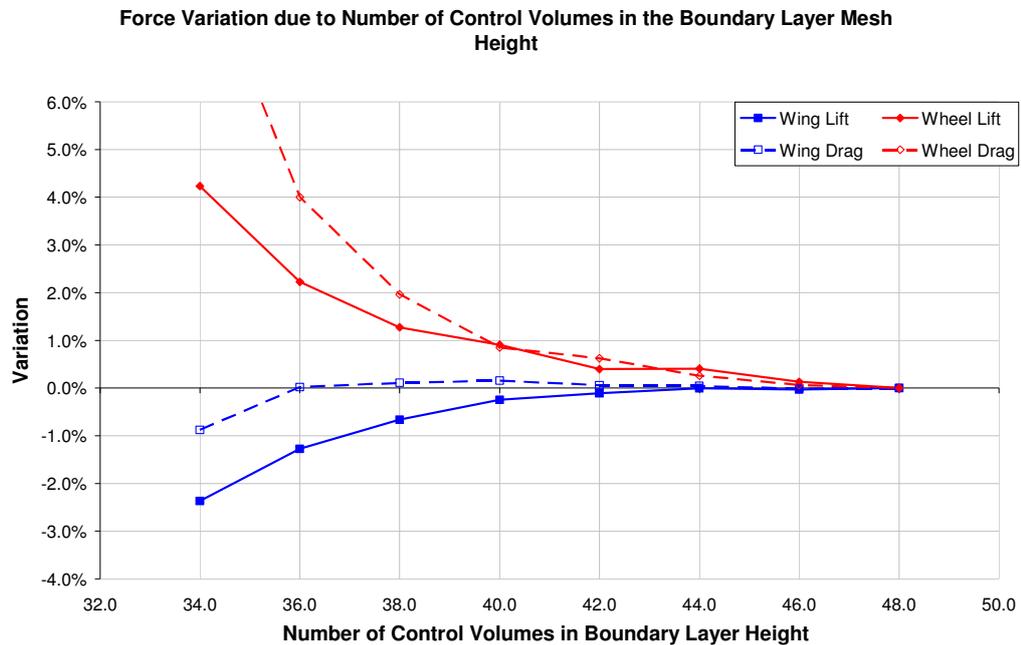


Figure 3.7 Variation in wing and wheel, lift and drag due to number of control volumes in boundary layer height

Through this investigation, it was determined that 40 control volumes were required to obtain lift and drag results for the wing and wheel within 1% of that obtained with the greatest number of control volumes in the height of the boundary layer tested. Reviewing the y^+ values over the ground, wing and wheel also indicated that the highest y^+ value obtained is approximately 1.5 which is approximately half of what is required for the two layer wall function (Fluent, 2006). It was decided therefore to proceed with this resolution in the boundary layer mesh for all subsequent computational results as well as an off surface grid characteristic length of 0.0266c.

3.2.1.3. Inlet, Outlet, Top and Side Boundary Positions

The position of the inlet, outlet, top and side boundaries were all independently adjusted to ensure that their position had little effect on the lift and drag values obtained of the wing and wheel with the full-scale computational models. The boundaries were tested in the order shown in Figure 3.8 and once each of the optimum boundary positions were selected, they were maintained for the subsequent tests. The results of adjusting these

boundaries are shown in Figure 3.8 and are presented as a comparison to the largest value tested for each respective boundary position.

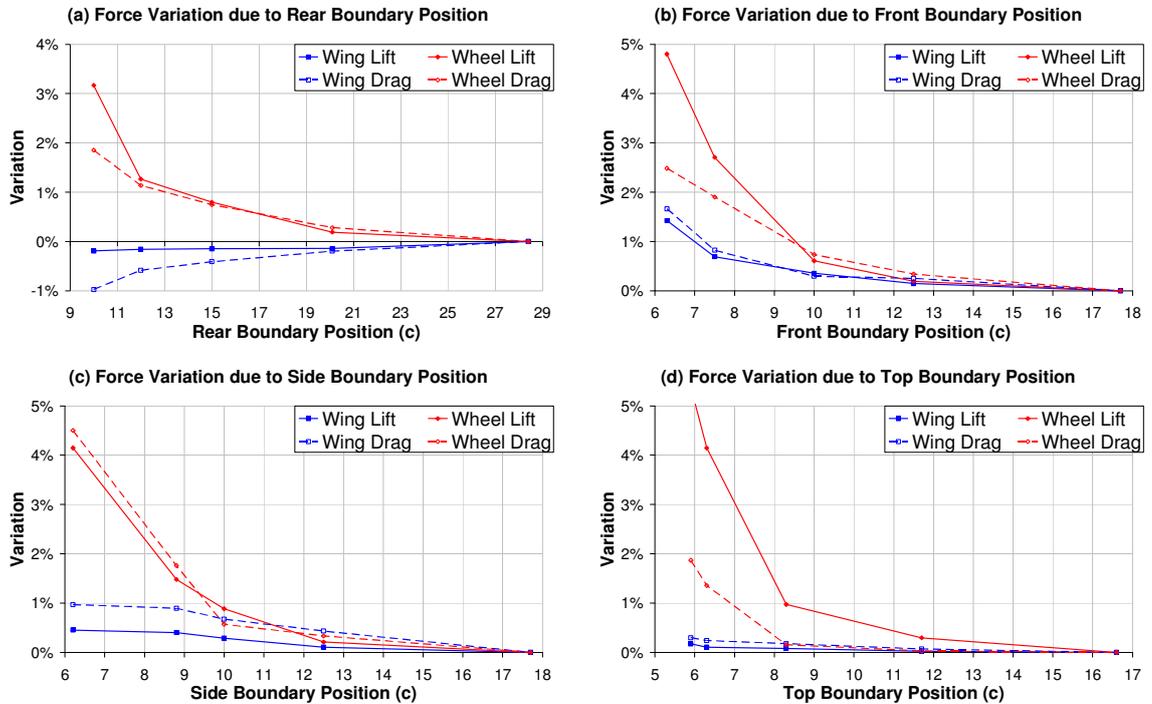


Figure 3.8 Variation in wing and wheel, lift and drag due to boundary positions

It was decided to maintain the boundary in a position which ensured that the lift and drag of the wing and wheel was not altered by more than 1% when compared to a boundary position approximately twice the chosen value. This value was chosen as it was less than the smallest GCI calculated for the selected grid characteristic reference length. With the exception of the front boundary at the smallest distance tested (Figure 3.8b), the lift and drag of wing was always within the chosen tolerance for the boundary positions tested, while the wheel lift and drag demonstrated greater sensitivity to the boundary positions. As a result, the lift and drag of the wheel became the determining factor for the location of the boundaries (as shown in Figure 3.4) and therefore, the inlet (x_{IFS}) and outlet (x_{OFS}) was chosen to be positioned 9.3c and 15.6c from the wheel centre respectively while the side (y_{FS}) and top (z_{FS}) boundaries were located 8.8c from the symmetry plane and 8.3c from the ground respectively.

3.2.2. Scaled computational model

The scaled computational model was created with the sole intention of being used to compare directly to the LDA results in order to determine the validity of the computational method employed. For this reason, the scaled computational model has been developed to replicate the experimental setup described in Chapter Two while trying to maintain as many of the features of the full-scale computational model as possible. In order to mimic the experimental set-up, the wheel sting, moving ground fairing geometry and the wind tunnel test section walls have all been included in this computational model (Figure 3.9). Additionally, due to the smaller scale of the experimental apparatus, the computational model was scaled such that the wing chord and the wheel diameter are equal to that of the wind tunnel models (75mm and 88mm respectively).

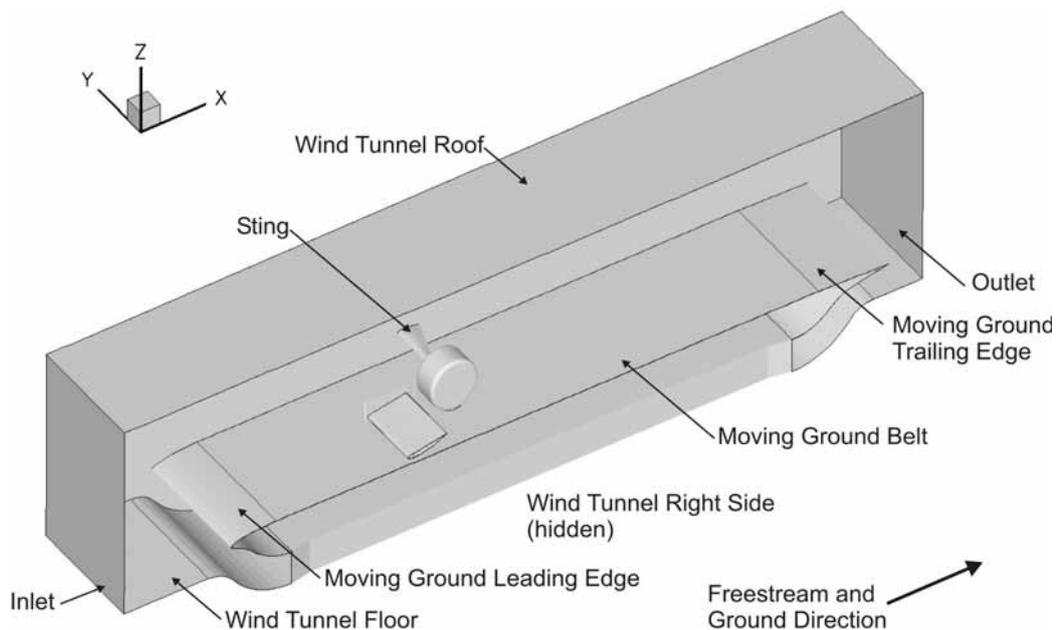


Figure 3.9 Computational domain and boundaries of the scaled computational model

In order to duplicate the experimental freestream conditions, the inlet velocity and turbulent length scale were modified to be 10ms^{-1} and 0.0462 respectively. The turbulence intensity was maintained at 0.15% as this was the average value originally measured at the inlet of the tunnel using the LDA system. The inlet was positioned at the start of the test section and given that this was further upstream than the 9.3c used by the full-scale computational model, this was not investigated any further. In order to have the outlet in the same relative

position as that of the full-scale computational model (15.6c downstream of the wheel rotation axis), it was necessary to extrude the rear of the test section further rearward. As in the full-scale computational model, the outlet was once again modelled as a pressure outlet.

Due to the variation in scale and the reduction in the freestream velocity, the velocity of the moving ground was also set to 10ms^{-1} while the angular velocity of the wheel was modified to be 227.3rads^{-1} . This angular velocity once again ensured that the tangential velocity of the wheel circumference was equal to the freestream velocity and that a zero slip condition was modelled at the contact of the wheel and the moving ground belt. The wheel and the wing surfaces were again modelled as smooth walls with the only additional modification made to the boundaries of the scaled computational model relative to the full scale computational model was the removal of the symmetry plane which was replaced by the left wind tunnel wall. Like the wheel sting, the moving ground fairings, duct and remaining wind tunnel walls were modelled as a smooth surface.

3.2.2.1. Mesh structure description and verification

While the off surface grid structure and characteristic length is identical to the full-scale computational model (0.0266c), the additional boundaries and the lower freestream velocities of the scaled computational model required that some modifications be made to the boundary layer mesh. For this computational model, the boundary layer mesh was required to be created offset not only from the wing, wheel, and ground, but also from all the wind tunnel walls, sting, duct, and moving ground fairings.

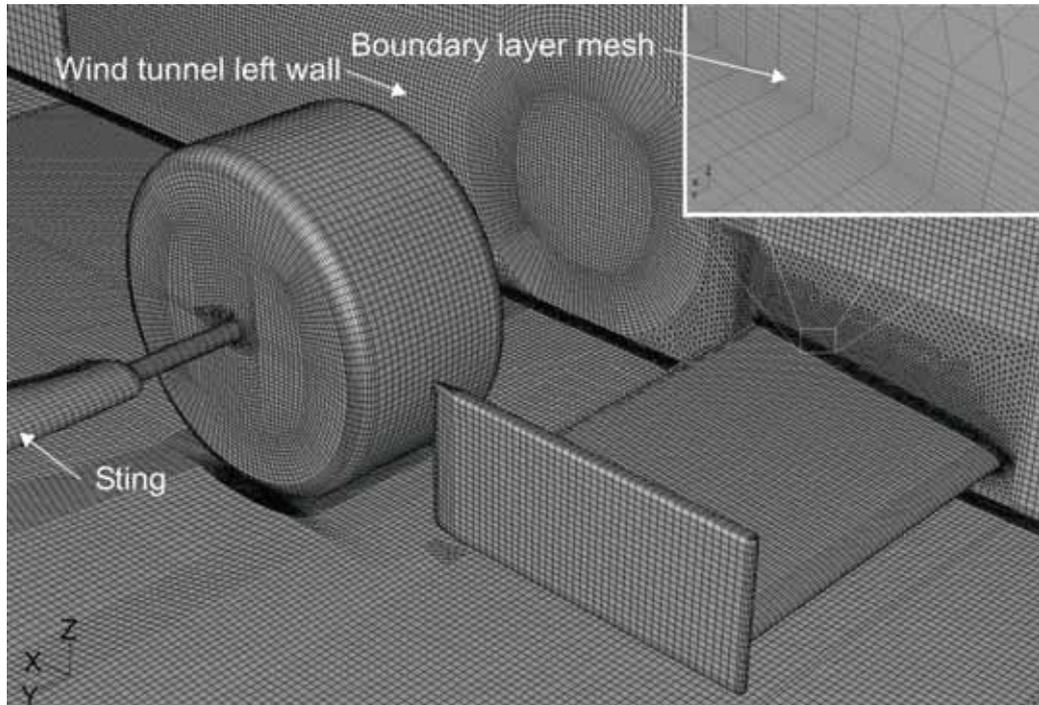


Figure 3.10 Surface mesh indicating grid structure of scaled computational model

Due to the additional regions that required a boundary layer mesh and the reduced freestream velocity, the number of control volumes in the boundary layer mesh height was reinvestigated in order to make the scaled computational model less computationally expensive. A similar method to that used previously for the full-scale model was once again employed to determine the number of control volumes required in the height of the boundary layer. Values in the range of 10 to 20 were tested in increments of 2 of which the results are shown in Figure 3.11.

This investigation determined that the lift and drag of the wheel for the scaled computational model required 14 control volumes in the height of the boundary layer mesh. While this is a significant reduction to the number of control volumes required in the boundary layer mesh in comparison to the full scale computational model, this did not significantly alter the y^+ values obtained with the highest values of approximately 2 being reordered on the wing and wheel surfaces. Due to the significantly reduced number of control volumes in the boundary layer mesh in comparison to the full-scale computational model, the complete scaled computational model consisted of approximately 6.5×10^6 control volumes.

Force Variation due to Number of Control Volumes in the Boundary Layer Mesh Height

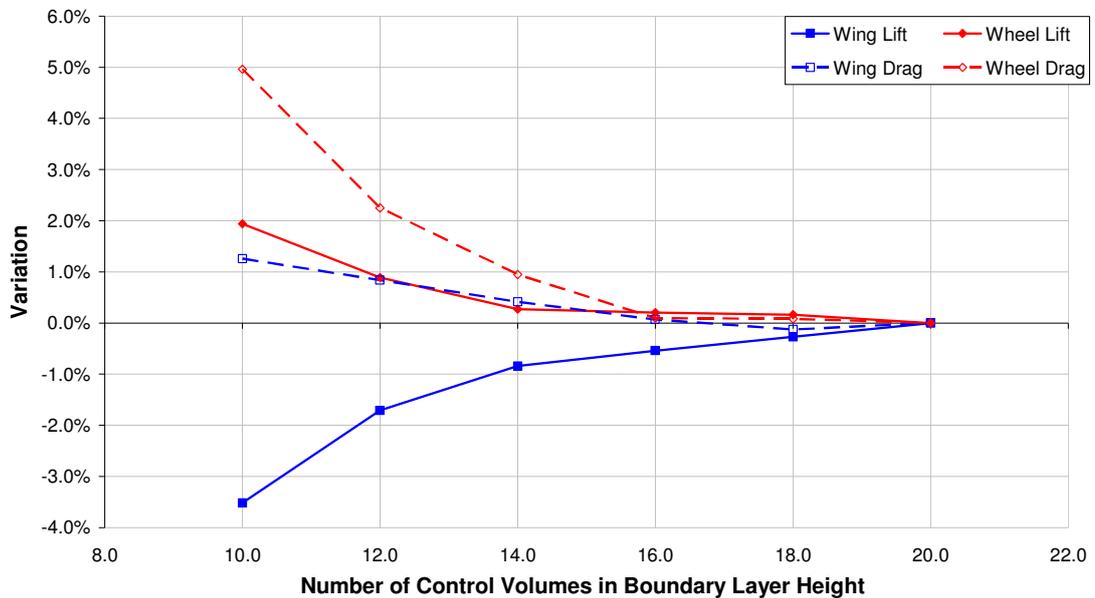


Figure 3.11 Variation in wing and wheel, lift and drag due to number of control volumes in boundary layer height for the scaled computational model

This computational model can now be used to obtain an indication of how reliable the computational method will be at predicting the flow structures associated with an interacting wing and wheel prior to the full-scale model being used to investigate the wing and wheel interaction.

3.3. Computational Hardware Requirements

Given that the full scale computational model consisted of approximately 8×10^6 control volumes, it was necessary to employ a cluster in order to solve the computational model. For all the computational results presented in this thesis, the “Barossa” cluster at the Australian Centre for Advanced Computing and Communications was used which has available 155 dual 3GHz Pentium 4 nodes with each node consisting of 4GB of memory. In order to obtain the necessary memory requirements to solve the computational models, five nodes were used in parallel and therefore, each simulation required approximately 24 hours for to be completed.

3.4. Summary

Two computational models have been created to replicate either the conditions experienced by a wing and wheel operating on a full scale open wheel racing car or that of the wind tunnel apparatus previously described in Chapter Two. Both computational models utilise the incompressible RANS equations, a segregated pressure based solver, and an implicit formulation in conjunction with the finite volume method. For the convective and viscous terms of the RANS equations, a second order upwind discretization scheme was employed while pressure-velocity coupling was implemented by utilising the SIMPLEC algorithm. For results presented during the course of the verification study determining the full-scale model's sensitivity to the grid resolution, y^+ values and boundary positions, closure was provided to the RANS equation with the aid of the $k-\varepsilon$ realizable turbulence model with an enhanced wall function. Several different turbulence models will be tested in the proceeding chapter using the scaled computational model in order to demonstrate that the $k-\varepsilon$ realizable turbulence is the most appropriate turbulence model for a combined wing and wheel investigation.

Chapter 4: Validation of Computational Model

Prior to conducting any investigations, a validation study was undertaken to ensure that the computational model realistically portrays the flow features associated with a wing and wheel working independently or in unison. As stipulated by the AIAA Guide to Validation and Verification (1998), the aim of this validation study is to demonstrate that trends obtained experimentally can be reproduced by the computational model. Initially, results obtained with several different turbulence models were compared to LDA measurements made in the wake of the wing and the wheel in order to determine the most suitable turbulence model. Then, published experimental results by Zerihan (2001) and Fackrell (1975) were used to demonstrate that previously reported variations in lift, drag and flow structures of an isolated wing or wheel could be reproduced by the computational model. Additionally, a comparison was also conducted to computational results obtained by McManus (2006) using an unsteady model to demonstrate that the same flow features can be obtained using a steady state model. Lastly further comparisons are made with LDA results to demonstrate that the computational model can accurately reproduce the variations in flow structures associated with changes in the wing span and angle of attack of the wing (parameters that will be investigated in the following wing and wheel interaction study).

4.1. Selection of Turbulence Model

Five different turbulence models that have been previously used in the computational modelling of wheels (Axon 1998 and Wray, 2003), or wings (Zerihan and Zhang, 2000), have been tested here, using the scaled computational model, to determine the most suitable in predicting the three-dimensional flow characteristics of the interacting wheel and wing in ground effect. These included the Spalart-Allmaras, $k-\epsilon$ standard, $k-\epsilon$ Realizable, $k-\epsilon$ RNG and $k-\omega$ SST turbulence models. For all the comparisons shown here using a $k-\epsilon$ turbulence model, an enhanced wall model has also been used (Fluent, 2006). To choose the most appropriate turbulence model, a single operating condition for the wing and wheel combination was selected as the test case. For this case, the wing span, ride height, angle of attack, wheel track, and wheel width were chosen to be $S/c=1.40$,

$h/c=0.13$, 8° , $T/c=1.60c$, and $W/c=0.63c$ respectively. This configuration, and the planes on which the comparisons were conducted at, are depicted in Figure 4.1.

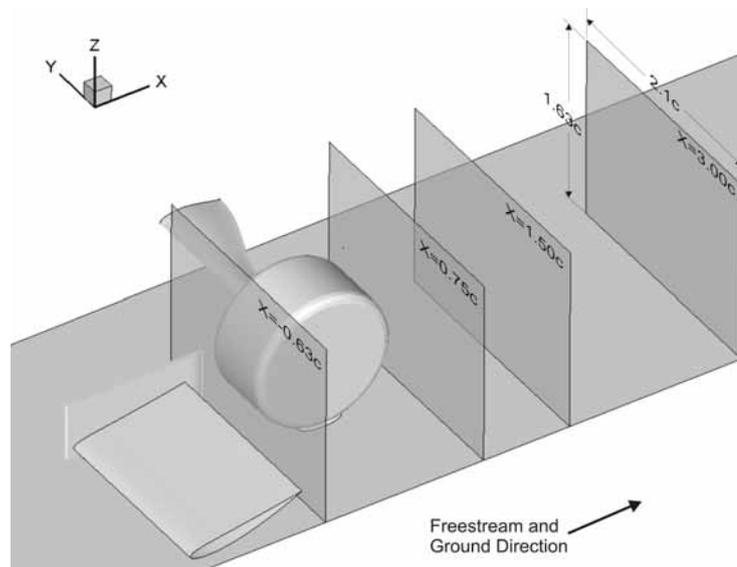


Figure 4.1 Planes on which comparisons are conducted on

Using the freestream velocity as the reference velocity, normalized x-velocity and in-plane velocity vectors were initially used (Figure 4.2 to Figure 4.4) to compare each turbulence model with the experimental LDA results, to determine which model best predicted the flow structures. This comparison was then repeated using the turbulence intensity at the same planes (Figure 4.5 to Figure 4.7). Based upon these results, a turbulence model was then chosen to be validated further against other LDA and published experimental results.

4.1.1. Turbulence Model comparisons of x-velocity and x-plane velocity vectors

For the plane located between the wing and wheel ($x/c=-0.63$) shown in Figure 4.1, all turbulence models have predicted the normalised x-velocity and in plane velocity magnitude with varying degrees of success. Qualitatively, all turbulence models adequately predict the x-velocity deficit in front and approximately mid height of the wheel as well as forward and above the contact patch region (Figure 4.2). The first of these two regions, located at $z/c=0.6$, $y/c=1.3$, indicate the stagnation point expected to form at the most upstream location of the wheel (McManus, 2006). For this reason, large horizontal and vertical in plane velocity components approximately equal to the free stream velocity

have been obtained surrounding this point. All the turbulence models successfully predict the location and effect of the stagnation region and little variation is observed for this feature amongst the different turbulence models tested.

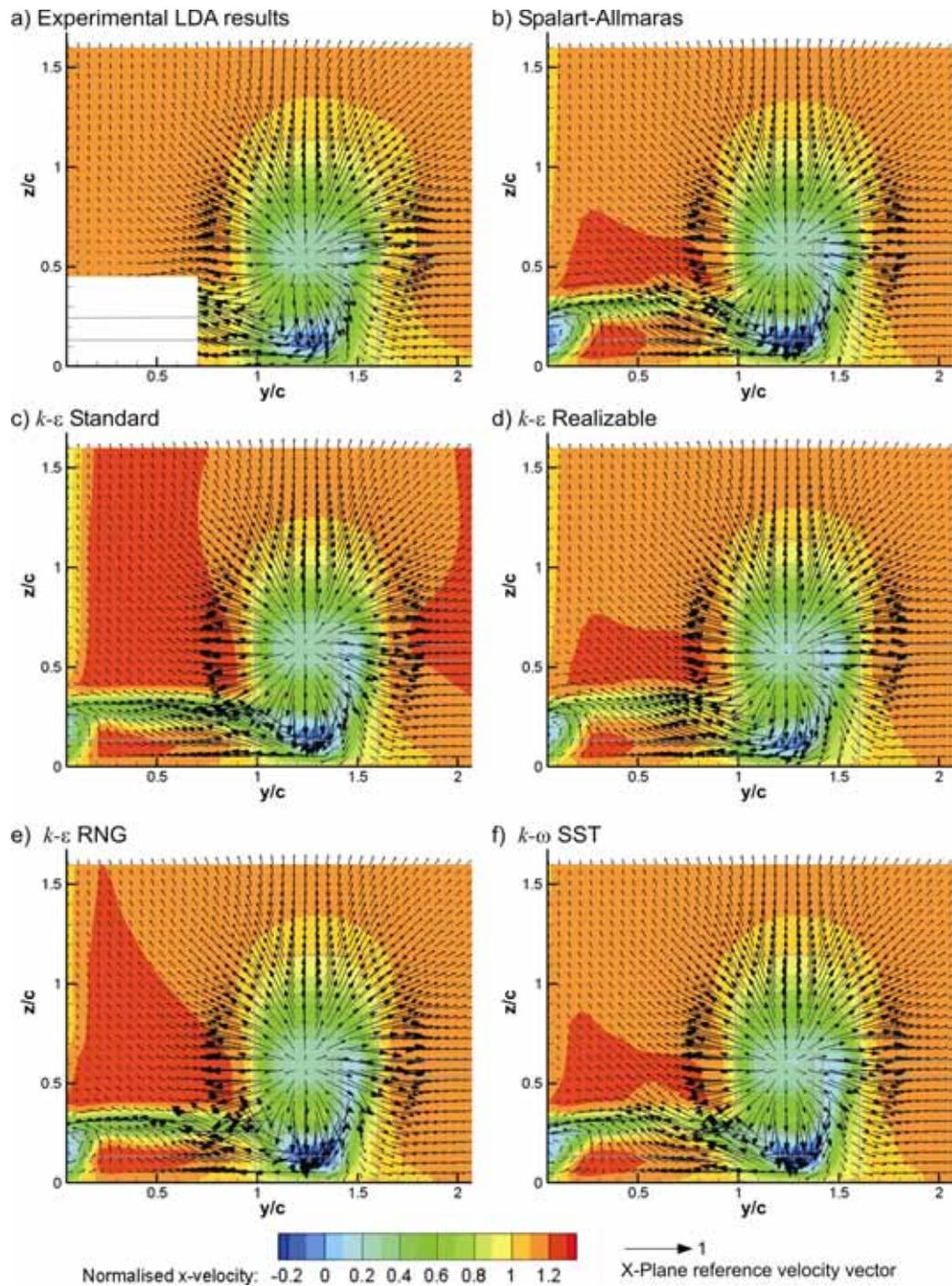


Figure 4.2 Normalised x-velocity and in plane comparisons to LDA results on $x/c=-0.63$ plane

The second region, located at $z/c=0.2$, $y/c=1.3$, indicates the location that the main wing vortex passes through the $x/c=-0.63$ plane. As indicated by Zerihan (2001), this vortex is formed by the pressure difference created about the bottom edge of the wing's endplate. Consistent with this explanation, this flow feature is located inboard of the endplate's bottom edge which is indicated by the grey outline. The core of this vortex is expected to pass through the $x/c=-0.63c$ plane, forward of the wheel with an oblique angle relative to this plane due to the influence of the high pressure region created forward of the wheel's contact patch (Fackrell, 1970). The local normalised x-velocity component in this region due to this flow structure was measured to be a normalised value of approximately -0.2 (Figure 4.2a). Additionally, the formation of a secondary wing vortex generated from the pressure differential across the top edge of the endplate (Zerihan, 2001) is also evident at $y/c=1.5$, $z/c=0.6$ by a third, smaller region where the x-velocity reduces to a value of 0.2 (Figure 4.2a). Once again, all the turbulence models indicate a similar velocity deficit and location for both these vortex structures.

An additional flow feature measured behind the wing and forward of the wheel is a strong cross component velocity adjacent to the ground in the region of $0.7 < y/c < 1.3$ (Figure 4.2a) caused by the suction generated beneath the downforce producing wing and the subsequent upwash created behind it. The extent of the inboard and vertical component of the cross flow is consistent amongst the computational results obtained with the $k-\epsilon$ RNG model being the only exception, indicating a larger vertical velocity component (Figure 4.2e) in this region. Another weakness of the $k-\epsilon$ RNG model was the inability to predict the effect of the blockage of the wing, wheel and sting in the tunnel. As a result, the region inboard of the wheel (Figure 4.2c) was accelerated to an x-velocity value approximately 10% faster than which was measured during the experiments (Figure 4.2a). The $k-\epsilon$ standard model also suffered from a similar problem (Figure 4.2c) to a much greater extent with the outboard region also experiencing a similar velocity increase.

Two features predicted by all the turbulence models tested are; the formation of a vortex at the junction of the wind tunnel wall and the wing ($y/c=0.05$, $z/c=0.2$); and the wake of the wing ($0 < y/c < 1$, $z/c=0.25$). This region could not be accessed by the LDA systems measurement volume as the laser beams were inhibited by the presence of the wheel and the wing and therefore no measurements could be taken in this region. In order to

determine the effectiveness of the turbulence models for these flow features, results obtained at the subsequent, downstream plane ($x/c=0.75$) plane will be considered (Figure 4.3).

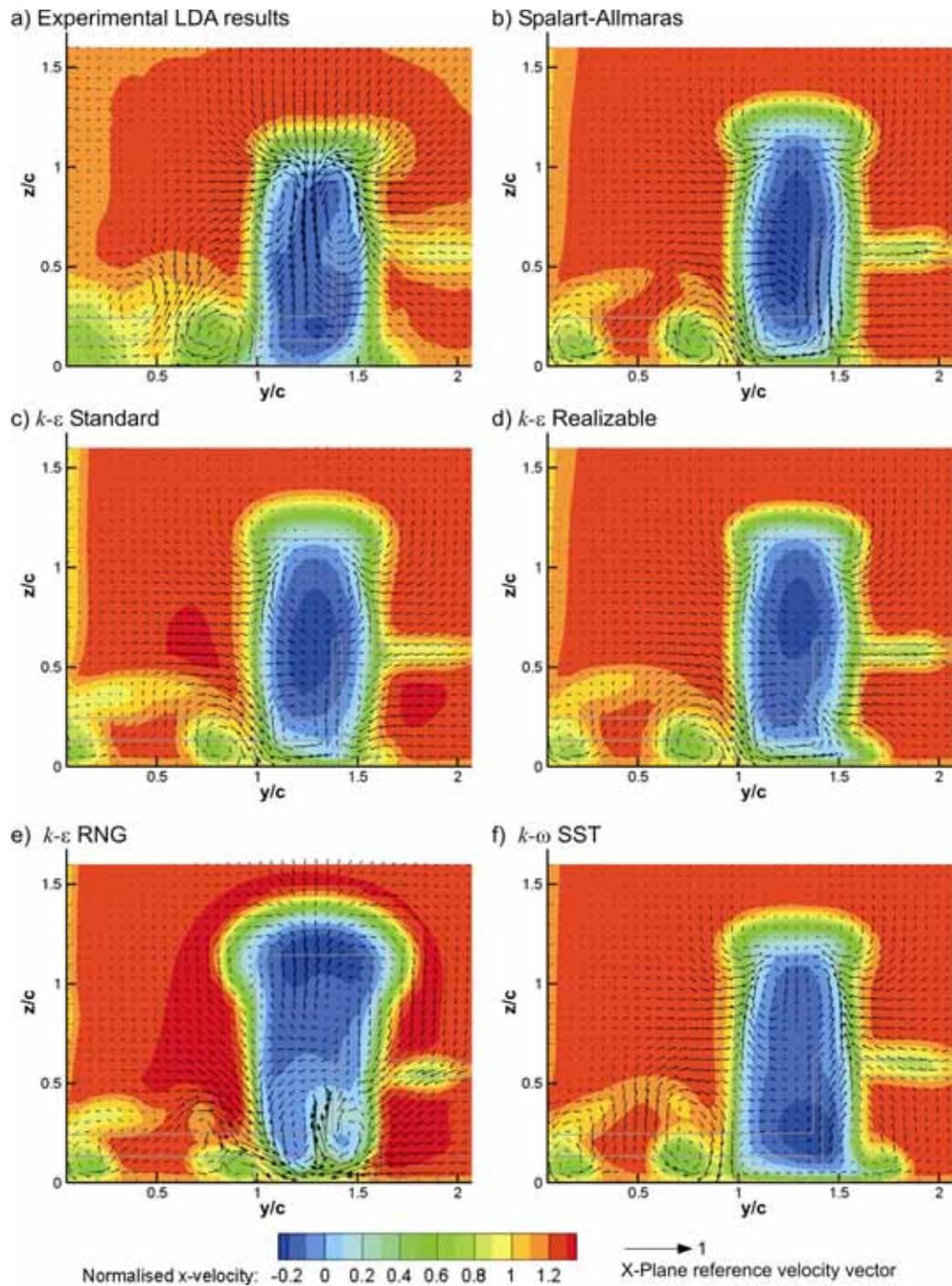


Figure 4.3 Normalised x-velocity and in plane comparisons to LDA results on $x/c=0.75$ plane

While the results obtained with several turbulence models differed only slightly for the $x/c=0.63$ plane, larger variations were seen on the $x/c=0.75$ plane located within the wing and wheel wake. Considering the LDA results initially (Figure 4.3a) indicates that the wheel wake ($0.9 < y/c < 1.7$, $0 < z/c < 1.25$) is directly positioned behind the wheel and consists of two upper, counter rotating vortices ($y/c=1.05$, $z/c=0.95$ and $y/c=1.45$, $z/c=0.95$) formed by the separation from the top of the wheel tread (McManus, 2006). Above the wheel wake, the flow is being entrained into the wheel wake and in the process; a downward velocity component in the centre of the wake is created. The wing wake can be observed between the wind tunnel wall ($y/c=0$) and extending across to the inner face of the wheel ($y/c=0.9$) at a height of $z/c=0.4$. Within the wing wake two additional counter rotating vortices can be observed ($y/c=0.4$, $z/c=0.3$ and $y/c=0.8$, $z/c=0.2$) where between them a vertical velocity component of 0.2 has been measured, created by the downforce producing wing located further upstream. The inboard vortex of this pair is believed to be the junction vortex previously indicated by the results obtained with the different turbulence models, while the outboard vortex is the main wing vortex. Outboard and at mid height of the wheel ($1.7 < y/c < 2.1$, $z/c=0.6$), the sting wake is also evident. This appears to play no significant role in the wing and wheel interaction and will therefore not be discussed further.

Comparing the LDA results to those obtained with the Spalart-Allmaras model (Figure 4.3b) indicate that this turbulence model over predicts the height of the wheel wake by a value of $0.1c$ and that the two upper vortex structures are positioned slightly lower and closer to the centre of the wheel wake ($y/c=1.15$, $z/c=0.9$ and $y/c=1.4$, $z/c=0.85$). The extent of the downwash between these two vortex structures is approximately a third of that measured and this turbulence model also suggests that an additional vortex is formed at the base of the wheel wake adjacent to the main wing vortex. A similar additional vortex structure was also obtained within the wheel wake with the $k-\varepsilon$ standard (Figure 4.3c) model and the height off the wake was also over predicted by the same amount as that observed by the Spalart-Allmaras model. An additional concern with the results obtained with the $k-\varepsilon$ standard model was the over prediction of the width of the wheel wake by approximately $0.1c$ in comparison to the experimental results. Additionally, the upper wheel vortices are much weaker making them more difficult to identify using the cross component velocity vectors alone. By plotting the x -vorticity (not shown), the upper wheel vortices were determined to be located at $y/c=1.2$, $z/c=0.9$ and $y/c=1.35$, $z/c=0.9$. The

reduction in strength of these vortices is also related to the extent of the downwash generated in the centre of the wheel wake.

The largest and least realistic wheel wake structure was calculated with the $k-\varepsilon$ RNG turbulence model (Figure 4.3e) which suggests that the wheel wake is narrower at the base than the top. No upper wheel wake vortices were obtained with this turbulence model and instead two vortices were formed adjacent to the ground causing an upwash in the centre wheel wake. This flow structure causes the flow to be entrained into the wake from the ground instead from above. Additionally, the formation of the main wing vortex at this plane is adversely altered by this variation in wheel wake structure, a flow feature that is expected to play a significant role in the interaction of the wing and wheel. The larger wake calculated by the $k-\varepsilon$ RNG turbulence model artificially increases the blockage and can be attributed to the increase in x-velocity observed on the $x/c=-0.63$ (Figure 4.2e) and $x/c=0.75$ (Figure 4.3e) planes surrounding the wing and wheel wakes. A similar effect, but to a lesser extent, has been obtained with the $k-\varepsilon$ standard turbulence model in the same regions (Figure 4.2e and Figure 4.3c).

The width and the height of the wheel wake was most accurately predicted with the $k-\varepsilon$ realizable (Figure 4.3d) model with the width being equal to that measured experimentally and the height being over estimated by approximately $0.05c$. Unfortunately, the wheel wake structure indicates significantly weaker upper wheel vortices positioned similarly to that observed with the $k-\varepsilon$ standard model ($y/c=1.2$, $z/c=0.9$ and $y/c=1.35$, $z/c=0.9$). The formation of an additional vortex in the lower wheel wake was also observed with the $k-\varepsilon$ realizable turbulence model as previously reported for the Spalart-Allmaras and $k-\varepsilon$ standard turbulence models. One additional region where the $k-\varepsilon$ realizable model excelled in comparison to the others tested was the prediction of the main wing vortex and the velocity deficit calculated across the wing wake.

Where the $k-\varepsilon$ realizable model faltered, the $k-\omega$ SST model excelled (Figure 4.3e). The upper wheel vortices and the subsequent downwash in the wheel wake were best predicted with this turbulence model and no additional vortex structure was obtained in the lower wheel wake on this plane. Unfortunately, the height and width of the wheel wake was over predicted in a similar magnitude to that previously reported for the $k-\varepsilon$ standard model and the main wing vortex shape and position was poorly predicted.

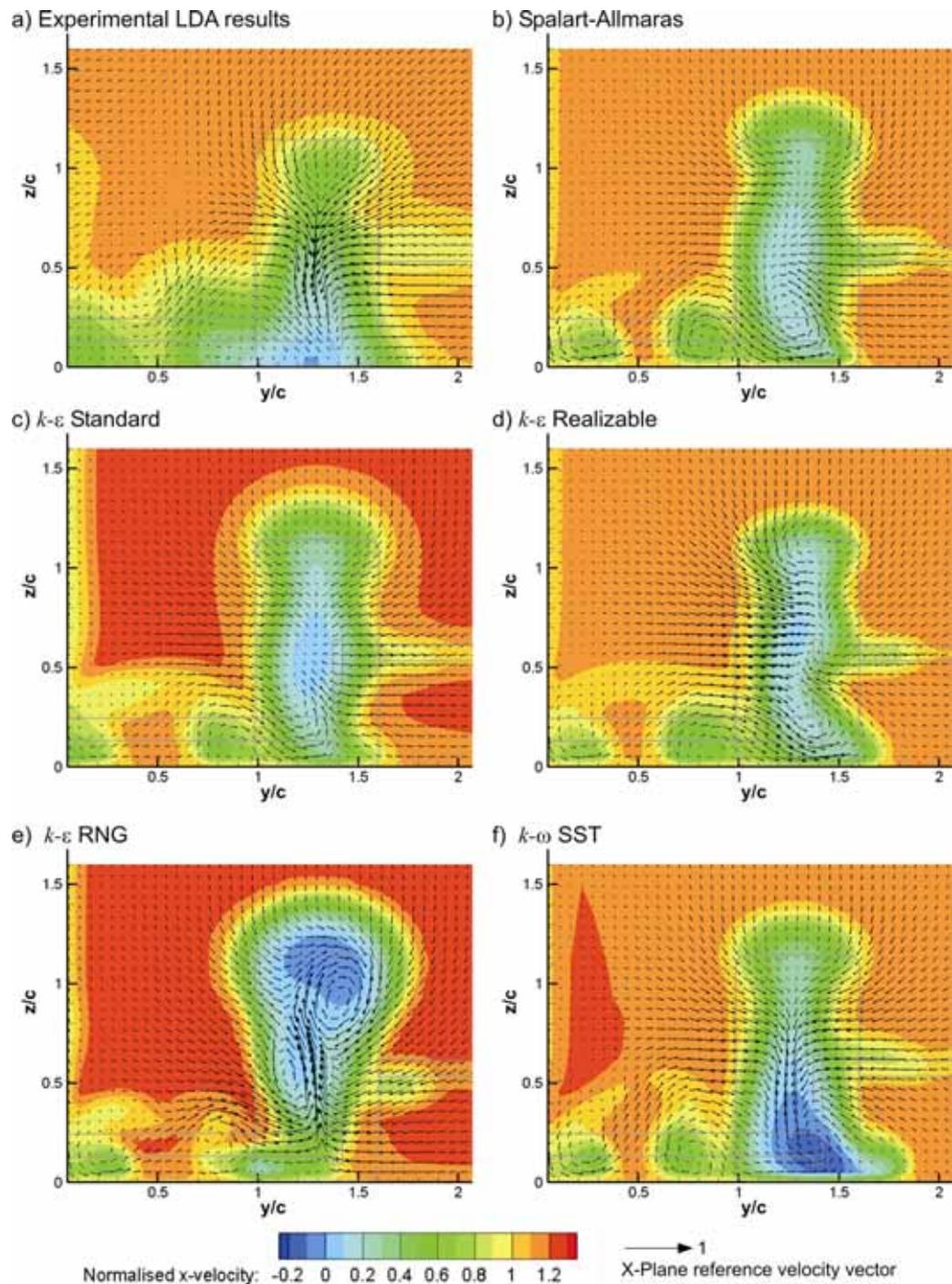


Figure 4.4 Normalised x-velocity and in plane comparisons to LDA results on $x/c=1.5$ plane

Progressing further downstream to the plane located at $x/c=1.5$ (Figure 4.4a), the experimental results indicate that the upper wheel wake vortices have completely dissipated at this stage and that this region of the wheel wake is mostly dominated by the

downwash component ($y/c=1.3$, $0.3 < z/c < 0.8$) which was first observed on the $x/c=0.75$ plane. Without the upper wheel wake vortices, the flow entrainment into the wheel wake is no longer solely from the top centre, but now also includes the sides. While all the turbulence models demonstrate the dissipation of the upper wheel vortices by the $x/c=1.5$ plane with the exception of the $k-\varepsilon$ RNG model (Figure 4.4e), the flow entrainment and downward flow component is best captured by the $k-\omega$ SST model (Figure 4.4f).

The experimental results also indicate that the height of the wheel wake remains the same and that the upper region progresses outboard. The general height and position of the upper wheel wake has been captured best by the $k-\varepsilon$ realizable model (Figure 4.4d). The $k-\omega$ SST (Figure 4.4f) and the Spalart-Allmaras (Figure 4.4b) models maintain the height of the wheel wake from the previous plane, but indicate no variation in the horizontal position. The remaining turbulence models predict that the upper wheel wake continues to increase in height suggesting that these models may have poorly determined the separation point from the wheel tread which causes a taller wheel wake to be determined.

Another feature calculated with greater success by the $k-\varepsilon$ realizable and $k-\omega$ SST models in comparison to the other turbulence models tested was the width at the base of the wheel wake. Like the experimental results, the lower wheel wake in both these models broadens and on the inboard region encroaches that of the wing wake. The $k-\varepsilon$ RNG model continues to compare poorly to the experimental results with the complete opposite trend being observed in this region (Figure 4.4e). Surprisingly the lower wheel wake of the $k-\omega$ SST model now also includes a lower vortex structure (Figure 4.4f, $y/c=1.4$, $z/c=0.2$) that was previously observed for all the other turbulence models tested on the $x/c=0.75$. On the $x/c=1.5$ plane, the same vortex structure is no longer evident for the $k-\varepsilon$ standard (Figure 4.4c) and realizable (Figure 4.4d) models. This vortex structure that has been observed in the computational results for the $x/c=0.75$ plane could be the main outboard wheel vortex that has been previously described by both Fackrell (1975) and McManus and Zhang (2006) and may not be evident in the LDA results as it may have dissipated prior to the $x/c=0.75$ plane for the experiments. If this assumption is true, then this would suggest that the lower wheel wake is better predicted by the $k-\varepsilon$ realizable model as opposed to the $k-\omega$ SST model.

Another region where the $k-\varepsilon$ realizable model out performs the $k-\omega$ SST model is in the vicinity of the wheel wake with the $k-\varepsilon$ realizable model better predicting the x-velocity deficit in this region. The experimental results also indicate that the core of the main wing vortex is located in the same position relative to the previous plane ($y/c=0.8$, $z/c=0.2$). Reductions in the surrounding cross component vectors that define the main wing vortex indicate that the strength of this vortex has been reduced. Similarly, the wing and wall junction vortex also reduces in strength, but the core is now located approximately 0.1c higher ($y/c=0.4$, $z/c=0.4$). The reduction in strength and the variation in the direction of the subsequent flow between these two vortices has been best predicted by the $k-\varepsilon$ realizable model.

In conclusion, it appears that either the $k-\omega$ SST and $k-\varepsilon$ realizable turbulence models could be considered suitable for use during a computational study of the wing and wheel interaction. While all the turbulence models behaved similarly on the plane located between the wing and wheel, downstream of the wheel, the $k-\omega$ SST model clearly performs better in predicting the upper and mid wheel wake structures while the $k-\varepsilon$ realizable model was best in the wing wake and lower wheel wake structures as well as the general size and position of the wheel wake. Despite being a simpler turbulence model, the Spalart-Allmaras more accurately predicted the wheel separation point, the wheel wake shape and the wing and wheel wake interaction in comparison to the $k-\varepsilon$ RNG and $k-\varepsilon$ standard models, yet was inferior in comparison to the $k-\omega$ SST and $k-\varepsilon$ realizable turbulence models.

4.1.2. Comparisons to LDA Results of turbulence intensity

The performance of the turbulence models is now considered using comparisons of the turbulence intensity. Given the poor mean velocity performance of the $k-\varepsilon$ RNG model and that the turbulence intensity is not calculated for the Spalart-Allmaras model, results obtained with these turbulence models have been omitted from the subsequent comparisons (Figure 4.5 to Figure 4.7). Considering the plane located between the wing and the wheel ($x/c=-0.63$), the experimental results indicate (Figure 4.5a) that the largest peak turbulence intensity occurs inboard of the main wing vortex core ($y/c=1.3$, $z/c=0.2$). A local increase is also seen at the core of the secondary wing vortex ($y/c=1.55$, $z/c=0.55$),

but other than in the wake of the wing ($0.7 < y/c < 1$), no other regions of increased turbulence have been recorded. All the turbulence models indicate that the core of the main wing vortex is a region of increased turbulence intensity, but the $k-\varepsilon$ realizable turbulence model most accurately predicts the magnitude in this region (Figure 4.5c) with a variation of approximately 10% in comparison to the LDA measurements while the other two were greater. Similarly, an increase in turbulence was also predicted in the region of the wing wake, but given that it was not possible to obtain LDA measurements in this region for this plane, this feature will once again be compared on planes located further downstream.

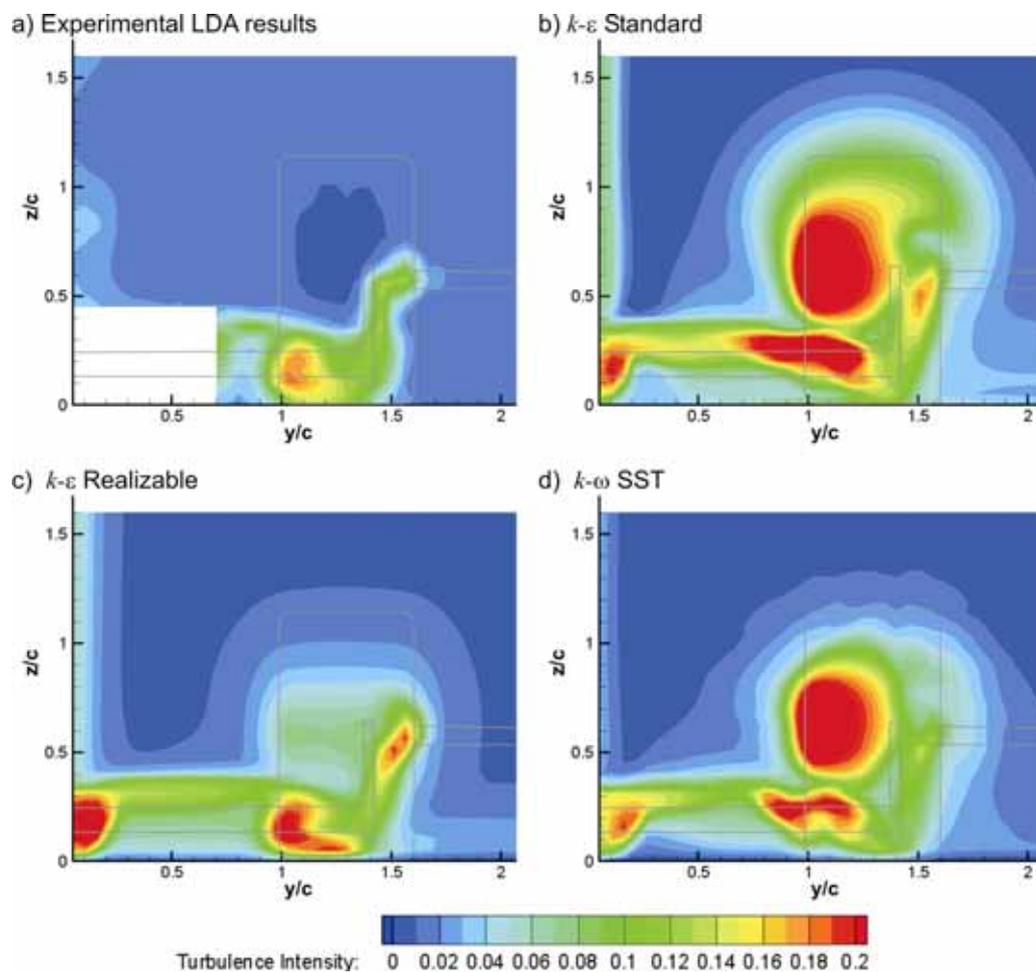


Figure 4.5 Turbulence intensity comparisons to LDA results on $x/c=-0.63$ plane

The local maximum obtained at the core of the secondary wing vortex was also predicted by all the turbulence models with the $k-\omega$ SST (Figure 4.5d) model determining this feature

most accurately with a turbulence intensity variation of approximately 5% to that measured experimentally. This was the only region where the $k-\varepsilon$ realizable model was outperformed by the other turbulence models. Unfortunately, all the turbulence models calculated a large increase in turbulence intensity forward of the wheel corresponding to the location of the expected stagnation region. The worst performing models in this region were determined to be the $k-\omega$ SST and $k-\varepsilon$ standard (Figure 4.5b) models with variations exceeding 100% in comparison to that which was measured experimentally.

Progressing to the first plane located downstream from the wheel ($x/c=0.75$), the highest level of turbulence intensity value (0.19) was measured around the perimeter and more specifically, at the base, of the wheel wake (Figure 4.6a). The wheel wake centre experienced values approximately half to three quarters of that experienced around the perimeter. Similar values were also recorded in the wing wake with a peak turbulence intensity value of approximately 0.15 being obtained at the location of the main wing vortex core ($y/c=0.7$, $z/c=0.2$). An additional feature evident on this plane is the sting wake ($1.6 < y/c < 2.1$, $z/c=0.6$) which also produced a region of increased turbulence aft of the wheel with a maximum value of 0.17.

In comparison, all the turbulence models generally predicted that the peak turbulence intensity would occur around the perimeter of the wheel wake for this plane. The magnitude was once again best predicted by the $k-\varepsilon$ realizable model with the peaks also being obtained at the base of the perimeter (Figure 4.6c). Both the $k-\omega$ SST (Figure 4.6d) and $k-\varepsilon$ standard (Figure 4.6b) turbulence models over predicted the extent and the magnitude of the variation in the upper wheel wake which should be expected given that during the previous comparisons of the mean flow, both turbulence models also over predicted the height of the wheel wake (Figure 4.3c,f). The $k-\varepsilon$ realizable model under predicted the turbulence intensity in the wing and sting wake regions, in some portions by up to 20% and 10% respectively. The turbulence intensity was also marginally better predicted in the wing and sting wake by the $k-\varepsilon$ standard model. The $k-\omega$ SST model under predicted the turbulence intensity in the wing wake, but was best at predicting the turbulence intensity in the sting wake. Given that the unbounded computational model will not include the sting, this argument can not be used as a valid reason for using the $k-\omega$ SST model for the oncoming investigation into the wing and wheel interaction.

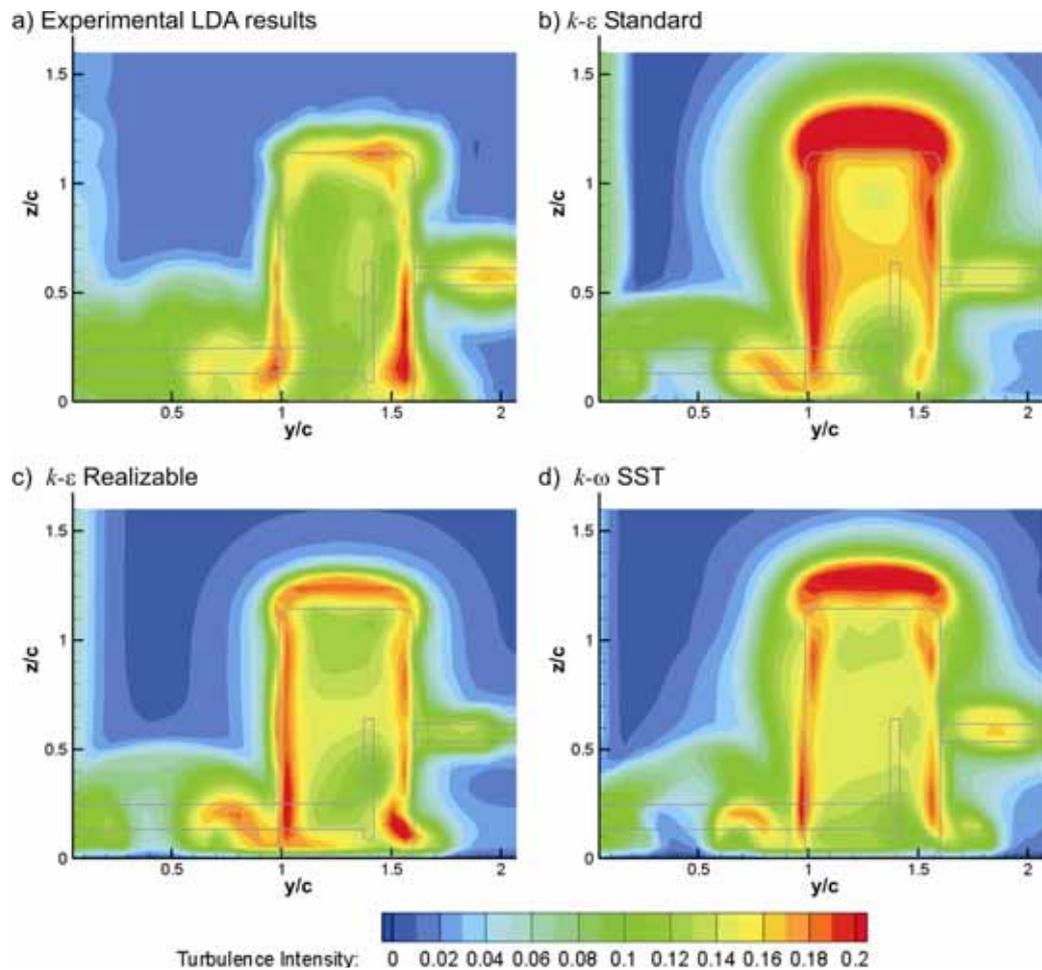


Figure 4.6 Turbulence intensity comparisons to LDA results on $x/c=0.75$ plane

For the final turbulence comparison conducted at the $x/c=1.5$ plane, similar features are evident with one exception. While on the $x/c=0.75$ plane the experimental results indicated that the peak turbulence was obtained around the perimeter of the wheel wake, on the $x/c=1.5$ plane, the peak turbulence intensity was obtained at the base and in the centre of the wheel wake (Figure 4.7). Also evident on this plane is the increased turbulence due to the wing and wheel wake but given that the variations obtained for this plane are the same as that seen for the $x/c=0.75$ plane, they will not be discussed further here and instead the discussion will focus on the variations within the wheel wake.

Both the $k-\varepsilon$ realizable and the $k-\omega$ SST models indicate that the base of the wake in general contains higher values of turbulence intensity than that of the upper wheel wake region. The turbulence intensity in the upper region of the wheel wake is over predicted by

both of these models. Despite this, the $k-\varepsilon$ realizable model predicted a result which is marginally better than the $k-\omega$ SST given that the upper wheel wake region is smaller. Of the same two turbulence models, the $k-\varepsilon$ realizable model indicates that the outboard side of the wheel wakes base should have larger turbulence intensity values than the inboard side. While inferior to the $k-\varepsilon$ realizable model, the $k-\omega$ SST outperformed the $k-\varepsilon$ standard turbulence model as variations in the upper wheel wake region were determined to be even greater. As on the $x/c=0.75$ plane, and also indicated by the mean velocities for the same plane, the extent of the upper wheel wake also appears to be significantly greater than that measured with the LDA.

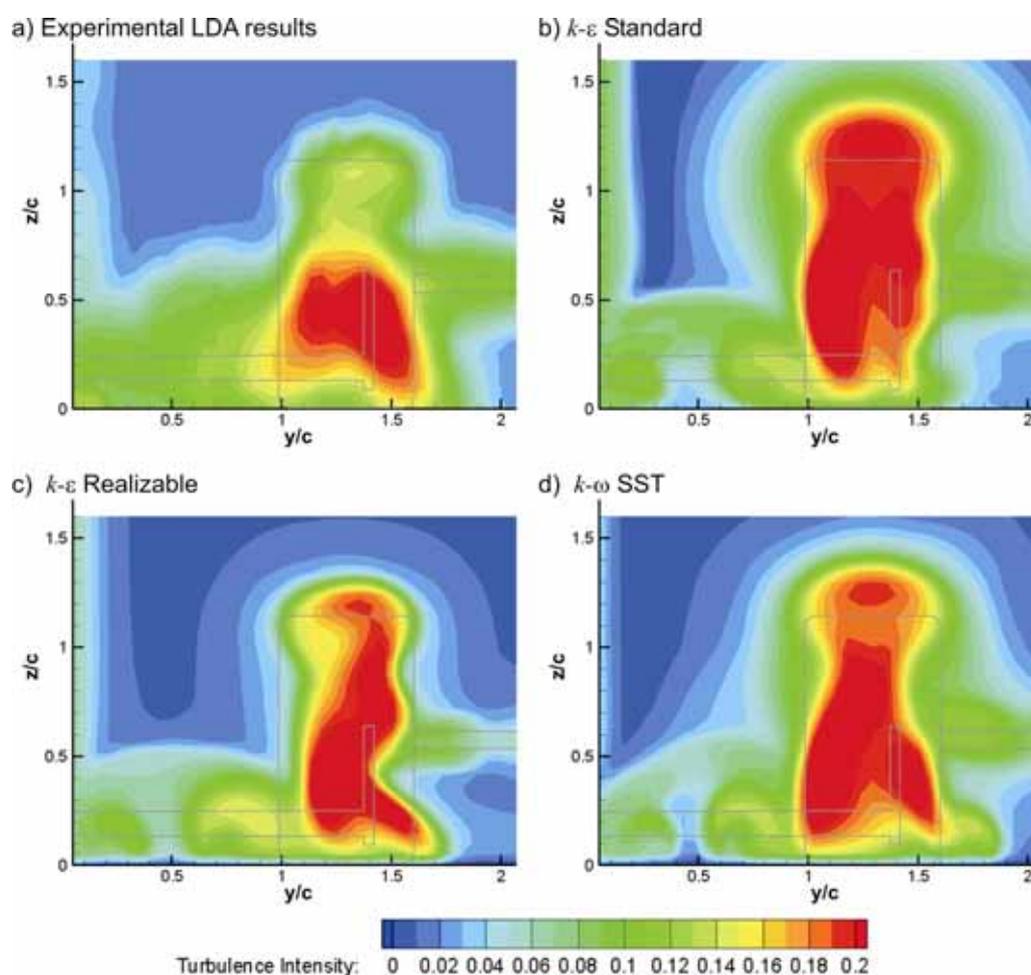


Figure 4.7 Turbulence intensity comparisons to LDA results on $x/c=1.5$ plane

Reviewing the performance of the various turbulence models by comparing them to the experimental LDA results for both the mean velocities and the turbulence intensity, it was

finally decided to continue the validation process using solely the $k-\varepsilon$ realizable turbulence model. While none of the turbulence models proved definitively to be the most suitable, this turbulence model was considered to be the best compromise amongst those tested predicting the flow structures that the author envisages will be the most dominant features of a wing and wheel interaction. This model was shown to most accurately predict the size and the velocity deficit of the wheel wake indicating its superiority at predicting the separation point from the wheel tread and side walls. The $k-\varepsilon$ realizable turbulence model also outperformed the other turbulence models tested in predicting the flow structures associated with the wing wake particularly the main wing vortex shape and position. Additionally the, turbulence intensity comparison indicates that the variation in the velocities calculated with the $k-\varepsilon$ realizable model were the most consistent with that which was measured with the LDA and significantly better than the $k-\omega$ SST model, which was also a likely candidate when only considering the mean flow velocities. In agreement with the conclusion obtained here, Mahon and Zhang (2005) have also shown this turbulence model, to provide the best agreement between experimental and computational data for a downforce producing wing in ground effect. Similarly, a comparison conducted by McManus (2006) of the numerical results obtained in comparison to Fackrell's (1975) experimental results also concluded that the $k-\varepsilon$ realizable model was most suitable when used to model the flow about the wheel.

The validation investigation will now continue to determine with what accuracy the computational model can predict the pressure coefficients, forces and wake structures of either an isolated wing or wheel using published experimental data. This was considered necessary given that the published experimental data has been obtained at higher Reynolds number which should be more representative of the flow conditions that are experienced by a wing and wheel attached to an open wheel racing car and that are intended to be modeled by the full-scale computational model.

4.2. Isolated Wing in Ground Effect Validation

Due to the speed and scale limitations of the wind tunnel used to obtain the LDA results, it was considered necessary to further validate the computational model at a higher Reynolds number. The calculated lift and drag results will also be investigated for

variations in wing and wheel geometries and therefore it was determined to be necessary to validate this aspect of the computational model as well. Additionally, it is recommended by the AIAA (1998) that a “building block” approach be taken when validating a computational model. For the above stated reasons, it was decided to conduct comparisons to the experimental results obtained by Zerihan (2001) of an isolated downforce producing wing in ground effect.

Maintaining all the characteristics of the unbounded computational model, the span, profile, chord length and endplate of the wing was modified to replicate the geometry of the single element wing used by Zerihan (2001). Additionally, the position of the boundaries and the inlet conditions were modified to replicate the flow conditions and the wall positions in the test section of the wind tunnel used by Zerihan (Figure 4.8). Based on the chord length (223.4mm), and the freestream velocity (30ms^{-1}) used during his experiments, the Reynolds number of Zerihan’s experiments and that of the computational model replicating his experiments was determined to be 4.56×10^5 .

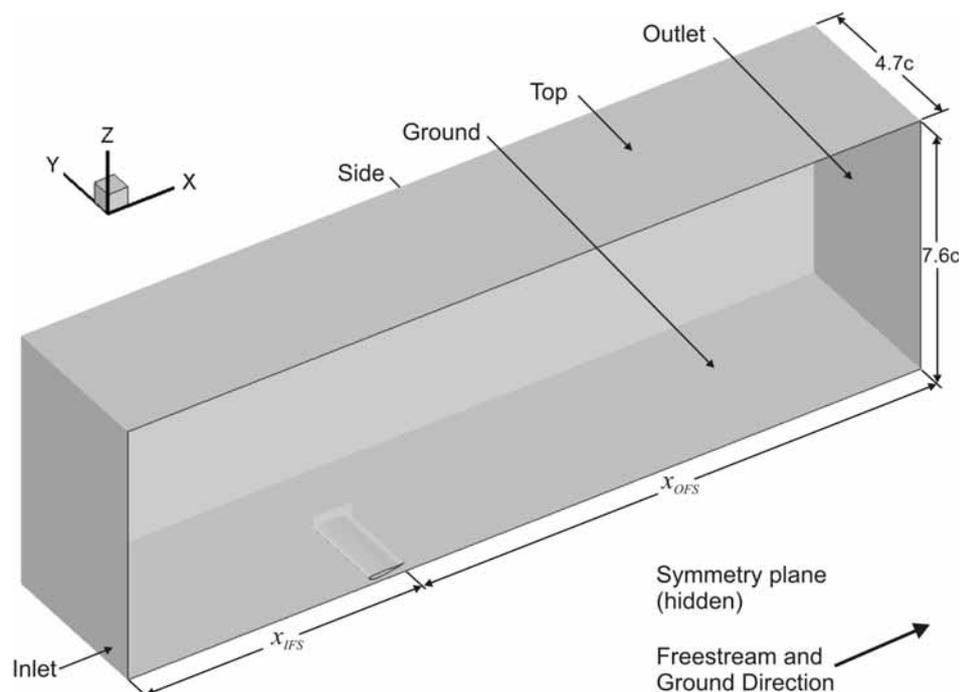


Figure 4.8 Computational domain and boundaries for comparisons to Zerihan’s (2001) experimental results

By recording the lift of the wing as the height was reduced, at several angles of attack, Zerihan was able to demonstrate the downforce loss phenomenon. This experiment was repeated numerically at Zerihan's reference angle of attack (1°) to determine with what accuracy the computational model used for this study could predict the position at which the lift loss phenomenon occurs at. This was undertaken within a height range of $0.053c$ to $0.313c$. The minimum height that this comparison could be conducted at was limited by the way in which the mesh was constructed as heights less than $0.053c$ would have compromised the cell quality in the boundary layer mesh between the endplate and the ground and were therefore not considered to be a valid comparison and therefore not conducted.

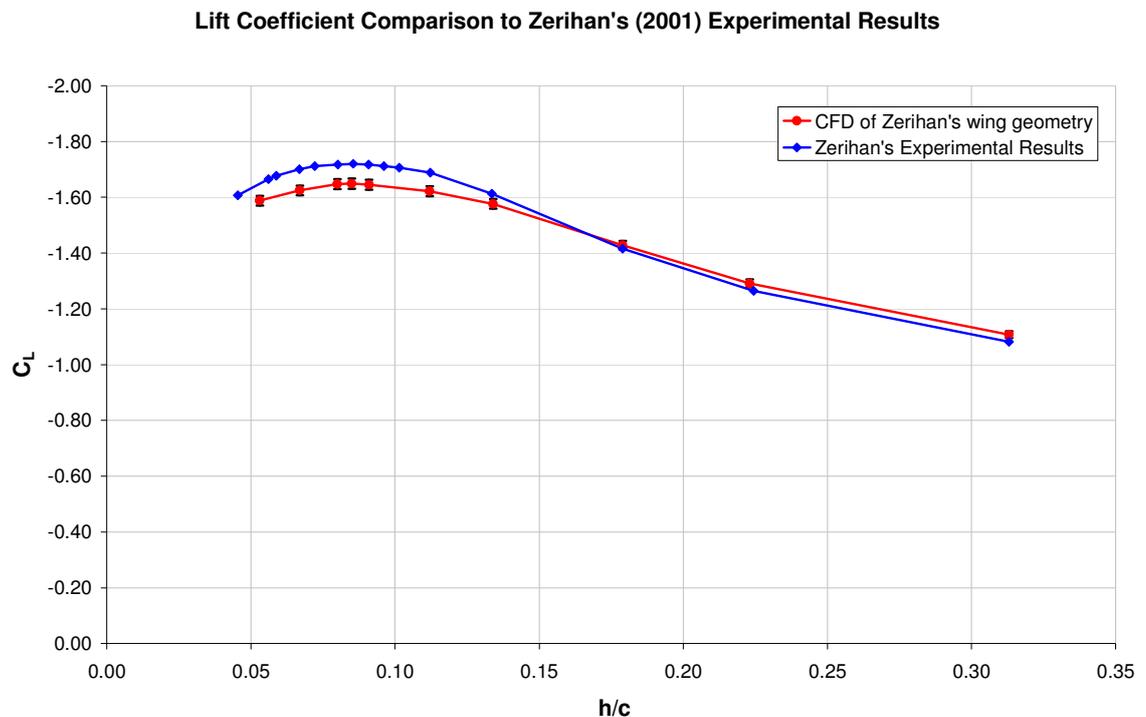


Figure 4.9 Comparison of the lift coefficients for Zerihan's wing at various heights and AOA

Figure 4.9 compares the lift results obtained experimentally by Zerihan (2001) to those obtained with the computational model used for this study. The lift coefficients have been calculated using the same reference area as that used by Zerihan (2001). These results indicate the excellent prediction of the numerical model being able to predict the height at

which the lift loss phenomenon occurs ($h=0.091c$) within the same resolution determined by Zerihan experimentally ($\pm 0.005c$).

Zerihan indicated that the lift loss phenomenon occurs when the flow separates from the bottom surface of the wing, due to the adverse pressure generated by the expansion between the bottom surface of the wing and its close proximity to the ground. As is requested by the AIAA, this comparison demonstrates that the computational model has successfully predicted the downforce trend. To investigate why the variation in magnitude exists, the pressure coefficients in the centre of the wing calculated were also compared to those measured by Zerihan (Figure 4.10). Four different ride heights were used for this comparison, two above, one below and one at the height at which the lift loss phenomenon occurred at.

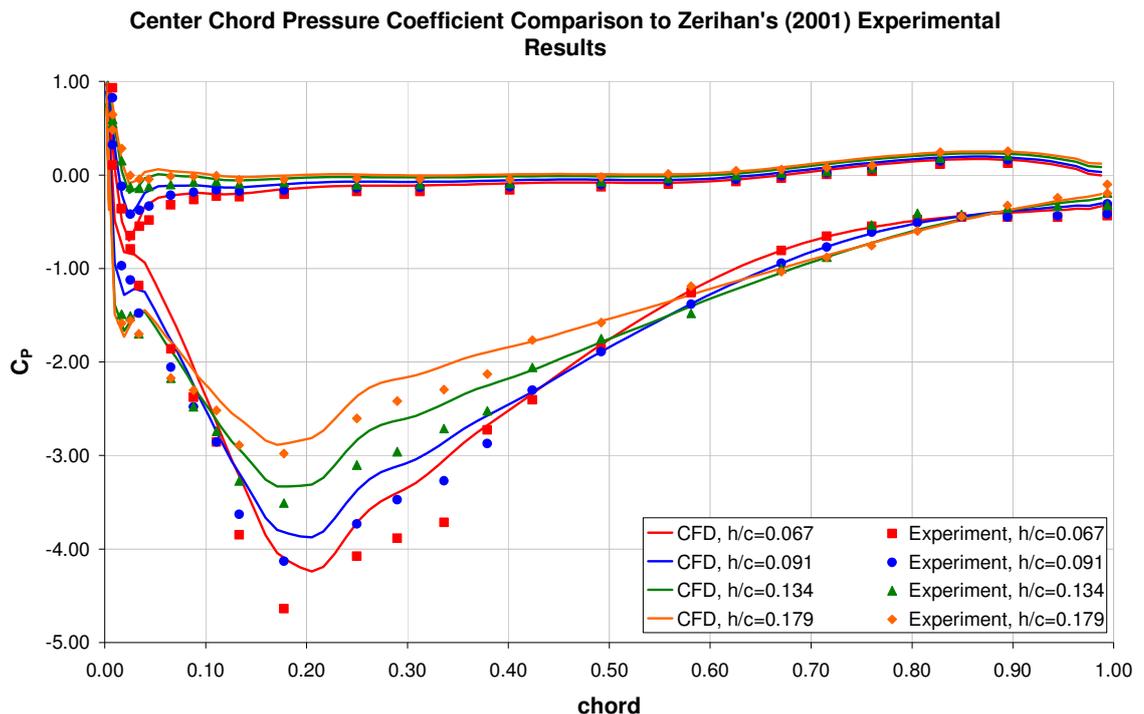


Figure 4.10 Comparison of the pressure coefficients obtained at the centre of the wing

The surface pressure comparisons along the central chord confirm that the computational model is least successful in the adverse pressure gradient regions where separation is expected ($0.2 < x/c < 0.43$). As a result, the separation point on the bottom surface of the

wing is predicted approximately $0.15c$ further upstream than that which Zerihan determined experimentally. The earlier separation on the bottom surface is expected to reduce the acceleration experienced by the flow beneath the wing and for this reason the computational model has under predicted the minimum pressure value and the positive pressure gradient upstream of the minimum pressure value ($0.05 < x/c < 0.2$). This may also explain why the total downforce generated by the wing has also been under predicted. Despite this limitation, the variation in the separation point between the shown computational results varies in an identical manner to that determined by Zerihan and for this reason, the position that the lift loss phenomenon occurs at for this wing has been predicted accurately.

Over the remaining portion of the centre chord, the pressure coefficient variation between the computational model and the experimental results is no more than 0.02. This includes the top and the leading edge of the centre chord where no adverse pressure gradients are expected. The computational model has also been able to predict the local pressure coefficient minimum obtained in close proximity to the leading edge. This is expected to be due to the acceleration caused by the large leading edge radius used by this wing geometry coupled with the stagnation point located on the leading edge. As the height of the wing is reduced, the stagnation point moves towards the upper surface, the acceleration over the leading edge reduces on the upper surface and then increases over the bottom portion of the leading edge. For this reason the local minimum varies in the same manner as the height is reduced in the results above.

During this study of the wing and wheel, the effect that varying the span has on the performance of the wing, as well as the influence that the wheel has on the wing loading is to be investigated. For this reason, a span wise comparison, from the endplate ($\eta=0$) to the wing centre ($\eta=1$), has also been undertaken and is included as Figure 4.11.

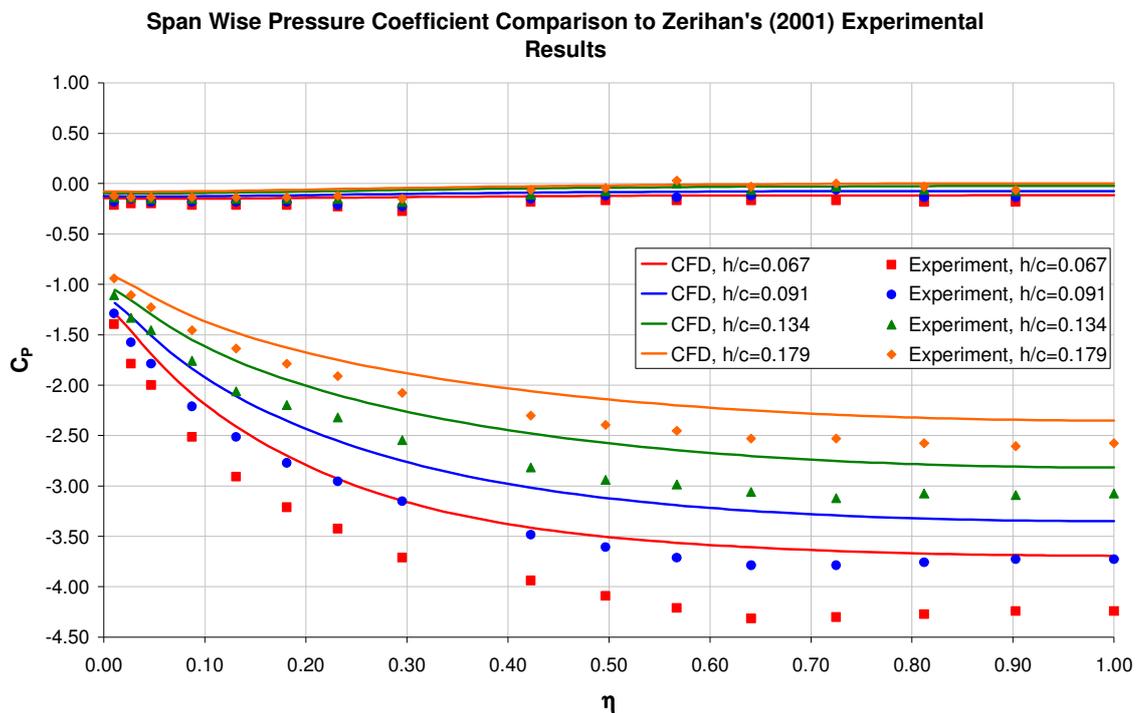


Figure 4.11 Comparison of span wise pressure coefficients obtained along the quarter chord

Both the computational and experimental results indicate that the wing loading is greater in the centre and this gradually reduces towards the endplate on the wing tip. At the wing centre, a discrepancy between the computational and the experimental results is evident which also reduces towards the wing tip. As indicated previously during the centre chord comparison, the quarter chord is positioned in an adverse pressure region where the static pressure predicted is lower than that measured by Zerihan and therefore this should be expected. This is likely to be the case along a large portion of the wing span, but since the wing loading reduces towards the wing tip, it would be expected that the adverse pressure gradient towards the wing tips would also be less than that in the centre and for this reason the comparison improves at the wing tips. Additionally, Zerihan had suggested that a vortex formed from the bottom edge of the endplate also assists with alleviating the separation at the wing tip and this could also be a reason why the computational model performs better at the wing tips than in the centre. For this to be true, the formation of the wing tip vortices would also be required to be representative of those measured by Zerihan.

Figure 4.12 compares the wing tip vortices measured by Zerihan (coloured contours) using PIV to those calculated using the computational model (overlaid contour lines) for three different heights. Also shown is the wing and endplate profile, while the ground and symmetry plane are located at $z/c=0$ and $y/c=0$ respectively. In all these results, two vortices are evident, the secondary vortex close to the top edge of the endplate and the main wing vortex close to the bottom edge of the endplate which this comparison will focus on. At a height of $0.091c$ (Figure 4.12a) the size of the main wing vortex is predicted accurately with the core position approximately $0.2c$ further inboard and $0.05c$ lower than that which was measured by Zerihan. A similar discrepancy also exists at a height of $0.134c$ (Figure 4.12b), but at this height the maximum strength of the core calculated is approximately half of that measured experimentally. At a height of $0.224c$, the largest ride height at which the comparison was conducted at, there is almost no variation in the position or peak strength in the main wing vortex. The core of the secondary vortex also appears to be offset towards the wing centre by approximately $0.1c$ for all the comparisons made.

Initially it would be expected that the lowest ride height would produce the least accurate correlation, but when considering that Zerihan and Zhang (2002) also demonstrated during their study that the wing tip vortex is related to the rate of change of the downforce curve, it becomes apparent why this is not the case. At a height of $0.134c$, the rate of downforce change measured by Zerihan begins to decrease as the height is reduced. At lower heights, the main wing vortex was also observed to reduce in strength and increase in size, or burst, as depicted in Figure 4.12a. Figure 4.9 indicates that the computational lift curve slope begins to decrease for reduced heights from a height of $0.179c$, therefore vortex burst should be expected at heights less than this value for the computational model. The comparison conducted at a height of $0.134c$ (Figure 4.12b) actually demonstrates this and for this reason the discrepancy in the magnitude and the core position exists between the computational and experimental results. Despite this variation, it is encouraging to see that the computational model is able to reproduce this complex phenomenon, if only at a slightly higher height.

A region of increased vorticity is also recorded above the trailing edge that spans towards the centre of the wing caused by the wing separation and the subsequent wake for all heights compared. This region increases in strength and size as the wing approaches the

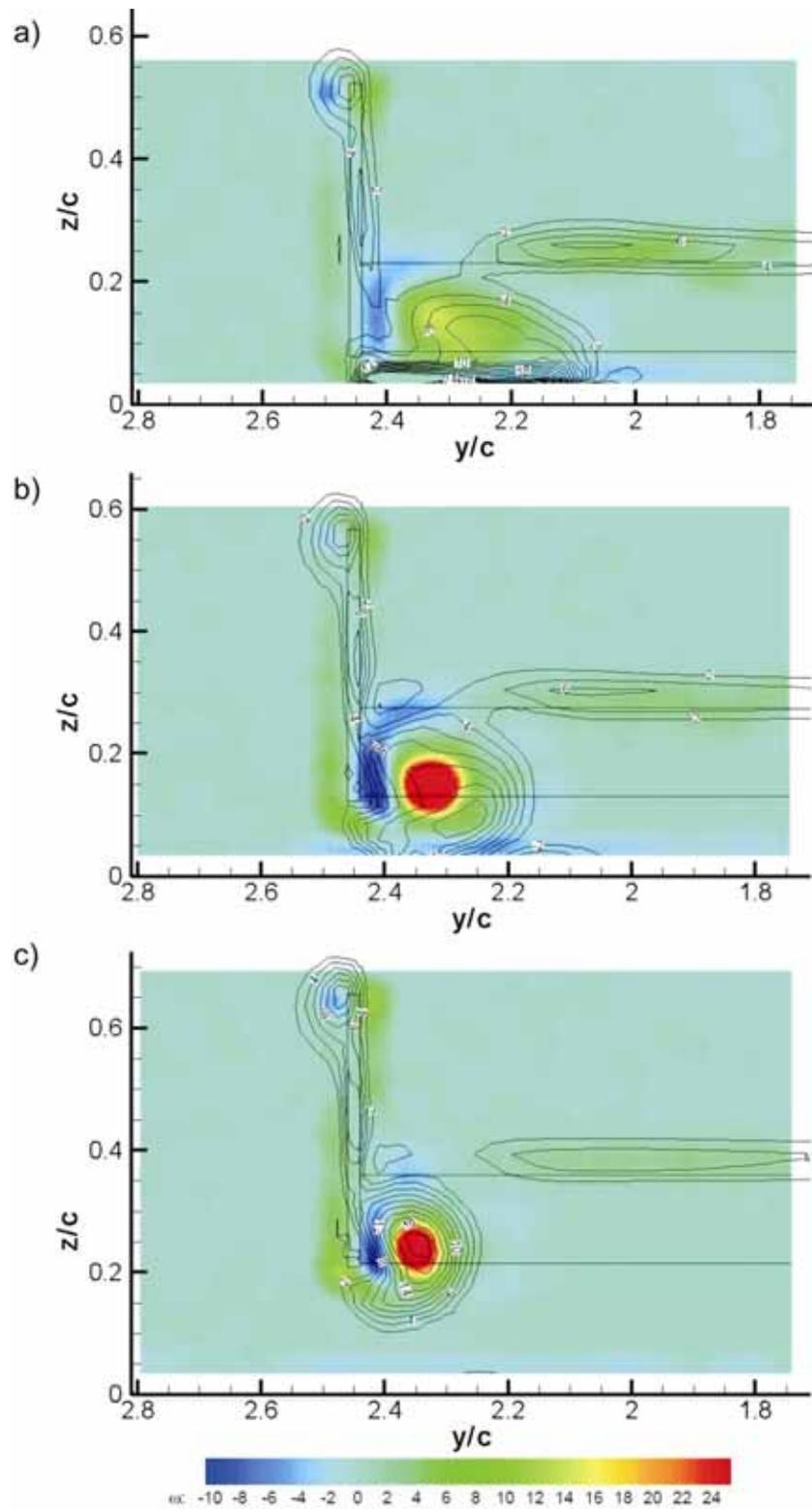


Figure 4.12 Comparison of Vortex positions at; a) $h=0.091c$, b) $h=0.134c$ c) $h=0.224c$

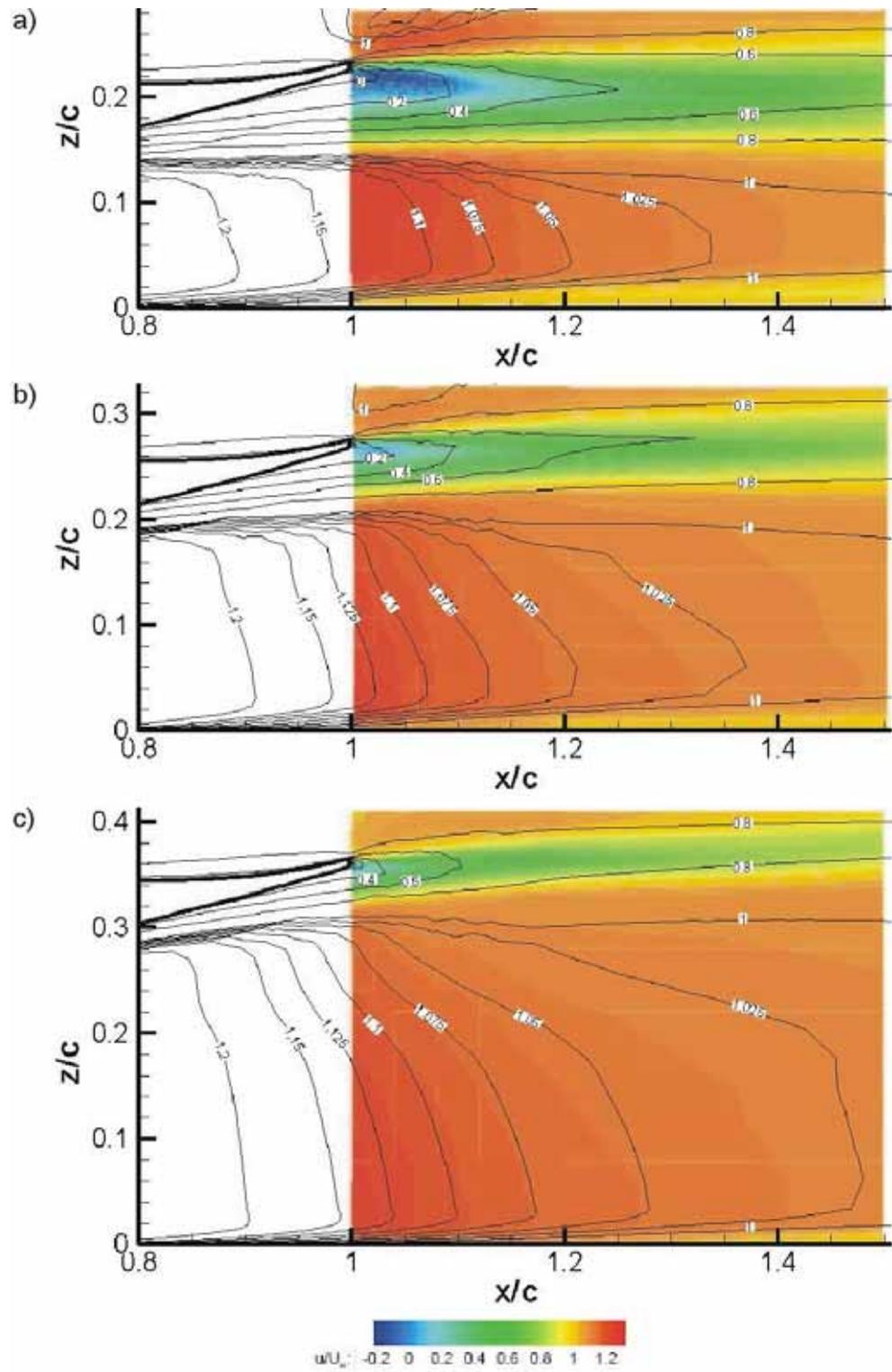


Figure 4.13 Comparison of Zerihan's (2001) wing wake at; a) $h=0.091c$, b) $h=0.134c$ c) $h=0.224c$

ground. Despite the computational model having difficulty in predicting the correct separation point, the x-vorticity in the wake is accurately calculated both in size and magnitude.

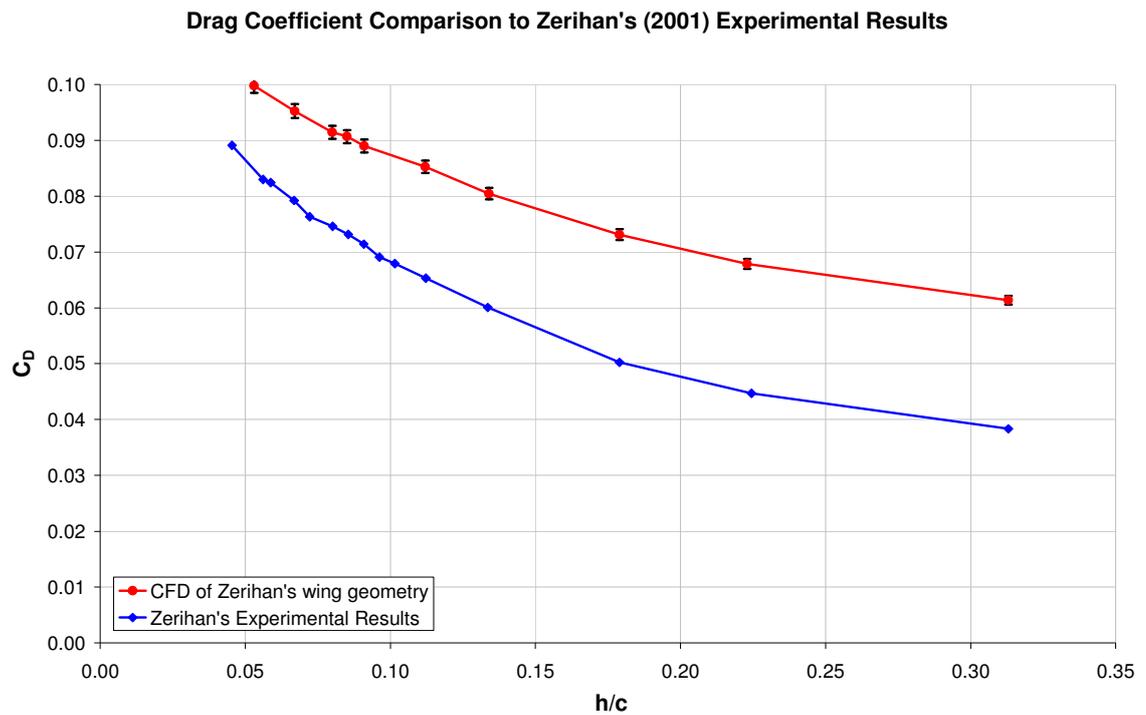


Figure 4.14 Comparison of the drag coefficients for Zerihan's wing at various heights

A better indication of the computational model's performance in the wing wake can be achieved by comparing LDA results obtained along the central plane, behind the wing. This is included as Figure 4.13 where the flooded contours are the normalised x velocity obtained by Zerihan experimentally while the contour lines are those obtained using the computational model. The ground plane is located at $z/c=0$, while the leading and trailing edges of the wing are located at $x/c=0$ and 1 respectively. This comparison also allows the variation of the flow beneath the wing to be determined. Consistent with the assumption made earlier explaining why the positive pressure gradient and the peak pressure value was underestimated, the accelerated flow beneath the wing is under predicted for all three ride heights by the computational model. An earlier separation point, as indicated by the pressure plots, would also suggest that the wake calculated by the computational model of the wing should be larger. This is also confirmed by the LDA comparison. The earlier

separation point should therefore also result in a higher wing drag than that which was measured experimentally. A comparison of the drag values (Figure 4.14) indicates that the computational model consistently over predicts the drag coefficient by approximately 0.025 as expected.

While the computational model is still lacking in predicting accurately the separation point from the wings bottom surface, this has not prevented the computational model from predicting the lift loss phenomenon and associated vortex bursting. The trends associated with both of these features have been reproduced by the computational model in a consistent manner to that which has been measured by Zerihan (2001) experimentally. Additionally, the downforce and drag values of the wing follow trends representative of those obtained experimentally indicating that the computational model is also robust at a greater Reynolds number than that which the turbulence model comparisons were initially conducted at. The validation will therefore progress to determine with what accuracy the flow around a wheel can be predicted.

4.3. Isolated Wheel Validation

4.3.1. Comparison to Experimental Study Conducted by Fackrell

Because the flow structures generated by a bluff body vary significantly to those created by a streamlined body, and to continue the building block approach suggested by the AIAA (1998), it was necessary to conduct a comparison of a wheel at a higher Reynolds number. A previously published study conducted on an isolated wheel by Fackrell (1975) was therefore used to validate the computational model. The unbounded computational model was once again modified so that the wheel geometry would be identical to that used by Fackrell and that the boundary conditions would be representative of the wind tunnel used by him. Additionally, the computational domain was mirrored about the symmetry plane to allow Fackrell's asymmetric wheel geometry to be modelled. The modifications made to the computational model also allowed it to be more similar to the one used by McManus and Zhang (2006) during their unsteady numerical study which will be discussed after this comparison. Therefore, a direct comparison can also be made with their results to evaluate the errors may arise from using a steady state model for a bluff body analysis.

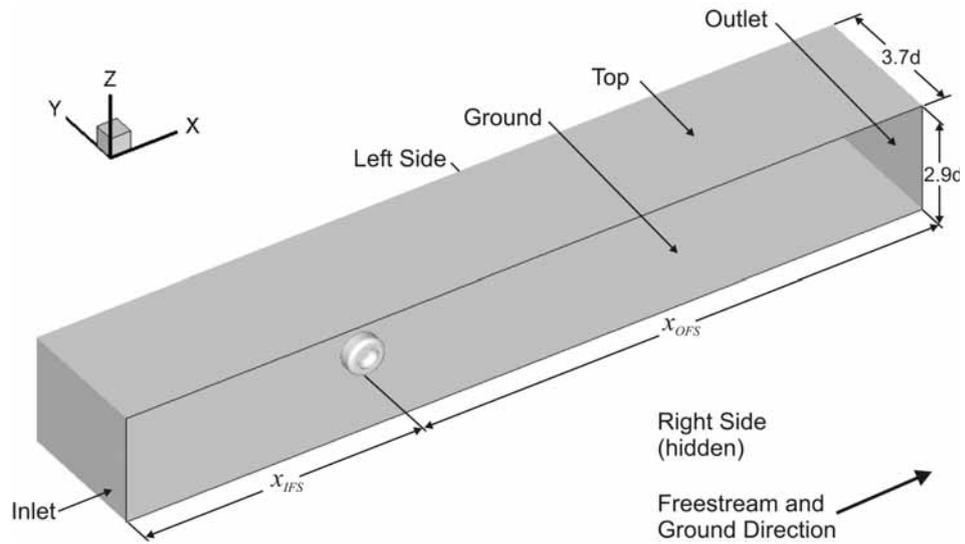


Figure 4.15 Computational domain and boundaries for comparisons to Fackrell's (1975) experimental results

During Fackrell's (1975) study, a variety of wheel widths and profiles representative of those used for open wheel race cars during the seventies were tested. This was achieved using three different tread widths, called A, B and C which could be fitted to one of two profiles, called 1 and 2. For this validation study, the A2 and B2 (Figure 4.16) wheels were used as they were most representative of the aspect ratio intended to be used for the wheel during this study and additionally, stationary and rotating results were obtained by Fackrell for the B2 wheel. Additionally, Fackrell's results indicated that the results obtained for the two different wheel profiles are very similar and therefore the chosen profile was considered to be less important than the aspect ratio. Therefore the profile with the most available experimental results was chosen.

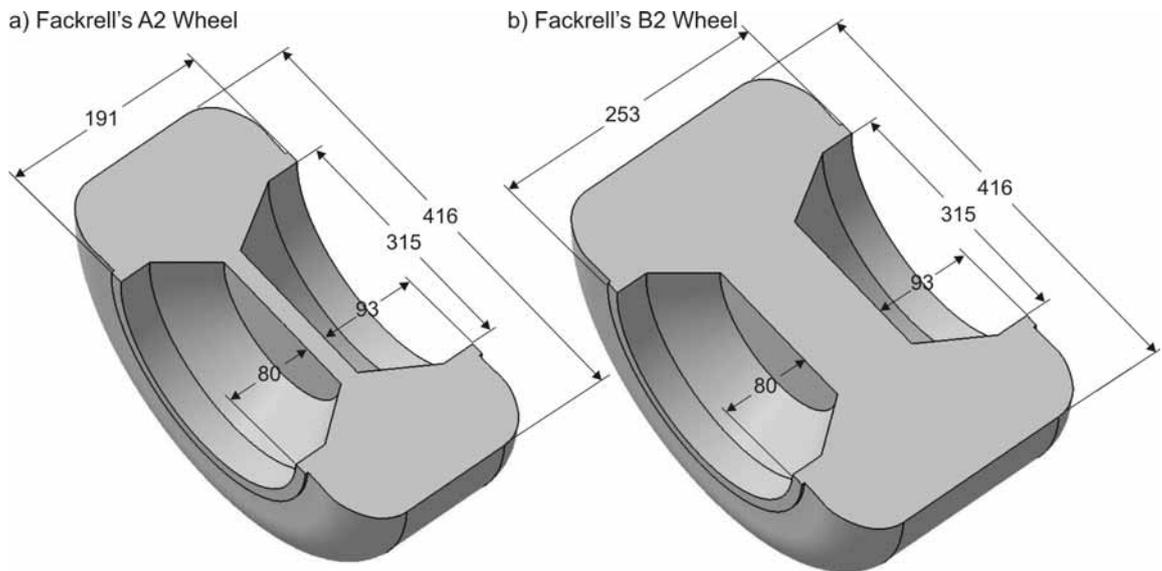


Figure 4.16 Geometry of Fackrell's (1975) wheels (shown to closest millimetre)

The comparisons commenced by comparing the forces obtained for Fackrell's stationary and rotating B2 wheel. Even though there is no intention of using a stationary wheel during this study, a comparison between a rotating and stationary wheel appears to be a logical method to determine if the wheel rotation is being modelled correctly. This was considered necessary as not all previous computational investigations of an isolated wheel have been able to achieve this (Skea *et al.* 1998). Fackrell (1975) obtained lift and drag results by integrating the measured static pressure recorded from approximately 25 pressure tappings distributed across the tread, wheel shoulders and inner hubs of the wheel as it rotated. Fackrell estimated that this method allowed him to determine the lift and drag coefficient of the B2 wheel within an accuracy of $\pm 10\%$. Improvements to his system made after these measurements were taken improved the accuracy to a value of $\pm 5\%$. Unfortunately, time restrictions prevented Fackrell from retaking the B2 measurements. Therefore the comparisons shown in Figure 4.17 include error bars for the error value associated with these results as indicated by Fackrell. The comparison to the computational results indicates that the drag of the wheel is calculated within the accuracy of the experimental results for both the rotating and stationary cases. Unfortunately, the lift is under estimated by the computational model for the rotating and stationary cases by approximately 30% and 20% respectively. Despite this, both the lift and drag values for the stationary case are greater than that for the rotating case. An increase in drag and lift

of 15% and 48% respectively was obtained with the computational model which compares favourably to a variation of 24% and 42% for the same comparison.

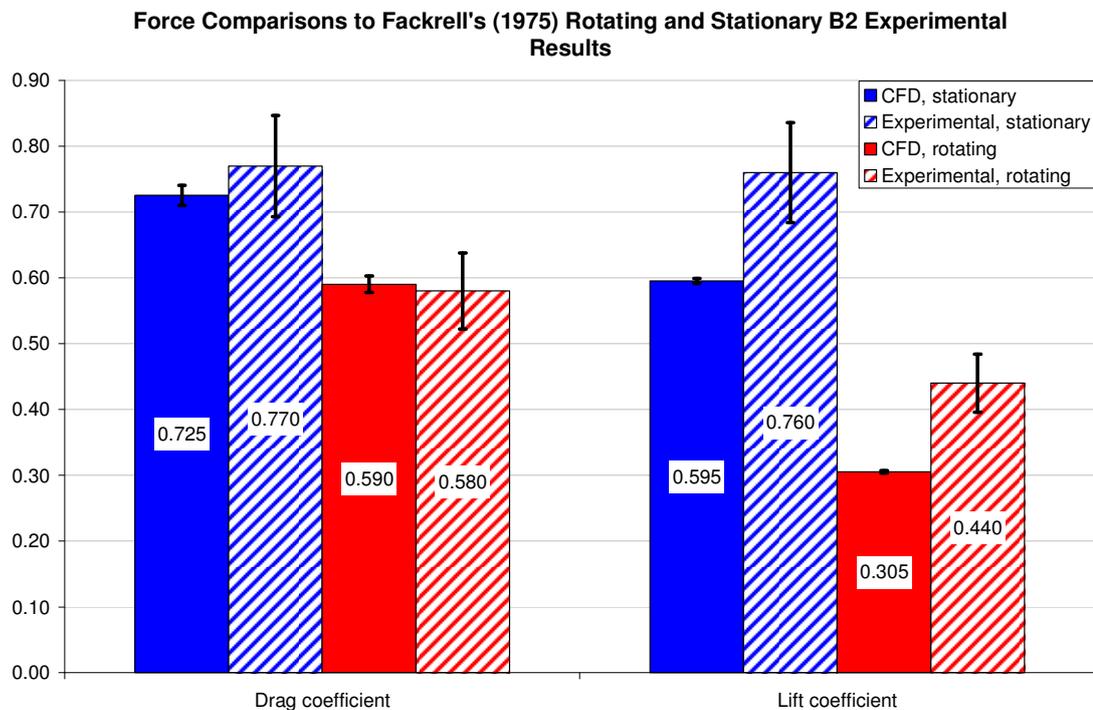


Figure 4.17 Force comparisons for Fackrell's (1975) rotating and stationary B2 wheel

It should be noted that Fackrell's method for measuring the lift and drag on the wheel does not take into account the viscous forces acting on the wheel while the lift and drag values presented from the computational model do. As mentioned by Fackrell, the contribution that the viscous forces make to the forces experienced by a bluff body are negligible and therefore this is unlikely to be responsible for the discrepancies seen above. This was determined to be no more than 3% for all the computational results presented in Figure 4.17.

The flow structures associated with a rotating and stationary wheel vary significantly and for this reason large variation in the forces are obtained. To investigate the computational models ability to predict the variations further, a comparison was also made to the static pressure measurements taken by Fackrell along the centre of the wheel and are presented in Figure 4.18.

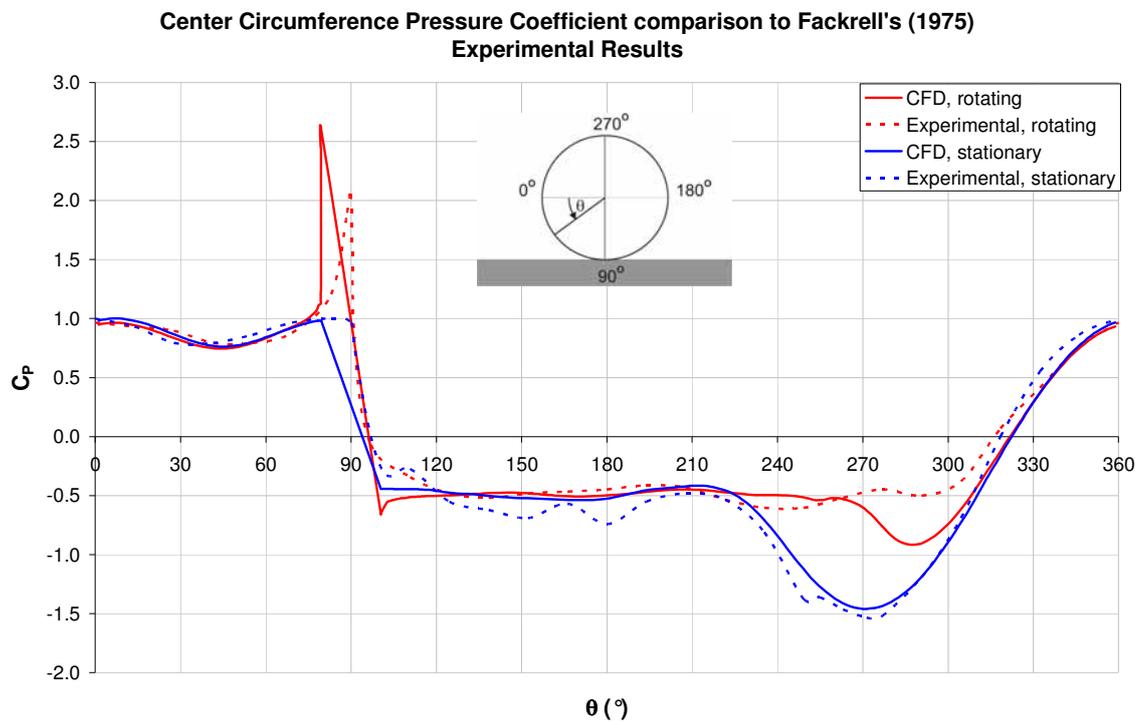


Figure 4.18 Centre pressure coefficient comparisons for B2 stationary and rotating wheels

This comparison indicates that the two main features that differentiate a rotating and stationary wheel have been successfully reproduced by the computational model. The stagnation pressure greater than 1 for a rotating wheel (Figure 4.18, $80^\circ < \theta < 90^\circ$) and the variation in the low pressure region that is generated over the top portion of the wheel (Figure 4.18, $240^\circ < \theta < 310^\circ$) have both been reproduced. The computational model has determined that the stagnation pressure for both the rotating and stationary wheel occurs 10° degrees further forward than measured by Fackrell ($\theta = 80^\circ$). This is because of the compromise made in modelling the contact patch to avoid the creation of highly skewed cells in this region. How this compromise has affected the position of the peak pressure and its magnitude is unknown, this will be further investigated in Section 5.1.2. Similar measurements also made by Hinson (1999) indicate that variations of ± 1.25 can occur in this region. Therefore the computed value of 2.7 in comparison to Fackrell's 2.2 was considered to be satisfactory. Significantly, the peak stagnation pressure at the same position for the stationary wheel was correctly determined to be 1. Given that the only variation between the rotating and stationary wheel calculations is the rotation of the wheel and the application of the moving ground, this is the first confirmation that the wheel

rotation is being modelled correctly. Not all previous computational investigations have been able to demonstrate this variation previously (Skea *et al.* 1998).

Another indication is the variation between the minimum pressure obtained over the top portion of each of the wheels. The agreement between the Fackrell's experiment and the computational model is excellent in this region for the stationary wheel while the rotating wheel has a significant discrepancy. A minimum pressure of -1 has been computed for the rotating wheel while Fackrell measures a local minimum value in the same region of approximately -0.4. This is surprising when considering that the flow from the stagnation point ($\theta=0^\circ$) until the separation point indicated by Fackrell ($\theta=280^\circ$) would be expected to be accelerated and therefore lead to a lower pressure coefficient. After the separation point, and in the separation region, it would be expected that the pressure would recover to be closer to a freestream value. The computational model indicates that this is the case as do results presented by McManus (2006) and Hinson (1999) for the same portion of a rotating wheel which may suggest that this discrepancy may be due to an error associated with Fackrell's experiment. Similarly, a much more consistent pressure value was obtained over the separated regions, $90^\circ < \theta < 220^\circ$ and $90^\circ < \theta < 260^\circ$ for the stationary and rotating wheels respectively, by both McManus and Zhang (2006) and Hinson (1999). Unfortunately, a direct comparison to Hinson's results could not be undertaken since no details were provided of the wheel geometry used. This is not the case with the study conducted by McManus and Zhang (2006) which a comparison has been conducted and is included in the Section 4.3.2.

Fackrell also took off-surface measurements at planes located 1.7" (0.10d), 5.7" (0.35d) and 8.5" (0.52d) downstream of the wheel centre to determine the wake structure behind the rotating wheel. This was only conducted for half of the wheel wake as the opposite half was expected to be affected by the presence of the wheel struts. The 0.9 total pressure coefficient contour line was presented as this was expected to be indicative of the wake's extremities. Given the query regarding the minimum pressure value for the rotating wheel at $\theta=280^\circ$ and the consistent pressure obtained over the separated portion of the wheel obtained during the centre pressure comparisons (Figure 4.18), a wake comparison was also considered to be valuable and has been included as Figure 4.19. In this figure, the results obtained using the computational model have been presented as flooded contours

with the total pressure coefficient value of 0.9 highlighted with a solid black line. The results obtained experimentally by Fackrell are overlaid using a black dashed line.

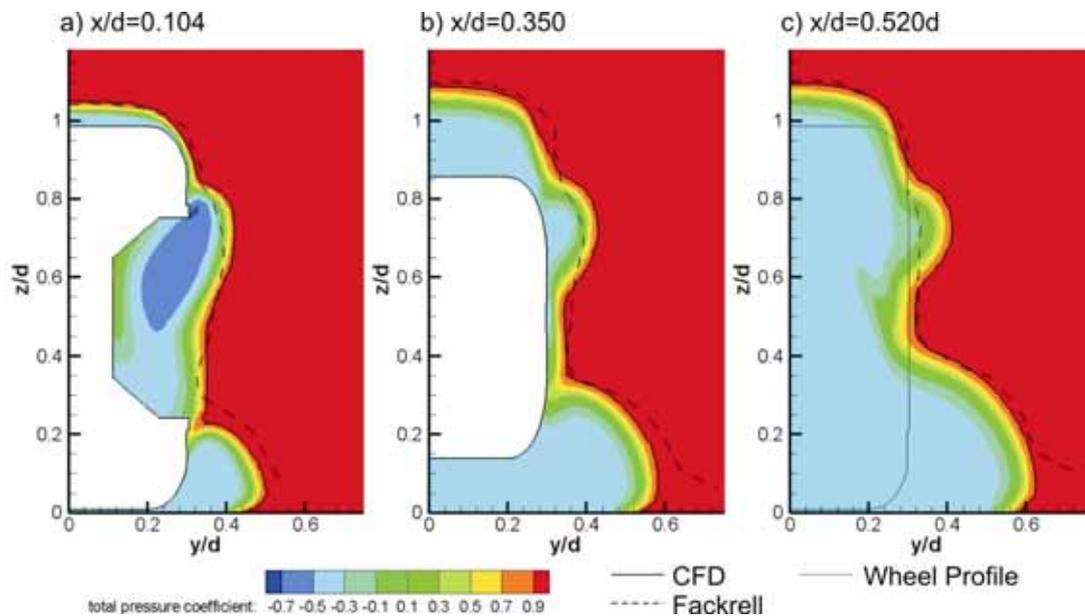


Figure 4.19 Total pressure comparison for Fackrell's B2 rotating wheel

The total pressure coefficient comparison suggests that the separation point for the rotating wheel over the wheel tread, or centre circumference, has been accurately predicted. Similarly, the wheel wake width also shows excellent agreement suggesting that the separation point from the wheel shoulder is also well predicted. The main variations occur where a vortex is formed in the wheel hub and the lower wake region where one of the two main wheel vortices are expected to form ($z/d=0.7$). The variation in predicting the inner hub vortex is not considered to be a problem as it is intended to use a simplified wheel geometry for this study which has completely flat sides and therefore this flow feature is not expected to occur. The variation from the main wheel vortex is not expected to be that significant either given that the experimental and numerical are no more than $0.05d$ apart. Despite these variations, this comparison for the wheel wake has shown better agreement than the previous comparison conducted at a lower Reynolds number during the selection of the turbulence model. The better correlation obtained is confirmation that the modelling procedure used, which assumes a completely turbulent boundary layer, is better suited to predicting a higher Reynolds number flow. This is a positive outcome for this study considering that the wing and wheel investigation is

intended to be conducted at a Reynolds number closer to that used by Fackrell than that used during the LDA comparisons.

Since it is intended to vary the wheel width during this study, a comparison has also been conducted to the results obtained by Fackrell for the A2 and B2 rotating wheels (Figure 4.16). This commenced by comparing the lift and drag coefficients obtained by Fackrell for the two wheel geometries (Figure 4.20). The computational model has accurately predicted the drag coefficient of the two wheels within the experimental accuracy indicated by Fackrell (5% and 10% for the A2 and B2 wheels respectively) with a variation for both cases of +/-2%.

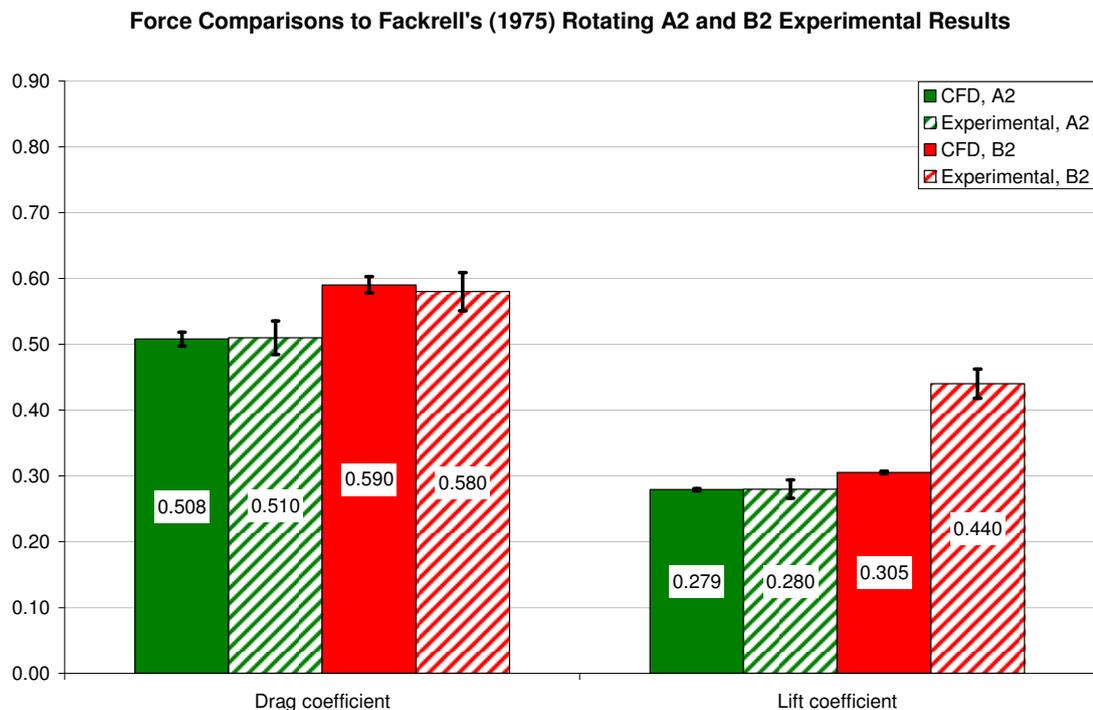


Figure 4.20 Force comparisons for Fackrell's A2 and B2 rotating wheels

The most significant differences exist for the wheel lift. The lift correlation with the narrower wheel (A2) appears to be significantly better than that for the wider wheel (B2) with a variation of 9% in comparison to 30%. Upon further investigation, it was determined that the B2 wheel lift coefficient stated by Fackrell was greater than the widest wheel, tested by him (Table 4.1). This seems counter intuitive as both the lift and drag coefficients would be

expected to increase as the wheel width would increase which was the case for the results obtained for the alternate wheel shoulder profile.

Wheel	Wheel shoulder profile 1			Wheel shoulder Profile 2		
	Width	C _D	C _L	Width	C _D	C _L
A	0.50	0.52	0.28	0.46	0.51	0.28
B	0.66	0.63	0.40	0.61	0.58	0.44
C	0.81	0.70	0.43	0.76	0.70	0.43

Table 4.1 Lift and drag coefficients obtained by Fackrell based on frontal area

Fackrell also indicated that very little variation was obtained for the results for the two different wheel shoulders. Unfortunately, the lift and drag coefficients for the B2 rotating wheel do not agree well with those obtained with the B1 supporting his concerns for the results obtained for the B2 wheel. This may suggest that the large variation seen for the lift and drag of the rotating and stationary wheel is more likely to be due to some experimental error rather than the computational model performing poorly. Unfortunately, no other experimental investigation has been conducted of a rotating wheel which provides as much detail of the geometry being tested and also correctly modelled the rotating wheel in contact with a moving ground. Therefore, despite the deficiencies in the results obtained by Fackrell, it is still the most suitable data to be used for correlation of an isolated rotating wheel.

4.3.2. Comparison to Numerical Study Conducted by McManus

Separated flows from bluff bodies are expected to generate flow features that vary with time. Therefore, an unsteady approach would be considered more appropriate for computing the flow associated with bluff bodies such as a wheel. This approach was undertaken by McManus and Zhang (2006) using Fackrell's (1975) A2 wheel geometry and therefore a comparison will be made to McManus and Zhang's results to determine what effect this compromise has for modelling the flow structures. While McManus and Zhang's approach is strictly more appropriate for a wheel, the computational resources required to conduct such an investigation are much greater than those required for a steady state model. Given the number of parameters intended to be investigated for the

wing and wheel interaction, an unsteady investigation would have been unfeasible at the time that this research was conducted. For this reason a steady state model was chosen. To determine what effect this compromise has on the flow structures associated with a rotating wheel, comparisons were conducted to the results obtained by McManus. Unfortunately, these results are somewhat limited and therefore qualitative comparisons can only be conducted.

McManus and Zhang solved an unsteady RANS computational model and used two different turbulence models to provide closure. The Spalart-Allmaras and $k-\epsilon$ realizable turbulence models both gave very similar results, but McManus and Zhang also determined that the $k-\epsilon$ realizable model proved to be best at predicting the flow structures associated with a rotating and stationary wheel. Therefore, all results obtained by McManus and Zhang with this turbulence model have been used for comparisons here. This computational model allowed McManus and Zhang to create a schematic representation of the flow structures to demonstrate the variation between a rotating and stationary wheel. A comparison to this schematic has been undertaken and is included as Figure 4.21.

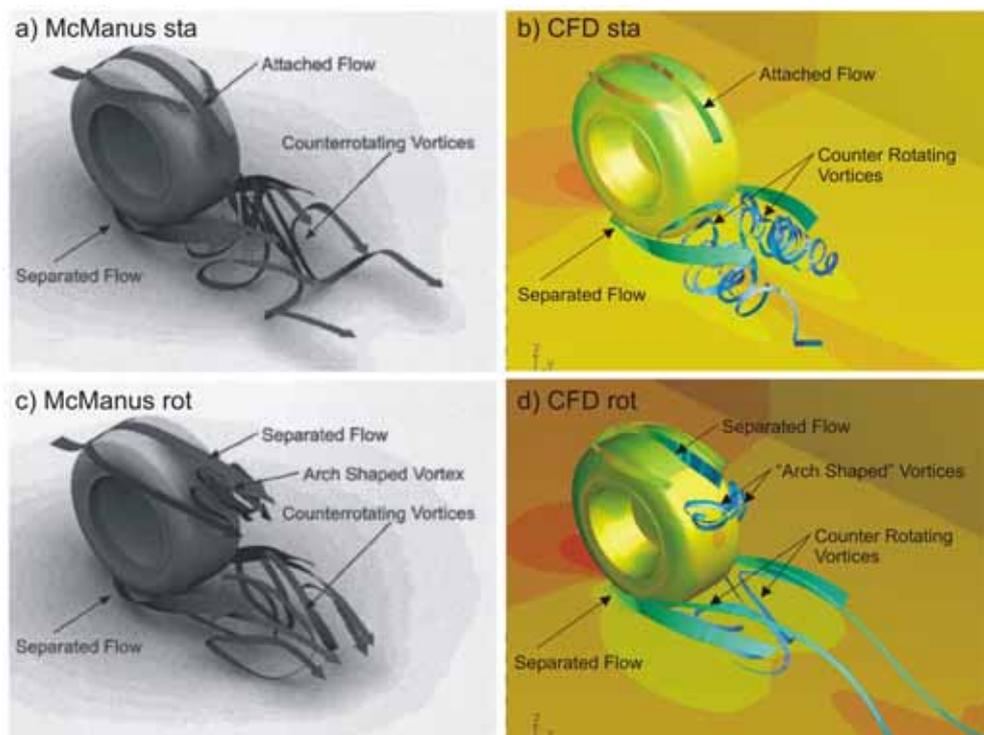


Figure 4.21 Schematic comparison to McManus and Zhang's results for Fackrell's A2 wheel

For the comparison to McManus and Zhang's schematic, streamlines have been released in the regions where key flow structures are expected to exist. This has indicated that the flow structures obtained with McManus and Zhang's unsteady model can also be obtained with a steady state model. The variations obtained in the separation point for the rotating (Figure 4.21c) and a stationary wheel (Figure 4.21a) by McManus and Zhang has been reproduced by the steady state computational model. The flow over the top of the rotating wheel (Figure 4.21d) separates while the stationary wheel (Figure 4.21a) remains attached. The separation experienced by the rotating wheels causes the flow to be entrained into the upper wheel wake region and as a result two additional vortices referred to as the "arch shaped" vortices by McManus and Zhang, have formed in this region only for the rotating wheel. As McManus and Zhang have indicated, both the rotating and stationary wheels produce separated flow either side of the front contact patch which assists the formation of two counter rotating vortices at the bottom of the wheel wake. The structure of the main wheel vortices for the stationary and rotating wheels differs. McManus and Zhang demonstrated this by comparing vectors and vorticity values located on a plane one diameter downstream of the wheel centre for one side of the wheel wake. A comparison to these results has also been conducted and is included as Figure 4.22.

McManus and Zhang's wake structure indicates that the main wheel vortex core for the stationary wheel (Figure 4.22a) is lower, broader and has a greater strength than that of the rotating wheel (Figure 4.22c). A similar trend has also been obtained for the stationary (Figure 4.22b) and rotating wheels (Figure 4.22d) with the steady state model. The downwash in the wheel centre also varies similarly between the two cases as should be expected as this is dependant on the separation point from the top of the wheel. McManus and Zhang's rotating result also indicate that the upper wheel vortex is rotating in the opposite direction and with a peak x-vorticity value less than that of the lower main wheel vortex. This feature has also been reproduced despite the x-vorticity values been greater than those indicated by McManus. Also consistent with McManus's results is the stronger entrainment from the side of the wheel wake obtained for the rotating wheel in comparison to that of the stationary wheel.

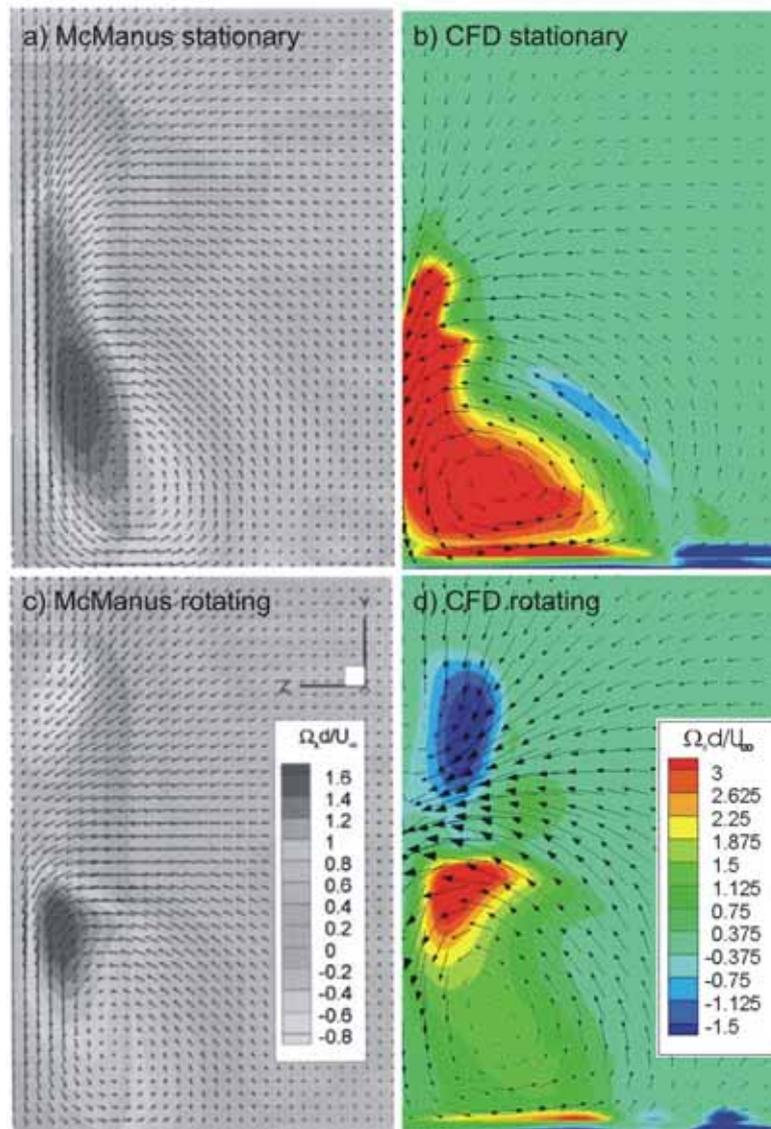


Figure 4.22 Wake comparison to McManus' time averaged results for Fackrell's A2 wheel

The use of an unsteady computational model would allow an indication of how the strength and positions of vortices vary over time to be obtained. Variations of these flow structures are likely to affect the separation and the forces experienced by the wheel. Unfortunately, McManus has only presented averaged results and how significant these variations are can not be determined as a result. Despite this, the comparisons conducted to McManus and Zhang's results have indicated that the mean flow structures associated with a rotating or stationary wheel can be predicted as accurately using a steady state solver as that of an unsteady computational model. Therefore, the validation will progress to investigate how

effective the computational model can predict the interaction of a wing and wheel when parameters of interest are adjusted.

4.4. Combined Wing and Wheel Validation

Up until this point, it has been demonstrated that previously published experimental trends obtained for variations in geometric features of an isolated wing or isolated wheel can be reproduced with the computational model intended to be used for the combined wing and wheel study. While the comparisons to the individual bodies were necessary in order to make comparisons at a higher Reynolds number, and also to make a force and surface pressure comparison, it was also considered necessary to demonstrate that the variation in the interaction of a combined wing and wheel could also be faithfully reproduced by the computational model. Given that no experimental published data exists for such an interaction, the author obtained LDA results for variations in wing span, angle of attack, and height as well as wheel width to conduct comparisons to results obtained with the sub-scale computational model. These results were obtained for an isolated wing and isolated wheel as well as both operating in unison. All the results of this comparison have been included as Appendix C, but it has been decided to only discuss four of these configurations of the above matrix here. The four cases selected for this discussion all have a common wheel width and track values of $T/c=0.631$ and $W/c=1.6$ respectively and wing height of $h/c=0.13$. Two wing angles of attack of 0° and 12° are presented at two different wing span values of $S/c=0.97$ and $S/c=1.6$.

4.4.1. Comparisons to LDA Results for wing with span $S/c=0.97$

Commencing with the comparison for the shorter span configuration ($S/c=0.97$), the experimental results indicate that on the $x/c=-0.63$ plane, located between the wing and wheel (Figure 4.1), a number of key flow variations exist due to increasing the wing angle of attack from 0° (Figure 4.23a) to 12° (Figure 4.23b). The most noticeable difference is the increase in the strength of the main wing vortex which are both located inboard of the wheel ($y/c=0.7$, $z/c=0.2$) for the two different angles of attack presented here. Also associated with the increase of angle of attack was a general increase in the upwash experienced behind and above the wing and an increase in the x-velocity component in

the same region ($0 < y/c < 0.8$, $0.5 < z/c < 1$). Comparing the computational results (Figure 4.23c,d) indicates that the computational model is able to predict the same trends for the same change in the wing angle of attack with the variation in strength of the main wing vortex, the increase in the x-velocity component and upwash behind and above the wing all being accurately simulated. Another flow feature noticeable in the experimental results recorded for the $x/c = -0.63$ plane is the wheel stagnation point located forward of the wheel ($y/c = 1.3$, $z/c = 0.55$). This feature was unaffected by the variation in the angle of attack for the wing located forward of the wheel for this span which was also replicated by the computational model.

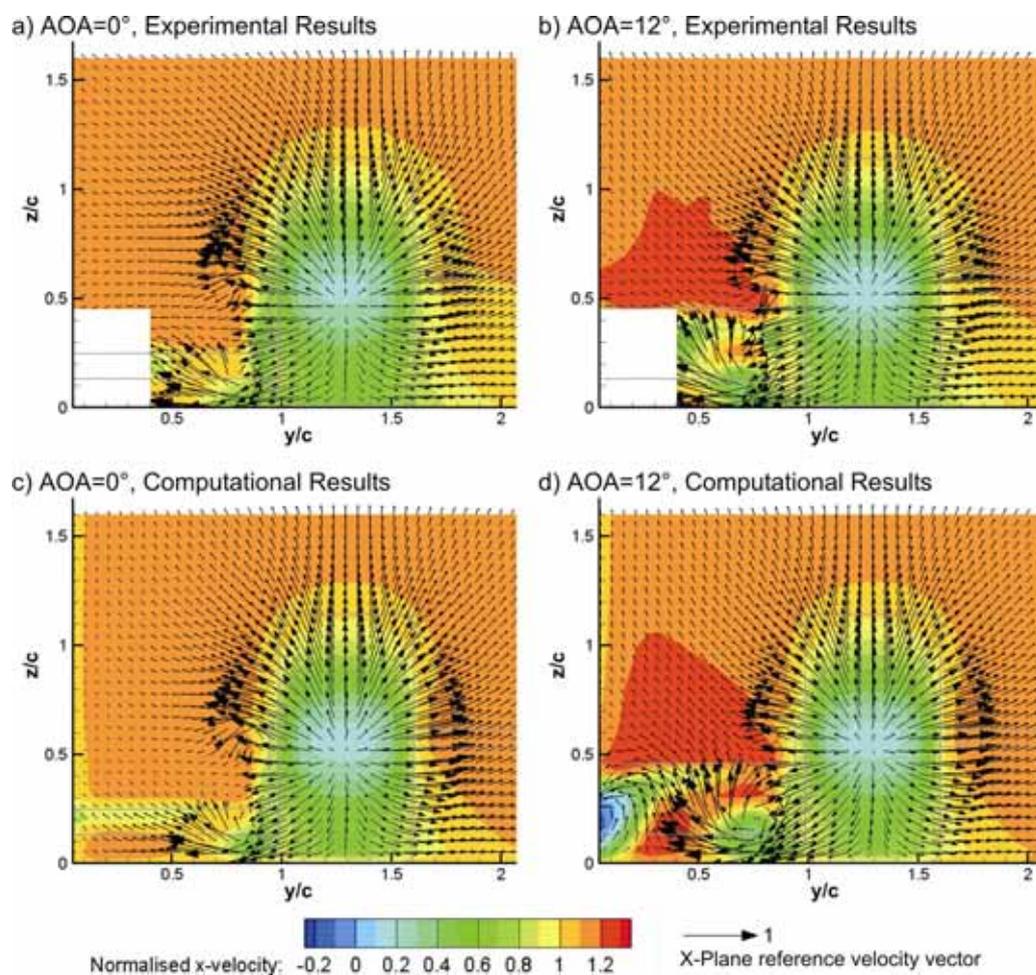


Figure 4.23 Comparisons to LDA for 0° and 12° angles of attack for span $S/c=0.97$ at $x/c=-0.63$

An additional feature noticeable within the computational results was a reduction in x-velocity in the region directly behind and spanning across the wing which was positioned higher when the wing angle of attack was increased. This velocity deficit indicates the position and height of the wing wake with the computational results suggesting that this feature is positioned in the region of $0 < y/c < 0.9$, $z/c = 0.2$ and $0 < y/c < 0.9$, $z/c = 0.4$ for the wing with angle of attack of 0° (Figure 4.23c) and 12° (Figure 4.23d) respectively. This feature could not be captured entirely due to the wing and wheel geometries preventing the LDA system measurement volume from accessing portions of this region, but from what has been measured, it appears that a similar variation has obtained experimentally. Portions of the wing wake have been captured in the regions of $0.4 < y/c < 0.9$, $z/c = 0.2$ and $0.4 < y/c < 0.9$, $z/c = 0.4$ for the experimental results of the 0° (Figure 4.23a) and 12° (Figure 4.23b) cases respectively.

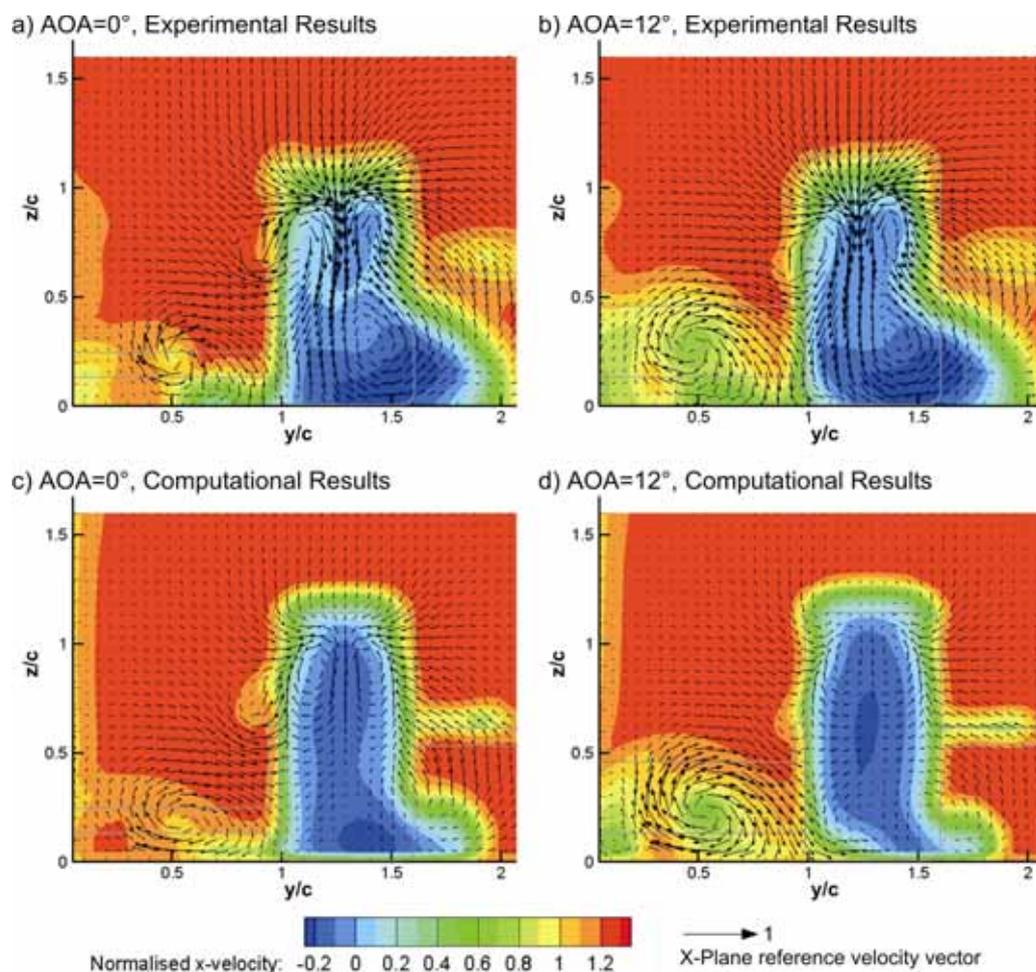


Figure 4.24 Comparisons to LDA for 0° and 12° angles of attack for span $S/c=0.97$ at $x/c=0.75$

The variation in the wing wake, and the ability of the computational model to capture this variation, is confirmed by the results obtained for the $x/c=0.75$ plane (Figure 4.24). The experimental results indicate that for an increase in wing angle of attack of 12° , the upper extremity of the wing wake rises from approximately $z/c=0.4$ (Figure 4.24a) to $z/c=0.65$ (Figure 4.24b) while the computational model determined that the same variation in angle of attack raises the upper extremity of the wing wake from $z/c=0.4$ (Figure 4.24c) to $z/c=0.6$ (Figure 4.24d). Within the wing wake, both the computational and experimental results again indicate that the main wing vortex is significantly stronger for the 12° case as should be expected, but of greater significance is the accuracy in which the position of this vortex has been determined by the computational model. For the 0° angle of attack comparison, the core of the main wing vortex was determined to be located at approximately $y/c=0.5$, $z/c=0.25$ and $y/c=0.5$, $z/c=0.2$ for the experimental and computational results respectively. For the 12° angle of attack cases, the main wing vortex core was located at $y/c=0.45$, $z/c=0.3$ and $y/c=0.5$, $z/c=0.25$.

One unique feature captured by the LDA at both wing angles of attack tested for the $S/c=0.97$ wing is what appears to be the secondary wing vortex rotating in the opposite direction to the main wing vortex. This vortex was also found to be stronger for the 0° angle of attack wing (Figure 4.24a, $y/c=0.85$, $z/c=0.7$), rather than the 12° angle of attack wing (Figure 4.24b, $y/c=0.85$, $z/c=0.65$). For an isolated wing, the secondary wing vortex has been shown to rotate in the same direction as that of the main wing vortex (Jasinski and Selig, 1998) and increase in strength with increases in angle of attack (Zerihan, 2000). The opposite rotation of the secondary vortex obtained here is likely to be due to the presence of the wheel and the high pressure region created forward of the wheel causing a pressure difference acting over the top edge of the endplate opposite to what is experienced by a wing in isolation. This feature will be investigated further during the wing and wheel investigation, but it is encouraging to see here that the same direction and variation has been obtained with the computational model. Additionally, the position of the vortices have also been captured by the computational model with the secondary vortex being located at $y/c=0.85$, $z/c=0.75$ and $y/c=0.85$, $z/c=0.65$ for the 0° (Figure 4.24c) and 12° (Figure 4.24d) computational results respectively.

Both the experimental and the computational results indicate that the wheel wake is asymmetric in structure and larger at the base on the outboard side. Little variation was obtained in the height and the width of the wheel wake with the height being over estimated once again as initially indicated during the comparison undertaken to determine which turbulence model is best suited to a wing and wheel interaction (Section 4.1). The comparison of the wheel wake to the total pressure results obtained by Fackrell (1975) indicated better agreement with no variation in the overall width and height of the wheel wake (Figure 4.19). As mentioned during this comparison (Section 4.3.1), this is expected to be due to the variation in the boundary layer properties between the modelling technique used by the computational model (completely turbulent) and the boundary layer produced over the experimental models due to the limited Reynolds number that the experimental results have been obtained at (mostly laminar). Given the improved performance of the computational model at the higher Reynolds number comparisons, it is expected that this will not hinder the full-scale models ability to predict a wing and wheel interaction at the higher Reynolds number that this investigation will be conducted at.

Another variation measured in the wheel wake is a reduction in the downwash acting along the centre of the upper wheel wake for the higher flap angle of approximately 20% ($y/c=1.3$, $0.5 < z/c < 1$). While the downwash calculated by the computational model is less than that measured experimentally in the same region, the trend of a reduction of downwash with an increase in angle of attack was reproduced by the computational model. Additionally, the two counter rotating vortices expected in the upper wheel wake region of a rotating wheel are evident in both experimental results and, unlike the initial comparison of the $k-\varepsilon$ realizable turbulence model, both these vortex structures have also been reproduced by the computational model for this comparison. The position of the upper wheel vortices remains mostly unchanged ($y/c=1.1$, $z/c=0.75$ and $y/c=1.4$, $z/c=0.8$) between the two experimental results and this is also replicated by the computational model despite the position of these vortices being calculated to be slightly different ($y/c=1.15$, $z/c=0.8$ and $y/c=1.4$, $z/c=0.8$). By the $x/c=1.5$ plane, the experimental results indicate that the upper wheel wake vortices have dissipated for both angles of attack (Figure 4.25a,b), but the stronger downwash in the centre of the wheel wake still remains for the 0° angle of attack wing relative to the 12° angle of attack wing. Both these features have also been reproduced by the computational model on the $x/c=1.5$ plane with the main variation in the wheel wake to that which was measured being that no cross flow

component has been predicted within the central region of the wheel wake (Figure 4.25c,d).

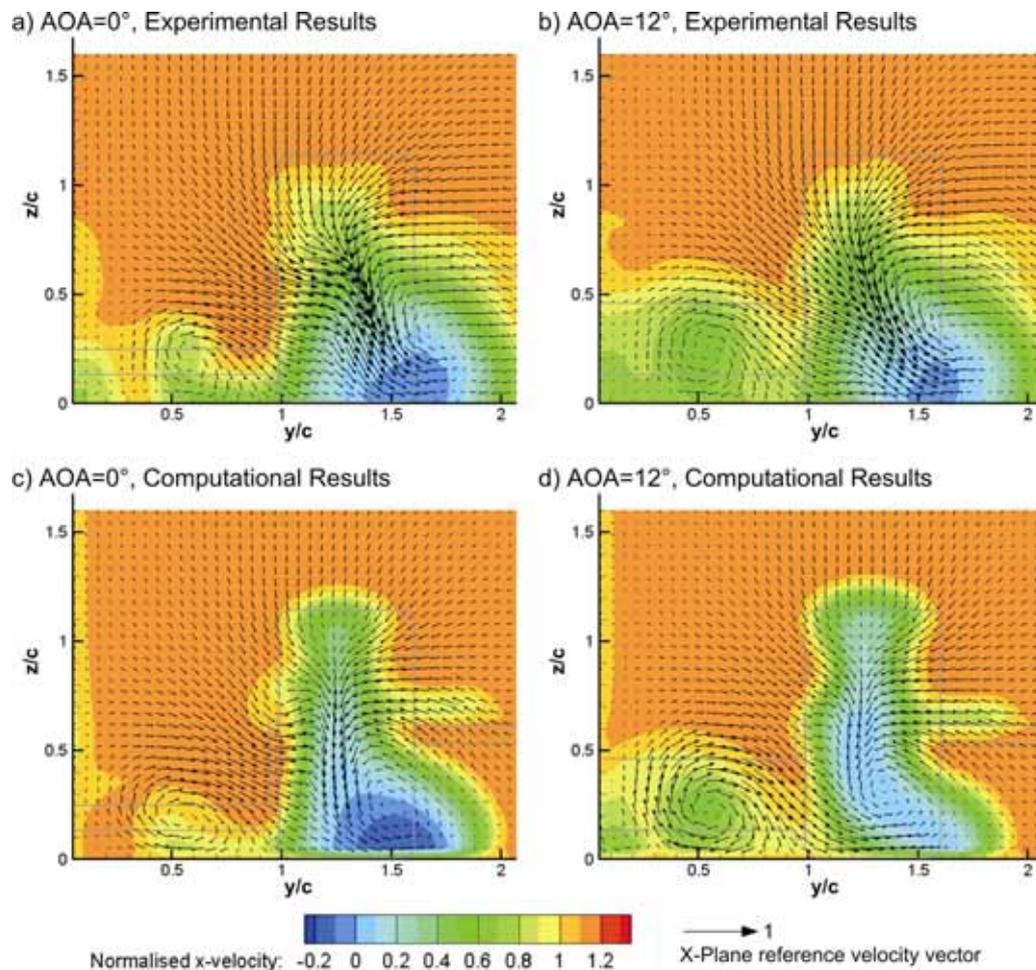


Figure 4.25 Comparisons to LDA for 0° and 12° angles of attack for span $S/c=0.97$ at $x/c=1.5$

By the $x/c=1.5$ plane, the experimental results also indicate that the secondary wing vortex has also dissipated with the only two vortex structures remaining by this plane being the outboard primary wheel vortex and the main wing vortex. The experimental results indicate that the position of the outboard primary wheel vortex is also influenced by the wing angle of attack with the core of the primary wheel vortex being located at $y/c=1.75$, $z/c=0.35$ and $y/c=1.65$, $z/c=0.35$ for the 0° and 12° angle of attack wings respectively. While the absolute location of the primary wheel vortex varied to that measured experimentally, the relative shift associated with the variation in angle of attack was reproduced by the computational model. For the computational results of the 0° and 12° angle of attack wings

the primary wheel vortex was calculated to be located at $y/c=1.5$, $z/c=0.3$ and $y/c=1.4$, $z/c=0.3$ respectively.

Consistent with the previous planes, the stronger main wing vortex from the 12° angle of attack wing is still evident on the $x/c=1.5$ plane in both the computational and experimental models. The location of this vortex is also accurately reproduced by the computational model for the two different wing angles of attack with the 0° and 12° wing angles of attack main wing vortex cores being measured and calculated to be located at approximately $y/c=0.55$, $z/c=0.2$ and $y/c=0.55$, $z/c=0.25$ respectively.

In general, it can be said that the flow structures and the variations associated with a change in the wing angle of attack for a wing with span value of $S/c=0.97$ calculated by the computational model agree well with that measured experimentally. Therefore, the comparison will continue by considering the variation in wing angle of attack for a wing span of $S/c=1.6$.

4.4.2. Comparisons to LDA Results for wing with span $S/c=1.6$

Comparison conducted between the computational and experimental results for a wing and wheel combination where the span of the wing is equal to $S/c=1.6$ and the angle of attack is either 0° or 12° are included as Figure 4.26 to Figure 4.28. Commencing with the experimental results of the 12° angle of attack wing on the plane located between the wing and the wheel, it is clear that this wing produces a clearly definable vortex which is located at $y/c=1.4$ and $z/c=0.15$ (Figure 4.26b) which is not evident for the wing with 0° angle of attack (Figure 4.26a). Given that this vortex is generated via a pressure differential established either side of the bottom edge of the endplate (Zerihan and Zhang, 2003), this would suggest that the 0° wing in the presence of the wheel does not produce adequate suction beneath the tip of the wing in order to overcome the high pressure region generated forward of the wheels contact patch (Fackrell and Harvey, 1975). The experimental results indicate that increasing the wing angle of attack to 12° appears to be sufficient to establish the pressure differential required to create the main wing vortex. This unique interaction feature of a wing and wheel combination has been reproduced by the computational model with the position of the main wing vortex in the 12° angle of attack case also being accurately reproduced (Figure 4.26d).

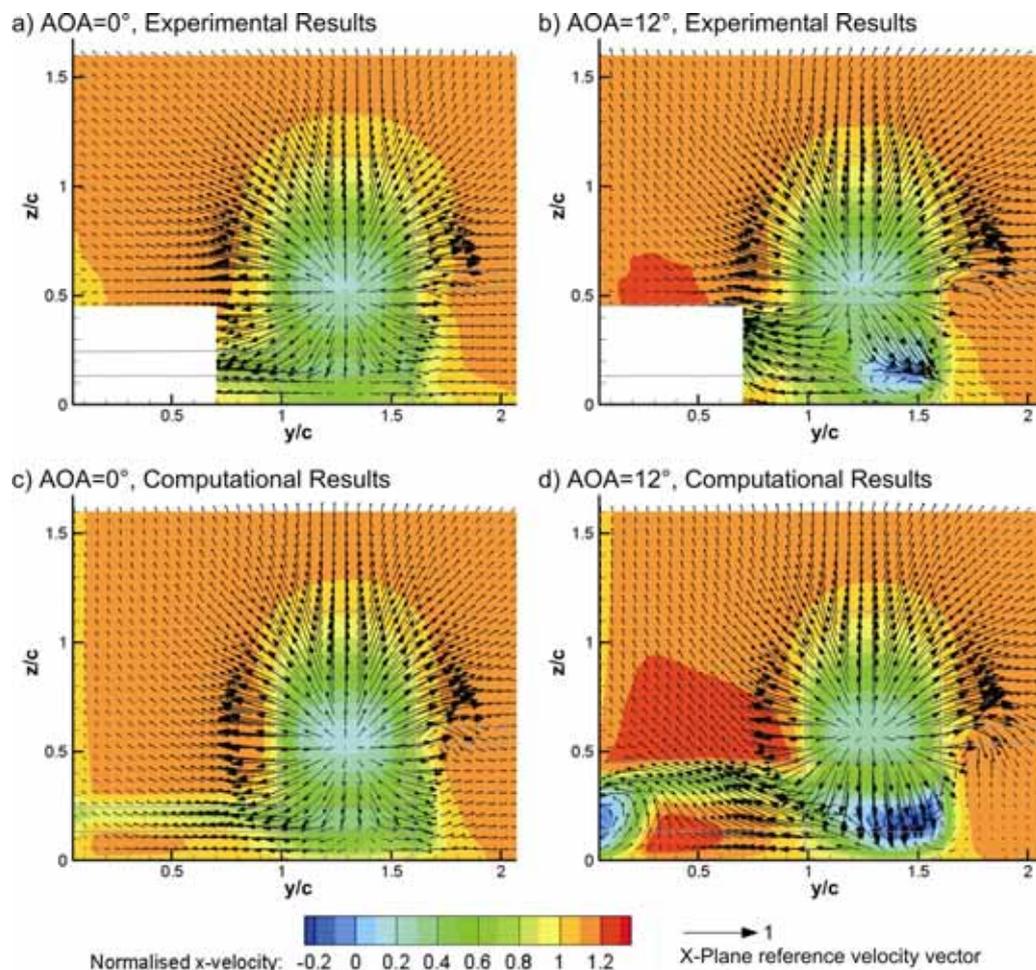


Figure 4.26 Comparisons to LDA for 0° and 12° angles of attack for span $S/c=1.6$ at $x/c=-0.63$

As a consequence of the formation of the main wing vortex and also due to the greater suction generated by the higher angle of attack wing, an increase in the cross flow component has been obtained for the 12° wing. This is most vividly demonstrated when comparing the vectors located in the vicinity of $y/c=1.3$ and $z/c=0.1$ for the two experimental results (Figure 4.26a, b). This region indicates the point at which the flow travelling towards the contact patch diverges and passes either side of the wheel not only for the wing with 0° angle of attack, but also for the previous span that the comparison was conducted at (Figure 4.23a,b). Increasing angle of attack at this span appears to influence the distribution of flow either inboard or outboard of the base of the wheel. The computational results indicate similar variations but also demonstrate that the increase in the cross flow component is greater further inboard of the wing. Unfortunately, the

previously discussed limitations of the LDA system for this plane prevented this feature from being measured.

Another variation with wing angle of attack both measured experimentally and calculated by the computational model is an increase in height of the stagnation point forward of the most upstream location of the wheel. This was determined to be located at $y/c=1.3$, $z/c=0.5$ and $y/c=1.3$, $z/c=0.55$ for the wing with 0° (Figure 4.26a,c) and 12° (Figure 4.26b,d) angles of attack respectively. This feature was found to remain in the same position for the shorter span wing comparison (Figure 4.23).

One common feature measured with an increase in wing angle of attack for both span wings has been a general increase in the upwash experienced behind and above the wing and an increase in the x-velocity component in the same region ($0 < y/c < 0.8$, $0.5 < z/c < 1$). The experimental results indicate that this feature is more enhanced for the shorter span wing (Figure 4.23c) rather than the wing spanning across the entire face of the wheel (Figure 4.26c). Comparing the computational results for the same angle of attack variation for the $S/c=1.6$ wing (Figure 4.26c,d) and also the variation in span for the two 12° wing angle of attack cases (Figure 4.23d and Figure 4.26d), the same conclusion can also be obtained with both trends being reproduced by the computational model.

Like the previous results presented for the $S/c=0.97$ wing, the computational results for the $S/c=1.6$ wing once again indicate that an additional vortex is formed at the junction of the wing and wall for the 12° wing angle of attack case (Figure 4.26d, $y/c=0.1$, $z/c=0.2$) which is not evident for the 0° case (Figure 4.26c). While it was not possible to measure this flow feature at the $x/c=-0.63$ plane, evidence of this vortex structure has been obtained once again further downstream for the measurements made at the $x/c=0.75$ plane (Figure 4.27c). The position of this vortex varies between the experimental measurements and the computational results with the core being located at $y/c=0.4$, $z/c=0.3$ and $y/c=0.2$, $z/c=0.2$ respectively. While this variation exists in the position of the junction vortex, this flow feature is not expected in the unbounded computational model as the wind tunnel wall will be replaced with a symmetry plane. Regardless, the experimental results indicate that this vortex interacts with the main wing vortex (Figure 4.27b, $y/c=0.9$, $z/c=0.35$) and creates a region of enhanced upwash between them. While the interaction of the junction vortex and the main wing vortex has been reproduced by the computational model, the position of the

main wing vortex appears to be less accurate than that which has been obtained for previous comparisons. The computational model calculated that the core of the main wing vortex is located lower and more inboard (Figure 4.27d, $y/c=0.8$, $z/c=0.25$) than that which was measured. Given the close proximity of the junction vortex, this variation may be due to the interaction with the poorly predicted junction vortex. The computational model being able to reproduce the measured position of the main wing vortex for the 0° angle of attack case (Figure 4.27a, b, $y/c=0.9$, $z/c=0.25$) supports this suggestion.

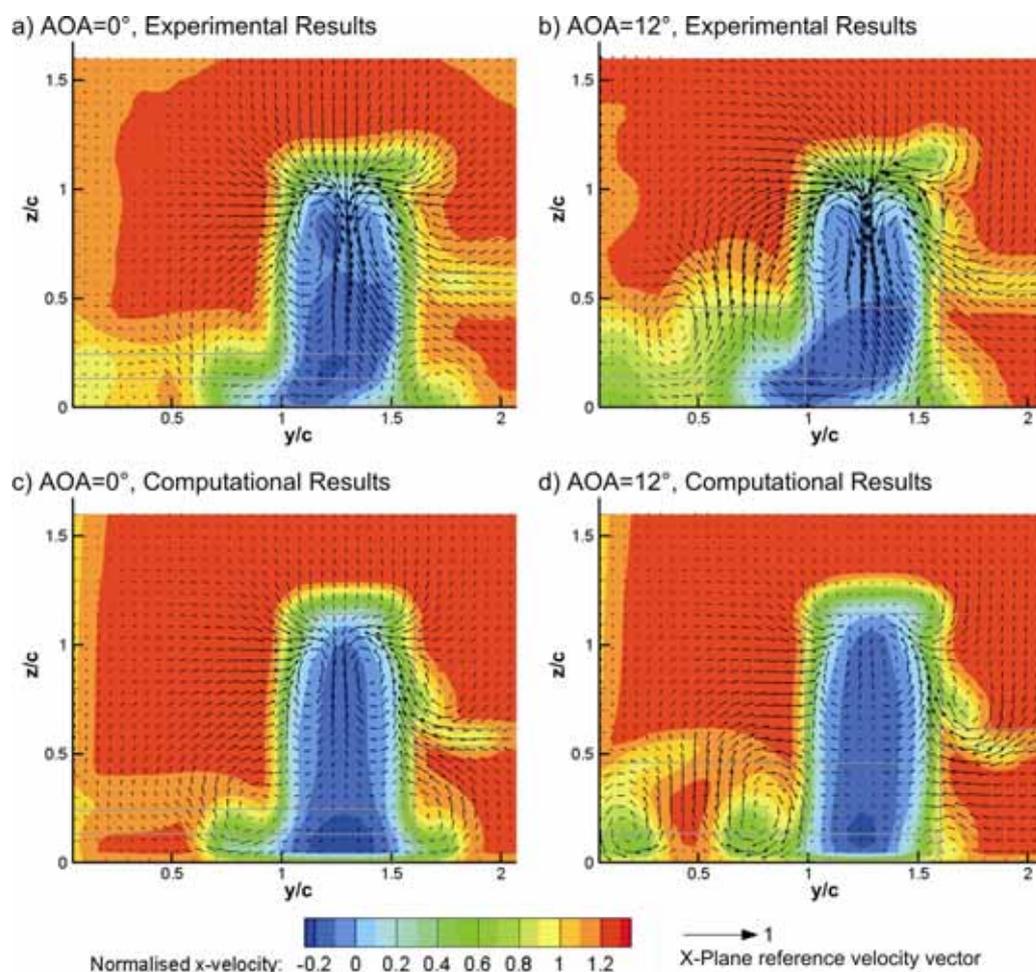


Figure 4.27 Comparisons to LDA for 0° and 12° angles of attack for span $S/c=1.6$ at $x/c=0.75$

The experimental results obtained for the $x/c=0.75$ plane also demonstrate that the 12° wing produces a secondary wing vortex that is located at $y/c=1.7$, $z/c=0.85$ (Figure 4.27b). Unlike the previous comparison conducted with the $S/c=0.97$ wing, the secondary vortex is rotating in the same direction as the main wing vortex. While a secondary vortex is also

expected for the wing with 0° angle of attack and $S/c=1.6$, it is believed to have dissipated prior to reaching the $x/c=0.75$ plane due to its reduced strength. In both cases, the computational model correctly determines that the secondary vortex has dissipated by the $x/c=0.75$ plane for the 0° angle of attack wing (Figure 4.27c) and the existence of the secondary wing vortex for the 12° angle of attack wing albeit in a lower position (Figure 4.27d, $y/c=1.7$, $z/c=0.75$). By the $x/c=1.5$ plane, no secondary vortex is evident in either the computational or experimental results for either angle of attack wing (Figure 4.28).

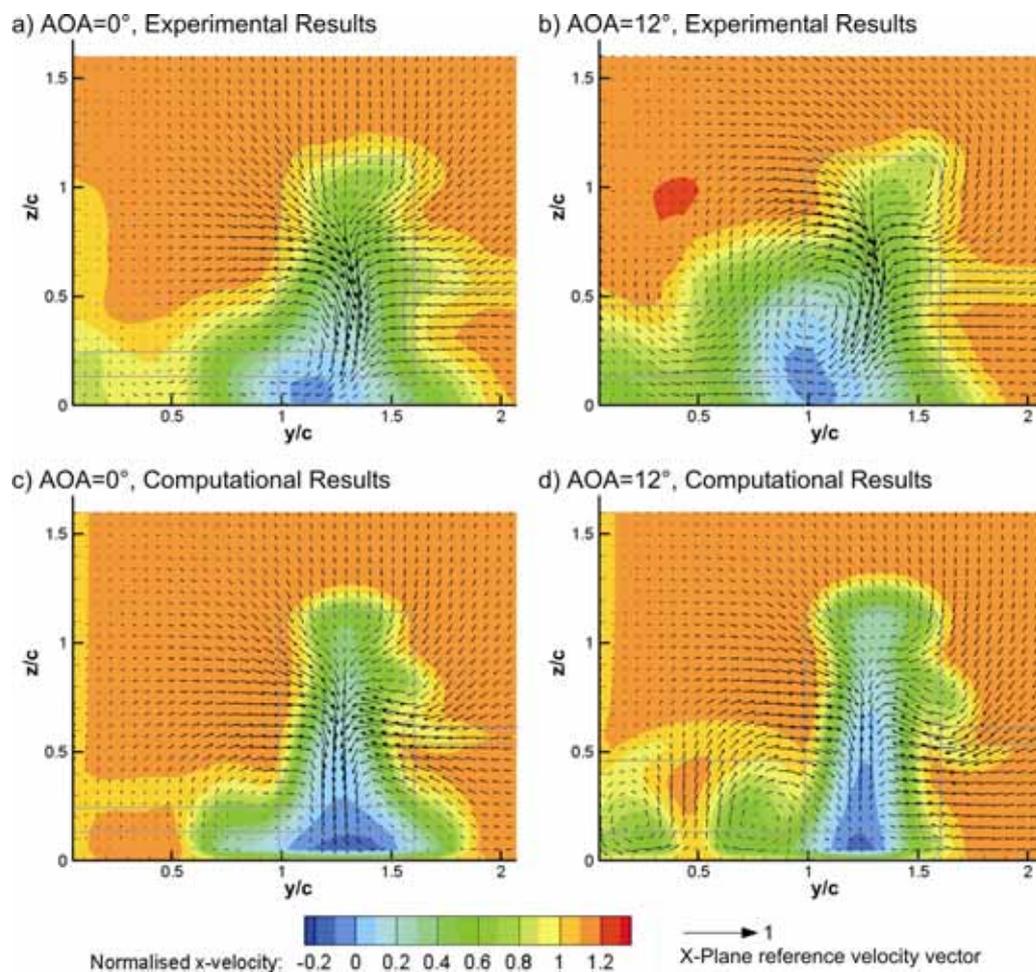


Figure 4.28 Comparisons to LDA for 0° and 12° angles of attack for span $S/c=1.6$ at $x/c=1.5$

The only vortex structures evident in the experimental results obtained at the $x/c=1.5$ plane (Figure 4.28b) for the 12° angle of attack wing was the main wing vortex and the junction vortex. Unlike the $S/c=0.97$ wing with 12° angle of attack, no outboard primary wheel vortex is evident on this plane despite a significantly smaller outboard primary wheel vortex being

visible on the $x/c=0.75$ plane (Figure 4.27b, $y/c=1.65$, $z/c=0.1$) for the same case. At the $x/c=0.75$ plane, the 0° angle of attack wing with $S/c=1.6$ span has a stronger outboard primary vortex (Figure 4.27a, $y/c=1.65$, $z/c=0.1$) suggesting that the cross flow variation obtained by increasing the wing angle of attack at this span forward of the wheel (Figure 4.26a,b) has reduced the separation obtained at the outer side of the wheel and the subsequent vortex that forms in the wheel's wake (McManus, 2006). Subsequently, the only vortex structures measured on the $x/c=1.5$ plane downstream of the $S/c=1.6$ wing with 0° angle of attack (Figure 4.28a) was the main wing vortex ($y/c=1$, $z/c=0.2$) and a weak outboard wheel vortex ($y/c=1.5$, $z/c=0.1$). Once again the position of the main wing vortex was better predicted for the 0° wing angle of attack by the computational model in comparison to the 12° angle of attack, but most importantly, the trends discussed for the variation in the outboard primary wheel vortex associated with the change in angle of attack and span have been reproduced by the computational model.

The last feature to be discussed for this comparison is the variation in downwash obtained for the $S/c=1.6$ wing at the two different angles of attack tested. The experimental results indicate a slightly taller wheel wake with a reduced downwash in the centre of the wake for the wing with 12° angle of attack (Figure 4.28a,b) which has also been reproduced by the computational model. Subsequently, the 0° wing angle of attack wheel wake appears to be shorter and wider at the base for both the computational and experimental results.

In conclusion, it has been demonstrated that the computational model adequately reproduces the flow structure associated with variations in the angle of attack for a wing span of $S/c=1.6$ for a wing in the presence of the wheel. Comparisons between the two different spans at common angles of attack have also agreed well demonstrating that the computational model can successfully predict the variation associated with both angles of attack as well as span.

4.5. Summary

Computational results obtained using the scaled computational model with several different turbulence models have been compared to experimental results to determine the most appropriate for a combined wing and wheel investigation. From this comparison, it was concluded that the $k-\varepsilon$ realizable turbulence model offered the best compromise

amongst the several different turbulence models tested when considering both the mean flow structures and the turbulence intensity. Subsequently, further validation was conducted with the computational model solely using this $k-\varepsilon$ realizable turbulence model at higher Reynolds number which is more representative of the speed and scale that the final wing and wheel investigation will be conducted at. Comparisons were made with results obtained by Zerihan (2001) of an isolated downforce producing wing demonstrating that the downforce loss phenomenon is predicted within the same resolution as that which was measured by Zerihan and that flow structures associated with this body vary in a consistent manner to that which he has described. Comparisons have also been made with experimental results obtained by Fackrell of an isolated wheel and have shown that the computational model can successfully predict the force variations associated with the wheel rotation and also changes in width. Comparisons of the wake extremities also agree favourably with the results obtained with the computational model as do the central circumference pressure distribution for all the variations compared. Using the same computational results, a comparison to results presented by McManus and Zhang (2006) also qualitatively demonstrate that the mean flow structures predicted by an unsteady approach can also be predicted using a steady state approach. Finally, a comparison was made with experimental results obtained of a combined wing and wheel interaction which demonstrated that for variations in the span and angle of attack of the wing variations in the interacting wing and wheel wakes are reproduced by the computational model. In doing so, the AIAA's (1998) recommended validation procedure has been fulfilled by demonstrating that the computational model can reproduce trends obtained experimentally, not only for sub-systems of the final geometry intended to be investigated, but also for the final complete system intended to be investigated. As a result, the computational model can now be used with confidence to conduct the desired investigations.

Chapter 5: Independent Wheel or Wing Investigations

5.1. Independent Wheel Investigations

In this section, four features of an isolated wheel are investigated. The first relates to the variation in the wheel wake associated with the wheel rotation as previous investigations in this area have been inconclusive. The second is the geometry used to model the contact between the ground and the wheel; this region is difficult to model accurately numerically and as a result some compromise must be made. The third investigation will focus on the effect of simplifying the wheel geometry, and the final investigation considers the variation associated with having two wheels adjacent to each other (as previous investigations have typically focussed on a solitary wheel working in isolation).

5.1.1. Lift, drag and wake structure dependency on wheel rotation

Previous experimental investigations of an isolated wheel have demonstrated that the primary wheel vortices form closer to the centre and at a greater height for a rotating wheel than that of a stationary wheel (Fackrell, 1975). It is also widely accepted that the wheel rotation increases the jetting action forward of the contact patch which leads to an increase in the horizontal velocity components in this region. Intuitively, this would suggest that the primary wheel vortices of a rotating wheel should be positioned lower and wider than that of a stationary wheel, yet no explanation has been provided thus far for why this anomaly exists. Given a wing positioned upstream of the wheel is likely to alter the flow forward of the contact patch, and the subsequent jetting action that contributes the formation of the primary vortices, it was decided that this phenomenon should be investigated in order to ascertain how flow variations in this region can influence the flow structures of a combined wing and wheel.

An initial hypothesis proposed by Fackrell (1975) to explain the variation in the primary wheel vortices position suggested that a pair of additional vortices form forward of the rotating wheel, due to the flow separating from the ground. It was believed that these vortices alleviate the path of the oncoming flow around the front contact patch allowing the

primary wheel vortices to form in a more central and higher position within the wake of a rotating wheel. The computational results obtained thus far of Fackrell's isolated rotating wheels have provided no evidence of these vortices, which also agrees with previous reports from McManus and Zhang (2006). Since this and no previous investigations have been able to demonstrate that these vortices exist, it seems fair to discount this hypothesis as a plausible explanation for the reduced lower wake width associated with the rotation of the wheel.

McManus and Zhang (2006) provided an alternative explanation. They proposed that the cause of the wider and lower position of the primary wheel vortices associated with a stationary wheel is due to the ejected flow from the front contact patch being deflected less by the oncoming flow due to the boundary layer formation over the stationary ground. As a result, the jetting action was expected to contribute a greater cross component in the stationary wheel wake than that which would be experienced by the rotating wheel with a moving ground, but no attempt was made by McManus and Zhang to prove this theory.

In an attempt to prove McManus and Zhang's theory, it was decided to replace the stationary ground with a slip condition so that the boundary layer would be completely eliminated. The computational model used to validate against Fackrell's (1975) experimental results of the stationary A2 wheel (Figure 4.15) was used to do this. A moving ground condition was not used as it was not expected to completely remove the boundary layer that develops over the ground as the flow around the wheel varies from the freestream velocity and therefore a boundary layer, albeit smaller, is still expected to develop. According to McManus and Zhang's hypothesis, a wheel wake structure that contains the primary vortices in a position that more closely resembles that of a rotating wheel should be obtained since the ejected flow can now be deflected to the full extent of the oncoming free stream velocity.

Total pressure contours and in plane vectors located on the $x/c=0.75$ plane were plotted to determine if a flow structure consistent with McManus and Zhang's proposal was obtained with the wheel outline shown in grey for reference (Figure 5.1). These results indicate that replacing the stationary ground with a slip condition does not alter the lower wheel wake in any significantly manner in comparison to that obtained of a stationary wheel. Despite the wheel wake taking a more asymmetric shape, the primary wheel vortices have formed in a

similar position (Figure 5.1b, $y/d=-0.2$, $z/d=0.2$ and $y/d=0.15$, $z/d=0.15$) to that found for a stationary wheel (Figure 5.1b, $y/d=-0.2$, $z/d=0.15$ and $y/d=0.15$, $z/d=0.2$). Additionally, the lift and drag values also closely resemble that of a stationary wheel further confirming that no significant variation has been obtained (Figure 5.1d). Therefore the influence that the boundary layer developing over a stationary ground has on the jetting action can be eliminated as a possible explanation for the variation in the lower wheel wake shape between a stationary and rotating wheel.

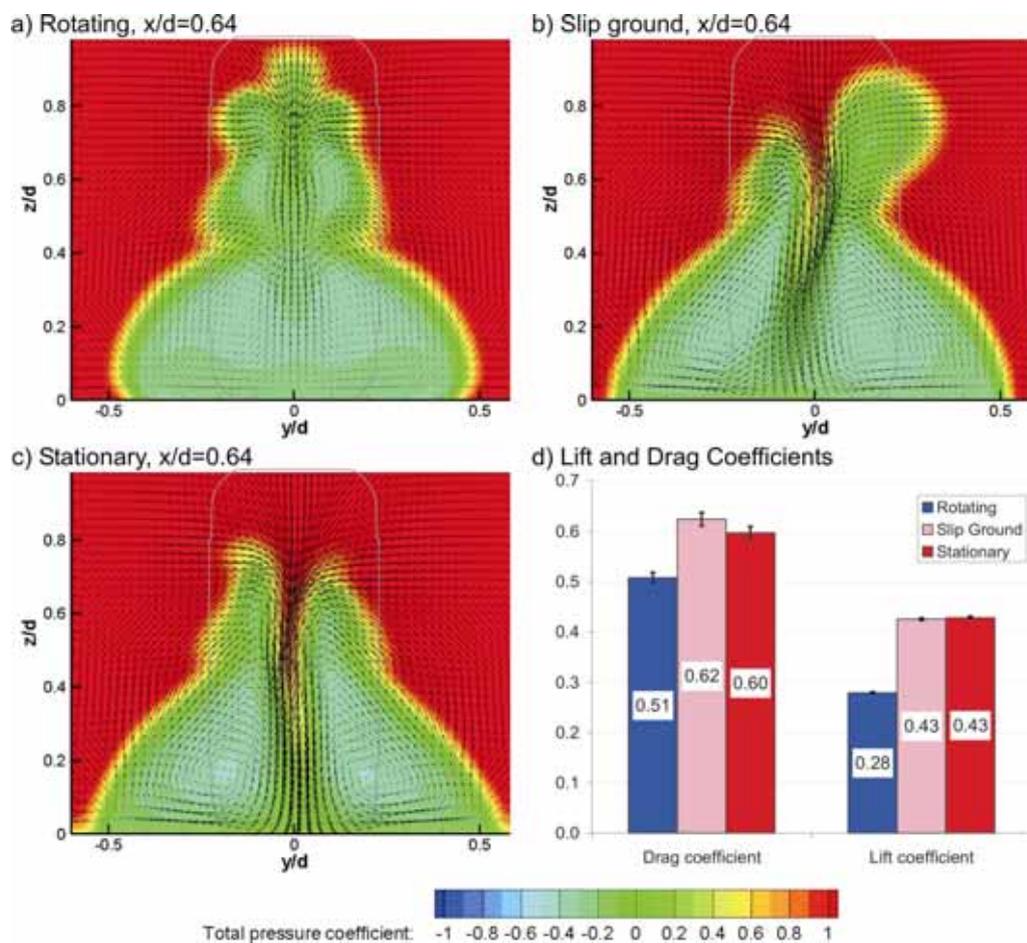


Figure 5.1 Comparison of wheel wake structure and forces obtained with slip ground condition

In an attempt to provide a valid explanation for the wheel rotation creating higher and more inboard positioned vortices despite the increased jetting action forward of the wheel, the computational model used to validate against Fackrell's A2 experimental results was used to independently reproduce each of the two flow features associated with the wheel

rotation. Additional to the increased jetting action forward of the front contact patch, Fackrell has also indicated that the wheel rotation causes an earlier separation point from the top wheel tread. Isolating these two characteristics of a rotating wheel was achieved by splitting the wheel boundary into upper and lower boundaries and then only applying the wheel rotation to either boundary. In the case where the lower wheel region was rotated, a moving ground was also employed. As demonstrated in Figure 5.2, the lower wheel boundary included the region of the wheel between $-45^{\circ} < \theta < 135^{\circ}$ while the remaining portion of the wheel was included in the upper wheel boundary.

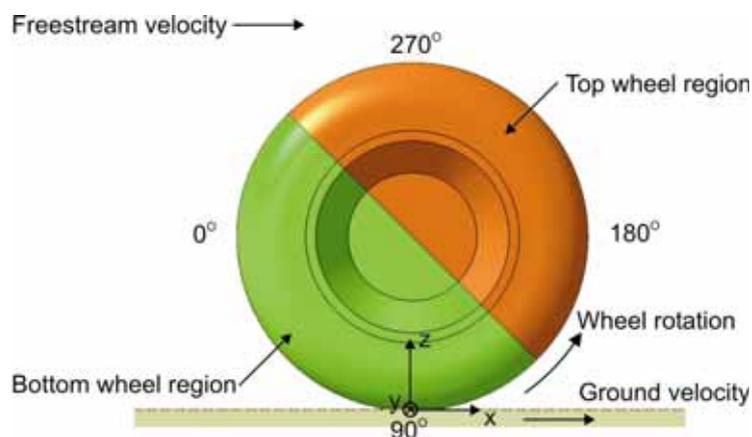


Figure 5.2 Separated Top and Bottom wheel regions for Fackrell's A2 wheel

Prior to commencing this investigation, it was necessary to determine if this unorthodox approach to treating the wheel rotation could be used to isolate the variation in the separation point and the jetting action forward of the contact patch due to the wheel rotation. While this approach may be physically difficult to achieve, the results presented in Figure 5.3 indicate that it has successfully managed to independently create the features associated with a rotating wheel. The ability to apply such a boundary condition with ease also demonstrates one advantage of using a computational model for such an investigation in comparison to taking an experimental approach. By applying the wheel rotation at the top, an earlier separation point (Figure 5.3c) that closely resembles that of the rotating wheel has been achieved while at the base, the y-velocity components indicates that no additional jetting action has been produced (Figure 5.3d). The opposite is also true when the wheel rotation is applied only to the bottom portion of the wheel with the separation being representative of the stationary case (Figure 5.3e) while the jetting action experienced is indicative of a rotating wheel (Figure 5.3f).

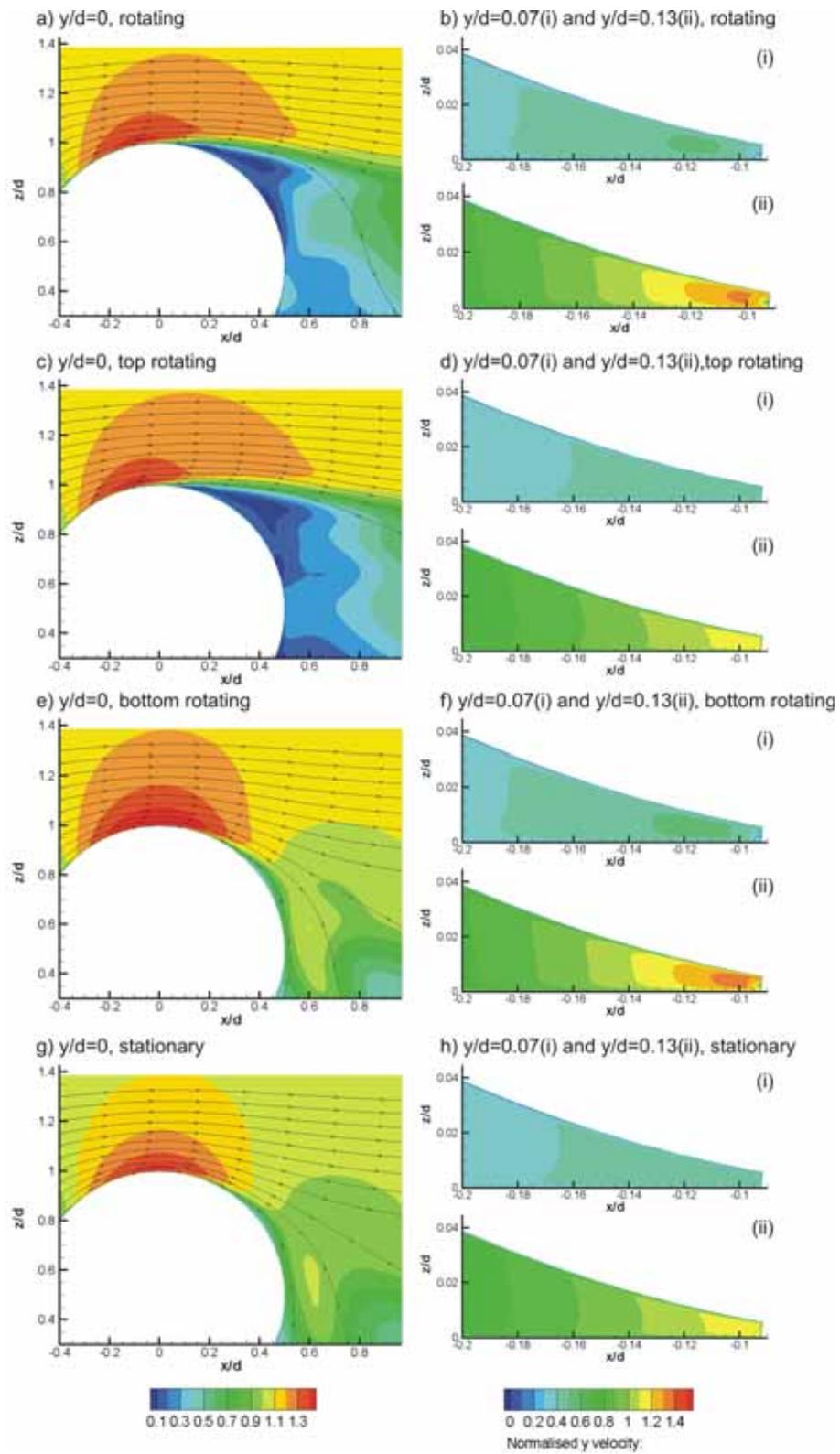


Figure 5.3 Streamlines indicating separation for tested boundary conditions

The central pressure coefficients (Figure 5.4) also confirm that the flow features located at the base or at the top of a rotating wheel have been reproduced and that the two characteristics associated with the wheel rotation have been created independently. The greater than 2 pressure coefficient experienced by a rotating wheel, which is responsible for the increased jetting action, has been replicated when only the bottom portion of the wheel has been rotated. This has had no effect on the separation point from the top of the wheel with pressure coefficients in the region of $190^\circ < \theta < 360^\circ$ of the wheel being identical to those associated with a stationary case. This would suggest that when the bottom portion of the wheel is rotated only, the lift should closely resemble that experienced by a stationary wheel. When the top of the wheel has been rotated, the opposite is also true and therefore the lift created for this boundary condition should be closer to that experienced by the rotating wheel. This has been confirmed by the forces obtained which will be discussed later during this section.

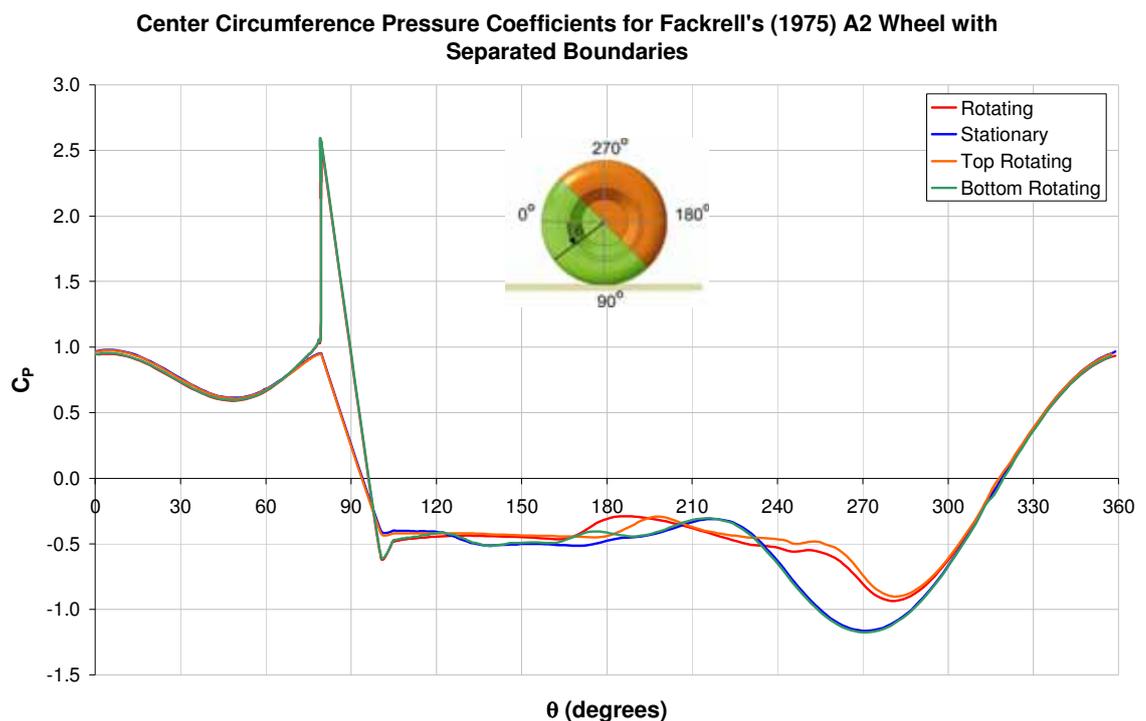


Figure 5.4 Central pressure coefficients obtained for wheels with separated boundaries

In order to determine the influence that each of the characteristics associated with a wheel rotation have on the vortices within the wake structure, total pressure contours and in

plane velocity vectors were used to compare the wake on the $x/c=0.75$ plane (Figure 5.5). Based upon these results, the separation point from the top wheel tread appears to be the critical flow feature that causes the primary wheel vortices to form in a higher and more inboard position (Figure 5.5b, $y/d=-0.1$, $z/d=0.45$ and $y/d=0.15$, $z/d=0.4$). As should be expected, the top rotating wheel has also reproduced the upper wheel vortices associated with the wheel tread separation (Figure 5.5b, $y/d=-0.1$, $z/d=0.75$ and $y/d=0.1$, $z/d=0.75$). It is also interesting to note that when only the top portion of the wheel boundary is rotated, the primary wheel vortices are located more inboard and higher than those associated with a completely rotating wheel (Figure 5.5b, $y/d=-0.15$, $z/d=0.3$ and $y/d=0.15$, $z/d=0.3$) suggesting that the jetting action does in fact draw the primary wheel vortices outboard and lower.

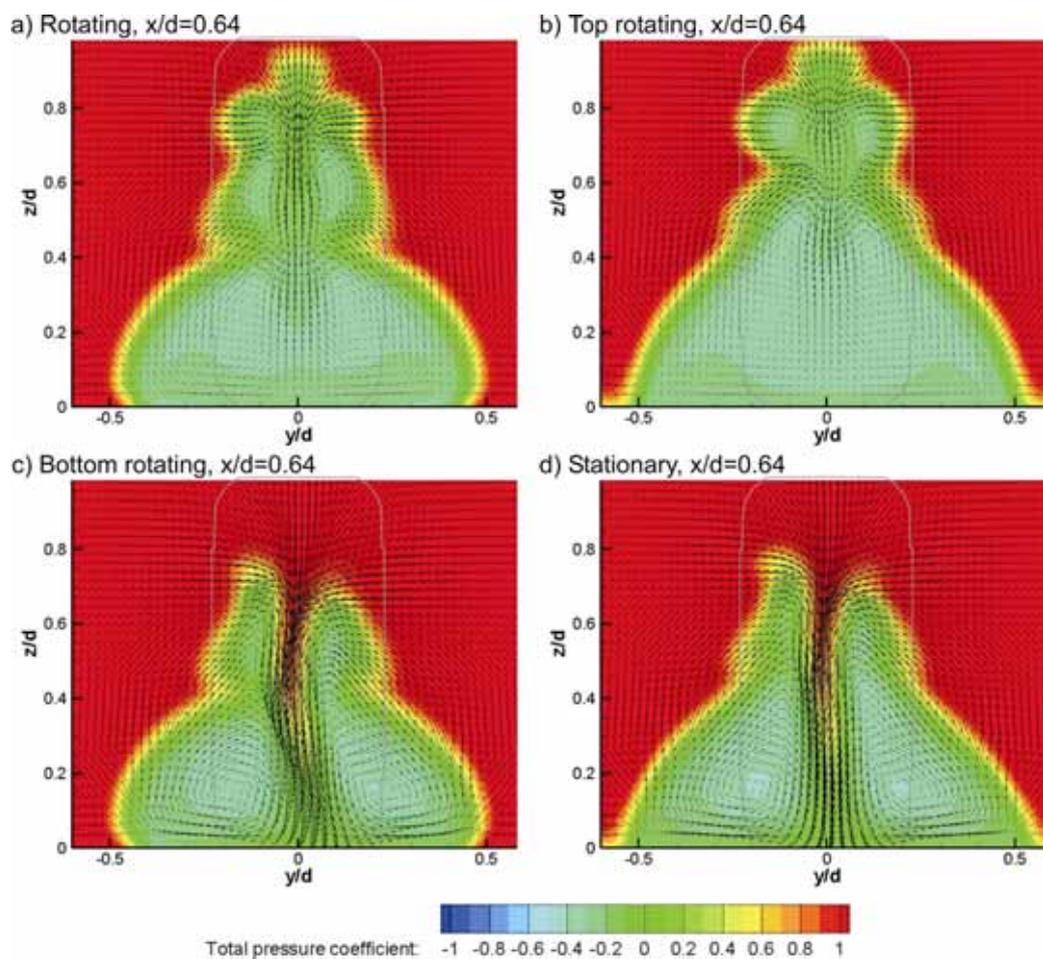


Figure 5.5 Wheel wake structures obtained with wheels with different boundaries

This result also indicates that the wheel tread separation point controls the distribution of flow entrainment into the wheel wake from either the top of the wheel or around the sides and is therefore independent of the extent of the jetting action forward of the wheel. As the separation point from the top surface of the wheel moves forward, less flow is entrained from the top of the wheel and this is compensated by an increased entrainment from the sides of the wheel. For this reason the rotating wheel lacks the large downwash component in the central wake region as experienced by the stationary wheel (Figure 5.5d). The main vortices for the stationary wheel are forced down and apart by this downwash component and therefore form further from the central plane and closer to the ground causing the wider lower wheel wake. Therefore, while the jetting action may make a small contribution to the final position of the primary wheel vortices, when the top wheel tread separation is delayed, the downwash in the wheel wake becomes the dominant feature to determine the final position of the primary wheel vortices.

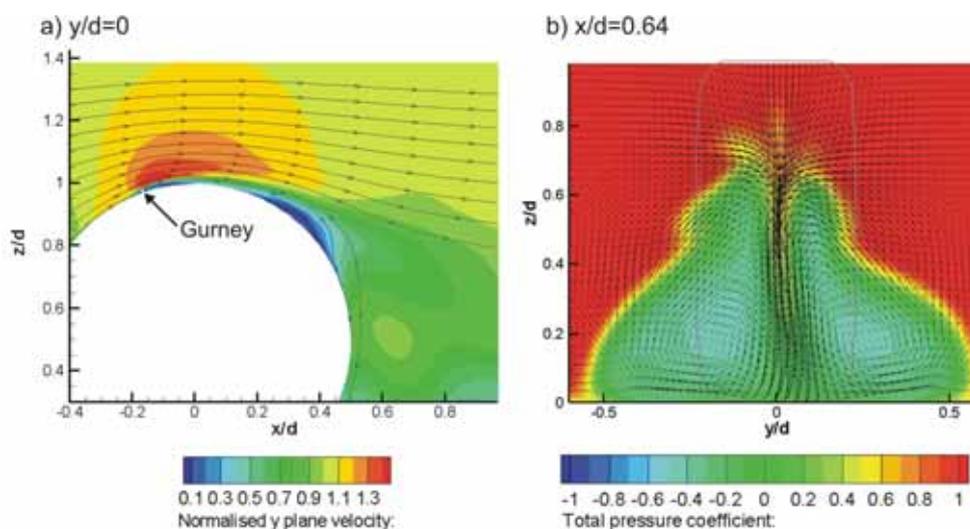


Figure 5.6 Flow structures obtained with attempted “gurney” trip

Based on this theory, if it was possible to deliberately separate the flow from the wheel tread of a stationary wheel in a comparable position as that experienced by a rotating wheel, it would be expected that a similar wake structure to a rotating wheel will be obtained without the wheel rotation or moving ground being employed. If such a solution could be applied, it would be particularly useful for experimental research being conducted for automotive applications that do not have a moving ground and where the wheel can not be rotated. This was attempted by incorporating a perpendicular surface to the wheel tread

of a stationary wheel (similar to a gurney flap) at the location that separation occurs from a rotating wheel tread (Figure 5.6).

While the flow from the wheel tread was initially separated by the addition of the gurney (Figure 5.6a), the high positive pressure gradient experienced by the flow passing over the top of a stationary wheel caused the flow over the wheel to eventually reattach. Subsequently, no variation was obtained in the wake structure (Figure 5.6b) or forces experienced for this configuration in comparison to that of a stationary wheel. Similarly unsuccessful results were obtained with using regions of increased roughness on the wheel tread. Therefore, it was determined that applying the wheel rotation independently to the top region of the wheel was the only way to obtain the desired separation location.

Another way considered to prove this theory was to adjust the location of the separation point from the top wheel tread and see if the primary wheel vortices varied in a manner consistent with the explanation provided. Up until this point, all the rotations applied to either the top, bottom or entire wheel have created a tangential velocity equal to the freestream velocity to satisfy the zero slip condition expected for a rotating wheel at the contact patch. In order to control the location of the separation point from the top of the wheel tread, the wheel rotation ratio of the top portion of the wheel was reduced from 1 to 0 in increments of 0.2 while the bottom portion of the wheel and the ground remained stationary.

The results obtained with the varied top wheel rotation are included as Figure 5.7 and demonstrate the relationship between the separation point and the position of the primary wheel vortices. As the wheel tread separation point moves rearward, the downwash generated in the central region of the wheel wake incrementally increases in strength as the main wheel vortices move closer to the ground as well as further apart. Also apparent is the trend for the flow entrainment into the wheel wake to reduce from the sides and increase from the top as the separation point moves rearward consistent with the proposed theory. Based on these results, it would be expected that the lift would follow an incremental variation dependant on the location of the separation point from the top wheel tread. The lift and drag have been plotted against the angle at which the separation occurs at on the wheel's central plane ($y/d=0$) for all the results obtained during this investigation and is included as Figure 5.8.

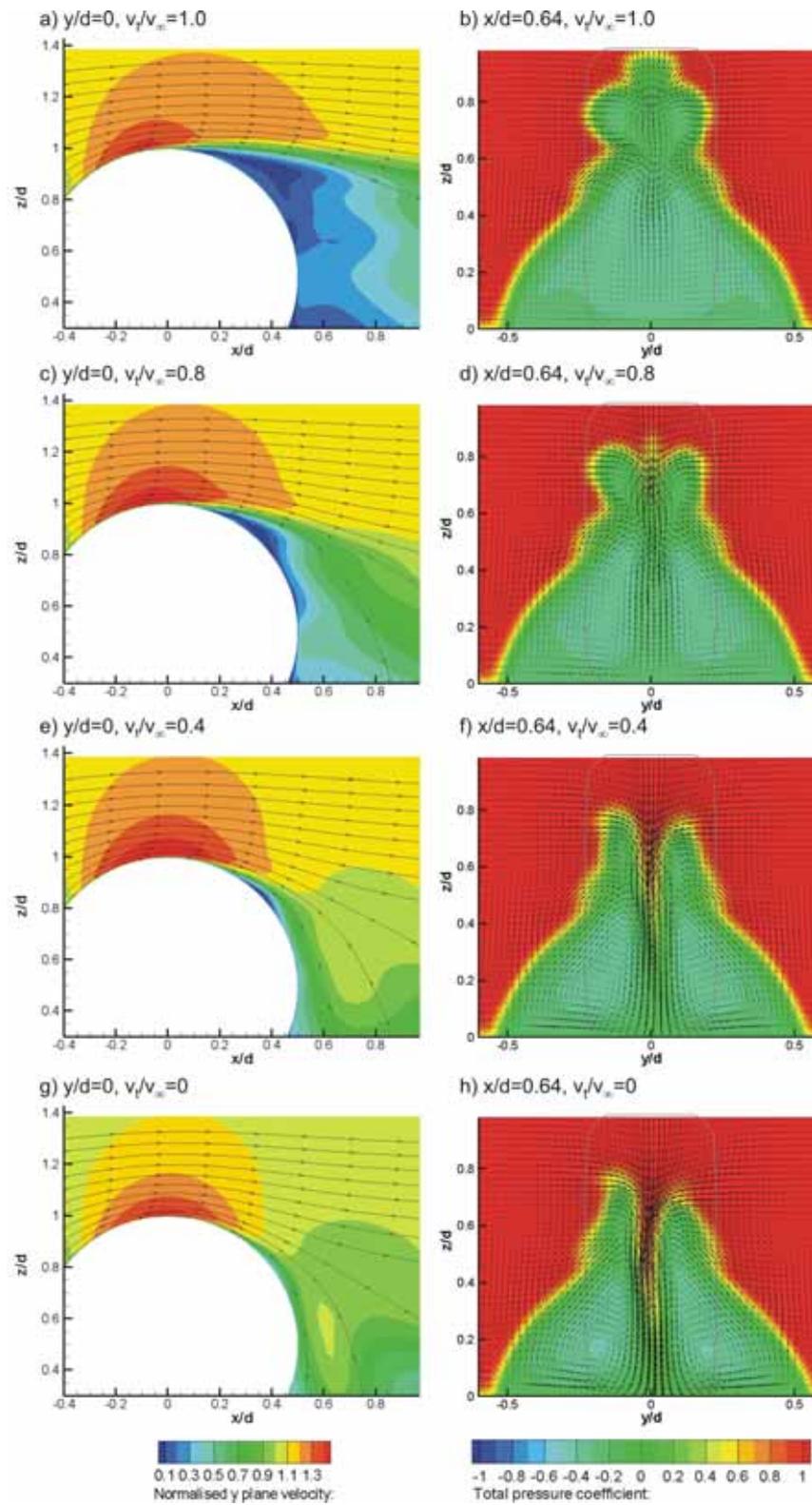


Figure 5.7 Comparison of wheel wake structure obtained when varying the separation

Lift and Drag Comparisons for Varying the the Top Wheel Tread Separation Point

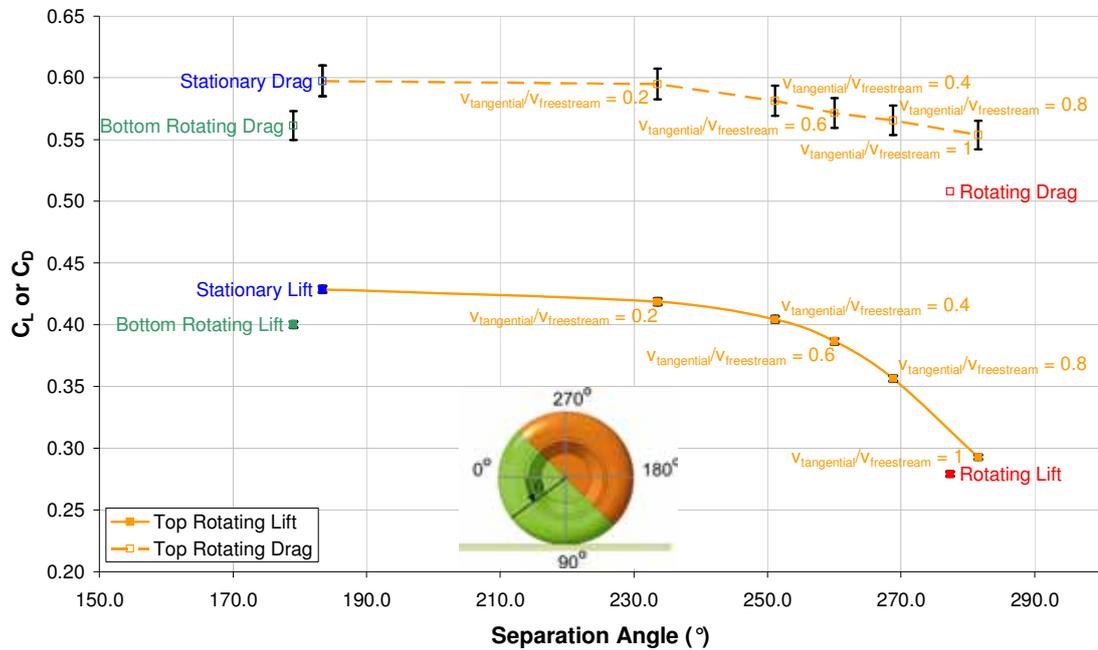


Figure 5.8 Force coefficients obtained for wheels with separated boundaries

These results confirm that both the lift and drag are related to the separation point and that a more forward separation point will result in a reduction in both lift and drag as demonstrated previously by Fackrell (1975). It is not expected that this trend will continue indefinitely, as at some point it will not be possible to separate the wheel from a further forward position. For example, the method used here is limited by the portion of the wheel that is rotated and therefore it would not be expected that the wheel could be separated close to or further forward than $\theta=315^\circ$. For this reason, attempts were not made to force a separation point further forward than those experienced here.

By separating the rotation of the upper and lower boundaries, it has also been possible to isolate the force variation contribution made by the increased jetting action from the front contact patch. By comparing the forces of the bottom rotating wheel only to the completely stationary wheel (Figure 5.8) it can be determined that the jetting action makes a small contribution to the lift reduction experienced by a rotating wheel in comparison to the effect that the separation point has. When only considering the central pressure coefficients (Figure 5.4), this may seem somewhat counter intuitive. While the large pressure increase

created by the rotation forward and at the centre of the contact patch may be expected to increase the lift of a wheel, the increase in cross flow experienced at either side of the contact patch (Figure 5.3) as a result of this pressure increase as well as the pressure drop experienced at the rear of the contact patch ($95^\circ < \theta < 110^\circ$) more than compensates for any additional lift provided by the localised pressure increase at the wheel centre. The reduction in pressure forward of the contact patch located at either side of the wheel centre was also measured by Fackrell (1975) and Hinson (1999) experimentally. The earlier separation point and the increased jetting action for the same reasons also contribute equally to the drag reduction experienced by a rotating wheel in comparison to its stationary equivalent. It is also interesting to note that the contribution made by the jetting action is consistent when the comparison is made with top of the wheel stationary or rotating.

In conclusion, it has been demonstrated that the previous explanation for the variation of the wheel wake shape associated with the wheel rotation provided by McManus and Zhang (2006) is incorrect. The main wheel vortices form in a higher and more central position because of the earlier separation caused by the wheel rotation. This causes a reduction of flow entrainment from the top removing the downwash from the central wake region associated with a stationary wheel, and is replaced by an increase in entrainment from the sides for a rotating wheel. The lift and drag have also been shown to be sensitive to the separation location with a more forward separation point causing both the lift and drag to decrease. Only the drag has been found to be sensitive to the jetting action. This is significant for the wing and wheel interaction study that will be discussed in the next chapter as the wing is likely to influence the flow incidence experienced by the wheel and also the flow upstream of the contact patch.

5.1.2. Variations due to size of the contact patch

One difficult aspect of numerically modelling the flow around a solid wheel is accurately portraying the contact line. This arises because the wheel tread is theoretically tangent to the ground for a solid wheel (Figure 5.9a) and meshing this geometry will lead to highly skewed cells around the contact line. This effect is further exacerbated with the number of cells and the height of the first cell required by the enhanced wall model used during this computational study. To overcome the grid skewness issues associated with a solid wheel,

the geometry of the wheel was modified to include a small face around the wheel's contact patch that subtended an equal angle to the ground and the wheel tangent as shown in Figure 5.9b. Axon (1998) had also utilised a step around the contact patch during his numerical study, but other authors conducting numerical investigations have not indicated how this problem has been approached or overcome. Up until this point, all computational results presented previously as part of this research project that have included a wheel have used a step height of $0.0028d$ after the wheel has been sunk into the ground the same amount. This height was initially chosen as it was the smallest step that could be achieved without adversely affecting the quality of the mesh surrounding the contact patch.

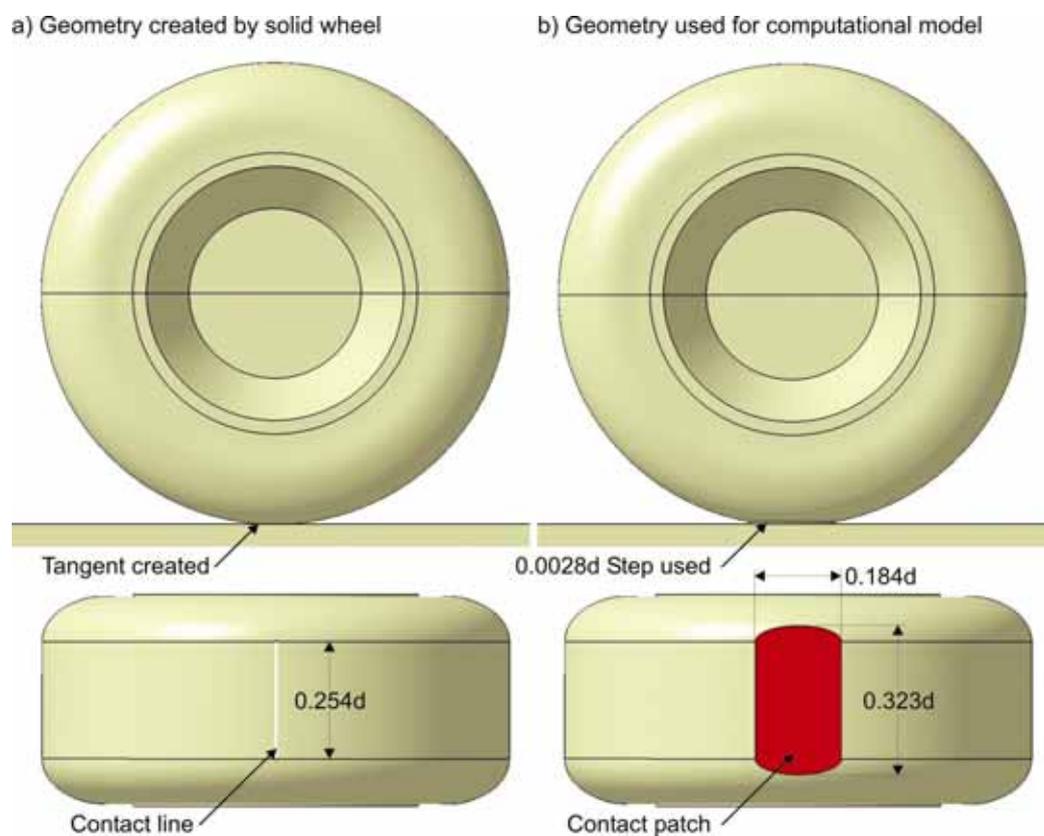


Figure 5.9 Contact made by solid wheel and geometry used for computational model

Varying the size of the contact patch by increasing the height of the step is also expected to give some insight into the validity of using a commonly used solid wheel during wind tunnel testing to model a pneumatic tyre which is used in reality. While the intention was to create a geometry that replicates a solid wheel in contact with the ground with the computational model, as used by Fackrell and during the authors own experimental

investigations, inadvertently the geometry used for the computational model is more representative of that of a pneumatic tyre. A deformable tyre in contact with the ground creates a contact patch instead of contact line of which the size depends on the stiffness characteristics and the load of the tyre (Pacejka, 2005). Therefore, it may also be considered that varying the size of the step would give some indication of the wheel's aerodynamic characteristics dependency on the size of the contact patch. The step sizes tested, and the extent of the variation that this effect has to the dimensions of the contact patch are shown in Figure 5.10. Given that a reduction in the step size beyond 0.0028d was not possible due to the mesh quality being compromised, the sensitivity of the flow to this simplification was tested by increasing the height of the step between the ground and the wheel using the same computational model used to validate against Fackrell's A2 wheel geometry.

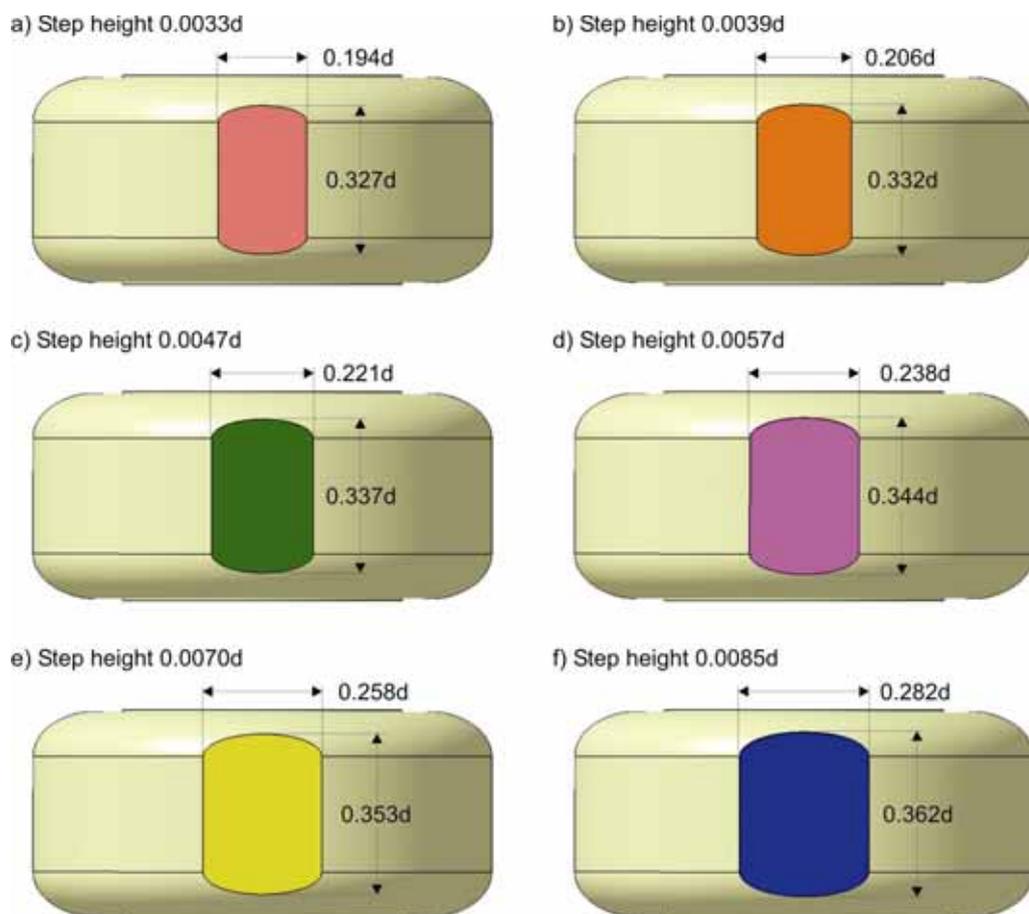


Figure 5.10 Variations in contact patch step height tested with Fackrell's A2 wheel

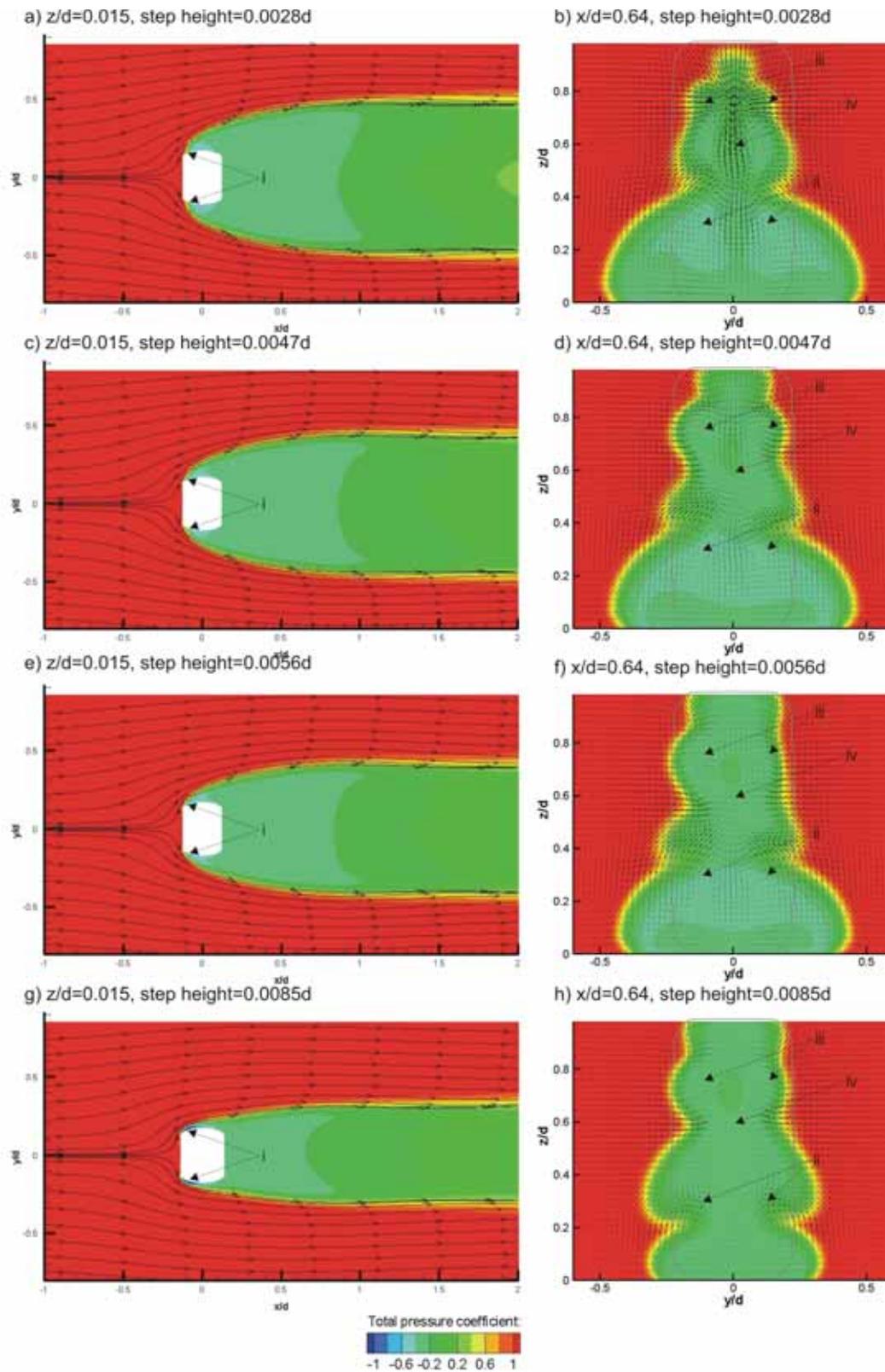


Figure 5.11 Variations in wheel wake obtained when increasing the step height

Increasing the step height through the range of geometries depicted in Figure 5.10 resulted in the wheel wake reducing in width and increasing in height (Figure 5.11). The cause for this large variation in the wheel wake was determined to be the variation in the separation point from the front contact patch. As the step height was increased, this separation point moved towards the rear of the wheel reducing the departure angle of the jetting flow from the front contact patch (Figure 5.11i). This is likely to be due to the variation in the contact patch's aspect ratio. Increasing the height of the step increases the length of the contact patch a greater amount than its width resulting in the side portions of the step becoming straighter (Figure 5.10).

This result is consistent with Fackrell's (1975) explanations on how the main wheel vortices form. They describe that the separation caused by the jetting action at each side and forward of the contact patch is responsible for the main wheel vortices and here it has been demonstrated that when this separation is delayed or reduced by increasing the height of the step surrounding the contact patch, the strength and size of the main wheel vortices is also reduced (Figure 5.11ii).

Two other variations are also evident as a result of the change in step height. The upper wheel wake was found to increase in height (Figure 5.11iii) while the downwash in the centre wheel wake reduced in magnitude (Figure 5.11iv). These variations have been observed previously and have been associated with a forward shift in the separation point from the upper wheel tread region. Streamlines generated over the central y-plane confirm that the separation point does move forward as the step height is increased in size (Figure 5.12). During the wake study preceding this investigation (Section 5.1.1), it was demonstrated that adjusting the wheel tread separation point allows the location of the main wheel vortices to be influenced. The results presented here suggest that the wheel tread separation point can also be influenced by the strength of the primary wheel vortices and that the relationship between these two features is not solely dependant on the wheel tread separation point, but instead an interaction exists between the two.

These results indicate that the primary wheel vortices strength is responsible for the downwash reduction in the central wheel wake region for a rotating wheel. These vortices draw flow from the central wake region due to the direction of their rotation creating a downwash as a result. Prior to being drawn into the centre of the wheel wake, the flow

passes over the top of the wheel tread and therefore the downwash generated by the rotation of the primary wheel vortices provides a downward component to the flow passing over the top of the wheel tread and also has an influence on the location of the separation point. By reducing the strength of the primary wheel vortices, as has been achieved by increasing the size of the step at the contact patch, the central downwash is also reduced and for this reason the top wheel tread separation point also shifts forward as a result.

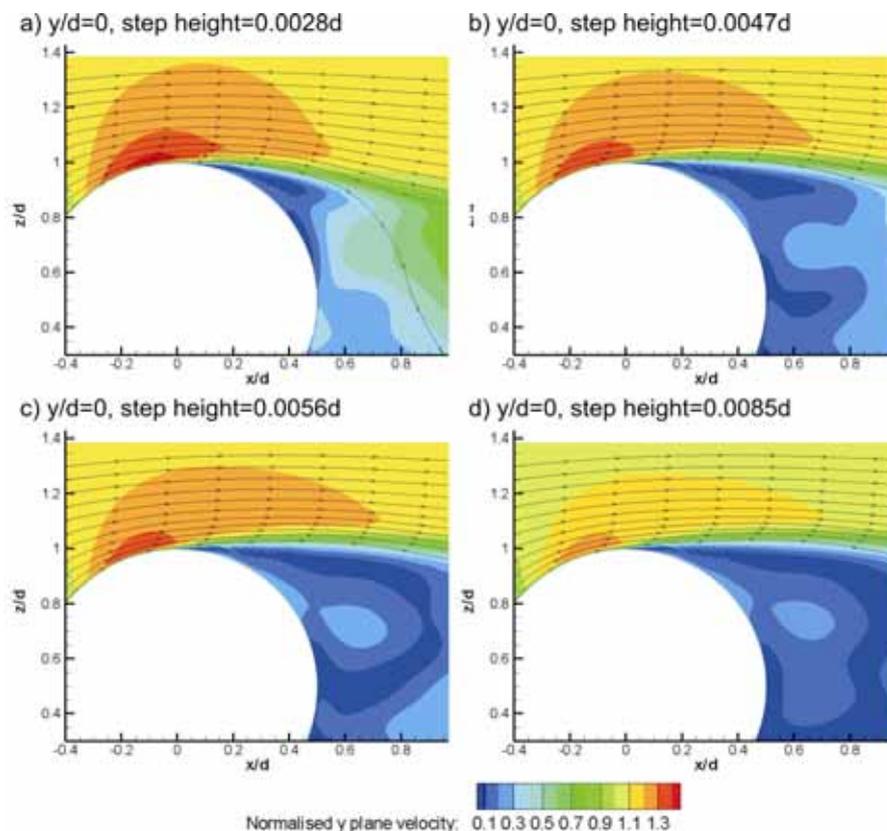


Figure 5.12 Wheel tread separation due to the variation in the contact patch step height

Another feature of an isolated wheel that was previously found to be sensitive to the separation point was the drag of the wheel. During the wake investigation, it was determined that as the separation point moves further forward on the top of the wheel tread, the drag of the wheel also reduces. This trend was repeated during this investigation demonstrating that the drag is also sensitive to the height of the step surrounding the contact patch. At the largest step height tested (0.0085d) the drag was approximately 20% less than that obtained with the original step height of 0.0028d. The trend obtained with the drag also suggests that as the step height is increased, it would converge towards a value

of approximately 0.4 while if the step height was further reduced it would converge to a value of approximately 0.5 (Figure 5.13). This may suggest that the results presented here have been obtained within a transition period where the vortex strength gradually decays and the separation point moves further forward as Figure 5.11 demonstrates. Further increases in the height of the step surrounding the contact patch above 0.007d would not be expected to result in a further reduction of the main wheel vortices strength or a further forward translation of the separation point from the top of the wheel tread as it is unlikely that the separation point at the base of the wheel can be further delayed. Similarly the strength of the main wheel vortices and the separation point are not expected to reduce further if the step height was reduced less than that which has been tested here.

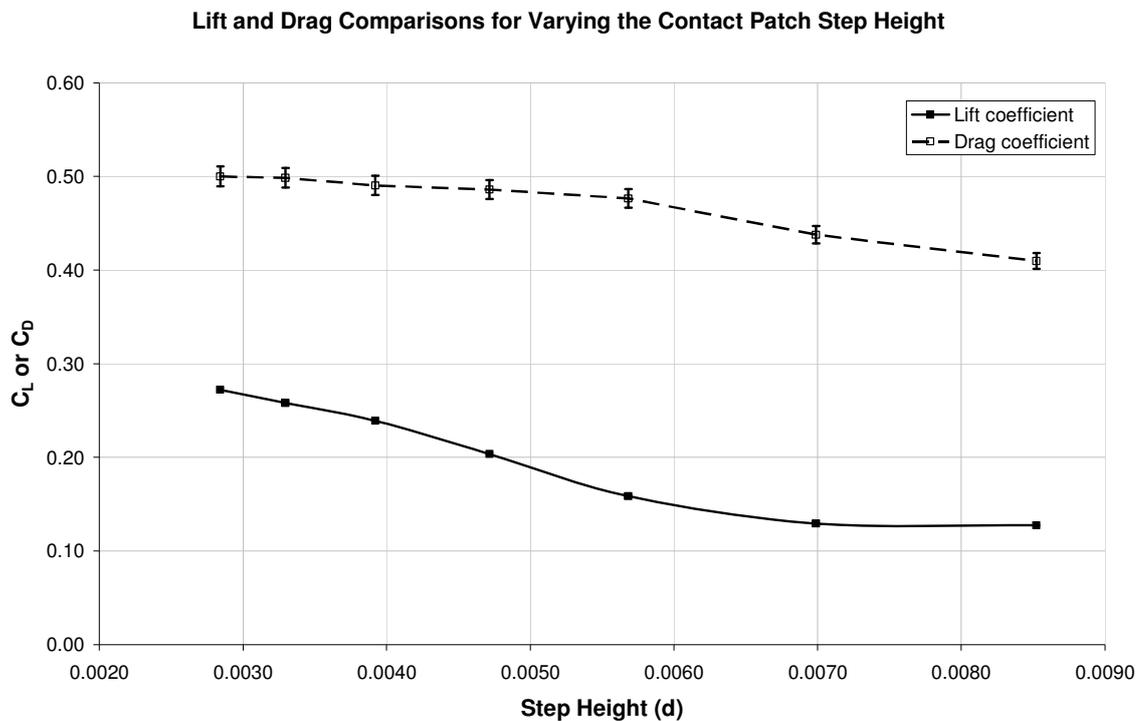


Figure 5.13 Force coefficients obtained for variations in the contact patch step height

Ideally, the results obtained with the computational model should be independent of the step height given that this geometric simplification has been introduced to ensure that the grid quality is not compromised. To satisfy this requirement the step height could either be less than 0.0028d or greater than 0.007d. Given that it has already been demonstrated that with a height of 0.0028d the wake structure closely resembles that measured

experimentally by Fackrell (1975) and that significant variations are obtained for heights greater than $0.007d$, it is recommended that the step height used for computational models should be as small as the meshing technique allows without being greater than $0.0028d$.

The lift also follows a similar trend as the drag where the results seem to be converging to a value on each extreme of the range tested (Figure 5.13). A similar trend should be expected given the previous relationship between the lift and drag results obtained during the wake investigation study (Section 5.1.1). As demonstrated previously, when the separation point moves forward, the opportunity that the flow over the top of the wheel tread has to be accelerated is reduced resulting in a lower peak velocity (Figure 5.12). Therefore, the minimum peak pressure coefficient is reduced (Figure 5.14, $\theta=285^\circ$) causing the lift that the wheel experiences to also be reduced. The lift also proves to be more sensitive to the variations in the separation point with the largest step height resulting in a lift reduction of 50% over the original step height. The significant variations obtained with the forces that move away from Fackrell's (1975) lift and drag coefficients measurement of 0.28 and 0.51 respectively also give a clear indication that the step height should be $0.0028d$ or less.

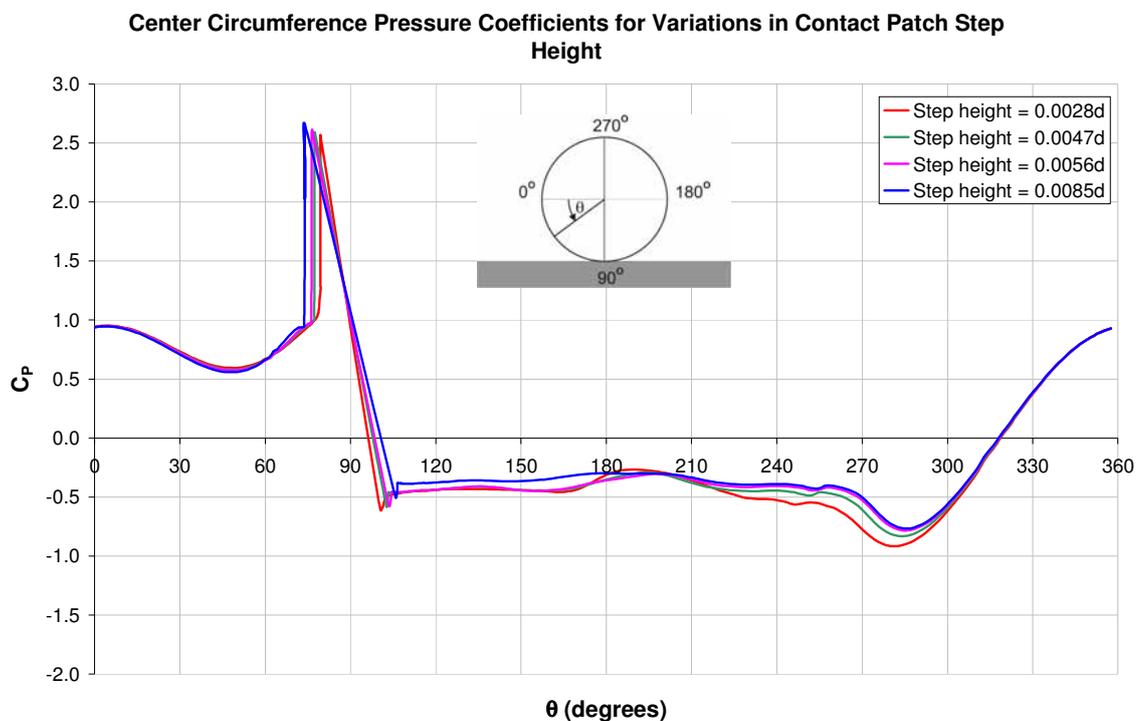


Figure 5.14 Central pressure coefficients obtained for variations in the step height

During the Section 4.3 it was assumed that the peak pressure value obtained forward of the contact patch (before $\theta=90^\circ$) varied from that which was measured experimentally by Fackrell (1975) due to the wheel simplification used at the contact patch. The results presented in Figure 5.14 show that the peak positive pressure occurs further forward and that the maximum value also increases in magnitude as the height of the step around the contact patch is increased confirming this assumption. In the event that a contact line would exist, the peak pressure measurement should be obtained at an angle of $\theta=90^\circ$. To determine a theoretical value for the peak positive pressure, the peak positive pressure values obtained with all the step heights were used to determine a function that could be extrapolated to an angle of 90° . Doing this yielded a theoretical value of 2.05 which is 5% smaller than the maximum pressure coefficient value of 2.15 measured by Fackrell (1975) with the A2 wheel geometry. Variations in this theoretical value to that measured by Fackrell (1975) could be attributed to either the large variations in the peak pressure measurements as demonstrated by Hinson (1999), or the possibility that despite using a solid wheel, the wheel may have created a small contact patch, much smaller than that which has been tested here. To truly obtain a contact line, not only would a solid wheel be required but also a belt surface that would not deform in any way under the load placed on it by the wheel. Given how unlikely it is for a belt used for a moving ground to exhibit such a quality, it would be fair to say that both explanations for the variation could be considered possible.

This investigation offers some insight into how appropriate it is to use solid wheels to model pneumatic tyres on vehicles during wind tunnel testing. By varying the height of the step surrounding the contact patch, it has been demonstrated how sensitive the flow features and the forces associated with a rotating wheel are to the separation point at the front contact patch. This is particularly relevant to a deformable tyre as the base of the tyre is expected to flex under load not only altering the shape of the contact patch but also the shape of the tyre's side wall above the contact patch. Both of these features are likely to alter the separation point at the base of the wheel and therefore would both be expected to be considered as important features to reproduce during wind tunnel testing, particularly when conducting studies on components that operate downstream or in the wake of a rotating wheel. Therefore, it would be expected that if solid wheels are used during wind tunnel testing of a road vehicle that uses pneumatic tyres, this simplification could contribute to correlation issues between the wind tunnel model and the full scale vehicle.

To achieve a realistic wind tunnel model, a tyre that can be deformed in the wind tunnel to reproduce the same contact patch and side walls as that of the tyre on a full scale vehicle would be recommended.

Given that the aim of this work is to obtain an understanding of the interaction of a rotating wheel and an inverted wing, and there is no intention to correlate this work with a full scale vehicle, it has not been considered necessary to consider the shape of the side wall and contact patch any further. In line with the recommendations outlined above, the step height surrounding the contact patch from here on will be maintained at $0.0028d$. The sensitivity of the separation point from the side contact patch is also expected to be relevant to the wing and wheel interaction to be discussed in the proceeding chapter as the wing is expected to induce a cross flow to the face of the wheel and this may affect the separation point at the base of the wheel in a similar manner to that which was experienced when increasing the step height.

5.1.3. Effects of geometry simplification to wheel characteristics

Pressure measurements taken during both Fackrell (1975) and Hinson's (1999) experimental studies have indicated that the pressure acting on the wheel hubs make small contributions to the lift and drag of the wheel. During the same study, Fackrell also came to the conclusion that the lift and drag did not vary significantly between two different wheel shoulder profiles that were similar in size and shape provided that the wheel tread remained the same. Since these two experimental studies, numerous numerical investigations have been undertaken for stationary and rotating wheels using simplified wheel geometries. These simplifications have included removing the wheel hubs and simplifying the wheel shoulder profile (Axon *et al.* 1998 and Hedges *et al.* 2002) or the wheel shoulder has been completely removed so that it is sharp (Skea *et al.* 2000). The only computational study previously conducted of a wheel with hubs was undertaken by McManus and Zhang, (2006). While their results confirm that the lift and drag of the hubs do not contribute significantly to the lift and drag of the wheel, they do demonstrate that they interact with the flow alongside the wheels and the upper wheel wake. Therefore, it would be expected that removing the wheel hubs must affect the wheel wake in some manner and consequently the lift and drag of the wheel.

Despite the geometric variations amongst all these studies, it has not yet been investigated the effect that these simplifications have on the flow structures associated with a wheel. Since it was intended to use a simplified wheel geometry to study the interaction of a wing and wheel, it was decided to investigate the implications this might have. This was undertaken by firstly removing the wheel hubs (Figure 5.15a) from Fackrell's (1975) A2 wheel geometry, and then replacing the wheel shoulder profile with a constant radius (Figure 5.15b). This is the narrow wheel geometry intended to be used for the wing and wheel investigation and from here on will be referred to as the W1 wheel. All the three wheel geometries tested have an identical aspect ratio (0.46) and frontal area ($7.9 \times 10^{-2} \text{m}^2$) as these parameters are typically consistent amongst the previous computational investigations regardless of the extent of the simplification in geometry. This investigation was undertaken with both a stationary and rotating wheel.

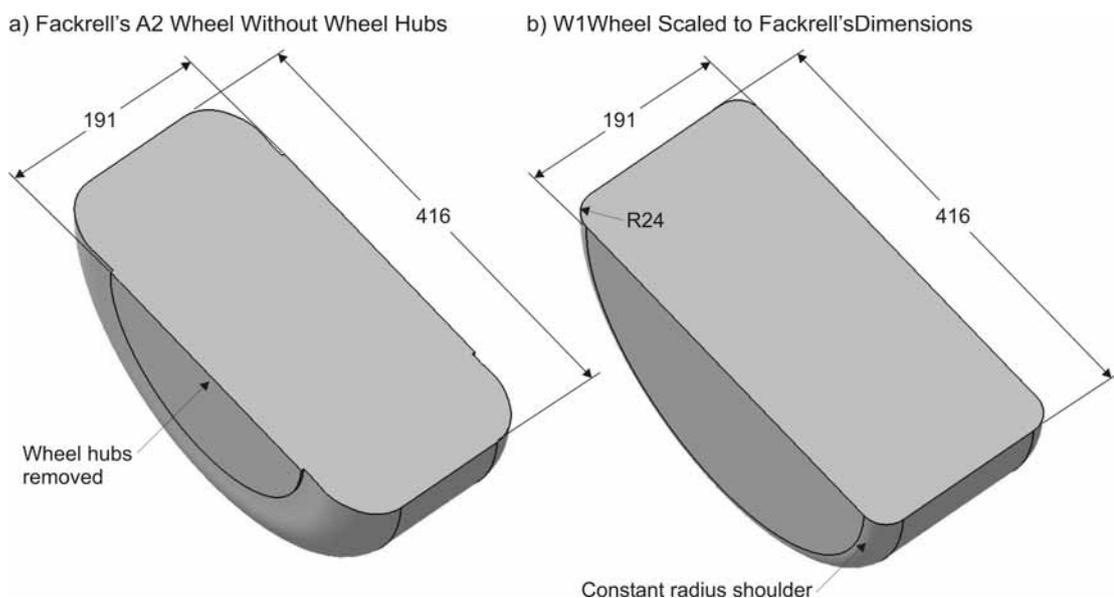


Figure 5.15 Simplified wheel geometries tested (measurements shown to closest millimetre)

Agreeing with previous results obtained by Fackrell and Hinson, the lift and drag results (Figure 5.16) indicate that the removal of the hubs has a small effect. Despite small, this effect was more pronounced for the rotating wheel's lift and drag with a reduction of 20% and 6% respectively while the stationary wheel had no variation in drag and a 4% increase in lift. Changing the wheel shoulder was found to be significantly more sensitive than the removal of the hubs. Comparing the results to the A2 wheel with no hubs, in order to isolate the effect that the shoulder has, a 33% and 25% increase in lift and drag

respectively was obtained for the rotating wheel while the stationary wheel experienced a 24% and 30% increase respectively. In all cases the rotating wheel lift and drag was lower than that of the stationary equivalent which may suggest that the wheel geometry is not critical to understanding the effect that the wheel rotation has on the flow structures.

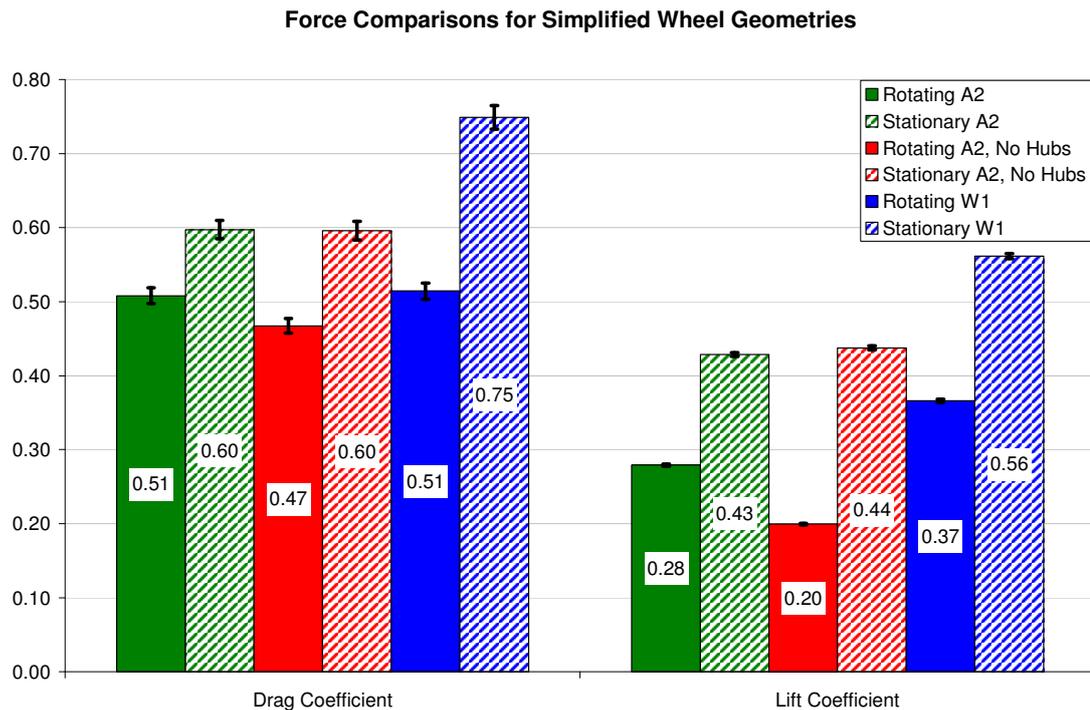


Figure 5.16 Force comparisons for simplifying Fackrell's A2 wheel geometry

Beginning with the rotating wheels investigated, the centre pressure coefficients indicate that the geometry simplifications are responsible for some small variations in the flow structure around the wheel. Removing the hubs from the A2 wheel geometry shifted the separation point approximately 5° forward and reduced the peak pressure obtained over the top of the wheel. The positive pressure gradient (360° to 285° , Figure 5.17) produced by these two wheels ahead of their respective peak pressure locations is very similar suggesting that the earlier separation point is also responsible for the reduced peak pressure value obtained in this region. The reduced speed flow and the increased separation from the top surface explain the reduction in the lift, but explaining the reduction in wheel drag and why these features occur will require some further investigation of the variation in the flow structures between these two cases.

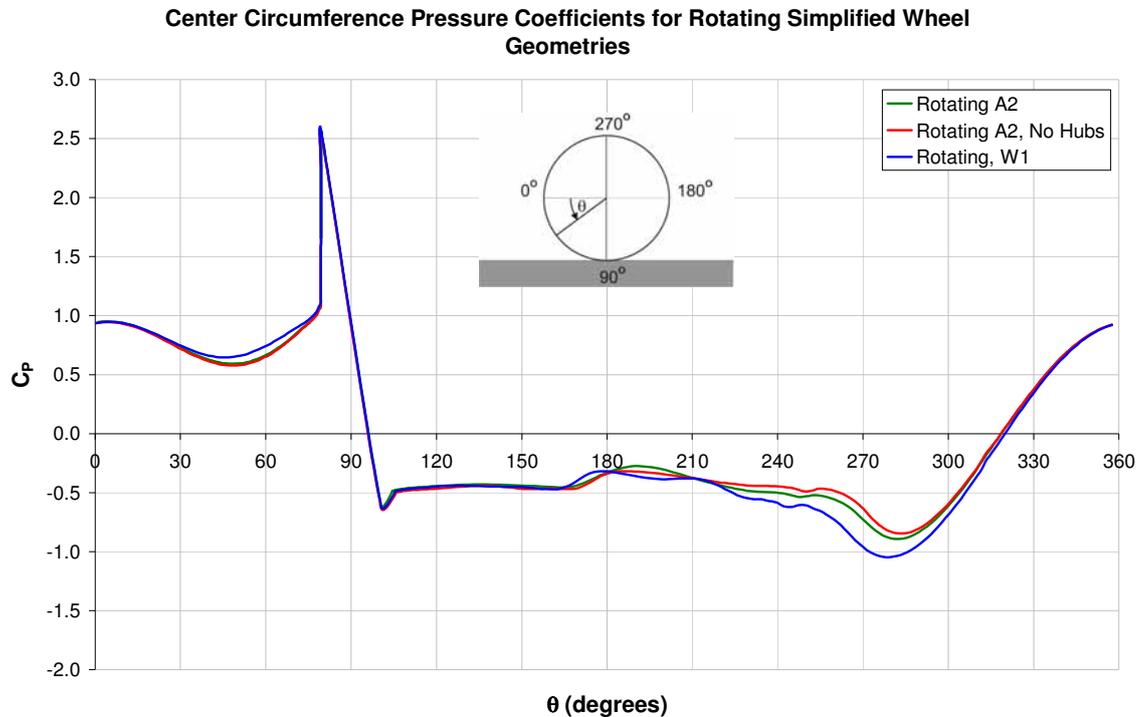


Figure 5.17 Centre pressure coefficients for simplified rotating wheel geometries

A unique feature observed for the A2 wheel without wheel hubs was the formation of two additional vortices in the wake that are located at approximately $z/d=0.55d$ (Figure 5.18b i) which may also explain the offset obtained in the central pressure coefficients between the angles of 180° and 210° (Figure 5.17) for the two flat sided wheels and Fackrell's A2 wheel geometry. This location corresponds with the height that these additional vortices would pass at. The author believes that they are formed due to the shear effects induced by the rotating flat side faces of the wheel and for this reason are significantly smaller than the remaining four vortices formed by the separation from the top and bottom of the rotating wheel (Figure 5.18 ii and iii). This has been previously proposed by Cogotti (1978), but no experimental evidence of these vortices has been obtained previously to support his theory. He proposed that these vortices should exist after considering the flow structures that would be expected to form independently from a stationary finite width cylinder in freestream and that due to the rotation of the same body in still air. Two pairs were expected for the first case, while an additional pair was expected for the second case caused by the above mentioned reason. Since a rotating wheel exhibits both

characteristics, Cogotti came to the conclusion that six vortices should exist in the wake of a rotating wheel as shown here when the wheel hubs have been removed.

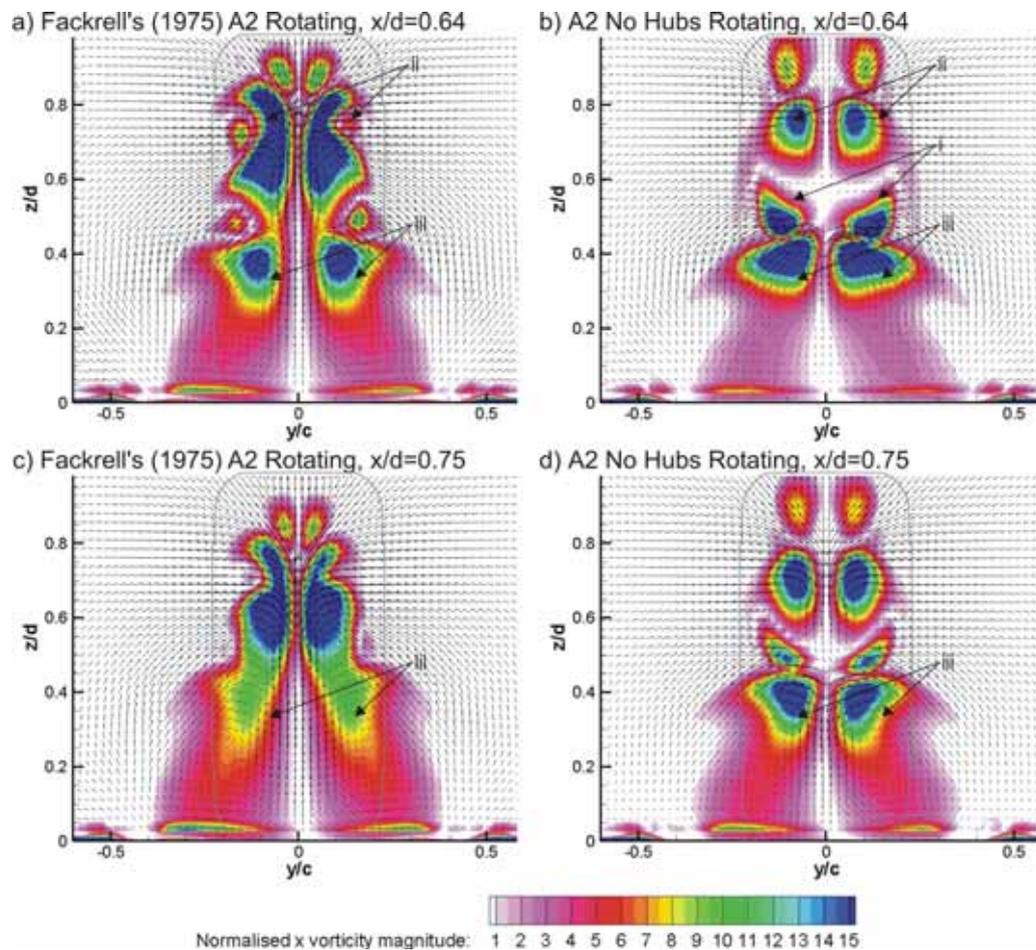


Figure 5.18 Flow structures associated with Fackrell's A2 wheel with and without the hubs

While McManus and Zhang (2006) and Fackrell (1975) found no evidence of a third pair of vortices in the wheel wake, the results here suggest that this could simply be because previous experimental research conducted with rotating wheels has been carried out with hubs and not with flat sided wheels. While small in comparison to the main wheel vortices, the vectors presented in Figure 5.18 for a plane located at $x/d=0.64$ indicate that Cogotti's theoretical model of a rotating wheel is, to some degree, correct. These vortices have been found to be significantly smaller than that of the other four vortices since they are formed solely by a shear interaction with wheel's side walls while the four others are formed by significant pressure variations that occur in the wheel wake due to boundary

layer separation. As a result, these two vortices dissipate by the $x/d=0.75$ (Figure 5.18d) plane leaving the four initial vortices commonly reported further downstream.

It should also be noted that McManus and Zhang (2006) had indicated that the flow within the hubs rotated more for the rotating wheel than that for the stationary wheel case. While no evidence had been obtained of a third pair of wheel wake vortices, this statement indicates that an additional pair of vortices are formed in Fackrell's (1975) wheel geometry that are influenced by the shear interaction with the wheel hub surfaces. While Cogotti's (1978) vortices created by the shear stress are located in the wake, the vortices affected by the shear from the hubs remain trapped within the wheel hubs and do not propagate downstream. This phenomenon would have been difficult for Fackrell (1975) and Hinson (1999) to observe during experiments using pressure tapings only located in the surface of the wheel and this may explain why a computational study conducted by McManus and Zhang (2006) was required to observe this variation.

Consistent with the phenomenon linking the separation point with the wake width and height previously discussed, the A2 wheel without hubs was observed to have a narrower and higher wake in comparison to Fackrell's (1975) A2 wheel geometry. This smaller wake structure should be expected given the reduction in drag for this configuration already reported. The formation of the two mid vortices is expected to increase the entrainment experienced from the sides in the lower wheel wake region and reduce the downwash behind the wheel caused by the earlier separation point from the top surface.

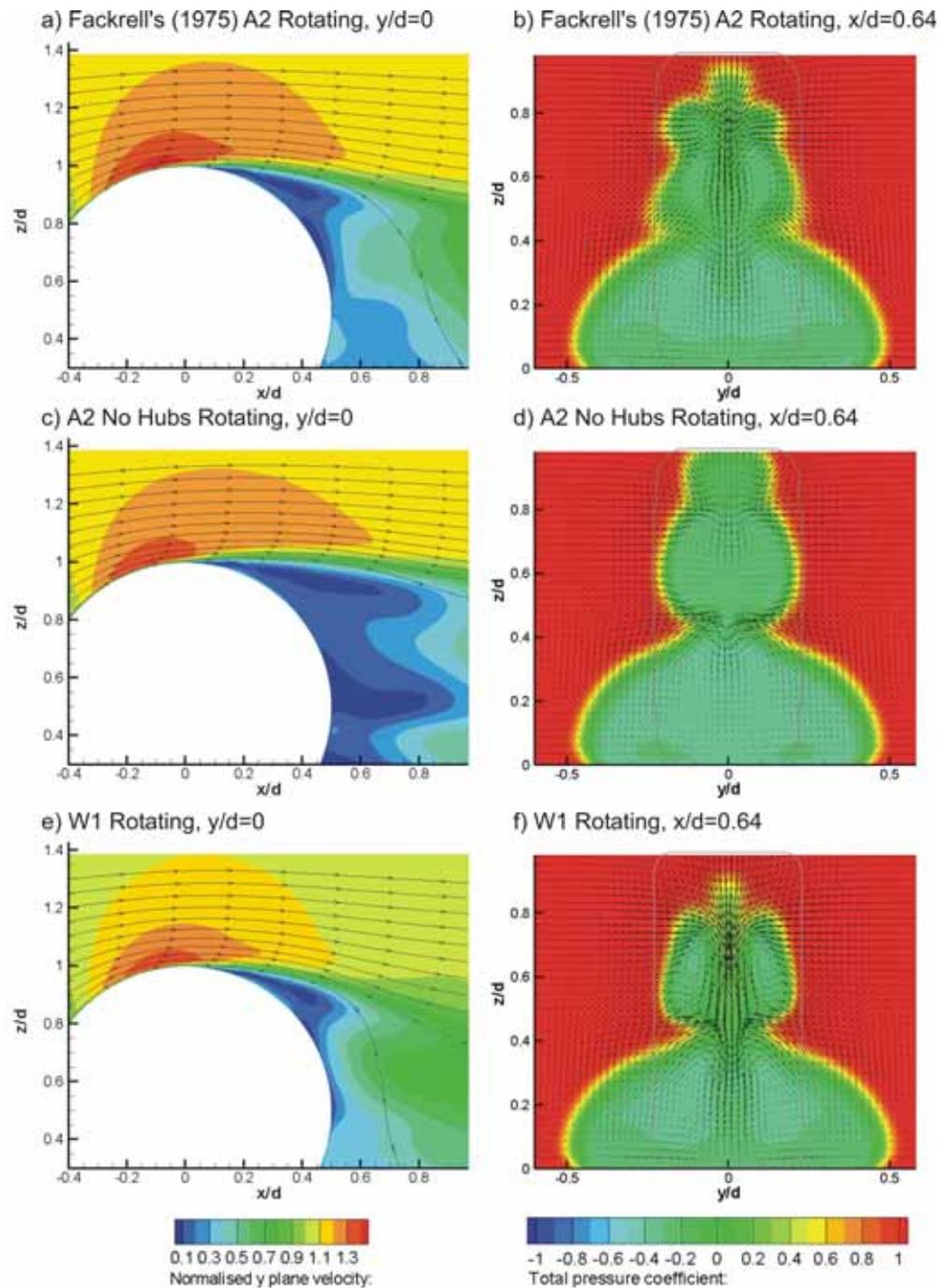


Figure 5.19 Wake comparisons of Fackrell's A2 wheel with and without the hubs

The variations obtained with the radiused wheel shoulders appeared to be more significant than that obtained for removing the wheel hubs. This was somewhat surprising given Fackrell's comments regarding his wheel shoulder variation results. When Fackrell modified the wheel shoulder during his experiment, the wheel tread was maintained while

the wheel width was slightly reduced due to the narrower wheel shoulder that was tested. A different approach has been taken here which may explain the discrepancy with Fackrell's comments. As indicated by Figure 5.15, the overall width of the wheel was maintained and the wheel shoulder was replaced effectively allowing the wheel tread to increase in width. The larger variation obtained here in comparison to that obtained by Fackrell may suggest that the wheel tread width is a more sensitive parameter than the total wheel width. Comparing to the A2 wheel with no hubs, a larger region of increased static pressure was observed forward of the wheel (Figure 5.20) that is likely to be responsible for the steeper pressure gradient that is shown in the central pressure coefficients (360° to 285° , Figure 5.17) and would also be expected to contribute to the drag increase obtained by this wheel geometry.

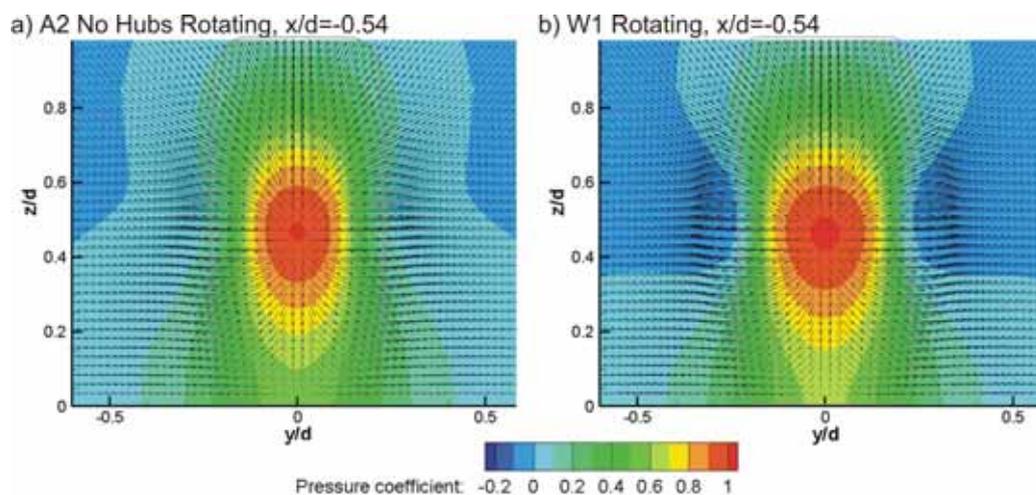


Figure 5.20 Static pressure comparisons of A2 wheel without hubs and W1 wheel

Another feature that was observed for this wheel geometry was a wider and lower wheel wake. The larger wheel tread results in a contact patch that is wider and therefore the jetting action for this wheel occurs further from the wheel centre line than that which was experienced previously for the A2 wheel without hubs (Figure 5.19f). This forces the lower wheel vortices to form further outboard in the wheel wake and, as demonstrated previously, this influences the separation point located on the upper portion of the wheel tread. In the middle of the upper wheel wake region, a larger downwash component has been obtained for this geometry which is caused by an increased flow over the top surface of the wheel and a reduced entrainment from the sides. This variation assists with delaying

the separation point, as indicated by Figure 5.17, and is also responsible for the 85% increase in lift obtained by changing the wheel shoulder.

Despite these variations in the flow around the wheel, the main flow structures associated with a rotating wheel have been maintained. Additional to the two lower wheel vortices, the two upper wheel vortices are evident and appear to have increased in strength. This may be due to the increased entrainment experienced in the upper central wake region and the steeper adverse pressure gradient experienced by the flow when passing around the rearward portion of the radiused wheel shoulder. The central vortices created by the shear interaction of the rotating sides, obtained in the previous case were repeated here, but were found to be smaller in size than observed for the previous geometry. This may be due to the increased strength of the original four vortices in the wheel wake.

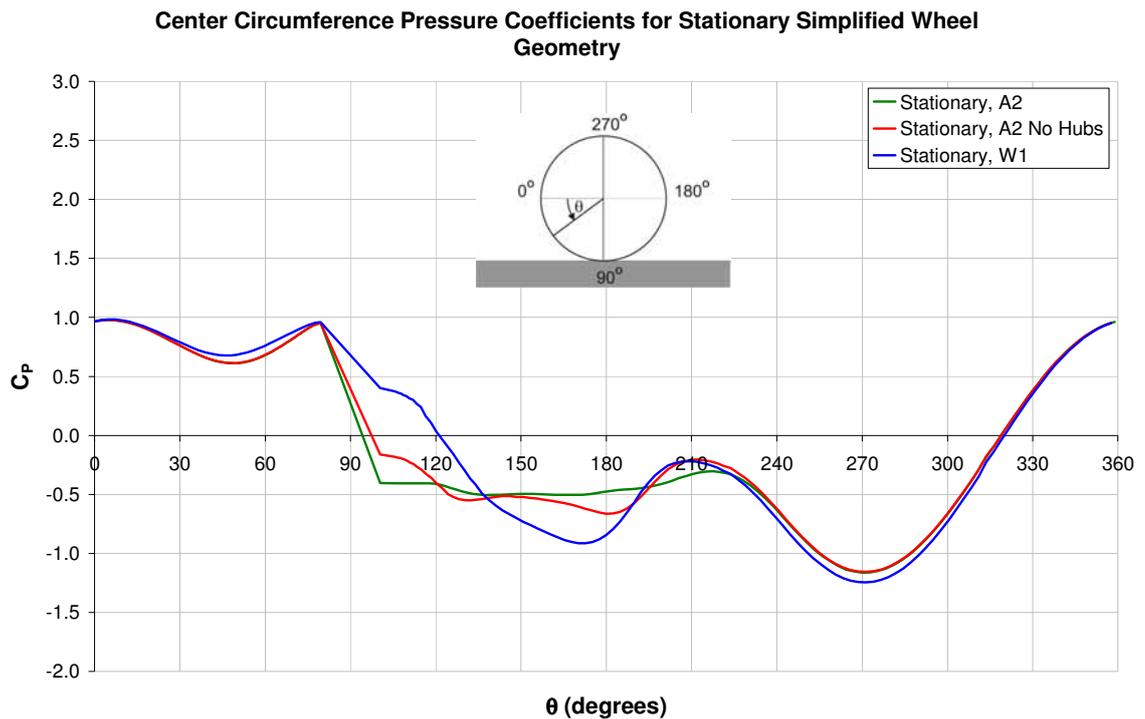


Figure 5.21 Centre pressure coefficients for simplified rotating wheel geometries

The geometries were also tested in a stationary configuration to determine what effect the geometry would have on the variations due to the rotation. As mentioned earlier, all the stationary wheels experienced greater lift and drag than their rotating equivalent (Figure

5.16). Despite this, the variation between the rotating and stationary conditions changed quite significantly. The lift reduction due to the wheel rotation for Fackrell's A2 wheel, the A2 wheel with no hubs and the W1 wheel was determined to be 40%, 55% and 34% respectively, while the drag reduction was 17%, 22% and 32% respectively. As expected for a stationary wheel, the central pressure coefficients of all the geometries (Figure 5.21) had a maximum stagnation pressure of 1 and the minimum pressure coefficient obtained over the top of the wheel is greater than that experienced by the rotating equivalent (Figure 5.17). The variations in the geometries performance once again can be related to changes in the separation point from the wheel tread. These variations are more significant than those experienced by the rotating equivalents. In the case of the stationary A2 wheel without hubs, the separation point is delayed while the opposite was experienced for the rotating case giving some insight into why this geometry experienced the most significant lift variation due to the wheel rotation.

For Fackrell's stationary A2 wheel geometry, it was determined that the flow in the wheel hubs exits from the top and is then entrained into the downwash generated in the mid wake region (McManus and Zhang, 2006). The flow over the wheel tread in this region (270° to 220° , Figure 5.21) is undergoing an adverse pressure gradient that eventually separates, at 220° , after the hub flow has been entrained. The flow from the wheel hubs has a much lower total pressure than that of the flow over the top surface of the wheel tread. For this reason, it is believed that the removal of the hubs delays the separation for the stationary wheel as the downwash produced over the top wheel tread surface entrains flow with a higher total pressure from the sides of the wheel where the hubs would have been. This provides the boundary layer with sufficient energy to overcome the adverse pressure gradient experienced and to delay the separation point until a location of 180° . Despite the flow exiting the hubs in a similar position for the rotating case, this variation is not as significant as the flow from the hubs is ejected into a portion of the wake after the separation point and the flat sides create a vortex that reduces the downwash behind the wheel. For this reason the separation point for the stationary case moves in the opposite direction to the rotating case when the hubs are removed and the large lift variation occurs between the stationary and rotating cases relative to the other two wheel geometries tested.

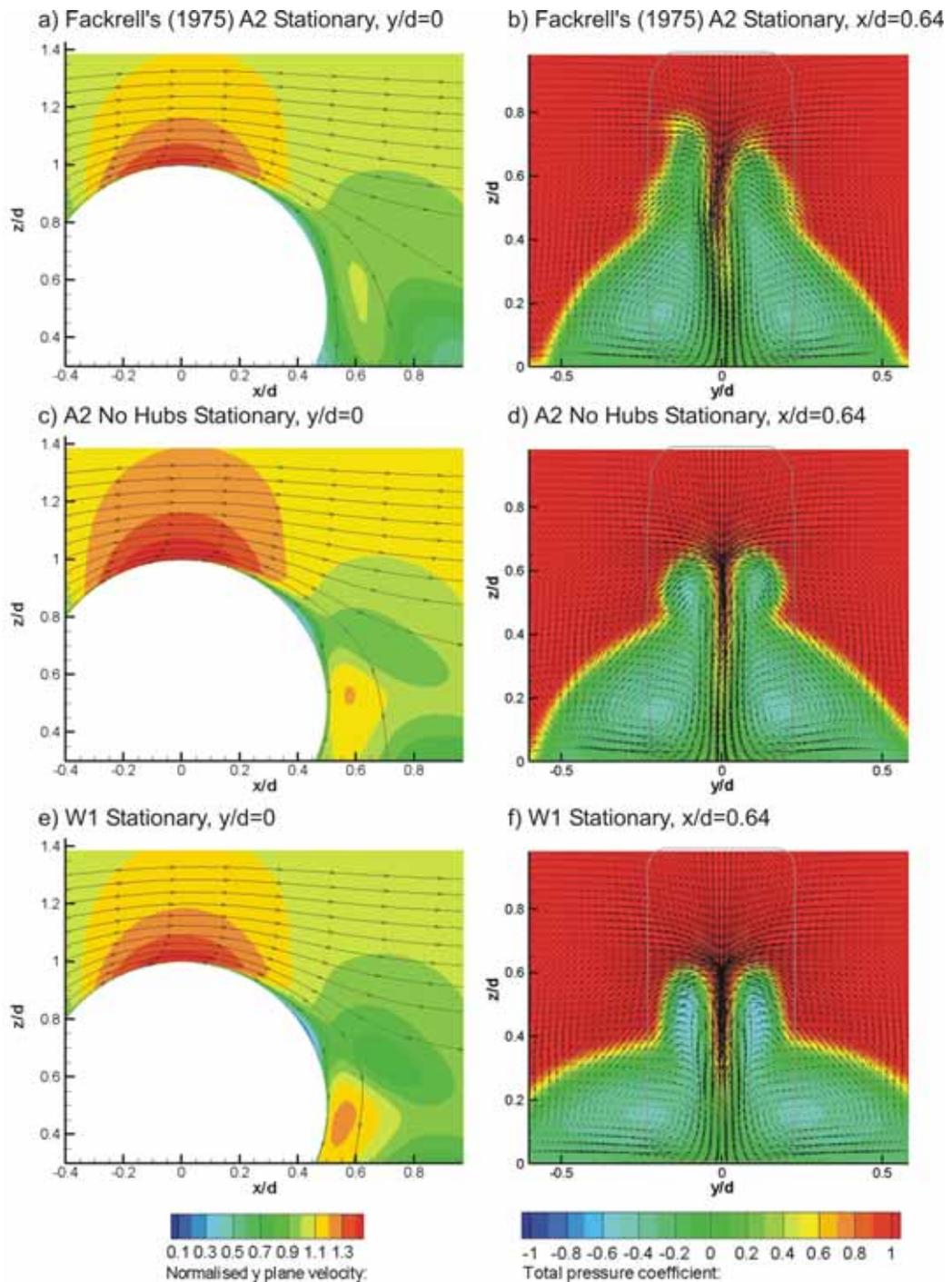


Figure 5.22 Entrainment into wheel wake for Fackrell's A2 wheel with and without hubs

One surprising aspect of this result is that while the separation point has varied significantly in a direction that would create an increase in lift and drag to occur, the results presented in Figure 5.16 indicate that little or no variation has been obtained in either

when removing the hubs from the stationary wheel. While it is difficult to quantify the variations due to the separation point, Fackrell had indicated that the lift and drag contribution made by the hubs was approximately 5% of the total lift and drag. Therefore it may be possible that the increase in lift and drag that would be expected due to the variation in the separation point could be of a similar magnitude as the contribution that is made by the hubs and therefore little total lift and drag variation is obtained for this geometric change.

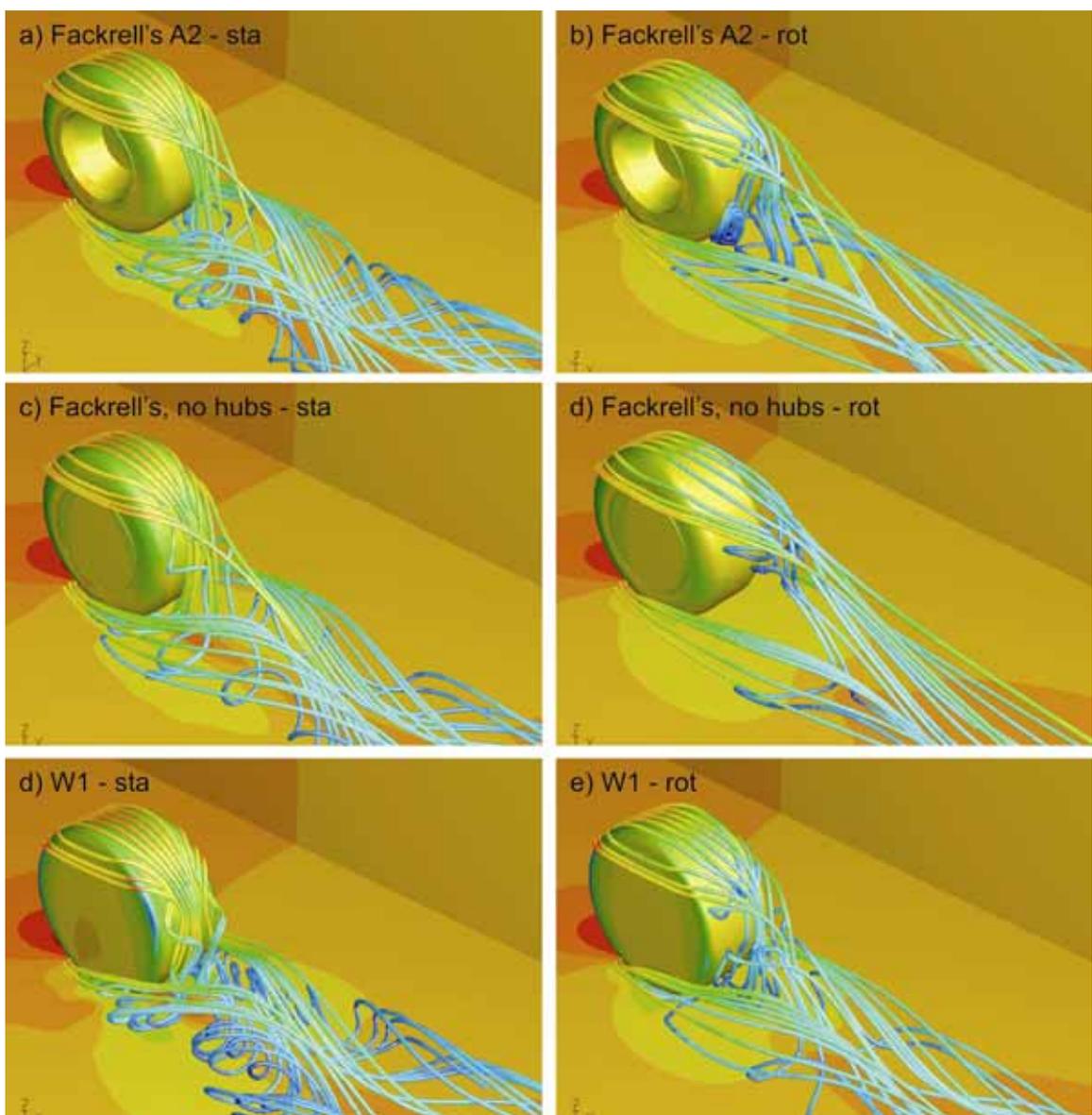


Figure 5.23 Flow structures associated with simplified wheel geometries

Replacing the wheel shoulder (W1) for the stationary case created similar variations as those experienced by the rotating equivalent and therefore will not be discussed in great detail. In short, the wider wheel tread provided by the new wheel shoulder produces a larger region of increased static pressure ahead of the wheel and can be seen by the variation in the pressure coefficients obtained in Figure 5.21 between an angle of 30° and 60°. This produces a steeper pressure gradient over the top surface of the wheel tread up until the minimum pressure location which also has a larger magnitude relative to the previous stationary geometries. This variation also creates a stronger downwash behind the wheel forcing the lower wheel wake and vortices to form further apart than the other cases as shown in Figure 5.23. The stronger downwash coupled with the completely flat and smooth sides also assists with keeping the boundary layer attached over the rear wheel tread surface. These variations in flow characteristics have already been demonstrated to produce increases in lift and drag values during the wheel wake investigation discussed in Section 5.1.1.

In conclusion it has been demonstrated that geometric variations can alter the details in flow of either a rotating or stationary wheel and as a result create significant changes to the final lift and drag values obtained for a wheel. Therefore, the simplified wheel geometries used by Axon *et al.* (1998) and Skea *et al.* (2000) for their computational investigations are likely to have contributed to the poor correlation that they obtained when comparing to the measurements undertaken by Fackrell (1975). This argument is further supported by the excellent correlation obtained during the isolated wheel validation study presented in Section 4.3 which utilised a wheel geometry that faithfully reproduced that used by Fackrell. While detailed variations in the flow have been obtained with the flow structures, they all demonstrated the fundamental variations for a rotating and stationary wheel previously published. Given that these variations are now understood and there is no future intention to compare the computational results to the experimental results obtained by Fackrell, the wheel investigation will progress using the simplified W1 wheel geometry.

5.1.4. Variations in characteristics for adjacent wheel pair relative to isolated wheel

While most vehicles utilise two front wheels positioned side by side, all previous investigations conducted specifically on the aerodynamics of a wheel have been

undertaken with a single wheel in isolation. The experimental investigation undertaken by Cogotti (1983) is one exception. Unfortunately, Cogotti utilised a stationary ground that required a gap to be left beneath the wheels so that the wheels may be rotated. Since then, the ground representation technique utilised by Cogotti has been demonstrated to be inappropriate and therefore there is a lack of understanding on the effect a second wheel placed alongside the first would have on the flow structures and forces for each wheel. Given that it is intended to model two adjacent wheels and to vary the wheel track during the wing and wheel study that will proceed in Chapter Six, it was decided to determine what effect the same variations would have in comparison to an isolated wheel.

So that the results may be comparable to those obtained with the combined wing and wheel investigation, this investigation was undertaken using the unbounded computational model utilising a freestream velocity of 33.3ms^{-1} and a wheel diameter of 660mm. Based on this diameter, the Reynolds number is 1.5×10^6 . These values were chosen to be more representative of the Reynolds number experienced by a wheel attached to an open wheel race car, as opposed to the Reynolds number used during Fackrell's experimental investigation. The wheels used for this investigation include both the W1 and W2 wheels which have a width of $0.46d$ and $0.54d$ respectively.

As figure 1.9 demonstrates, the wheel track has being defined during this study as the distance from the symmetry plane to the outer face of the wheel. The largest wheel track value of $1.52d$ tested is representative of the maximum wheel track permitted by the F1 regulations prior to the 1998 season (FIA, 1997) while the second largest wheel track value of $1.36d$ is the maximum permissible track as specified by the current regulations and used since 1998 (FIA, 2009). While it is unlikely that significantly smaller track values are representative of those used by open wheel race car, in order to exaggerate the effect that a wheel placed alongside the first would have, the wheel track was reduced by two additional increments to a minimum value of $0.92d$. Since the Reynolds number and the surrounding boundaries (and therefore the effective blockage experienced by the wheel) have now changed in comparison to that used during the previous isolated wheel investigations, the W1 and W2 wheels were again tested in isolation using the unbounded computational model for comparison to the results presented here as part of the wheel track investigation. For this reason the lift and drag coefficient values of 0.40 and 0.48

respectively, presented here in Figure 5.24 for the W1 wheel, are less than those indicated by Figure 5.16.

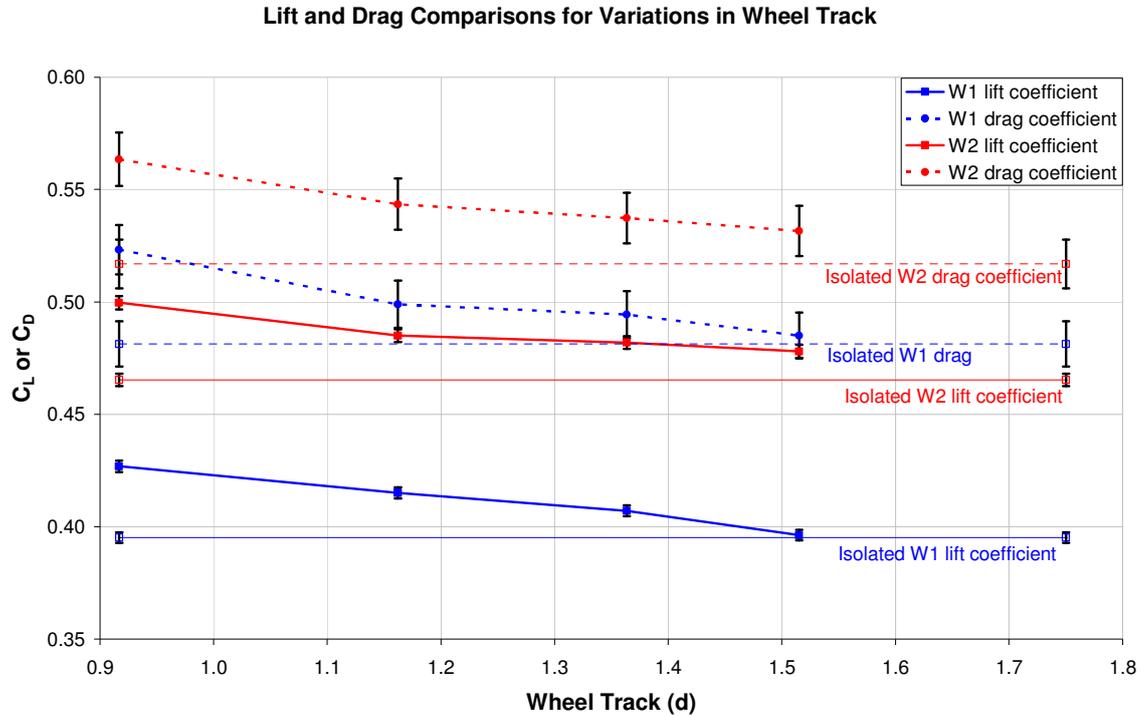


Figure 5.24 Lift and drag forces experienced by both wheels side by side and in isolation

The lift and drag coefficients presented in Figure 5.24 were calculated using the frontal area of 0.210m^2 and 0.234m^2 as the reference area for the W1 and W2 wheel's respectively for both the side by side configuration with varied wheel track and the isolated case. These results predictably demonstrate that as two wheels that are positioned adjacent to each other have their wheel track increased, the forces obtained on each wheel will reduce and approach that of a single wheel in isolation. At the narrowest wheel track tested ($T/d=0.92$) the lift and drag of both wheels increased by approximately 7.5% and 9% respectively in comparison to the same wheel in isolation. While the W1 wheel experienced a smaller than 1% increase in lift and drag at the greatest wheel track tested ($1.52d$), the W2 wheel experienced a larger increase in lift and drag of approximately 3%. This is likely to indicate that an increase in the width of the wheel also increases the sensitivity of the lift and drag variations as a wider wheel at the same wheel track will result in the distance between the inner face and the symmetry plane to be smaller. This is also

confirmed by the results obtained for the maximum permissible wheel track values for the current F1 regulations ($T/d=1.36$) where the W1 wheel experienced an increase of approximately 3% in both lift and drag while the W2 wheel experienced a slightly higher increase of 4%.

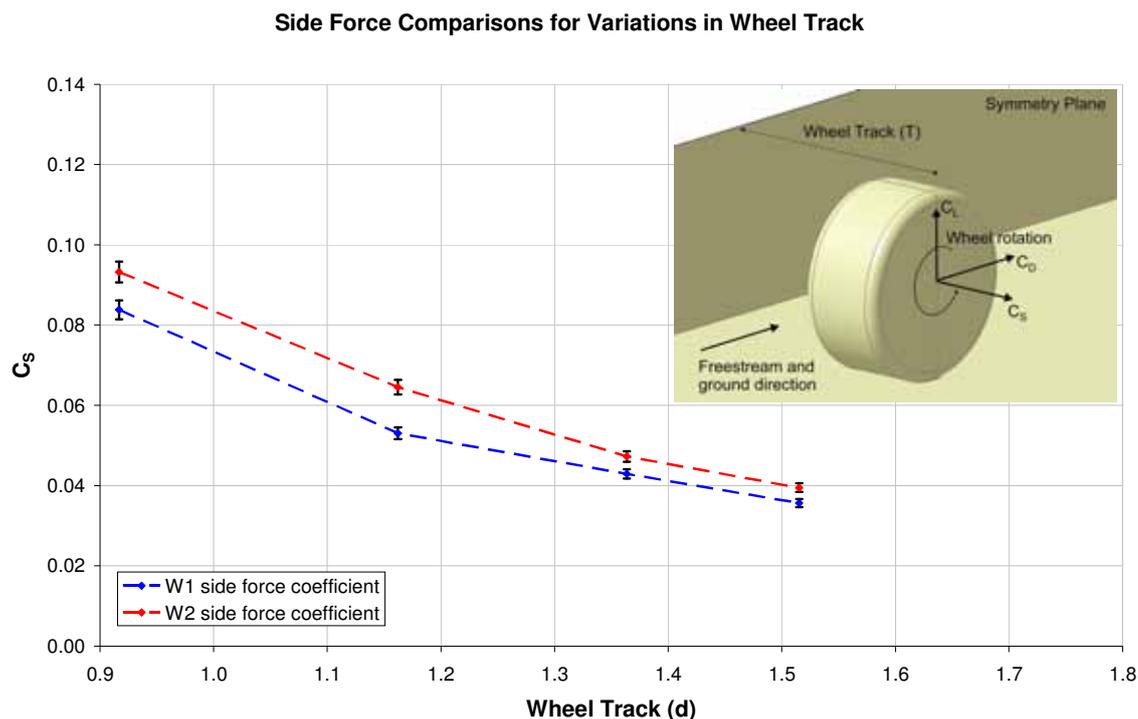


Figure 5.25 Side forces obtained for both wheels when side by side

Positioning two wheels adjacent to each other also introduces an additional side force on each wheel in comparison to that which would be experienced in isolation. The variation of this side force is shown in Figure 5.25 where a positive value indicates a direction acting away from the symmetry plane. No values are provided for the side force acting on the isolated W1 and W2 wheels as both wheel geometries are symmetrical and located in the centre of the flow field and therefore the side force expected in this configuration would be zero. At the narrowest track the side force experienced by the W1 and W2 wheel is approximately 18% of the respective isolated wheel drag. Like the lift and drag, as the wheel track is increased, the side force experienced reduces. At the two maximum wheel tracks values of $T/d=1.36$ and $T/d=1.52$, the side force is approximately 7.5% and 9% of the isolated wheel drag respectively for both wheel widths tested.

In order to understand what mechanism is responsible for the generation of the side force, pressure coefficient plots were taken around the circumference of the wheel made with several intersecting planes parallel to the ground for a wheel in isolation and for the minimum wheel track value tested ($T/d=0.92$). These two cases were used for comparison as it was expected that these would provide the largest variations in the static pressure acting over the wheel and that larger wheel tracks tested would only reduce the magnitude of the variation relative to the isolated wheel case. The planes used to intersect with the wheel were located at heights of $z/d=0.107$, $z/d=0.239$ and $z/d=0.503$ and a schematic of each of these intersections is included in Figure 5.26. Additionally, in each schematic the angles subtended by the start and end of the upstream and downstream wheel shoulders and tread, as well as the inner and outer faces, when viewed from above, have been included.

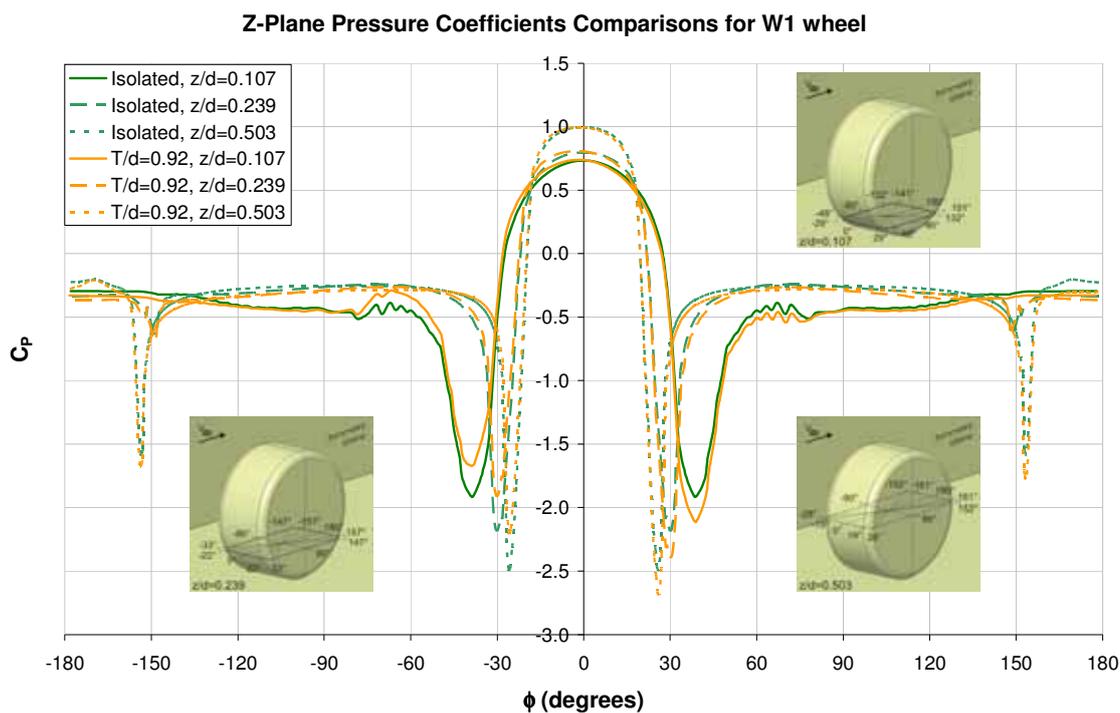


Figure 5.26 Pressure coefficients on W1 wheel at $z/d=0.107$, $z/d=0.239$ and $z/d=0.503$

Viewing the pressure coefficients around the circumference of the wheel at a given height highlights a number of key flow features associated with a rotating wheel. When considering the $z/d=0.503$ profile for the isolated wheel case as an example (Figure 5.26),

the peak pressure value of 1 obtained at $\phi=0^\circ$ indicates the stagnation point that occurs at the front of the wheel. The static pressure drastically reduces from this point towards the upstream wheel shoulder ($19^\circ < \phi < 28^\circ$) where the minimum pressure values are obtained indicating that the flow is accelerated around this portion of the wheel geometry. Alongside the side wheel face ($28^\circ < \phi < 152^\circ$) the pressure coefficients remain constant until the rear wheel shoulder ($152^\circ < \phi < 161^\circ$) where the flow undergoes a second, smaller acceleration as the flow is entrained into the separated region behind the rear of the wheel ($152^\circ < \phi < 180^\circ$). For the isolated wheel case, the flow is symmetric and therefore the negative ϕ values, indicating the opposite side of the wheel, replicate the corresponding positive ϕ values. In the case of the two adjacent wheels, the negative ϕ values indicate the side that is closest to the symmetry plane.

The pressure coefficients presented in Figure 5.26 for all the profiles demonstrate that the flow on both sides of the wheel is accelerated further by the presence of an adjacent wheel relative to the same wheel in isolation, but the inside face generally experiences a slightly greater acceleration than that of the flow travelling along the outer face. The cause for the increased velocity on the inside face of the wheel is due to the sudden contraction in the flow that is caused by the close proximity of the two wheels when they are positioned side by side and this is likely to also contribute to the increase in lift and drag experienced by the wheel while in this configuration. Despite this, larger and more significant variations were obtained for the suction peaks acting over the upstream wheel shoulders with the inboard and outboard shoulder experience a reduction and increase in suction respectively. Given that this is the largest variation obtained for the pressure coefficients when comparing the isolated wheel to one with a second placed adjacent to it, it would be expected that the cause for this variation will also be responsible for the side force experienced by the wheel.

The acceleration variations obtained over the wheel shoulders is believed to be linked to the inboard shift in the position of the maximum pressure as also indicated by Figure 5.26. Therefore, before understanding why this variation occurs over the shoulders, it was considered necessary to understand why the shift in maximum pressures occurs. The peak pressure values obtained on the $z/d=0.107$, $z/d=0.239$ and $z/d=0.503$ indicate a line along the front face of the wheel which indicates where the oncoming flow diverges and

then travels on either side of the wheel. This “divergence” line joins the two main stagnation points at the contact patch and the most upstream position of the wheel tread generating large cross flow components forward of the wheel at either side (McManus and Zhang, 2006). By placing a second wheel alongside the first, it is possible that the inboard acting components of the crossflow generated by the stagnation zones oppose each other reducing the magnitude of the inboard crossflow component and subsequently enhancing the outboard component. Vectors and pressure coefficients plotted on a plane located at $x/d=-0.63$ relative to the wheel’s axis of rotation confirm that this is the case (Figure 5.27). Therefore while the inboard crossflow components act against each other reducing in magnitude, the remaining flow has been forced to travel either above or outboard of the wheel resulting in higher velocities in these direction. As a consequence, the stagnation zones move inboard and as does the divergence line that joins them as indicated by the maximum pressure peaks obtained for the wheel with a track value of $0.92d$. The shift in the location of the stagnation zone and the divergence line was determined to be approximately 5% of the wheel width. The increase in lift previously reported as the wheel track is reduced is a possible consequence of the increased flow over the top of the wheel tread.

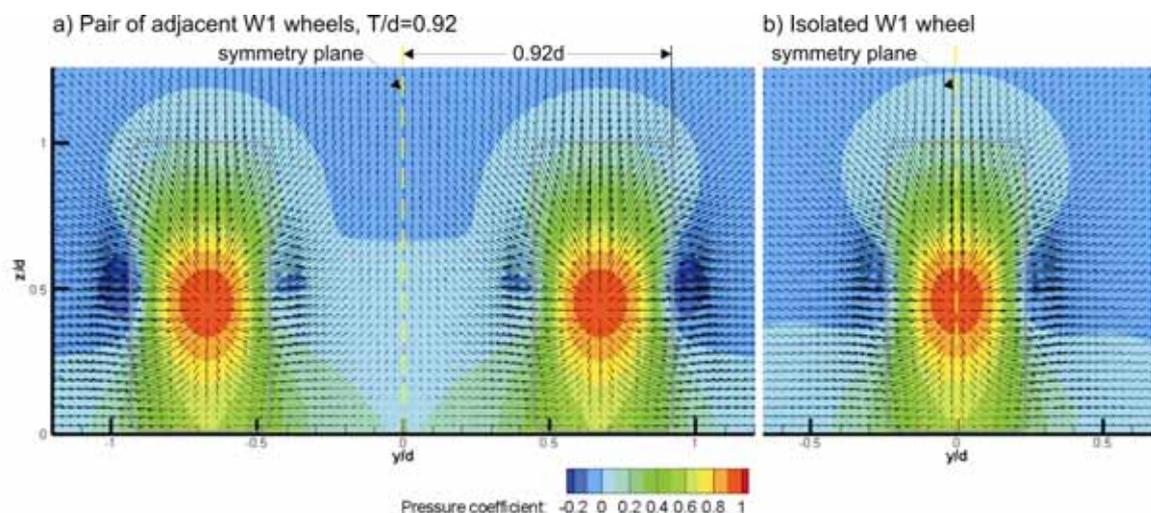


Figure 5.27 Pressure coefficients and cross component velocity at $x = -0.63d$ for W1 wheel

The variation of the minimum pressures registered over the upstream shoulders (Figure 5.26) can also be explained by the adjustment in crossflow obtained when two wheels are positioned adjacent to each other. Reducing the inboard crossflow component would

require less flow to travel around the inner shoulder requiring a reduced acceleration in this region and also explaining the reduction in minimum pressure obtained on all the inner wheel shoulders for the side by side configuration when compared to the isolated wheel. Similarly the outboard shoulder experiences a greater suction peak due to the increased quantity of flow travelling outboard of the wheel and this is why an asymmetric flow is generated around the wheel when positioned adjacent to another. As a result the peak pressure coefficients from the forward shoulder go from being equal for the isolated case to varying by approximately 20% for two adjacent wheels with a wheel track value of $T/d=0.92$. The change in quantity of flow travelling outboard of the wheel also explains the variation in static pressure acting on the outer face of the wheel even though small in magnitude compared to the variation obtained for the front wheel shoulders. This pressure reduction on the outer face can assist in alleviating some of the side force generated by the suction increase on the inner shoulder further suggesting that the variations over the front wheel shoulders is a significant factor in determining the direction of the side force.

Another variation that is evident and supporting the theory of an interaction of the two cross flow components is an increase in static pressure inboard of the wheel relative to that experienced on either side of an isolated wheel. This variation could also contribute to the drag increase experienced by the wheel as the wheel track is reduced and also explain the upwash generated along the symmetry plane for the two adjacent wheels which is not obtained for the isolated wheel at a similar distance on either side for the isolated wheel. The opposite also occurs on the outer regions of the wheel.

Increasing the width of the wheel maintained the same trend while the magnitude of the variations for the pressure distributions around the perimeter of the wheel was increased. Due to the definition of the wheel track used here, when the wider W2 wheel is positioned to have the same wheel track as that used for the W1 wheel ($T=0.92d$ in this case), the distance between the inner face of the wheel and the symmetry plane is 16% less and therefore a greater acceleration should be obtained for the flow travelling between the symmetry plane and the inner face of the wheel than that which was obtained by the W1 wheel.

Z-Plane Pressure Coefficients Comparisons for W2 wheel

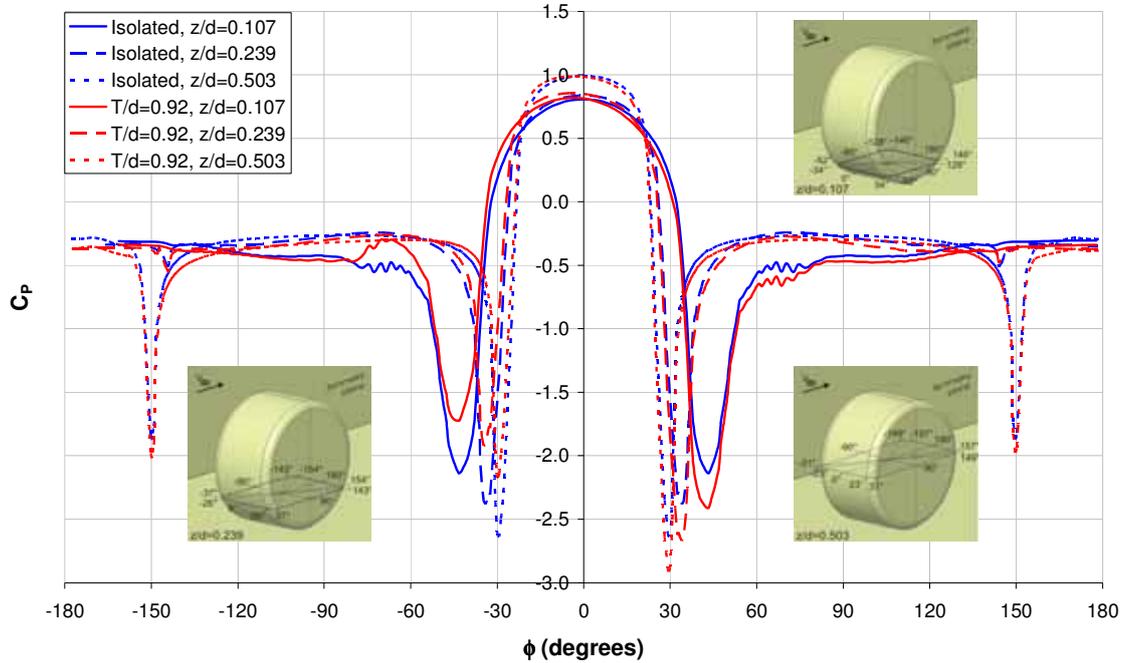


Figure 5.28 Pressure coefficients on W2 wheel at $z/d=0.107$, $z/d=0.239$ and $z/d=0.503$

The results presented in Figure 5.28 relative to Figure 5.26 confirm that this is the case with the W1 and W2 wheel exhibiting pressure reductions of 15% and 25% respectively on the inboard face. Not only should the inner face of the wheel be closer, but also the wheel's stagnation points. As a result, the maximum pressure obtained at each plane also shifts a greater portion inboard due to the increase interaction by the inboard component of the flow generated by these regions (Figure 5.29) as well as the pressure variation is larger when comparing the inboard and outboard portions of the flow forward of the wheel.

As a result more flow is forced outboard and therefore the variation of the suction peaks of the inner and outer wheel shoulders is approximately 30%, 10% greater than that obtained by the W1 wheel and is also a likely explanation why the W2 wheel's lift, drag and side force is more sensitive to equal wheel track variations in comparison to the W1 wheel (Figure 5.24 and Figure 5.25). These results seem to further support the proposed theory here that the interaction of the stagnation regions and the opposing inboard cross flow component is the main cause for the variations in flow for two wheels positioned adjacent to each other in comparison to a single isolated wheel.

All profiles, taken through the wheel demonstrated a common variation in the flow around the wheel with the exception of those obtained at $z/d=0.0015$, or at the contact patch (Figure 5.30). The peak pressure value that is greater than one found on this plane is due to the viscous interaction of the converging wheel and ground surfaces that occurs forward of the contact patch (Fackrell, 1975) while the minimum pressures indicate the maximum acceleration experienced by the flow prior to separating and being ejected from either side of the front contact patch. For this reason the peak pressure for the isolated W1 wheel is located at $\pm 62^\circ$, the exact location that the wheel tread ends and the wheel shoulder is in contact with the ground. After these peaks, the static pressure remains mostly constant within the separated region of the lower wheel wake (McManus and Zhang, 2006).

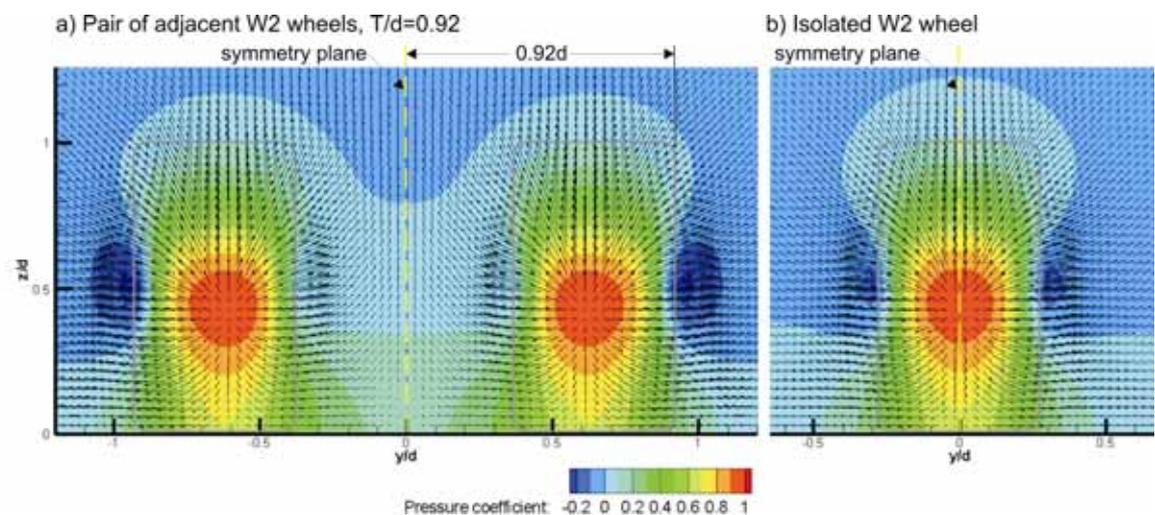


Figure 5.29 Pressure coefficients and cross component velocity at $x = -0.63d$ for W2 wheel

Unlike the previous planes, positioning two wheels adjacent to each other resulted in an increase in the acceleration on the inner side and a deceleration for the outer side, at the contact patch. This is because the flow around the wheel's contact patch is separated and therefore the increase in pressure generated on the inboard region of the wheel due to the interacting inboard cross flow results in the separation point being delayed for the inboard region of the contact patch. Conversely, the outboard region experiences a more forward separation point.

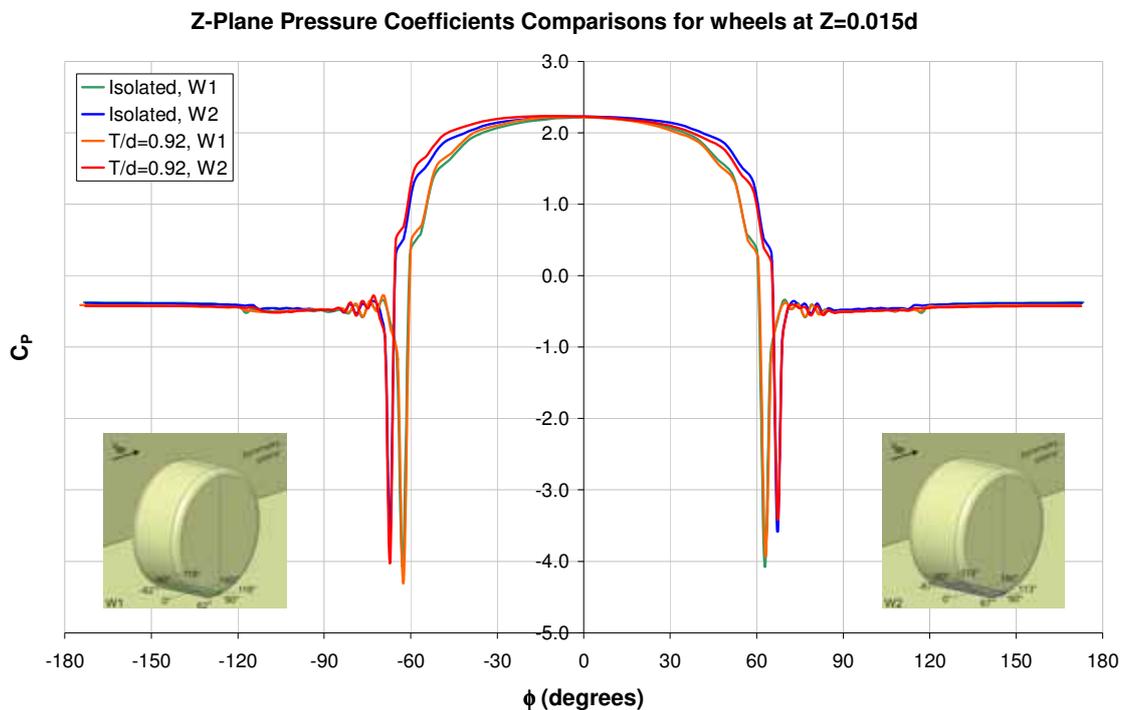


Figure 5.30 Pressure coefficients on W1 and W2 wheels at $z/d=0.0015$ (contact patch)

Streamlines located on the same plane for the isolated W1 wheel with a wheel track of $0.92d$ (Figure 5.31g) demonstrate that this is the case indicating that the cross flow interaction that occurs for two adjacent wheels can also alter the separation point at the contact patch of each wheel in comparison to that which is experienced in isolation (Figure 5.31a). It should be noted that while only a single wheel is shown, the results presented in Figure 5.31c-h are for pairs of wheels positioned adjacent to each other with varied wheel track and the symmetry plane located at $y/d=0$. A clear trend also exists as the wheel track is increased showing that the separation at the contact patch tends to that obtained for an isolated wheel (Figure 5.31a and b) which is also replicated by the results obtained with the W2 wheel (Figure 5.32a, c, e and g).

Reducing the wheel track also caused the upper inboard vortex to become larger and be positioned higher while the outboard vortex becomes weaker and is positioned lower. Given that these vortices are created due to the separation that is obtained over the upper portion of the wheel tread (McManus and Zhang, 2006), the variation in these vortex structures indicate that the separation over the wheel tread also becomes asymmetric

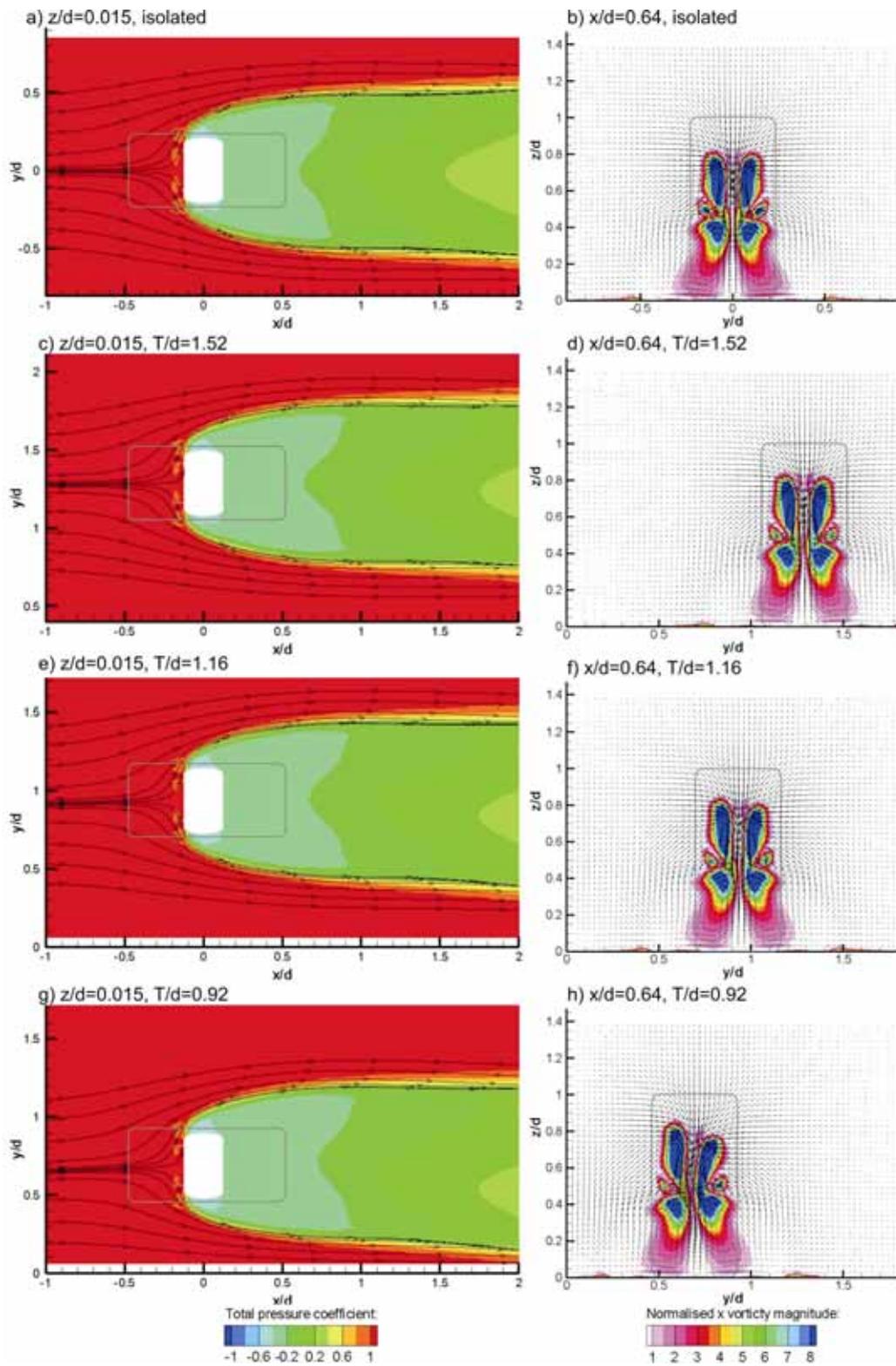


Figure 5.31 Variations in W1 wheel wake obtained when varying the wheel track

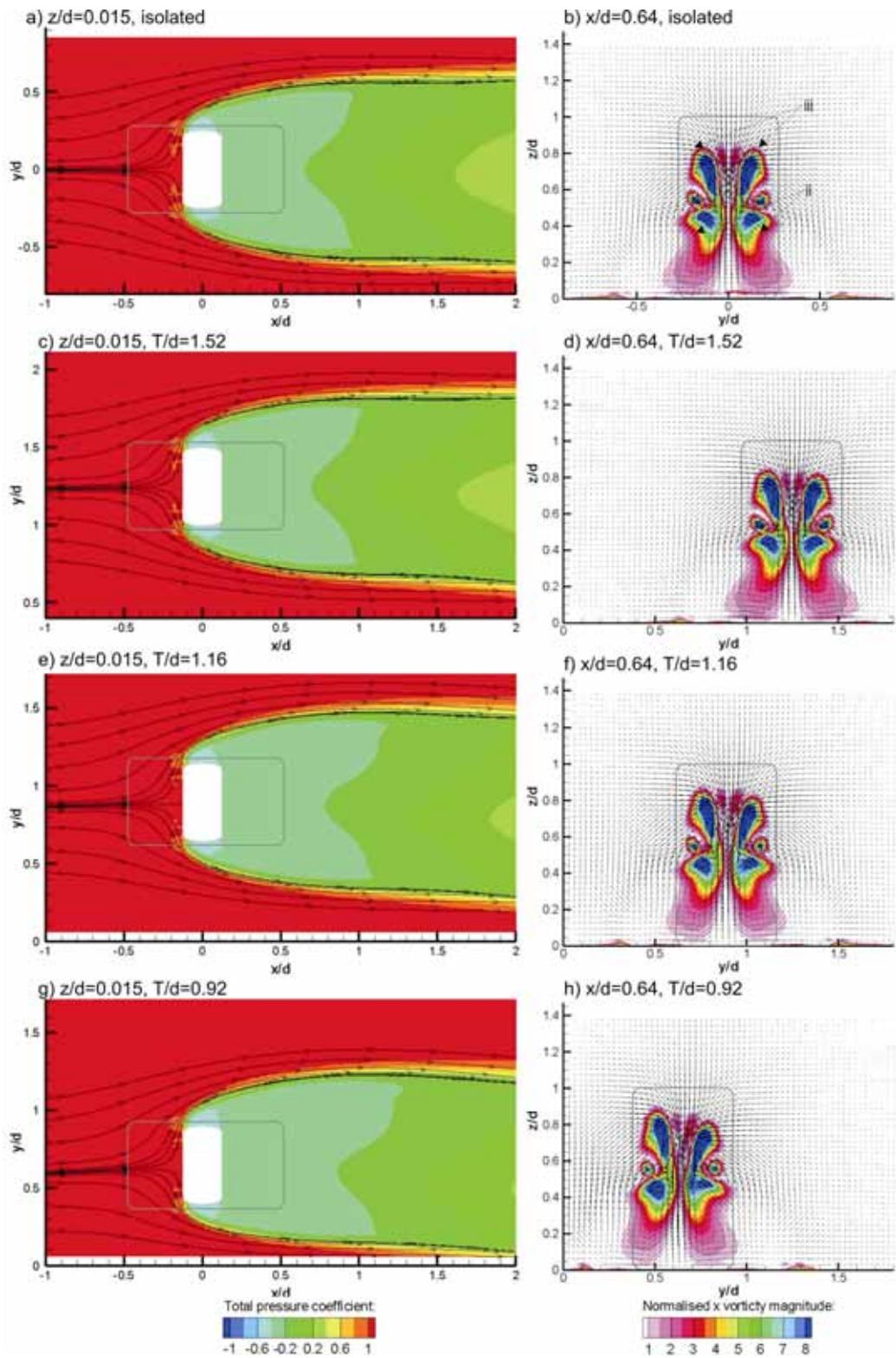


Figure 5.32 Variations in W2 wheel wake obtained when varying the wheel track

when two wheels are positioned adjacent to each other. The relationship between the wheel tread separation position and the contact patch separation previously seen during the contact patch dependency study (5.1.2) was again repeated here. The smallest wheel track tested indicated that on the inboard side, the separation was delayed at the contact patch and this was coupled with an increase in separation from the wheel tread and size of the inner upper wheel vortex. The opposite occurred on the outer side of the wheel with the separation at the contact patch being increased and therefore the size of the upper outer wheel vortex reducing.

Another feature that has been previously observed with a wheel track value of $0.92d$ that can also contribute to the increased separation from the inboard upper wheel tread is the increased upwash generated by the close proximity of the wheels stagnation points (Figure 5.27 and Figure 5.29). The imbalance of these vortex structures has also induced a crossflow in the central region of the wheel wake which has only previously been seen for asymmetric wheel geometries (Figure 5.5). This may explain why the wheel wake has a tendency to be drawn inboard as it travels downstream. Another contributing factor could also be the size variation of the lower wheel vortices also being caused by the changes in the cross flow experienced forward of the contact patch and the subsequent variation in separation obtained in this region. This causes the size of the lower outboard vortex to increase relative to the lower inboard vortex as the wheel track is reduced. The results obtained for the widest wheel track tested appeared to be very similar to those obtained for the isolated wheel suggesting that with a wheel track of $1.52d$, the positioning of a second wheel alongside the first has little influence on the flow associated with each wheel. The small force variations obtained at the wheel track of $1.36d$ also suggest that the same can be said for this wheel track for both wheels tested.

In conclusion, it has been demonstrated that by positioning two wheels side by side, an interaction occurs reducing the inboard cross flow components and enhancing the outboard cross component that occurs forward of a rotating wheel and promoting flow around the outer face of the wheel. Subsequently, the separation that occurs due to the jetting action from the front contact patch results in asymmetric trailing vortex structures that cause the wheel wake to travel inboard as it propagates downstream. The net effect on the wheel causes the lift and drag to increase over that obtained for an isolated wheel and for a side force to be introduced that pushes the two wheels apart (or away from the

symmetry plane). This effect reduces as the wheel track is increased and at the largest wheel track tested, the variations obtained relative to an isolated wheel were negligible. In order for these observations to be made, it was necessary to use a much smaller track value than what would realistically be used for an open wheel vehicle. Therefore, based on these results, it is likely that the influence of the interaction associated with the positioning of two wheels side by side for the wing and wheel study that will be presented in the following chapter (Section 6.5), will be small.

5.2. Isolated Wing Investigations

One parameter that has not been previously investigated for a downforce producing wing is the effect that the wing span will have on the performance of the wing. Given that this is a characteristic that will be varied during the wing and wheel study, it was decided to determine what effect this would have on an isolated wing first. During Zerihan's (2001) study of a single element, downforce producing wing in ground effect, he determined that the downforce loss phenomenon is caused when a reduced proximity to the ground causes a severe adverse pressure gradient on the bottom surface of the wing that leads to boundary layer separation. Additionally, surface flow visualisation conducted by Zerihan indicated that the separation was more pronounced at the centre of the wing than at the tips. The cause of this was attributed to the main wing vortex that forms on the bottom edge of the endplate re-energising the boundary layer and preventing separation from occurring near the wing tips and that the centre experiences a greater adverse pressure gradient due to the larger peak suction values achieved there. Based on these explanations, it is expected that as the wing span is decreased the height at which the maximum downforce occurs at would also reduce since the main wing vortex that prevents separation at the tips will effectively act over a greater portion of the bottom surface.

To determine if this was the case, the computational model used to validate against Zerihan's experimental results in the previous chapter (Section 4.2) was used to test four additional increments of reduced span ($S/c=2, 1.6, 1.24$ and 0.97) of Zerihan's original wing geometry (span of $2.46c$). The wing profile, chord ($0.2234m$), and freestream velocity ($30ms^{-1}$) used by Zerihan were maintained such that the comparison was conducted at the same Reynolds number of 4.56×10^5 .

Lift Coefficients of Zerihan's (2001) Wing Geometry for Variations in Span

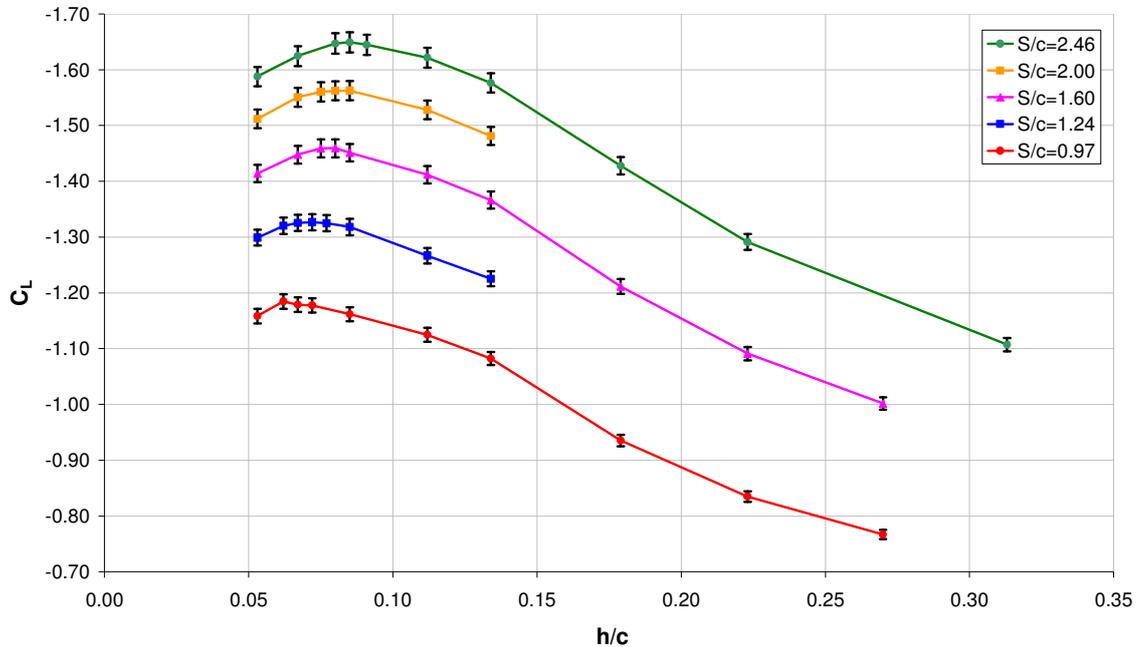


Figure 5.33 Lift coefficient obtained for variations in span of Zerihan's wing

The lift coefficients calculated using the computational model (and evaluated by using each wing's plan view area as the reference area) are shown in Figure 5.33. These results indicate that reducing the span of the wing results in a clear trend indicating that a relationship exists between the span and the height at which the downforce loss phenomenon occurs at. For the wing span values tested of 2.00c, 1.60c, 1.24c and 0.97c, it was determined that the height at which the downforce loss phenomenon occurred at was reduced to 0.080c, 0.078c, 0.072c and 0.062c respectively instead of 0.085c as originally determined by Zerihan for his span of 2.46c. To determine if the cause for this variation was caused by the main wing vortex acting over a larger portion of the wing, the variation of the separation along the span of the wing was investigated. In order to achieve this, it was determined that the shear stress experienced by the bottom surface of the wing could be an indicator as where the separation was likely to occur over the bottom surface of the wing. To determine if this was possible, the shear stress values obtained using the computational model of Zerihan's wing at a height of 0.067c were compared to on surface flow visualisation conducted by Zerihan during his experimental investigation at the same height and is included as Figure 5.34.

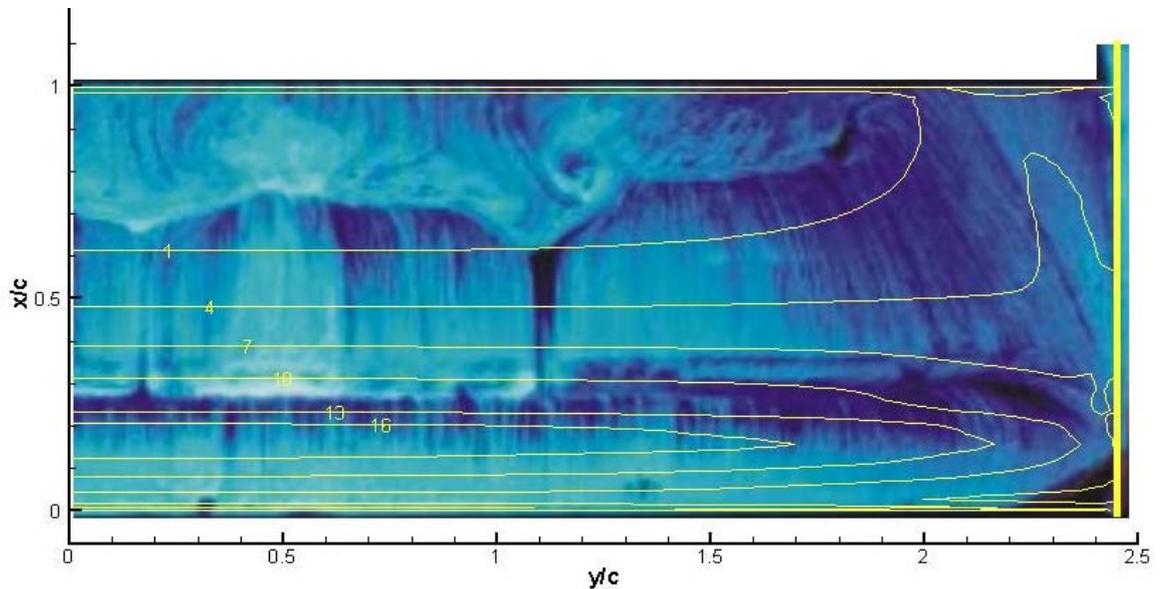


Figure 5.34 Comparison of Zerihan's on surface flow visualisation to shear stress values

Comparing the iso-contour lines of the shear stress values indicates that a shear stress value of less than 1 can be used to indicate which regions of the flow over the bottom surface of the wing should be expected to be separated. As Zerihan was able to demonstrate with the flow visualisation shown in Figure 5.34, the shear stress values obtained with the computational model indicate that the separation is more pronounced over the centre portion of the wing while a region closer to the wing tip where the main wing vortex is expected to pass remains attached. Using the wall shear stress in a similar manner for the shorter span wings at the maximum downforce height demonstrate that this trend is continued but the size of the vortex appears to remain fairly constant and therefore acts over a larger portion of the wing as the span is reduced (Figure 5.35 a, c, e, g). The results shown here indicate that the separated region is expected to form from the centre of the wing until $0.4c$ inboard from the endplate. This suggests, that for a wing span of $0.97c$, $1.60c$, $2.00c$ and $2.46c$, the region of which the vortex acts over preventing separation from occurring is approximately 40%, 25%, 20% and 16% of the span respectively agreeing with the original assumption made for why a shorter span wing will experience the downforce loss at a later height.

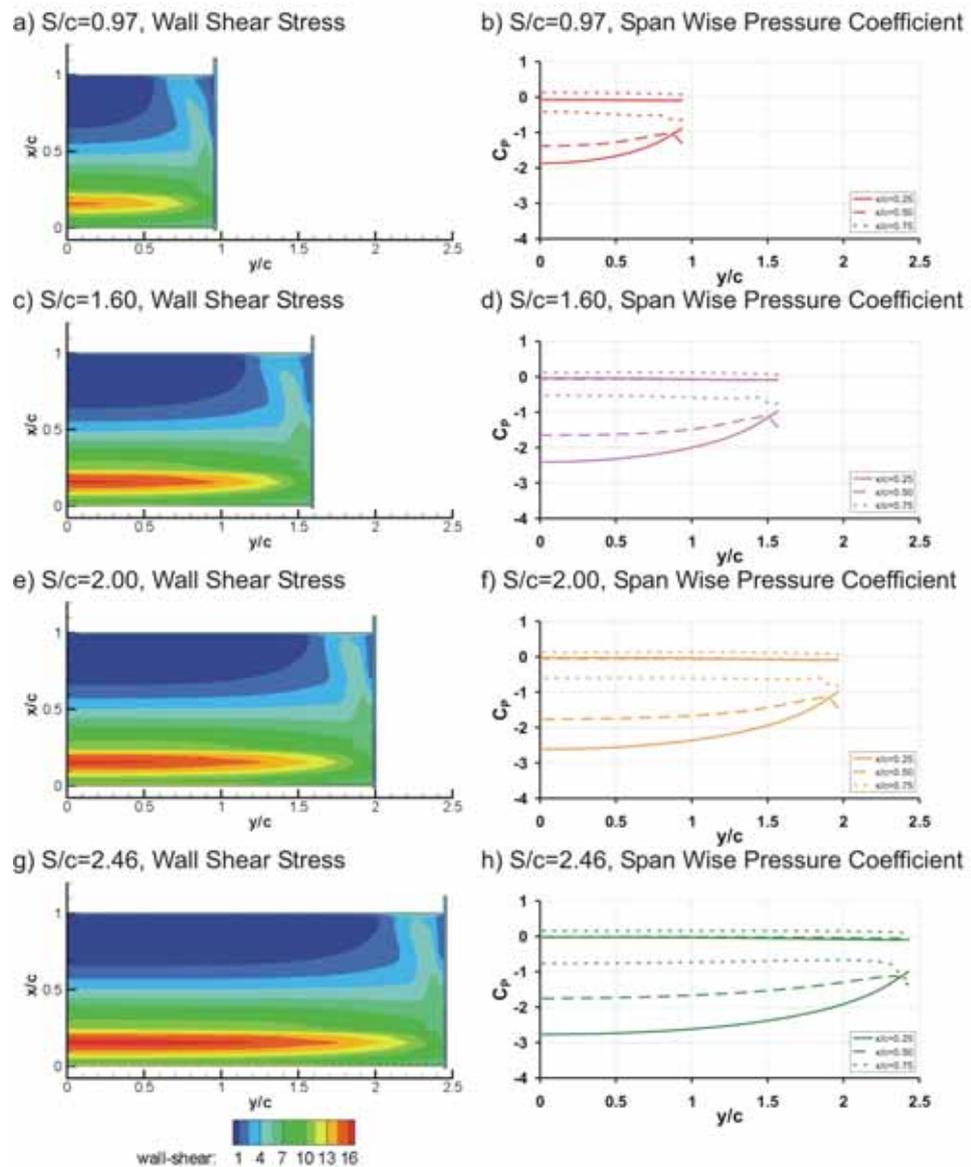


Figure 5.35 Shear stress and spanwise pressure for Zerihan wing with varied spans

In order for the vortex to act over a constant area, the vortex strength would have to remain unchanged for variations in span. It is widely accepted that the main wing vortex is created by the pressure difference created either side of the endplates bottom edge and this is dependant on the pressure difference that can be achieved by the upper and lower surfaces. Spanwise pressure distributions located at $x/c=0.25$, 0.5 and 0.75 (Figure 5.35 b, d, f and h) give an indication that the vortex strength remains unchanged by the variation of span with the pressure difference remaining fairly constant at 0.8, 1.2 and 0.7 at

$x/c=0.25, 0.5$ and 0.75 respectively at the corresponding height at which the maximum downforce occurs at for each wing span tested. Vorticity plots on a plane located at $x/c=0.75$ (Figure 5.36), downstream from the wing's leading edge, also indicate that at the height at which the maximum downforce is achieved for each wing, the main wing vortex has a diameter that remains between $0.5d$ and $0.55d$.

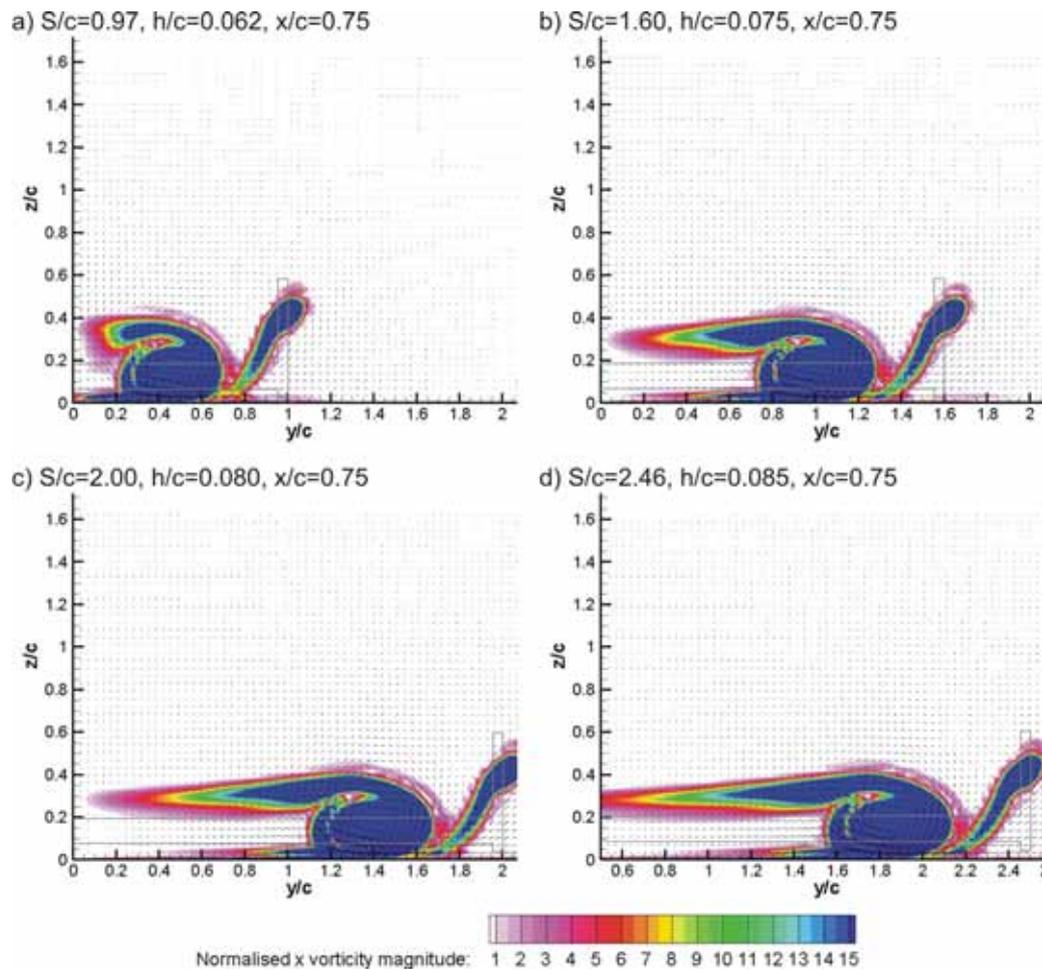


Figure 5.36 X-Vorticity on a plane located at $x/c=0.75$

The spanwise pressure coefficients indicate that the most significant variation occurs at the centre of the wing ($y/c=0$) where reductions in span result in reduced levels of suction acting on the bottom surface that are responsible for the variation in downforce obtained for the shorter spans. This would suggest that there is a second possible reason why the downforce loss phenomenon is delayed as the span is reduced and is best explained by

considering the pressure distribution over the central chord of each wing at a fixed height (Figure 5.37).

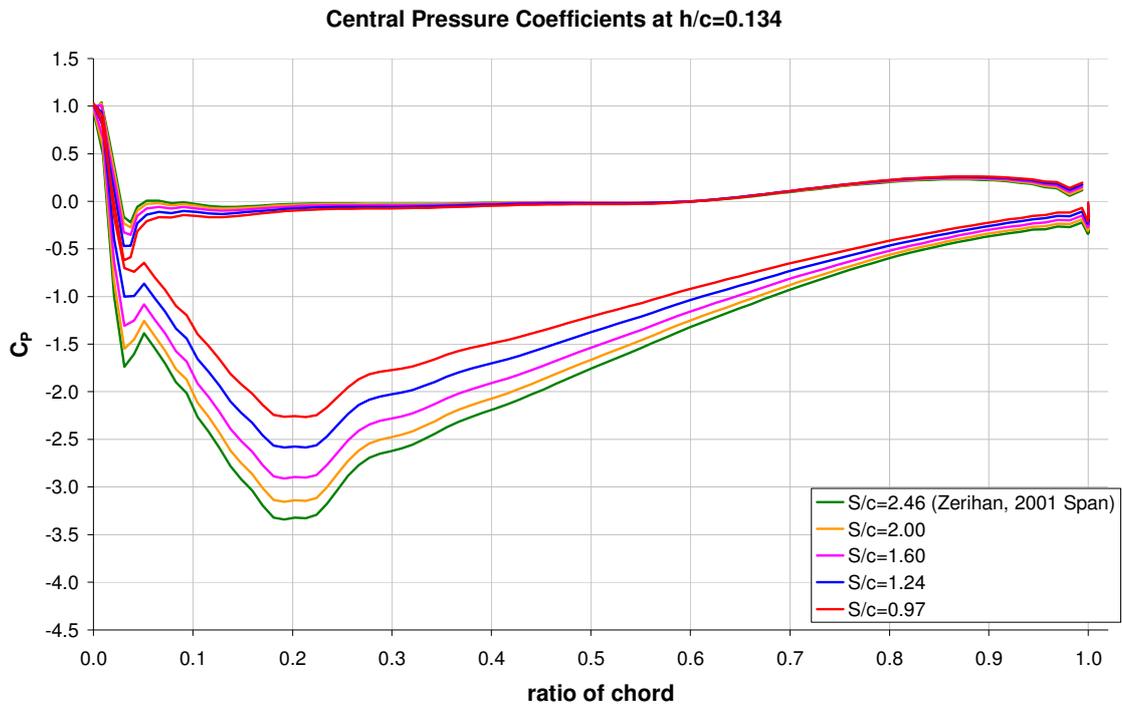


Figure 5.37 Centre chord pressure coefficients for Zerihan's wing with varied span at $h/c=0.134$

For a given height, as the span is reduced, the minimum pressure experienced by the bottom surface also reduces. This results in a less severe adverse pressure gradient ensuring that as the span is reduced, the flow over the centre portion of the bottom surface of the wing will remain attached at further reduced heights. Comparing the same spans at the maximum downforce height (Figure 5.38) indicates that the peak suction pressure obtained for each span varies less than that obtained at a common height ensuring that the adverse pressure gradient is experienced on the bottom surface of the wing is also similar and therefore the extent of the separation should also be similar. The shear stress plots of the bottom wing surface indicate that at the maximum downforce height, the separation occurs from a point approximately located at $x/c=0.6$ along the centre chord. This would suggest that the reduced ability of the a shorter span wing to create high levels

of suction on the bottom surface of the wing would also be a contributing factor for why reduced span wings experienced a delayed downforce loss phenomenon.

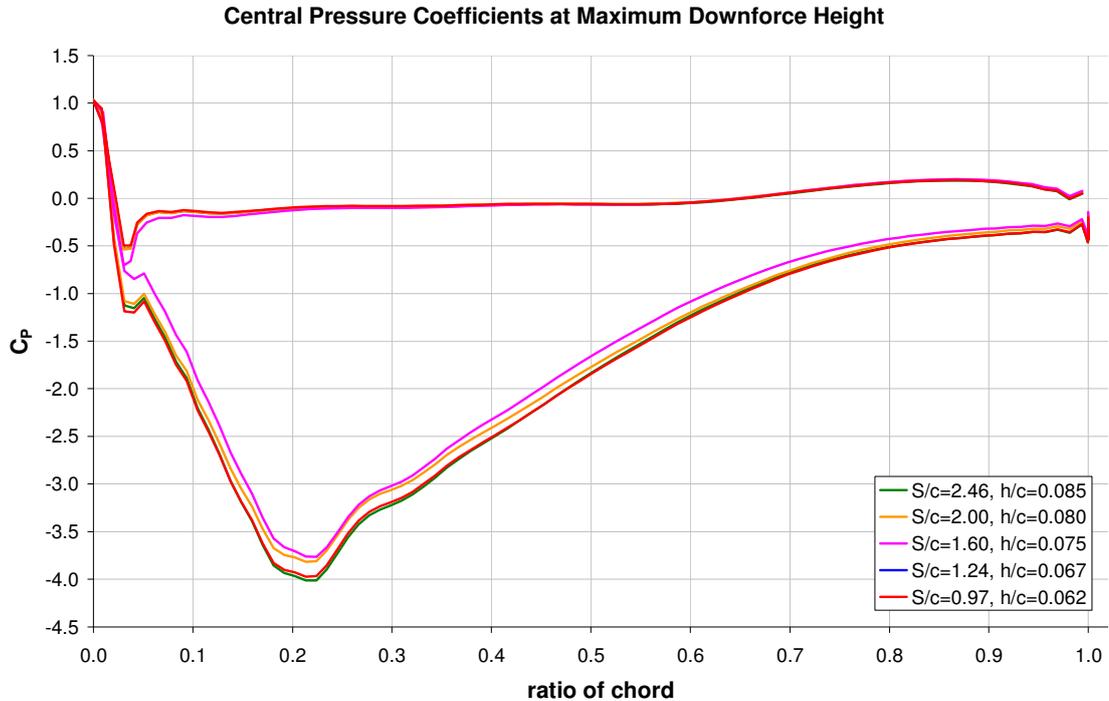


Figure 5.38 Centre chord pressure coefficients for Zerihan’s wing with varied span at the respective maximum downforce heights

Given that the wing vortex size remains fairly constant, and that the main variations that cause the reduced levels of downforce are due to the variation of pressure acting on the surface of the wing, it would be expected that as the wing span is reduced, the induced drag created by the formation of the main wing vortex of the wing would be of greater significance. The drag coefficients presented in Figure 5.39 suggest that this is the case with the shortest span tested ($S=0.97c$) indicating that the maximum drag coefficient is obtained at the same height at which the maximum downforce is achieved ($h=0.062c$). At subsequent heights, the wing vortex is expected to burst and as a result the induced drag of the wing is also expected to reduce accounting for the subsequent reductions in drag obtained at this span as the height is further reduced. As the span is increased, the significance of the induced drag is outweighed by the increases in the pressure drag caused by the separation from the bottom surface of the wing. For this reason the

relationship of the drag coefficients for variations in the height tend to increase for reductions in height at a more rapid rate as the span is increased and as separation effects greater portions of the bottom surface of the wing. The reduced significance of the induced drag is consistent with previous investigations in the effect that increasing span has on lifting wings in freestream conditions (Abbott and Von Doenhoff, 1959) as well as those in ground effect (Barber, 2000).

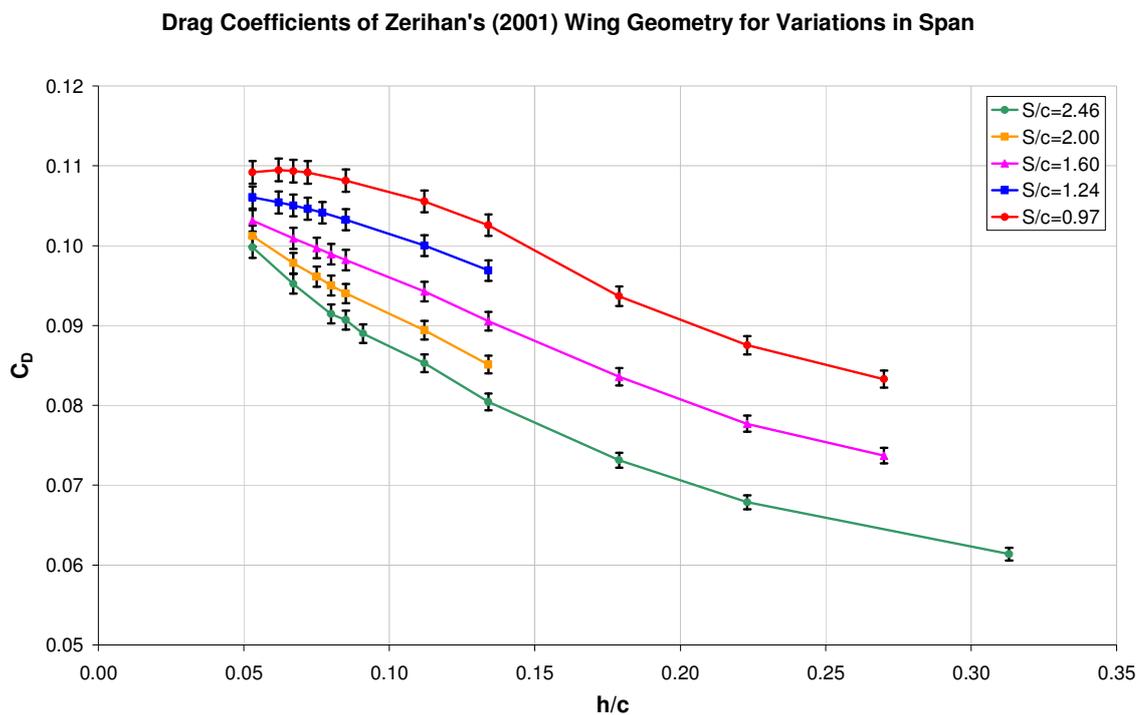


Figure 5.39 Drag coefficient obtained for variations in span of Zerihan's wing

During this investigation, it has been demonstrated that reducing the span of a wing allows the wing to operate closer to the ground before the downforce loss phenomenon occurs. The cause of this is due to two reasons; the first being that the main wing vortex that prevents separation from occurring at the wing tip remains unchanged effectively acting over a greater portion of the wing. Secondly, the shorter spans wings have reduced ability to increase suction on the bottom surface and as a result, the wing can operate much closer to the ground before an adequately severe pressure gradient is obtained that results in excessive separation on the bottom surface of the wing. Both the ability of the wing to generate suction on the bottom surface of the wing, and the main vortex strength of the

wing is likely to be affected by the presence of the wheel and therefore it would be expected that these trends will also vary when the wheel is also included in the investigations that will proceed in the Chapter Six.

5.3. Summary

Flow structures associated with an isolated wheel or isolated wing have been investigated in this chapter. Investigations concerning an isolated wheel have determined that the cause of the variation in the formation and the strength of the primary wheel vortices and the subsequent reduced wheel wake width are caused by a reduction in the downwash experienced by a rotating wheel. The downwash associated with the wake of a stationary wheel was found to force the primary wheel vortices to be stronger and form in a lower and more outboard position. A rotating wheel does not exhibit this downwash component in the wheel wake due to the more forward wheel tread separation point and for this reason the vortices associated with the rotating wheel are weaker, form higher and closer to the centre plane causing the lower wheel wake to be narrower despite the increased jetting action experienced forward of the contact patch. The effect that the increased jetting action has on the lower wheel wake width was determined to be small in comparison to the separation point, but accounts for approximately half of the drag reduction obtained by a rotating wheel.

Changing the height of the step surrounding the contact patch allowed the same interaction to be observed in reverse. Doing so delayed the flow from separating from the wheel shoulders allowing the primary wheel vortices to form in a higher position and with reduced strength. This caused the separation point from the wheel tread to shift further forward and as a result the upper wheel vortices formed due to this separation strengthened. This was undertaken to ensure that this geometric simplification did not adversely affect the results obtained of an isolated wheel. By doing so, it was determined that when modelling a wheel, the step used around the contact patch should be no more than $0.0028d$ otherwise unrealistic lift and drag values are obtained when comparing to experimental results obtained with a solid wheel.

Similar interactions between the lower wheel wake structure and the wheel tread separation point were also observed in a study conducted to determine what effect

simplifying the wheel geometry would have. Removing the wheel hubs caused an additional pair of vortices to form in the wheel wake due to the shear interaction provided by the flat sides. This also increased the downwash in the centre wake causing consistent variations to the lower wheel wake width as discussed above. Cogotti (1983) had previously postulated that these vortices would also exist in the wake of the wheel but prior to this investigation no evidence of these vortices has been found. Simplifying the wheel geometry however did not vary the effect of the wheel rotation and the most simplified wheel geometry (W1) that will be used for the wing and wheel investigations had an increase in lift of 48% with almost no variation in drag in comparison to Fackrell's (1975) A2 wheel.

The W1 wheel was subsequently used to determine how the flow structures of a pair of adjacent wheels would vary in comparison to those belonging to a single wheel in isolation. This was also repeated with a wider version of the W1 wheel (W2 wheel). Doing so indicated that the stagnation point expected at the most upstream location of the wheel is shifted towards the symmetry plane reducing the flow travelling between the two wheels and increasing the velocity of the flow passing around the outer surface and the top of the wheel. This causes the wheels to experience a side force pushing the two wheels apart as well as an increase in drag and lift for each wheel. The conclusions described here were obtained by investigating a wheel track value much less than what is representative of that found for an open wheel racing car and which will be used for the final wing and wheel investigation. At the larger, more representative wheel track values these effects can be considered to be negligible as the stagnation regions for the two adjacent wheels are too far apart for the cross flow to influence the flow structures associated with the adjacent wheel.

The investigation undertaken for an isolated wing considered the effect that the wing span has on the downforce loss phenomenon. It was demonstrated that reducing the wing span caused the downforce loss phenomenon to be delayed and that this is caused by two reasons. The first and most significant is that when the span of the wing is reduced, the maximum suction generated at the centre of the wing also reduces causing the adverse pressure gradient experienced in this region to be less severe. As a result, the wing can be brought closer to the ground before the same level of separation is obtained. Secondly, the size of the main wing vortex is independent of the span of the wing and Zerihan (2001) has

demonstrated that this vortex can assist with preventing the flow beneath the wing at the tips from separating. By reducing the span of the wing, the main wing vortex can have the same effect over a greater proportion of the wing.

Chapter 6: Combined Wing and Wheel Investigations

Now that a better understanding of how various geometric characteristics of as isolated wing or wheel affect the flow structures associated with them, the two bodies will be considered together. The investigations undertaken of a wing working in unison with a wheel pair, which are presented throughout this chapter, are summarised in Figure 6.1.

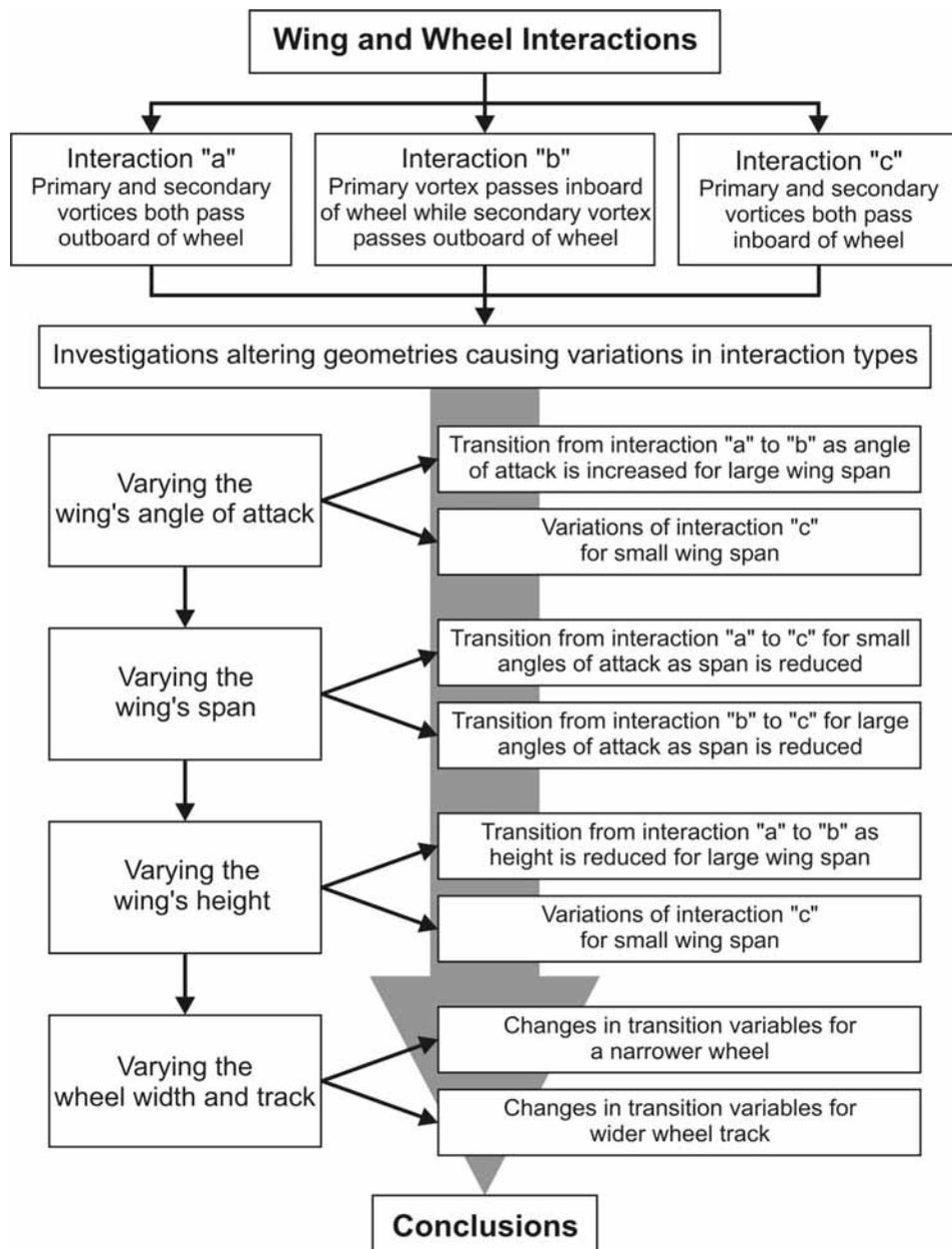


Figure 6.1 Flow chart outlining investigations undertaken of a combined wing and wheel pair

In the process of conducting these investigations, it was determined that three main wing and wheel vortex interactions can be achieved. More detailed investigations were then carried out to determine how varying the span and the angle of attack of the wing may alter the state of interaction between these governing flow structures. As mentioned in previous investigations, the presence of the wheel is expected to alter the downforce produced by the wing and the size of the main wing vortex. Therefore, using the knowledge obtained during the study conducted with an isolated wing with varied span, it would be expected that the height that the downforce loss phenomenon would occur at would also be altered by the presence of the wheel and therefore this was also investigated. The last investigation considers the implications of altering the wheel width and track. All results presented in this chapter were obtained using the unbounded computational model which was previously described in Chapter Three.

6.1. Main Interacting States of Wing and Wheel Vortices

Numerous computational results were obtained for a combination of varied wing span, angle of attack and height as well as wheel widths and tracks. Doing so indicated that three main wing and wheel interactions may occur depending on the combination of wing and wheel parameters chosen. The main variation between the three states is dependant on the path that the main and secondary wing vortices take around the wheel and subsequently how they interact with the wheel wake. The three alternatives paths that the wing vortices may take were determined to be;

- a) both main and secondary wing vortices travel outboard of the wheel (interaction a)
- b) the secondary wing vortex travels outboard of the wheel while the main wing vortex is drawn inboard (interaction b), and
- c) both the main and secondary vortices travel inboard of the wheel (interaction c).

By releasing streamlines from the top and bottom edges of the endplate for three cases with common wheel width and track values of $0.631c$ and $1.6c$ respectively, it is possible to visualise the three different interactions (Figure 6.2). With 0° angle of attack and a span equal to the wheel track both wing vortices were able to travel around the outer face of

the wheel (Figure 6.2a). From this configuration, increasing the angle of attack to 12° caused the main wing vortex to travel inboard of the wheel (Figure 6.2b). Reducing the span of the wing such that the endplate was in line with the inner face of the wheel resulted in the secondary vortex also travelling along the inside face of the wheel (Figure 6.2c).

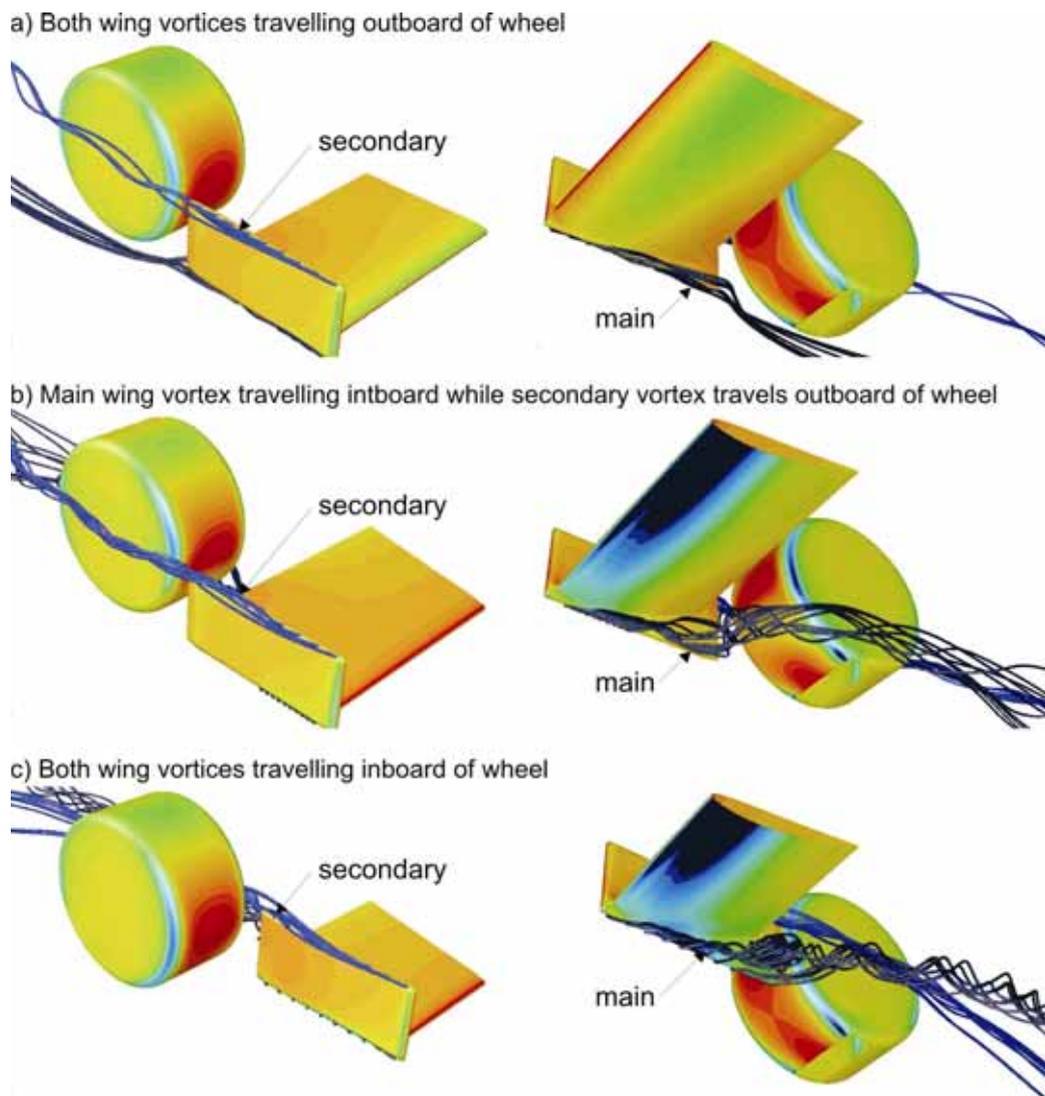


Figure 6.2 The three wing and wheel vortex interactions; a) both outer, b) main inner and secondary outer, and c) both inner

Depending on the path that the wing vortices take around the wheel, the forces experienced by both the wing and wheel can be altered relative to that which is experienced in isolation for each body. Figure 6.3 indicates the variations in lift and drag for each of the examples depicted in Figure 6.2 in comparison to the same wing in

computational investigation of a wing and wheel with a fixed wing span and angle of attack. Interaction “c” showed an opposite trend with the wing in the presence of a wheel experiencing an increase in downforce and drag of 10% and 22% respectively when operating in the presence of the wheel.

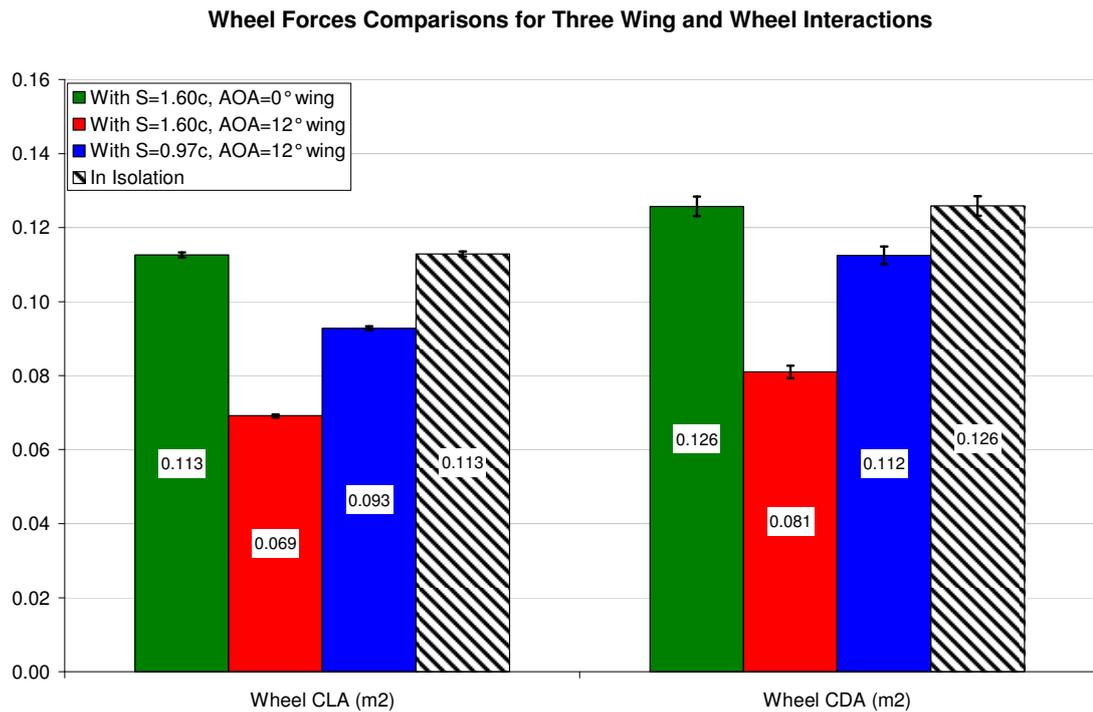


Figure 6.4 Force variation experienced by wheel in the three interacting states

Like the wing forces, the variation of the wheel forces relative to the isolated case also differed for each configuration (Figure 6.4). With the wing at an angle of attack and span of 0° and 1.6c respectively, the wheel experienced no change in lift and drag. Increasing the angle of attack to 12° resulted in both the downforce and drag of the wheel reducing to be 45% and 28% of that experienced by the isolated case. Reducing the span of the wing to 0.97c increased both the lift and drag of the wheel so that the drag was equal to that experienced in isolation and the lift would be 25% less than that experienced by the isolated wheel. The reason for the significant variations in the forces for both the wing and wheel caused by the three different states will now be investigated individually in greater detail.

6.1.1. Causes and consequences of both wing vortices travelling outboard of wheel

In order to demonstrate how the vortex structures that form from the front wing endplates differ in the presence of a wheel to that in isolation, normalised x-vorticity and in plane vectors have been included as Figure 6.5 for x planes located between the wing and wheel ($x/c=-0.63c$) and at the wheel centre ($x/c=0$). The outline of the wing and wheel bodies have also being included in these figures for reference which depict the interaction where both wing vortices travel outboard of the wheel. In order to make a direct comparison, both the equivalent isolated wing (Figure 6.5 a, b) and isolated wheel (Figure 6.5 c, d) have been included with the results obtained for the combined wing and wheel case (Figure 6.5 e, f).

From the results of the isolated wing case, it is evident that the main wing vortex is approximately 4 times stronger than that of the secondary vortex (Figure 6.5a). While moving downstream from the $x/c=-0.63$ plane to the $x/c=0$ plane (Figure 6.5b), the main wing vortex travels inboard $0.2c$ and slightly higher while the secondary vortex moves outboard and lower. When considering that the position of the main wing vortex ($y/c=1.4$, $z/c=0.1$) corresponds to the position of the wheel on the $x/c=0$ plane (Figure 6.5d), it is clear that the same vortex path can not be maintained for the combined wing and wheel. Considering the $x/c=-0.63$ plane for the pair of isolated wheels (Figure 6.5c), the vectors demonstrate that the stagnation point forward of each wheel can generate cross flow components up to a value of 0.7 times that of the free stream velocity. Similarly, regions of cross flow created by the ejected flow from the either side of the contact patch (Figure 6.5d) were determined to reach magnitudes 0.6 time that of the free stream velocity.

When combining both the wing and wheel it becomes apparent that the presence of the wheel alters the formation of the main wing vortex (Figure 6.5e) and the direction that it travels in for this interaction state. The outboard cross flow component created by the large pressure rise associated with the viscous jetting action forward of a rotating wheel (evident on the $x/c=-0.63$ plane) remains. This forces the main wing vortex, which is now approximately half the strength of that for the isolated case, outboard of the wheel (Figure 6.5f). Static pressures located on a plane coincident with the top and bottom edges of the wings ($z/c=0.1$ and $z/c=0.59$) endplate also assist with demonstrating the explanation for these variations Figure 6.6.

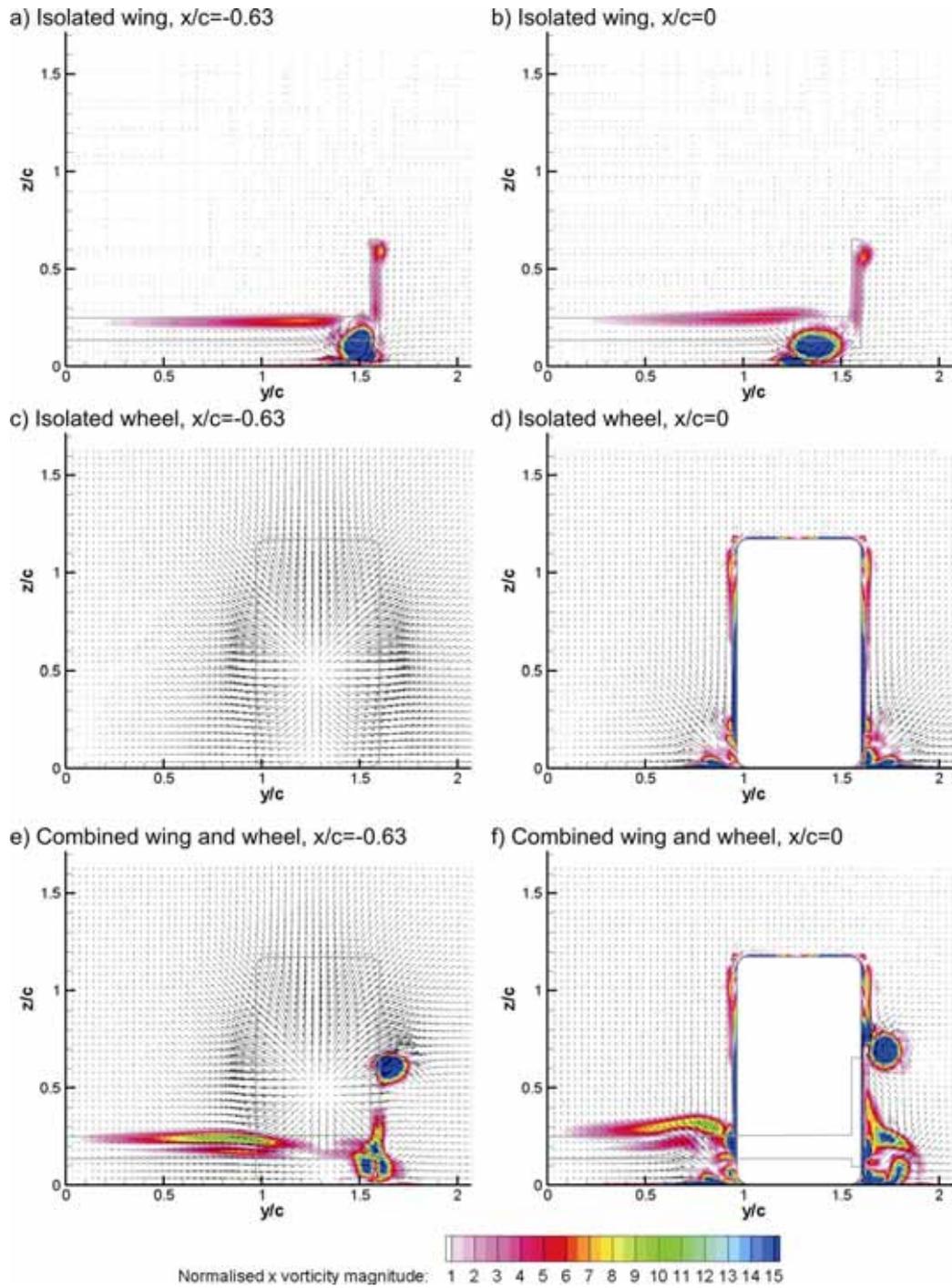


Figure 6.5 Vectors and Vorticity on x-planes for a wing and/or wheel with $W/c=0.63$, $T/c=1.6$, $h/c=0.13$, $S/c=1.6c$ and $AOA=0^\circ$

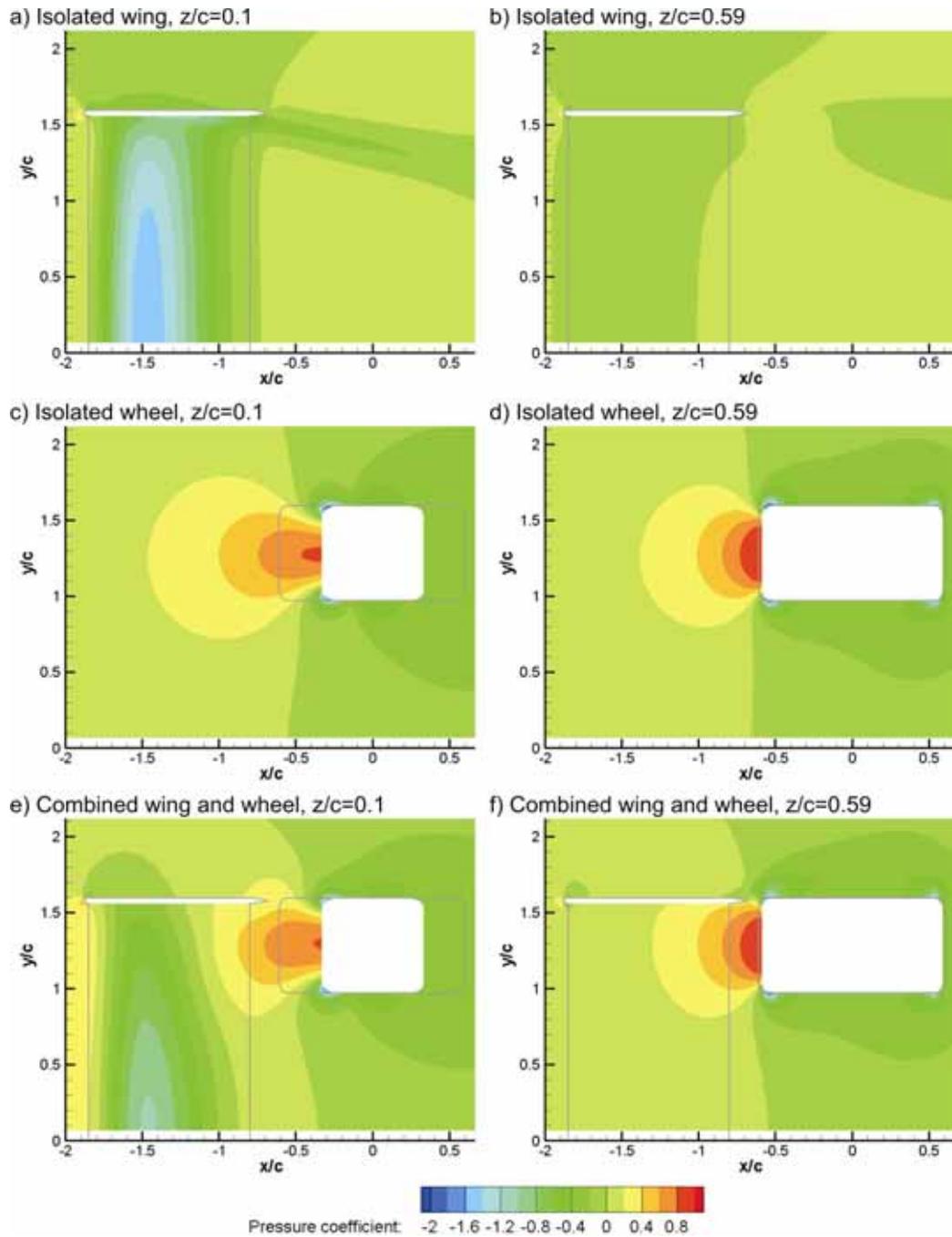


Figure 6.6 Pressure coefficients around endplate on z-planes for a wing and/or wheel with $W/c=0.63$, $T/c=1.6$, $h/c=0.13$, $S/c=1.6c$ and $AOA=0^\circ$

As has been previously demonstrated both experimentally (Fackrell, 1975) and numerically (McManus and Zhang, 2006) Figure 6.6c shows the regions of large pressure increases ($x/c=0.4$, $y/c=1.3$) that are expected forward of the wheel's contact patch, while

Figure 6.6a demonstrates regions of reduced pressure ($x/c=1.5$, $0 < y/c < 1.5$) that are expected beneath an isolated wing (Zerihan, 2001). Both these features exist in the combined wing and wheel case Figure 6.6e, but the pressure rise at the front of the contact patch has been reduced while the pressure drop beneath the wing has also been altered. This would agree with the previously proposed hypothesis that the pressure rise that forms forward of a rotating wheel adversely affects the ability of the lower surface of the wing to generate suction and for this reason, a wing in the presence of the wheel produces less downforce (Thisse, 2004).

The reduction in the main wing vortex strength is consistent with previous reports linking the downforce produced by an isolated wing to the strength of the wing's main vortex (Zerihan, 2001), but an additional variation in the main wing vortex structure also exists. While the main wing vortex for the isolated case is round in shape and completely coherent (Figure 6.5a), the main wing vortex for the combined wing and wheel appears to consist of three individual components (Figure 6.5e, $y/c=1.6$, $z/c=0.15$). The main wing vortex forms from the variation in pressure that occurs across the bottom edge of the endplate (Zerihan, 2001). Figure 6.6a indicates that the pressure is consistently lower on the inboard section of the endplate ($-1.85 < x/c < -0.85$, $y/c < 1.57$) in comparison to the pressure outboard of the endplate ($-1.85 < x/c < -0.85$, $y/c > 1.6$) for the isolated wing case. For the combined wing and wheel (Figure 6.6e), this pressure difference varies along the length of the endplate such that at the front of the endplate ($-1.85 < x/c < -1.1$, $y/c=1.6$) it is determined by the suction beneath the wing while at the rear ($-1.1 < x/c < -0.85$, $y/c=1.6$), the pressure rise created forward of the wheel causes the pressure variation to be in the opposite direction. It is expected then that this inconsistent variation along the length of the endplate would be the cause for the vortex that sheds from the bottom edge of the endplate to be less coherent in the presence of the wheels.

Another variation observed was the relationship between the main and secondary vortices strengths. In the presence of the wheel, the upper vortex is three times stronger than that of the main wing vortex (Figure 6.5e, f) and more than three times the strength of the same vortex for the isolated wing case (Figure 6.5a, b). Like the main wing vortex, the secondary vortex forms due to the pressure variation obtained at the top of the endplate. The pressure variation for the combined wing and wheel (Figure 6.6f) case increases due to the presence of the stagnation region formed at the most upstream location of the wheel

($x/c=0.45$, $y/c=1.3$). This stagnation region for the combined wing and wheel is unaffected by the presence of the wing (Figure 6.6f) and continues to produce large cross flow components (Figure 6.5e) equal to that obtained for the isolated case (Figure 6.5c). Therefore, when combining the wing and the wheel, the crossflow produced by the wheel interacts with the upper edge of the endplate to shed a stronger secondary vortex. Total pressure planes located at $x/c=0.75$ and $x/c=3$ indicate that the secondary vortex passes the outer side of the wheel cleanly (Figure 6.7e $y/c=1.65$, $z/c=0.85$) and is then entrained into the upper wheel wake (Figure 6.7f $y/c=1.65$, $z/c=0.85$). The increased strength of the secondary vortex also appears to allow this vortex to travel further downstream than that which is achieved by the same vortex for the isolated wing (Figure 6.7a, b).

Total pressure contours plotted on planes located downstream from the wheel centre also indicate that the upper wheel wake becomes lower and wider for this wing and wheel interaction (Figure 6.7e) relative to the wake belonging to the same isolated wheel pair (Figure 6.7c). These variations in the wake structure indicate that the separation point from the upper wheel tread is positioned more rearward due to the presence of the wing. Despite the rearward shift in the separation point, no variation in lift and drag was obtained for the wheel due to the presence of the wing for this interaction which should be expected when considering the results presented during the investigation of the wake structure of an isolated wheel (Section 5.1.1). Therefore, a second phenomenon is expected to be acting on the wheel to also reduce the lift and drag. When comparing the static pressures forward of the wheel with a wing present and also for an isolated pair (Figure 6.6c, d, e and f) it is apparent that the suction of the wing also acts on the wheel reducing the static pressure experienced by the most upstream portion of the wheel tread and near the contact patch. This variation is likely to be reducing the lift and drag of the wheel and counter balancing the lift and drag increase expected by the delayed separation from the upper wheel tread. For this reason no variation is observed for the forces experienced by the wheel due to the presence of the wing for this configuration. As the lower wheel wake propagates further downstream to the $x/c=3$ plane, the wheel wake produced by the combined wing and wheel (Figure 6.7f) appears to become more asymmetric and travels closer towards the symmetry plane relative to that which is experienced by the isolated wheel pair (Figure 6.7d). Additionally, the stagnation point forward of the wheel was determined to be located approximately $0.1c$ further outboard which was also observed during the experimental results obtained and included as Appendix C.

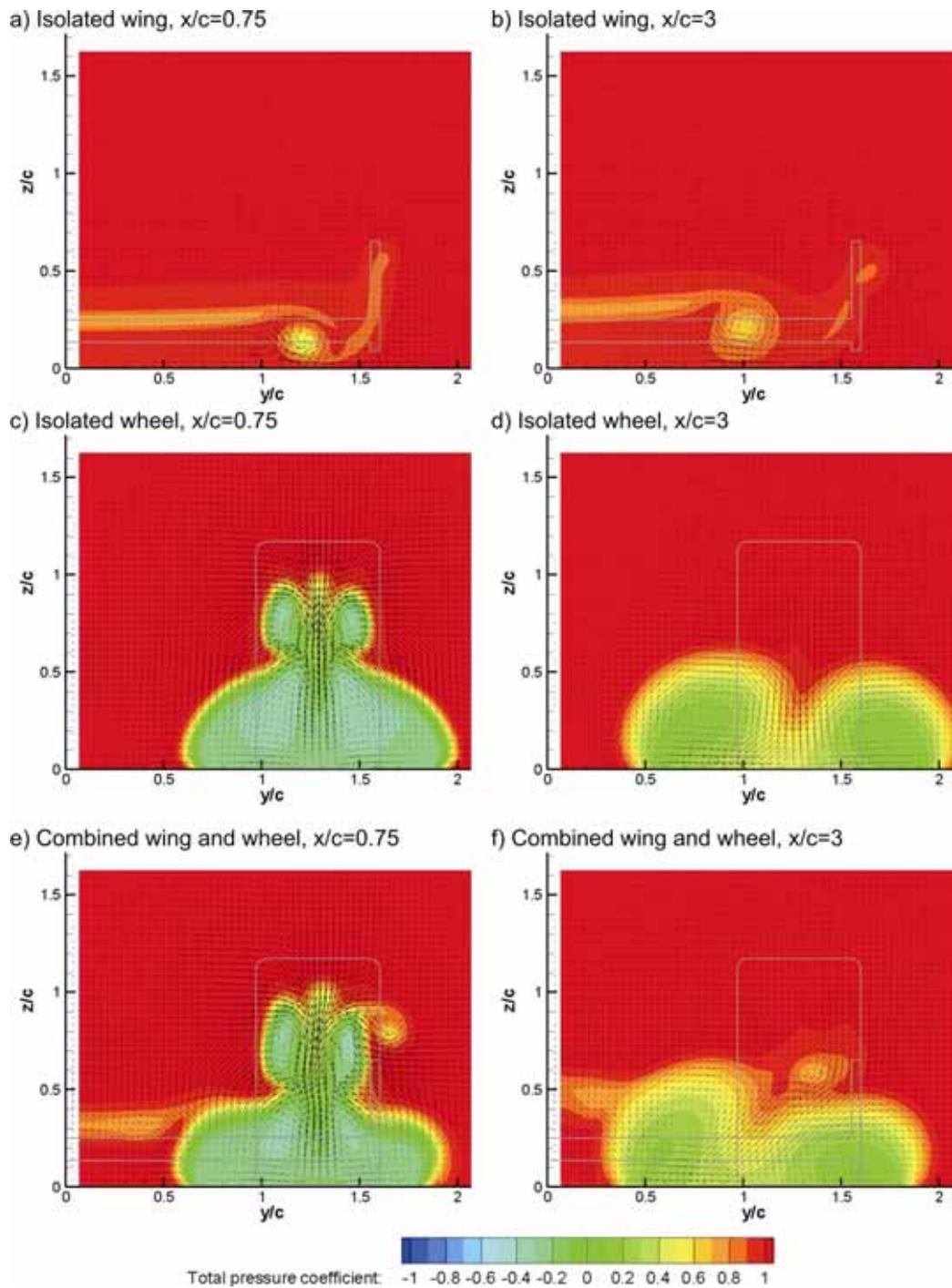


Figure 6.7 Vectors and Total Pressure on x-planes for a wing and/or wheel with $W/c=0.63$, $T/c=1.6$, $h/c=0.13$, $S/c=1.6c$ and $AOA=0^\circ$

The cause for the wheel wake travelling closer to the symmetry plane and being asymmetric is believed to be due to the increased inboard component created by the

inclusion of the wing ahead of the wheel. This is evident when comparing the vectors located in front of the wheel on the $x/c=-0.63$ plane for the isolated wheel and the combined wing and wheel (Figure 6.5c, e). The increased cross flow experienced by the inboard section of the wheel is expected to increase the separation experienced along the inner face and therefore increase the strength of the vortex that forms rearward of the wheel as a consequence of this separation. As a result the inner wheel vortex is now larger than the outer wheel vortex, and subsequently draws the outer wheel vortex inboard as they both travel downstream. The lower wheel wake was determined to be between $0.1c$ and $0.2c$ closer to the symmetry plane on the $x/c=0.75$ and $x/c=3$ planes respectively (Figure 6.7e, f) as a result of the addition of the wing with this configuration.

6.1.2. Causes and consequences of main wing vortex travelling inboard while secondary vortex travels outboard of wheel

Increasing the wing angle of attack from 0° to 12° , while maintaining the remaining wing and wheel parameters, caused the main wing vortex to travel inboard of the wheel while the secondary vortex remained outboard of the wheel (Figure 6.8f). As expected for the corresponding isolated wing case, the 12° increase in angle of attack of the wing has increased the suction beneath the wing (Figure 6.9a) and subsequently the strength of the main wing vortex and the flow entrainment generated towards the symmetry plane downstream of the wing (Figure 6.8a,b). Comparing the main wing vortex size and position for the isolated wing case with an angle of attack of 0° (Figure 6.5b) to that of the 12° case (Figure 6.8b) demonstrates that the vortex is now almost twice the strength and that the vortex centre has moved from $y/c=1.5$ to $y/c=1.35$ at the $x/c=-0.63$ plane, and $y/c=1.35$ to $y/c=1.2$ for the $x/c=0$ plane. In the presence of the wheel, a similar suction increase has been obtained beneath the wing (Figure 6.9c) in comparison to the 0° case and this has caused a similar inboard shift for the vortex position on the $x/c=-0.63$ planes (Figure 6.8e). The variation in position of the main wing vortex, relative to the peak pressure region created forward of the contact patch is expected to be the main cause for the main wing vortex to be travelling inboard of the wheel. In order for the vortex to take this path, the main wing vortex is required to be drawn across the face of the wheel and when comparing the vortex shape on the $x/c=0$ plane downstream of the wing in isolation to that of the wing in the presence of the wheel, it appears that the main wing vortex structure is affected as a result. It is believed that this is due to the vortex being trapped between the

converging ground and wheel surfaces and is subsequently “squashed”. The accuracy of this conclusion will be investigated further in a proceeding section investigating the effect that the wheel has on the downforce loss phenomenon (Section 6.4).

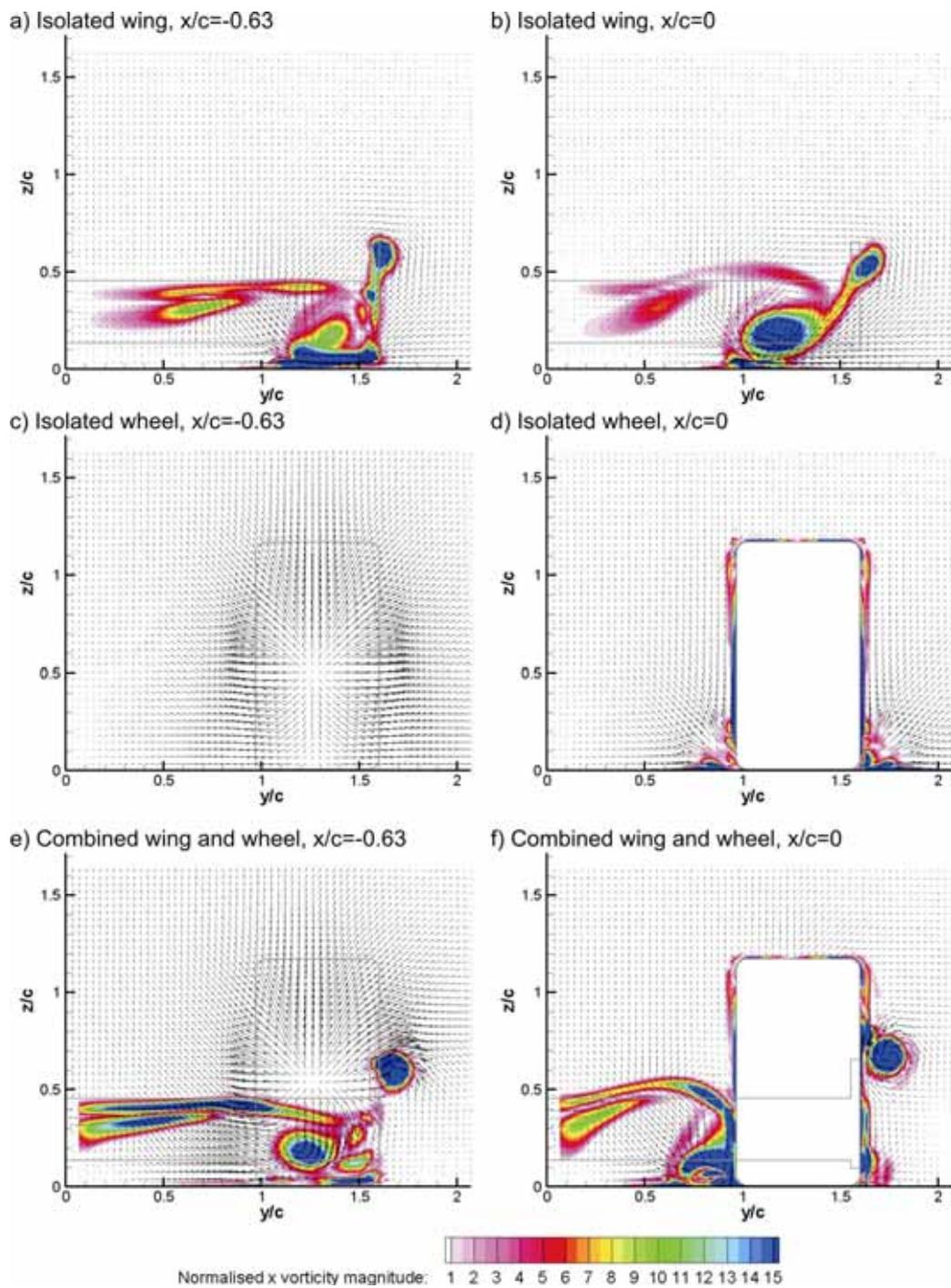


Figure 6.8 Vectors and Vorticity on x-planes for a wing and/or wheel with $W/c=0.63$, $T/c=1.6$, $h/c=0.13$, $S/c=1.6c$ and $AOA=12^\circ$,

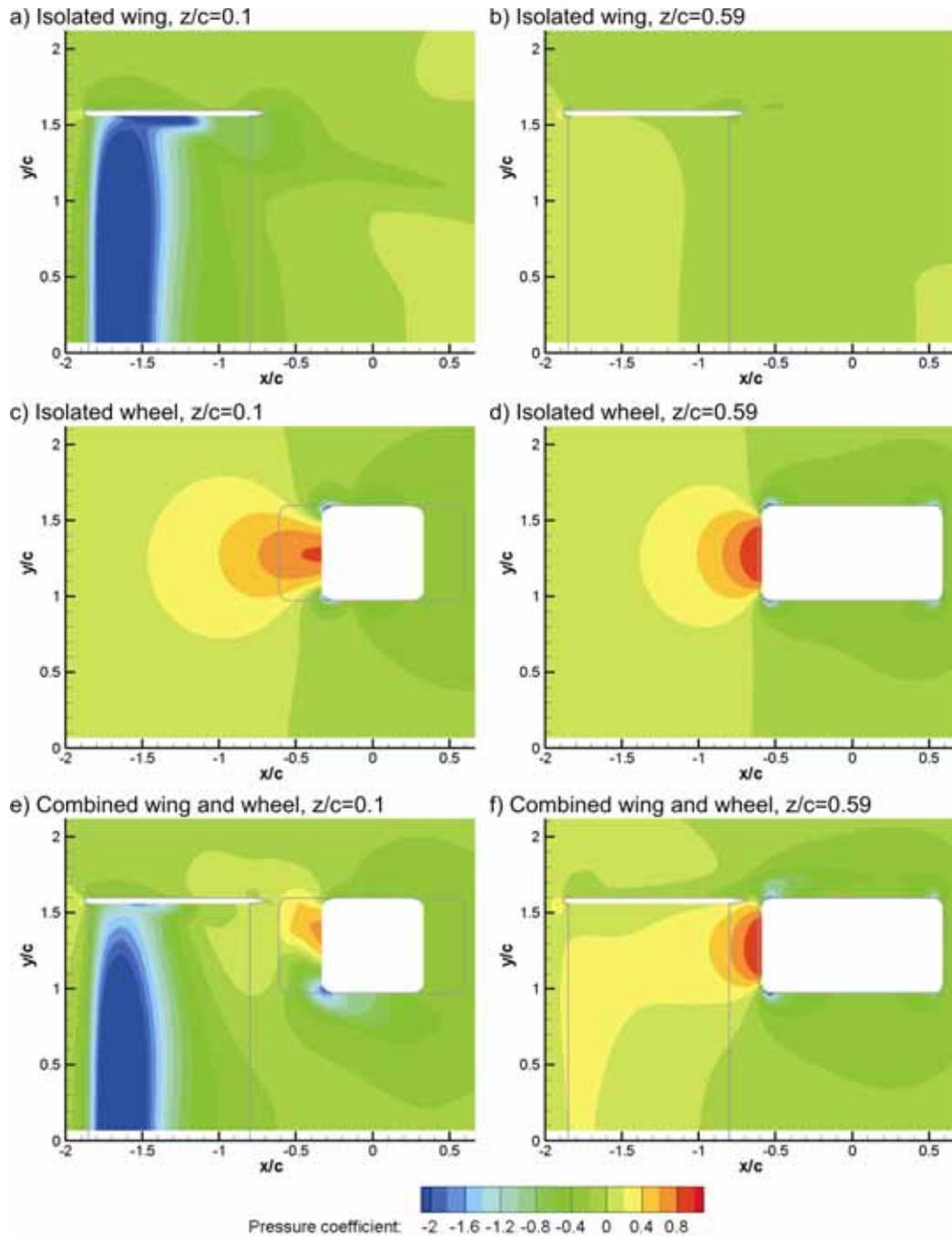


Figure 6.9 Pressure coefficients around endplate on z-planes for a wing and/or wheel with $W/c=0.63$, $T/c=1.6$, $h/c=0.13$, $S/c=1.6c$ and $AOA=0^\circ$

On the more upstream plane of $x/c=-0.63$, the main wing vortex for the isolated wing (Figure 6.8a) appears to be less coherent than that which was obtained for the combined wing and wheel (Figure 6.8e). The main wing vortex shape obtained for the isolated wing

appears to be “bursting” as previously described by Zerihan (2001) suggesting that in this configuration, the wing is beneath the height at which the maximum downforce can be obtained. In the presence of the wheel, the wing was determined to be producing 12% less downforce and the vortex structure suggests that the wing is able to operate closer to the ground without reducing the downforce that it may produce. A similar trend was observed during a previous investigation relating to the effect that varying the span has on the downforce loss phenomenon. The shorter aspect ratio wing produced less downforce and subsequently suffered from a less severe adverse pressure gradient in the centre of the wing. This was determined to be partly the reason why a shorter span wing could operate closer to the ground before suffering from the downforce loss phenomenon than that which a larger span wing was able to. Comparing the suction generated by the wing in isolation (Figure 6.9a, $x/c=0.4$, $0 < y/c < 1.5$) and in the presence of a wheel (Figure 6.9b) provides an initial indication that the same phenomenon may be occurring here. Therefore the effect that a wing and wheel interaction has on the downforce loss phenomenon will also be investigated in greater detail in Section 6.4.

The cause for the 12% reduction in downforce obtained for this wing in the presence of the wheel appears to be for the same reason as that described for interaction “a”. The low pressure region beneath the wing has been adversely affected by the high pressure region generated forward of the wheel with the only variation in this interaction being the extent at which the high pressure region forward of the wheel is affected by the suction generated beneath the wing. This more significant reduction in pressure beneath the front of the wheel may be due to the main wing vortex passing through this region and also be a contributing factor to the 26% reduction in lift obtained by the wheel in this configuration. Unlike interaction “a”, the reduction in the high pressure region forward of the wheel (Figure 6.9e) has ensured that the static pressure remains less inboard of the endplate ($-1.85 < x/c < -0.85$, $y/c < 1.57$) in comparison to that experienced outboard along the entire endplate length ($-1.85 < x/c < -0.85$, $y/c < 1.57$) allowing a more coherent vortex structure to form. Additionally, the location of the maximum pressure forward of the wheel has shifted from $y/c=1.25$ for the isolated wheel pair to $y/c=1.4$ for the combined wing and wheel. This is also additional evidence that the flow entrainment towards the symmetry plane downstream of the wing has increased with this interaction in comparison to interaction “a”.

Another aspect of interaction “b” that is quite similar to interaction “a” is the size and strength of the secondary wing vortex ($y/c=1.7$, $z/c=0.6$ in Figure 6.5e and Figure 6.8e). In both interactions, the secondary vortices are of equal strength, size, position and are rotating in the same direction as the main wing vortex. This is despite the isolated wing with an angle of attack of 12° (Figure 6.8a) having a secondary vortex twice the strength of that obtained for the isolated wing with an angle of attack of 0° (Figure 6.5a). The variation in the secondary vortex in the isolated condition is due to the pressure increase obtained on the top surface of the wing when the angle of attack is increased. The increase in pressure along the inner edge of the endplate that leads to the stronger vortex is evident when comparing Figure 6.9b to Figure 6.6b. The angle of attack appears to have little influence on the secondary vortex when the same two wings are operating with the wheel. This is because the pressure increase provided by the stagnation point at the most upstream location of the wheel is greater than that which may be obtained by increasing the angle of attack.

Total pressure contour plots downstream indicate that the secondary vortex maintains the same position for interaction “b” (Figure 6.10e,f) as it did for interaction “a” (Figure 6.7e,f). The most significant variation in the wake structure of this configuration of combined wing and wheel, in comparison to that of the isolated wheel, was determined to be an increase in height and reduction in width. This change in the combined wing and wheel wake is completely the opposite of that obtained for interaction “a” where the wheel wake became slightly lower and broader. It is suspected that the cause of this variation in the wake is due to the increase in front wing angle causing the upwash seen by the wheel to increase and subsequently the separation point shifting further forward than that which is obtained for the isolated wheel. Velocity vectors located above the wheel on the $x/c=0$ plane for the combined wing and wheel (Figure 6.8f) have a positive z velocity component four times greater than that obtained for the same isolated wheel pair (Figure 6.8d) confirming that the wheel in the presence of the wing does have a separation point further forward. The 0.2c increase in wake height and the 28% reduction in drag for the combined wing and wheel over the isolated wheel at the $x/c=0.75$ plane is again consistent with the previous isolated wheel investigation linking the drag to the separation point. It is also expected that the variation in the separation point would also be a significant contribution to the 45% reduction in lift also obtained and that the effect that the vortex passing beneath the forward portion of the wheel would not be solely responsible for this variation.

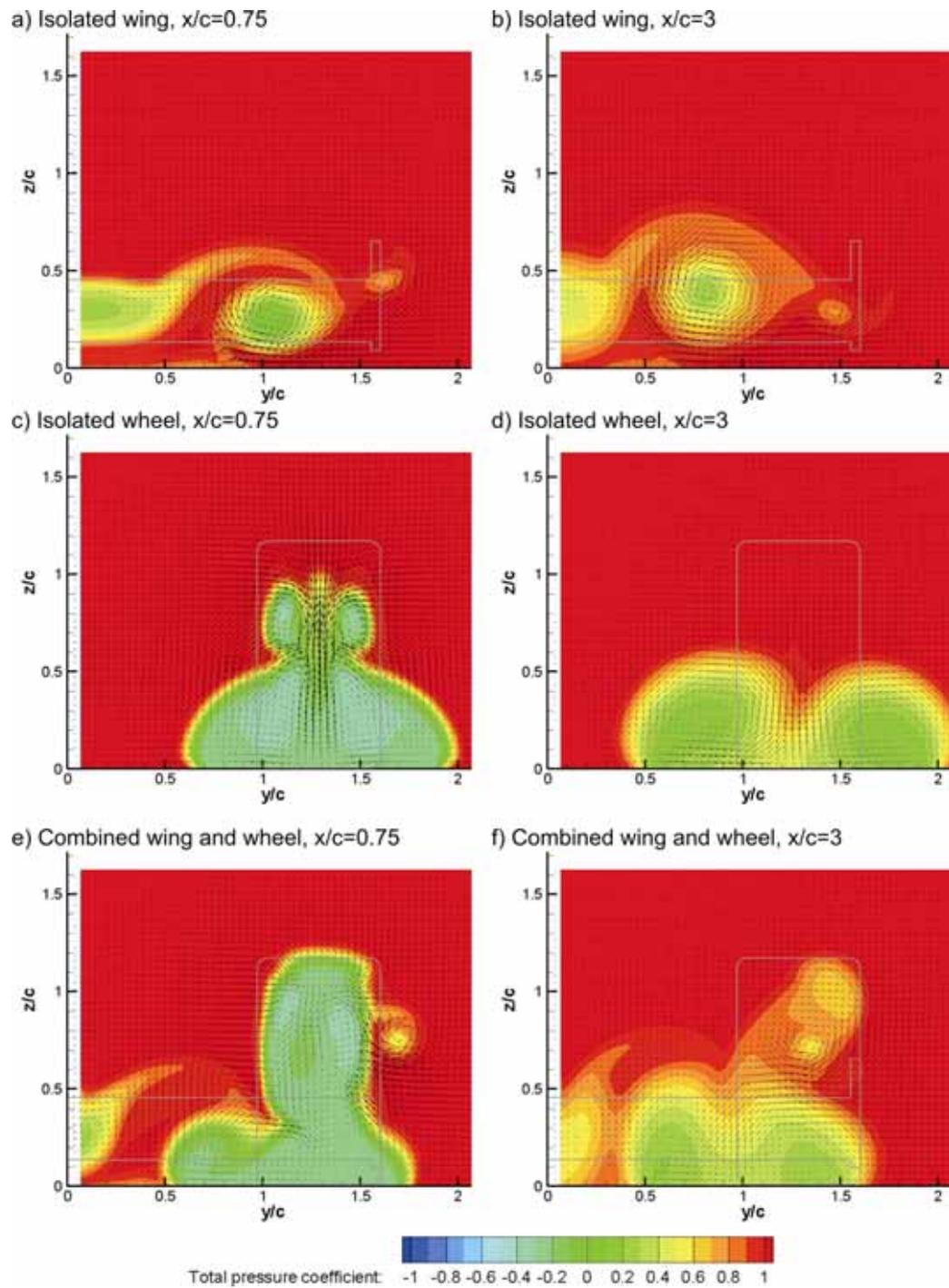


Figure 6.10 Vectors and Vorticity on x-planes for a wing and/or wheel with $W/c=0.63$, $T/c=1.6$, $h/c=0.13$, $S/c=1.6c$ and $AOA=12^\circ$,

Also consistent with the previous investigation, the wheel wake on the $x/c=3$ plane is reduced from a width of $1.7c$ for the isolated wheel (Figure 6.10d) to a width of $1.1c$ for the

combined wing and wheel (Figure 6.10f). Despite the reduction in the wheel wake width, the most inner position of the lower wheel wake is still positioned approximately $0.1c$ further inboard on the $x/c=0.75$ and the $x/c=3$ planes in comparison to the isolated wheel pair. This is likely to be once again due to the flow entrainment obtained towards the symmetry plane as was discussed for interaction “a”. It should also be noted that the main wing vortex is not evident downstream of the wheel as it is expected to have combined with the inner primary wheel vortex. This may also be a contributing factor as to why the wheel wake has moved further inboard.

6.1.3. Causes and consequences of both wing vortices travelling inboard of wheel

Reducing the span from $1.6c$ to $0.97c$ from the previously discussed interaction “b”, such that the outer endplate aligns with the inner face of the wheel, allowed both the main and secondary vortices to travel inboard of the wheel (Figure 6.11e, f). One unique feature of this interaction in comparison to the previously discussed interactions “a” and “b” is the direction of rotation of the secondary vortex. In the previously discussed interactions, and for all the isolated wing results, the secondary vortex has always rotated in the same direction as the main wing vortex. For this interaction, the secondary vortex (Figure 6.11f, $y/c=0.88$, $z/c=0.6$) is rotating in the opposite direction of the main wing vortex (Figure 6.11f $y/c=0.5$, $z/c=0.2$). Both interaction “a” and “b” demonstrated that the pressure rise provided by the stagnation region at the most upstream position of the wheel (Figure 6.6f and Figure 6.9f) was responsible for an increase in the pressure differential about the top edge of the endplate and as a result the secondary vortex in these two interactions was always stronger than the same vortex for the corresponding isolated wings. Considering static pressures on the $z/c=0.59$ plane for the combined wing and wheel (Figure 6.12f) indicate that the same mechanism is responsible for the variation in the vortex rotation. At this span, the endplate sits inboard of the high pressure region created by the stagnation at the most upstream location of the wheel and therefore the pressure is now greater outboard of the endplate than inboard. Vectors located on the $x/c=-0.63$ plane also confirm that the new endplate position relative to the wheel stagnation is the likely cause for the variation in the rotation with the crossflow component created by the stagnation region acting on the upper edge of the endplate (Figure 6.11e) being in the opposite direction of that seen in the previous interactions (Figure 6.5 and Figure 6.8f). The variation in the secondary wing vortex also appears to contribute with increasing the static pressure experienced by the

top surface of the wing in the presence of the wheel pair (Figure 6.12f) and this may be contributing to the 10% increase in downforce obtained by the wing in this configuration.

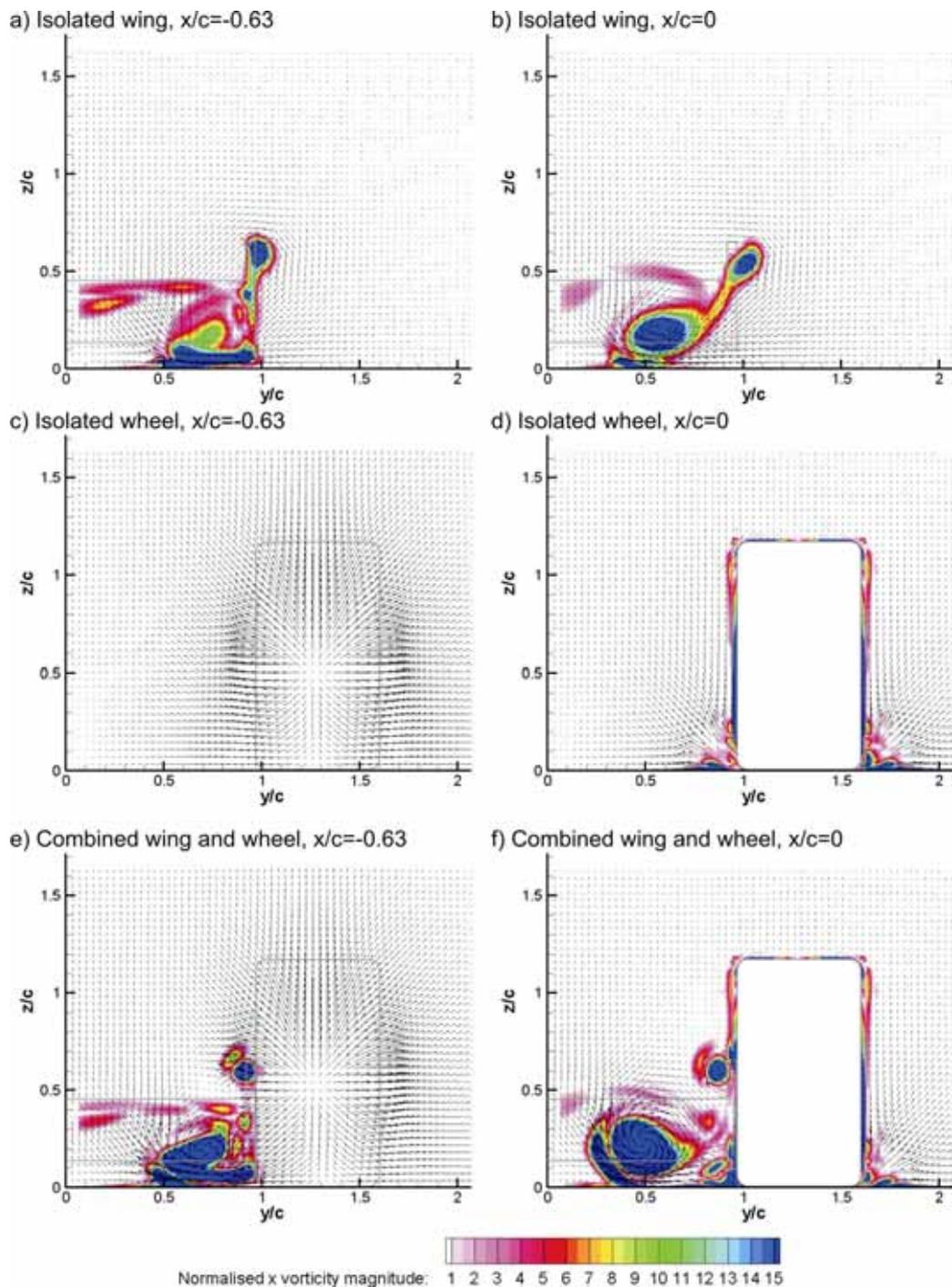


Figure 6.11 Vectors and Vorticity on x-planes for a wing and/or wheel with $W/c=0.63$, $T/c=1.6$, $h/c=0.13$, $S/c=0.97c$ and $AOA=12^\circ$,

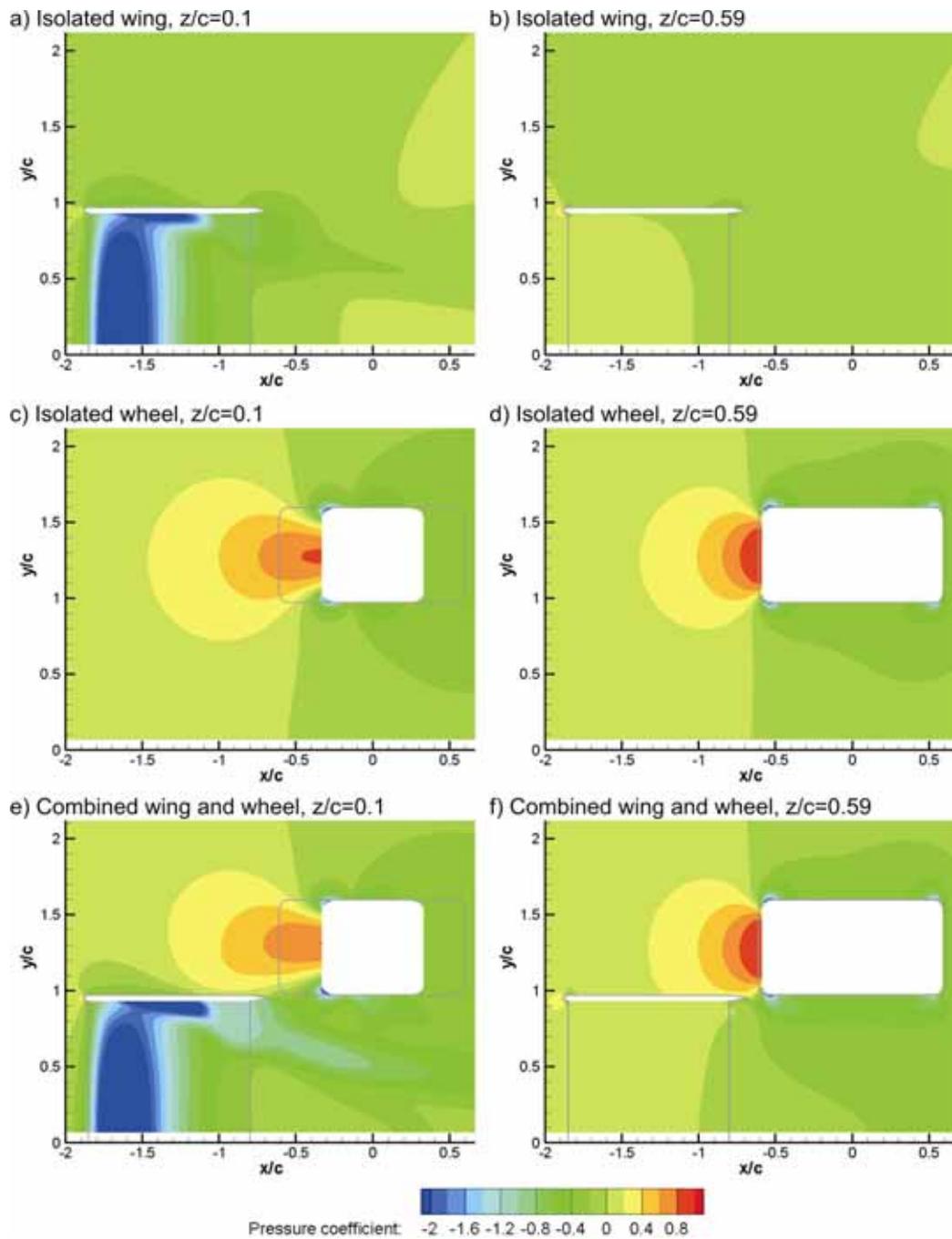


Figure 6.12 Pressure coefficients around endplate on z-planes for a wing and/or wheel with $W/c=0.63$, $T/c=1.6$, $h/c=0.13$, $S/c=1.6c$ and $AOA=0^\circ$

The increase in front wing downforce has again coincided with a consistent variation in size and strength of the main wing vortex as seen before (Zerihan, 2001). While for interaction “a” and “b” the main wing vortex in each case was reduced in strength by the

presence of the high pressure region created at the front contact patch, interaction “c” experiences an increase in main wing vortex strength ($y/c=0.5$, $z/c=0.2$, Figure 6.11f) over the same wing in isolation ($y/c=0.5$, $z/c=0.2$, Figure 6.11b) due to the same flow feature ($x/c=-0.4$, $y/c=1.3$, Figure 6.12e). For the previous interactions, the high pressure region acted on the bottom surface of the wing reducing the ability of the wing to create low pressure (Figure 6.6e and Figure 6.9e). At this wing span, the high pressure assists with increasing the pressure difference on the bottom edge of the endplate and subsequently provides an increased pressure differential along the bottom edge of the endplate ($-1.85 < x/c < -0.85$, $y/c=0.95$, Figure 6.12e) increasing the inboard y velocity component of the flow beneath the endplate ($y/c=0.95$, $z/c=0.05$, Figure 6.11e) and subsequently creating a stronger vortex ($y/c=0.5$, $z/c=0.2$, Figure 6.11f).

Consistent with Zerihan’s experimental investigation (2001), the previously conducted span investigation for an isolated wing demonstrated that the main wing vortex can also assist with reducing the separation experienced by the wing. Therefore in this interaction it would be expected that the increased vortex size and strength would be coupled with a reduction in separation for the wing. Total pressure contours on planes located at $x/c=0.75$ confirm that the separation experienced by the wing ($y/c=0.1$, $z/c=0.5$, Figure 6.13a) has been reduced in the presence of the wheel pair ($y/c=0.1$, $z/c=0.5$, Figure 6.13e). It is expected that the reduced separation from the bottom surface of the wing has enabled the flow drawn beneath the wing to increase and for this reason the suction generated by this wing in the presence of the wheel pair ($x/c=-1.6$, $0 < y/c < 0.95$, Figure 6.12e) is greater than that experienced by the same wing in isolation ($x/c=-1.6$, $0 < y/c < 0.95$, Figure 6.12a). This is also likely to be a contributing factor to the 10% increase in downforce for the wing while the increased vortex strength would be expected to contribute to the 22% increase in drag obtained for the wing in the presence of the wheel pair.

Unlike the previously discussed wing and wheel interactions, the main wing vortex continues downstream of the wheel without combining with the wheel wake structure and is clearly defined on the $x/c=0.75$ ($y/c=0.4$, $z/c=0.3$, Figure 6.13e) and $x/c=3$ ($y/c=0.4$, $z/c=0.4$, Figure 6.13f) planes. Including the main wing vortex, six individual vortices are evident on the $x/c=0.75$ plane (Figure 6.13e). These also include: the two main wheel vortices ($y/c=1.15$, $z/c=0.2$ and $y/c=1.35$, $z/c=0.45$); the two upper wheel vortices ($y/c=1.1$, $z/c=0.8$ and $y/c=1.4$, $z/c=0.8$); and the decaying secondary wing vortex ($y/c=0.95$, $z/c=0.6$).

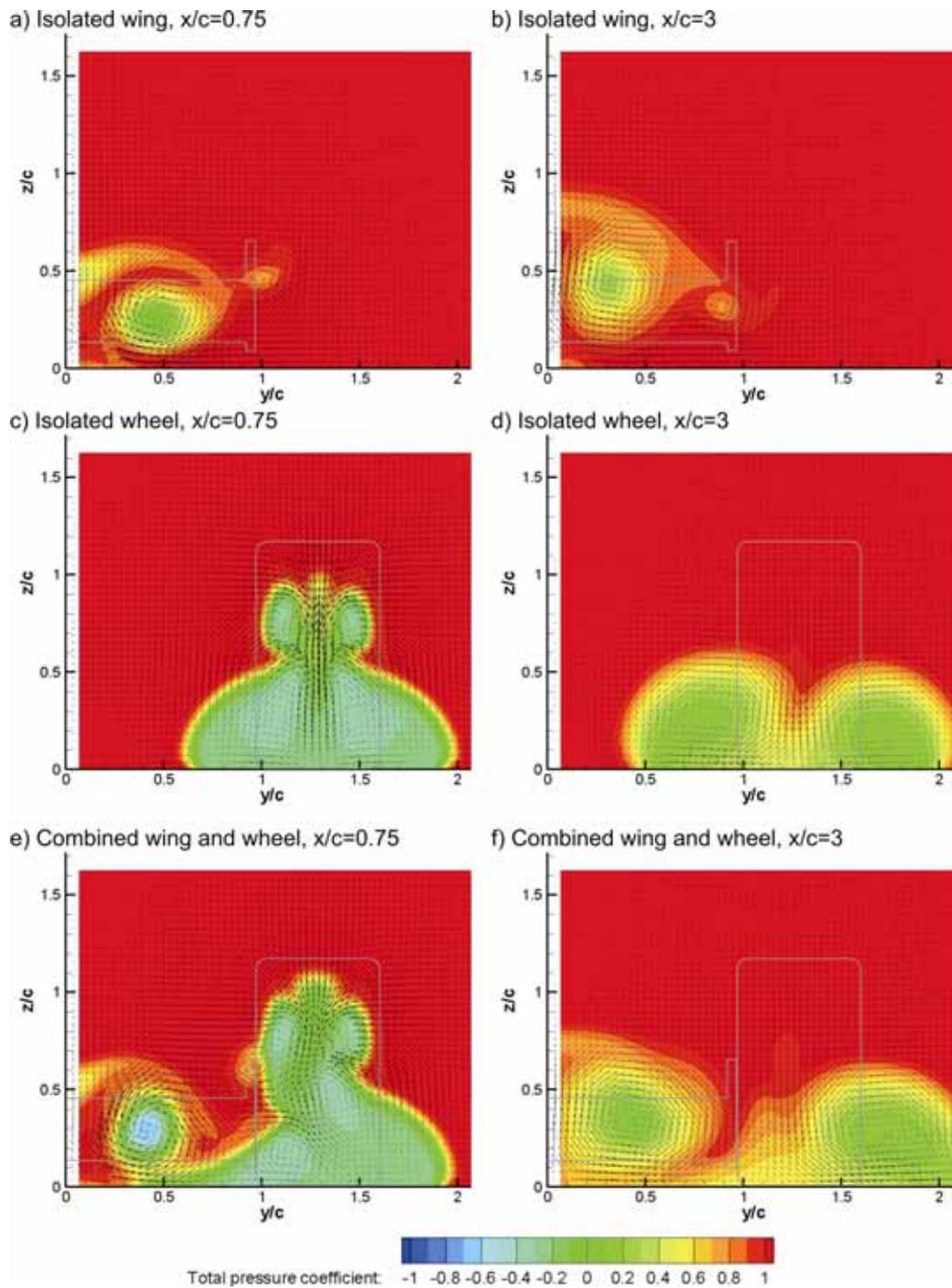


Figure 6.13 Vectors and Vorticity on x-planes for a wing and/or wheel with $W/c=0.63$, $T/c=1.6$, $h/c=0.13$, $S/c=0.97c$ and $AOA=12^\circ$,

By the $x/c=3$ plane (Figure 6.13f) only the main wing vortex ($y/c=0.5$, $z/c=0.4$) and outer primary wheel vortex remain ($y/c=1.7$, $z/c=0.3$). While the subsequent wake structure

resembles that of the isolated wheel (Figure 6.13d), but with the vortex centres approximately one chord further apart, it must be noted that a significant variation exists in that the inner wheel vortex has decayed further upstream and therefore the two remaining vortices at this plane are not from the same source as that of the isolated wheel pair. The inner wheel vortex strength has been reduced and subsequently decays prior to reaching the $x/c=3$ plane as a result of the interaction with the wing. It is possible that the main wing vortex has reduced the separation experienced by the wheel and this has caused the inner wheel vortex to have a reduced strength, but this will have to be confirmed in a proceeding investigation.

An additional variation observed for the wheel wake of the combined wing and wheel is the more inboard location and increased height of the upper wheel wake on the $x/c=0.75$ plane (Figure 6.13e) relative to that experienced by the isolated wheel pair (Figure 6.13c). As stated previously the higher position is likely to be due to a more forward separation point from the wheel tread as experienced by interaction “b” and can again be linked to the 25% lift reduction experienced by the wheel over that for the isolated case. The $0.05c$ inboard shift of the upper wheel wake may be explained by the position and rotation of the secondary wing vortex, but this will also have to be further investigated.

With the results discussed up until this point, it appears that the angle of attack can control the transition from interaction “a” to “b” and that from either interaction, adjusting the span will lead to achieving interaction “c”. At which point the transition will occur is unclear and will therefore be investigated further in the proceeding sections (6.2 to 6.5).

6.2. Variations in Interaction due to Wing Angle of Attack

Two major variations have been identified in the flow structures associated with interaction “a” and “b” which include the path that the main wing vortex takes around the wheel and the subsequent shape of the combined wing and wheel wake. It has also been demonstrated depending on the interaction state, either an increase or decrease in lift and drag can be experienced by the wing and wheel relative to the same bodies in isolation. It was therefore decided to further investigate the effect that the wing angle of attack has on a combined wing and wheel in greater detail to obtain a better understanding of not only the differences of interaction “a” and “b”, but also the transition between these two states.

This investigation was also extended to include the effect that the angle of attack may have on interaction “c”, achieved when the span of the wing is reduced to be inline with the inner face of the wheel. This was undertaken by obtaining results for wings with variations in angle in the range of 0° to 12 ° for a span of 1.6c and 0.97c in the presence of a wheel pair and in isolation. The wheel configuration used for this study is identical to that used previously to outline the three different interaction states ($W/c=0.63$, $T/c=1.6$). Similarly the wing height was also maintained from the previous investigation ($h/c=0.13$).

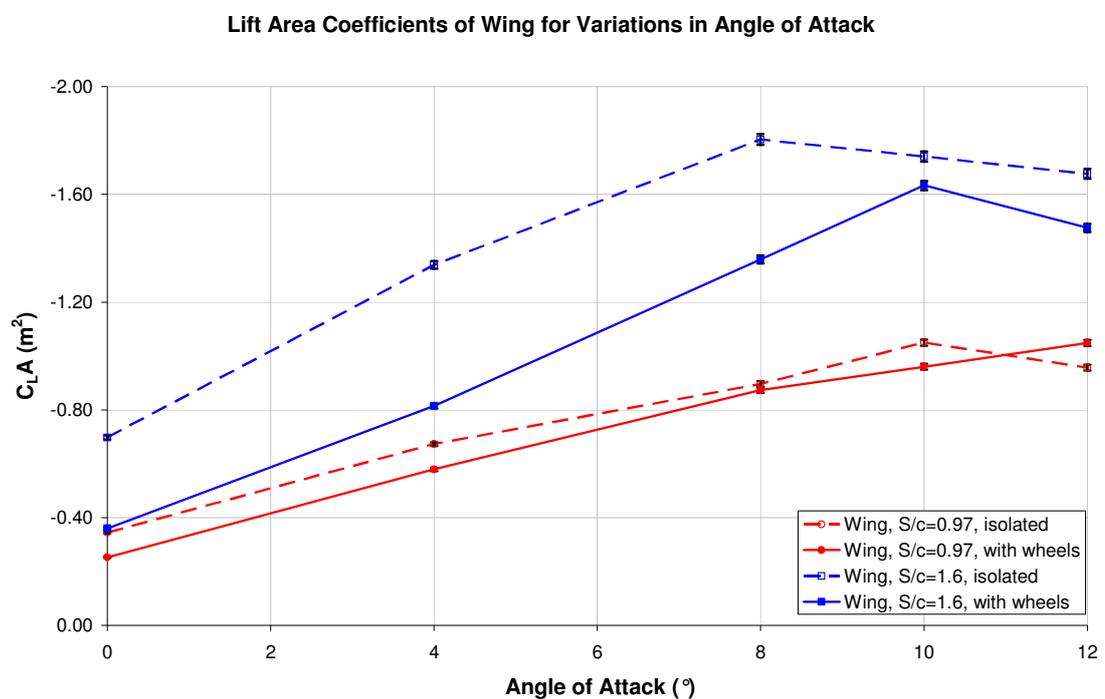


Figure 6.14 Wing lift results for variations in angle of attack for an isolated wing ($h/c=0.13$) and also in the presence of a wheel pair ($W/c=0.63$, $T/c=1.6$)

Figure 6.14 outlines the lift coefficient area obtained for the wings in isolation (dashed lines) and in the presence of a pair of wheels (solid lines) for two span values of $S/c=0.97$ (red) and $S/c=1.6c$ (blue). For the isolated wing with the larger span, it appears that at an angle of attack of 8° the wing stalls while in the presence of the wheel this is delayed to an angle of attack of 10°. Up until the relevant stall angle is reached, the gradient of the lift curve slope for variations in angle of attack are equal for both the isolated wing and for the wing in the presence of the wheel and therefore the lift coefficient variation between these two cases remains at a constant value approximately equal to 0.45m^2 . While the variation

in downforce prior to the isolated wing stalling is consistent, the percentage of downforce lost, as previously quoted by Thisse (2004) and the author, incrementally reduces as the angle of attack is increased and therefore with a span value of $S/c=1.6c$ and an angle of attack of approximately 5° a downforce reduction of approximately 36% would be expected, demonstrating that it is possible to reproduce the condition previously reported by Thisse (2004).

Similar trends were obtained for the $S/c=0.97$ wing as that of the $S/c=1.6$ wing albeit the variation in the downforce coefficient generated by the isolated shorter span wing in comparison to the same wing in the presence of a pair of wheels is only approximately $0.1m^2$. As a result when the isolated wing with $S/c=0.97$ exceeds an angle of attack of 10° , where stall occurs, the downforce produced by the wing in the presence of the pair of wheels exceeds that obtained for the same wing in isolation. Once again the wing in the presence of the wheels experienced a delayed stall; unfortunately it was not possible to determine exactly at which angle stall will occur as it is expected to be an angle greater than the maximum tested here.

The mechanism that causes the wing to stall would be expected to be an increase in separation experienced by the suction surface of the wing due to a more severe adverse pressure gradient as the wing's angle of attack is increased. Therefore, further increases in angle of attack result in increased regions of separation and reductions in the lift that the wing can generate (Smith, 1975). An identical explanation has been provided by Zerihan (2001) for the cause of the downforce loss phenomenon experienced by a downforce producing wing as the height is reduced. One would therefore expect that parallels can be drawn between the results obtained here for the two different span wings in the presence of a wheel pair and in isolation to those obtained during the previously presented study to determine the effect that the span has on the height at which the maximum downforce is achieved. This feature has been shown to be influenced by both the relative size of the vortex in comparison to the wing span as well as the central wing loading and the subsequent adverse pressure gradient experienced by the wing. Both of these features are expected to change when a wing is placed in front of a wheel and one must therefore expect that this will also be responsible for variations in the stall angle seen here. This will be investigated in greater detail for each span configuration to ascertain which of the two possibilities is more likely to be responsible for the variations observed here.

Drag Area Coefficients of Wing for Variations in Aspect Ratio

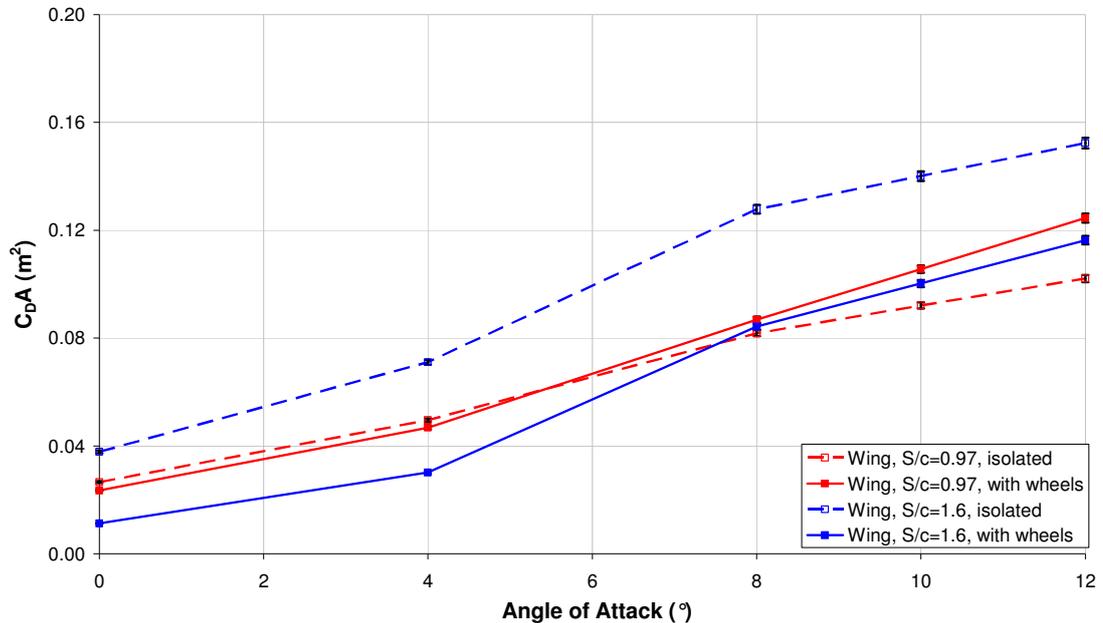


Figure 6.15 Wing drag results for variations in angle of attack for an isolated wing ($h/c=0.13$) and also in the presence of a wheel pair ($W/c=0.63$, $T/c=1.6$)

As expected, the drag of the wing increases as the angle of attack is increased for all the wing configurations tested and for the isolated wing with the shorter span has a smaller drag magnitude than that of the larger span (Figure 6.15). In the presence of the wheel pair, the $S/c=1.6$ wing experiences a consistent drag reduction of 0.04m^2 throughout the angle of attack range tested. It would therefore be expected that the high pressure region formed forward of the wheel's contact patch acting on the bottom surface of the wing would be responsible for this drag reduction as indicated previously (Figure 6.6e and Figure 6.9e). This may also explain why the short span wing experienced no variation in drag up to an angle of attack of 8° given that with this span, the wing does not encroach into any regions where the wheel is expected to produce pressure increases that may act on any of the wing surfaces (Figure 6.12e). Only at angles of attack greater than 8° were drag variations obtained relative to the same wing in isolation with the 12° case, for example, experienced a drag increase of 0.03m^2 relative to the same isolated wing. While the lift forces indicate that at this angle of attack the wing has not stalled in the presence of the wheel, one possible explanation for the increase in drag seen at this angle of attack could be due to an increase in induced drag as this wing configuration has previously

shown to produce a main wing vortex that is stronger in the presence of the wheel than that obtained in isolation (Figure 6.11e, f).

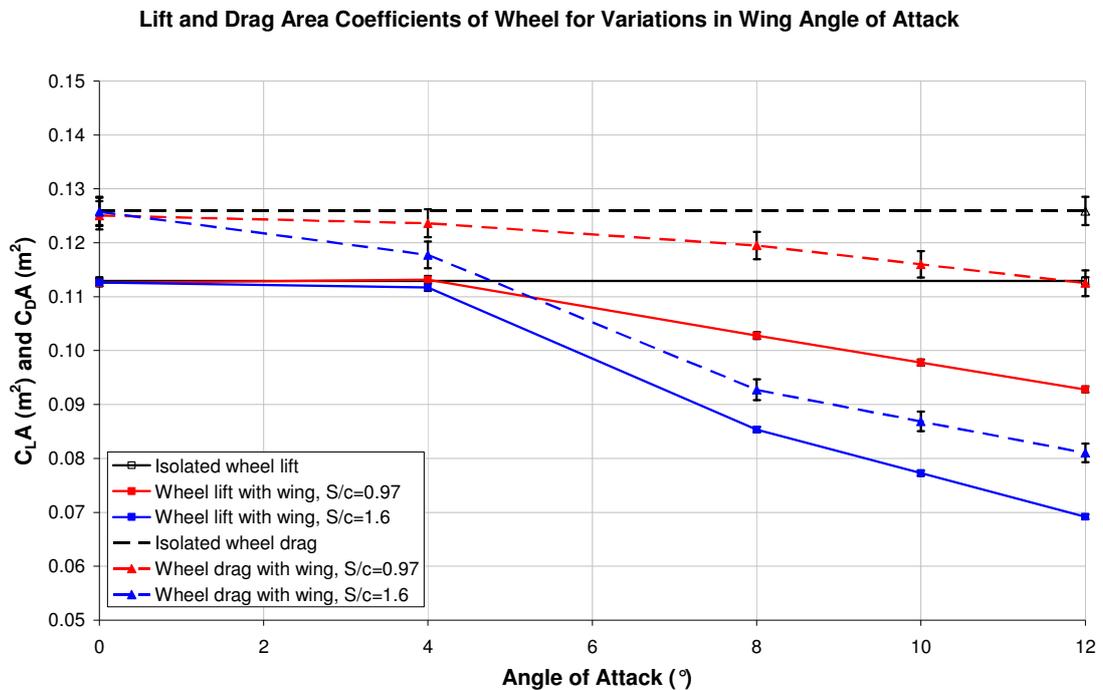


Figure 6.16 Wheel lift and drag results for an isolated wheel pair ($W/c=0.63$, $T/c=1.6$) and also in the presence of a wing ($h/c=0.13$) with varied angle of attack

As indicated by Figure 6.16, variations were also obtained for the wheel lift (solid lines) and drag (dashed lines) as the wing angle of attack was varied for the two different span wings ($S/c=0.97$ in red and $S/c=1.6$ in blue) in comparison to the lift and drag obtained for the isolated wheel (black solid and dashed lines respectively). For all the variations in the wing angle of attack at the two different spans, the lift of the wheel was generally reduced by the presence of the wing. At angles of attack between 0° and 4° , no variations in lift were obtained in comparison to the isolated wheel. As the angle of attack was further increased, the lift reduces linearly up to the maximum reduction obtained at 12° where the wheel in the presence of the $S/c=1.6$ wing experienced a 45% reduction in lift and the wheel in the presence of the $S/c=0.97$ wing obtained an 18% reduction. This suggests that for the $S/c=1.6$ wing, interaction “a” is occurring for an angle of attack of 0° and 4° . This will be confirmed later in this section.

Similar trends were also observed for the variation in the wheel drag. Up to an angle of attack of 4° the drag remains constant for the $S/c=0.97$ wing, while at larger wing angles of attack, the wheel drag begins to reduce linearly to a value 11% less than that experienced by an isolated wheel pair. For the $S/c=1.6$ wing, the drag reduces almost linearly from no variation at a wing angle of attack of 0° to a 28% reduction in wheel drag at a wing angle of attack of 12° when comparing to the drag experienced by an isolated wheel pair.

It should also be noted that both the lift and drag forces for the wheel vary relative to the same wheel pair in isolation in a similar manner to that which was observed previously during the isolated wheel investigations. This would therefore suggest that while there may be additional phenomena affecting the wheel lift and drag, the key phenomenon dictating the variation in the wheel lift and drag in the presence of the wing is likely to be the separation point from the upper wheel tread.

Also of interest is the variation of the side forces experienced by the wheel (Figure 6.17) as this is likely to offer greater insight into the variation of the flow structures around the wheel. Previously it has been observed that placing two wheels adjacent to each other created a side force that pushed the two wheels apart and that this was influenced by the rate at which the flow was accelerated about the inner and outer forward shoulders. This trend also changes when a wing is placed forward of a wheel pair with almost all variations of wing span and angle of attack tested here resulting in a side force acting towards each other with the exception of the $S/c=1.6$ wing at an angle of attack of 0° . This would also suggest that the variation of the side force may be linked to the path that the main wing vortex takes given that it is known that in this configuration the main wing vortex travels outboard of the wheel (interaction "a"). The side force reduces with the wing angle of attack such that at the maximum angle of attack the $S/c=1.6$ and $S=0.97$ wings experience a side force not only opposite, but five and three times greater respectively than that obtained by the isolated wheel pair. In order to confirm that this is the cause for the variation, further analysis will be required for each wing span which will now commence in the proceeding sections.

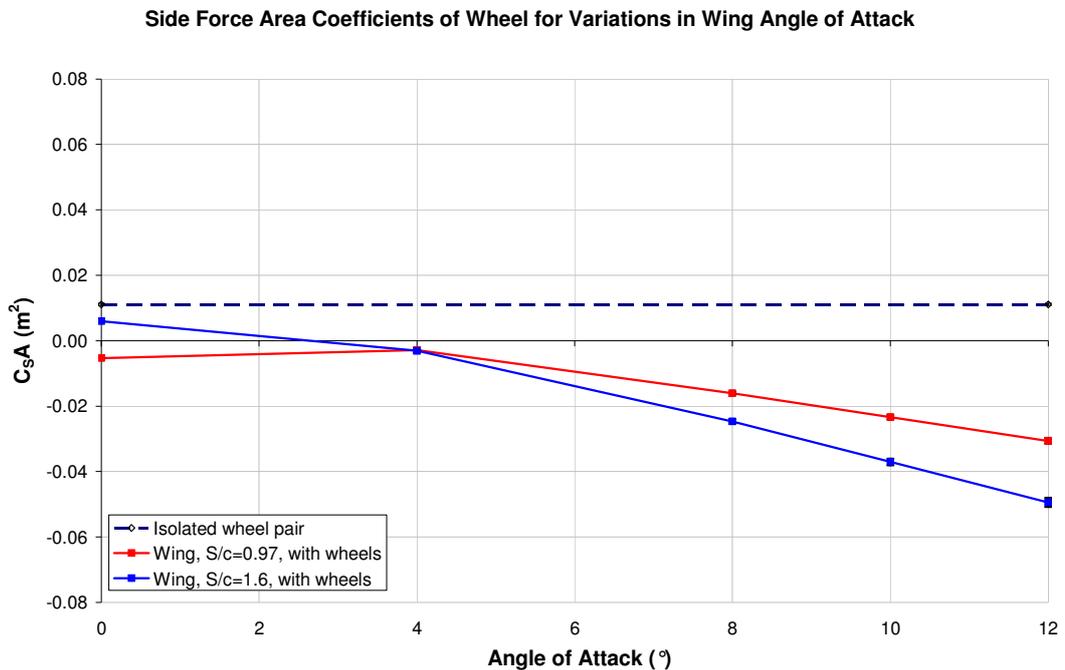


Figure 6.17 Wheel side force results for an isolated wheel pair ($W/c=0.63$, $T/c=1.6$) and also in the presence of a wing ($h/c=0.13$) with varied angle of attack

6.2.1. Adjustments in angle of attack causing transition from interaction “a” to “b”

When considering the lift and drag force coefficients obtained for the wheel in the presence of the $S/c=1.6$ wing (Figure 6.16), two distinct trends emerge that are dependant on the wing angle of attack. For angles of attack of a value of 0° and 4° , the lift and drag offset for the wheel in the presence of the wing remains constant relative to the same wheel in an isolated pair, while at the higher angles of attack tested the lift and drag reduces linearly as the angle of attack is increased. It has already been shown in the preceding section (6.1) that in this span configuration, two different interactions can be obtained dependant on the wing angle of attack and it is therefore likely that the lift and drag coefficients of the wheel are indicating that for angles of attack less than or equal to 4° , interaction “a” is occurring while at 8° , 10° and 12° the interaction “b” is likely to occur. To determine if this hypothesis is correct, vectors and x-vorticity were plotted on an x plane located $-0.63c$ upstream of the wheel centre line (Figure 6.18) to determine on which side of the wheel the main wing vortex passes for four of the angles of attack tested.

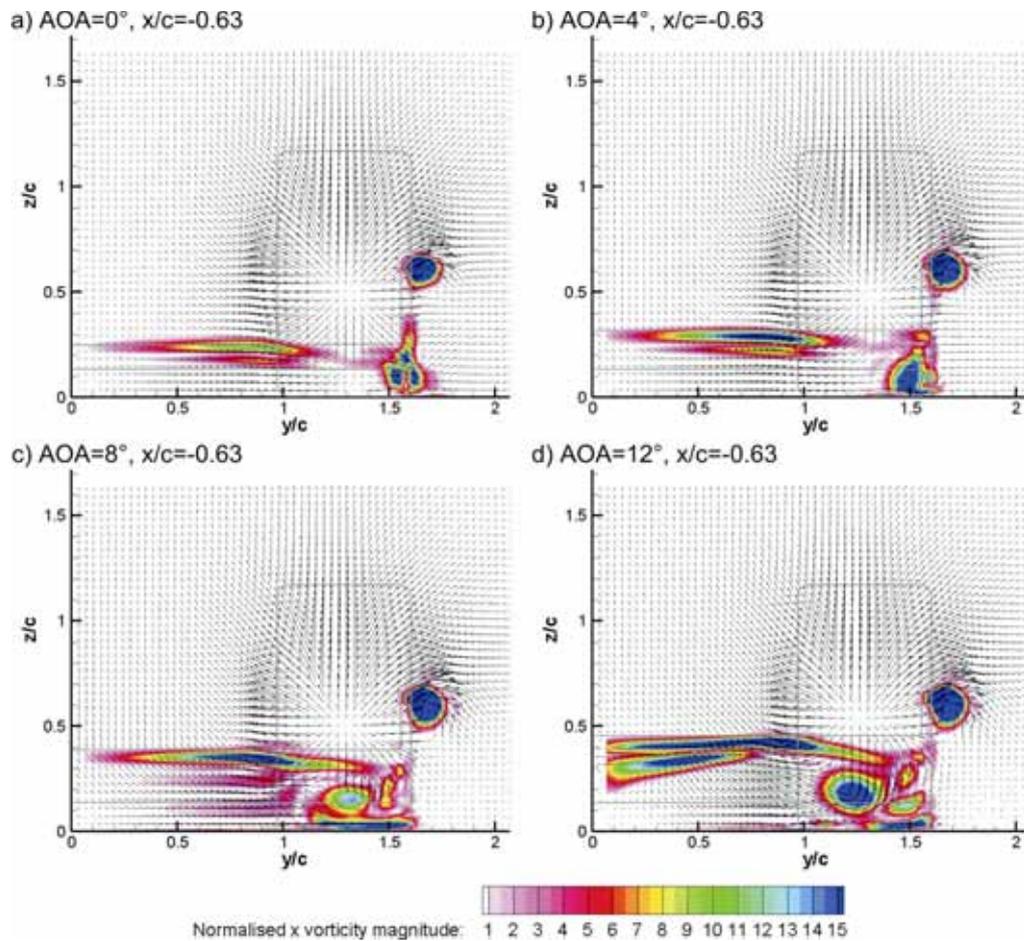


Figure 6.18 Vectors and Vorticity on x-planes for a wing with varied AOA and with a wheel

Doing so confirmed that the 0° and 4° angle of attack allows the wing vortex to travel outboard of the wheel while the angles of attack between 8° and 12° are drawn inboard. While it has been demonstrated previously that the main wing vortex is drawn inboard by the low pressure generated beneath the wing and the subsequent cross flow that this low pressure generates towards the symmetry plane, it was not clear if other angles of attack besides the 12° case tested would be sufficient to generate a cross flow to overcome the large pressures generated forward of the contact patch. This would therefore suggest that other wing parameters could also alter the transition point from interaction “a” to “b”. For example, varying the height of the wing will also be expected to vary the magnitude of the low pressure region generated beneath the wing and should therefore also influence the angle of attack that the switch will occur at between the two states. This will be investigated in section 6.4 where the height of the wing will be varied in order to determine how the downforce loss phenomenon varies in the presence of a wheel pair.

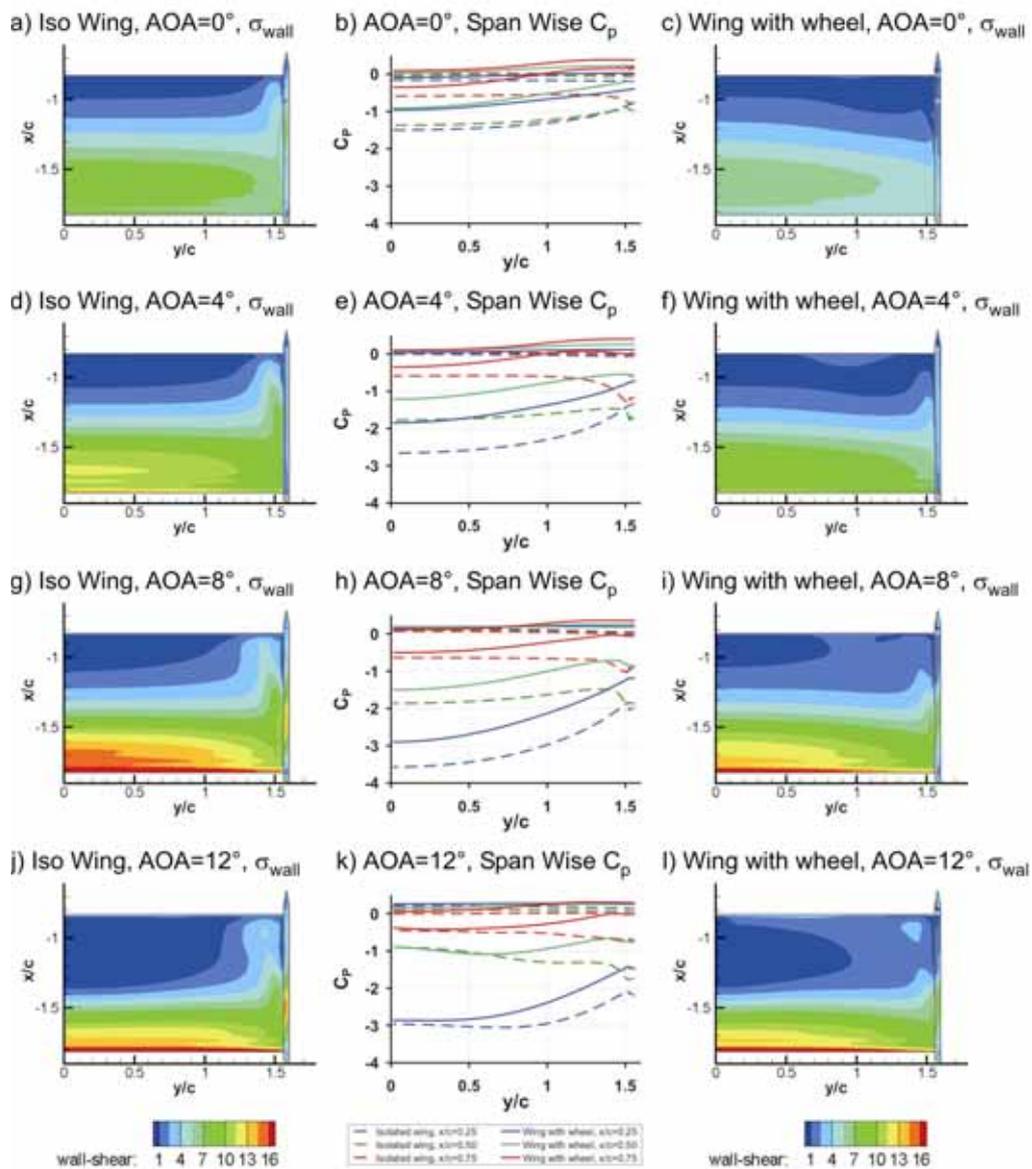


Figure 6.19 Wall shear stress and spanwise pressure distribution for variations in AOA

Another feature observed for the $S/c=1.6$ wing was a delayed angle at which stall occurs relative to the same wing in isolation (Figure 6.14). Two possible explanations exist why this may occur due to the addition of the wheel including either; a reduction in the peak pressure drop obtained beneath the wing; or the main wing vortex may act over a larger portion of the wing's bottom surface. Given that the $S/c=1.6$ wing produces consistently less downforce in the presence of the wheel, the more likely cause would be a reduction in the adverse pressure gradient experienced by the wing. In order to confirm this, spanwise

pressure coefficients and the shear stress experienced by the bottom surface of the wing in isolation and in the presence of a wheel pair were considered at four different angles of attack (Figure 6.19).

When comparing the shear stress experienced by the bottom surface of the wing at an angle of attack of 8° (Figure 6.19g, i) and 12° (Figure 6.19j, l) the general increase in shear stress experienced by the wing confirms that the bottom surface of the wing suffers less from separation in the presence of the wheel than in isolation. The span wise pressure distribution indicates that for angles of attack of 8° and less, the ability of the wing across the whole span to produce suction is adversely affected by the high pressure region generated forward of the wheel (Figure 6.19b,e,h) and not only at the wing tips. This confirms that the cause for the delayed stall for the $S/c=1.6$ wing is due to the less severe pressure gradient experienced in the centre of the wing given that between 0° and 8° the wings bottom surface generates approximately a pressure coefficient magnitude of 1 less suction in the presence of the wheel pair. Additionally, the coefficient of pressure values at the symmetry plane for the $12^\circ S/c=1.6$ wings are equal (Figure 6.19k), suggesting that both wings have exceeded the adverse pressure gradient that the boundary layer may maintain alone. The isolated wing at this angle of attack appears to load the region closer to the tip further than the centre ($y/c=1$) which may be once again evidence that the main wing vortex may prevent separation from occurring over larger portions of the wing while in this configuration.

In order for the main wing vortex to assist with preventing separation from occurring on the bottom surface of the wing in the presence of the wheel, an increase in vortex strength would be required, or the vortex would have to travel further inboard. While it has been shown that the main wing vortex does travel further inboard in the presence of the wheel, (Figure 6.8a, e) the main wing vortex strength is also reduced negating any positive effect that the more inboard position the main wing vortex may have. Also confirming that the wing generates a weaker main wing vortex in the presence of a wheel is the pressure differential at the wing tip ($y/c=1.6$) for all the angles of attack shown in Figure 6.19 (b, e, h and k).

For the $0^\circ S/c=1.6$ wing, the shear stress on the bottom surface of the wing indicates that separation is more likely to occur at the wing tip with larger regions of shear stress values

less than 1 (Figure 6.19c, $x/c=1.05$, $y/c=1.5$). This is expected to occur due to the inconsistent pressure variation obtained along the bottom edge of the endplate previously discussed for interaction “a” and attributed to the less coherent wing tip vortex.

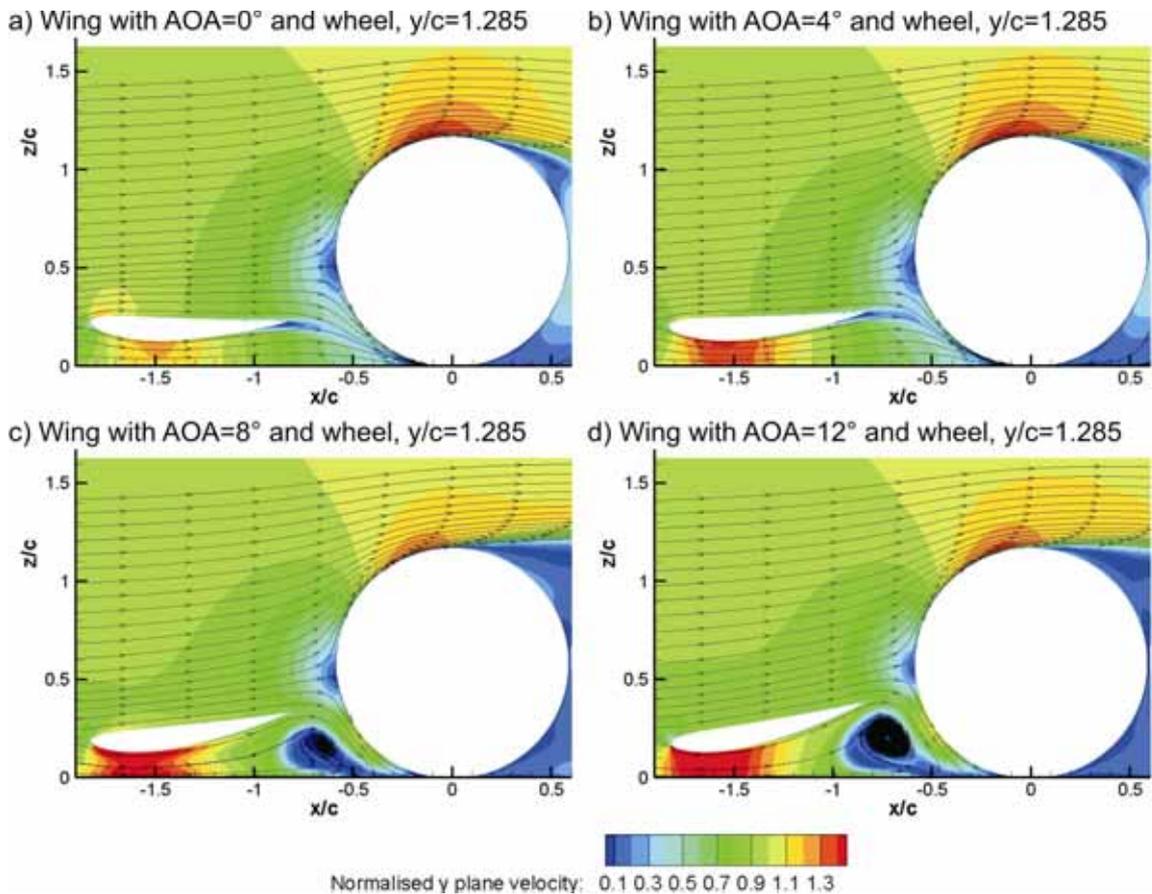


Figure 6.20 Streamlines indicating upwash variation due to changes in wing angle of attack

In plane velocity and streamlines on a y plane passing through the centre of the wheel (Figure 6.20) indicates the position that the main wing vortex passes the front face of the wheel for the 8° and 12° angles of attack ($x/c=-0.7$, $z/c=0.15$). As the main wing vortex passes the face of the wheel, it is expected that it will also have some influence on the static pressure experienced by that region of the wheel. This is confirmed by the centre circumference pressure coefficients (Figure 6.21) which experience a large pressure drop between an angle of 10° and 60° that coincide with the region that the main wing vortex passes the wheel at for the 8° and 12° cases. This would be expected to contribute to the drag and lift reduction that has been experienced by the wheel between wing angles of attack of 8° and 12° but is not expected to be the solitary cause for these variations.

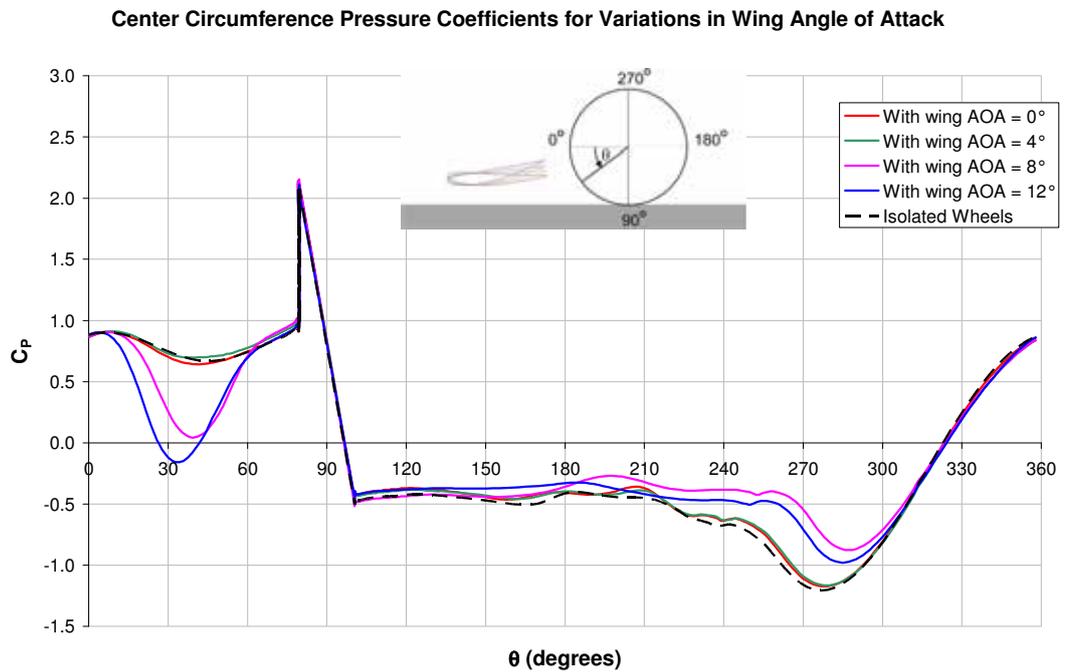


Figure 6.21 Central pressure coefficients obtained for wheel with varied wing angle of attack

Previously reported isolated wheel studies (Section 5.1.1) have also indicated that the wheel lift and drag are sensitive to the separation point of the wheel. The streamlines located on a y plane passing through the wheel centre confirm that as the angle of attack of the wing is increased up to an angle of 8° , the upwash experienced by the wheel also increases allowing the separation point from the wheel tread to shift further forwards as was assumed the cause for the drag and lift reduction was for interaction “b” previously. For this reason the maximum velocity that may be obtained over the top of the wheel is reduced (Figure 6.20 $x/c=-0.1$, $z/c=1$) and therefore the peak low pressure that is experienced by the wheel on the top surface of the wheel tread is also reduced (Figure 6.21, $240^\circ < \theta < 300^\circ$). Similarly to that which was determined during the isolated wheel study previously, the drag reduction is achieved by an increase in flow entrainment from the sides of the wheel reducing the lower wheel vortex strengths and reducing the entrainment into the wheel wake from above the wheel. For this reason, the wheel wake has also become narrower and taller as the upwash has been increased (Figure 6.22) with the only exception being that the wheel wake for the 12° is a little smaller and wider at the base than the 8° case. This is believed to be because the 12° wing has stalled and therefore is expected to produce less upwash than that created by the 8° wing. It should

be noted that the wheel in the presence of the 12° angle of attack wing still experienced the lowest drag and lift values. One possible explanation for this could be the stronger main wing vortex produced by the 12° wing which is evident in both the x sections behind the wing (Figure 6.18d, $y/c=1.25$, $z/c=0.2$) and the y sections (Figure 6.20d, $x/c=-0.7$, $z/c=0.2$) causing a further pressure reduction on the upstream portion of the wheel tread than what the same vortex does for the 8° wing (Figure 6.18c, $y/c=1.3$, $z/c=0.15$ and Figure 6.20d, $x/c=-0.7$, $z/c=0.15$).

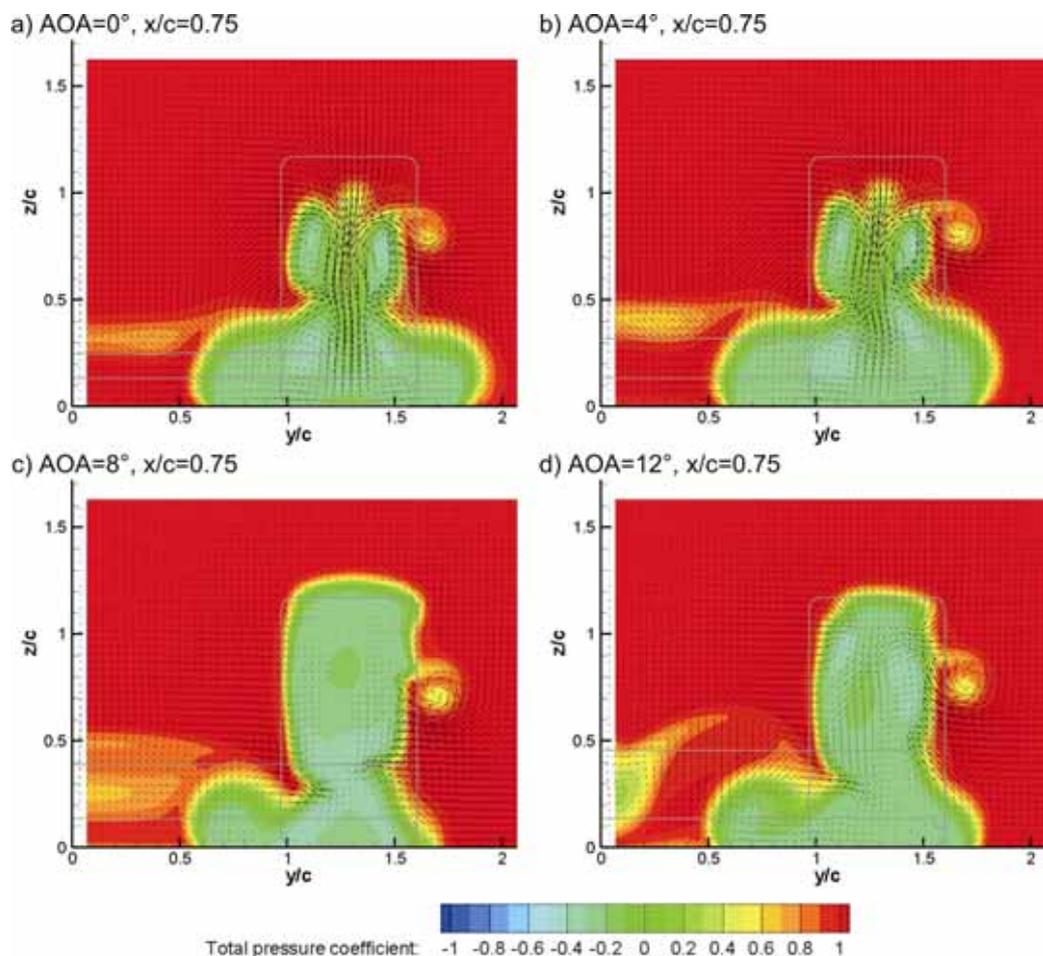


Figure 6.22 Vectors and Total Pressure on x-planes for a wing and wheel with varied angle of attack

The centre circumference pressure coefficients (Figure 6.21) confirm that this is the case with the lowest peak in the region of $10^\circ < \theta < 60^\circ$ being obtained with the 12° wing. This variation is also significantly larger than the separation point variation seen between 240°

and 300° which indicates that the wheel in the presence of the 8° wing has an earlier separation point.

An additional variation previously reported for the wheel in the presence of the $S/c=1.6$ wing was a consistent reduction in the side force as the angle of attack was increased. For the largest angle of attack tested (12°) a side force in the opposite direction and five times larger than that which was experienced by the same wheel in an isolated pair was obtained. In order to determine the cause for this variation, pressure coefficients around the circumference of the intersection of three z planes and the wheel were compared for a wheel in an isolated pair and in the presence of a wing with 0° and 12° angle of attack (Figure 6.23 and Figure 6.24 respectively). On each graph, the result obtained for the isolated wheel pair is shown in black, while the red and blue lines indicate the pressure coefficients for the wheel operating in the wake of the 0° and 12° wings respectively.

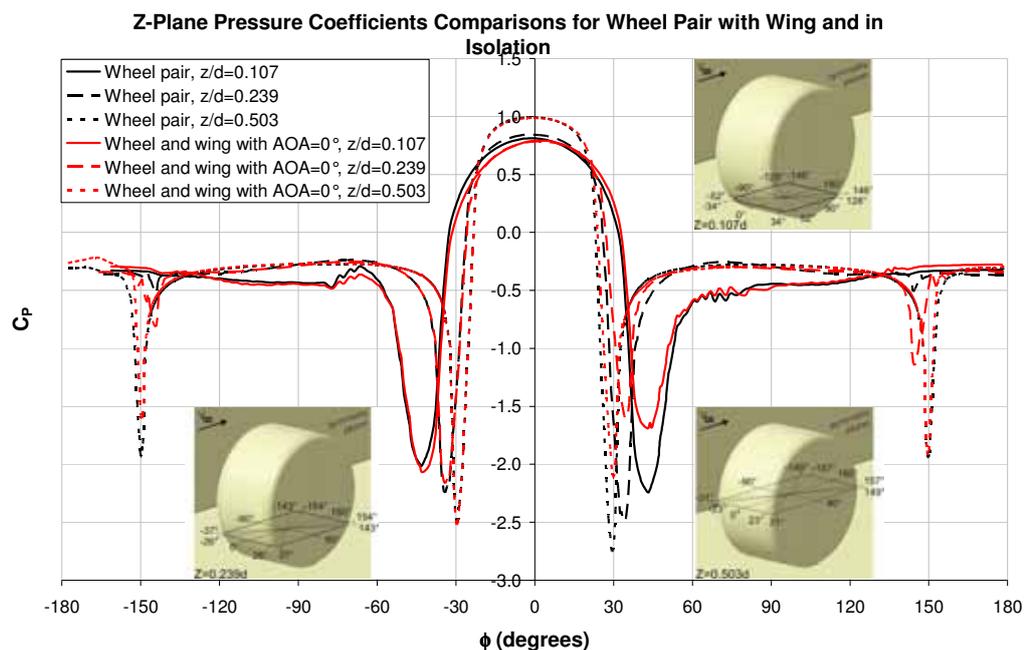


Figure 6.23 Pressure coefficients on wheel at $z/d=0.107$, $z/d =0.239$ and $z/d =0.503$ in isolation and in the presence of a wing with 0° angle of attack

For the wheel in the presence of the 0° wing, the comparison to the wheel from the isolated wheel pair indicates that the surface pressures experienced on the inner face is unchanged by the presence of the wing (Figure 6.23, $\phi < 0^\circ$). Variations are limited to the

outer shoulder of the wheel where the peak pressure reduction has been reduced ($25^\circ < \phi < 50^\circ$). As mentioned previously during the wheel width and track investigation, the pressure peaks in this region represent the acceleration experienced by the flow travelling around the forward outer wheel shoulder. For the isolated wheel pair, the location of the stagnation point relative to the inner and outer shoulders determines the acceleration obtained about each wheel shoulder and this imbalance is responsible for the side force experienced by a wheel operating in a pair. The addition of the wing shifts the location of the stagnation point outboard ($-15^\circ < \phi < 10^\circ$). When considering the static pressure plots on z planes (Figure 6.6e, f), it appears that the endplate position could be partly responsible for this change limiting the flow that can travel around the outside of the wheel. This will be considered further on during the span investigation.

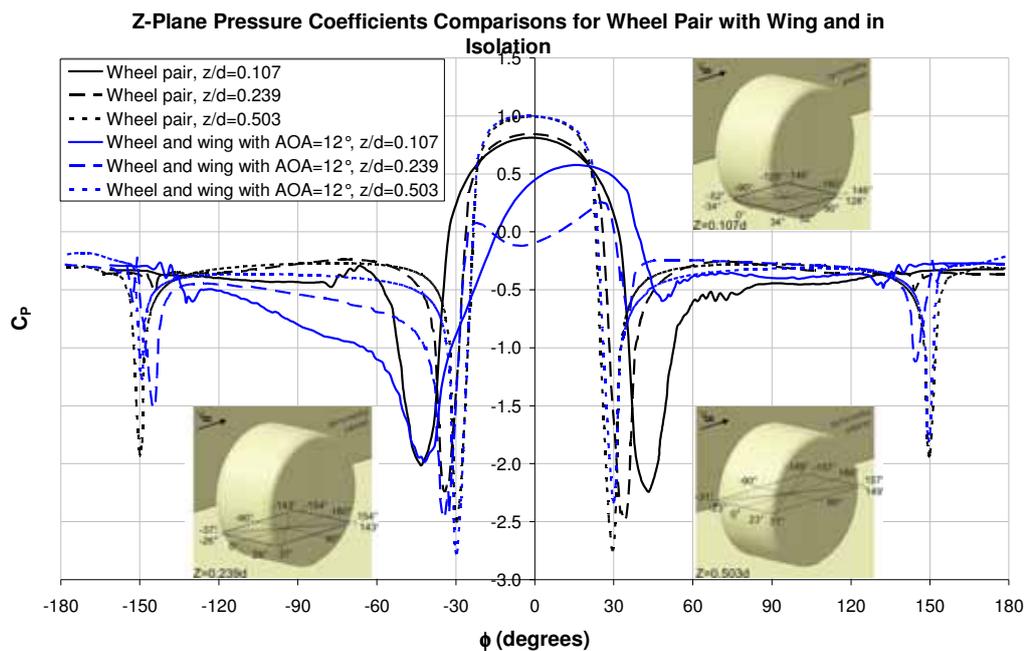


Figure 6.24 Pressure coefficients on wheel at $z/d=0.107$, $z/d =0.239$ and $z/d =0.503$ in isolation and in the presence of a wing with 12° angle of attack

Figure 6.24 indicate a similar but more drastic variation to the accelerated flow about the front outer wheel shoulder and the stagnation position on the wheel tread. This is likely to be due to the increased cross flow component produced when the wing angle of attack is increased. Increasing the angle of attack of the wing to 12° also allows the main wing vortex to travel inboard of the wheel which has already shown to have a significant

influence on the lift and drag values of the wheel. When comparing the static pressures obtained on the inside face of the wheel, significant reductions in pressure ($-120^\circ < \phi < -50^\circ$) suggest that the main wing vortex can also be responsible for the side force that is five times stronger and in the opposite direction to that obtained for a wheel belonging to an isolated wheel pair.

6.2.2. Adjustments to angle of attack causing variations for interaction “c”

The transition from interaction “b” to interaction “c” was initially achieved by reducing the wing span from $S/c=1.6$ to $S/c=0.97$. The main variation of interaction “c” relative to interaction “b” is the inboard path that the secondary vortex takes about the wheel and the direction of its rotation. Like interaction “b”, the main wing vortex is also expected to pass along the inner side of the wheel. While altering $S/c=1.6$ wing’s angle of attack could control the transition from interaction “a” to “b”, all angles of attack tested with the $S/c=0.97$ wing were expected to maintain variations of interaction “c”. To confirm this, vectors and x-vorticity contours were plotted on a plane located $0.63c$ upstream from the wheel’s axis of rotation for four angles of attack and have been included as Figure 6.25.

As initially assumed, all angles of attack presented here for the $S/c=0.97$ wing maintained the interaction “c” with both the main and secondary wing vortices travelling on the inboard side of the wheel. Increasing the angle of attack was found to reduce the strength of the secondary vortex (Figure 6.25, $y/c=0.95$, $z/c=0.65$). As explained previously, the secondary vortex is formed due to the pressure differential that exists on either side of the endplate’s top edge created by the stagnation region forward of the wheel and the flow above the top of the wing’s top surface (Figure 6.12f). Therefore, increasing the wings angle of attack will increase the static pressure generated on the top surface of the wing and in turn, this will reduce the difference relative to the stagnation pressure generated forward of the wheel and create a weaker secondary vortex. It should be noted that the opposite was achieved for the $S/c=1.6$ wing, but this should be expected given that the pressure differential experienced by the top edge of the endplate for this wing is in the opposite direction to that of the $S/c=0.97$ wing. This will be investigated further during the span study (Section 6.3).

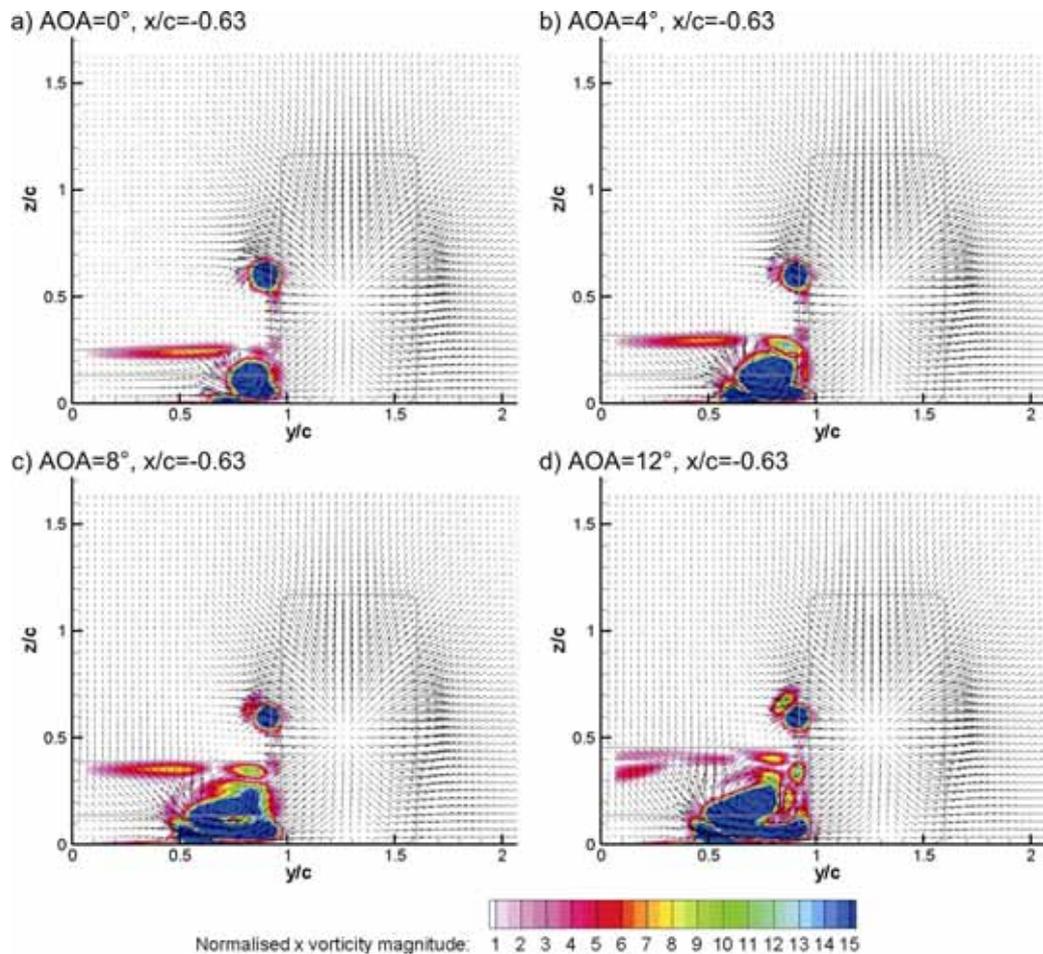


Figure 6.25 Vectors and Vorticity on x-planes for a wing with varied AOA and with a wheel

Like the $S/c=1.6$ wing, the $S/c=0.97$ wing also experienced a delayed stall in comparison to the same wing in isolation but the cause for this is expected to differ for the two wings. Another unique feature associated with interaction “c” was that the main wing vortex produced by the $S/c=0.97$ wing with an angle of attack of 12° in the presence of the wheel pair was 20% stronger than that achieved by the same wing in isolation. Therefore it was decided to once again use spanwise pressure coefficients and the shear stress experienced by the wings at several angles of attack to determine if this larger vortex was the cause for the delayed stall or the much less significant reduced wing loading was the cause as was determined for the $S/c=1.6$ wing.

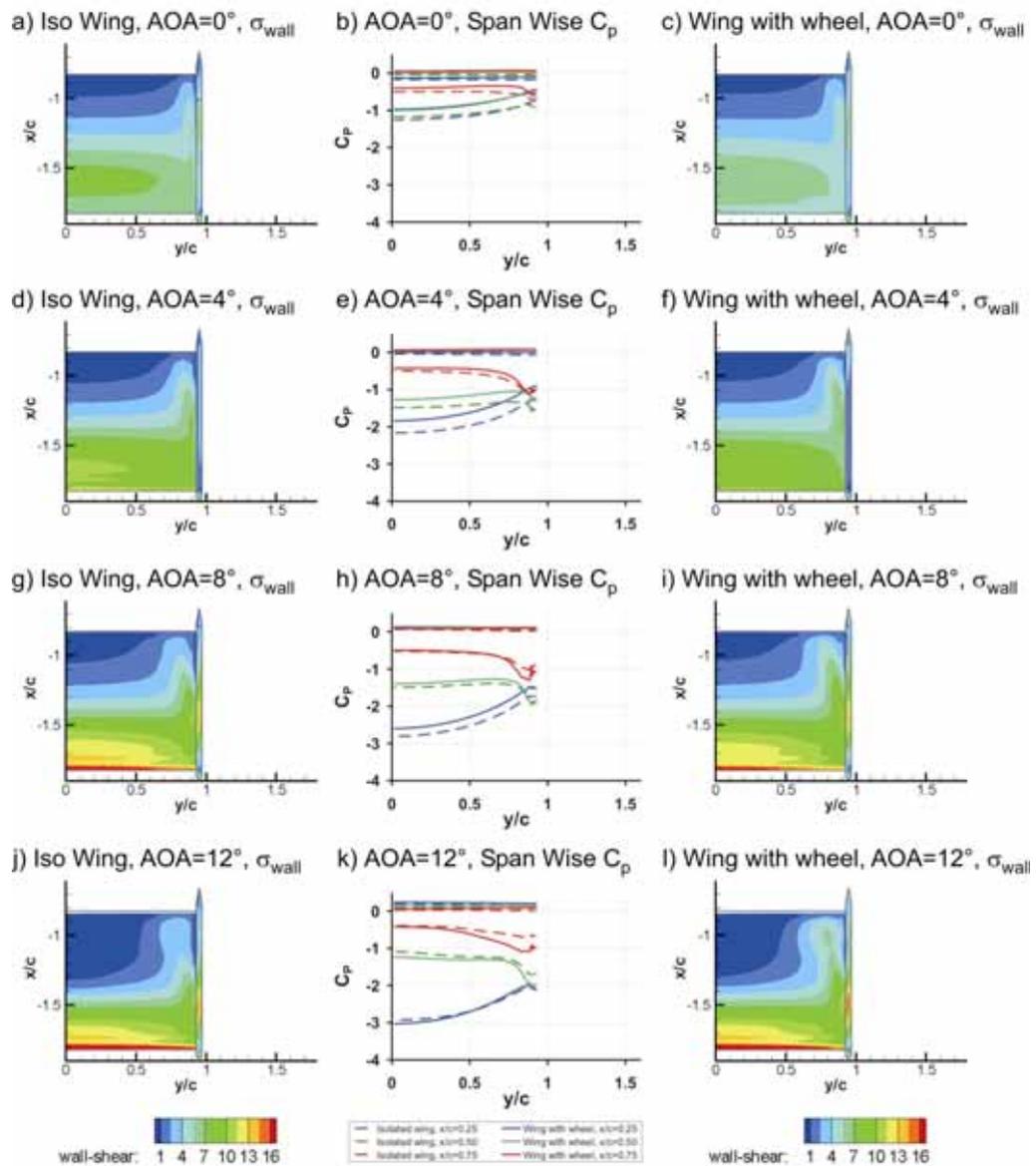


Figure 6.26 Wall shear stress and spanwise pressure distribution for variations in AOA

Comparing the wall shear stress for the isolated wings to those in the presence of the wheel pair between angles of attack of 0° and 8° inclusive indicates that very little variation is achieved in the separation due to the presence of the wheel (Figure 6.26). Likewise, the spanwise pressure coefficient variation is also small but generally the wing loading ($y/c=0$) is less in the centre of the wing agreeing with this wing producing slightly less downforce in the presence of the wheel pair in this angle of attack range (Figure 6.14). As the angle of attack is increased between 0° to 8° , the tip of the wing ($y/c=0.95$) begins to approach and

eventually exceed the suction generated by the wing in isolation providing evidence that the stronger main wing vortex is assisting with the generation of downforce for this wing. The most significant variation is achieved by the highest angle of attack tested where the stronger main wing vortex appears to significantly reduce the separation near the tip of the wing (Figure 6.26l, $y/c > 0.5$) relative to the same wing in isolation (Figure 6.26j, $y/c > 0.5$). Subsequently, the suction generated by the bottom surface increases at the tip and also propagates towards the symmetry plane ensuring that the entire bottom surface of the wing is generating equal or greater levels of suction relative to the same wing in isolation. Therefore, it is likely that the delayed stall is due to the increased main wing vortex strength reducing the separation experienced by the wing in the presence of the wheel for the $S/c=0.97$ wing.

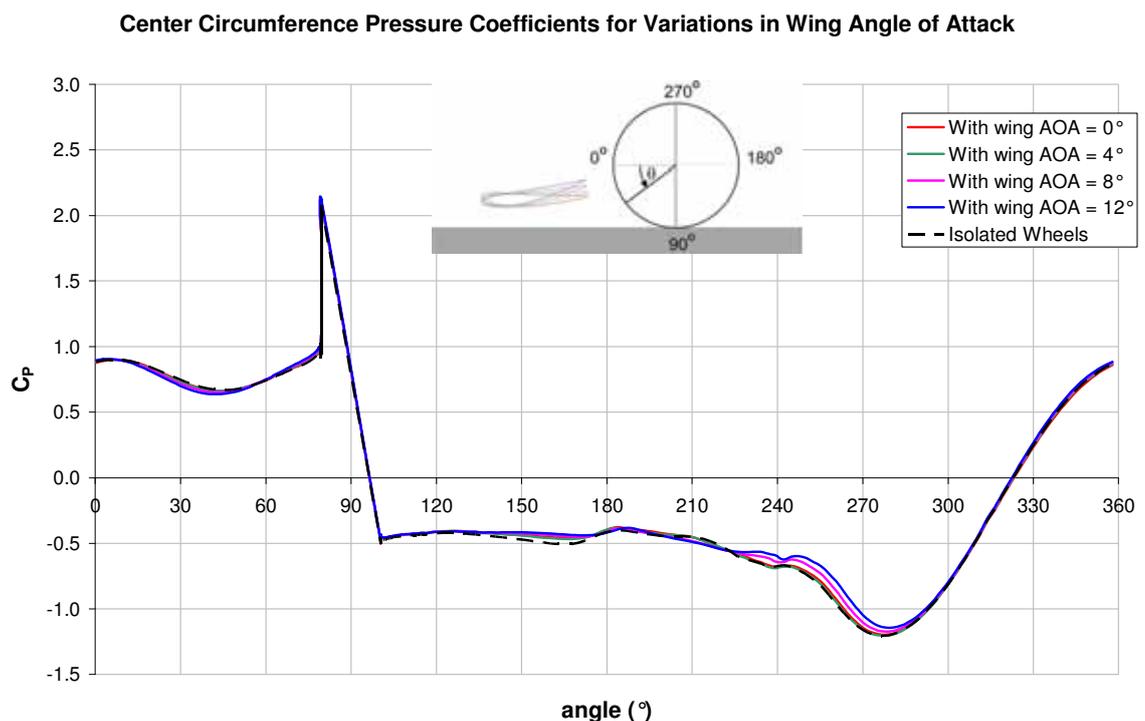


Figure 6.27 Central pressure coefficients obtained for wheel with varied wing angle of attack

Another common feature between the two different wing spans for which the angle of attack was varied was a reduction in the wing lift and drag as the angle of attack was increased relative to the same wheel of a pair in isolation (Figure 6.17). Given that the $S/c=0.97$ wing does not extend across the front of the wheel, it is not possible for the main

wing vortex to travel across the face of the wheel. Consequently, no variation was seen on the central circumference pressure coefficients for the wheel in the presence of the wing relative to that of the same wheel in isolation with the only exception being a subtle change in the separation point and the subsequent pressure drop achieved above the wheel ($240^\circ < \theta < 280^\circ$). This was also at first unexpected given that this variation was previously obtained due to the up wash generated by the portion of the wing forward of the wheel with the $S/c=1.6$ wing, but when considering the effect that the main wing vortex has on the lower wheel wake (Figure 6.28), the cause for this variation becomes apparent.

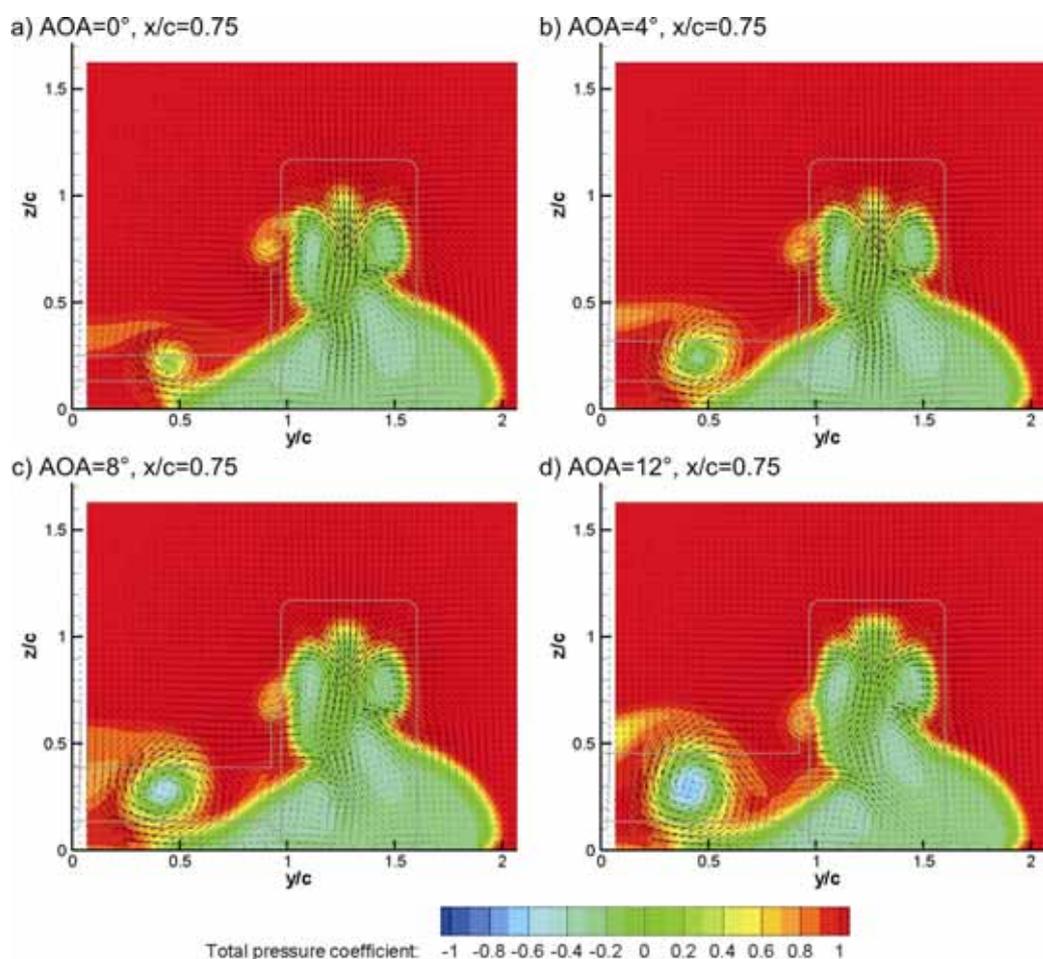


Figure 6.28 Vectors and Total Pressure on x-planes for a wing and wheel with varied angle of attack

During the study into the effect of the step used at the contact patch of the wheel, it was determined that altering the separation point at the base of the wheel could also influence the distribution of flow entrainment into the wake from either the top of the wheels or the

side by varying the strength of the vortices formed at the base of the wheel. It is expected that with the $S/c=0.97$ wing, a similar interaction is occurring and is therefore the cause for the small variation in the separation point from the top wheel tread. Total pressure contours and vectors located at a plane $0.75c$ downstream of the wheel centre indicate that an interaction exists between the main wing vortex (Figure 6.28, $y/c=0.45$, $z/c=0.25$) and the inner lower wheel vortex ($y/c=1.1$, $z/c=0.15$). As the angle of attack is increased and the main wing vortex strength increases, it is likely that the main wing vortex reduced the separation experienced on the inside face of the wheel which is required to create the lower wheel vortices. Subsequently, increasing the main wing vortex strength reduces the inner lower wheel vortex strength and the downwash generated in the centre of the wheel wake ($y/c=1.25$, $z/c=0.7$) which has previously been shown to be linked to the separation point from the top wheel tread. For this reason it is believed that increasing the angle of attack of the $S/c=0.97$ wing also reduces the lift and drag of the wheel and causes the wheel wake to be less symmetrical.

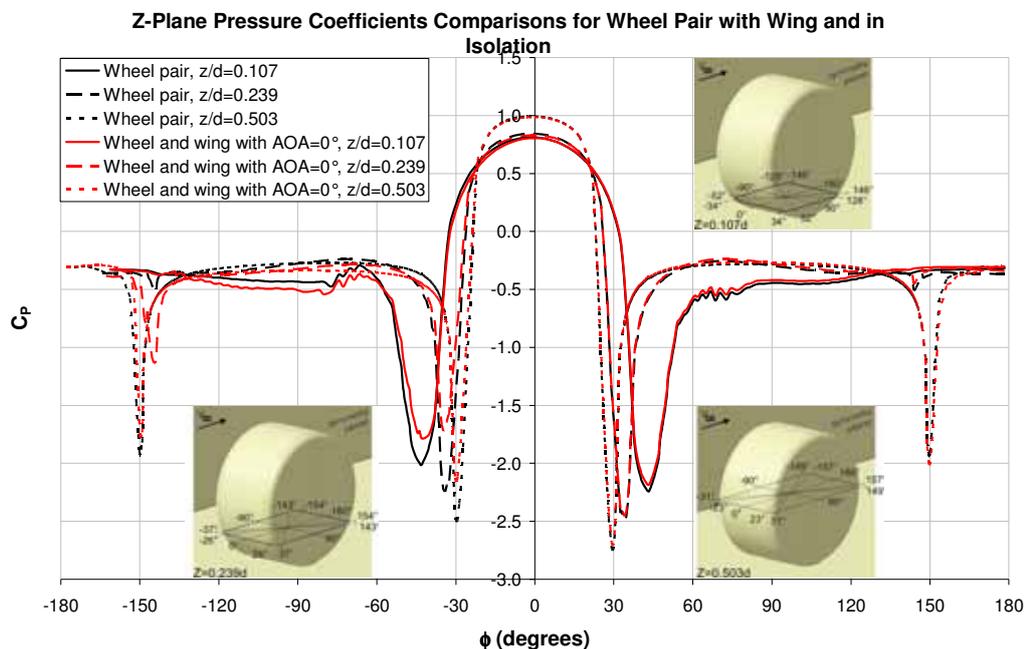


Figure 6.29 Pressure coefficients on wheel at $z/d=0.107$, $z/d =0.239$ and $z/d =0.503$ in isolation and in the presence of a wing with 0° angle of attack

The reduced wing span also generally experienced reduced side forces as the wing angle of attack was increased. Pressure coefficients around the circumference of the intersection

of three z planes and the wheel for the $S/c=0.97$ wing with 0° angle of attack (Figure 6.29) indicate that aligning the endplate with the inner face of the wheel has reduced the acceleration experienced about the forward inner shoulder ($-50^\circ < \phi < -20^\circ$) while the stagnation regions ($-15^\circ < \phi < 15^\circ$) and the flow about the outer face ($20^\circ < \phi < 180^\circ$) of the wheel remain unchanged. This on its own would be expected to produce a larger side force pushing the two wheels apart, but the main wing vortex travelling along the inside face of the wheel ($-130^\circ < \phi < -60^\circ$) has created a lower pressure on the inner face of the wheel in comparison to the same wheel in an isolated pair. Subsequently, the wheel in the presence of this wing configuration experiences a side force acting towards the symmetry plane approximately equal in magnitude to the force experienced by a wheel belonging to an isolated wheel pair.

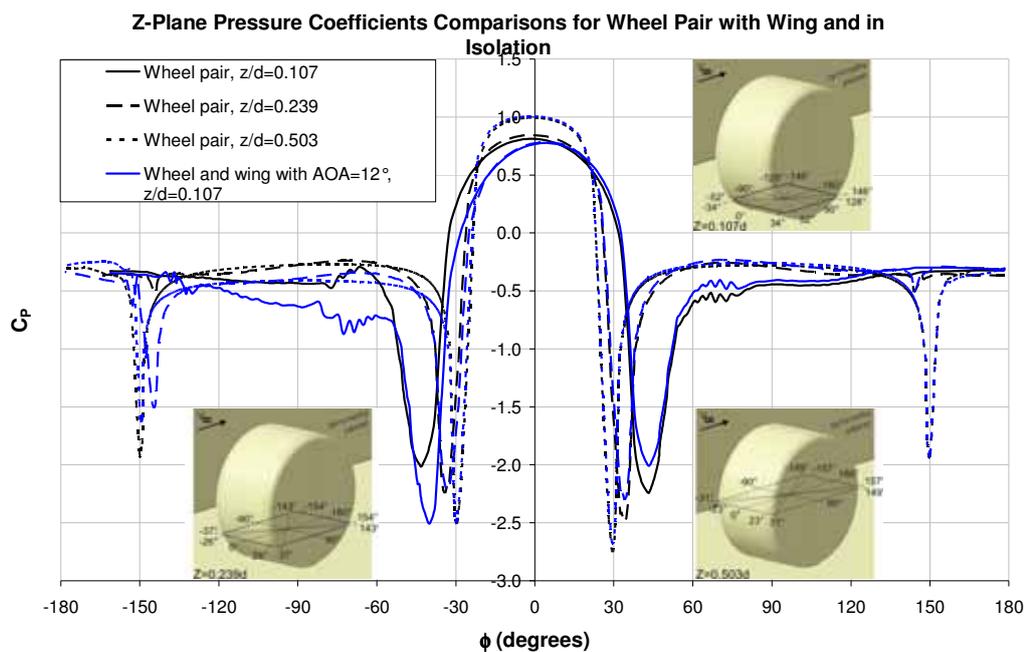


Figure 6.30 Pressure coefficients on wheel at $z/d=0.107$, $z/d =0.239$ and $z/d =0.503$ in isolation and in the presence of a wing with 12° angle of attack

Increasing the angle of attack of the $S/c=0.97$ wing to 12° causes far more significant variations that not only alter the static pressure on the inside face of the wheel, but also on the outside (Figure 6.30). While the endplate in all the previous cases has restricted the acceleration about the closest wheel shoulder, this case seems to be one exception with the flow being accelerated about the inboard shoulder to a greater extent than that which

is experienced by the isolated wheel ($-50^\circ < \phi < -20^\circ$). This may be due to the pressure drop generated on the inboard side of the endplate encouraging flow to pass between the trailing edge of the endplate and the inner forward wheel shoulder (Figure 6.12e). Other variations also include a shift in the stagnation regions ($-20^\circ < \phi < 20^\circ$) outboard for the $Z=0.107d$ profile as well as reduced pressure drops for the outboard front wheel shoulder ($20^\circ < \phi < 50^\circ$) and outer face ($60^\circ < \phi < 120^\circ$). The opposite is experienced by the inner wheel face ($-120^\circ < \phi < -60^\circ$) and this is likely to be due to the suction that the main wing vortex creates encouraging more flow around the inner face of the wheel as opposed to the outer face. All these features are expected to contribute to the reversed side force experienced by the wheel which is three times greater than that experienced by the same wheel in an isolated pair.

6.3. Variations in Interaction due to Wing Span

Investigations carried out thus far considering the interaction of a wing and wheel have demonstrated that the $S/c=1.6$ wing is dependant on the angle of attack in order to determine whether interaction “a” or “b” would be achieved, while the $S/c=0.97$ wing would always experience interaction “c” regardless of the angle of attack. Therefore, the effect that varying the span has on the interaction of a wing and wheel was also investigated to determine at which wing span the switch will occur to interaction “c” and also to determine how the forces on the wing and wheel vary with this parameter. This was undertaken at four different angles of attack (0° , 4° , 8° and 12°) and with the same wheel pair configuration as that used for the previous wing and wheel investigations ($W/c=0.63$, $T/c=1.6$).

The results of the lift forces experienced by the wing in the presence of a wheel pair while the span is varied (Figure 6.31) indicates that the maximum wing downforce should be expected to occur at the maximum span within the angle of attack range tested here (0° to 12°). For the 0° angle of attack wings, the reduction in downforce relative to the same wing in isolation varied from 27% at $S/c=0.97$ to 48% at $S/c=1.6$ in a linear manner. Similarly, the downforce reduction experienced by the 4° angle of attack wing also had a linear relationship varying from 14% to 39% over the same span range. Increasing the angle of attack further to 8° also showed that the reduction in downforce experienced by the wing in

the presence of a wheel pair also increased as the span was increased to a maximum variation of 19%, but this was no longer in a linear manner and at the two shortest spans tested ($S/c=0.97$ and $S/c=1.06$) equal levels of downforce as the corresponding wings in isolation were obtained.

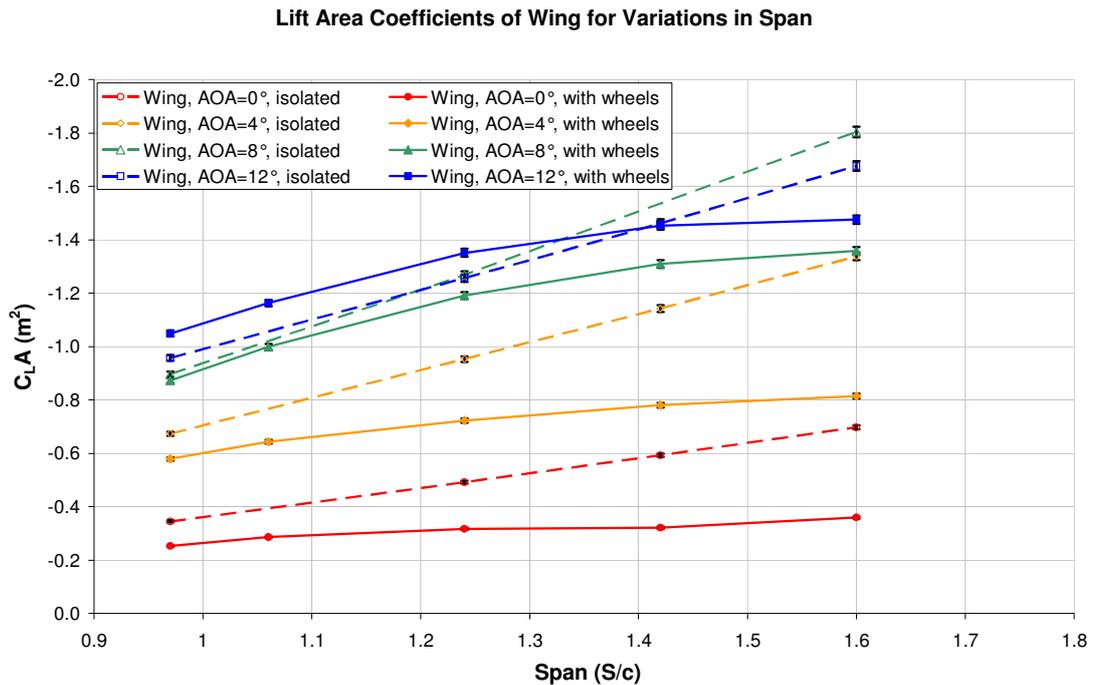


Figure 6.31 Wing lift results for variations in span and angle of attack for an isolated wing ($h/c=0.13$) and also in the presence of a wheel pair ($W/c=0.63$, $T/c=1.6$)

As shown previously for the $S/c=0.97$ wing, only the 12° angle of attack wing benefited from the presence of the wheel with increased levels of downforce being obtained up to a span of $1.42c$. The increased wing performance for the largest angle of attack tested has already been demonstrated to occur due to the reduced separation obtained on the bottom surface of the wing which delays stall from occurring for the $S/c=0.97$ wing. This was caused by a stronger main wing vortex created by the increased pressure differential provided by the high pressure regions generated forward of the wheel contact patch and the suction obtained beneath the wing surface. It is unclear if this is the cause for the improved front wing performance at the larger spans ($S/c=1.06$ and $S/c=1.24$) as it is expected that increasing the span will eventually cause the endplate to be positioned on the opposite side of this high pressure region and therefore the main wing vortex strength

will not be able to benefit from the presence of the wheel. Therefore this will be given some greater consideration further on in this section.

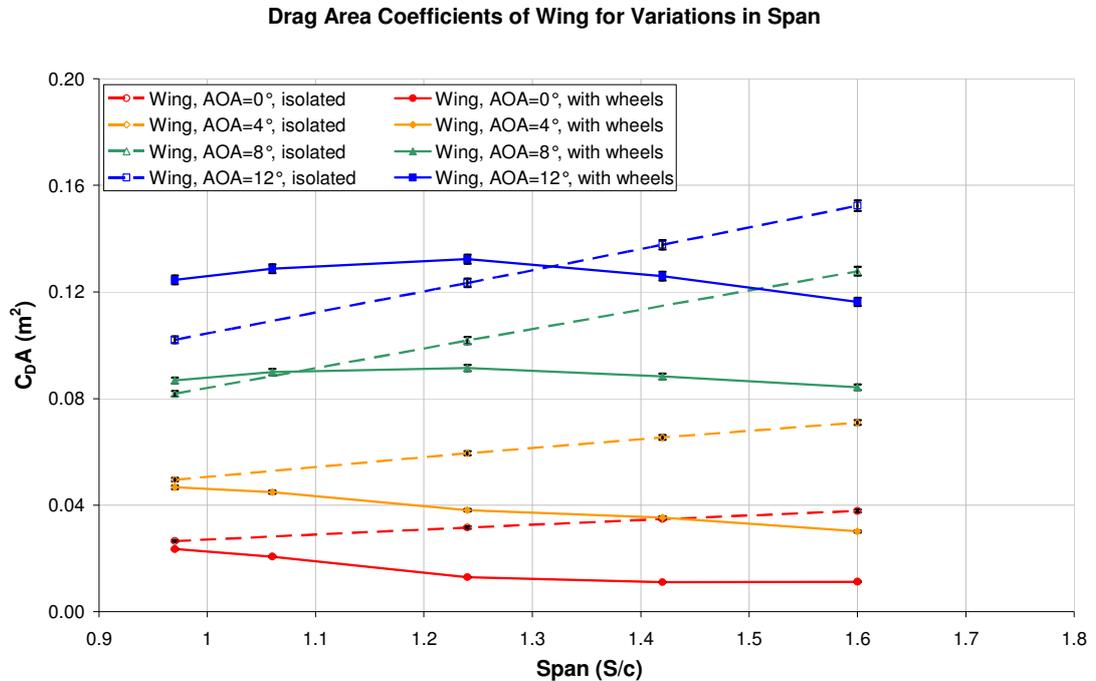


Figure 6.32 Wing drag results for variations in span and angle of attack for an isolated wing ($h/c=0.13$) and also in the presence of a wheel pair ($W/c=0.63$, $T/c=1.6$)

Consistent with the previous findings, the drag of the 12° wing (Figure 6.32) in the presence of the wheel is higher than the same wing in isolation for the three spans where the downforce was also greater. This may be due to a stronger main wing vortex causing an increase in the induced drag experienced by the wing and will be investigated further later in this section. At greater wing spans, the 12° wing had reduced levels of drag relative to the same wing in isolation with the peak drag being obtained at $S/c=1.24$. A similar trend was also obtained for the 8° wing while the 0° and 4° wings experienced an incremental reduction in drag as the wing span was increased relative to the same wing in isolation. Both wings in the presence of a wheel pair experience approximately equal drag at $S/c=0.97$ as the corresponding wings in isolation, while at $S/c=1.6$, the 0° and 4° angle of attack wings experience approximately a 70% and 50% reduction in drag respectively.

Lift and Drag Area Coefficients of Wheel for Variations in Wing Span

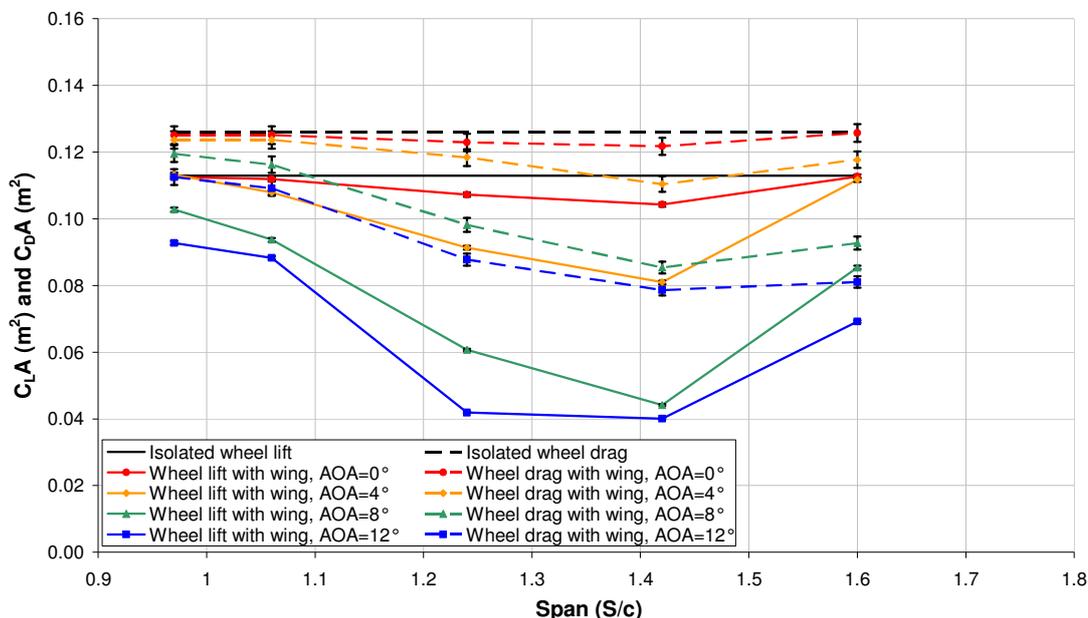


Figure 6.33 Wheel lift and drag (a) and side force (b) results for an isolated wheel pair ($W/c=0.63$, $T/c=1.6$) and also in the presence of a wing ($h/c=0.13$) with varied span and AOA

The wheel lift and drag coefficients variations with span have been included as Figure 6.33 and indicate once again that the lift and drag variations for the wheel exhibit common trends. This is likely to suggest that varying the span across the face of the wheel is altering the wheel tread separation point as well. The previously discussed trend where the lift and drag of the wheel incrementally reduces with increases in angle of attack for the two extreme spans tested ($S/c=0.97$ and 1.6) has been maintained throughout the range of spans tested here. Minimum lift and drag forces have been obtained at each angle of attack tested for the $S/c=1.42$ wings with the lift of the wheel being reduced by 8%, 28%, 61% and 65% with the wing angle of attack being 0° , 4° , 8° and 12° respectively while the wheel drag reduction was determined to be 3%, 12%, 32% and 38% respectively over the same wheel belonging to an isolated pair. For all the spans tested less than $S/c=1.42$, the lift and drag reductions incrementally reduce as the span is reduced. The cause for the wheel in the presence of the $S/c=1.42$ wings experiencing the greatest lift and drag reductions is expected to be due to a combination of the upwash generated by the wing and the effect that the main wing vortex has directly acting on the forward wheel tread and the subsequent alteration to the wheel wake vortex structures.

Side Area Coefficients of Wheel for Variations in Wing Span

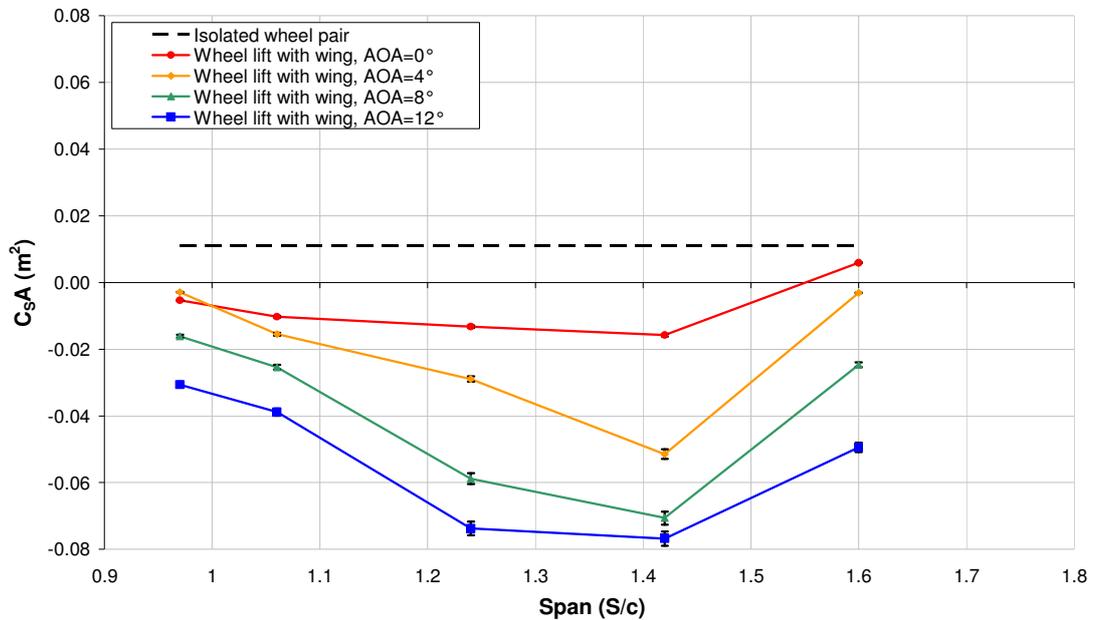


Figure 6.34 Wheel side force results for an isolated wheel pair ($W/c=0.63$, $T/c=1.6$) and also in the presence of a wing ($h/c=0.13$) with varied span and AOA

Previously it has been demonstrated that the side force experienced by the wheel is partly due to the influence that the main wing vortex has as it passes either the inner or outer face of the wheel. The magnitude and the direction of the side forces (Figure 6.34) indicate that the main wing vortex is likely to be passing on the inner face for all the combinations of spans and angle of attack tested with the exception of the $S/c=1.6$ wing at 0° and 4° which have previously been shown to be examples of interaction “a”. Given that the peak side force for the wheel has also been obtained at the span at which the minimum lift and drag has also been obtained, this may also be considered as an indication that the main wing vortex is playing a significant role in the lift and drag of the wheel operating in the presence of a wing and therefore this factor will be considered further at a later point in Section 6.3.1 and 6.3.2.

Total Lift Area Coefficients for Variations in Span

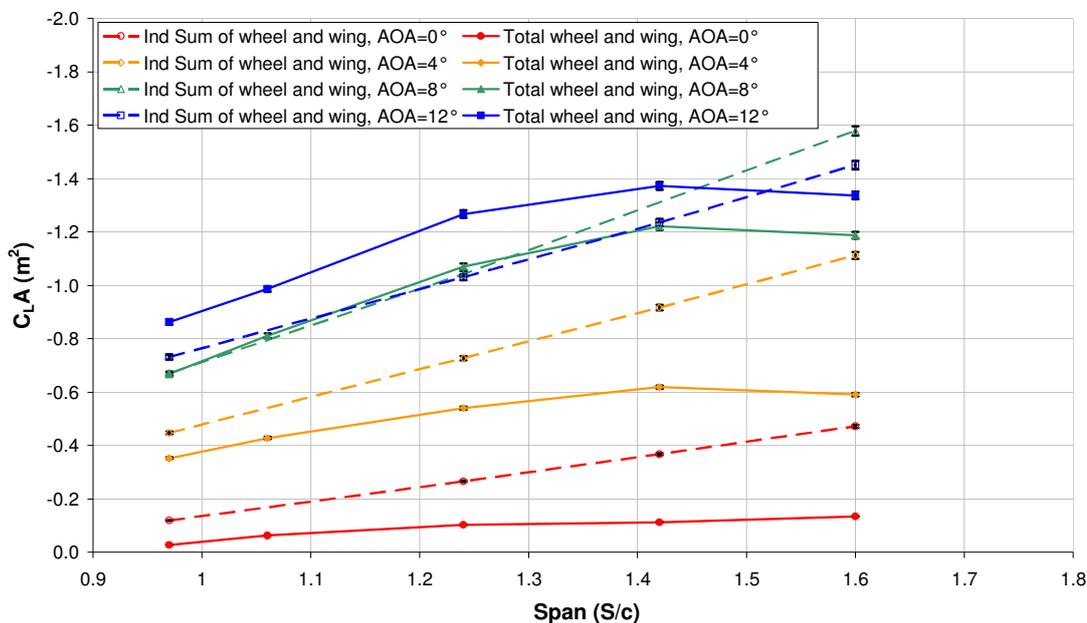


Figure 6.35 Total lift results for variations in span and angle of attack for an isolated wing ($h/c=0.13$) and also in the presence of a wheel pair ($W/c=0.63$, $T/c=1.6$)

While the individual aerodynamic performance of the wing and wheel is important, for the application of an open wheel racing car, it would be expected that the sum of the wing and wheel lift would be of greater significance given that this would be more representative of the total vehicle downforce. Therefore, the total lift (Figure 6.35) and drag (Figure 6.36) have been presented with the sum of the isolated wing and wheel results also plotted for comparison. When considering the total lift of the wing and wheel, the $S/c=1.42$ wing in the presence of the wheel produces the greatest total downforce for all the angles of attack tested with the exception of the wing with 0° angle of attack. Even though the $S/c=1.42c$ wings generally produces less downforce in the presence of a wheel pair than the respective wings in isolation (Figure 6.31), the lift reduction obtained on the wheel when working in unison with this wing allows these combinations to produce the most downforce in total for the 4° , 8° and 12° angles of attack. If only the individual sum of the isolated wing and isolated wheel were to be considered, this trend would not be evident and the results would suggest that the maximum span would produce the greatest total downforce. Additionally, with the exception of the $S/c=0.97$ to $S/c=1.42$ wings at an angle of attack of 8° and 12° , the total downforce for all the remaining wing span and angle of attack

combinations tested would be over estimated by up to 77% ($S/c=0.97$, $AOA=0^\circ$) if the individual sum was considered instead of the total downforce. Likewise the total downforce for the $S/c=0.97$ to $S/c=1.42$ wings at 12° angle of attack would be underestimated by up to 23% if the individual sum was considered with only the wing with an angle of attack of 8° in the same span range exhibiting comparable downforce values.

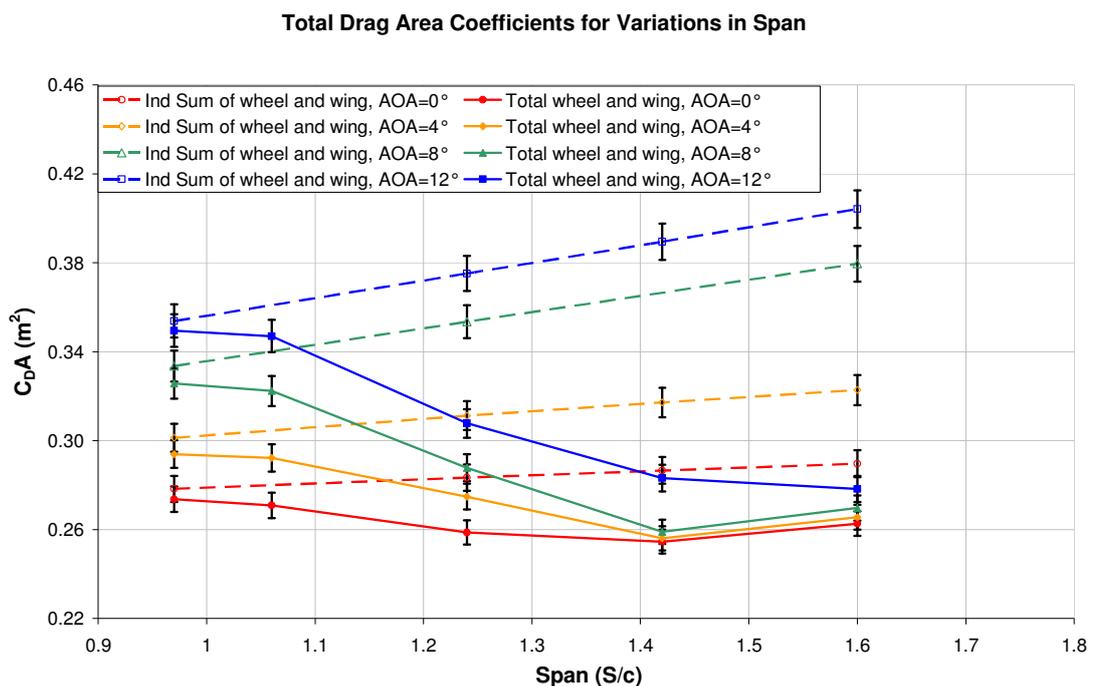


Figure 6.36 Total drag results for variations in span and angle of attack for an isolated wing ($h/c=0.13$) and also in the presence of a wheel pair ($W/c=0.63$, $T/c=1.6$)

The total drag results also indicate that the minimum drag would be achieved by the $S/c=1.42$ wing for all angles of attack tested except for the 12° case. This trend is due to the combination of drag reduction experienced by both the wheel and the wing compared to the same bodies when working in unison. Of greater significance is the opposite trends obtained with variations in drag as the span is varied when comparing the individual sum to the wing and wheel total. While the individual sum suggests that increasing the span will result in increase in a combined drag of the wing and wheel, the total indicates that the opposite will occur with the exception being the minimum achieved at 0° , 4° and 8° with a span value of $S/c=1.42$. As a result the drag variation between the individual sum and the

wing and wheel total can be up to 31% ($S/c=1.6$, $AOA=12^\circ$). Only for the shortest span tested can the individual sum be representative of the total wing and wheel drag with variations for these spans not exceeding 3% for all the angles of attack presented here. Therefore, further investigation will be required to determine why the $S/c=1.42$ wing proves to be an optimum span for both lift and drag performance and why the wheel lift and drag is so significantly reduced with this wing span. The variations between the total and the individual sum of the wing and wheel forces indicate that understanding of the interaction of the wing and wheel is of significant importance given that it is possible to further optimise a wing and wheel combination than that which may be achieved for either in isolation. Additionally, one must also consider that the wing and wheel is only a small proportion of an entire open wheeler's geometry and therefore it is unlikely that only considering a total wing and wheel optimum would provide a total vehicle optimum.

6.3.1. Variations caused by changes of span for a wing with 0° angle of attack

At an angle of attack of 0° , it has previously been identified that two different wing and wheel interactions can occur dependant on the wing spans investigated thus far. With a wing span value of $S/c=1.6$, both the main and secondary vortices travel outboard of the wheel (interaction "a"), while at a wing span value of $S/c=0.97$ both wing vortices travel inboard of the wheel (interaction "c"). For this wing angle of attack, it has yet to be proven at which span the switch will occur from interaction "a" to "c" and if some transition interaction will occur in between. When considering the secondary wing vortex alone, it is expected that the path that this vortex will take will switch when the wing endplate is positioned in the middle of the wheel and the pressure differential created either side of the endplate is equal. At this span configuration, it would also be expected that the formation of the secondary vortex will be prevented given that no pressure differential will exist about the top edge of the endplate. Therefore it is expected that as the wing span is reduced from a value of $S/c=1.6$, the secondary vortex strength will reduce to zero and continue travelling outboard of the wheel until a span value of approximately $S/c=1.3$. Then it will be expected to begin to form again in the opposite direction and travel inboard of the wheel continuing to gain strength until the shortest span tested ($S/c=0.97$) is achieved. To determine if this is the case, vectors and normalised x-vorticity plotted on a plane between the wing and the wheel ($x/c=-0.63$) have been included as Figure 6.37 for variations in span for a wing with 0° angle of attack.

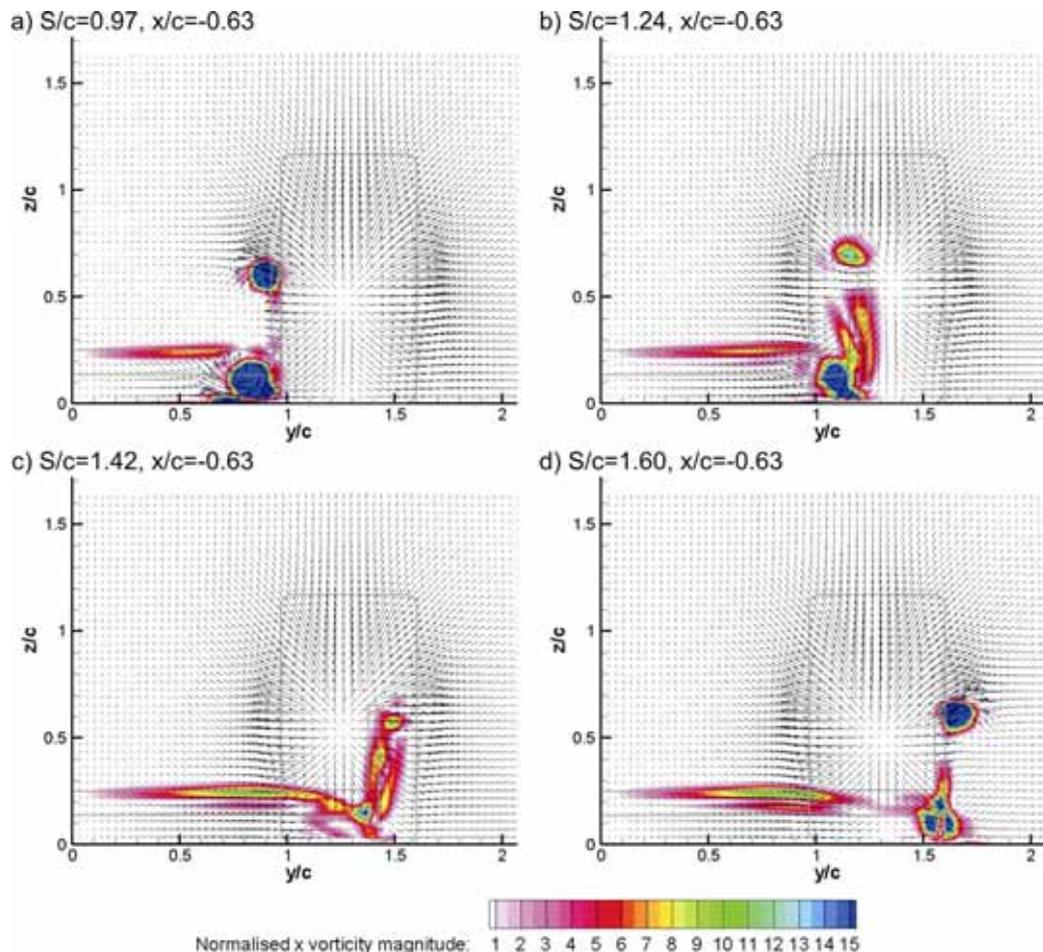


Figure 6.37 Vectors and Vorticity on the $x/c = -0.63$ plane for a wing in isolation and in the presence of a wheel with varied span, $AOA = 0^\circ$, $h/c = 0.13$ and wheel with $W/c = 0.63$, $T/c = 1.6$

The vectors and x-vorticity plots confirm that the proposed variation to the secondary vortex with the span of the wing does in fact occur. The two spans tested greater than a value of $S/c = 1.3$ indicate that a clockwise rotating vortex is achieved that on the $x/c = -0.63$ plane is located outboard of the stagnation region formed forward of the most upstream location of the wheel (Figure 6.37c, $y/c = 1.5$, $z/c = 0.55$ and Figure 6.37d, $y/c = 1.7$, $z/c = 0.65$). Given these vortices position relative to the stagnation point ahead of the wheel, it would be expected that both will travel outboard of the wheel consistent with the proposed theory. Also consistent with the proposed theory, the $S/c = 1.6$ wing produced a secondary vortex more than twice the strength of the $S/c = 1.42$ wing. For the wing span values less than $S/c = 1.3$, the same can also be said with a counter clockwise secondary vortex forming that is becoming stronger as the wing span is further reduced (Figure 6.37b,

$y/c=1.2$, $z/c=0.7$ and Figure 6.37a, $y/c=0.95$, $z/c=0.7$). Both these vortices are positioned on the inboard side of the wheel stagnation region and would also be expected to travel towards the inner side of the wheel. While the strength of the secondary vortex for the two extreme spans tested are adequate for the secondary vortex to remain visible at the $x/c=0$ plane (Figure 6.38a, $y/c=0.9$, $z/c=0.7$ and Figure 6.38d, $y/c=1.7$, $z/c=0.7$), the same can not be said for the span vales of $S/c=1.24$ and $S/c=1.42$ (Figure 6.38c, d). Despite the path that the secondary vortex takes about the wheel for the $S/c=1.42$ wing, it appears that the main wing vortex does not pass about the outside face of the wheel as observed for the $S/c=1.6$ wing (Figure 6.38d, $y/c=1.7$, $z/c=0.2$).

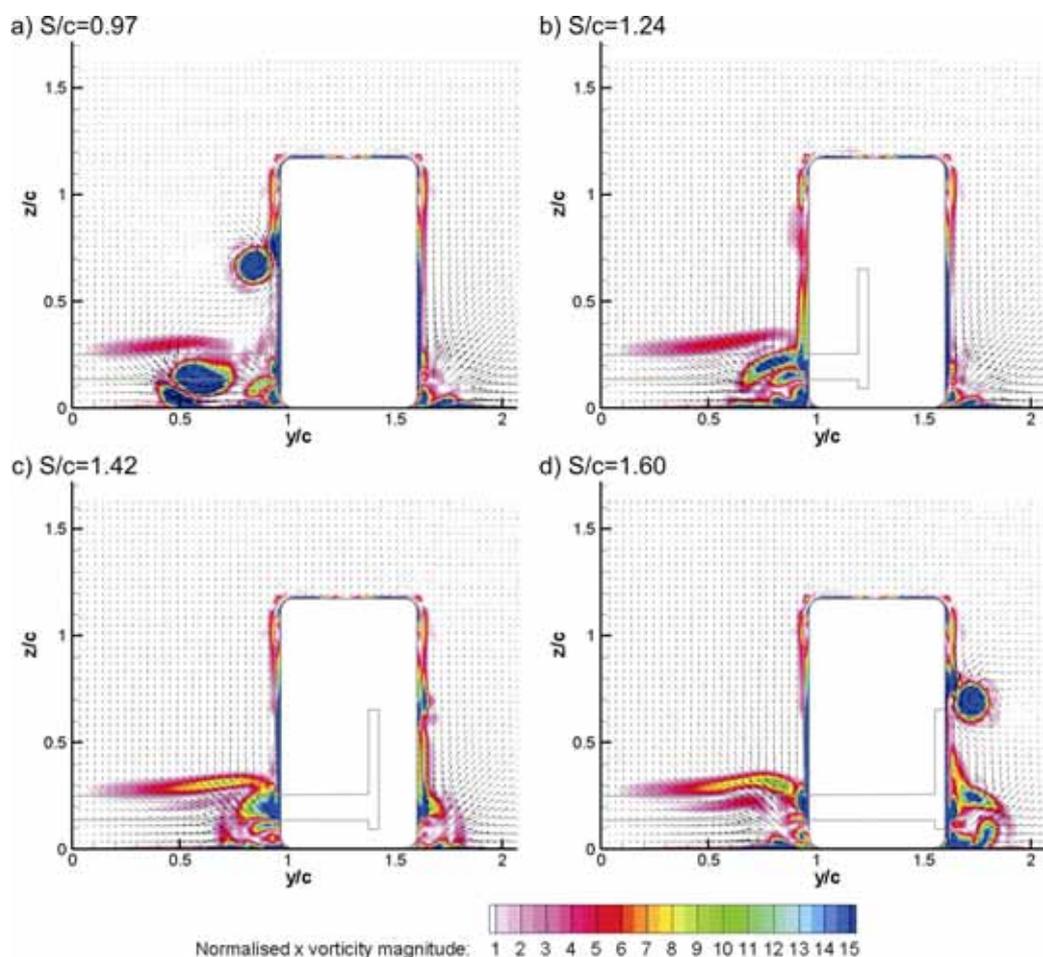


Figure 6.38 Vectors and Vorticity on the $x/c=-0.63$ plane for a wing in isolation and in the presence of a wheel with varied span, $AOA=0^\circ$, $h/c=0.13$ and wheel with $W/c=0.63$, $T/c=1.6$

Instead, it appears that the main wing vortex for the $S/c=1.42$ wing travels inboard of the wheel indicating that the transition interaction between “a” and “c” is in fact interaction “b”. When considering the x-vorticity on the $x/c=-0.63$ plane, the main wing vortex appears to be weaker and being drawn inboard by the cross flow generated by the wing (Figure 6.37c, $y/c=1.5$, $z/c=0.55$). Further reducing the wing span allows the main wing vortex to become stronger in the presence of the wheel. This is expected to be because of the greater pressure differential created either side of the bottom edge of the endplate due to the presence of the high pressure region created forward of the wheel. This will be confirmed during a more detailed investigation considering the variation in span with the 12° angle of attack wing (Section 6.3.2). This wing angle of attack was chosen to investigate this feature because it is expected to provide the greatest variation in the flow structures in comparison to the smaller angles of attack which also reacted in a similar manner.

6.3.2. Variations caused by changes of span for a wing with 12° angle of attack

In order to determine the cause of the increased wing downforce in the presence of the wheel relative to the same wing in isolation previously reported, vectors and x-vorticity have been plotted on the $x/c=-0.63$ plane and included as Figure 6.39 and Figure 6.40. In both these figures, the isolated wing results are shown on the left at several spans, while the combined wing and wheel results are on the right. When comparing the $S/c=0.97$ and $S/c=1.24$ wings in isolation to that in the presence of the wheel (Figure 6.39), it is evident that increasing the wing span has no effect on the shape or structure of the main wing vortices for the wing in isolation. This trend is continued for further steps in span of $S/c=1.42$ and $S/c=1.6$ (Figure 6.40). Albeit for a different wing profile, the consistent shape and strength of the main wing vortex being formed by an isolated wing with varied span has been discussed during the previous investigation considering the downforce loss phenomenon dependency on the wing span (Section 5.2) and will therefore not be discussed further here.

In the presence of the wheel pair the main wing vortex appears to become smaller and weaker as the wing span is increased. The stronger main wing vortex in the presence of the wheel for the $S/c=0.97$ wing (Figure 6.39b) relative to the same wing in isolation (Figure 6.39a) has been previously shown to be caused by an increase in the pressure

differential about the bottom edge of the endplate due to the presence of the high pressure region formed forward of the wheel (Figure 6.41a). In turn, the stronger vortex prevented separation from occurring from the bottom surface of the wing, increasing the suction generated at the tip of the wing and allowing the wing in the presence of the wheel to produce greater downforce than the same wing in isolation. The high pressure region forward of the wheel is located approximately in the middle of the wheel in an isolated pair (Figure 6.12c) but for a wheel in the presence of a wing with angle of attack of 12° and the maximum span previously investigated ($S/c=1.6$), the high pressure region forward of the wheel has been shown to be influenced by the pressure drop achieved below the wing. This is believed to also be the case for the intermediate steps of span tested (Figure 6.41b,c) and can be confirmed when considering the static pressure on z -planes at a height in line with the bottom edge of the endplate ($z/c=0.1$).

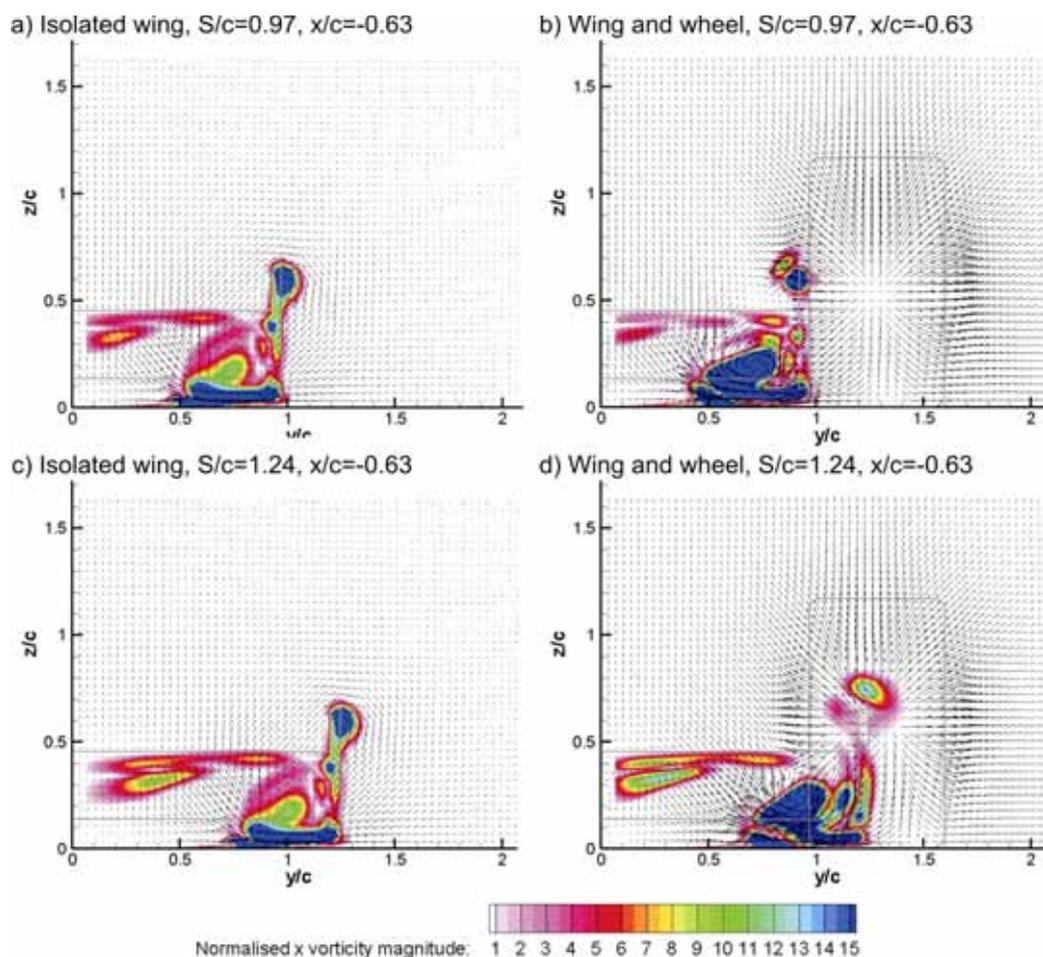


Figure 6.39 Vectors and Vorticity on the $x/c=-0.63$ plane for a wing in isolation and in the presence of a wheel with varied span, $AOA=12^\circ$, $h/c=0.13$ and wheel with $W/c=0.63$, $T/c=1.6$

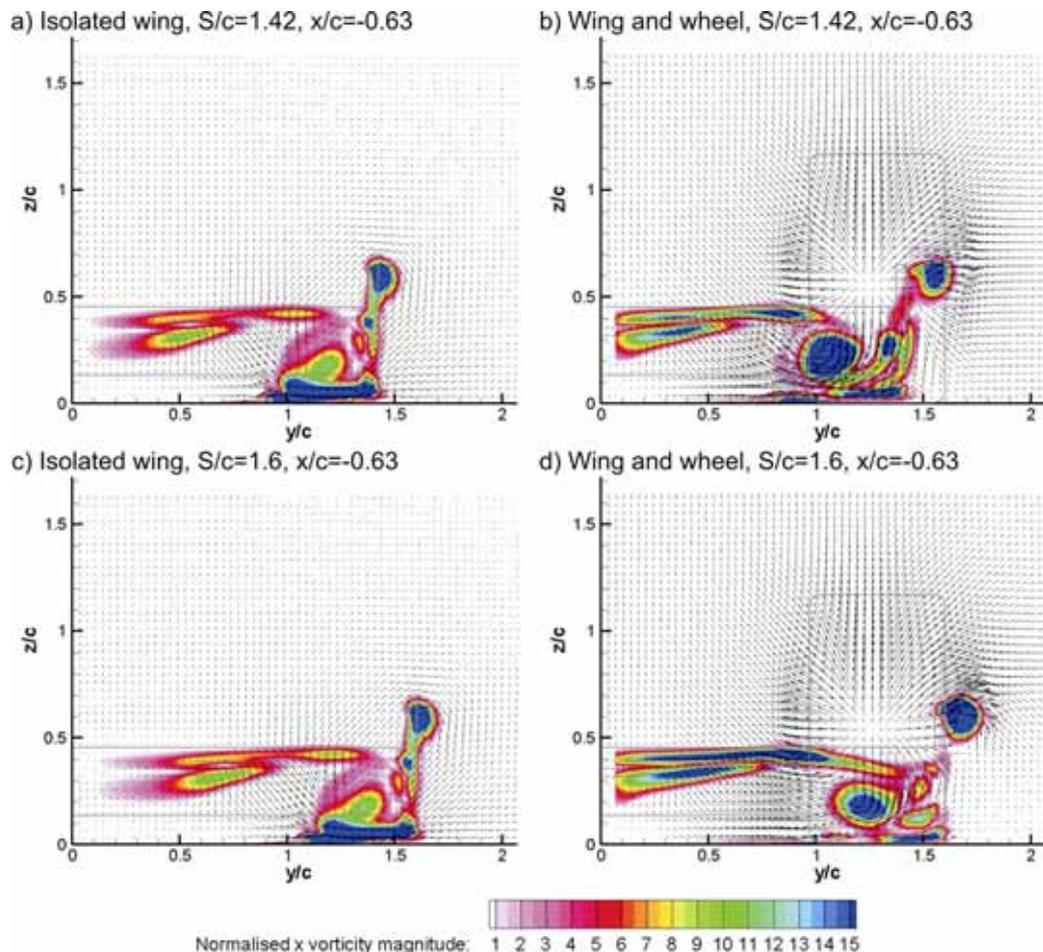


Figure 6.40 Vectors and Vorticity on the $x/c=-0.63$ plane for a wing in isolation and in the presence of a wheel with varied span, $AOA=12^\circ$, $h/c=0.13$ and wheel with $W/c=0.63$, $T/c=1.6$

Figure 6.41 demonstrates that as the span of the wing is increased, the endplate encroaches the area that is occupied by the high pressure region forward of the wheel. This allows the low pressure region generated below the bottom surface of the wing to reduce the strength of the high pressure region ahead of the wheel. For this reason, as the span of the wing is increased, the high pressure region formed ahead of the wheel propagates outboard. Despite this reduction in strength, the variation in position of the high pressure region ahead of the wheel still allows the main wing vortex strength to be increased for a wing in the presence of a wheel relative to the same wing in isolation up to the span value of $S/c=1.42$ (Figure 6.39 and Figure 6.40), but the increase in pressure differential provided to the bottom edge of the endplate becomes less as the span is further increased. As a consequence, the increase in strength that the main wing vortex

experiences for the wing in the presence of the wheel compared to that of the same wing in isolation is less as the span is increased. This is expected to be a contributing factor to explain why the 12° wing in the presence of the wheel produces more downforce than the same wing in isolation not only at a span value of $S/c=0.97$, but up to a value of and including $S/c=1.42$.

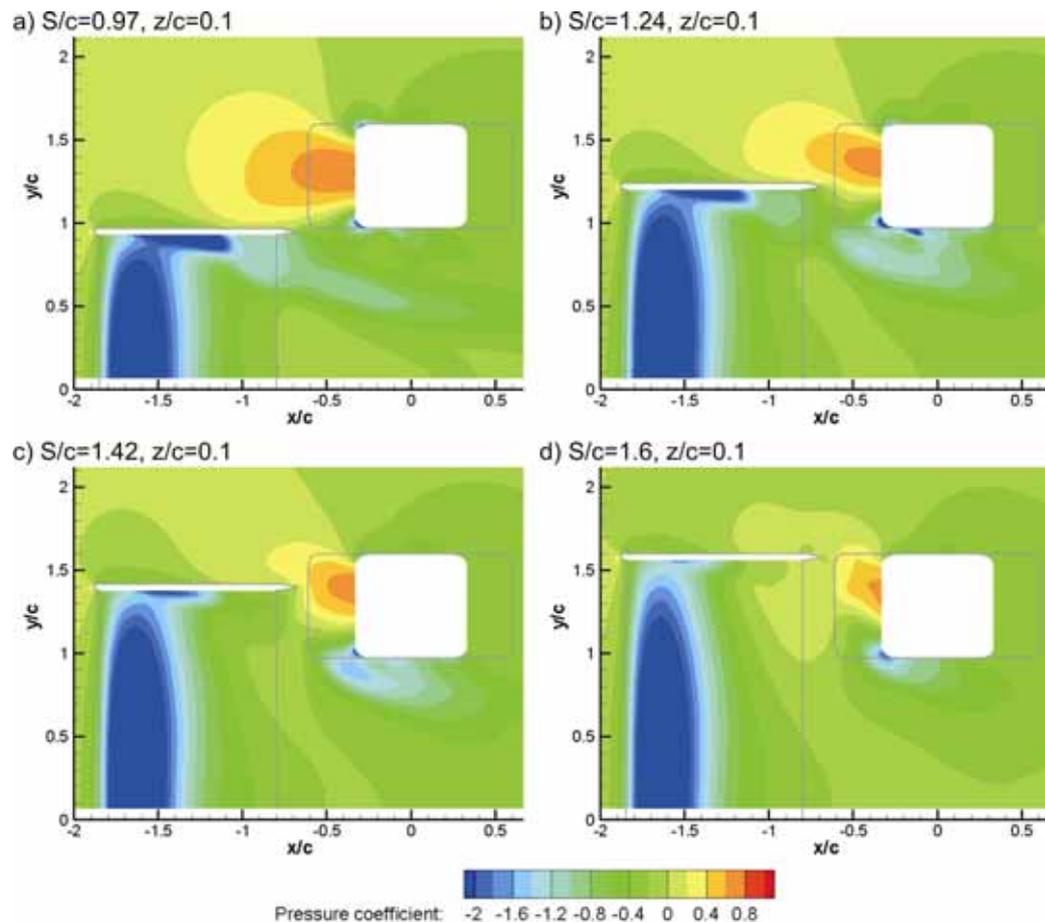


Figure 6.41 Pressure coefficients around endplate on z-planes for a wing and wheel with $W/c=0.63$, $T/c=1.6$, $h/c=0.13$, $AOA=0^\circ$ and varied span

Increasing the span of the wing not only appears to adversely affect the generation of the high pressure region forward of the wheel, but also the ability for the entire bottom surface of the wing to generate suction as previously reported by Thisse (2004). Increases in wing span increases the extent of this interaction explaining why increasing the span of the wing reduces the downforce that a wing can generate in the presence of the wheel relative to the same wing in isolation. The reduced suction being generated at the centre of the wing

will also be expected to improve the adverse pressure gradient experienced by the wing in this region and thus also assist with preventing stall from occurring.

This suggests that as the wing span is increased, the contribution that the main wing vortex has in reducing separation and preventing stall is decreased. Given that the main wing vortex strength also decreases, it would be expected that the reduction in adverse pressure gradient plays a more significant role in reducing separation as the span is increased. Therefore there are two contributing factors to why the wing with an angle of attack of 12° performs better in the presence of the wheel between spans of $S/c=0.97$ and $S/c=1.42$ relative to the same wings in isolation. It should be noted the effect that varying the span has in the presence of a wheel is the opposite of that which was previously reported during the investigation considering the effect that this parameter has on the downforce loss phenomenon for an isolated wing (Sections 5.2). This will be investigated further in Section 6.4 where the downforce loss phenomenon will be investigated for a wing in the presence of a wheel as well.

The results presented thus far indicate that Thisse's (2004) hypothesis that a wing in the presence of the wheel will produce less downforce due to the adverse effect of the high pressure region acting on the bottom surface is only true if two conditions are met. First, the wing in isolation must not be stalled, otherwise the addition of the wheel is likely to assist with the stall being delayed allowing the wing performance to be improved as was the case with the $S/c=0.97$ wing with an angle of attack of 12° , secondly the span is sufficiently large enough to encroach the area where the high pressure region will be able to act on the bottom surface of the wing.

The variations in the static pressures observed forward of the wheel are also expected to contribute to the variations in the lift and drag obtained for a wheel in the presence of a wing in comparison to that of an isolated pair (Figure 6.41). The static pressures around the central circumference of the wheel (Figure 6.42) indicate as the main wing vortex passes the front face of the wheel, a pressure drop is obtained in the region of $15^\circ < \theta < 45^\circ$ for the $S/c=1.6$ and $S/c=1.42$ wings. A similar yet smaller pressure reduction is also observed for the $S/c=1.24$. This is thought to be because the endplate position for this span wing does not allow the main wing vortex to pass the centre of the wheel and therefore the full extent of the pressure drop generated by the vortex is not experienced in

this region. Given that in this region the greatest pressure drop is achieved by the wheel operating in the presence of the $S/c=1.6$ wing, and that this is not the wing that provides the greatest drag or lift reduction to the wheel, the path that the main wing vortex takes about the front face of the wheel would be considered to be a secondary influence. Regardless, the path that the main wing vortex takes for several spans will be further discussed later in this section.

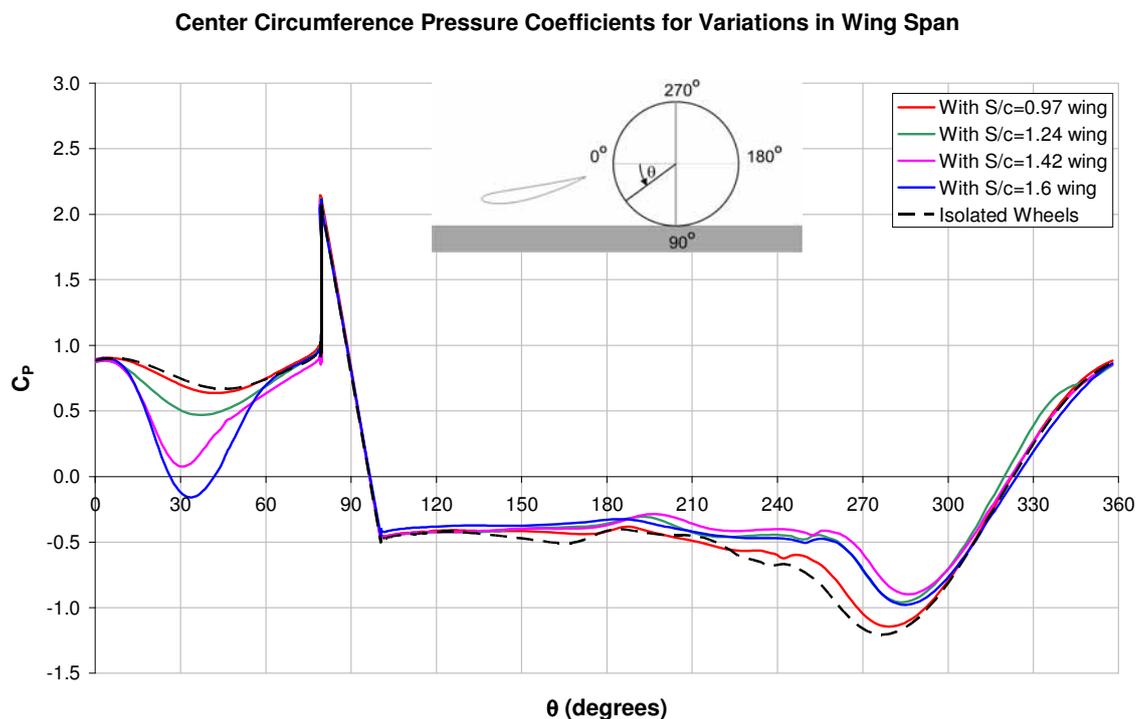


Figure 6.42 Central pressure coefficients obtained for wheel with varied wing span and 12° angle of attack

The one feature that does vary in a manner more representative of the variation in the lift and drag experienced by the wheel in the presence of the wing relative to the same wing in isolation is the wheel tread separation point (Figure 6.42, $240^\circ < \theta < 290^\circ$) and therefore this will be expected to be the most dominant feature for determining the wheel lift and drag. This is again consistent with the previous investigations that have also shown that the wheel tread separation point is the most critical flow feature for determining the wheel lift and drag. The cause for this variation in the separation point during the wing angle of attack investigation was previously explained to be due to an increase in upwash

generated by the wing forward of the wheel for the $S/c=1.6$ span wing while at the $S/c=0.97$ wing span, the interaction with the main wing vortex and the inboard wheel vortex was considered to be the cause for the variations. It is believed that by varying the span of the wing a combination of these features has caused a further reduction in the drag and lift of the wheel further than that which has been previously indicated for a wing with 12° angle of attack at either of the extreme wing spans tested.

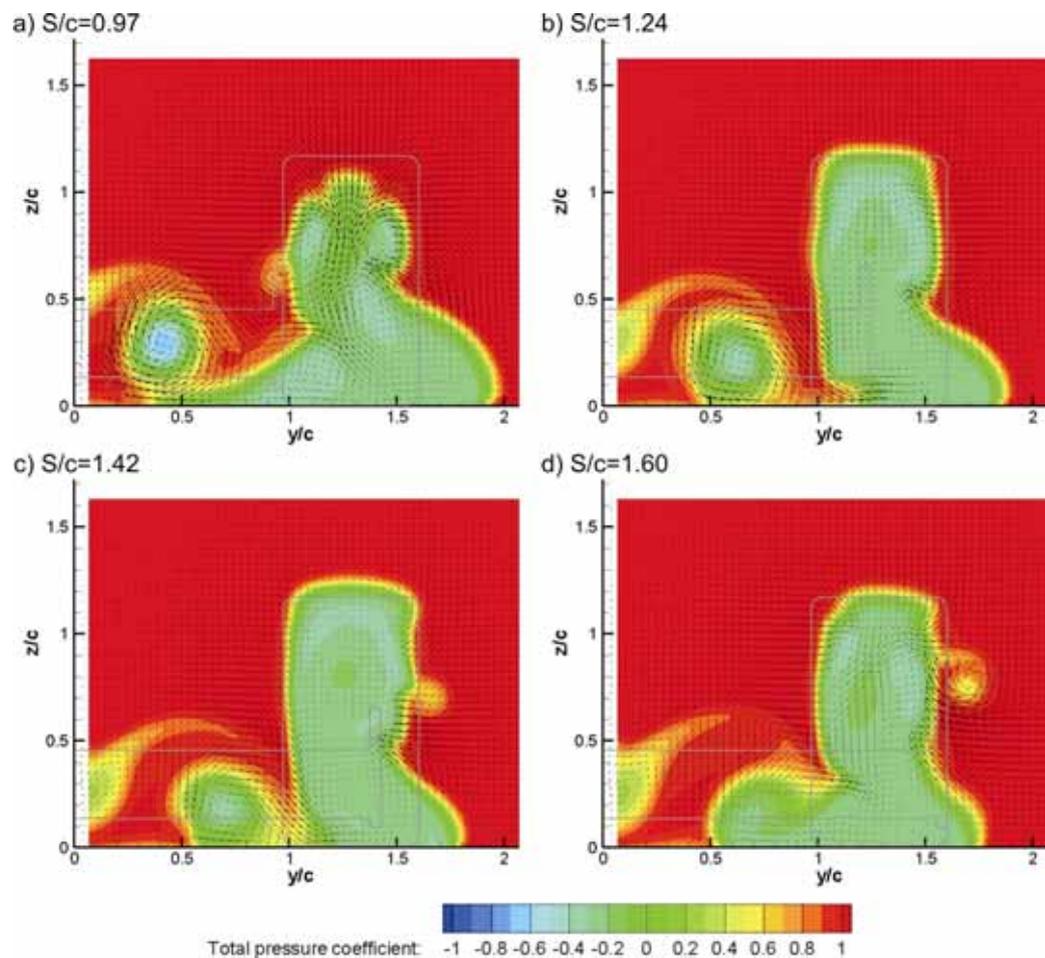


Figure 6.43 Vectors and Total Pressure on $x/c=0.75$ for a wing and wheel with varied span

Consistent with the previous investigations, the total pressure contour plots and vectors on the $x/c=0.75$ plane demonstrate (Figure 6.43) that the tallest and narrowest wheel wake is achieved with the wing that also provides the greatest lift and drag reduction for the wheel. It has already been demonstrated that the endplate position can alter the strength of the main wing vortex, and now it appears that the endplate position can also alter the vortex

position as it passes the inner face of the wheel. Therefore, by adjusting the wing span it has been confirmed that the largest lift and drag reduction of the wheel is achieved when an optimum between three parameters is obtained including; the upwash generated by the wing, the main wing vortex strength and the main wing vortex proximity to the inner wheel face. Previously it has been demonstrated that the main wing vortex can reduce the separation experienced by the inboard wheel shoulder which is required to form the inboard primary wheel vortex (McManus and Zhang, 2006). Reducing this separation also reduces the strength of the primary wheel vortex as previously demonstrated for a wheel working in combination with either the $S/c=0.97$ and the $S/c=1.6$ wings with an angle of attack of 12° . The same has occurred here for the two intermediate steps of span, but the strength of the main wing vortex and its position relative to the wheel has completely prevented the inboard primary wheel vortex from forming with the $S/c=1.24$ and $S/c=1.42$ wings. This occurs because the rotation of the main wing vortex promotes cross flow into the lower wheel wake preventing the inboard shoulder from separating (Figure 6.43b, c $y/c=1$, $z/c=0.2$). For this reason both the strength and relative position of the main wing vortex are sensitive parameters for determining the wheel tread separation point.

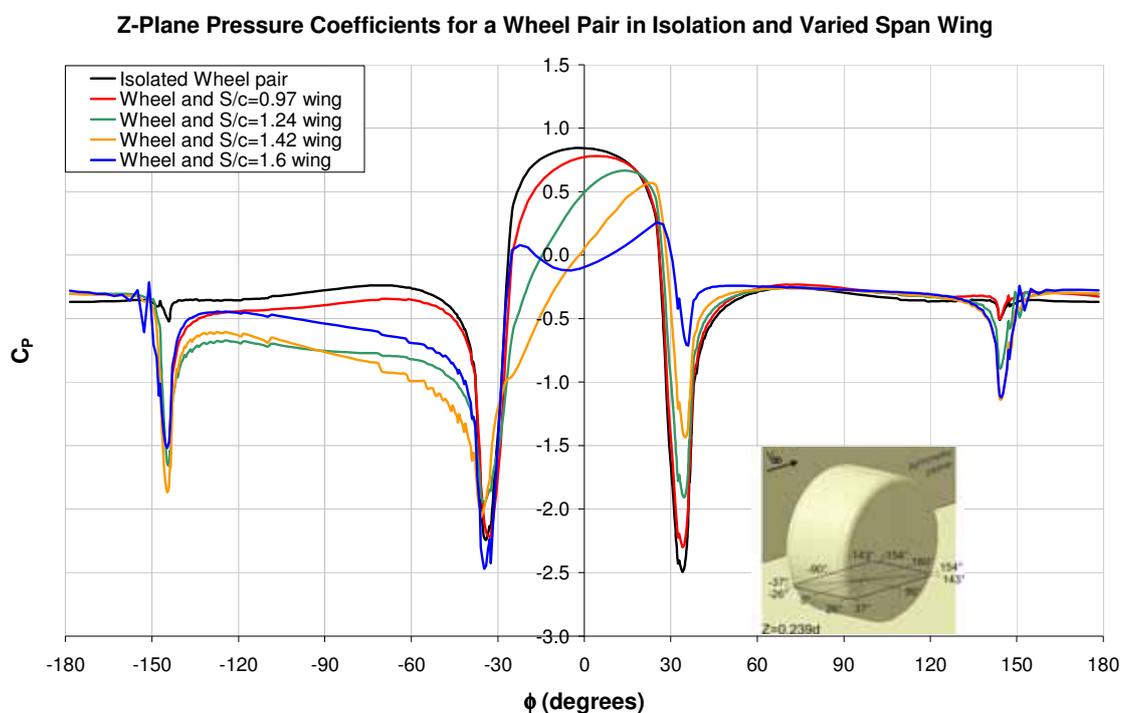


Figure 6.44 Pressure coefficients on wheel at $z/d=0.239$ in isolation and in the presence of a wing with 12° angle of attack and varied span

The side force generated by the wheel is also expected to be influenced by this and this may explain why the side force has followed similar trends as the lift and drag for the wheel. Pressure coefficients taken around the circumference of the intersection of the wheel and the $z/c=0.239$ plane demonstrate that the greatest pressure drop on the inner face is obtained for the wheel in the presence of the $S/c=1.42$ wing (Figure 6.44, $-140^\circ < \phi < -40^\circ$). The variation in the pressure drop obtained in this region for the wheel in the presence of the wings with other spans tested also follow the trend indicated by the side forces. Therefore it is likely that the side force variations for a wheel in the presence of a wing relative to that belonging to an isolated pair is also dependant on the position and strength of the main wing vortex as the pressure drop created in the core of the main wing vortex is expected to act on the inner surface of the wheel creating a force that draws the wheel towards the symmetry plane. Also evident from Figure 6.44 is the variation in the location of the peak pressure forward of the wheel ($-10^\circ < \phi < 30^\circ$) moving outboard as the wing span is increased which is also expected to alter the speed of the flow travelling either side of the wheel. This may also be contributing to the variation in the pressures obtained on either side of the wheel and the side force experienced by the wheel.

6.3.3. Main and secondary wing vortex variations for adjustments of wing span and angle of attack

Thus far, it has been stated that the position of the main wing vortex relative to the wheel is a key cause for the variations in the wheel forces obtained in the presence of a wing. In order to confirm this and to further understand that which alters the position of the main wing vortex, these features have been plotted (Figure 6.45 to Figure 6.48) for all the variations in wing angle of attack and span presented up until this point during this chapter. These figures include both the results for the isolated wing cases (shown as dashed lines) and also those obtained in the presence of a wheel pair (shown as solid lines). The core of the main wing vortex has been defined as the position within the vortex at which on specific x planes, the y and z velocity is equal to zero. The outline of the wing's and endplate's trailing edge, as well as that of the wheel have also been included in these figures to obtain an indication of the main wing vortex position relative to the respective wing and wheel.

Considering the horizontal position of the main wing vortex belonging to an isolated wing with 0° angle of attack and with variations in span (Figure 6.45a), it can be observed that the horizontal displacement towards the symmetry plane of the main wing vortex relative to the endplate increases as the wing span is also increased. For example, the main wing vortex created by the $S/c=0.97$ and the $S/c=1.6$ span wings are located approximately $0.35c$ and $0.61c$ inboard of their respective endplates. This variation is expected to be attributed to the increase cross flow component created in the wake of a wing producing an increase in downforce and is also expected to be a contributing factor for the path that the main wing vortex takes in the presence of the wheel. The vertical position (Figure 6.45a) of the isolated wing vortices remains unchanged for the different spans tested indicating that the upwash generated by these wings is similar.

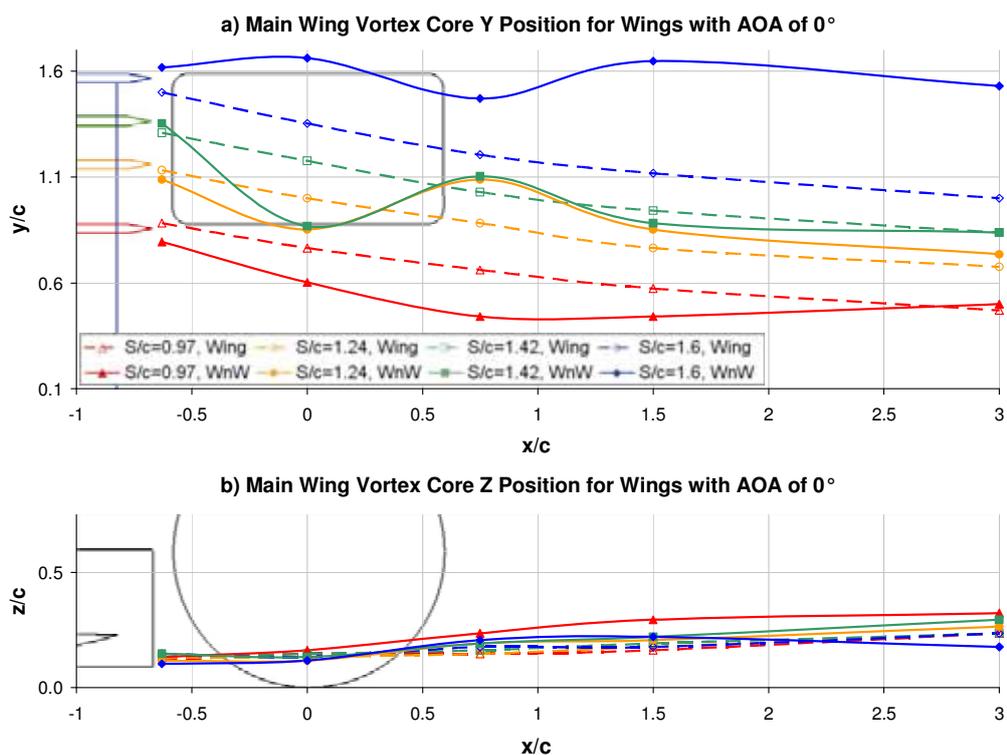


Figure 6.45 Main wing vortex core y (a) and z (b) position for $AOA=0^\circ$ wings in isolation and in the presence of a wheel pair

The main wing vortex that appears least affected by the presence of the wheel belongs to the $S/c=0.97$ span wing. In the presence of the wheel, the main wing vortex from this wing exhibits a shift in position towards the symmetry plane before returning to a similar position

as that of the isolated main wing vortex by the $x/c=3$ plane. While this wing has been shown to produce less downforce in the presence of the wheel in comparison to the same wing in isolation, the more inboard location of the main wing vortex can be attributed to the large cross flow component created forward of the wheel by the jetting action at either side of the contact patch (McManus and Zhang, 2006). While all the main wing vortices belonging to the isolated wing move towards the symmetry plane as they travel downstream, the addition of the wheel not only causes the main wing vortex to travel initially inboard, but once past the wheel centre, the flow entrainment into the wheel wake also causes the main wing vortex to be drawn outboard again. For this reason the final horizontal position of the main wing vortex for the $S/c=0.97$, $S/c=1.24$ and $S/c=1.42$ wings does not differ significantly in comparison to their respective isolated main wing vortex positions by the $x/c=3$ plane. This variation is more pronounced for the $S/c=1.24$ and $S/c=1.42$ wings as the main wing vortex is not only entrained into the wheel wake but also combines with the inboard primary wheel vortex.

A similar effect is experienced by the $S/c=1.6$ main wing vortex in the presence of the wheel but instead of being initially drawn inboard and then outboard the opposite occurs. As already mentioned the endplate for this span wing is located outboard of the high pressure region of the wheel and for this reason the main wing vortex is pushed outboard initially (interaction "a") before being entrained into the wheel wake (or drawn inboard) prior to combining with the outer primary wheel vortex. The same path has been taken by the main wing vortex of the $S/c=1.6$ wing with an angle of attack of 4° (Figure 6.46a) which is also an example of interaction "a". While the main wing vortex has also combined with the outer primary wheel vortex in the wake of the wheel, the position of this vortex relative to the 0° wing case is generally located approximately $0.2c$ more inboard. This is expected to be as a result of the increased cross component created by the increased wing angle of attack drawing the entire wheel wake towards the symmetry plane.

Comparing the isolated wing results obtained with an increase in wing angle of attack of 4° indicates that the increased inboard cross component has also caused the main wing vortex to travel further inboard. The extent of this variation is between $0.1c$ and $0.15c$ with the greater difference being obtained with the larger span wing at the $x/c=3$ plane. Once again the vertical position of the main wing vortex remains unchanged amongst the different wing spans tested at this angle of attack but the vertical position was measured to

have raised slightly by $0.05c$ in comparison to the 0° wing angle of attack at the $x/c=3$ plane (Figure 6.46b) which would be expected to be caused by an increase in upwash associated with the increase in angle of attack.

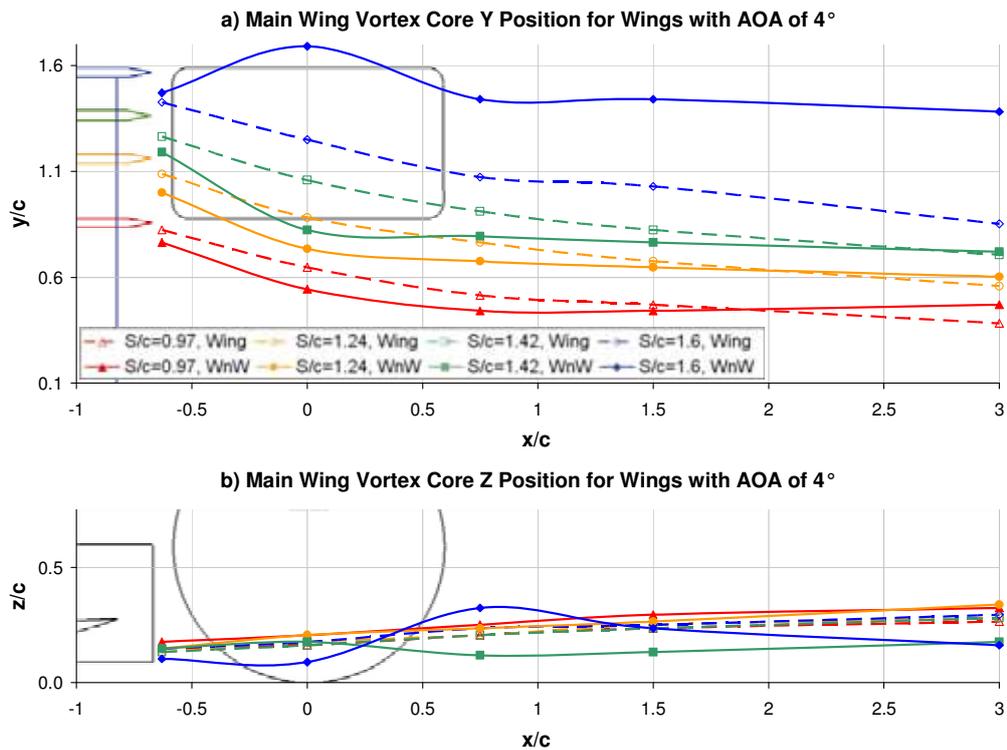


Figure 6.46 Main wing vortex core y (a) and z (b) position for AOA= 4° wings in isolation and in the presence of a wheel pair

Another variation observed with an increase in wing angle of attack of 4° is the more constant path taken by the main wing vortices for the $S/c=1.24$ and $S/c=1.42$ wings once the main wing vortex has past the wheel. Comparing the main wing vortex horizontal position for the two intermediate span wings at the $x/c=0$ plane to that obtained with a wing angle of attack of 0° (Figure 6.45a) indicates that the horizontal displacement of the main wing vortex due to the 4° increase in angle of attack is $0.15c$ and $0.08c$ for the $S/c=1.24$ and $S/c=1.42$ wings respectively. As a consequence, the main wing vortex is now positioned adequately far enough inboard, preventing it from being entrained into the wheel wake and subsequently continues to travel downstream alongside the lower wheel wake. A further shift in the same direction has been obtained with an additional increase in the wing angle of attack of 4° (Figure 6.47a). Relative to the corresponding span wings in

the presence of the wheel with an angle of attack of 0° , the translation of the main wing vortex was determined to be $0.25c$ and $0.1c$ for the $S/c=1.24$ and $S/c=1.42$ wings respectively. Once again, once past the rear of the wheel, the main wing vortex travels downstream on a path almost parallel to the symmetry plane while the main wing vortices belonging to the isolated wings continue to travel further inboard in comparison to the lower angle of attack wings in isolation.

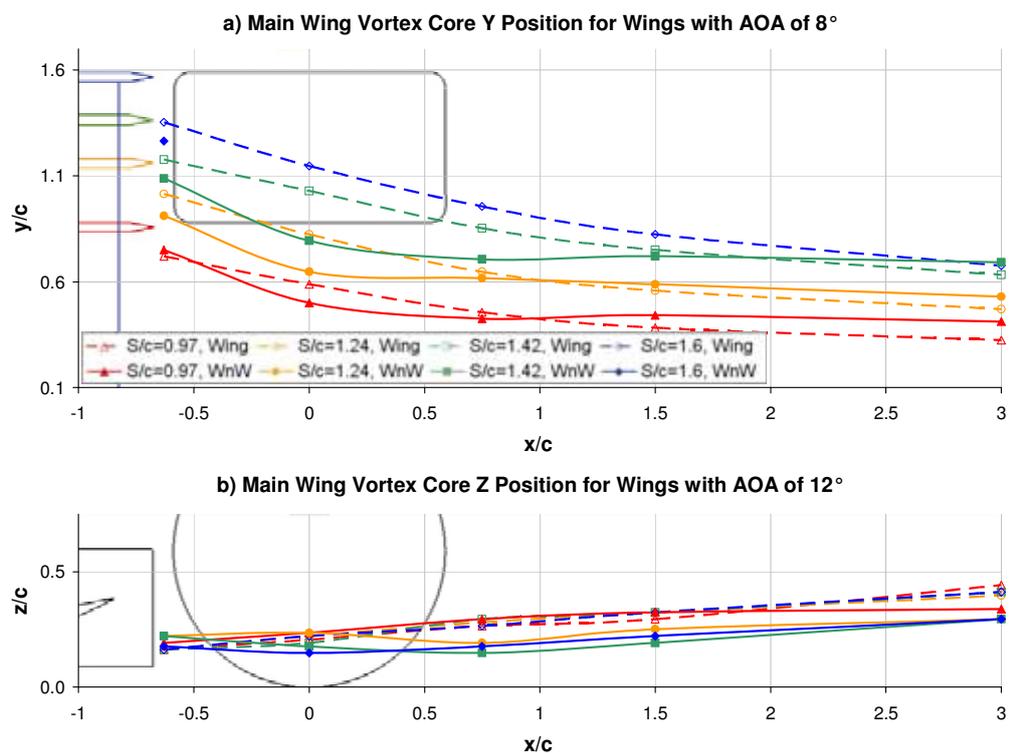


Figure 6.47 Main wing vortex core y (a) and z (b) position for $AOA=0^\circ$ wings in isolation and in the presence of a wheel pair

Also of significance is the switch that the main wing vortex undergoes at this angle of attack for the $S/c=1.6$ wing. It was previously reported in Section 6.2 that increasing the angle of attack causes this switch to occur, but while the suction generated beneath the wing is adequate to draw it inboard, the main wing vortex does not manage to travel across the face of the wheel before becoming trapped in the contact patch of the wheel. Due to this phenomenon, the main wing vortex does not propagate further downstream. This would suggest that there is a condition between interaction “a” and “b” where the main wing vortex does not pass either side of the wheel as it becomes trapped in the

wheel's contact patch and this will be discussed in greater detail during the downforce loss phenomenon investigation proceeding in Section 6.4. A further increase of 4° in the wing angle of attack was found to be adequate to draw the main wing vortex around the face of the wheel (Figure 6.48a) and as a result is positioned in a similar location on the $x/c=0$ plane to that obtained for the $S/c=1.24$ and $S/c=1.42$ wings with 0° angle of attack (Figure 6.45a). As a result, the main wing vortex in this case is also drawn into the wheel wake while the main wing vortex for the shorter span wings continue on a path almost parallel to the symmetry plane. It should also be noted that all the examples shown here where the main wing vortex travels along the inboard face of the wheel also corresponds to some degree with the wings that provide the greatest reduction in lift and drag for the wheel (Figure 6.33).

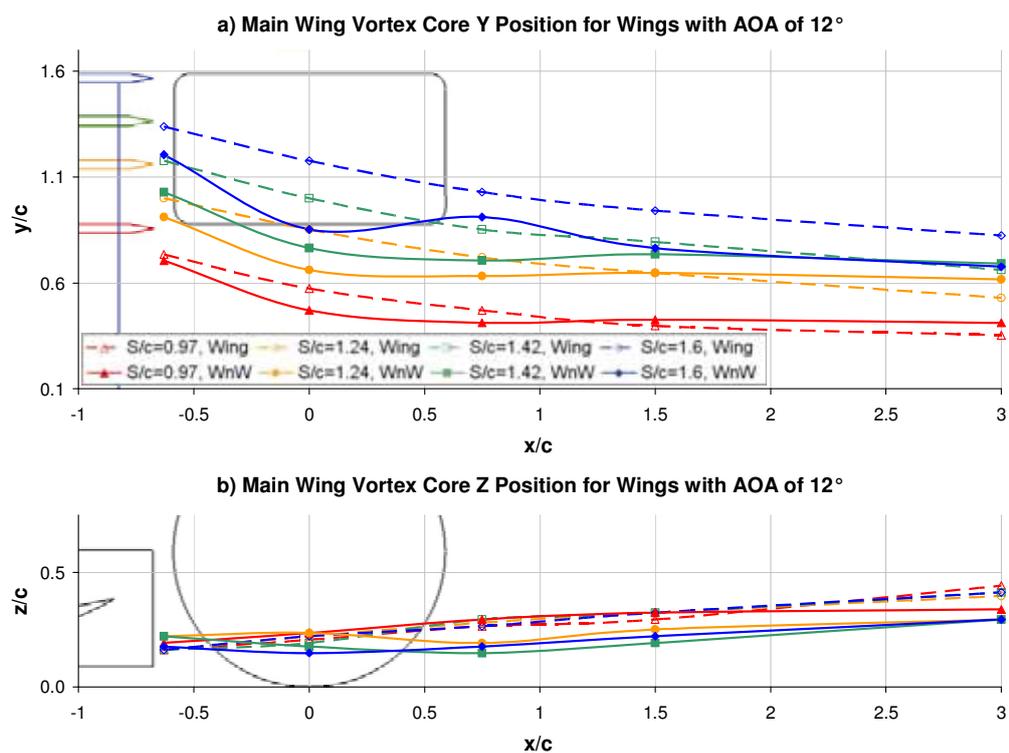


Figure 6.48 Main wing vortex core y (a) and z (b) position for AOA= 0° wings in isolation and in the presence of a wheel pair

Consistent with the observations made between the transition between the 0° and 4° angle of attack wings, the subsequent increases in the angle of attack also caused the main wing vortices to travel further inboard and higher regardless if the wheel was present or not for

the 8° and 12° wing angle of attack cases. Despite this, the core of the $S/c=0.97$ main wing vortex in the presence of the wheel at no stage was positioned less than $0.4c$ from the symmetry plane for any given longitudinal position. Reviewing the vectors located on a plane located at $x/c=0.75$ (Figure 6.43a) indicates that this value corresponds to the radius of the main wing vortex produced by the 12° wing in the presence of the wheel and therefore the size is a possible explanation for why the main wing vortex is unable to travel closer to the symmetry plane than that which has been indicated here. This differs for the same wing in isolation as the main wing vortex generated in this case has been demonstrated to be smaller in diameter and for this reason it can travel closer to the symmetry plane.

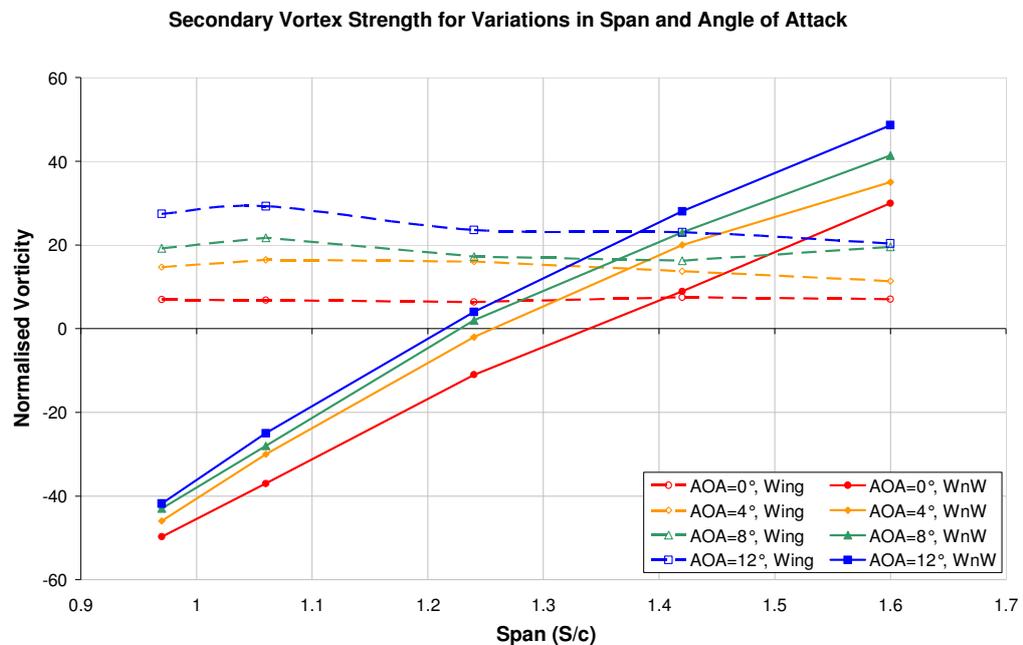


Figure 6.49 Secondary wing vortex strength for wings in isolation and in the presence of a wheel a pair

While the position of the main wing vortex relative to the wheel is the main distinguishing feature for determining if interaction “a” or “b” has been obtained by a wing and wheel combination, the direction of the secondary wing vortex determines when the switch occurs from interaction “b” to “c”. The secondary vortex is considered in order to confirm at which point the switch occurs between these two interactions. Figure 6.49 includes the x-vorticity of the secondary wing vortex for an isolated wing (dashed lines) and for that in the

presence of the wheel (solid lines). Positive x-vorticity indicates that the secondary wing vortex is rotating in the same direction as the main wing vortex. As has been stated previously, for all angles of attacks and spans tested, the isolated wing produces a secondary vortex that rotates in the same direction as the main wing vortex with its strength varying with changes in angle of attack and not span. The results presented here also confirm the statements made earlier linking the formation of the secondary vortex to the position of the endplate relative to the stagnation region obtained forward of the wheel. This is also the primary factor in determining the strength of the secondary vortex for a wing in the presence of the wheel while the angle of attack is secondary. Therefore, Table 6.1 can be considered a summary of which interaction will be obtained for the different combinations of wing angle of attack and span presented thus far. These results have been obtained with a wing with height $h/c=0.13$ and in the presence of a wheel pair with wheel track and width of $T/c=1.6$ and $W/c=0.631$.

	$S/c=0.97$	$S/c=1.06$	$S/c=1.24$	$S/c=1.42$	$S/c=1.6$
AOA=0°	c	c	c	b	a
AOA=4°	c	c	b/c	b	a
AOA=8°	c	c	b/c	b	a/b
AOA=12°	c	c	b	b	b

Table 6.1 Interaction types obtained for a wheel pair configuration of $W/c=0.63$, $T/c=1.6$

6.4. Wing Downforce loss Phenomenon in the Presence of a Wheel and Other Effects Due to Variations in Wing Height

During the previous investigations of the wing and wheel interaction, two variations observed related to the wing when placed in the presence of the wheel have included a change in the downforce produced by the wing and also the strength of the main wing vortex. Albeit with a different aerofoil profile, the previous isolated investigation into the effect that the span has on the downforce loss phenomenon indicated that both these features influence the height at which the maximum lift is obtained at. It would be expected then that the presence of the wheel will also vary the height at which the wing experiences the downforce loss phenomenon at.

Results were obtained at two different spans ($S/c=0.97$ and $S/c=1.6$) in isolation and in the presence of the wheel for a height range of $h/c=0.08$ to $h/c=0.27$. Results that included the

wheel used the same wheel configuration as previously reported combined wing and wheel investigations ($W/c=0.63$ and $T/c=1.6$). Also consistent with the previous wing and wheel investigations, the NACA 4412 profiled wing was used for this investigation with the angle of attack maintained at a value of 4° . This angle was chosen as it was anticipated that the downforce loss phenomenon will be observed within the height range that would be tested for two different span isolated wings and that if a lower angle of attack was used, the downforce loss phenomenon would be expected to occur at a lower height (Zerihan, 2001) than that which could be tested with this computational model.

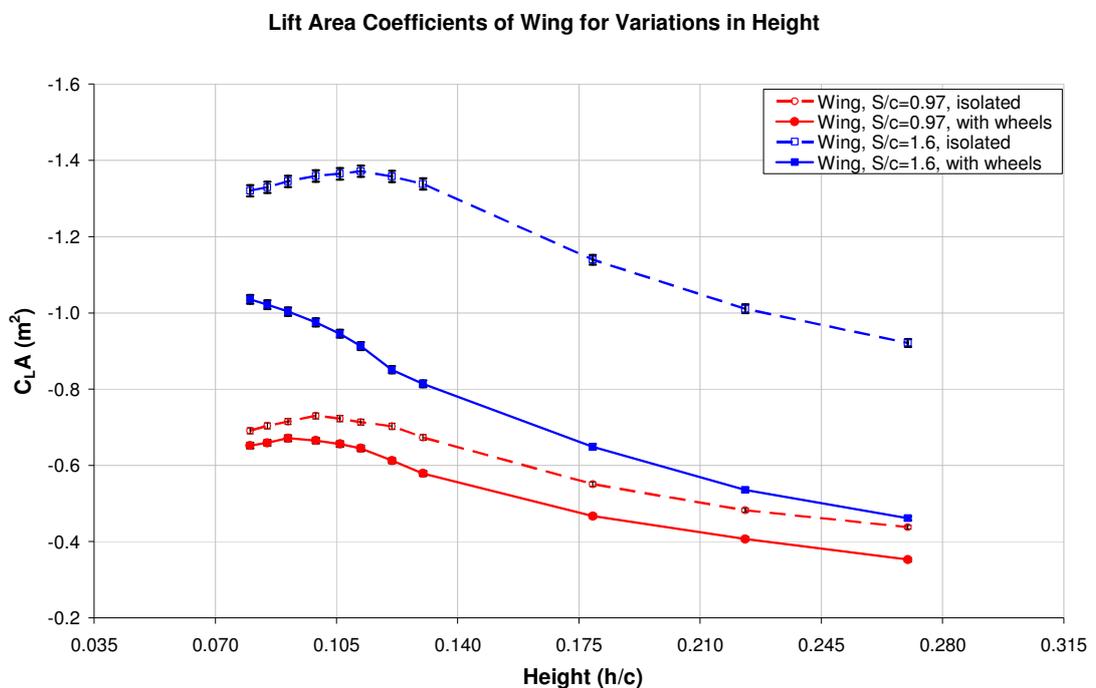


Figure 6.50 Wing lift results for variations in height for wings of two different spans in isolation and also in the presence of a wheel pair ($W/c=0.63$, $T/c=1.6$)

Considering the lift coefficient area (Figure 6.50) for the two different span wings in isolation (dashed lines) indicates that the downforce loss phenomenon for the NACA4412 profile wing has reacted in a similar manner to the Tyrrell profile wing used during the investigation considering the effect that the span has on the downforce loss phenomenon (Section 5.2). Reducing the span from $S/c=1.6$ to $S/c=0.97$ has resulted in the height at which the downforce loss phenomenon occurs at being reduced from $h/c=0.112$ to $h/c=0.099$. Of greater significance is the height at which the downforce loss phenomenon

occurs at in the presence of the wheel for the two different spans tested here (Figure 6.50 solid lines). The presence of the wheel for the $S/c=0.97$ wing resulted in the height at which the downforce loss phenomenon occurring at being reduced from $h/c=0.099$ to $h/c=0.091$ while the $S/c=1.6$ wing resulted in a more significant step with the height varying from $h/c=0.112$ to a value less than the smallest height that could be tested with the computational model ($h/c<0.08$). This also indicates that the trend between the wing span and the height at which the downforce loss phenomenon occurs at is reversed in the presence of a wheel.

Consistent with the previous combined wing and wheel investigations, the downforce produced by the $S/c=1.6$ wing in the presence of the wheel is always less than that of the same wing in isolation. A 54% reduction in downforce was obtained at the largest height ($h/c=0.270$) tested and this gradually reduced to a 22% loss in downforce at the smallest height tested ($h/c=0.08$). A similar trend was also obtained for the $S/c=0.97$ wing in the presence of the wheel losing between 6% and 20% of the downforce produced by the same wing in isolation.

From the results presented thus far, it would be expected that the reduction in height at which the downforce loss phenomenon occurs at for the $S/c=1.6$ wing would be due to the lower levels of suction produced beneath the wing in the presence of the wheel causing a subsequent reduction in the adverse pressure gradient obtained at the wing centre. As a result, the separation that would usually be expected to occur beneath the wing is expected to be delayed and obtained at lower ride heights. This will be confirmed during a more detailed discussion of the $S/c=1.6$ wing results that will follow. The $S/c=0.97$ wing is likely to be experiencing a similar phenomenon, but another possibility for the delay in the height at which the downforce loss phenomenon occurs at could be a stronger main wing vortex which was outlined in Section 6.1.3. It has already been demonstrated that in the presence of the wheel, this span wing produces a stronger main wing vortex and this may be assisting with alleviating the separation experienced by the bottom surface of the wing.

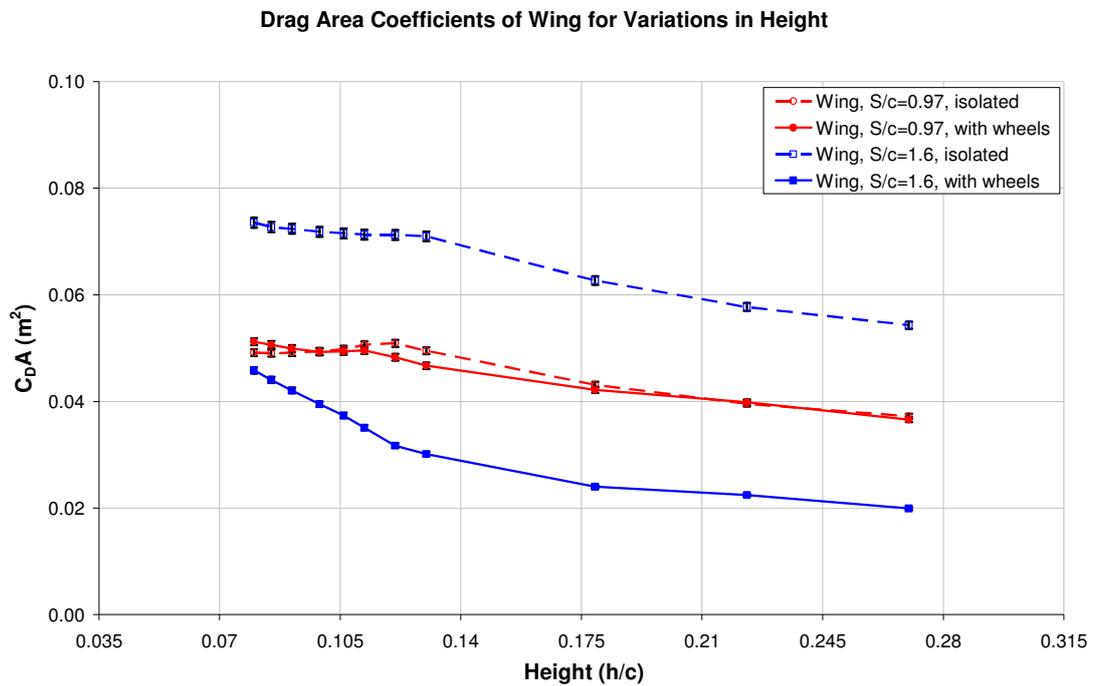


Figure 6.51 Wing drag results for variations in height for wings of two different spans in isolation and also in the presence of a wheel pair (W/c=0.63, T/c=1.6)

The variation in the wing drag results (Figure 6.51) are consistent with those obtained previously for a wing in the presence of the wheel. No significant variation was obtained in the wing drag for the range of heights tested with the S/c=0.97 wing when the wheel was added. The S/c=1.6 wing on the other hand experienced significant reductions in drag across the entire range tested which varied from 38% to 66%. The reduction in drag obtained for the S/c=1.6 wing in the presence of the wheel is once again expected to be due to the high pressure region that is obtained forward of the wheel acting on the bottom surface of the wing as originally indicated in Section 6.1.1. For the same reason, it is expected that the S/c=0.97 wing does not experience a significant drag variation as no portion of the wing overlaps the wheel for the high pressure regions generated forward of the wheel to act upon.

Lift and Drag Area Coefficients of Wheel for Variations in Wing Height

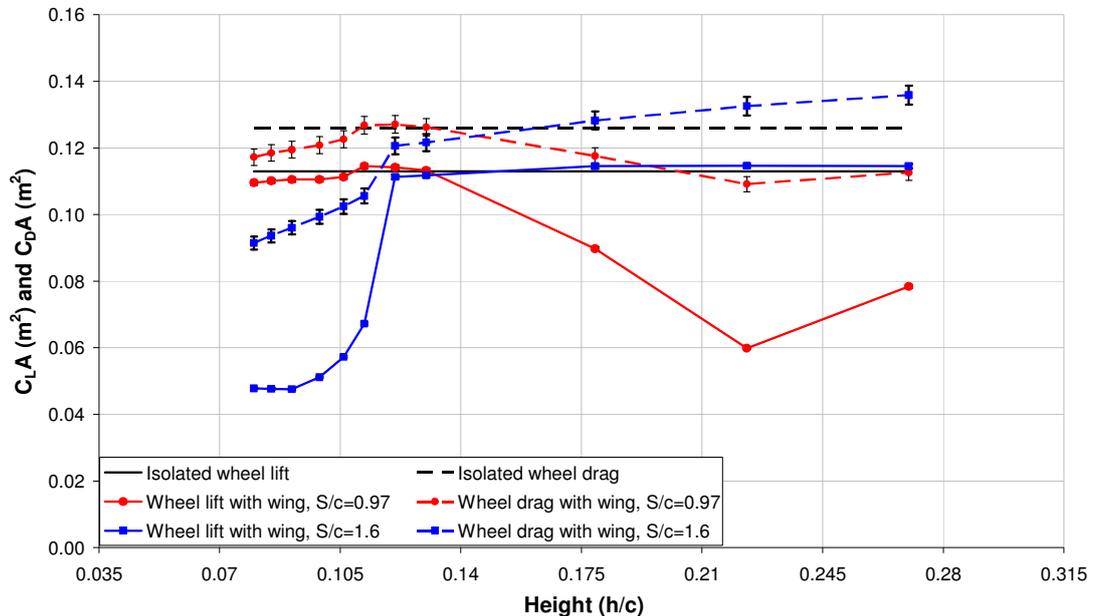


Figure 6.52 Wheel lift and drag results for variations in wing height for two different spans in isolation and also in the presence of a wheel pair ($W/c=0.63$, $T/c=1.6$)

Considering the lift and drag of the wheel in the presence of the wing also shows some strong trends associated with changes in the wing height for each span wing (Figure 6.52). The $S/c=1.6$ wing between the height range of $h/c=0.121$ and $h/c=0.27$ indicates little variation in both the lift and drag of the wheel. At heights below $h/c=0.121$, both the lift and the drag of the wheel experience reductions in lift and drag of up to 58% and 27% respectively. The change in the trend below and above $h/c=0.121$ suggests that two different wing and wheel interactions may be occurring within these ranges. For example, at a height and angle of attack of $h/c=0.13$ and 4° , it has already been demonstrated that the main wing vortex travels outboard of the wheel (interaction a) while increases in wing angle of attack can increase the suction generated beneath the wing such that the main wing vortex is drawn inboard of the wheel (interaction b). The second of these two interactions have consistently resulted in a reduction in wheel lift and drag while the first has had little influence on the lift and drag of the wheel (Figure 6.16). Both these trends appear to be reproduced by the results above and below a height value of $h/c=0.121$. Therefore, it is expected that by reducing the height of the wing, the suction generated beneath the wing increases to the extent where the main wing vortex switches from

travelling outboard of the wheel to inboard at a height value of approximately $h/c=0.121$. This will also be investigated further in the more detailed discussion of the $S/c=1.6$ wing result that will follow.

The opposite trend was obtained with the $S/c=0.97$ wing with the lift and drag of the wheel being reduced as the height of the wing was increased. This is expected to be caused by a variation in the position of the main wing vortex relative to the wheel. During the span investigation undertaken with a combined wing and wheel, it was shown that the most significant lift and drag reductions are obtained when the main wing vortex is positioned adjacent to the inboard face of the wheel. While the span has been maintained here, it is expected that the main wing vortex will be positioned further outboard as it travels downstream as the height of the wing is increased and the downforce that it produces is reduced. It would therefore be expected that a similar interaction will be achieved with the main wing vortex and the wheel wake as that observed while changing the wing span when the height of the wing is varied.

Increases in the height of the $S/c=0.97$ wing have also increased the side force (Figure 6.53) acting on the wheel in a consistent manner as that of the lift and drag for the same span wing. When in the presence of the wings with the two greatest heights tested, each wheel experiences a force opposite and four times greater than that experienced by each wheel belonging to an isolated pair. The side force following the same trends as the lift and drag forces has been previously seen during the wing span investigation where the variation of the main wing vortex position was also demonstrated to be responsible for the changes obtained in the wheel forces. Therefore, the position and the variation in the main wing vortex will be investigated in greater detail in Section 6.4.1 focussing solely on the results obtained with the $S/c=0.97$ wing.

For the $S/c=1.6$ wing, the wheel side force also indicates two distinct trends below and above the wing height value of $h/c=0.112$ consistent with the lift and drag forces obtained for a wheel in the presence of the same wing. Above this height the side force is close to 0 and does not vary significantly. Below a height of 0.112, the side force of the wheels approaches that experienced by each wheel belonging to an isolated pair up until a height of 0.099. At further reduced heights, the wheel side force once again changes direction in comparison to that experienced by a wheel belonging to an isolated pair. It is expected

that the side force is also being influenced by the position that the main wing vortex takes around the wheel and will therefore be discussed further in Section 6.4.2 dedicated to the $S/c=1.6$ wing in the presence of the wheel.

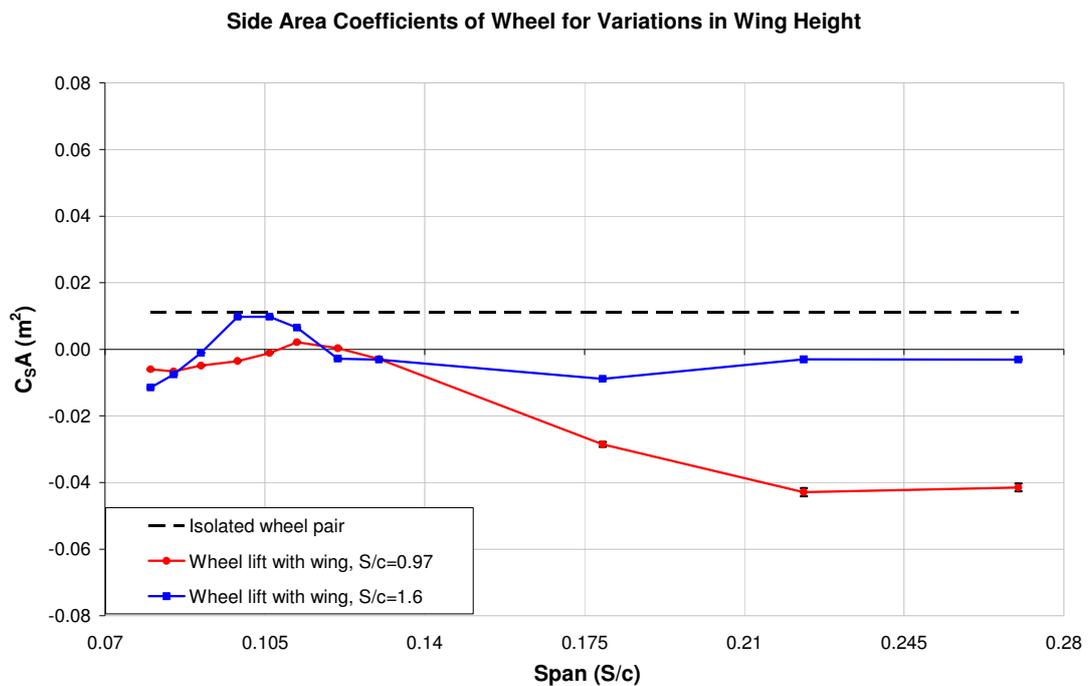


Figure 6.53 Side force results for variations in wing height for two different spans in isolation and also in the presence of a wheel pair ($W/c=0.63$, $T/c=1.6$)

6.4.1. Downforce loss phenomenon for $S/c=0.97$ wing in the presence of a wheel

During the combined wing and wheel investigation considering the effect of changing the angle of attack of the $S/c=0.97$ wing, it was demonstrated that the inclusion of the wheel allows the stall of the wing to be delayed (Figure 6.14). This was later shown to be due to a combination of a stronger wing tip vortex and a reduced adverse pressure gradient experienced by the bottom surface of the wing delaying the separation experienced by the wing and subsequently the angle of attack at which stall occurred at. In order to determine if the same mechanisms are responsible for the variation in the height at which the downforce loss phenomenon occurs at, the wall shear stress and the span wise pressure coefficients were plotted for the $S/c=0.97$ wing in isolation and combined with a wheel at

several different heights within the range that the downforce loss phenomenon was indicated to occur at (Figure 6.58).

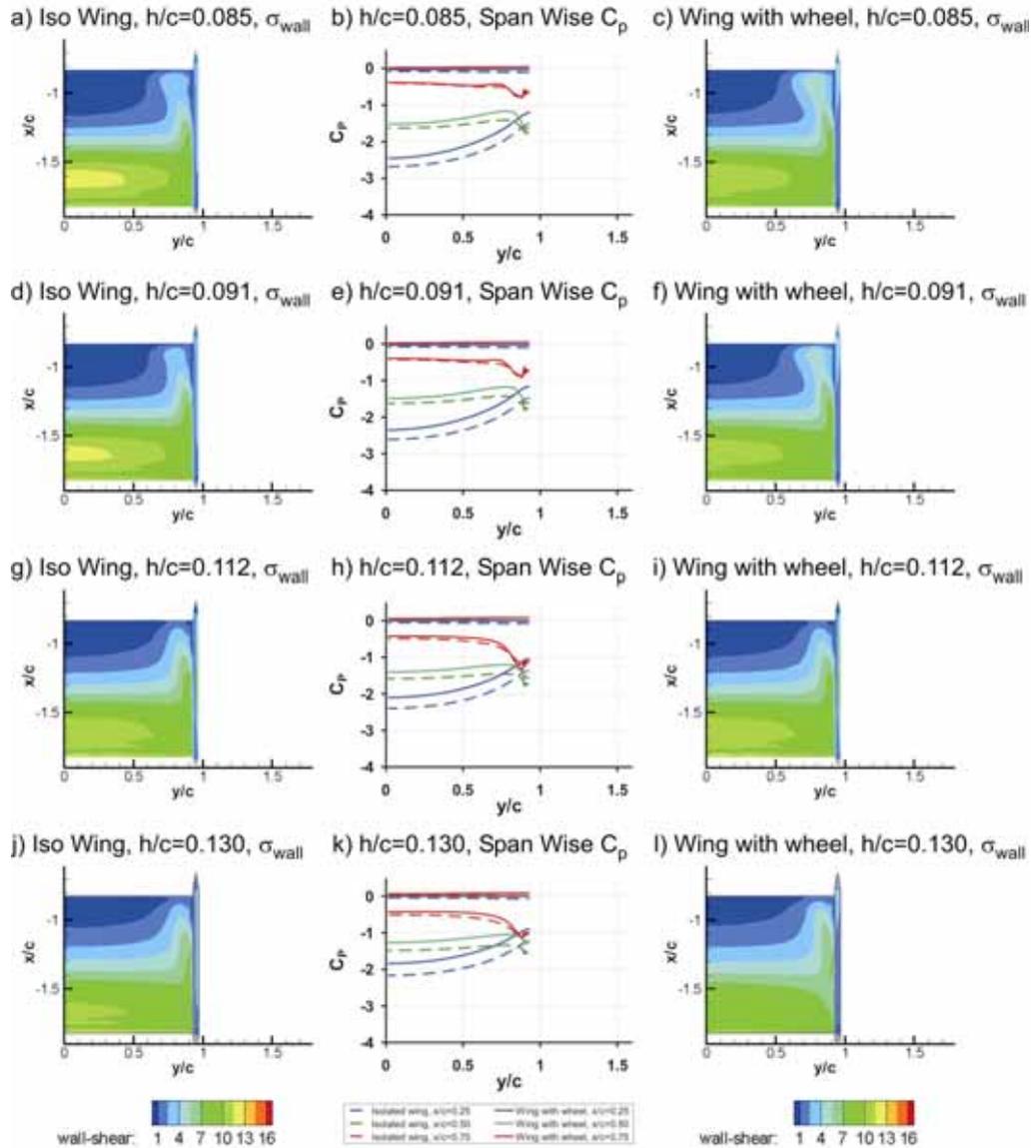


Figure 6.54 Wall shear stress and spanwise pressure distribution for variations in height for a wing with span $S/c=0.97$

Comparing the wall shear stress of the isolated wing (Figure 6.54a, d, g and j) to that of the wing in the presence of a wheel (Figure 6.54c, f, i, l) for the heights $h/c=0.085, 0.091, 0.112$ and 0.13 , an increase in shear stress has been obtained at the wing tip indicating

that a stronger main wing vortex has been obtained by the wing in the presence of the wheel. Despite this, no significant variation has been indicated by the span wise pressure coefficients between the isolated wings and those in the presence of the wheel in the corresponding region (Figure 6.54b, e, h and k). As should be expected due to the consistently lower downforce values obtained, the suction generated in the centre of the wing in isolation was always greater than that of the same wing in the presence of the wheel suggesting then that the cause for the delayed height at which the downforce loss phenomenon occurred at for this span wing is more likely to be due to the reduced adverse pressure gradient experienced at the wing centre. While it is evident for the examples given here that the increase in the main wing vortex strength has had little influence on the height at which the downforce loss phenomenon occurs at, the author believes that if this investigation was repeated with the wing at an angle of attack of 10° or greater, the main wing vortex would play a more significant role as it was demonstrated during the previous investigation varying the angle of attack of the $S/c=0.97$ wing.

During the previous investigations, it has also been demonstrated that the main wing vortex and the path that it takes can influence the aerodynamic performance of the wheel. Therefore, it was considered important to understand how the main wing vortex varies in size and position for adjustments in the height of the wing. Figure 6.55 includes the in plane velocity vectors and the x-vorticity for four different height wings on an x-plane located between the wing and the wheel ($x/c=-0.63$) in order to obtain some indication of this. As expected, these results indicate that reducing the height of the wing increases the strength of the main wing vortex (Figure 6.55, $y/c=0.8$, $z/c=0.2$) up until the height at which the maximum downforce is obtained ($h/c=0.91$) consistent with that which Zerihan had described for an isolated wing (2000). He also indicated that at heights below the height at which the maximum downforce is obtained, the main wing vortex “bursts” and this feature is also indicated by the incoherent vortex structure obtained for the wing with height of $h/c=0.085$ (Figure 6.55a). At the $x/c=-0.63$ plane, no significant variation has been obtained in the horizontal position of the main or secondary wing vortices, but the vertical position of the both these flow structures have been translated such that their relative position to the wing remains unchanged. This is not surprising given that both vortices form from either the top or bottom edges of the endplate which has also been translated with the wing when the height has been changed.

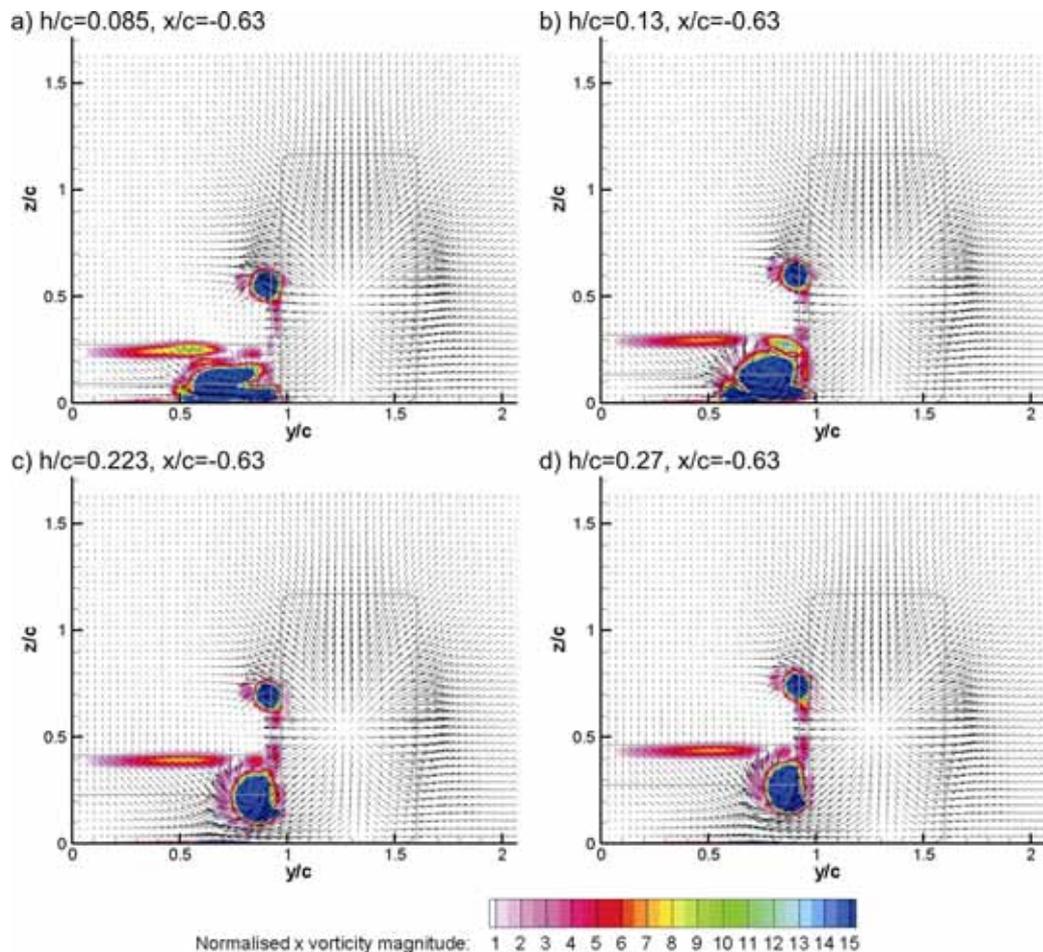


Figure 6.55 Vectors and Vorticity on x-planes for a wing wheel with $W/c=0.63$, $T/c=1.6$, $S/c=0.97c$ and $AOA=4^\circ$

Reductions in the size of the secondary wing vortex have also been obtained with an increase in wing height. Given that for this span it has already been demonstrated that the secondary wing vortex is rotating in an opposite direction to that of the same wing in isolation due to the high pressure created outboard of the endplates upper edge by the stagnation region forward of the wheel, it is expected the reduction of the secondary vortex with increases in wing height are due to the upper endplate edge being translated away from the stagnation region forward of the wheel. The secondary vortex up until this stage has had no significant influence on the wheel wake and therefore the focus will return to the main wing vortex position further downstream.

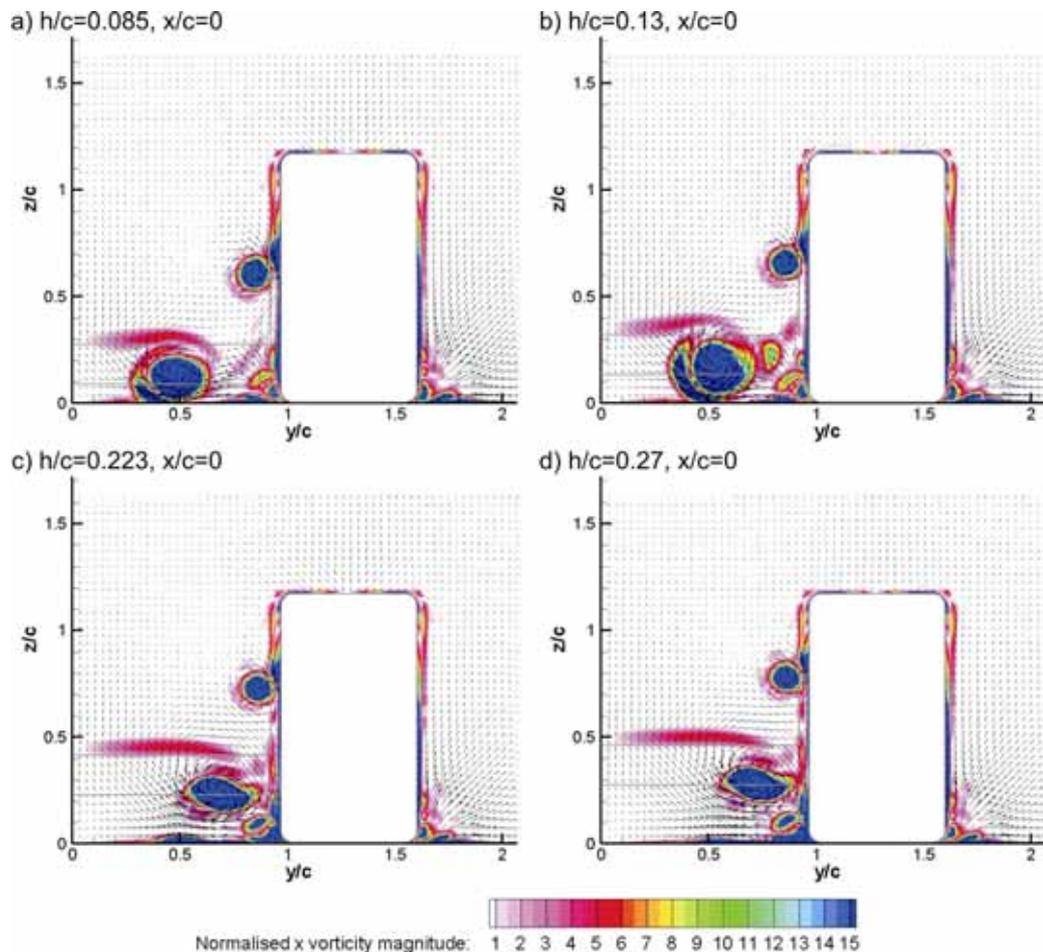


Figure 6.56 Vectors and Vorticity on x-planes for a wing wheel with $W/c=0.63$, $T/c=1.6$, $S/c=0.97c$ and $AOA=4^\circ$

When considering the x-vorticity and in plane velocity vectors for an x-plane located in line with the wheel centre (Figure 6.56), a better indication is obtained for the variation in the horizontal position of the main wing vortex relative to the inner face of the wheel. At wing heights of $h/c=0.085$, $h/c=0.13$, $h/c=0.223$ and $h/c=0.27$, the horizontal position of the main wing vortex core is located at $y/c=0.5$, $y/c=0.6$, $y/c=0.8$ and $y/c=0.8$ respectively. The variation in horizontal position of the main wing vortex with changes in wing height is consistent with what was assumed during the discussion of the trends obtained of the wheel lift, drag and side force in the presence of the wheel. Increasing the height of the wing reduces the horizontal translation that the main wing vortex undergoes as it travels downstream and therefore a similar interaction is obtained with the wheel wake as that of a wing with increased span. This can also be confirmed by considering the total pressure

and the in plane velocity vectors located on a plane located at $x/c=0.75$ downstream of the wheel and within its wake (Figure 6.57).

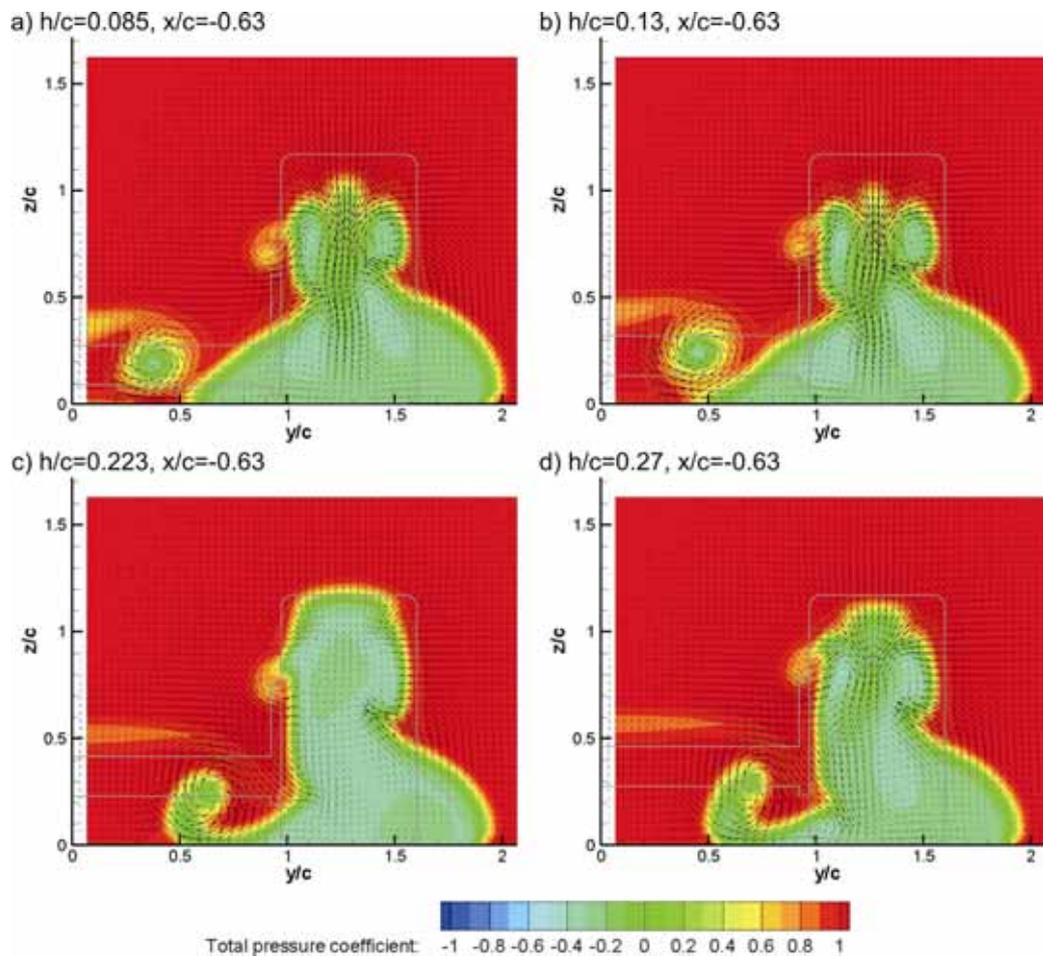


Figure 6.57 Vectors and Total Pressure on x-planes for a wing and wheel with $W/c=0.63$, $T/c=1.6$, $S/c=0.97c$ and $AOA=4^\circ$

Previously it has been shown that reductions in lift and drag can be obtained for a wheel by reducing the primary wheel vortex strength that also reduces the downwash generated in the centre of the wheel wake and subsequently shifts the wheel tread separation point forward. This is the effect that the main wing vortex has when it is positioned closer to the inner face of the wheel and Figure 6.57 indicates that as the main wing vortex is positioned more outboard as it passes the wheel centre, the wheel wake structure becomes taller and narrower. The only exception to this is the variation from the wing height of $h/c=0.223$ and $h/c=0.27$ where the opposite trend has been obtained. It should be noted no variation in

the horizontal position of the main wing vortex was obtained at these two wing heights and it is expected that this variation comes from the weaker main wing vortex strength associated with increases in wing height. This would then indicate that while the horizontal position of the main wing vortex is the primary factor for influencing the wheel lift and drag results, the strength and size of the main wing plays is a secondary factor. Therefore, in this case, the combination of main wing vortex strength and horizontal position for the $h/c=0.223$ case produces an optimum combination for the wing and wheel drags as indicated by Figure 6.52 for this span and angle of attack wing. This would be expected to vary with the wing angle of attack as the horizontal translation and the strength of the main wing vortex are both influenced by this parameter.

The same interaction can therefore also be used to explain the trends also seen in the side force acting on the wheel. The vortex produces a region of reduced static pressure that acts on the inner face of the wheel. This feature is enhanced as the main wing vortex is positioned closer to the wheel and the main wing vortex strength is increased.

6.4.2. Downforce loss phenomenon for $S/c=1.6$ wing in the presence of a wheel

While both the $S/c=0.97$ and $S/c=1.6$ wings experienced a reduction in height at which the downforce loss phenomenon occurs at in the presence of the wheel, the previous investigations comparing span have indicated that the interaction with the wheel for these two wings should be significantly different. Therefore it was decided to also consider in more detail the causes for the variation in performance with height of the $S/c=1.6$ wing when the wheel is present. Comparing the lift coefficients for the $S/c=1.6$ wing in isolation to that in the presence of a wheel pair indicates that the downforce is reduced by up to 54% due to the presence of the wheel pair. The cause of this has been previously shown to be due to the high pressure region formed forward of the wheel's contact patch reducing the suction that can be generated by the bottom surface of the wing and is indicated by the span wise pressure distribution for four different height wings in Figure 6.58. In the same figure, the wall shear stress has also been included for the isolated wing (Figure 6.58a, d, g and j) and also that of the same wing in the presence of a wheel pair (Figure 6.58c, f, i and l). These plots indicate that in the regions close to the tip, the isolated wing experiences larger wall shear stress values due to the presence of a stronger main wing vortex in comparison to the corresponding wing in the presence of a wheel pair.

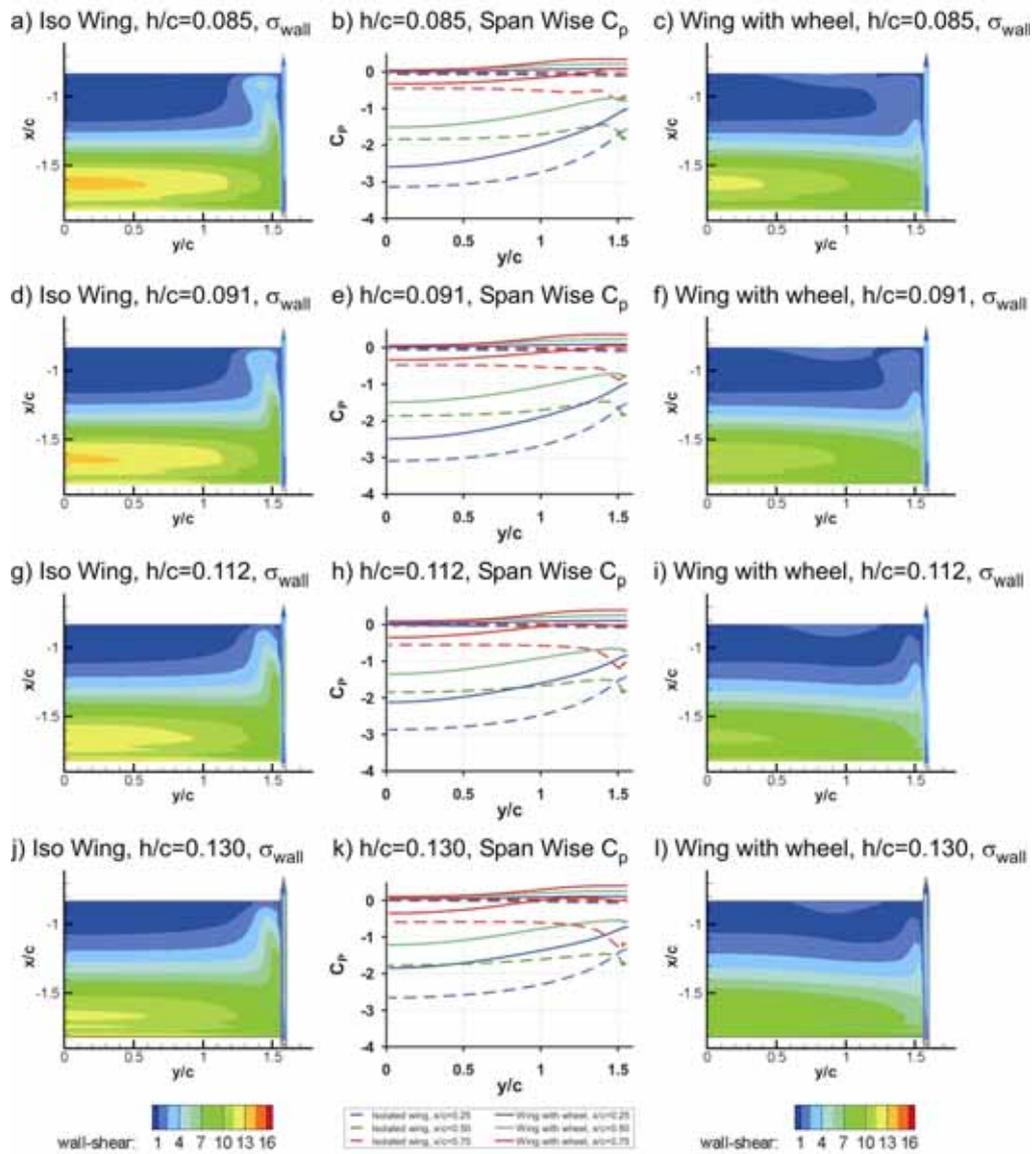


Figure 6.58 Wall shear stress and spanwise pressure distribution for variations in height for a wing with span $S/c=1.6$

Given that previous investigations considering the downforce loss phenomenon have indicated that either an increase in the main wing vortex strength or a reduction in adverse pressure gradient can delay this phenomenon from occurring, it is clear that the sole cause for the variation in the height at which the downforce loss phenomenon occurs at for the $S/c=1.6$ wing in the presence of a wheel pair is the reduction in the adverse pressure gradient experienced at the centre of the wing. While this is the same explanation given for

the $S/c=0.97$ wing, the significance of this result is the extent of the change at which the height that the downforce loss phenomenon occurs at can now be correlated to the reduction in the downforce obtained. Additionally, unlike the $S/c=0.97$ wing, at no angle of attack is the main wing vortex expected to contribute to reducing the height at which the downforce loss phenomenon occurs at as the main wing vortex has always been shown to be weaker for this span wing in the presence of the wheel for all the angles of attack tested.

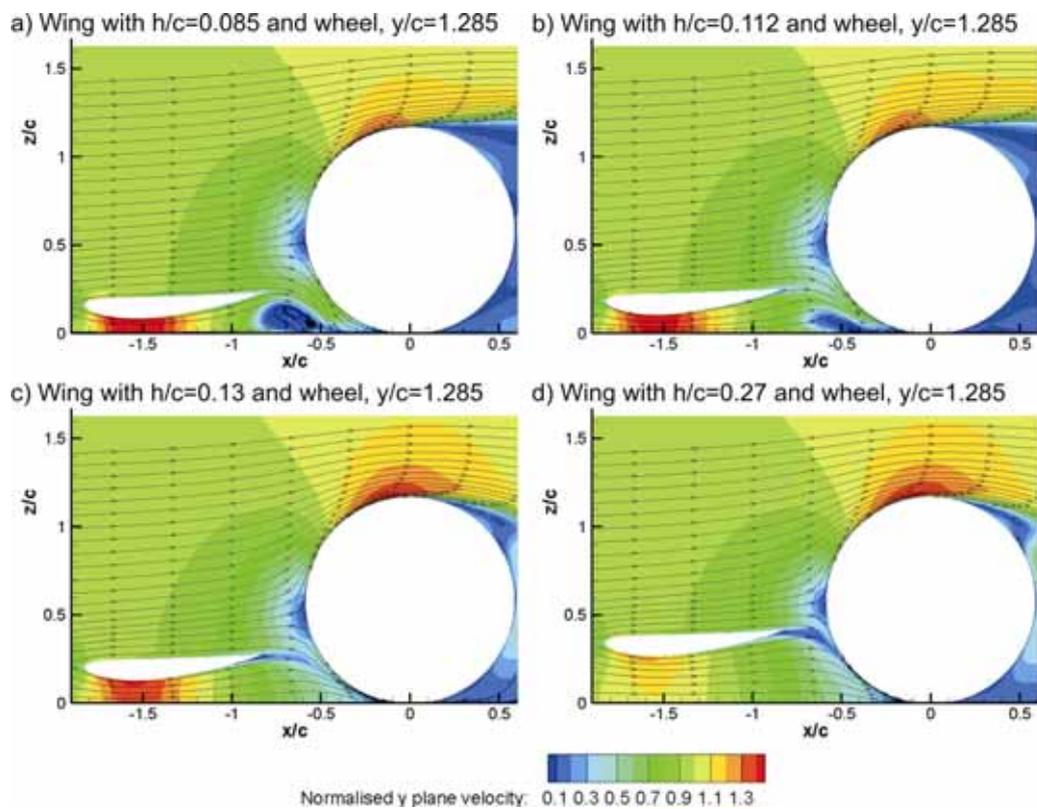


Figure 6.59 Streamlines indicating vortex path variation due to changes in wing height

Increasing the angle of attack for the $S/c=1.6$ wing has been demonstrated to draw the main wing vortex inboard, passing adjacent to the inboard face of the wheel (interaction b) as opposed to the outboard face of the wheel (interaction a). The cause of this was identified to be the increase in the inboard velocity component created behind the wing associated with an increase in downforce generated by a wing with a larger angle of attack (Zerihan, 2001). An increase in the inboard velocity component should also be obtained when the height of the wing is reduced as this also increases the downforce produced by

the wing. Therefore it would be expected that reducing the height of the wing could cause the main wing vortex to switch from travelling outboard of the wheel to inboard of the wheel while maintaining a constant angle of attack (as has been suggested during the discussion of the wheel forces for changes in height). In plane velocity magnitude plots and streamlines on a plane located through the centre of the wheel (Figure 6.59) for heights at either side of the assumed switch point have been used to confirm this. Evidence of the main wing vortex crossing the front face of the wheel was found on the $y/c=1.285$ plane at $x/c=-0.7, z/c=0.1$ and $x/c=-0.6, z/c=0.1$, for the $h/c=0.085$ and $h/c=0.112$ cases respectively, while for the greater heights, no evidence of the main wing vortex was found.

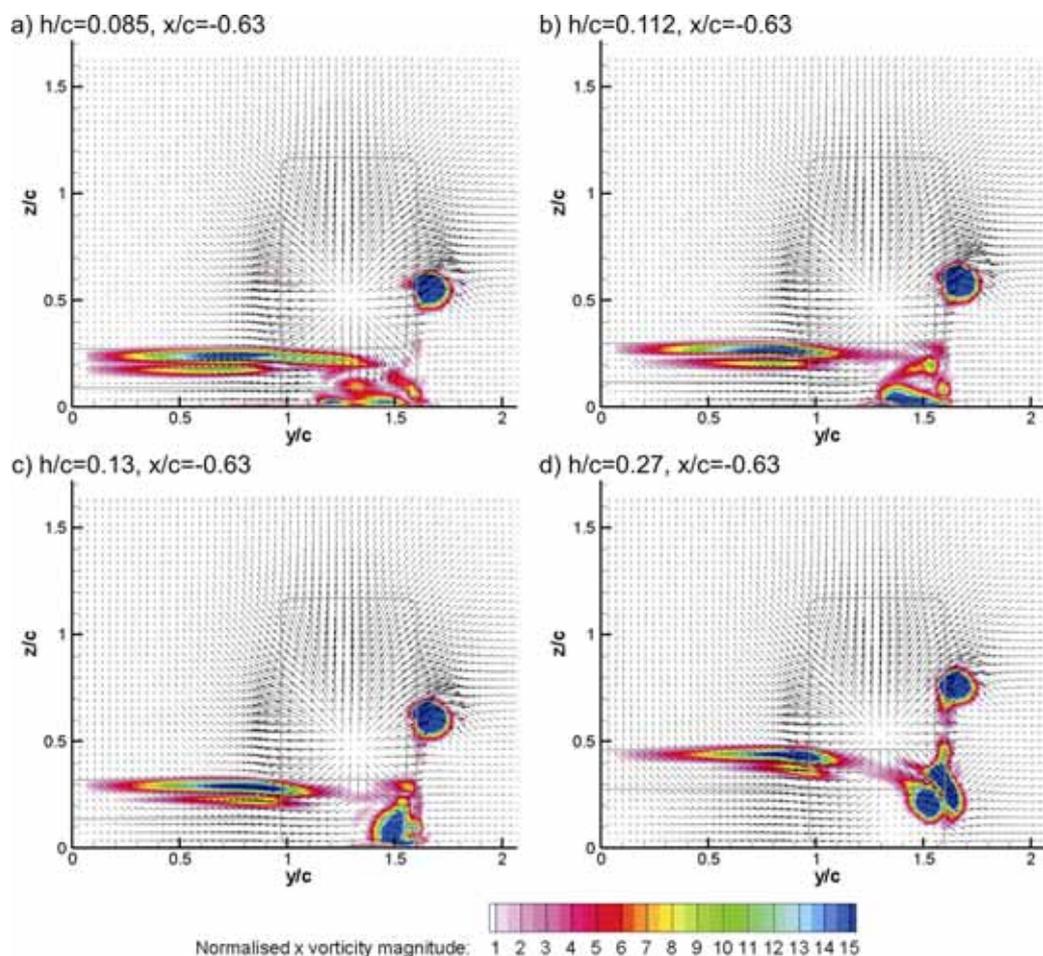


Figure 6.60 Vectors and Vorticity on x-planes for a wing and wheel with $W/c=0.63, T/c=1.6, S/c=1.6c$ and $AOA=4^\circ$,

In plane velocity vectors and x-vorticity plots for the $x/c=-0.63$ plane (Figure 6.60) also confirm this with the main wing vortex at a height of $h/c=0.13$ and $h/c=0.27$ being located closer to the outer edge of the wheel at $y/c=1.5$, $z/c=0.1$ and $y/c=1.5$, $z/c=0.25$ respectively while for the heights of $h/c=0.085$ and $h/c=0.112$ the main wing vortices are located at $y/c=1.3$, $z/c=0.1$ and $y/c=1.4$, $z/c=0.1$ respectively and appear to be drawn towards the symmetry plane. It should be noted that the incoherent vortex structure obtained for the wing with height of $h/c=0.085$ in the presence of the wheel (Figure 6.60a) is due to the vortex travelling in a direction that is normal to the plane at which it is being viewed on and for this reason the main wing vortex can be seen more clearly in the y-section shown previously (Figure 6.59a). This result also confirms the previous assumption that if the angle of attack investigation was conducted at a different height, the switch from “interaction a” to “interaction b” would also be obtained at a different wing angle of attack.

Interaction “b” has inherently displayed reduced levels of wheel lift and drag. This is consistent with the trend observed when reducing the height of the wing to values less than $h/c=0.112$. In this height range, a gradual reduction in the lift and drag of the wheel were obtained where at the smallest wing height tested a reduction of 58% and 27% respectively was obtained. The complete variation between the lift and drag of the wheel by changing the height of the wing differs to the trends that have previously been obtained when observing the transitions from interaction “a” to interaction “b” (Figure 6.16 and Figure 6.33). By varying the height, much less abrupt variations in wheel forces have been obtained. This indicates that there is some transitional phase that occurs between these two states. For the wing heights in question, the position of the main wing vortex forward of the wheel’s contact patch was considered with greater detail in order to understand what may be occurring during this transition. In Figure 6.61, results of in plane velocity have been included on several y-planes positioned ahead of the wheel for five different ride heights in the region in which the transition is expected to be occurring. These results indicate that as the height of the wing is increased, the strength and size of the main wing vortex becomes larger and stronger (Figure 6.33v). As the planes progress further towards the symmetry plane (Figure 6.33v to i) and to the inboard side of the wheel, it appears that the rotation of the wheel and the movement of the ground work to trap the main wing vortex in the contact patch and destroy it. Only for the two lowest heights shown here is the main wing vortex evident on the $y/c=1.027$ plane. This is believed to be a consequence of the extent of the cross flow component created by the wing reducing with increases in

the wing height and subsequently, the likelihood of the main wing vortex being drawn into the contact patch increases. While it is expected that a similar transitional phase would be obtained by either adjusting the wing span or angle of attack, it is expected that the transition phase has not been obtained previously because the variations in span and angle of attack made during these earlier investigations were not adequately fine to do so.

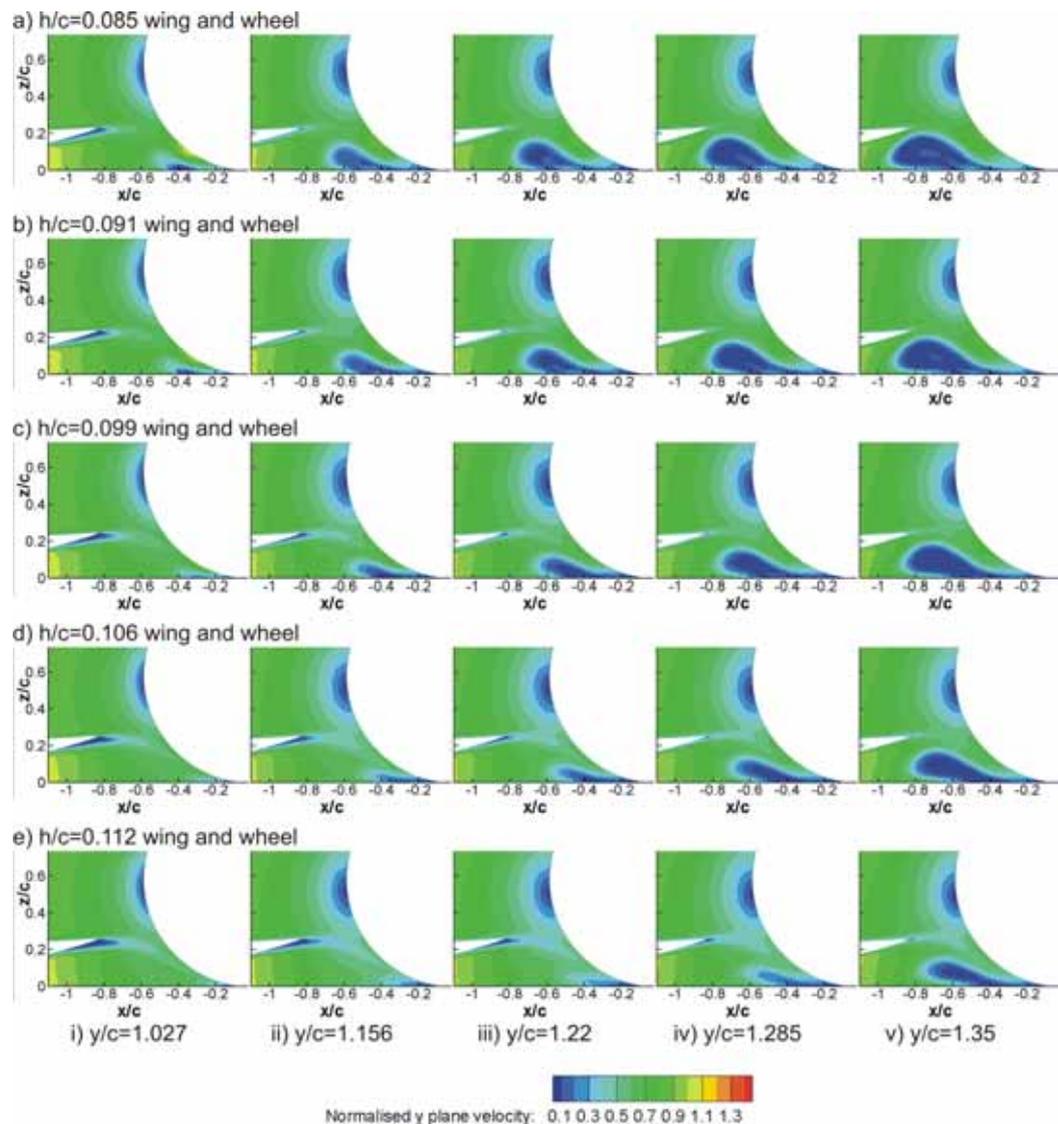


Figure 6.61 Y-plane velocity between the wing and wheel for variations in wing height

While the main wing vortex does not manage to cleanly pass the contact patch of the wheel, the effect that it has on the wheel wake structure remains quite similar to that described for interaction “b”. Total pressure and velocity vector plots for the $x/c=0.75$ plane

indicate that the wheel wake for the $h/c=0.112$ (Figure 6.62b) wing is taller and narrower than that of the $h/c=0.13$ and $h/c=0.27$ cases (Figure 6.62c, d) where the main wing vortex is expected to travel past the outer face of the wheel. As should be expected, the tallest and narrowest wheel wake (Figure 6.62a) once again corresponds with the case that produces the greatest reduction in lift and drag for the wheel in comparison that experienced by a wheel belonging to an isolated pair. This result once again demonstrates that the most desirable location for the main wing vortex to provide a lift and drag reduction to the wheel's lift and drag is adjacent to the inboard face of the wheel.

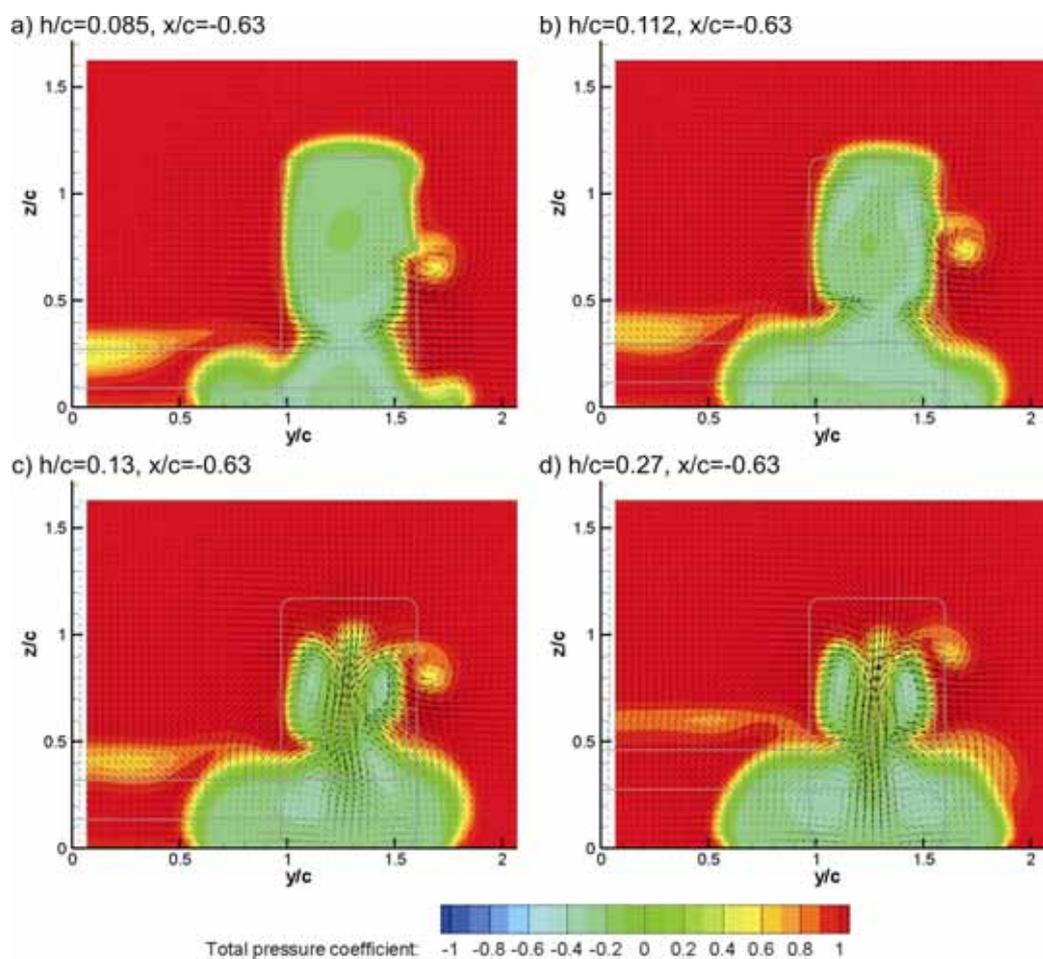


Figure 6.62 Vectors and Total Pressure on x-planes for a wing and wheel with $W/c=0.63$, $T/c=1.6$, $S/c=1.6c$ and $AOA=4^\circ$

6.5. Variations in Performance due to Wheel Width and Track

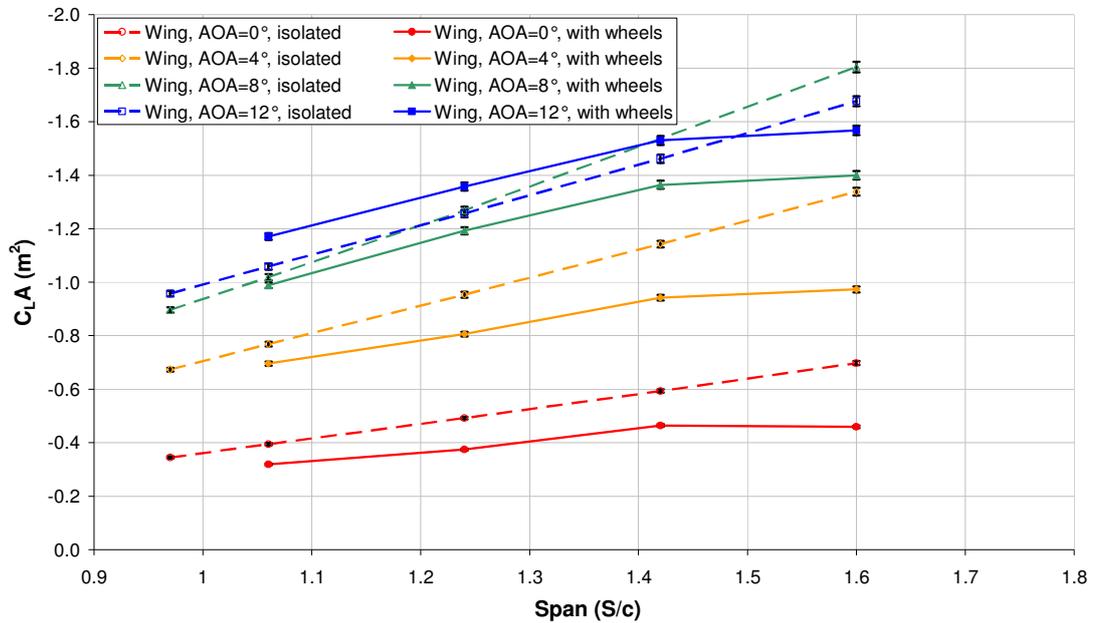
For all the investigations discussed thus far of a combined wing and wheel, a consistent wheel pair configuration has been utilised where the wheel width and track have been maintained at $0.63c$ and $1.60c$ respectively. The wheel track and width values thus far are the maximum permissible under the current F1 regulations (FIA, 2009). In this section, results are presented for several spans and angles of attack at a constant wing height of $0.13c$ for a single variation in wheel width initially, followed by an increase in wheel track. The interaction observed when adjusting these two features did not vary significantly to those obtained at the previous wheel width and track values. For completeness and comparison, the lift and drag results for these variations are discussed here as well as a summary of the interaction type obtained for each variation of either wheel width or track.

6.5.1. Force variations for a reduction in wheel width to $W/c=0.54$

In order to investigate the effect that the wheel width has on the interaction of the wing and wheel, the wheel width was reduced from the previous value of $W/c=0.63$ (or wheel W2) to 0.53 (or wheel W1) while the wheel track was maintained at a value of $T/c=1.60$. This variation in wheel width is representative of the minimum permissible front wheel width under the current F1 regulations (FIA, 2009). During this study, the wing span was varied from a value of $S/c=1.06$ to 1.60 in four increments for four different angles of attack (0° , 4° , 8° and 12°). The span values were chosen so that the wing and wheel overlap would once again vary from 0 to 100% and for this reason the minimum span tested during this investigation is greater than that used for the previous investigations.

Comparing the wing downforce generated for various span and angle of attack wings in the presence of the W1 wheel pair to the same wing in isolation (Figure 6.63a) demonstrates similar trends to those discussed previously for the W2 wheel pair (Figure 6.31). With the exception of the wing with an angle of attack of 12° and a span of $1.42c$ or less, the presence of the wheel reduced the wings ability to generate downforce. While this should be expected due to the high pressure regions generated forward of the wheel adversely affecting the wings ability to generate downforce, the extent at which the wing is adversely affected has been reduced at common wing spans and angles of attack.

(a) Lift Area Coefficients of Wing for Variations in Span



(b) Drag Area Coefficients of Wing for Variations in Span

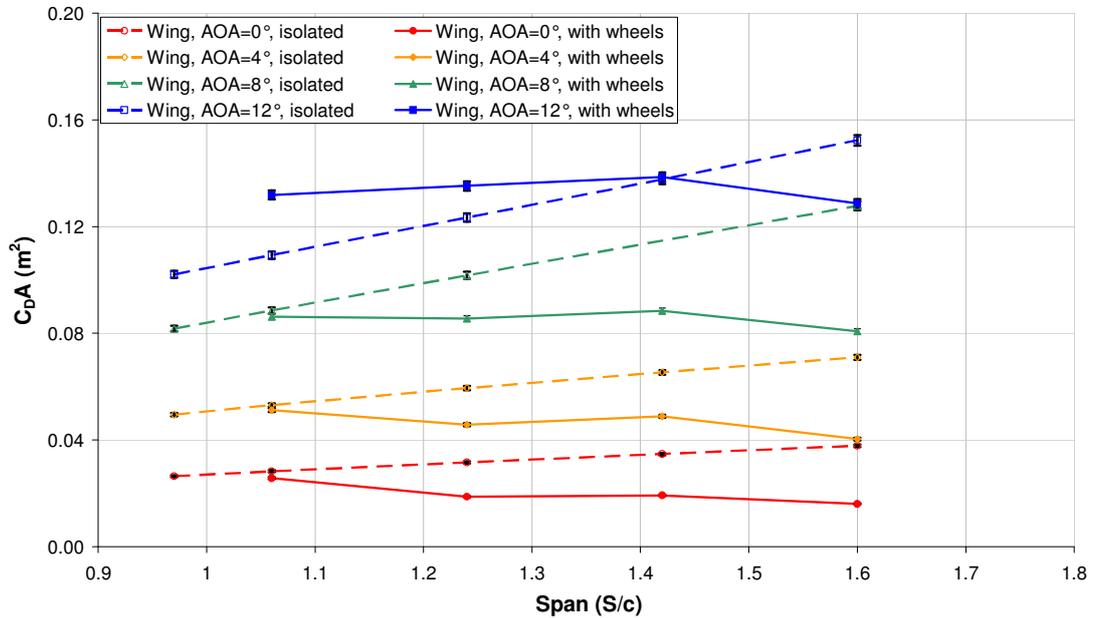


Figure 6.63 Wing lift (a) and drag (b) results for variations in span and angle of attack for a wing ($h/c=0.13$) in isolation and also in the presence of a wheel pair ($W/c=0.63$, $T/c=1.78$)

It has been demonstrated during the isolated wheel investigation (Section 5.1.4), that reducing the width of the wheel will also reduce the size of the high pressure regions created forward of the wheel. For this reason, it is expected that the wing in the presence of a narrower wheel will perform better than the same wing in the presence of a wider wheel. The most extreme variation in performance was obtained by the lowest angle of attack tested (0°) in combination with the largest span ($S/c=1.6$) where reducing the wheel width by approximately 16% caused the wing variation relative to the same wing in isolation to improve from a 48% reduction in downforce to a 23% reduction in downforce. While the adversely affected wing configurations suffered less in the presence of the W1 wheel, the wing configurations in which an improved performance would be obtained also demonstrated smaller variations. The wing drag (Figure 6.63b) also demonstrated similar trends to that seen previously (Figure 6.32) while also varying less for the same reasons.

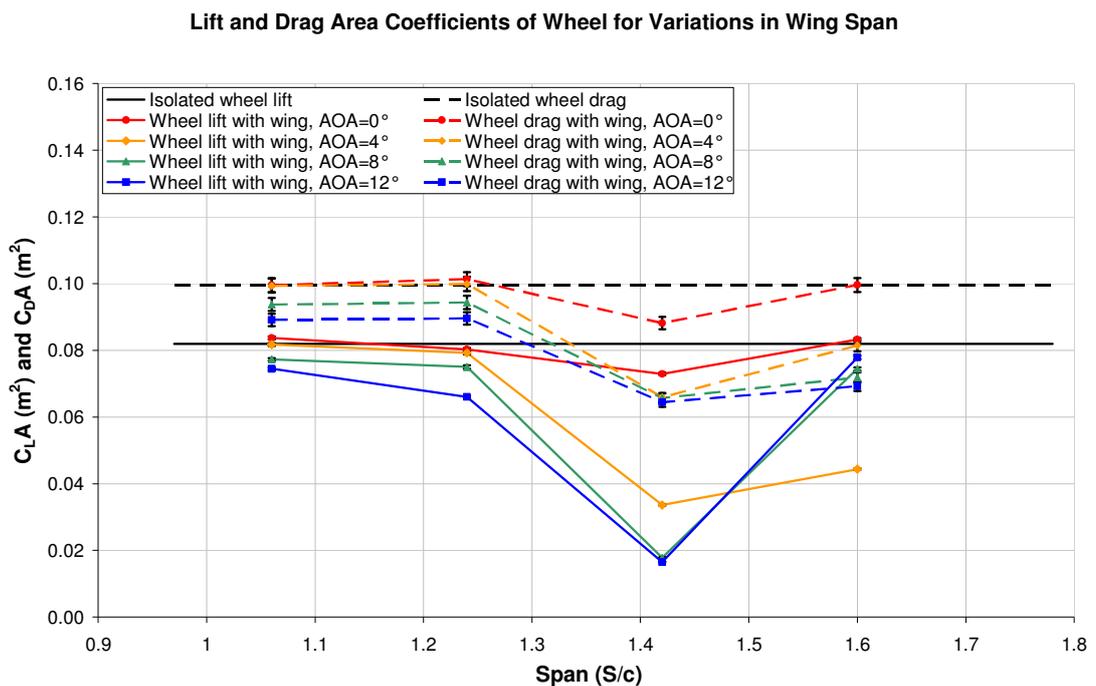


Figure 6.64 Wheel lift and drag results for an isolated wheel pair ($W/c=0.54$, $T/c=1.6$) and also in the presence of a wing ($h/c=0.13$) with varied span and AOA

The wheel lift and drag forces (Figure 6.64) have also shown similar trends as those demonstrated previously for a wider wheel (Figure 6.33). In all cases, the presence of the wing has reduced the wheel lift and drag with the largest variation relative to the same

wheel belonging to an isolated pair occurring at a span value of $S/c=1.42$. At this span, both the 8° and 12° angle of attack wings reduce the wheel lift and drag by approximately 75% and 35%. This is significantly greater than the previously reported reduction of approximately 65% and 30% for the W2 wheel pair in the presence of the same span wing. This is believed to be due to a combination of two reasons. The first relates to the size and strength of the main wing vortex. This flow structure is expected to be larger for the wing in the presence of the narrower wheel given that in the presence of this wheel pair, the same wing generates approximately 5% more downforce. Secondly, the primary wheel vortices associated with the narrower wheel will be weaker, and therefore even if the main wing vortex remains unchanged, the influence that it would have on the wheel will be greater. A stronger main wing vortex would also explain the more significant variations obtained in the side force for the wheel, which is evident when comparing Figure 6.65 and Figure 6.34.

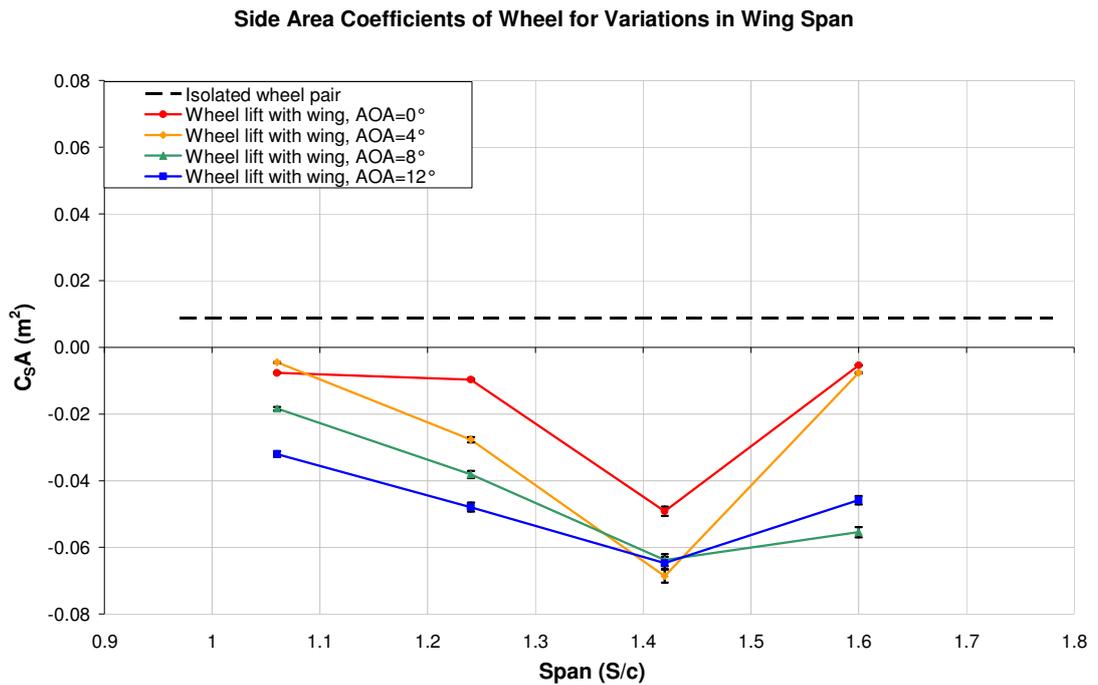
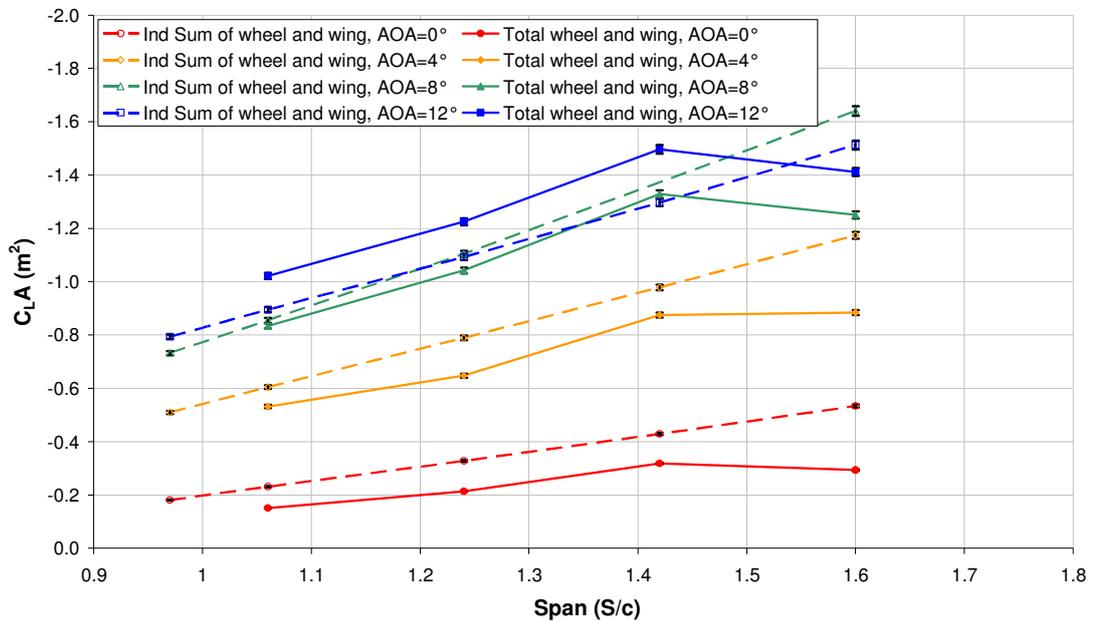


Figure 6.65 Wheel side force results for an isolated wheel pair ($W/c=0.54$, $T/c=1.6$) and also in the presence of a wing ($h/c=0.13$) with varied span and AOA

(a) Total Lift Area Coefficients for Variations in Span



(b) Total Drag Area Coefficients for Variations in Span

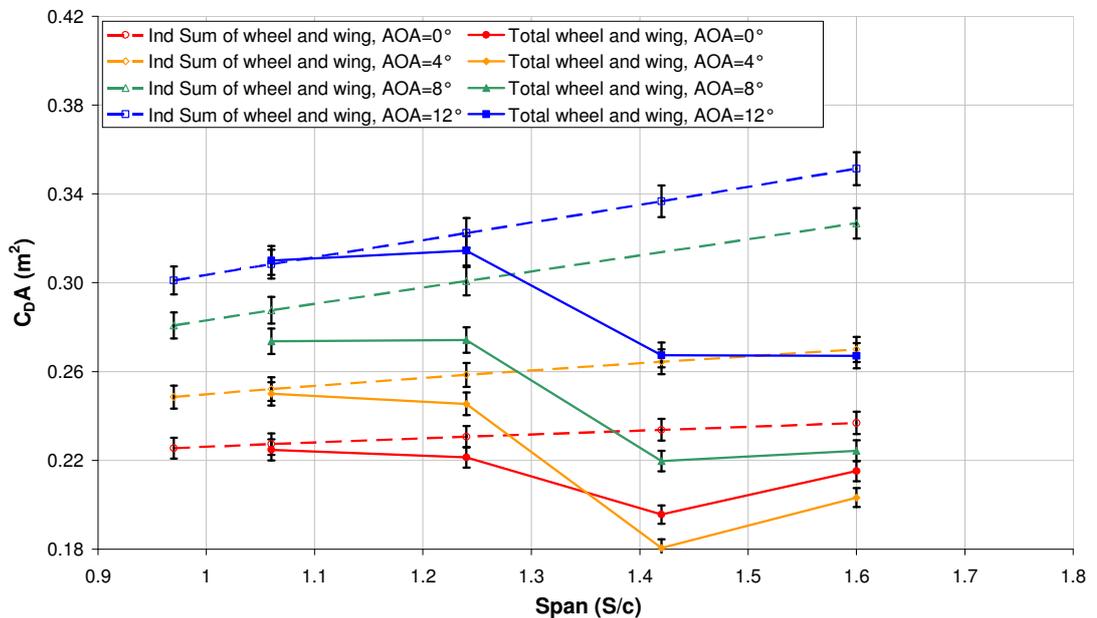


Figure 6.66 Total lift (a) and drag (b) results for variations in span and angle of attack for a wing ($h/c=0.13$) in isolation and also in the presence of a wheel pair ($W/c=0.63$, $T/c=1.78$)

The total lift of the wing and wheel (Figure 6.66a) indicates that the maximum downforce configuration will be provided by a wing configuration with the largest angle of attack tested and a span value of $S/c=1.42$. This is the same conclusion obtained for the wider wheel (Figure 6.35). In this configuration, the combination of the greater downforce produced by the wing and the reduced lift generated by the wheel allows the same wing in combination with the W1 wheel to produce approximately 9% more downforce than when combined with the wider W2 wheel. Also consistent with the previous investigation (Figure 6.36), the $S/c=1.42$ wing also consistently produced the least drag (Figure 6.66b) for each of the angles of attack tested with the exception of the $S/c=1.6$, 12° angle of attack wing which exhibits an equal drag value. In comparison to the wider wheel, the W1 wheel in combination with the $S/c=1.42$ wing at an angle of attack of 12° exhibits a drag reduction of approximately 6%. As mentioned previously, the lift and drag trends observed here would not have been evident had the two bodies been tested individually again, highlighting the importance of optimising a downforce producing wing for an open wheel racing car in the presence of the wheel.

	$S/c=1.06$	$S/c=1.24$	$S/c=1.42$	$S/c=1.6$
AOA= 0°	c	c	b	a
AOA= 4°	c	c	b	a
AOA= 8°	c	c	b	b
AOA= 12°	c	c	b	b

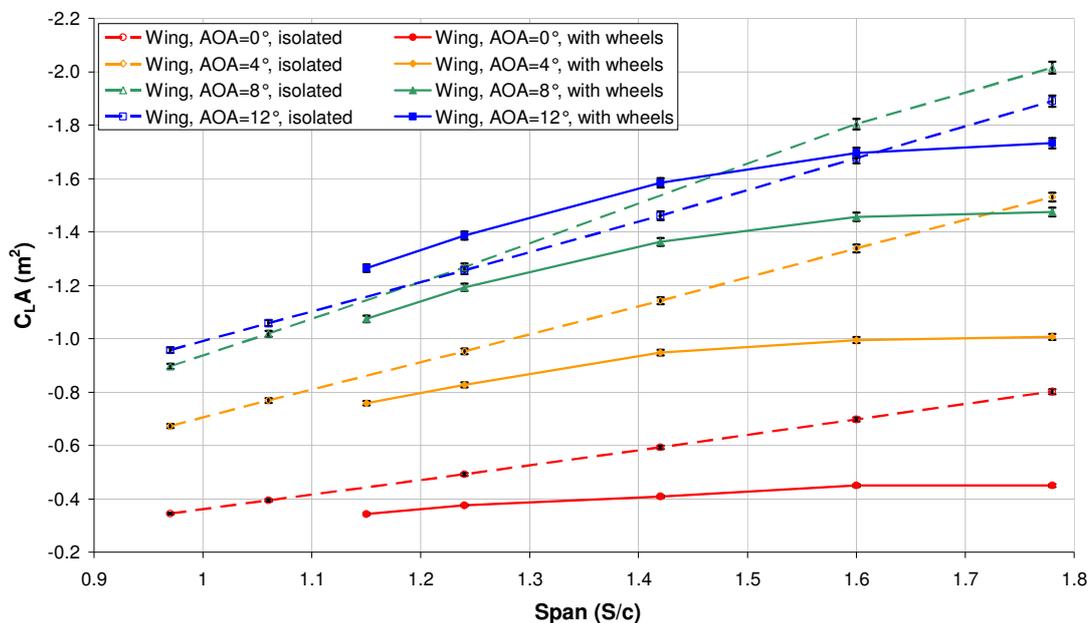
Table 6.2 Interaction types obtained for a wheel pair configuration of $W/c=0.54$, $T/c=1.6$

Table 6.2 summarises the interaction types obtained with the narrower W1 wheel. As has been discussed previously during Section 6.1 to 6.3, when the main wing vortex is too weak and passes outboard of the wheel (interaction type “a”) little variation is obtained in the lift and drag of the wheel (Figure 6.64) with the strongest variation in wheel forces being obtained when the main wing vortex passes adjacent to the inside face of the wheel (interaction type “b”).

6.5.2. Force variations for an increased wheel track value of 1.78c

A variation of wheel track was also investigated by obtaining results for the W2 wheel with an increased track value of $T/c=1.78$. This value was chosen as it is representative of the maximum wheel track allowed by the F1 regulations prior to the 1998 season (FIA, 1997).

(a) Lift Area Coefficients of Wing for Variations in Span



(b) Drag Area Coefficients of Wing for Variations in Span

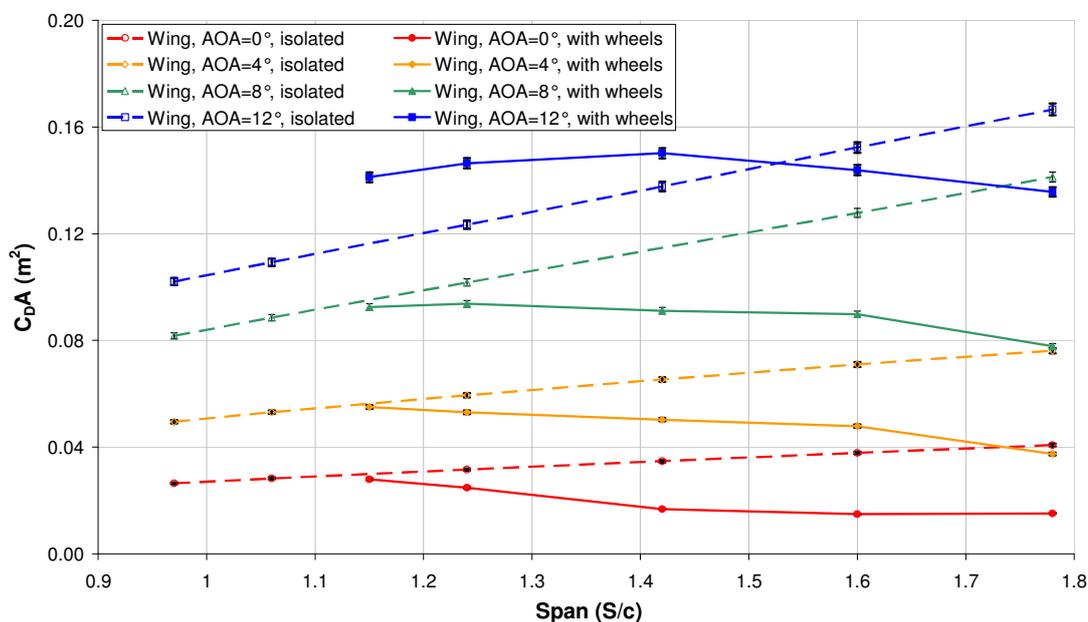


Figure 6.67 Wing lift (a) and drag (b) results for variations in span and angle of attack for a wing ($h/c=0.13$) in isolation and also in the presence of a wheel pair ($W/c=0.63$, $T/c=1.78$)

Results were again obtained for a variety of wing spans ($1.15 < S/c < 1.78$) that provided for a range of wing and wheel overlap values between 0 and 100% at four different angles of attack while maintaining the wing at a constant height of $h/c=0.13$. These results indicate that the lift and drag values for a wing in the presence of a wheel pair with the increased wheel track (Figure 6.67a and b) varied in a similar manner to that obtained for the same wheel width and track value of 1.6c (Figure 6.31 and Figure 6.32). The only variation in trends obtained here with that observed previously is that the 12° angle of attack wing benefits from the presence of the wheel pair up until a span of $S/c=1.6$ obtaining increased values of downforce in comparison to the same wing in isolation. When the narrower wheel track was tested with the same wheel, the largest span that benefited from the presence of the wheels was the $S/c=1.42$ wing. This result suggests that a better comparison can be made when considering the respective wing and wheel overlap instead of the span. In the case of the results obtained with a track of $T/c=1.6$, the $S/c=1.42$ wing overlaps the W2 wheel by approximately 71% while the $S/c=1.6$ wing overlaps the W2 wheel by 72%.

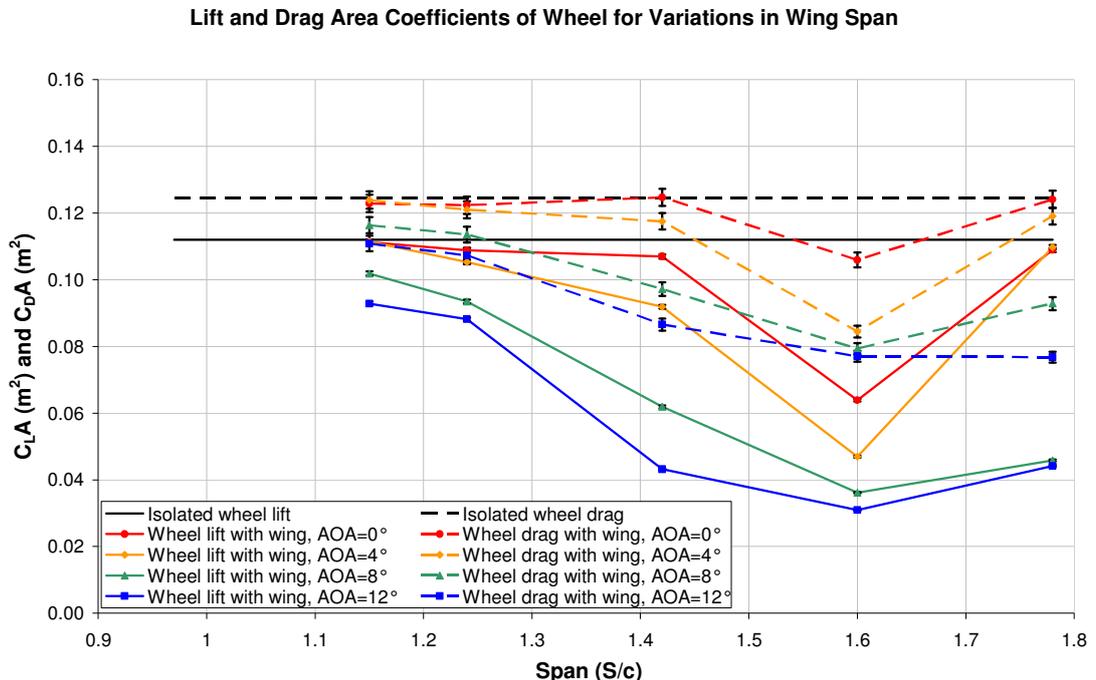


Figure 6.68 Wheel lift and drag (a) and side force (b) results for an isolated wheel pair ($W/c=0.63$, $T/c=1.78$) and also in the presence of a wing ($h/c=0.13$) with varied span and AOA

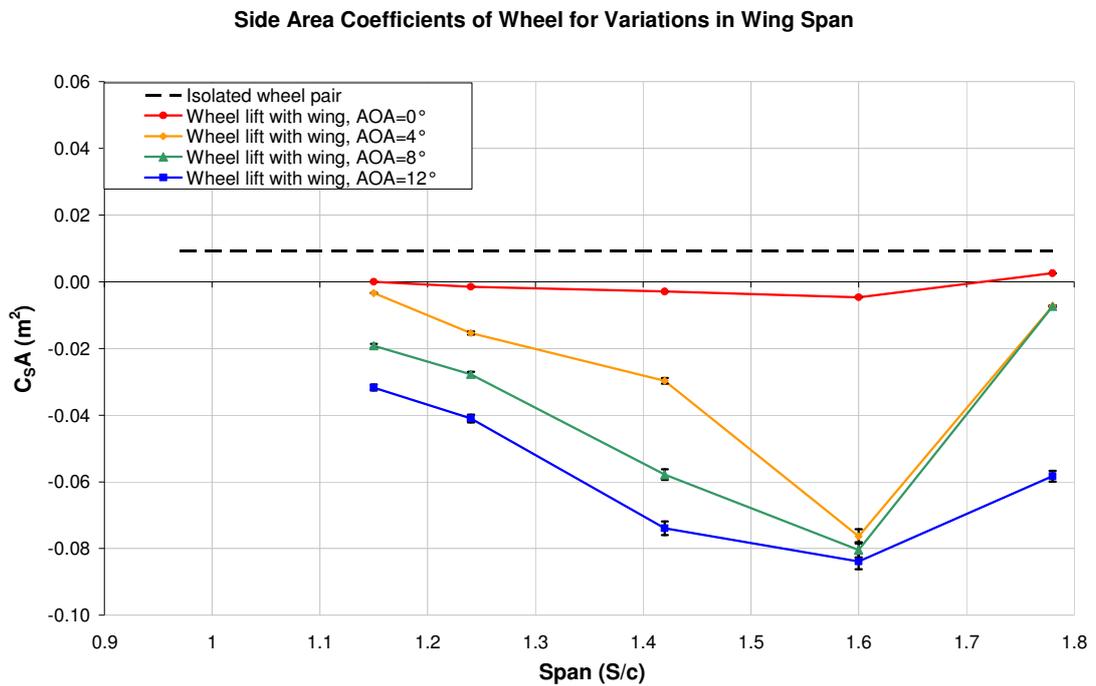
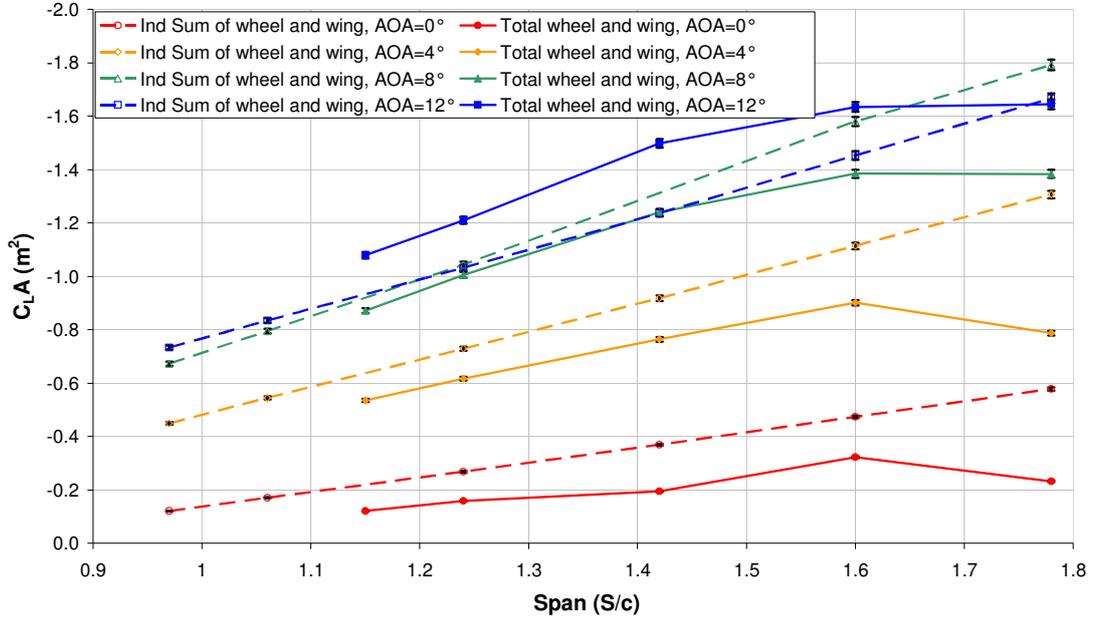


Figure 6.69 Wheel side force results for an isolated wheel pair ($W/c=0.63$, $T/c=1.78$) and also in the presence of a wing ($h/c=0.13$) with varied span and AOA

The minimum wheel lift and drag was also obtained at a span value of $1.6c$ in the presence of the wider wheel track for all the angles of attack tested (Figure 6.68). The lift and drag trends obtained for the wheel are also consistent with previous observations when considering that in both cases the minimum wheel lift and drag has been obtained at spans that equate to a wing and wheel overlap of approximately 72%. It should be noted that the lift and drag reductions obtained at this wing and wheel overlap do vary in magnitude to those obtained with the smaller wheel track; the maximum reduction in wheel lift and drag of 72% and 38% respectively found in comparison to the 65% and 30% obtained with the narrower wheel track. This is believed to occur due to the significant variation obtained in wing downforce produced by the two different span wings required to achieve the same wing and wheel overlap. At an angle of attack of 12° for example, this variation was calculated to be 17%. The large variation in wing downforce is expected to produce a stronger main wing vortex and therefore be able to provide a further reduction in the lift and drag of the wheel. For the same reason a 9% larger side force has also been obtained when making the same comparison (Figure 6.69).

(a) Total Lift Area Coefficients for Variations in Span



(b) Total Drag Area Coefficients for Variations in Span

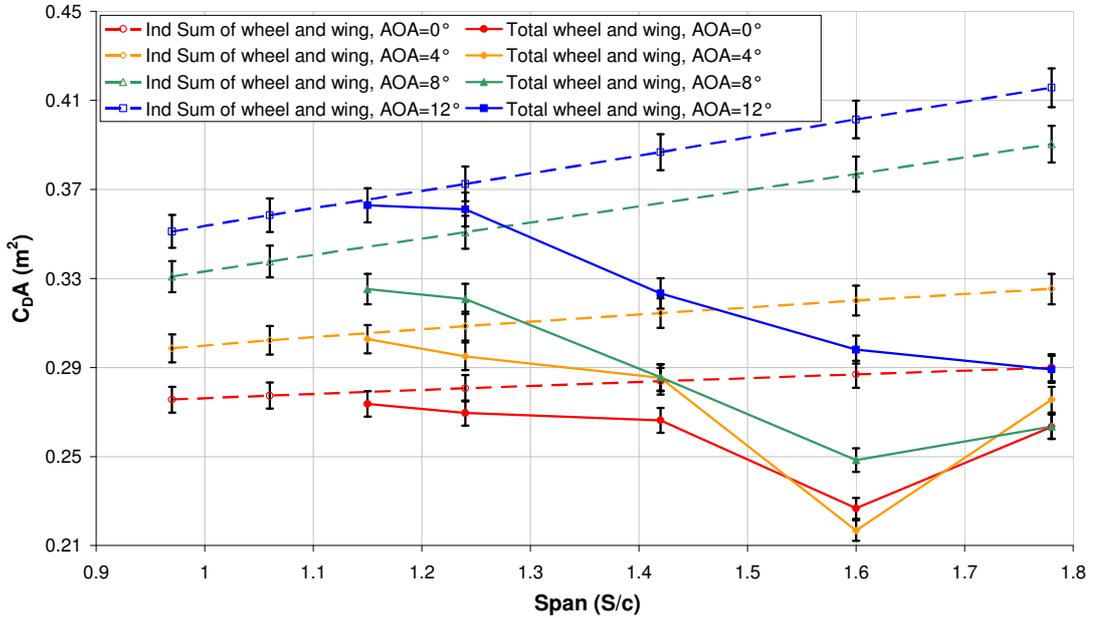


Figure 6.70 Total lift (a) and drag (b) results for variations in span and angle of attack for a wing ($h/c=0.13$) in isolation and also in the presence of a wheel pair ($W/c=0.63$, $T/c=1.78$)

The total lift and drag trends (Figure 6.70) have also been repeated for those obtained previously with the shorter track value of $T/c=1.6$, with the largest total downforce and minimum drag being achieved at a wing and wheel overlap of approximately 72% (Figure 6.35 and Figure 6.35). The wing and wheel overlap at which the optimum downforce and drag is obtained at also agrees with that obtained by the pair of narrower wheels (W1) in the narrower wheel track configuration ($T/c=1.6$). For this configuration, the optimum span for the total lift and drag values was found to be $S/c=1.42$ which allows 68% of the wheel to be overlapped by the wing.

It can be concluded that for wheel track values and wheel widths relevant to open wheel racing cars, the optimum wing and wheel total downforce will be achieved by a wing span that overlaps the wheel between 65% and 75%. Therefore, it is recommended that any study conducted to optimise the span of a wing in the presence of the wheel be concentrated within this wing and wheel overlap window.

	$S/c=1.06$	$S/c=1.24$	$S/c=1.42$	$S/c=1.6$	$S/c=1.78$
AOA=0°	c	c	c	b	a
AOA=4°	c	c	b/c	b	a
AOA=8°	c	c	b/c	b	b
AOA=12°	c	c	b	b	b

Table 6.3 Interaction types obtained for a wheel pair configuration of $W/c=0.63$, $T/c=1.78$

No change has also been obtained in the type of variations recorded for this wheel width and track as indicated by Table 6.3. The switch from interaction “a” to “b” was again found to again occur between an angle of attack of 4° and 8° at a span that provides a 100% wing and wheel overlap while between the same angles of attack at a span of 1.42c the switch was found to occur from interaction “b” to “c”.

6.6. Summary

It has been determined that there are three main interactions that may occur depending on the path that the main and secondary wing vortex takes around the wheel. Interaction “a” occurs when the main and secondary wing vortices both travel outboard of the wheel, interaction “b” is obtained when only the main wing vortex passes inboard of the wheel, while interaction “c” requires both wing vortices to travel inboard of the wheel.

In order for interaction “a” to occur, the endplate is required to be positioned outboard of the high pressure regions that exist forward of the wheel. The high pressure regions force the main wing vortex outboard and also reduce the pressure difference experienced on the bottom surface of the endplate causing a weakened main wing vortex to form in comparison to that obtained for the same wing in isolation. Due to the low strength of the main wing vortex, it has little impact on the wheel wake as well as the lift and drag values. Typically in this configuration, the wing produces a 40% reduction in downforce due to the low pressure surface of the wing being exposed to the high pressure regions generated forward of the wheel. This also assists in reducing the drag of the wing by up to 70%.

By increasing the angle of attack, the suction generated beneath the wing causes the main wing vortex to be drawn inboard and to pass the wheel along its inner face, satisfying interaction “b”. Despite the increased angle of attack, the wing’s ability to generate low pressure still suffers due to the high pressure regions generated by the wheel and as a result the wing produces approximately 10% less downforce in comparison to the same wing in isolation. These high pressure regions are also altered by the presence of the suction generated beneath the wing and have been observed to be weakened and positioned more outboard as a result. When this interaction is achieved, the influence of the main wing vortex on the wheel wake and the upwash generated by the wing forward of the wheel both contribute to lift and drag reductions of approximately 45% and 25% respectively for the wheel. The position of the main wing vortex was also able to increase and change the direction of the side force experienced by the wheel. For each angle of attack tested, the optimum wing and wheel configurations for obtaining maximum total downforce and reducing drag was found with this interaction type when the span allowed between 65% and 75% of the wheel to be overlapped by the wing. This optimum range was generally found to be independent of the wheel width but it is also important to note that this interaction can only be observed when considering the forces of the two bodies working in unison as opposed to studying them individually as has been the norm thus far.

Further reducing the span of the wing such that it overlaps the wheel by less than 50% allows interaction “c” to occur. While the main wing vortex also passes the inner face of the wheel for this interaction, its significant feature is that the endplate is located inboard of the stagnation regions ahead of the wheel and therefore the secondary vortex forms in the

opposite direction to that usually obtained for an isolated downforce producing wing. Additionally, in this configuration only, and when the wing in isolation was stalled, the presence of the wheel assisted the wing to generate up to 10% more downforce. This was also caused by the presence of the stagnation region outboard of the bottom edge of the endplate causing the main wing vortex to become stronger and alleviate some of the separation obtained at the tip of the wing. Lift and drag reductions were also observed for the wheel for this interaction, but this was to a smaller extent in comparison to that observed for the interaction "b". The cause for this variation was determined to be the position of the main wing vortex, which was found to be further inboard due to the shorter spans required to obtain this interaction and as a result had little influence on the wheel wake.

An investigation was also conducted to determine how the downforce loss phenomenon varied in the presence of the wheel relative to the same wing in isolation. This study was conducted using two span wings that positioned the endplate in line with either the inner or outer face of the wheel. Results obtained with the shorter span wing indicated that the increase in main wing vortex strength due to the presence of the wheel allowed the downforce loss phenomenon to occur at a height $0.08c$ closer to the ground. A more significant variation was obtained with the larger span wing in the presence of the wheel with no peak downforce being obtained in the height range tested and as a result the maximum downforce was calculated to occur at the lowest height tested ($h/c=0.08$). The downforce loss phenomenon for the same span wing in isolation was found to occur at a value of $h/c=0.112$. The more significant variation obtained with the larger span wing was shown to be caused by the reduced suction levels obtained beneath the wing due to the high pressure regions forward of the wheel. This caused the adverse pressure gradient to be experienced at the centre of the wing to be less severe and as a result the separation obtained in the centre was delayed. For all heights tested with the shorter span wing, only interaction "c" was observed while for the wider span, the height of the wing also influenced the interaction type obtained. At heights greater than values of $h/c=0.121$ where the suction beneath the front wing was not adequate to draw the main wing vortex inboard, interaction "a" was obtained. For height values less than $h/c=0.091$, interaction "b" was obtained and subsequently the main wing vortex was positioned inboard of the wheel allowing for wheel lift and drag reductions associated with this interaction type to be reproduced. Between these two states, the main wing vortex was found to be trapped

between the wheel and the ground and as a result was destroyed. Reducing the height for both span wings caused the main wing vortex and the lower wheel wake to travel further inboard. Increasing angle of attack had a similar effect and it was concluded that any increase in front wing downforce will also have the same result.

Previous investigations conducted by Thisse (2004) and Taylor (1992) showed conflicting results regarding whether the front wheels of an open wheel racing car hinder or assist the front wing in generating downforce. This investigation has demonstrated that depending on the wing span, height and angle of attack can influence the interaction type and subsequent variation in forces obtained by either the wheel or the wing in comparison to the same body in isolation. Therefore, the specific wing and wheel geometries used during the investigations undertaken by Thisse (2004) and Taylor (1992) can explain the discrepancies between their conclusions. The wheel track and width is unlikely to be responsible for this variation as it had little effect on the overall trends when comparisons were conducted considering the wing and wheel overlap as opposed to the span of the wing.

Chapter 7: Conclusions and Future Work

7.1. Summary of Conclusions

A computational model was developed to model the flow about a simplified wing and wheel geometry in conditions that would be representative of those experienced by an open wheel racing car. Prior to using this computational model, an extensive verification study was undertaken demonstrating that the computational model is independent of the spatial discretisation and boundary positions used. A validation study was also conducted testing several turbulence models demonstrating that the best compromise between accuracy in predicting the flow structures associated with a combined wing and wheel, as well as the required computational resources, is the $k-\varepsilon$ realizable turbulence model. Subsequently, this turbulence model was used to validate the computational model against measurements obtained by Fackrell (1975) and Zerihan (2001) of an isolated wheel and isolated wing respectively. These comparisons demonstrate that the computational model is capable of reproducing force, static pressure and wake measurements associated with variations in either the wing or wheel's geometry. Variations in flow structures associated with changes in angle of attack and span for a combined wing and wheel that were measured using LDA were also reproduced by the computational model.

A number of isolated wheel and isolated wing investigations were undertaken prior to conducting the combined wing and wheel study. The first investigation considered the cause for the primary wheel vortices associated with a stationary wheel forming closer to the ground and in a more outboard position in comparison to the same wheel when rotated. The wheel rotation should logically create primary wheel vortices that are located further outboard due to the increased jetting action experienced by a rotating wheel forward of the contact patch. Previous publications suggested that this anomaly was caused by vortices forming forward of a rotating wheel (Fackrell, 1975) or due to the boundary layer developing forward of a stationary wheel on the ground (McManus and Zhang, 2006), but both these hypotheses were disproved during this investigation. Instead, it was demonstrated that the primary wheel vortices are located depending on the distribution of flow entrainment from either the top or the side of the wheel wake. Due to the delayed separation associated with a stationary wheel, the flow is entrained into the

wheel wake from above the wheel causing a large central downwash which forces the primary wheel vortices to form lower and in a more outboard position. By progressively moving the separation point from the upper wheel tread forward towards the position associated with that of a rotating wheel, it was possible to reduce the downwash in the central wheel wake, as well as the flow entrainment into the wheel wake from above the wheel. This increased the flow entrainment from the sides and allowed the primary wheel vortices to progressively form in a higher and more central position. Reproducing the jetting action without the more forward separation point from the wheel tread caused the primary wheel vortices to form further apart as expected. This demonstrates that the variation in position of the primary wheel vortices is determined by the wheel tread separation point and the reduced downwash associated with a rotating wheel and not a flow feature that is expected to develop over the ground as proposed by Fackrell (1975) or McManus and Zhang (2006).

Similar variations in the wake of the wheel were also observed when increasing the step height surrounding the contact patch. This was undertaken to determine how this required simplification, to ensure grid quality, affects the forces and the flow structures predicted by a computational model of a rotating wheel. Increasing the size of the contact patch was observed to reduce the separation experienced at either side of the contact patch and therefore increase the flow entrainment from the sides of the wheel wake. Subsequently, the wheel tread separation point also moved forward allowing the primary wheel vortices to form in a higher and more central position. Consistent with Fackrell's (1975) previous findings, the wheel lift and drag was reduced the further forward the wheel tread separation point occurred. A lift and drag reduction of 52% and 18% respectively was obtained at the largest step height tested (0.0085d). This study indicated that a step height no greater than 0.0028d should be used in order to obtain computational lift and drag results of a rotating wheel comparable to those obtained experimentally using a solid wheel.

Simplifying Fackrell's (1975) A2 wheel geometry by removing the wheel hubs and replacing the shoulder geometry with a radius was also found to influence the flow structures associated with a rotating wheel. This simplified geometry (W1 wheel) was used for the wing and wheel investigation. Removing the hubs introduced two additional vortices in the wake of the wheel forming due to the shear interaction caused by the rotating wheel

sides with the flow. It was previously hypothesised by Cogotti (1978) that six vortices would be found in the wake of a rotating wheel, but no prior investigation into a rotating wheel has been able to demonstrate that six vortices exist in a wheel wake. This is likely to be due to the wheel geometry used during the previous investigations consisting of hubs and not the flat sides required to obtain the additional vortices. The rotation of these two vortices increased the flow entrainment from the sides of the wheel and subsequently the lift and drag of the wheel was reduced by 28% and 8% respectively. Simplifying the wheel shoulder to a radius increased the wheel lift and drag by 85% and 60% respectively. This was determined to be due to the increase in wheel tread width that was caused by the variation in shoulder geometry. For all the wheel geometries tested, the stationary wheel demonstrated similar variations in forces and flow structures to their rotating equivalents as described by Fackrell (1975) demonstrating that the effects of the wheel rotation are independent of the wheel geometry.

Most previous investigations concerning the aerodynamics of a wheel have focused on a single isolated wheel. Given that two wheels exist side by side on most vehicles, it was also decided to investigate what effect that this would have on the flow and the forces of each wheel. At the wheel track values that the wing and wheel investigation was conducted at ($T/d > 1.36$) the variations were found to be negligible and therefore the wheel track was further reduced to exaggerate the effect that this parameter might have. Doing so demonstrated that the inboard cross flow component generated by the wheel stagnation was reduced due to the same, but opposing flow feature belonging to the adjacent wheel. As a result the stagnation point moved inboard encouraging an increase in flow above and around the outer side of the wheel. This caused the wheel wake to be asymmetric and travel inboard, while a side force was also observed acting to push the two wheels apart while lift and drag increases were also obtained. Increasing the wheel width, while maintaining the wheel track, also increased the sensitivity of the wheel forces to the track variations.

The isolated wing study focused on the effect that the span has on the height at which the downforce loss phenomenon occurs at. Reducing the span of the wing from $S/c=2.46$ to $S/c=0.97$ reduced the height at which the downforce loss phenomenon occurred at from $h/c=0.085$ to $h/c=0.062$. The main cause for this variation was the reduced pressure drop generated in the centre by a shorter span wing which alleviates the adverse pressure

gradient in this region, delaying separation from occurring. This was confirmed by comparing the centre pressure coefficients at the height at which the downforce loss phenomenon occurs at for several different span wings which all demonstrated similar adverse pressure gradients at this height. The main wing vortex also contributed to delaying the downforce loss phenomenon as shorter span wings generated a main wing vortex equal in strength and size to the larger span wings and therefore was able to regenerate the boundary layer over a larger portion of the wing preventing separation from occurring.

The combined wing and wheel investigation commenced using a wheel with width and track values equal to $W/c=0.631$ and $T/c=1.6$ respectively. Three different flow interactions were observed that differed in the path that either the main or secondary wing vortices will take around the wheel and the subsequent effect that these flow structures have on the wheel wake. The main and secondary wing vortices would found to either pass:

- on the outboard side (interaction “a”)
- inboard and outboard of the wheel respectively (interaction “b”), and
- both inboard (interaction “c”)

For the above stated wheel width and track values, interaction “a” was observed to occur only when the span was equal to the wheel width and the wing angle of attack was less than or equal to 4° . Due to the wing spanning across the entire wheel, the high pressure regions formed forward of the wheel reduced the wing’s ability to generate suction beneath the wing. Subsequently, reductions in wing downforce and drag of up to 40% and 70% respectively were obtained in this configuration. The presence of the high pressure regions also acted to reduce the pressure differential experienced by the bottom edge of the endplate causing the main wing vortex strength and size to be reduced in comparison to the corresponding isolated wing. After passing on the outboard side of the wheel both the main and secondary wing vortices had little influence on the wheel wake structure or the forces experienced by the wheel in comparison to the same wheel belonging to an isolated pair.

Increasing the angle of attack to a value of 8° or greater at a span equal to the wheel track allowed interaction “b” to be obtained. Doing so increased the low pressure region beneath the wing sufficiently to allow the high pressure regions formed forward of the wheel to be

overcome, such that the main wing vortex travelled inboard of the wheel. The high pressure regions forward of the wheel were also observed to be weakened and positioned further outboard as a result of the increased suction generated by the wing in this configuration. As a result the wing's ability to generate downforce was generally found to be less affected with downforce reductions of 10% been obtained in comparison to an equivalent wing in isolation. Given that the endplate is still positioned outboard of the stagnation regions belonging to the wheel, the secondary wing vortex was observed to pass outboard of the wheel. This interaction was also achieved at all angles of attack tested with a span value of $S/c=1.42$ and also at 8° and 12° wing angles of attack at a span value of $S/c=1.24$. By reducing the span of the wing, it was determined that the suction required to draw the main wing vortex to the inboard side of the wheel was reduced, as was the wheel's ability to reduce the low pressure that could be achieved beneath the wing. For this reason, the lower angles of attack at the shorter wing spans also caused the main wing vortex to travel inboard. In doing so, the main wing vortex reduced the separation experienced on the inner face of the contact patch and increased the flow entrainment into the wake from the side. The main wing vortex interaction with the wheel wake also reduced the downwash experienced in the central wheel wake region allowing the wheel lift and drag to be reduced by up to 45% and 25% respectively. When considering the combined lift and drag of the wheel, interaction "b" was observed to produce the largest total downforce values when the wing span overlapped between 65% and 75% of the wheel. This optimum would not have been observed if the wing and wheel was studied individually and only the sum of both body's lift was considered, highlighting the importance of optimising the wing in the presence of the wheel.

Reducing the angle of attack of the $S/c=1.24$ wing to 0° and 4° allowed the secondary vortex to travel inboard of the wheel allowing interaction "c" to occur. Both the main and secondary wing vortices travelled inboard for all angles of attack tested with span values less than $S/c=1.24$. The most unique feature of this interaction being that the secondary wing vortex rotates in the opposite direction to that observed for interaction "a" and "b" as well as for the corresponding wings in isolation. This was found to occur due to the high pressure regions generated by the wheel being located outboard of the endplate and as a result the direction of the pressure differential across the top edge of the endplate was reversed. Only in this configuration, and when the corresponding wing in isolation was stalled, was the presence of the wheel observed to assist the wing to produce increases in

downforce. The high pressure region forward of the wheel was found to increase the pressure differential experienced about the bottom edge of the endplate allowing the main wing vortex to be stronger and therefore assist with alleviating the separation that would be experienced by the equivalent wing in isolation. When this was observed, wing downforce and drag increases of up 10% and 20% respectively were observed. Given that the path of the main wing vortex for interaction “c” was found to be similar to that of interaction “b”, lift and drag reductions were also obtained for the wheel for this interaction. The extent of the wheel lift and drag was found to reduce as the span of the wing was also reduced, as this caused the main wing vortex to travel further inboard. At the smallest span tested, the main wing vortex was found to remain independent of the wheel wake further downstream and therefore, have little influence on the wheel wake as well as lift and drag values.

The downforce loss phenomenon was also investigated in the presence of a wheel using a wing with 4° angle of attack at two different span values of $S/c=0.97$ and $S/c=1.6$. These span values were chosen as they allowed the wheel to be completely overlapped by the wing or not at all. In both cases the height at which the downforce loss phenomenon was observed to occur was lower than that of the corresponding wing in isolation, but the downforce loss phenomenon was achieved at a larger height for the smaller span wing in comparison to the larger span wing when in the presence of the wheel. While this trend is opposite to that determined during the isolated wing study investigating the effect that the span has on the downforce loss phenomenon, the causes for this variation in the presence of the wheel were found to be consistent with those described for the wing in isolation. The $S/c=0.97$ wing in the presence of the wheel was observed to have a stronger main wing vortex at all heights testing due to the greater pressure differential created about the bottom edge of the endplate by the high pressure regions formed forward of the wheel. The increase in size and strength of the main wing vortex assisted with re-energising a greater portion of the boundary layer allowing the height at which the downforce loss phenomenon occurred to be reduced by $0.08c$. At all heights tested for this wing span, interaction “c” was observed with the greatest lift and drag variation for the wheel being obtained at a wing height of $0.223c$ (47% and 13% respectively). At this height, the reduced cross velocity component generated by the wing, in comparison to that experienced at the lower heights, allowed the main wing vortex to be positioned adjacent to the inside face of the wheel and to interact in a favourable manner with the wheel wake.

The variation in the height obtained by the $S/c=1.6$ wing in the presence of the wheel was achieved due to the high pressure regions created by the wheel reducing the wing's ability to generate low pressure beneath the wing and therefore, also reduced the adverse pressure gradient experienced at the centre of the wing. As a result, the height that the downforce loss phenomenon was achieved at was reduced from $h/c=0.112$ to a value less than $h/c=0.08$ confirming that the adverse pressure gradient is a much more significant feature in determining the height at which the downforce loss phenomenon will occur in comparison to the strength of the main wing vortex. For the $S/c=1.6$ span wing, at heights greater than $0.121c$ interaction "a" was observed with little variation in the wheel lift and drag as previously reported for this interaction. As the height of the wing was reduced, the increase in suction generated by the wing drew the main wing vortex in board, but not until a height of $0.091c$ had the main wing vortex been observed to completely pass the wheel allowing interaction "b" to occur. Between these two heights, the main wing vortex was shown to be trapped by the converging surfaces of the rotating wheel and moving ground and being disturbed in the process. As lower heights allowed the main wing vortex to pass the wheel, the greatest lift and drag reduction experienced by the wheel in this configuration (57% and 27% respectively) was achieved at the lowest height tested ($h/c=0.08$). Given that the downforce loss phenomenon occurs due to increased levels of separation from the bottom surface of the wing, it would be expected that the height at which this occurs would also vary with the freestream velocity and turbulence intensity. Therefore, the height at which this phenomenon occurs at should be expected to be overestimated by computational models as well as wind tunnel tests in comparison to what would be experienced by an open wheel racing on track.

The conclusions discussed above also explain the discrepancy in previous reports which state that the presence of the wheel increases (Taylor, 1992) or reduces (Thisse, 2004) the downforce produced by the wing in comparison to the same wing in isolation. This investigation has demonstrated that the type of interaction that will occur is dependant on the span, angle of attack and height of the wing and the same parameters determine the variation in downforce experienced by a wing in the presence of a wheel in comparison to the same wing in isolation. Therefore, the variations in wing and wheel geometries used during Thisse (2004) and Taylor's (1992) investigation are legitimate causes for the discrepancy in the conclusion obtained for these two previous investigations.

Results were also obtained at the same angles of attack for a single variation of wheel width ($W/c=0.53$) and also a single variation in wheel track ($T/c=1.78$). During both of these investigations the span of the wing was varied such that results were obtained for a range of wing and wheel overlap values of 0 to 100%. As was determined by the isolated wheel study of two adjacent wings, the variations in the forces and the flow structures obtained for a combined wing and wheel when adjusting these parameters was determined to be insignificant. In both cases the optimum downforce condition was achieved with a wing and wheel overlap in the region of 65% to 75% for all wing angles of attack tested.

This investigation has determined that the combined downforce and drag of a wing and wheel operating in unison can vary by up to 77% and 31% respectively in comparison to the sum of the same bodies in isolation. These variations can be estimated to be equivalent to 23% and 12% of the total open wheeler's downforce and drag respectively when considering the contribution that these two bodies make to downforce and drag produced by an open wheel racing car. The span, angle of attack and height were found to be the most sensitive parameters, while the wheel width and track did little to vary the span at which the maximum downforce and drag was obtained at. For all wheel widths and tracks, the optimum was obtained with a wing and wheel overlap of 65% to 75%.

7.2. Recommendations for Future Work

In this study the interaction of a wing and wheel relevant to an open wheel racing car was investigated. Additional investigations could also be undertaken to further contribute to the understanding of this unique interaction. One extension of this work which has not been considered is the effect that steered wheels would have on the interaction of a front wing and wheel. While the freestream conditions for the full scale computational model were chosen to be representative of an open wheel racing car during cornering, in reality, the front wheels during this condition are yawed to the oncoming flow. Wray (2003) has undertaken an initial investigation considering the variation in vortex structures due to the yaw angle for a single isolated wheel demonstrating that the primary wheel vortex strengths asymmetrically vary as do the secondary wheel vortices. Given that these flow structures when interacting with the main wing vortex dictate the variation in the wheel lift and drag, it is likely that this interaction would vary for a steered wheel. Such an

investigation would require considerably more resources given that both sides will have to be modelled and that no symmetry condition can be applied and for this reason were not undertaken here.

Force trends obtained by Wray (2003) of a yawed wheel differ to those presented by Whitbread (2000) and therefore experimental data of a wheel at different yaw angles is also required for future validation. The experimental results most commonly used for validation of a computational model of an isolated wheel are those provided by Fackrell (1975). Unfortunately, Fackrell has admitted that there are some unexplainable errors in his results which time constraints prevented him from repeating. While Hinson (1999) also provided similar data, the lack of a detailed description of the wheel geometry utilised makes this data less suitable for validation. Therefore, published experimental measurements of an isolated wheel's pressure distributions and forces that also include details of the wheel geometry used would be expected to greatly benefit future computational investigations in this area. Such an experimental investigation could also be extended to consider the yaw angle of the wheel and the validity in using solid wheels for wind tunnel testing of an open wheel racing car given that pneumatic tyres are now the industry standard (Gillan, 2009).

While it was demonstrated that the mean flow structures associated with a rotating wheel which are predicted by a transient computational model can be reproduced by a steady state computational model, no reference is available of how the flow structures associated with a rotating wheel vary with time or if these results converge to a steady state solution. Given that the wake structure of the wheel alters with the addition of a wing upstream, it would also be valuable to see how the interaction of a wing and wheel would also vary with time to determine if the amplitude and frequency of these variations are adequately significant to alter the vehicles handling characteristics. This would be expected to be of greater significance when the wing height is less than that at which the maximum downforce is obtained, separation is expected to occur from the wing, and also for configurations where the main wing vortex does not pass the wheel contact patch cleanly (between interaction "a" and "b"). For such an investigation, the validity of using a symmetry plane would also have to be confirmed.

A combined wing and wheel experimental investigation considering the parameters investigated here using larger scaled models and a higher freestream velocity than that used during the experimental portion of this investigation would also be valuable. While comparisons to Fackrell's (1975) and Zerihan's (2001) experimental investigations were conducted at a higher Reynolds number than that which the LDA results were obtained at, it would have been preferred if a combined wing and wheel comparison could also have been conducted at a more representative Reynolds number. This would provide experimental data for a more valid comparison, particularly for selecting the most appropriate turbulence model, given that the experimental results used for this purpose were somewhat limited by the scale and freestream velocity of the experimental facility. By conducting an experimental investigation of a wing and wheel, it would be possible to determine with a higher resolution the span that provides the optimum total wing and wheel downforce. Additionally, several different endplates and multi-element wing geometries that are more realistic representations of those used by open wheel racing cars can also be investigated if the scale of the models are increased.

While the current study has demonstrated that the flow structures produced by the wing can influence the wake of the wheel, it has not been considered how these changes may affect other aerodynamic components further downstream belonging to an open wheel racing car. Therefore, a further computational and experimental study that modifies the span of the wing in the presence of a simplified complete car such that the variations in forces experienced by the rear wing, rear wheels, diffuser and floor can be measured would also be considered valuable.

List of Publications

Diasinos, S., Barber, T.J., Leonardi, E. and Hall, S.D., "A Two-Dimensional Analysis of the Effect of a Rotating Cylinder on an Inverted Aerofoil in Ground Effect," *Proceedings of the 15th Australasian Fluid Mechanics Conference, Dec 13-17, Sydney Australia, 2004*

Barber, T.J., Beves, C., Diasinos, S., Doig, G. and Leonardi, E., "Ground Effect Aerodynamics," *Proceedings of the 2nd European Automotive Conference, Jun 29-30, Frankfurt, Germany, 2005*

Diasinos, S., Barber, T.J., Leonardi, E. and Hall, S.D., "Validation of a 2D CFD Model for the Implementation of a Moving Ground in the UNSW 3x4ft Wind Tunnel," *Proceedings of the 5th Pacific Symposium on Flow Visualization and Image Processing, Sept 23-27, Daydream Island, Australia, 2005a*

Diasinos, S., Barber, T.J., Leonardi, E. and Hall, S.D., "An Experimental and Numerical Two-Dimensional Analysis of the Effect of a Rotating Cylinder on an Inverted Aerofoil in Ground Effect," *Proceedings of the 5th Pacific Symposium on Flow Visualization and Image Processing, Sept 23-27, Daydream Island, Australia, 2005b*

Diasinos, S., Barber, T.J., Leonardi, E., Gatto, A., "The Interaction of a Rotating Cylinder and an Inverted Aerofoil in Ground Effect: Validation and Verification," *AIAA 2006-3325, 2006*

Barber, T.J., Beves, C., Diasinos, S., Doig, G., Leonardi, E. and Neely, A., "Experimental and Computational Studies of Ground Effect Automotive Aerodynamics," *Proceedings of the FISITA Conference, October, 2006*

Barber, T.J., Beves, C., Diasinos, S., Doig, G., Leonardi, E. and Neely, A., "Studies of Ground Effect Automotive Aerodynamics," *Automotive Aerodynamics, Auto Technology, Edition: 2007-02, 2007*

Diasinos, S. and Gatto, A., "Experimental Investigation into Wing Span and Angle-of-Attack Effects on Sub-scale Race Car Wing/Wheel Interaction Aerodynamics," *Exp in Fluids, 45:537-546, 2008*

Diasinos, S. and Beves, C., "Design Features of the UNSW Low Speed 225x340mm Open Circuit Wind Tunnel and Moving Ground," *School of Mechanical and Engineering Internal Report, UNSW, 2009*

List of References

Abbott, I. and von Doenhoff, A.E., "Theory of Wing Sections," *Dover Publications*, 1959

Agathangelou, B. and Gascoyne, M., "Aerodynamic Considerations of a Formula One Racing Car," *SAE 980399*, 1998

AIAA, "Guide for the Verification and Validation of Computational Fluid Dynamics Simulations," *AIAA, G-077-1998*, 1998

Akanni, S., "Running Rampant," *Journal Articles By Fluent Software Users*, 1995

Albrecht, H.E., Borys, M., Damanshke, N., Tropea, C., "Laser Doppler and Phase Doppler Measurement Techniques," *Users (1999)*, 1998

Axon, L., "The aerodynamic Characteristics of Automobile Wheels," *PhD thesis, Cranfield University*, 1998

Axon, L., Garry, K., and Howell, J., "An Evaluation of CFD for Modelling the Flow Around Stationary and Rotating Wheels," *SAE 980032*, 1998

Axon, L., Garry, K., and Howell, J., "The Influence of Ground Condition on the Flow Around a Wheel Located Within a Wheelhouse Cavity," *SAE 1999-01-0806*, 1999

Barber, T.J., "A Study of a Lifting Wing in Ground Effect," *PhD thesis, University of New South Wales*, 2000

Barlow, J.B., Rae, W.H. and Pope, A., "Low-Speed Wind Tunnel Testing," *3rd Edition, John Wiley & Sons*, 1999

Bearman, P.W., De Beer, D., Hamidy, E. and Harvey, J.K., "The Effect of a Moving Floor on Wind Tunnel Simulation of Road Vehicles," *SAE 880245*, 1988

Beauvis, F.N., Tignor, S.C. and Turner, T.R., "Problems of Ground Simulation in Automotive Aerodynamics," *SAE 680121*, 1968

Benedict, L.H. and Gould, R.D., "Towards Better Uncertainty Estimates for Turbulence Statistics," *Exp. in Fluids*, 2006

Boussinesq, J., "Thorie de L'coulement Tourbillant," *Mem. Prsents par Divers Savant Acad. Sci. Inst. Fr.*, 1877

Carr, G.W., "A Comparison of the Ground Place Suction and Moving Belt Ground Representation Techniques," *SAE 880249*, 1988

Celik, I. and Zhang, W., "Calculation of Numerical Uncertainty in Computational Fluid Dynamics," *Journal of Fluids Engineering, Vol. 117, No.3, pp. 439-445*, 1995

Chou, P.Y., "On the Velocity Correlations and the Equations of Turbulent Vorticity Fluctuation," *Quarterly of Applied Mathematics* 1:33-54, **1945**

Chung, T. J., "Computational Fluid Dynamics," *Cambridge University Press*, **2002**

Cogotti, A., "Aerodynamic Characteristics of Car Wheels," *Int. Jou. Vehicle Design*, no. SP-3, pp. 173-196, **1983**

Corray, P., "Establishing a Particle Image Velocimetry System for Studying Heat Transfer Enhancements using Dimpled Surfaces," *MSc thesis, University of New South Wales*, **2005**

Cumming, R. J., "CFD Investigation on Front Wing Geometry of a Formula 3 Car," *MSc thesis, Cranfield University*, **2002**

Dantec, "BSA Flow Software Installation and User's Guide v4.10," *10th Edition, Dantec*, **2006**

Diasinos, S. and Beves C., "Design Features of the UNSW Low Speed 225x340mm Open Circuit Wind Tunnel and Moving Ground," *School of Mechanical and Engineering Internal Report, UNSW*, **2009**

Diasinos, S., Barber, T.J., and Leonardi, E., "The Interaction of a Rotating Cylinder and an Inverted Aerofoil in Ground Effect: Validation and Verification," *AIAA 2006-3325*, **2006**

Diasinos, S., Barber, T.J., Leonardi, E. and Hall, S.D., "Validation of a 2D CFD Model for the Implementation of a Moving Ground in the UNSW 3x4ft Wind Tunnel," *Proceedings of the 5th Pacific Symposium on Flow Visualization and Image Processing, Sept 23-27, Daydream Island, Australia*, **2005a**

Diasinos, S., Barber, T.J., Leonardi, E. and Hall, S.D., "An Experimental and Numerical Two-Dimensional Analysis of the Effect of a Rotating Cylinder on an Inverted Aerofoil in Ground Effect," *Proceedings of the 5th Pacific Symposium on Flow Visualization and Image Processing, Sept 23-27, Daydream Island, Australia*, **2005b**

Doddegowda, P., Bychkovsky, A. L. and George, A. R., "Use of Computational Fluid Dynamics for the Design of Formula SAE Race Car Aerodynamics," *SAE 2006-01-0807*, **2006**

Doig G., Barber T. J., Leonardi, E. and Neely A. J., "The Onset of Compressibility Effects for Aerofoils in Ground Effect," *Aeronautical Journal, Vol. 111, no1126*, pp. 797-806, **2007**

Dominy, J. A. and Dominy, R. G., "Aerodynamic Influences on the Performance of a Grand Prix Car," *V198 D p1-7 Pro Inst Mech Eng*, **1984**

Dominy, R. G., "Aerodynamics of Grand Prix Car," *Proceedings of the Institution of Mechanical Engineers, V206* pp. 267-274, **1992**

Fackrell, J. E. and Harvey, J. K., "The Flowfield and Pressure Distributon of an Isolated Road Wheel," *Imperial College Science and Technology*, **1972**

Fackrell, J. E. and Harvey, J. K., "The Flowfield and Pressure Distributon of an Isolated Road Wheel," *Advances in Road Vehicle Aerodynamics*, **1973**

Fackrell, J. E. and Harvey, J. K., "The Aerodynamics of an Isolated Road Wheel," *Proceedings of the 2nd Symposium on Aerodynamic of Sports and Competition Automobiles, AIAA*, **1975**

Fackrell, J.E., "The Aerodynamics of an Isolated Wheel Rotating in Contact with the Ground," *Ph.D. thesis, London, Imperial College of Science and Technology*, **1975**

Ferziger, J.H. and Peric, M., "Computational Methods for Fluid Dynamics," *Springer, 3rd edition*, **2002**

FIA, "1996 F1 Technical Regulations," *FIA*, **1996**

FIA, "1997 F1 Technical Regulations," *FIA*, **1997**

FIA, "2009 F1 Technical Regulations," *FIA*, **2009**

Fluent, "Fluent User Guide," *Fluent*, **2006**

Garchev, D. and Mortenson, B., "Discusions Regarding Methods of Aligning a Three Dimensional Laser Doppler Anemometer Using a Pin Holes," *Personal communication*, **2005**

Gatto, A., "Discusions Regarding Methods of Aligning a Three Dimensional Laser Doppler Anemometer Using a CCD Chip," *Personal communication*, **2004**

Gillan, M., "Discusions Regarding Reynolds Number and Tyre Modeling for Wind Tunnel Testing of Open Wheel Racing Cars," *Personal communication*, **2009**

Hinson, M., "Measurement of the Lift Produced by an Isolated Rotating Formula One Wheel Using a New Pressure Measurement Sytem," *MSc thesis, Cranfield University*, **1999**

Hinze, J.O., "Turbulence," *McGraw-Hill Publishing Co., New York*, **1975**

Hucho, W.H. and Sovran, G., "Aerodynamics of Road Vehicles," *Annu. Rev. Fluid Mech., Vol. 25, pp.285-537*, **1993**

Imaizumi, T. and Yoshida, Y., "The Aerodynamic Effect of Rotating Wheels," *JSAE Review 12(4):64-66*, **1991**

Jasinski, W.J. and Selig, M.S., "Experimental study of Open-wheel Race Car Front Wing," *SAE 983042*, **1998**

Jongen, T., "Simulation and Modeling of Turbulent Incompressible Flows," *PhD thesis, EPF Lausanne*, **1992**

Kahler, C.J., "The Significance of Coherent Flow Structures for the Turbulent Mixing in Wall-bounded Flows," *PhD thesis, Georg-August-Universitat*, **2004**

Katz, J., "High-Lift Wing Design for Race-Car Applications," *SAE 951976*, **1995**

Katz, J., "Aerodynamics of Race Cars," *Annu. Rev. Fluid Mech., Vol. 38*, pp.27-63, **2006**

Katz, J., "Aerodynamic Effects of Indy Car Components," *SAE 2002-01-3311*, **2002**

Kellar, W. P., Pearse, S.R.G. and Savill, A.M., "Formula 1 Car Wheel Aerodynamics," *Sports Engineering Journal, 2*, 203-212, **1999**

Kellar, W. P., Targett, G. J., Savill, A. M., Dawes, W. N., "An Investigation of Flowfield Influences Around the Front Wheel of a Formula 1 Car," *Proceedings of the 3rd International Conference on the Engineering of Sport*, pp. 353-360, Jun, Sheffield, United Kingdom, **2000**

Kim, M.S. and Geropp, D., "Experimental Investigation of the Ground Effect on the Flow Around Some Two Dimensional Bluff Bodies with Ground Effect," *J. of Wind Eng. & Industrial Aero., 74-76*, pp.511-519, **1998**

Knowles, K., Donoghue, D.T. and Finnis, M.V., "A Study of Wings in Ground Effect," *Proceedings of the Royal Aerospace Society Conference on Vehicle Aerodynamics*, pp. 22.1-22.13, **1994**

Knowles, R.D., Saddington, A. and Knowles, K., "On the Near Wake of Rotating, 40% Scale Champ Car Wheels," *SAE 2002-01-3293*, **2002**

Kolmogorov, A.N., "Equations of Turbulent Motion of an Incompressible Fluid," *Izvestia Academy of Sciences, Vol. 6, No. 1 and 2*, pp. 56-58, **1942**

Launder, B. E., Reece, G. J. and Rodi, W., "Progress in the Development of a Reynolds-Stress Turbulent Closure," *Journal of Fluid Mechanics, Vol. 68(3)*, pp. 537-566, **1975**

Launder, B.E. and Sharma, A., "Application of the Energy-Dissipation Model of Turbulence to the Calculation of Flow Near a Spinning Disk," *Letters in Heat and Mass Transfer. 1*, 131-138, **1974**

Launder, B.E. and Spalding, D.B., "Lectures in Mathematical Models of Turbulence," *Academic Press*, **1972**

Launder, B.E. and Spalding, D.B., "The Numerical Computation of Turbulent Flows," *Computer Methods in Applied Mechanics and Engineering, 3:269-289*, **1974**

Mahon, S. and Zhang, X., "Computational Analysis of Pressure and Wake Characteristics on an Aerofoil in Ground Effect," *ASME J. Fluids Eng., Vol. 127*, pp. 290-298, Mar, **2005**

McBeath, S., "Competition Car Downforce," *Haynes Publishing*, **1998**

McManus, J. and Zhang, X., "A Computational Study of the Flow Around an Isolated Wheel in Contact With Ground," *Journal of Fluids Engineering*, Vol. 128, No. 3, pp. 520-530, **2006**

Menter, F. R., "Two-Equation Eddy-Viscosity Turbulence Models for Engineering Applications," *AIAA Journal*, Vol. 32, No. 8 pp. 269-289, Aug, **1994**

Menter, F. R., Kuntz, M. and Langtry, R., "Ten Years of Industrial Experience with the SST Turbulence Model," *Turbulence, Heat and Mass Transfer 4*, pp. 652-653, **2003**

Mercker, E., Breuer, N., Berneburg, H. and Emmelmann, H.J., "On the Aerodynamic Interference Due to the Rolling Wheels of Passenger Cars," *SAE 910311*, **1991**

Metz, L. D., "Aerodynamic Properties of Indy Cars," *SAE 870726*, **1987**

Morelli, A., "Aerodynamic Effects of an Automobile Wheel," *MIRA Translation number 47/69 of A.T.A.*, Vol. 22, No. 6 pp. 281-288, **1969**

Morelli, A., "Aerodynamic Actions on an Automobile Wheel," *Proceedings of the 1st Symposium on Road Vehicle Aerodynamics*, London, United Kingdom, **1970**

Mortel, F., "The Front Wing," *MSc thesis, Cranfield University*, **2002**

Motson, B.C. and Archer, R.D., "Design Features of the Low Speed 4ftx3ft Return Circuit Wind Tunnel," *Report No. 19969/FMT/3*, UNSW, **1969**

Oswald, L.J. and Brone, A.L., "The Airflow Field Around an Operating Tire and its Effect on Tire Power Loss," *SAE 810166*, **1981**

Pacejka, H.B., "Tyre and Vehicle Dynamics," *2nd Edition, SAE International*, Dec, **2005**

Patanker, S.V., "Numerical Heat Transfer and Fluid Flows," *Hemisphere (McGraw-Hill) New York*, **1980**

Ramnefors, M., Bensryd, R., Holmberg, E. and Perzon, S., "Accuracy of Drag Predictions on Cars using CFD - Effect of Grid Refinement and Turbulence Models," *SAE 960681*, **1996**

Ranzenbach, R. and Barlow, J., "Two Dimensional Aerofoil in Ground Effect, Experimental and Computational Study," *SAE 942509*, **1994**

Ranzenbach, R. and Barlow, J., "Cambered Airfoil in Ground Effect - Wind Tunnel and Road Conditions," *AIAA 95-1909-CP*, **1995**

Ranzenbach, R. and Barlow, J., "Cambered Airfoil in Ground Effect - An Experimental and Computational Study," *SAE 960909*, **1996**

Ranzenbach, R. and Barlow, J., "Multielement Aerofoil in Ground Effect, Experimental and Computational Study," *AIAA 97-2238*, **1997**

- Sardou, M.**, "Reynolds Effect and Moving Ground Effect Tested in a Quarter Scale Wind Tunnel Over a High Speed Moving Belt," *J. of Wind Eng. & Industrial Aero.*, Vol. 22, pp.345-370, **1986**
- Sawley, M.L. and Richter, R.**, "Numerical simulation of the Flow around a Formula 1 Racing car," *Proceedings of the 9th EPFL Supercomputing Review*, **1997**
- Schubauer et al. 1958**, "Aerodynamic Characteristics of Damping Screens," *NACA Technical Note 2001*, **1958**
- Shaw, C.T.**, "Using Computational Fluid Dynamics," *Prentice Hall*, **1992**
- Shih T.H., Liou, W.W., Shabir, A., Yang, Z. and Zhu, J.**, "A New k-e Eddy Viscosity Model for High Reynolds Number Turbulent Flows," *Computers Fluids*, 24(3):227-238, **1995**
- Skea, A.F., Bullen, P.R. and Qiao, J.**, "The Use of CFD to Predict the Flow Around a Rotating Wheel," *Proceedings of the MIRA International Conference on Vehicle Aerodynamics, London, United Kingdom*, **1998**
- Skea, A.F., Bullen, P.R. and Qiao, J.**, "CFD Simulations and Experimental Measurements of the Flow Over a Rotating Wheel in a Wheel Arch," *SAE 2000-01-0487*, **2000**
- Smith, A.M.O.**, "High Lift Aerodynamics," *J. of Aircraft*, Vol 12 No 6 p501-530, **1975**
- Spalart, P.R., and Allmaras, S.R.**, "A One-Equation Model for Aerodynamic Flows," *AIAA 92-0439*, **1992**
- Stapleford, W.R. and Carr, G.W.**, "Aerodynamic Characteristics of Exposed Rotating Wheels," *MIRA Technical Report 1970/2*, **1970**
- Stapleford, W.R. and Carr, G.W.**, "Blockage Effects in Automotive Wind Tunnel Testing," *SAE 860093*, **1986**
- Swales, C., Rickards, J., Brake, C.J. and Barrett, R.V.**, "Development of a Pin-hole Meter for Aligning 3D Laser Doppler Anemometers," *Dantec Information No.12, February*, **1993**
- Taylor, R.M.**, "The Interaction of the Flow Around the Front Wheels and Wing of a Single Seater Racing Car," *MSc thesis, Cranfield University*, **1992**
- Thisse, E.**, "Influence of End-Plates on Tip Vortices in Ground Effect for a 2004 Formula One Front Wing," *MSc thesis, Cranfield University*, **2004**
- Van Doormal, J.P. and Raithby, G.D.**, "Enhancements of the SIMPLE Method for Predicting Incompressible Fluid Flows," *Numerical Heat Transfer, Vol. 7*, pp.147-163, **1984**
- Versteeg, H.K., and Malalasekera, V.**, "Computational Fluid Dynamics," *Prentice Hall*, **1998**

- Whitbread, L.**, "Measurement of the Lift Distribution on a Rotating Wheel," *MSc thesis, Cranfield University*, **2000**
- Wickern, G. and Dietz, S.**, "Gradient Effects on Drag Due to Boundary-Layer Suction in Automotive Wind Tunnels," *SAE 2003-01-0655*, **2003**
- Wilcox, D.C.**, "Turbulence Modeling for CFD," *DCW Industries Inc.*, **2000**
- Wordley, S. and Saunders, J.**, "Aerodynamics for Formula SAE: A Numerical, Wind Tunnel and On-Track Study," *SAE 2006-01-0808*, **2006**
- Wray, J.**, "A CFD Analysis Into the Effect of Yaw Angle on the Flow Around an Isolated Rotating Wheel," *MSc thesis, Cranfield University*, **2003**
- Yakhot, V. and Orszag, S.A.**, "Renormalization Group Analysis of Turbulence: One Basic Theory," *Journal of Scientific Computing*, **1986**
- Zahm, A. F. and Bear, R. M.**, "Ground-Plane Influence on Airplane Wings," *J. Franklin Inst.*, 191(5), pp. 687-693, **1921**
- Zerihan, J.**, "An Investigation into the Aerodynamics of Wings in Ground Effect," *PhD thesis, Southampton University*, **2001**
- Zerihan, J. and Zhang, X.**, "Aerodynamics of a Single Element Wing in Ground Effect," *J. of Aircraft*, Vol 37, No. 6, Nov-Dec, **2000**
- Zerihan, J. and Zhang, X.**, "Force Enhancement of Gurney Flaps on a Wing in Ground Effect," *AIAA 2000-2241*, **2000**
- Zerihan, J. and Zhang, X.**, "Aerodynamics of Gurney Flaps on a Wing in Ground Effect," *AIAA Journal Vol. 39, no. 5*, pp. 772-780, May, **2001**
- Zerihan, J. and Zhang, X.**, "A Single Element Wing in Ground Effect - Comparisons of Experiments and Computation," *AIAA 2001-0423*, **2001**
- Zhang, X. and Zerihan, J.**, "Off Surface Aerodynamic Measurements of a Wing in Ground Effect," *J. of Aircraft*, Vol. 40, No. 4, pp 716-725, Jul-Aug, **2003**
- Zhang, X. and Zerihan, J.**, "Aerodynamics of a Double Element Wing in Ground Effect," *AIAA 2002-0834*, **2002**
- Zhang, X. and Zerihan, J.**, "Edge Vortices of a Double Element Wing in Ground Effect," *J. of Aircraft*, Vol. 41, No. 5, pp 1127-1137, Sep-Oct, **2004**
- Zhang, X., Zerihan, J., Ruhrmann, A., and Deviese, M.**, "Tip Vortices Generated by a Wing in Ground Effect," *Proceedings of the 11th international Symposium on Applications of Laser Techniques to Fluid Mechanics, Jul 8-11, Lisbon, Portugal*, **2002**
- Zhang, X., Toet, W., and Zerihan, J.**, "Ground Effect Aerodynamics of Race Cars," *Applied Mechanics Reviews*, Vol. 59, Iss. 1, pp. 33-49, Jan, **2006**

Appendix A:

Detailed drawings of experimental models

A

B

C

D

4

4

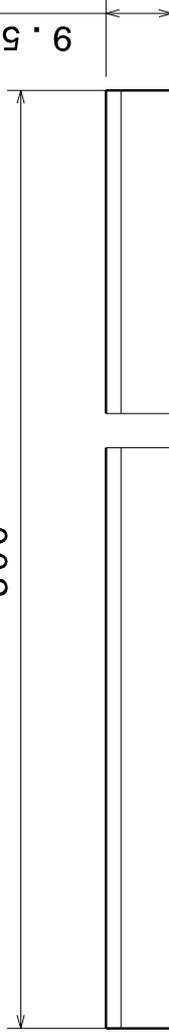
3

3

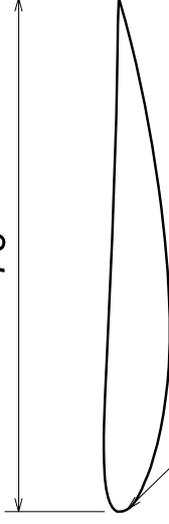
300

9.56

75



Front view



Right view

NC Code to be provided
for NACA 4412 profile

1

1

A

B

C

D

Name: Wing Section
Drawing No: AER-01
Drawn by: S. Diasinos

Scale: 1:1
Material: Acrylic
All dimension in mm

UNSW
The School of Mechanical and
Manufacturing Engineering

A

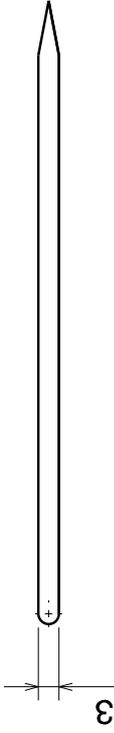
B

C

D

4

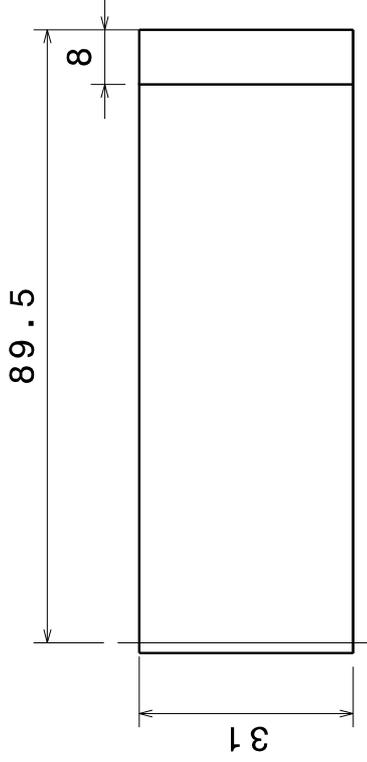
4



Top view

3

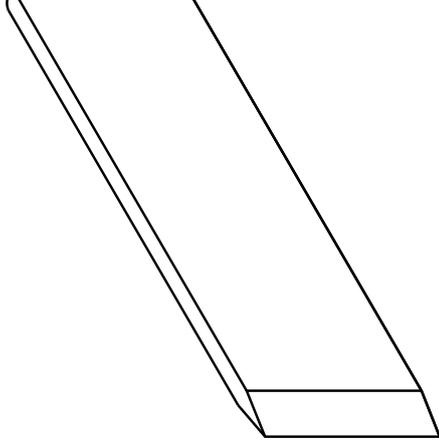
3



Front view

2

2



Isometric view

1

1

A

B

C

D

Name: Wing Endplate
 Drawing No: AER-02
 Drawn by: S. Diasinos

Scale: 1:1
 Material: Acrylic
 All dimension in mm

A

B

C

D

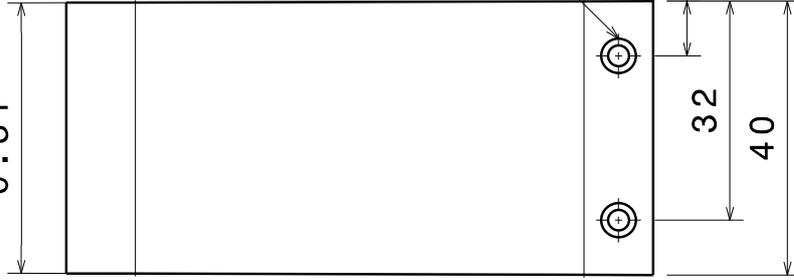
4

3

2

1

0.31°



2 Off $\phi 6$
 8 deep
 $\phi 3$ right
 through

Front view

A

B

C

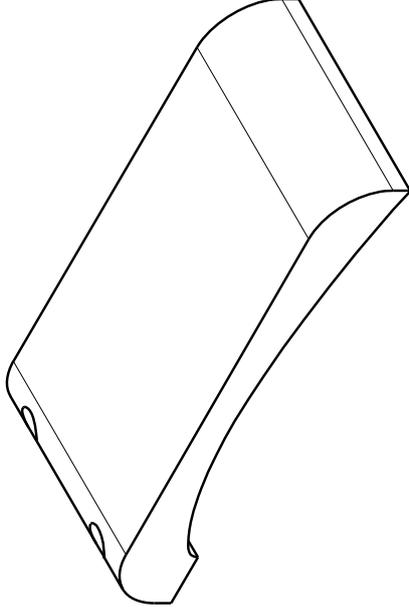
D

4

3

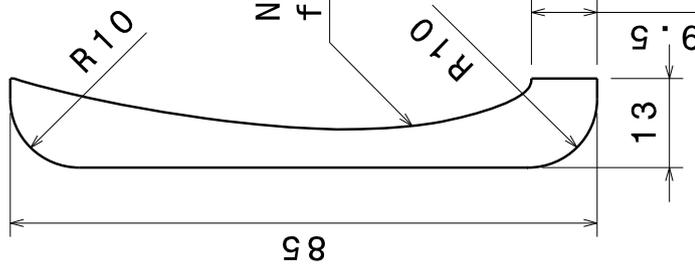
2

1



Isometric view

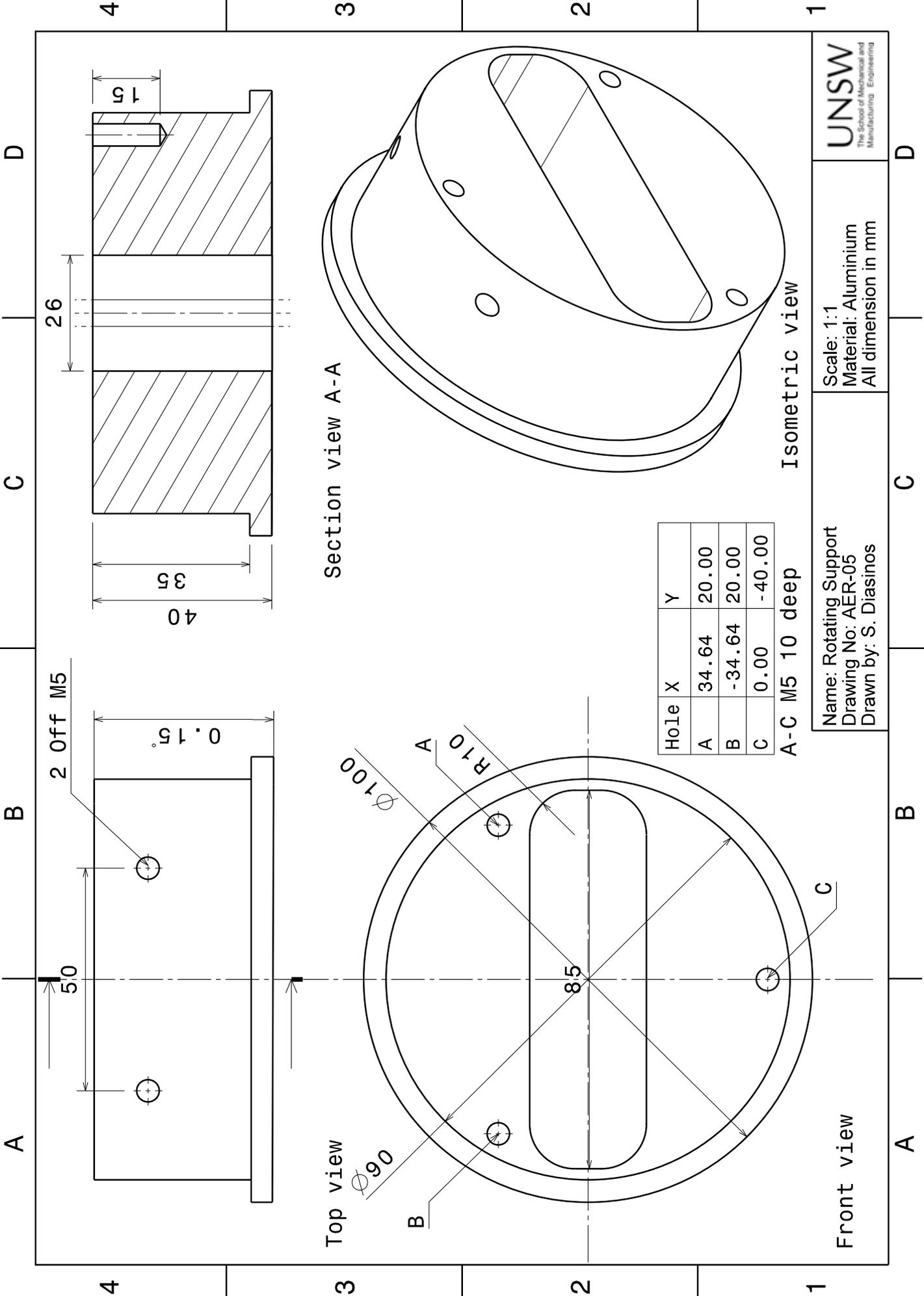
NC code to be provided
 for this surface



Right view

Name: Bottom Clamp
 Drawing No: AER-04
 Drawn by: S. Diasinos

Scale: 1:1
 Material: Renshape
 All dimension in mm



Section view A-A

Top view

Isometric view

Hole X	Y
A	34.64 20.00
B	-34.64 20.00
C	0.00 -40.00

A-C M5 10 deep

Front view

Name: Rotating Support
 Drawing No: AER-05
 Drawn by: S. Diasinos

Scale: 1:1
 Material: Aluminium
 All dimension in mm

A

B

C

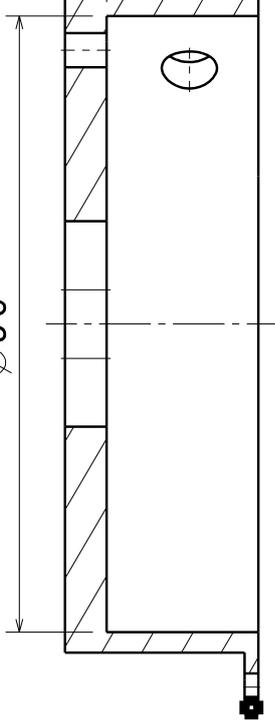
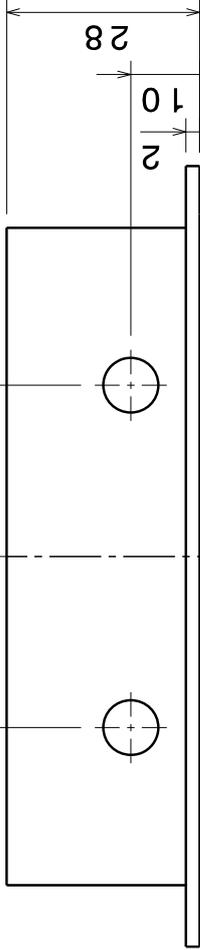
D

50

∅90

4

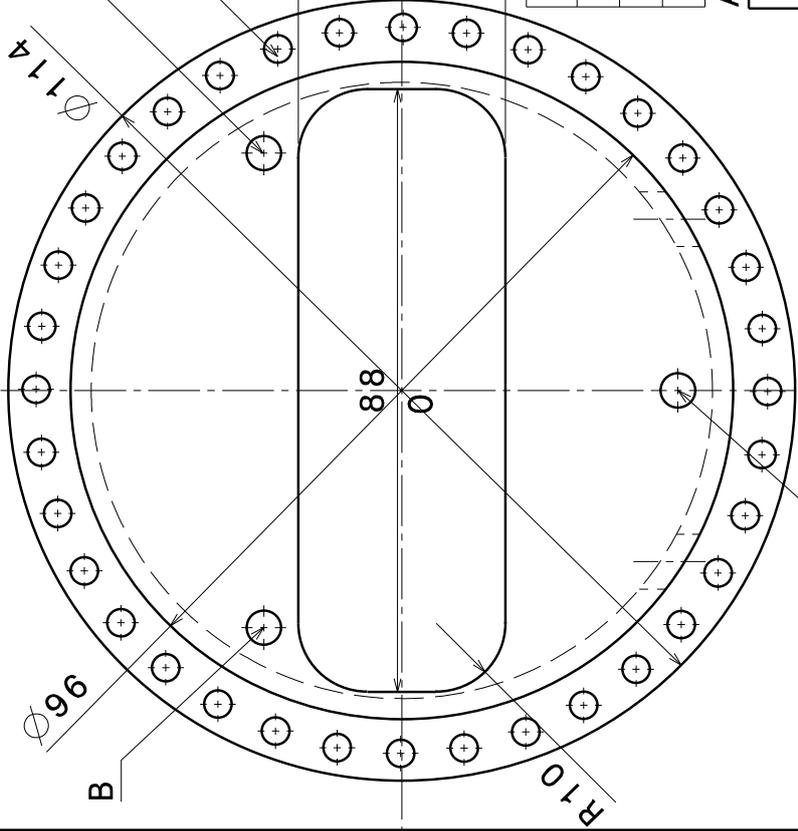
4



Section view A-A

3

3



36 off ∅4 PCD 106
Equispaced

2

2

∅8

88

Hole	X	Y
A	34.64	20.00
B	-34.64	20.00
C	0.00	-40.00

A-C ∅5

1

1

Name: End Cap
Drawing No: AER-06
Drawn by: S. Diasinos

Scale: 1:1
Material: Aluminium
All dimension in mm

A

B

C

D

A

B

C

D

4

3

2

1

A-C $\phi 4$ Chamfered 4 deep $\sphericalangle 90^\circ$
 D-L M4

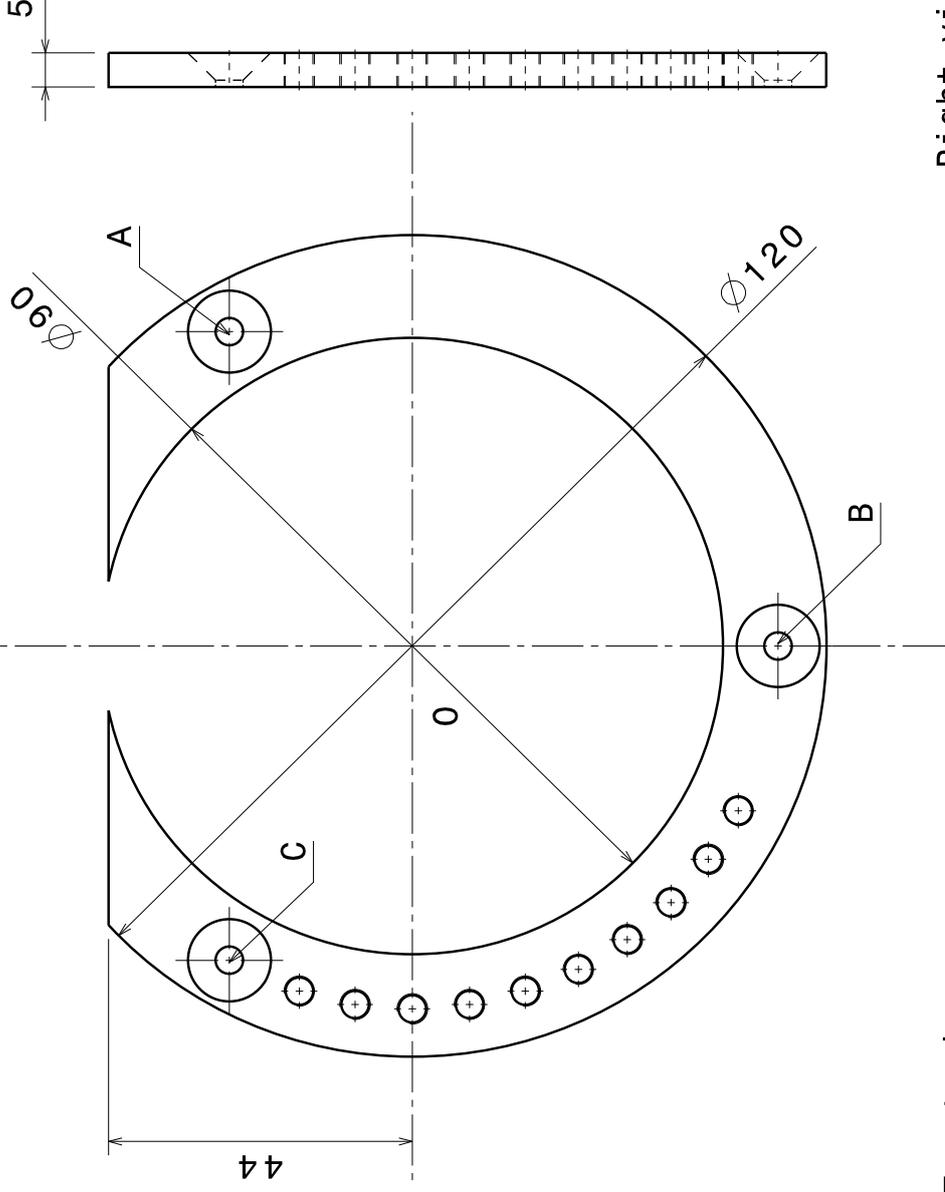
Hole	X	Y
A	45.47	26.25
B	0.00	-52.5
C	-45.47	26.25
D	-53.00	0.00
E	-52.35	-8.29
F	-50.41	-16.38
G	-47.22	-24.06
H	-42.88	-31.15
I	-37.48	-37.48
J	-23.23	-47.64
K	-15.50	-50.68
L	-7.38	-52.48

4

3

2

1



Front view

Right view

Name: C-Bracket
 Drawing No: AER-07
 Drawn by: S. Diasinos

Scale: 1:1
 Material: Mild Steel
 All dimension in mm

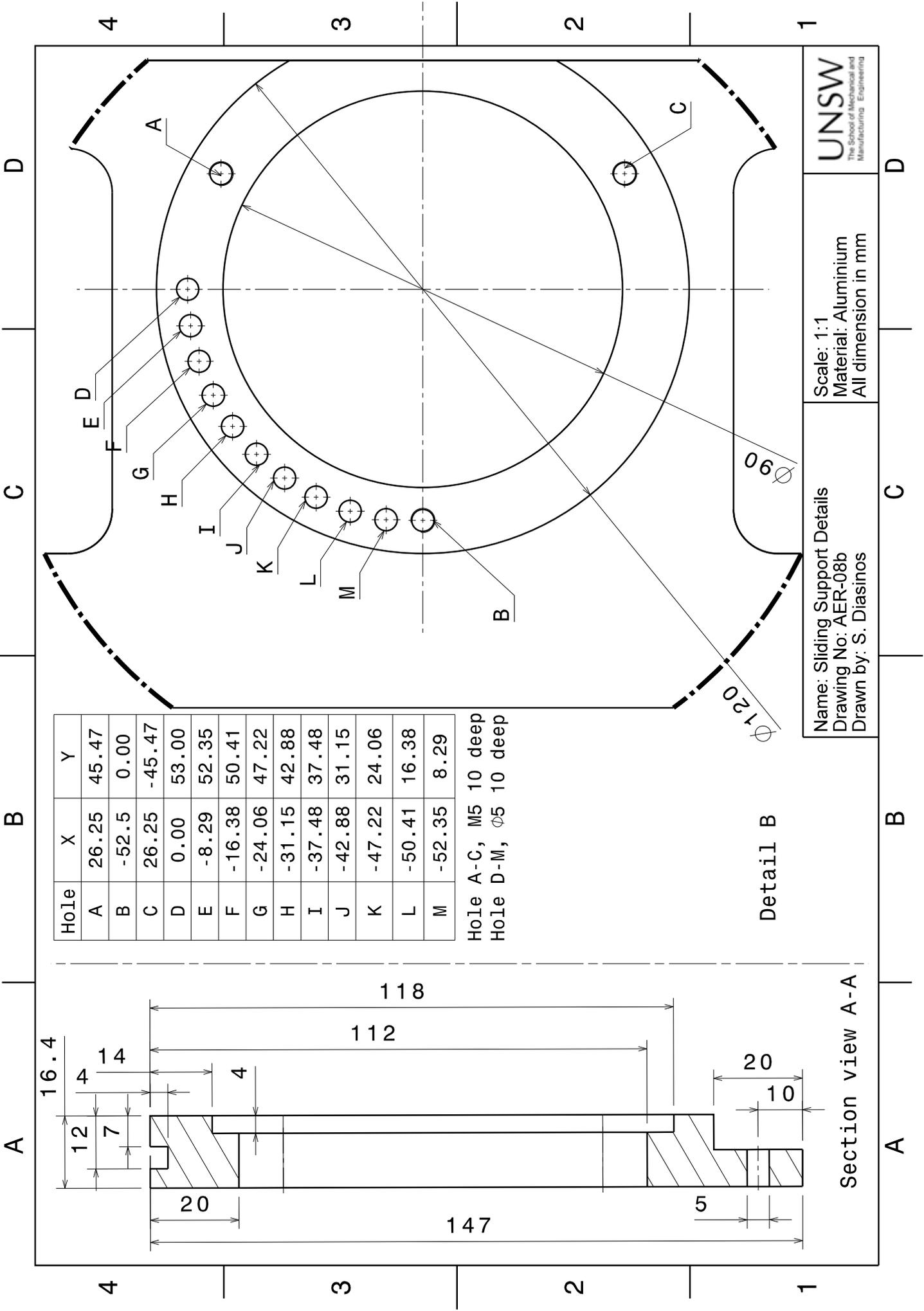
UNSW
 The School of Mechanical and
 Manufacturing Engineering

A

B

C

D



Hole	X	Y
A	26.25	45.47
B	-52.5	0.00
C	26.25	-45.47
D	0.00	53.00
E	-8.29	52.35
F	-16.38	50.41
G	-24.06	47.22
H	-31.15	42.88
I	-37.48	37.48
J	-42.88	31.15
K	-47.22	24.06
L	-50.41	16.38
M	-52.35	8.29

Hole A-C, M5 10 deep
Hole D-M, $\phi 5$ 10 deep

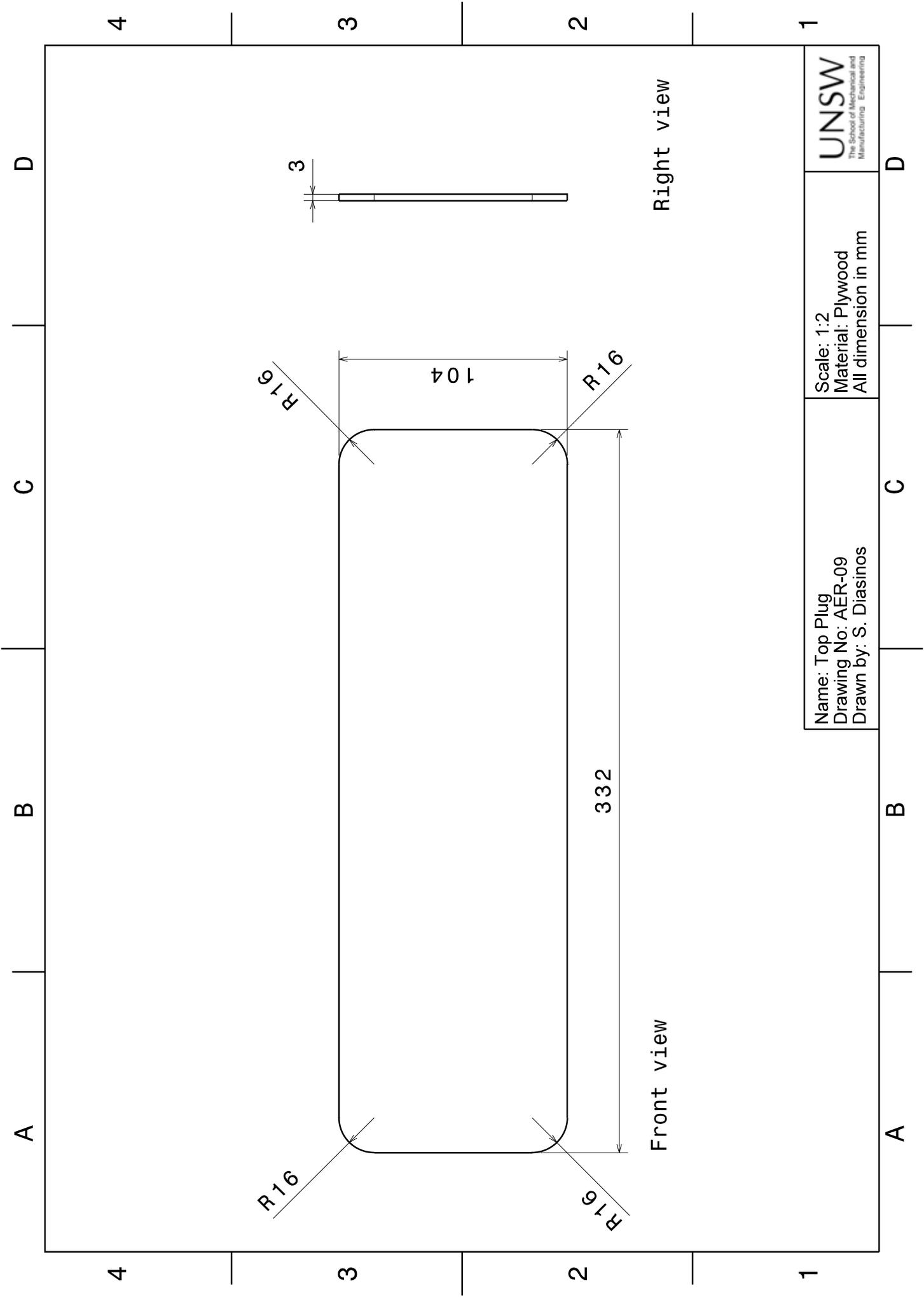
UNSW
The School of Mechanical and
Manufacturing Engineering

Name: Slicing Support Details
Drawing No: AER-08b
Drawn by: S. Diasinos

Scale: 1:1
Material: Aluminium
All dimension in mm

Section view A-A

Detail B



UNSW
The School of Mechanical and
Manufacturing Engineering

Scale: 1:2
Material: Plywood
All dimension in mm

Name: Top Plug
Drawing No: AER-09
Drawn by: S. Diasinos

Right view

Front view

4

3

2

1

D

C

B

A

4

3

2

1

D

C

B

A

R16

104

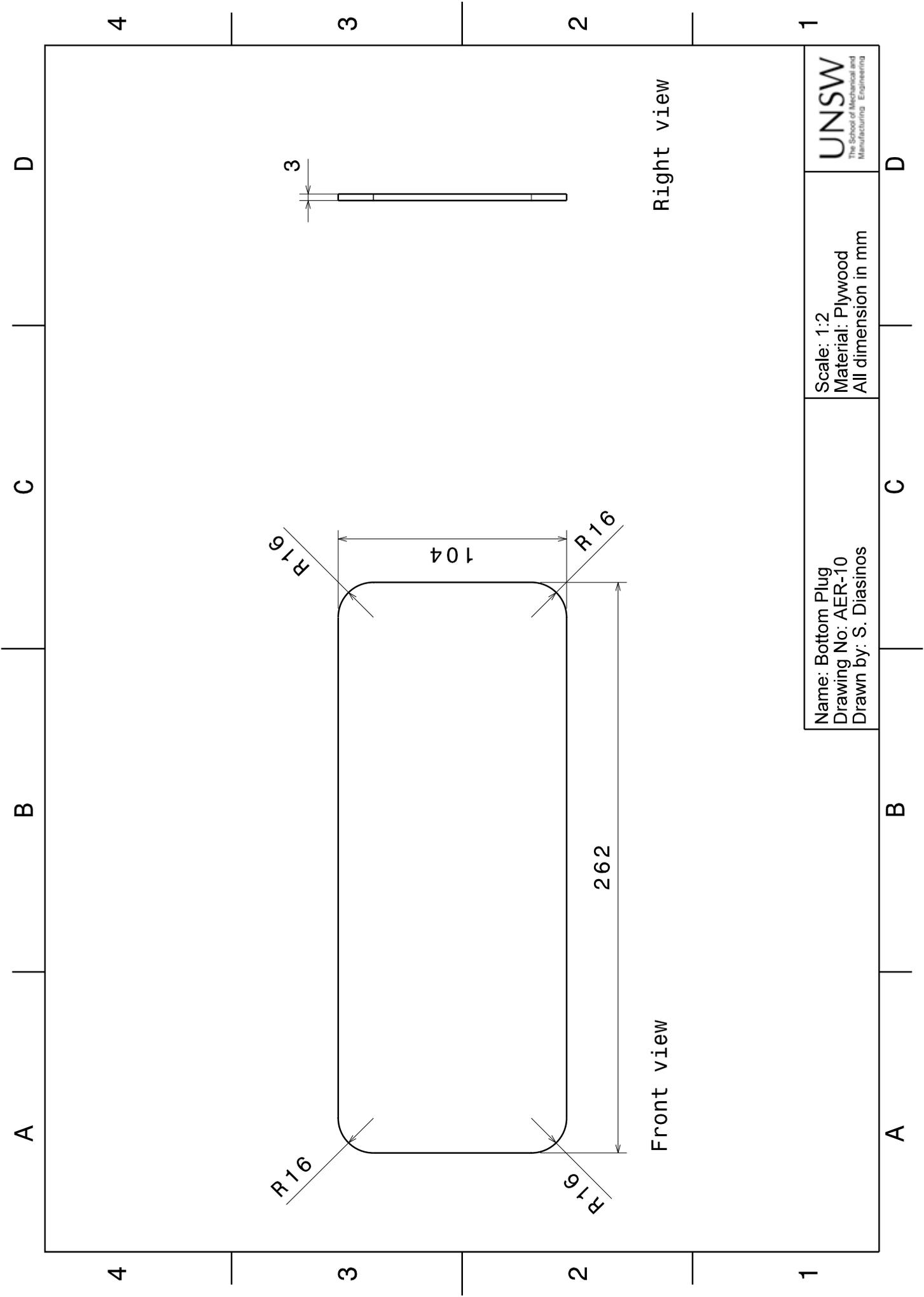
R16

3

332

R16

R16



Name: Bottom Plug Drawing No: AER-10 Drawn by: S. Diasinos	Scale: 1:2 Material: Plywood All dimension in mm	 UNSW The School of Mechanical and Manufacturing Engineering
--	--	---

A

B

C

D

16

14.5

8

$\phi 10 \pm 0.018$

$\phi 7$

$\phi 10 \pm 0.018$

11.5

106.5

18

4

18.5

6

81.5

94

Front view

Right view

4

3

2

1

4

3

2

1

Name: Wing Rest
Drawing No: REF-01
Drawn by: S. Diasinos

Scale: 1:1
Material: Brass
All dimension in mm

UNSW
The School of Mechanical and
Manufacturing Engineering

A

B

C

D

A

B

C

D

4

4

3

3

2

2

1

1

M5



Front view

10

10

342

Right view

∅ 10
-0.006
-0.017

2 off required

Name: Wing Rest Shaft
Drawing No: REF-02
Drawn by: S. Diasinos

Scale: 1:1
Material: Steel Rod
All dimension in mm

UNSW
The School of Mechanical and
Manufacturing Engineering

A

B

C

D

A

B

C

D

4

M4 Equispaced
3 Off PCD 17

9

113

3

30.6

4

3

X	Y
0.000	-8.500
7.361	4.250
-7.361	4.250

5

100.5

1

8

3

4

10

5

10

12.5

100.5

4

3

10

5

10

12.5

100.5

4

2

10

5

10

12.5

100.5

4

1

10

5

10

12.5

100.5

4

1

10

5

10

12.5

100.5

4

1

10

5

10

12.5

100.5

4

1

10

5

10

12.5

100.5

4

1

10

5

10

12.5

100.5

4

1

10

5

10

12.5

100.5

4

1

10

5

10

12.5

100.5

4

1

10

5

10

12.5

100.5

4

1

10

5

10

12.5

100.5

4

1

10

5

10

12.5

100.5

4

1

10

5

10

12.5

100.5

4

1

10

5

10

12.5

100.5

4

1

10

5

10

12.5

100.5

4

2 off required

Name: Wing Height Reference
Drawing No: REF-03
Drawn by: S. Diasinos

Scale: 1:1
Material: Aluminium
All dimension in mm

UNSW
The School of Mechanical and
Manufacturing Engineering

Right view

Front view

A

B

C

D

1

10

5

10

12.5

100.5

4

A

B

C

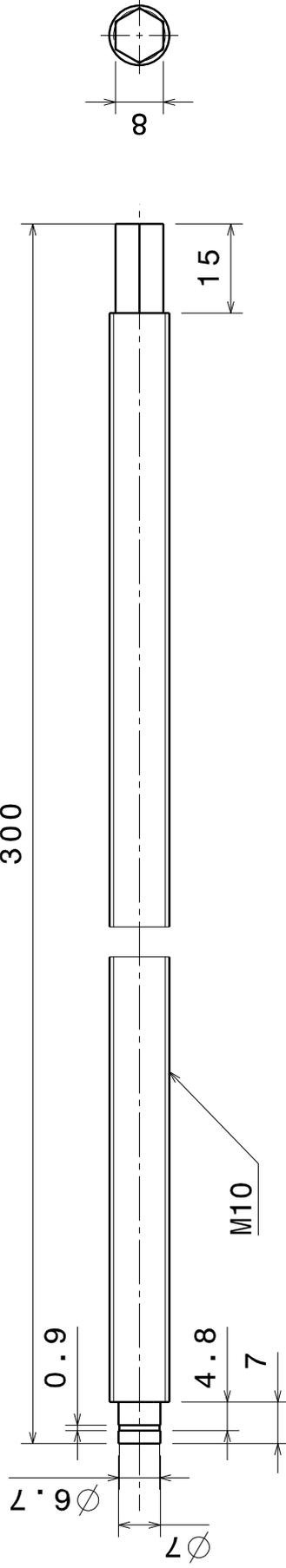
D

4

3

2

1



Name: Wing Brooker Rod
 Drawing No: REF-04
 Drawn by: S. Diasinos

Scale: 1:1
 Material: M10 Brooker rod
 All dimension in mm

UNSW
 The School of Mechanical and
 Manufacturing Engineering

A

B

C

D

4

3

2

1

A

B

C

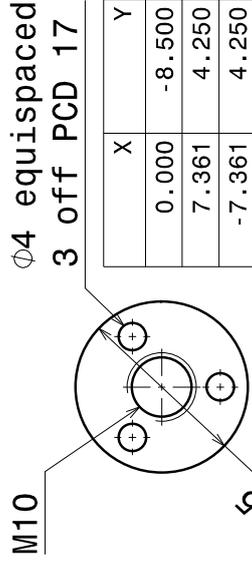
D

4

3

2

1



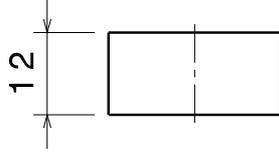
Ø4 equispaced

3 off PCD 17

M10

Ø2.5

Front view



12

Right view

4

3

2

1

Name: Threaded Driver
 Drawing No: REF-05
 Drawn by: S. Diasinos

Scale: 1:1
 Material: Brass
 All dimension in mm

A

B

C

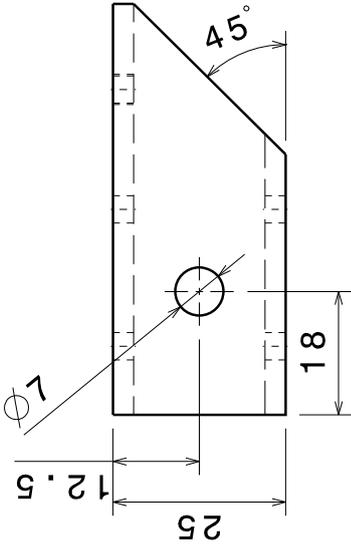
D

A

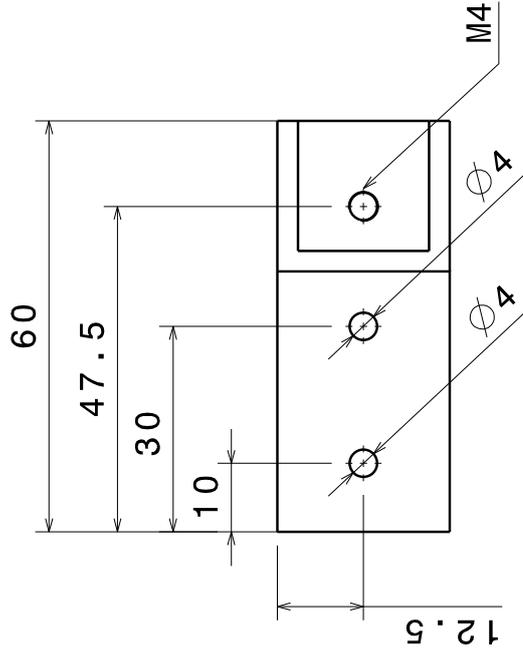
B

C

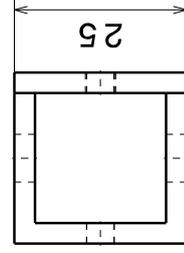
D



Top view



Front view



Right view

4

3

2

1

4 off required

Name: Vertical Offset
 Drawing No: REF-06
 Drawn by: S. Diasinos

Scale: 1:1
 Material: Mild Steel
 All dimension in mm

A

B

C

D

A

B

C

D

105.5

14.75

50

40

Top view

6.75

50

8

8

156

R2.5

88

44

4

3

2

1

Front view

Name: Endplate Jig
Drawing No: REF-07
Drawn by: S. Diasinos

Scale: 1:1
Material: Renshape
All dimension in mm

UNSW
The School of Mechanical and
Manufacturing Engineering

A

B

C

D

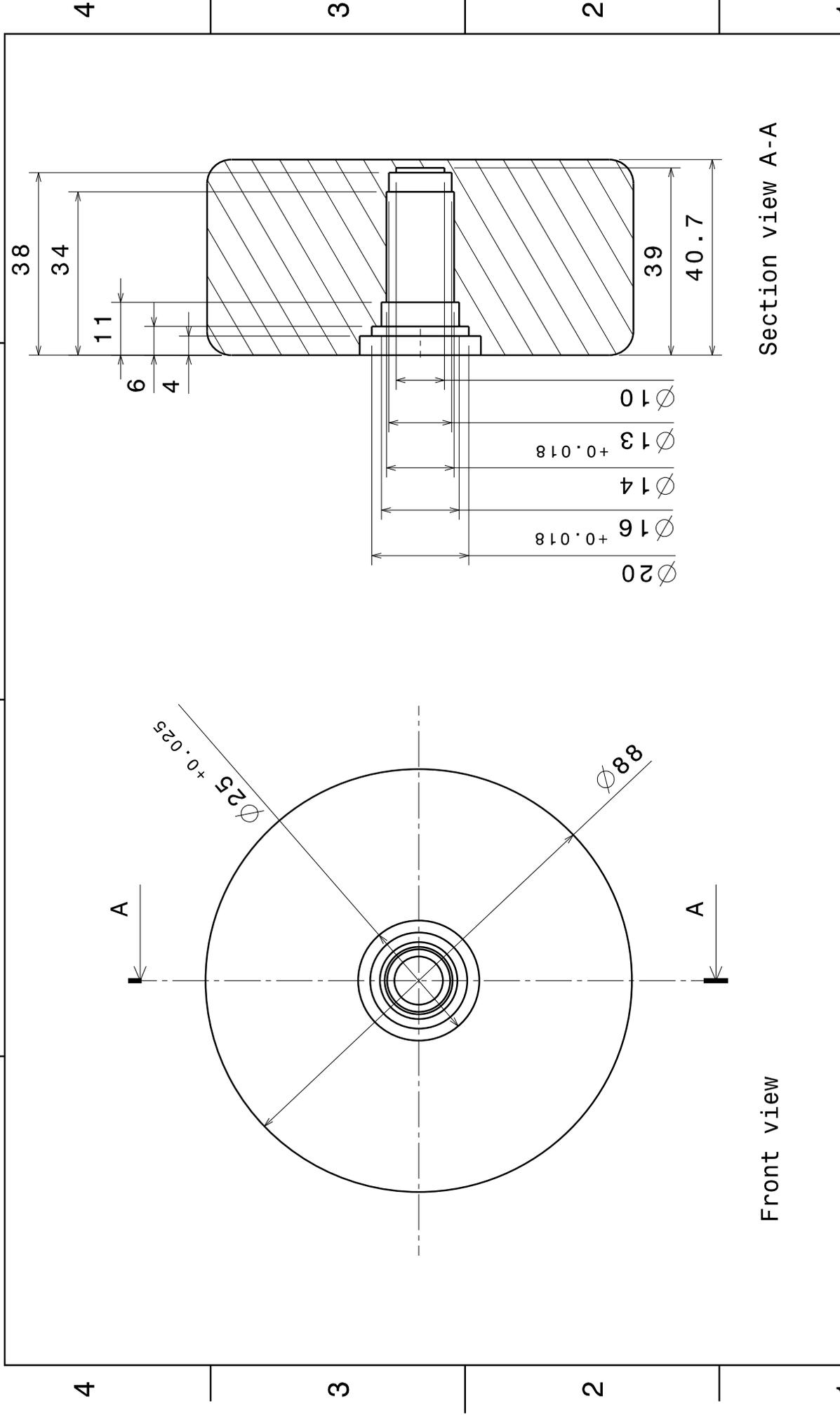
4

3

2

1

A B C D



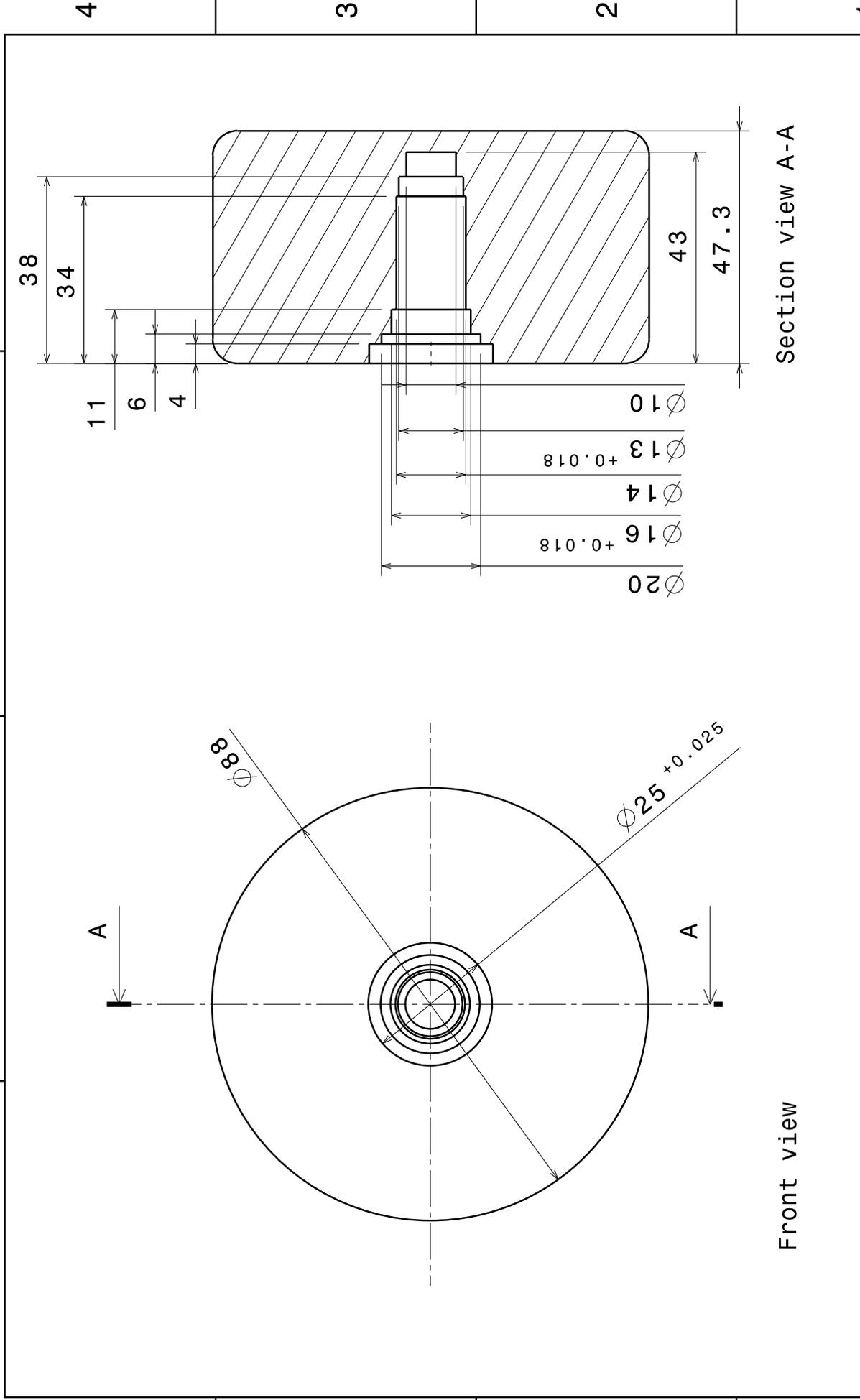
Section view A-A

Front view

1	UNSW The School of Mechanical and Manufacturing Engineering	Name: W1 Wheel Drawing No: WHL-01 Drawn by: S. Diasinos	Scale: 1:1 Material: Acrylic All dimension in mm
---	---	---	--

A B C D

A B C D

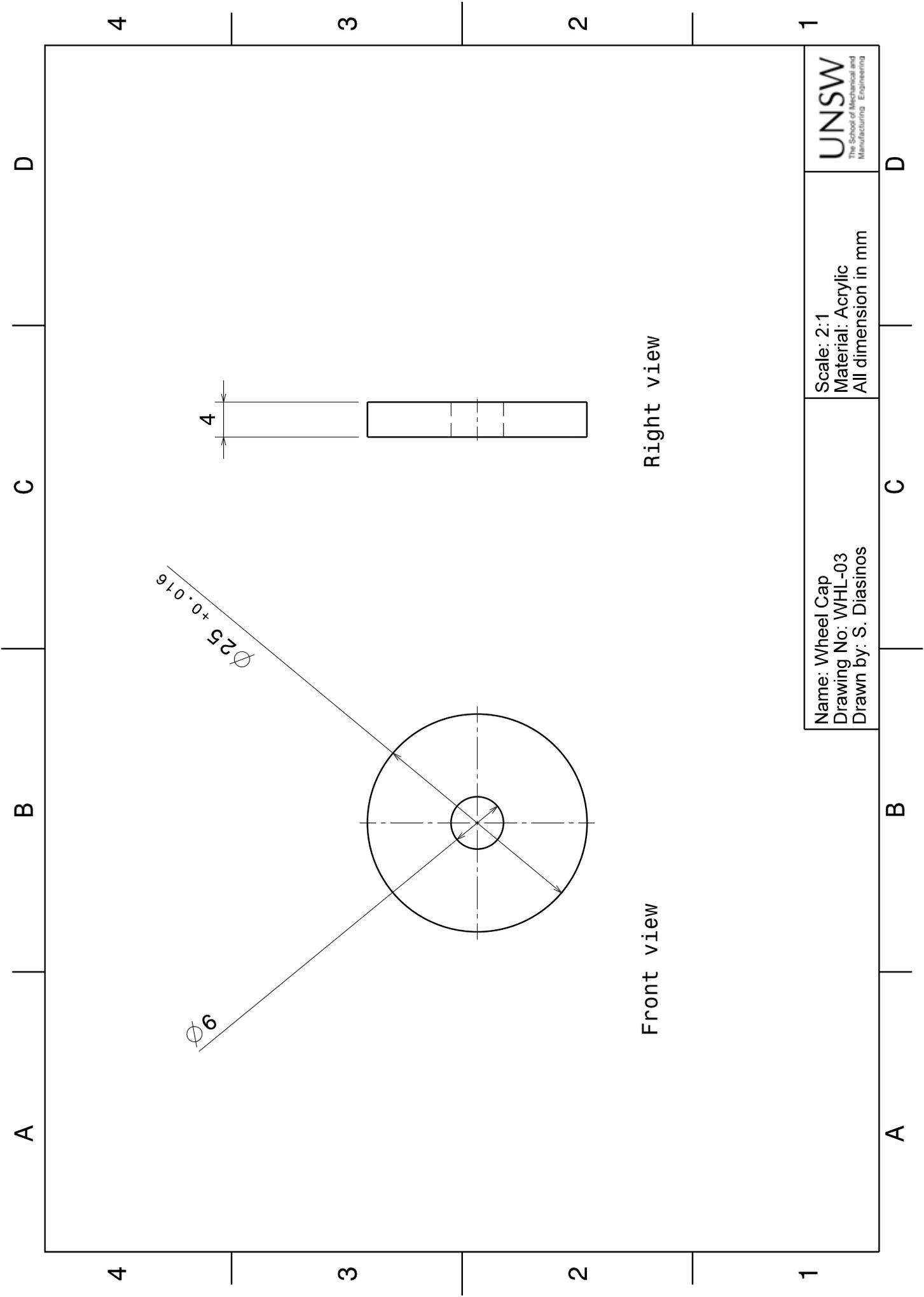


Section view A-A

Front view

1	Name: W2 Wheel Drawing No: WHL-02 Drawn by: S. Diasinos	Scale: 1:1 Material: Acrylic All dimension in mm	
---	---	--	--

A B C D

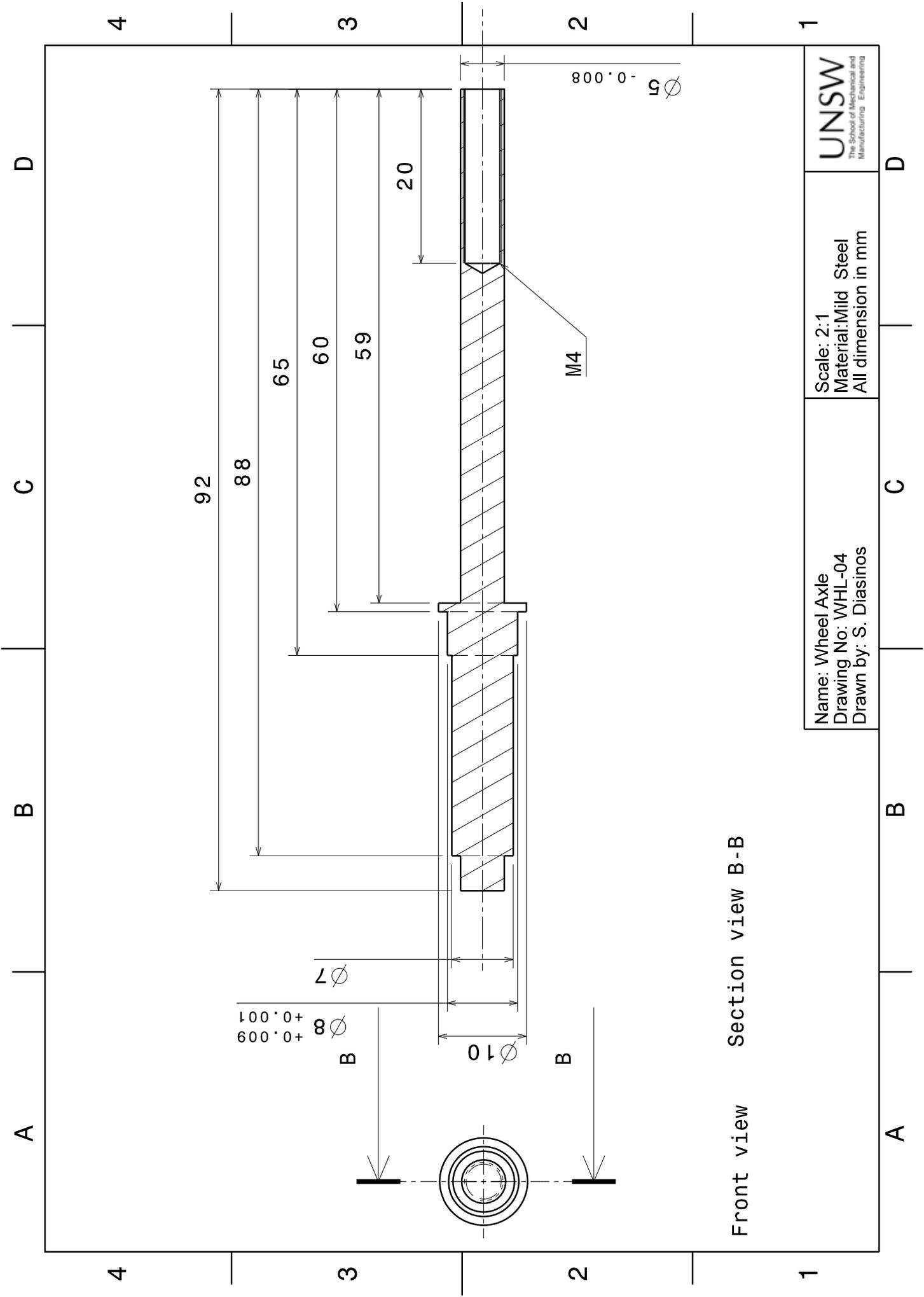


Right view

Front view

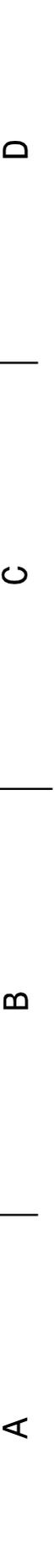
 <p>UNSW The School of Mechanical and Manufacturing Engineering</p>	<p>Scale: 2:1 Material: Acrylic All dimension in mm</p>	<p>Name: Wheel Cap Drawing No: WHL-03 Drawn by: S. Diasinos</p>
--	---	---

A B C D 1 2 3 4



Front view Section view B-B

UNSW The School of Mechanical and Manufacturing Engineering	Scale: 2:1 Material: Mild Steel All dimension in mm	Name: Wheel Axle Drawing No: WHL-04 Drawn by: S. Diasinos
---	---	---



A

B

C

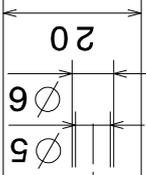
D

0.15°

21.5

59

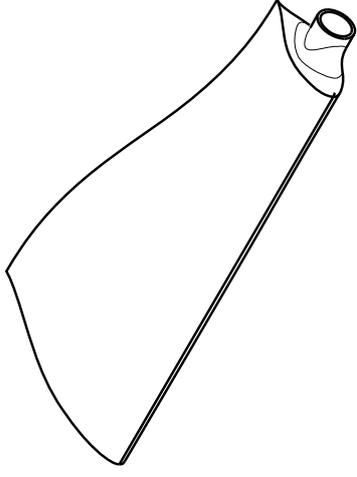
M4 x 20 deep



84

Section view C-C

M4 x 20 deep



Isometric view
Scale: 1:1

4

3

2

84

C

8

C

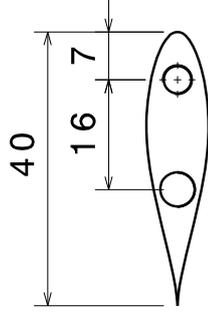
NC Code to be provided

Front view

40

16

7



Right view

2

1

A

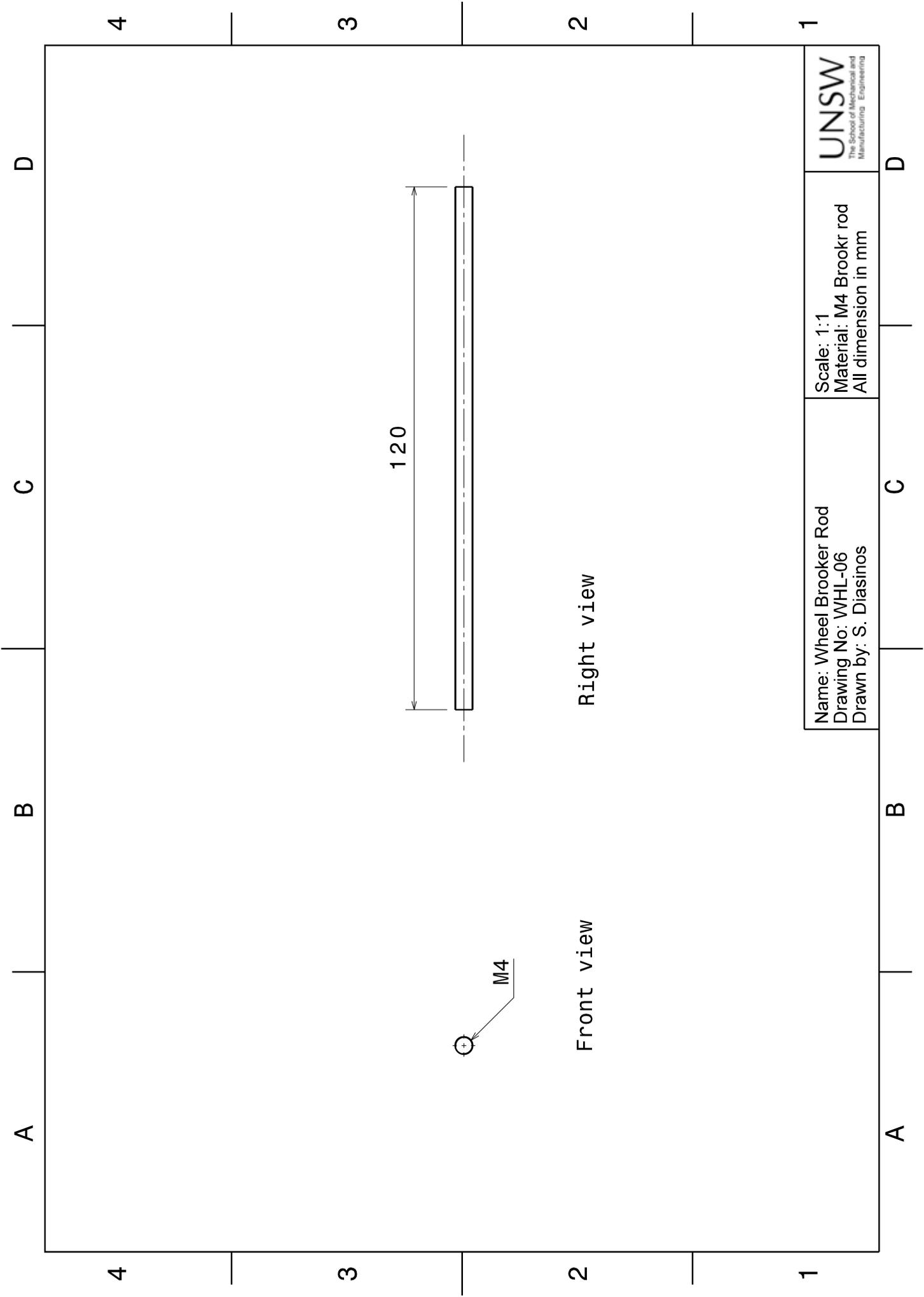
B

C

D

Name: Wheel Sting
 Drawing No: WHL-05
 Drawn by: S. Diasinos

Scale: 1:1
 Material: Aluminium
 All dimension in mm



A

B

C

D

1

2

3

4

1

2

3

4

A

B

C

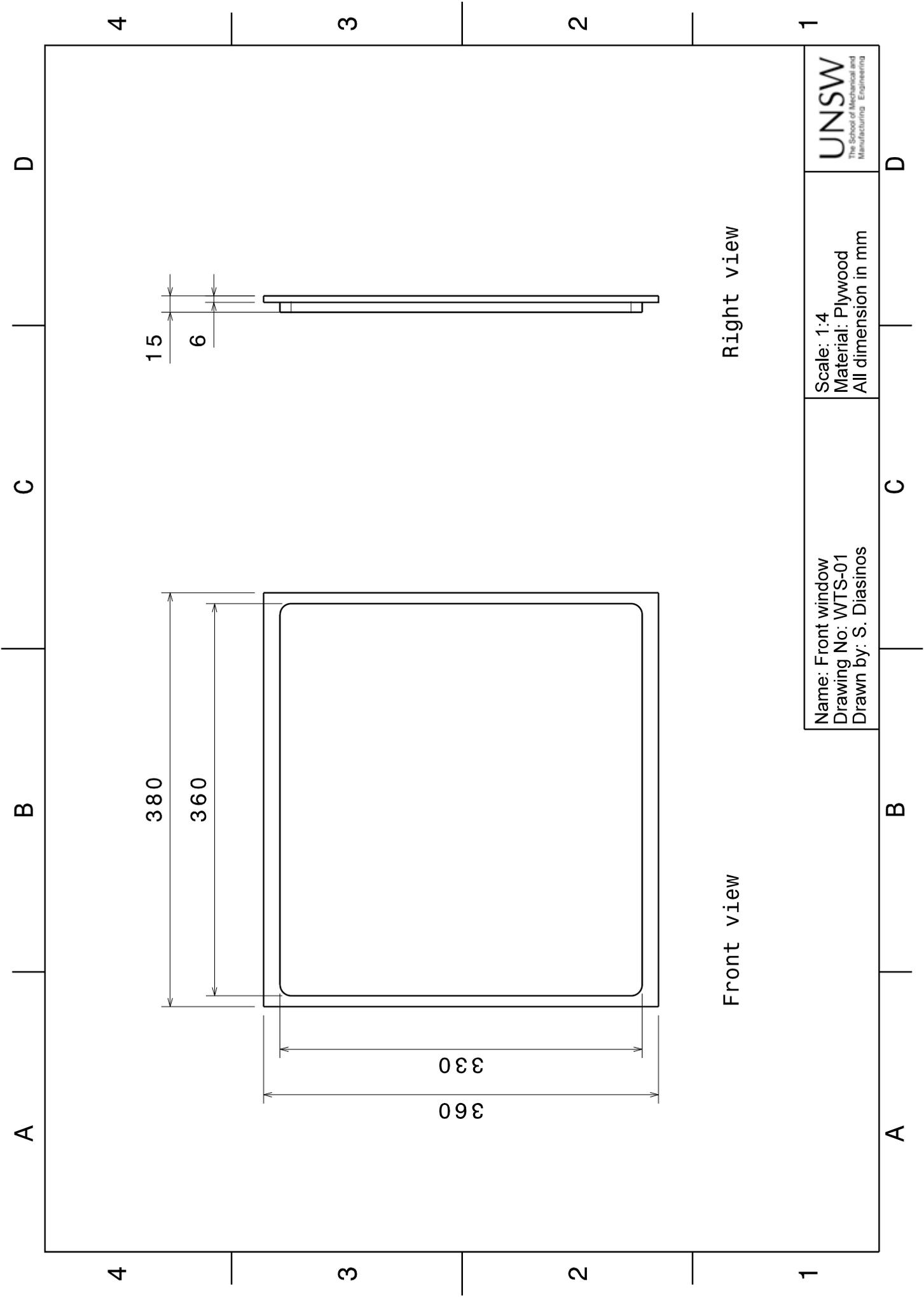
D

Front view

Right view

120

M4



15

6

380

360

330

360

Right view

Front view

UNSW
The School of Mechanical and
Manufacturing Engineering

Scale: 1:4
Material: Plywood
All dimension in mm

Name: Front window
Drawing No: WTS-01
Drawn by: S. Diasinos

D

C

B

A

D

C

B

A

4

3

2

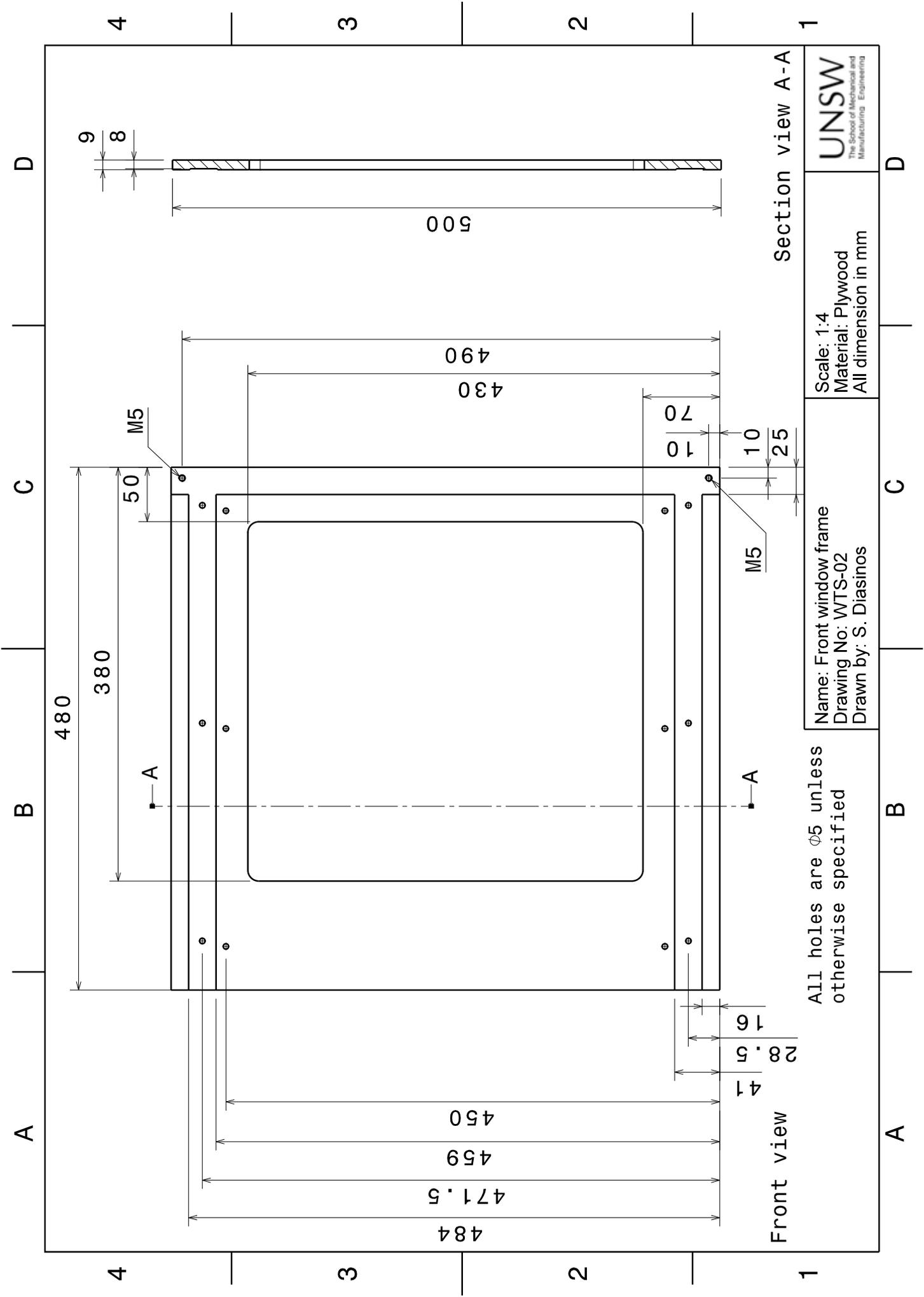
1

4

3

2

1



All holes are $\phi 5$ unless otherwise specified

Name: Front window frame
 Drawing No: WTS-02
 Drawn by: S. Diasinos

Scale: 1:4
 Material: Plywood
 All dimension in mm



Section view A-A

Front view

A B C D A B C D

A

B

C

D

4

3

2

1

335

310

478

508

9

15

Front view

Right view

Name: Rear window
Drawing No: WTS-03
Drawn by: S. Diasinos

Scale: 1:4
Material: Plywood
All dimension in mm

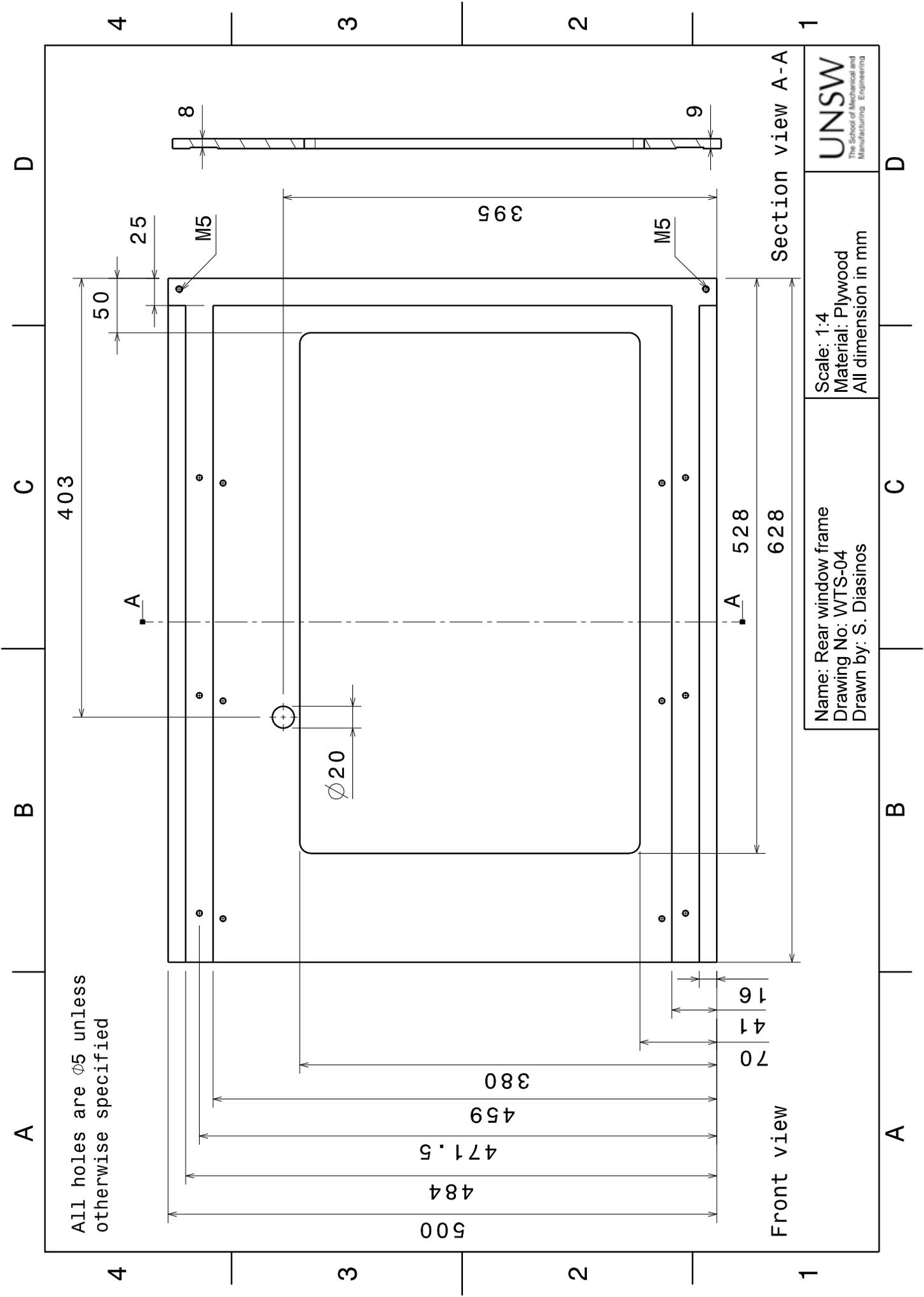
UNSW
The School of Mechanical and
Manufacturing Engineering

A

B

C

D



All holes are $\phi 5$ unless otherwise specified

Name: Rear window frame
 Drawing No: WTS-04
 Drawn by: S. Diasinos

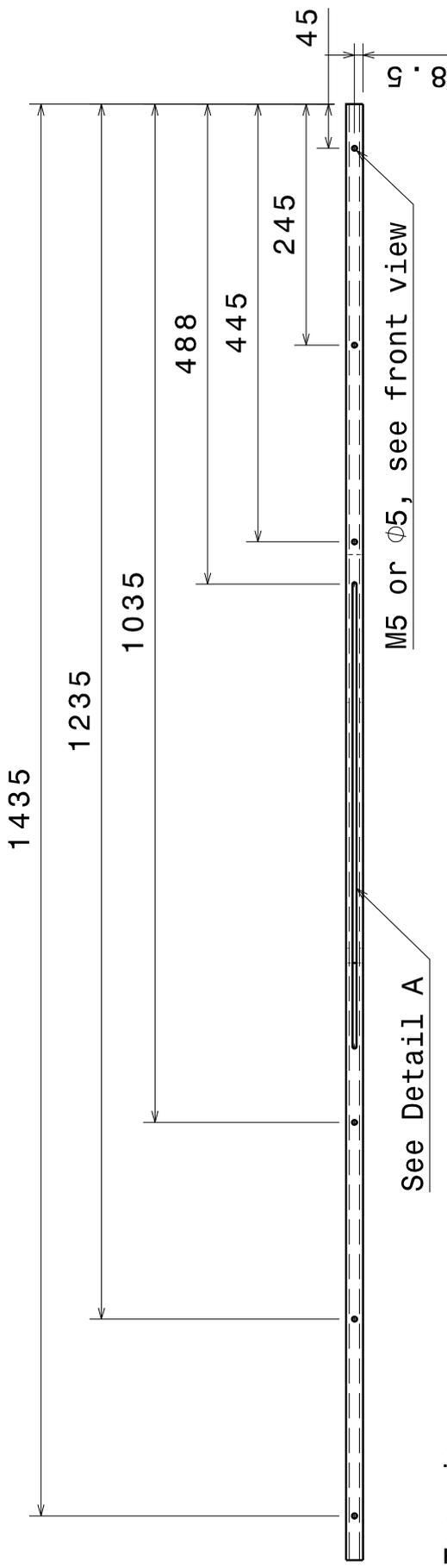
Scale: 1:4
 Material: Plywood
 All dimension in mm

A

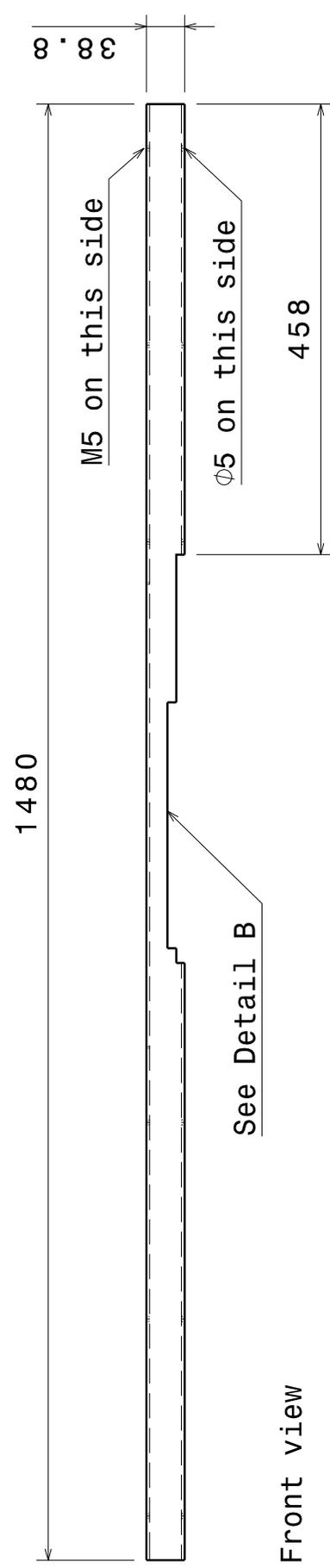
B

C

D



Top view



Front view

2 of required

Name: Horizontal Brace
 Drawing No: WTS-05a
 Drawn by: S. Diasinos

Scale: 1:6
 Material: Aluminium
 All dimension in mm

A

B

C

D

4

3

2

1

4

3

2

1

A

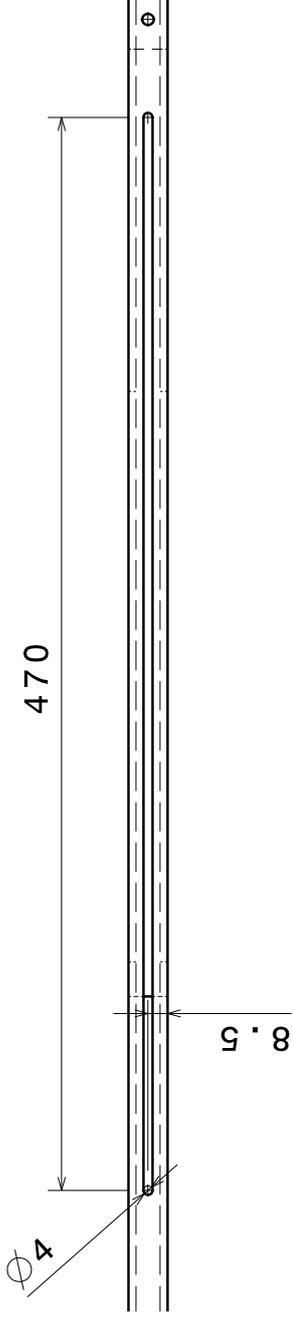
B

C

D

4

4



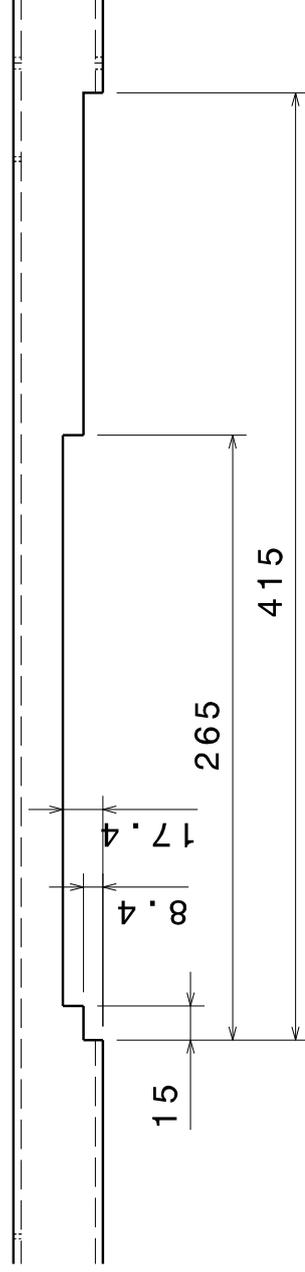
3

3

Detail A

2

2



Detail B

1

1

Name: Horizontal Brace Details
 Drawing No: WTS-05b
 Drawn by: S. Diasinos

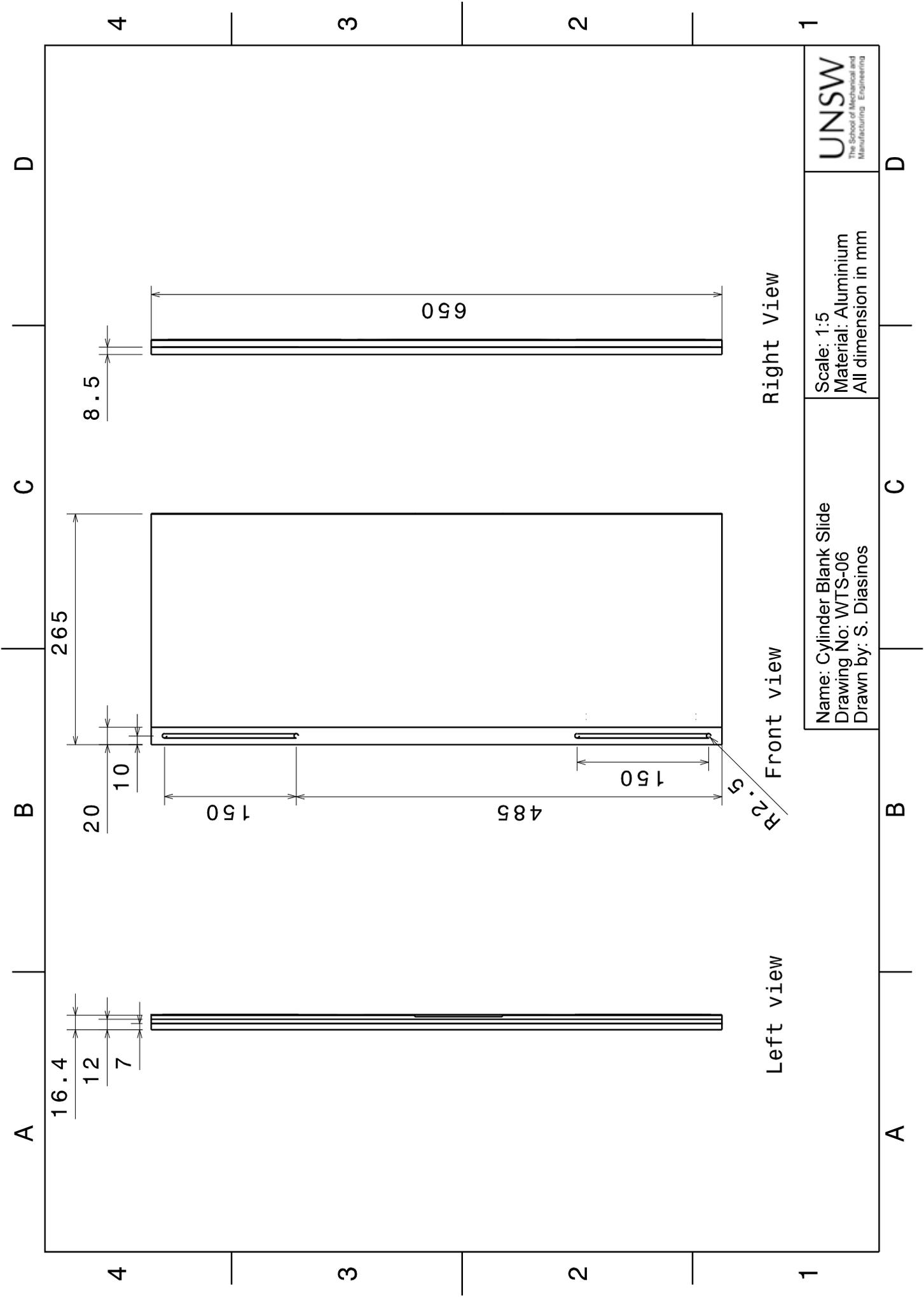
Scale: 1:3
 Material: Aluminium
 All dimension in mm

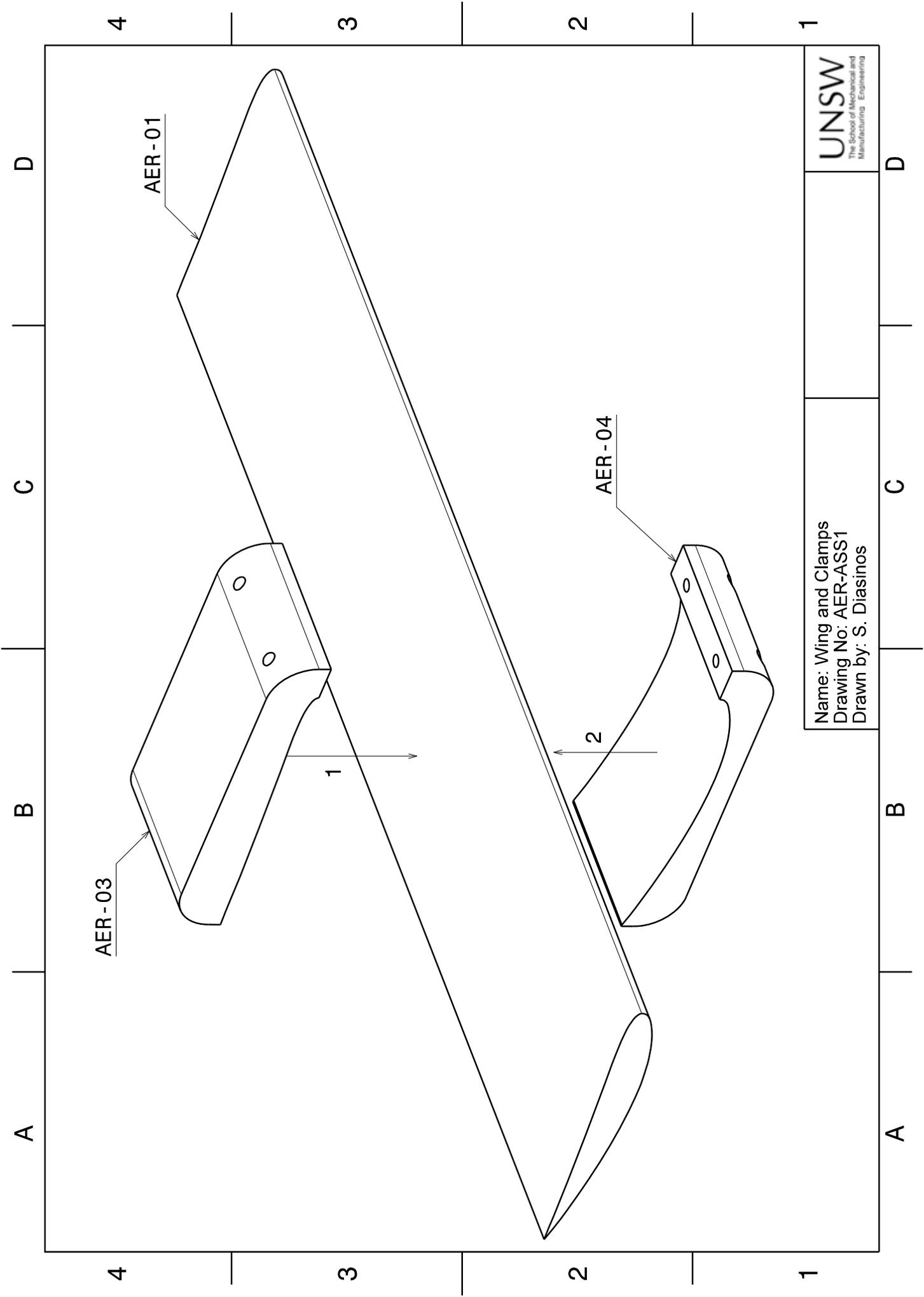
A

B

C

D





Name: Wing and Clamps
 Drawing No: AER-ASS1
 Drawn by: S. Diasinos

UNSW
 The School of Mechanical and
 Manufacturing Engineering

A

B

C

D

4

3

2

1

4

3

2

1

AER-09

AER-05

4

AER-ASS1

AER-10

5

2

6

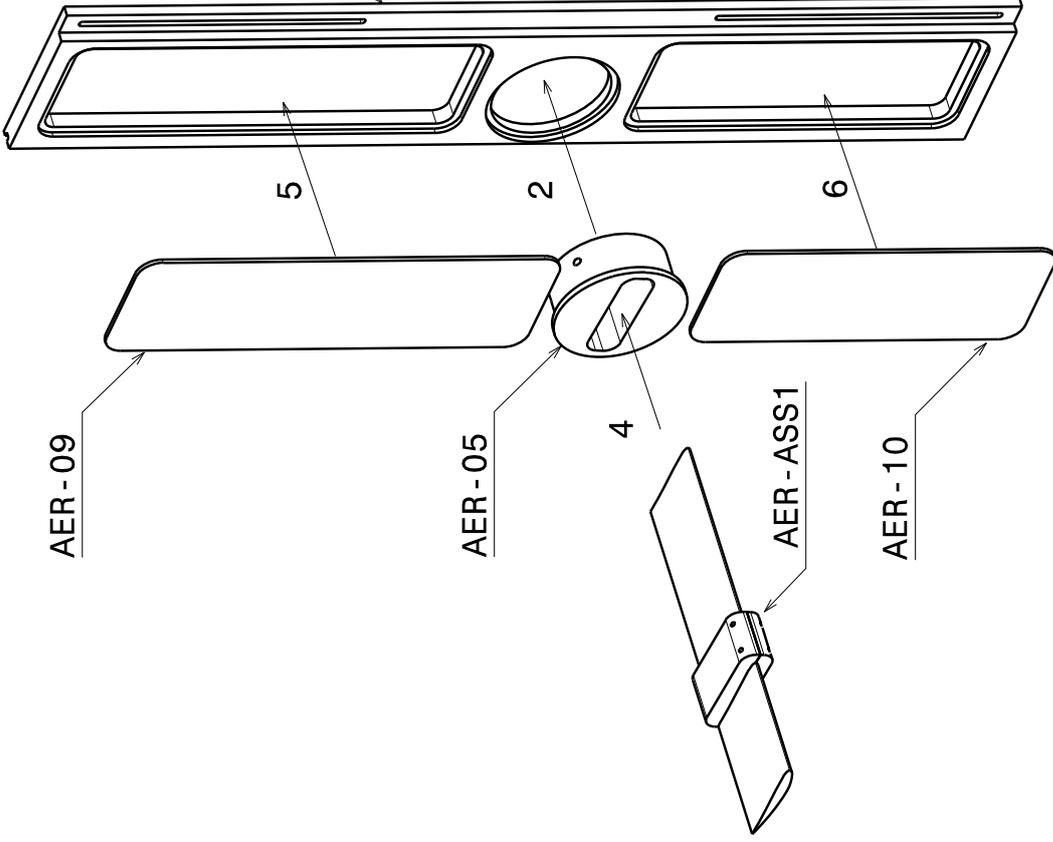
AER-08a

1

AER-06

3

AER-07



Name: Wing Slides Assembly
 Drawing No: AER-ASS2
 Drawn by: S. Diasinos

A

B

C

D

4

3

2

1

A

B

C

D

4

3

2

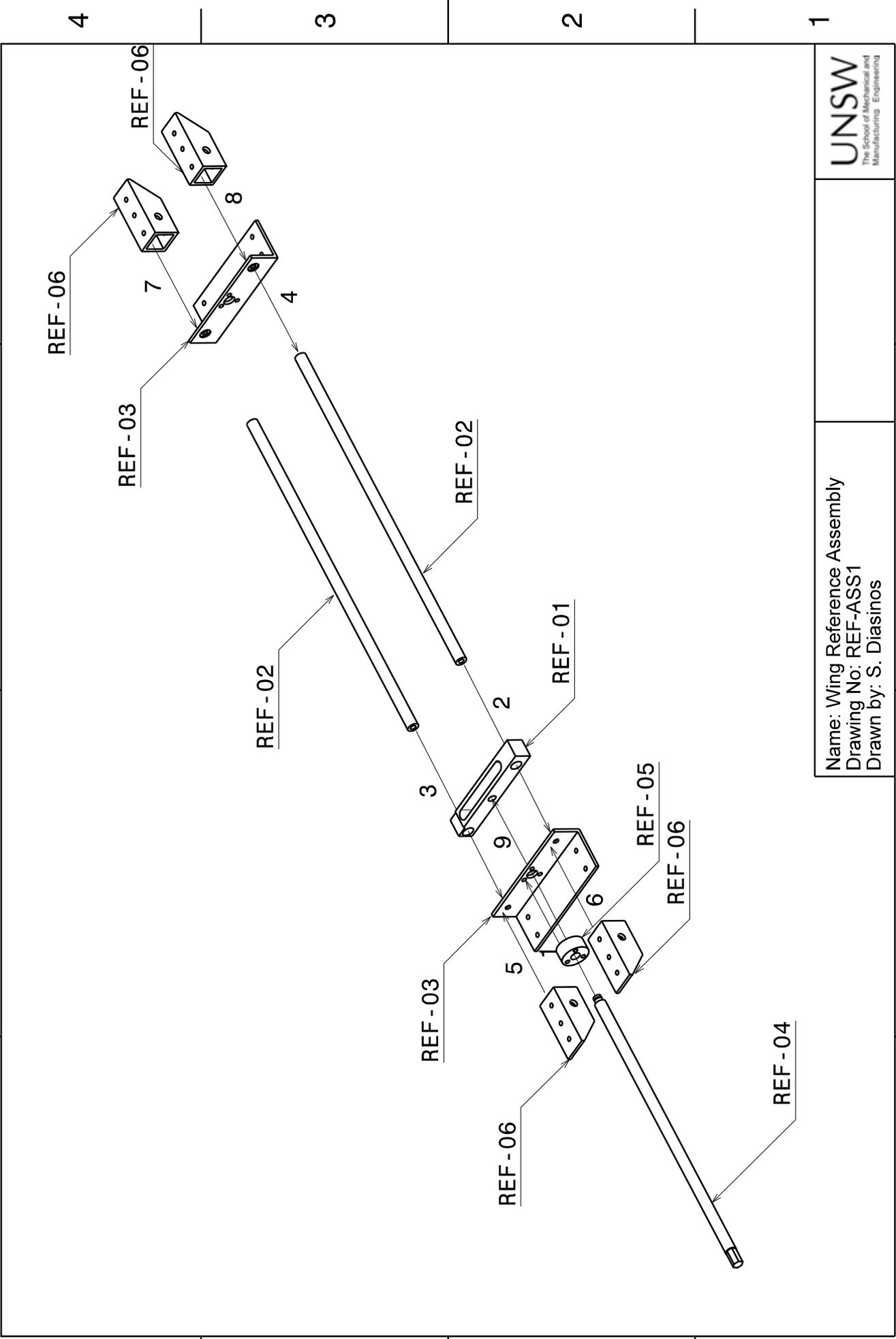
1

4

3

2

1



REF-06

REF-03

7

8

REF-06

REF-02

REF-03

5

3

2

REF-02

REF-01

9

6

REF-06

REF-06

REF-06

5

REF-06

REF-05

2

REF-02

REF-01

3

REF-02

REF-03

REF-06

REF-06

REF-04

Name: Wing Reference Assembly
 Drawing No: REF-ASS1
 Drawn by: S. Diasinos

A

B

C

D

4

3

2

1

4

3

2

1

A

B

C

D

4

4

3

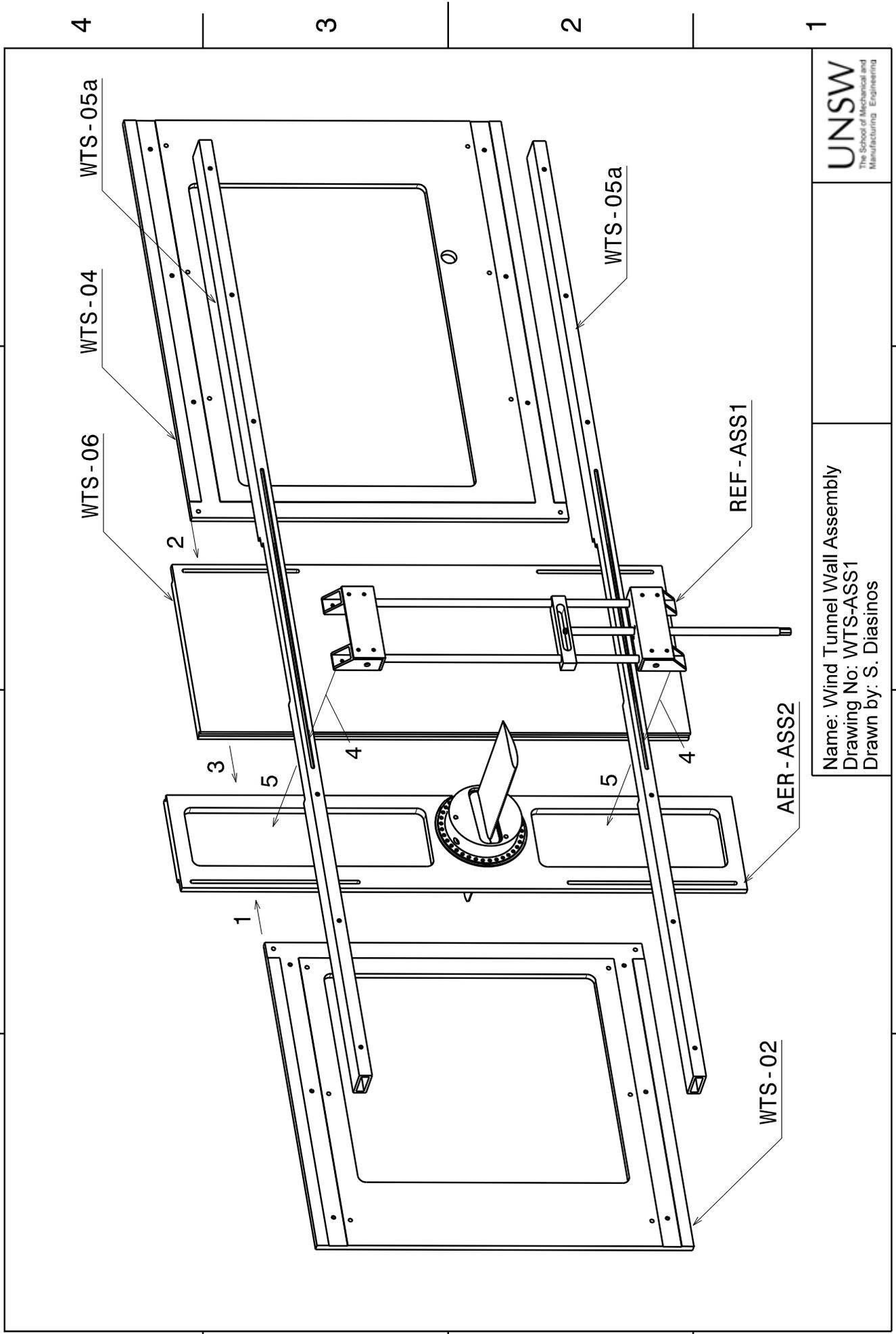
3

2

2

1

1



Name: Wind Tunnel Wall Assembly
 Drawing No: WTS-ASS1
 Drawn by: S. Diasinos

A

B

C

D

4

4

3

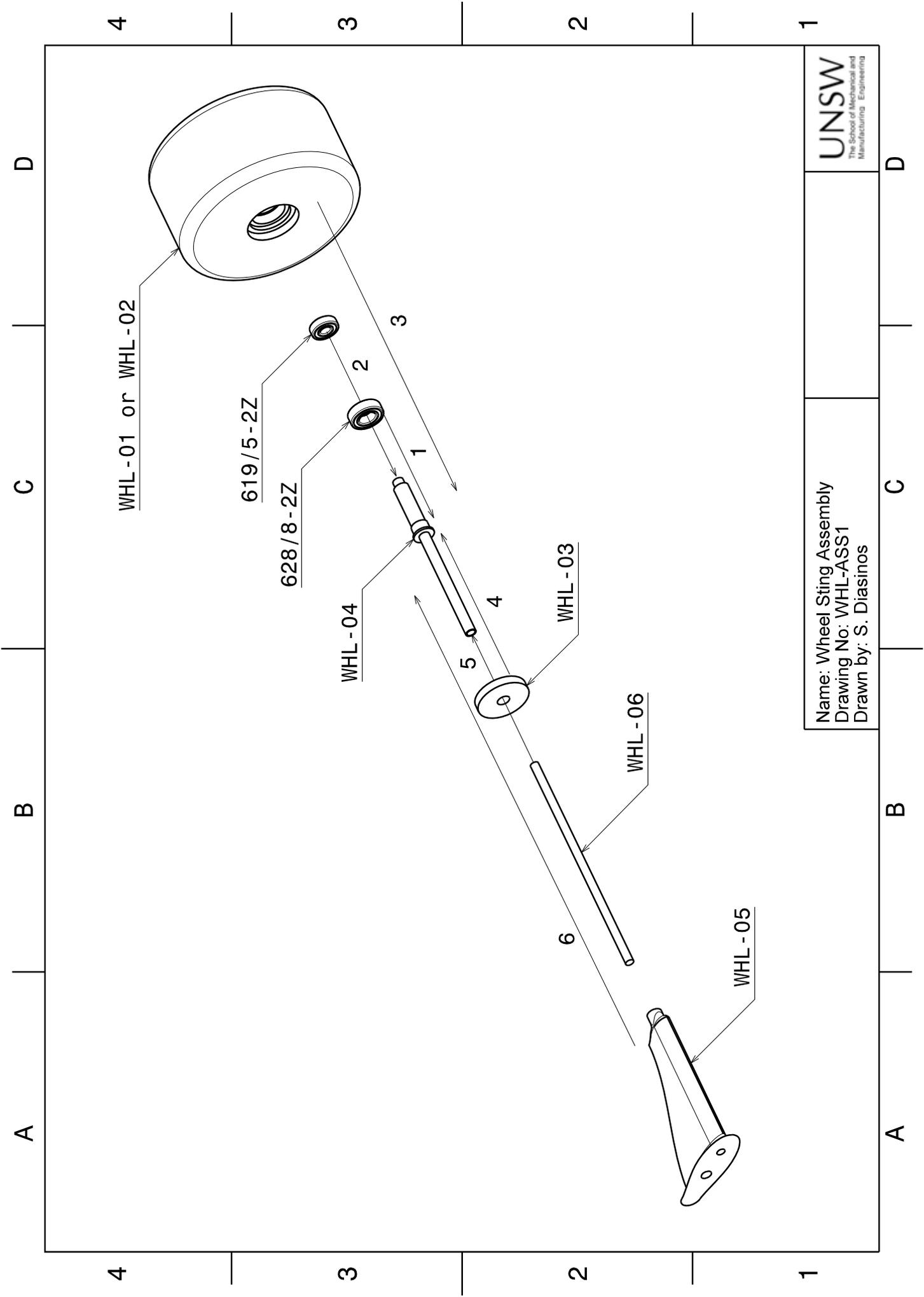
3

2

2

1

1



Name: Wheel Sting Assembly
 Drawing No: WHL-ASS1
 Drawn by: S. Diasinos

A

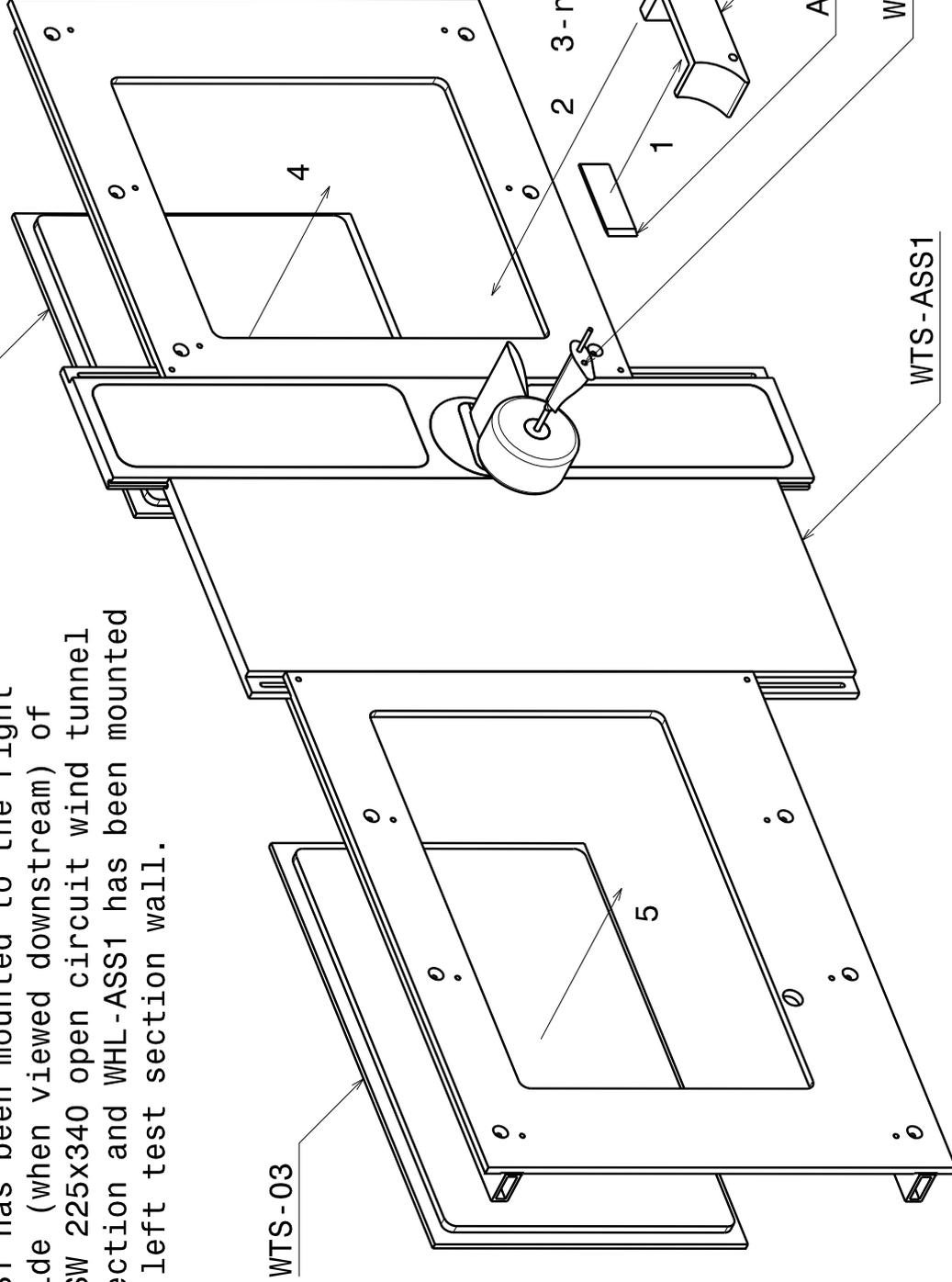
B

C

D

Note: This assembly takes place after WTS-ASS1 has been mounted to the right hand side (when viewed downstream) of the UNSW 225x340 open circuit wind tunnel test section and WHL-ASS1 has been mounted to the left test section wall.

WTS-01



4

3

2

1

4

3

2

1

Name: Final Assembly
 Drawing No: WTS-ASS2
 Drawn by: S. Diasinos

UNSW
 The School of Mechanical and
 Manufacturing Engineering

A

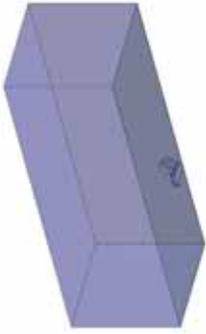
B

C

D

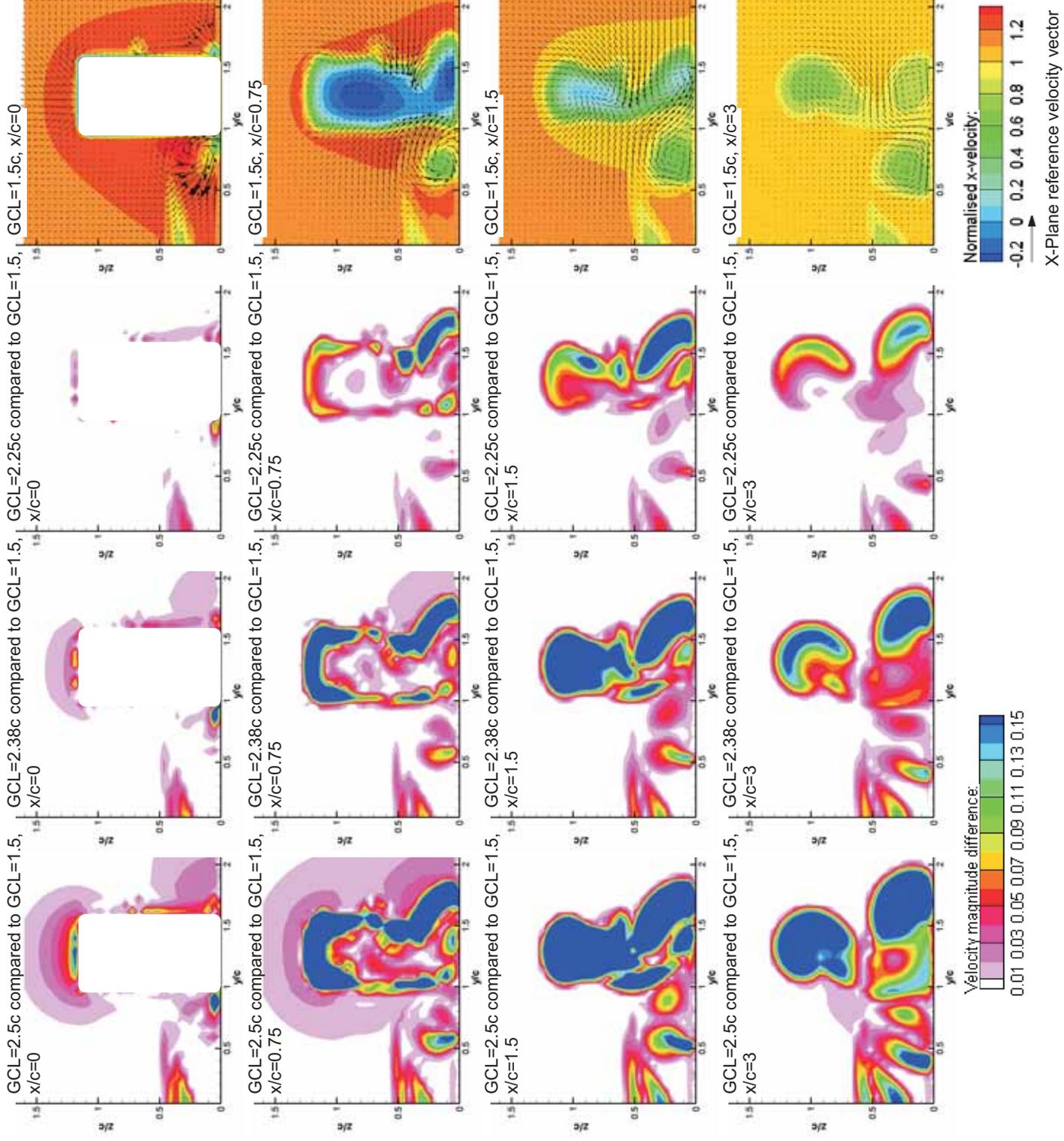
Appendix B:

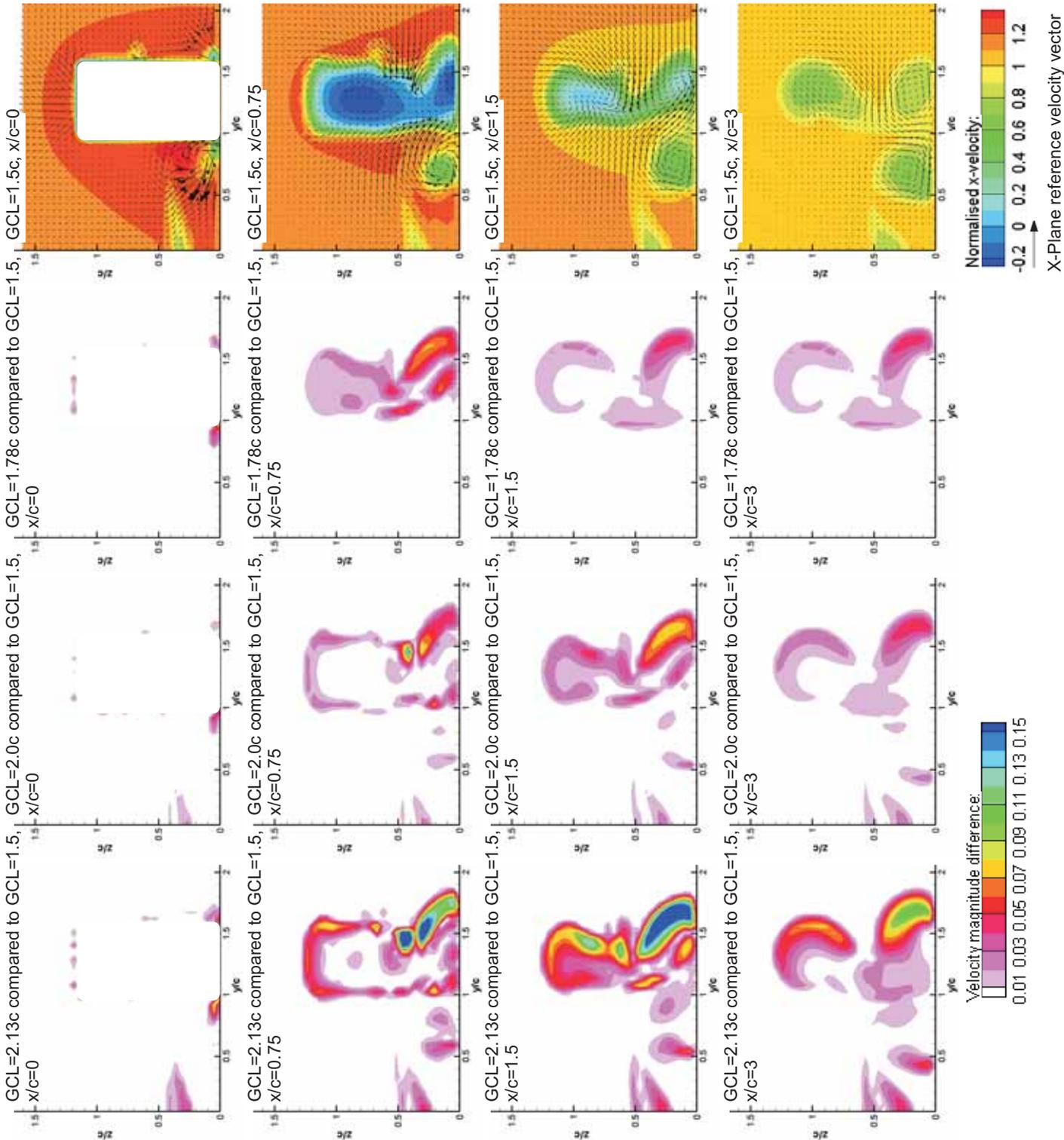
Verification comparisons of flow field

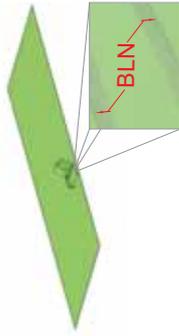


Off surface region depicted by blue volume above. Grid Characteristic Length (GCL) adjusted to obtain variations in total number of control volumes as indicated by table below for results shown here for the full-scale computational model.

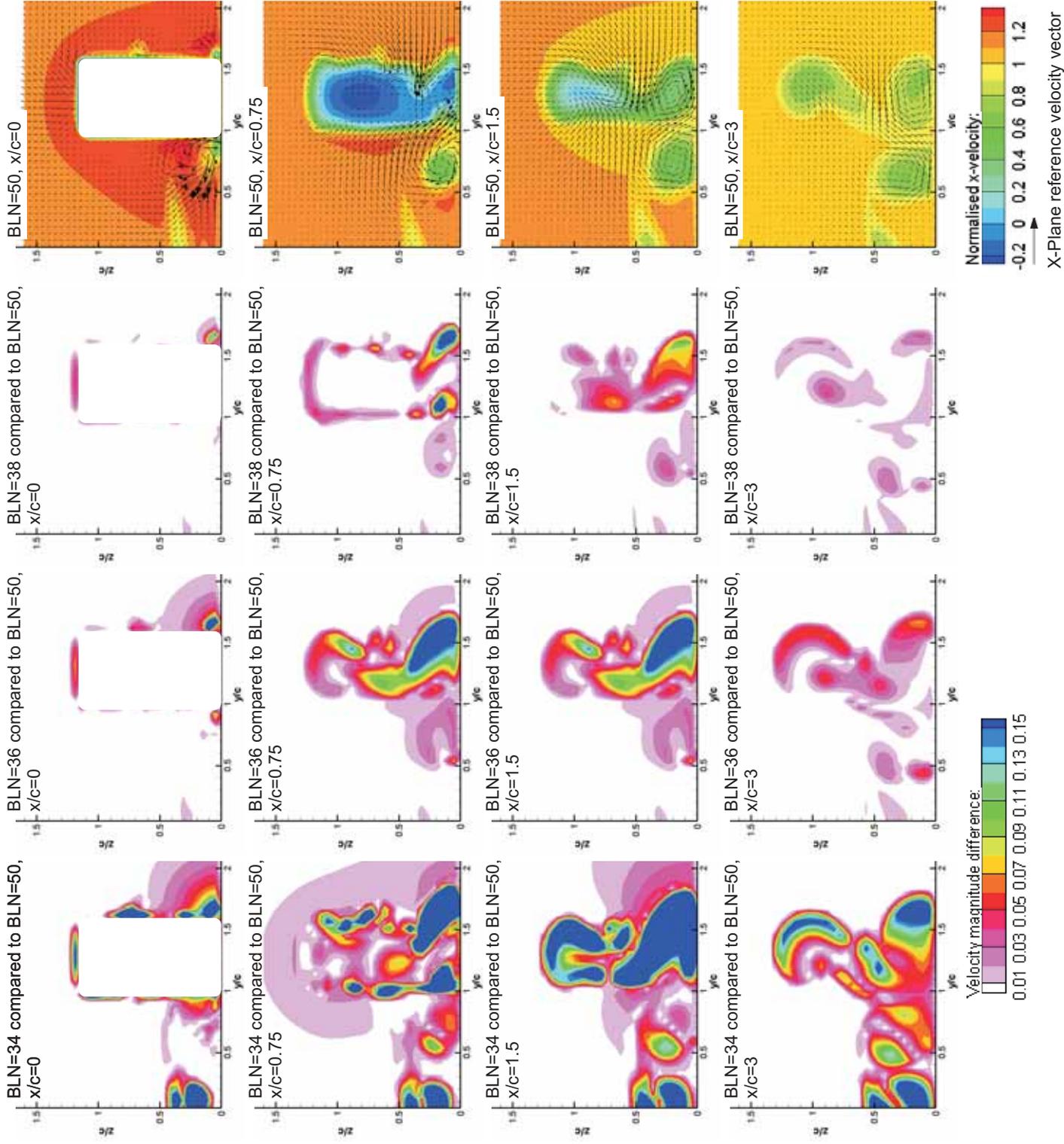
GCL (c)	Number of Control Volumes
2.50	4820270
2.38	5314729
2.25	6114069
2.13	6899270
2.00	7919548
1.78	10325775
1.50	15442990

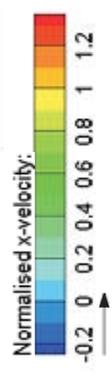
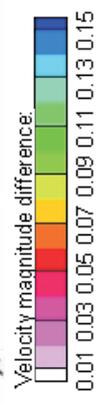
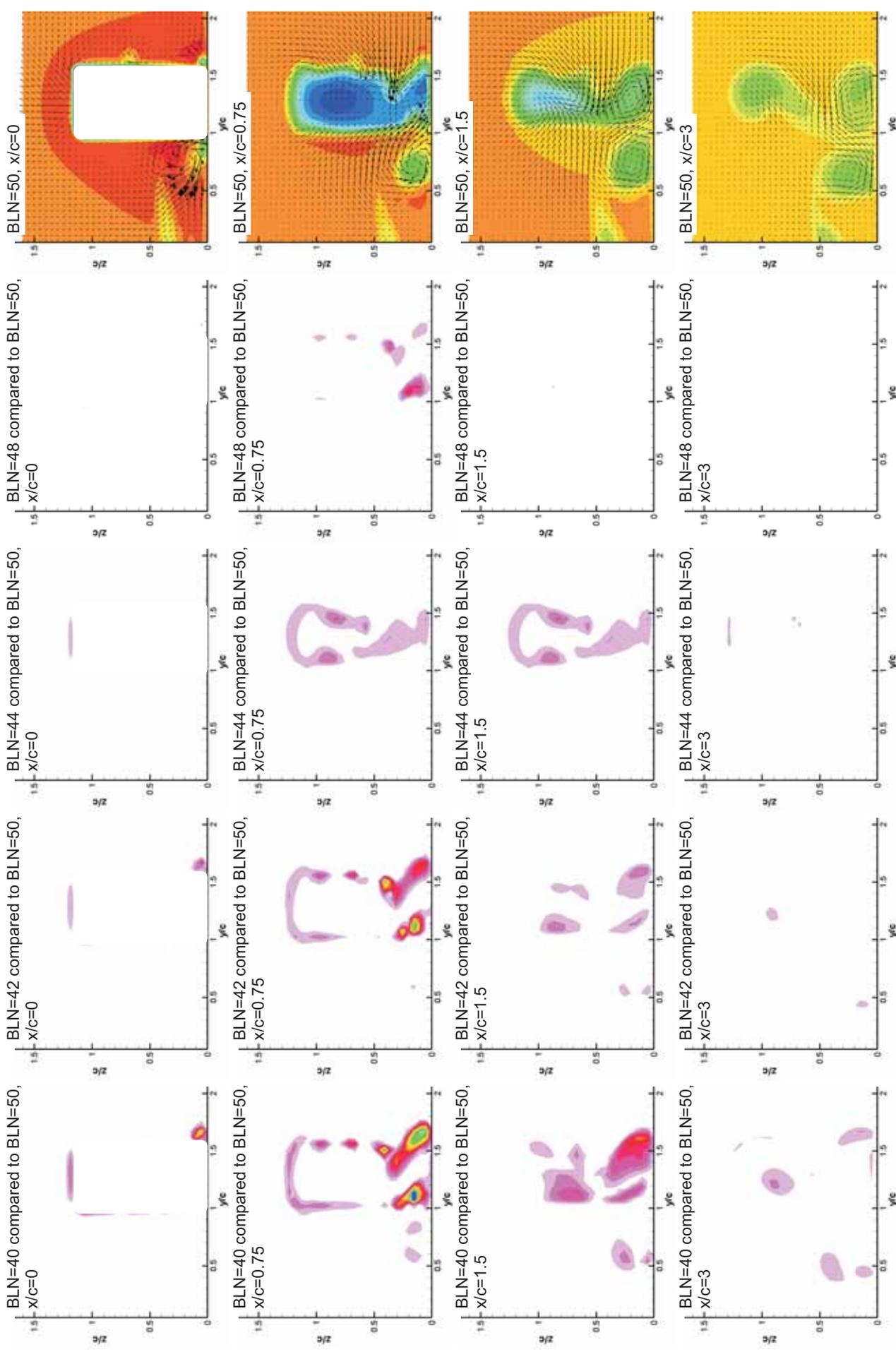




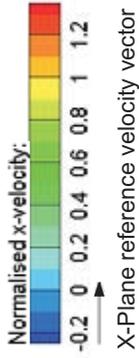
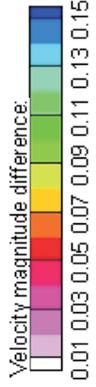
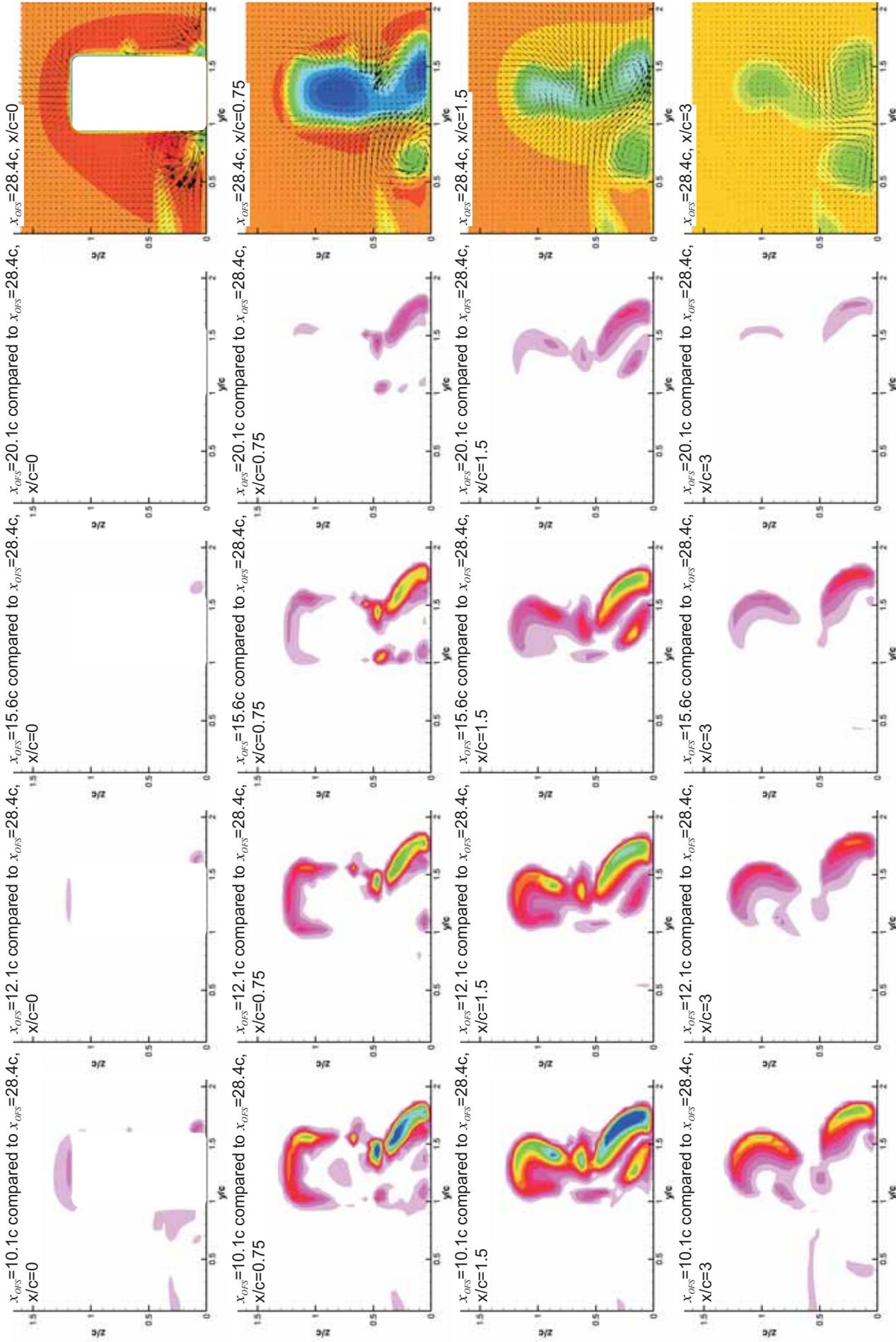


Boundary layer region depicted by green volume above. Number of control volumes perpendicular (BLN) to non-zero shear surfaces adjusted in the results shown here for the full-scale computational model.

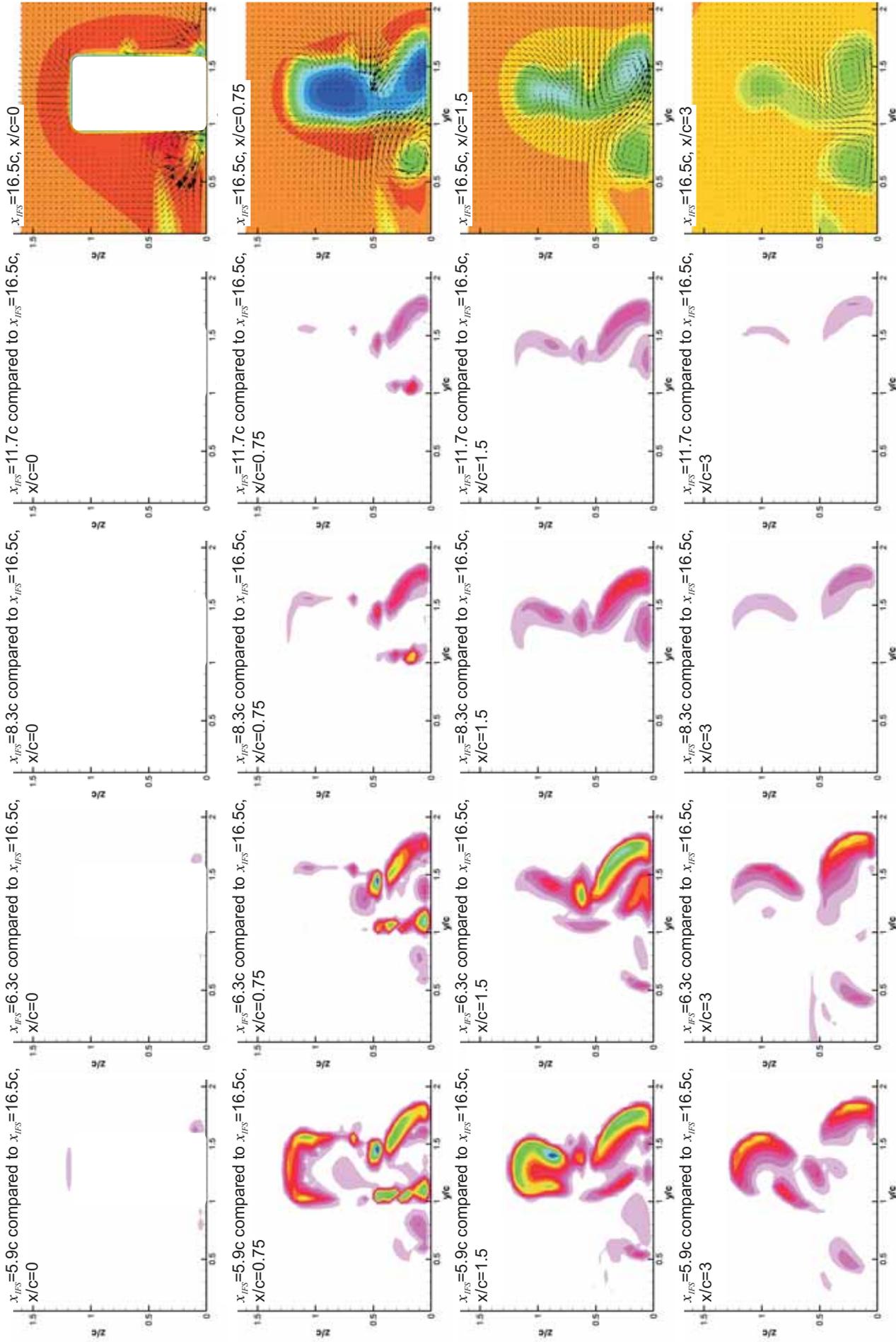




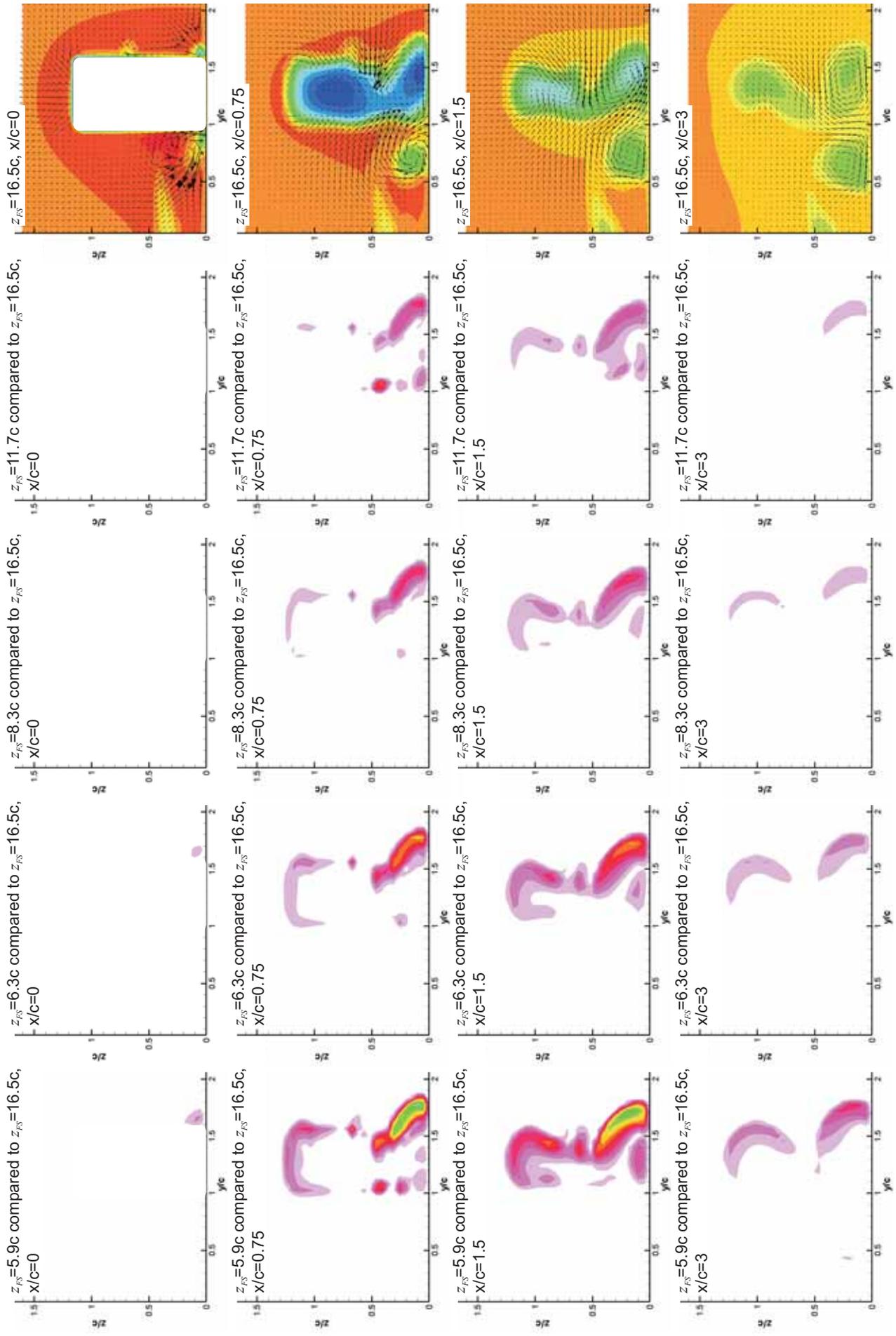
X-Plane reference velocity vector



Variations for changes in the outlet position for the full-scale computational model.



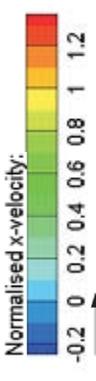
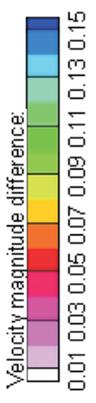
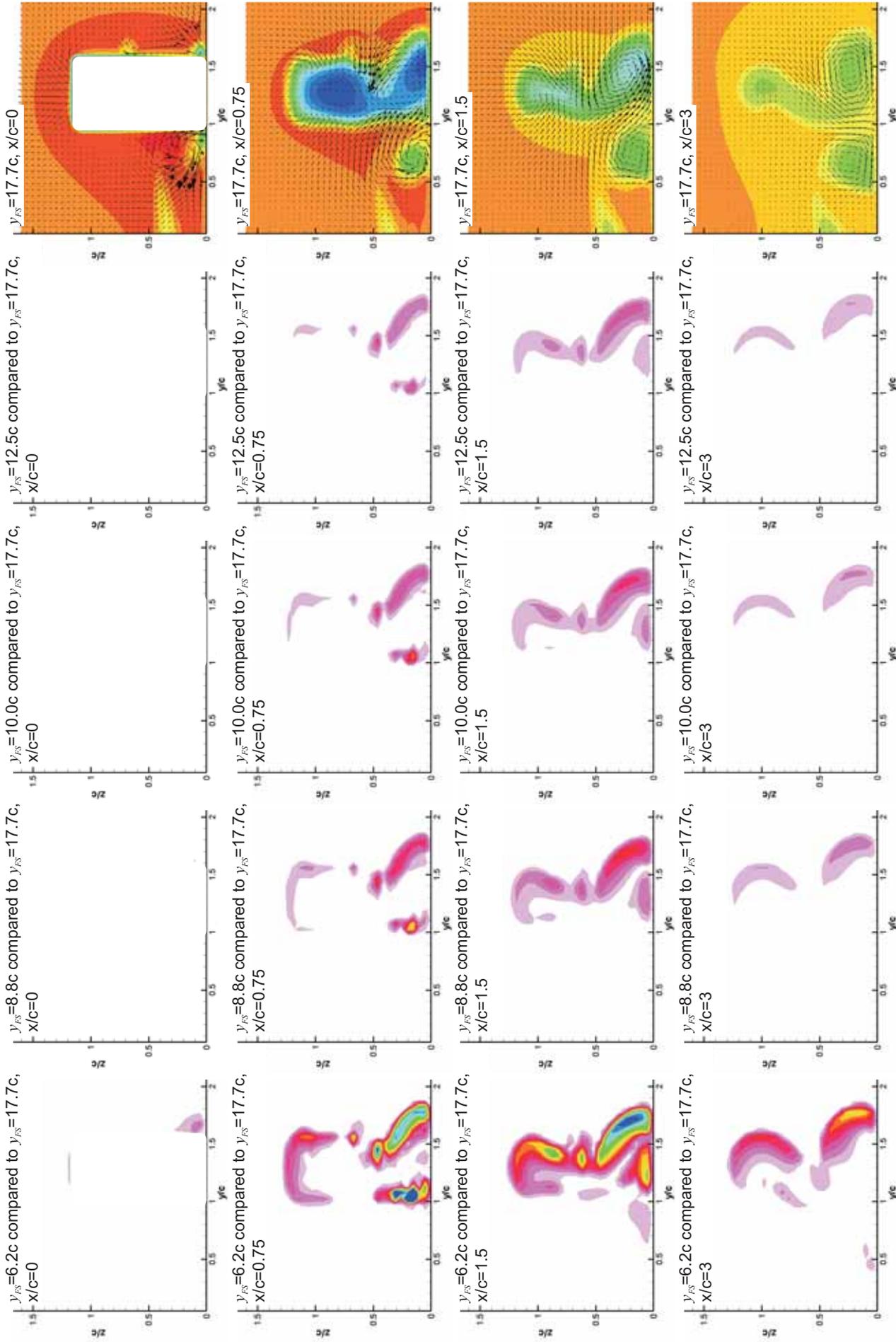
Variations for changes in the inlet position for the full-scale computational model.



Velocity magnitude difference:
 0.01 0.03 0.05 0.07 0.09 0.11 0.13 0.15

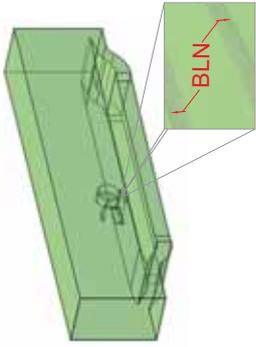
Normalised x-velocity:
 -0.2 0 0.2 0.4 0.6 0.8 1 1.2
 X-Plane reference velocity vector

Variations for changes in the top boundary position for the full-scale computational model.

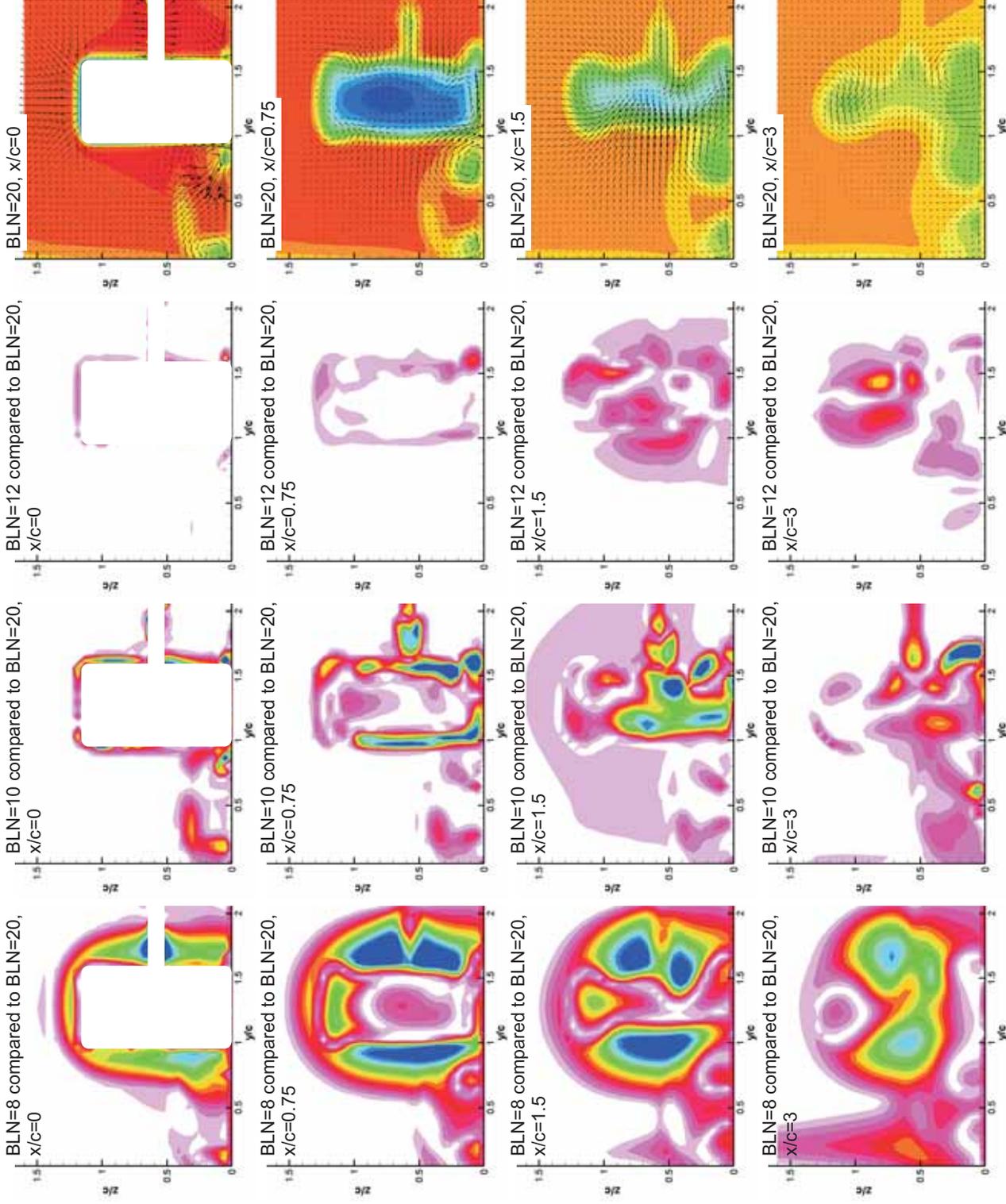


Variations for changes in the side boundary position for the full-scale computational model.

X-Plane reference velocity vector

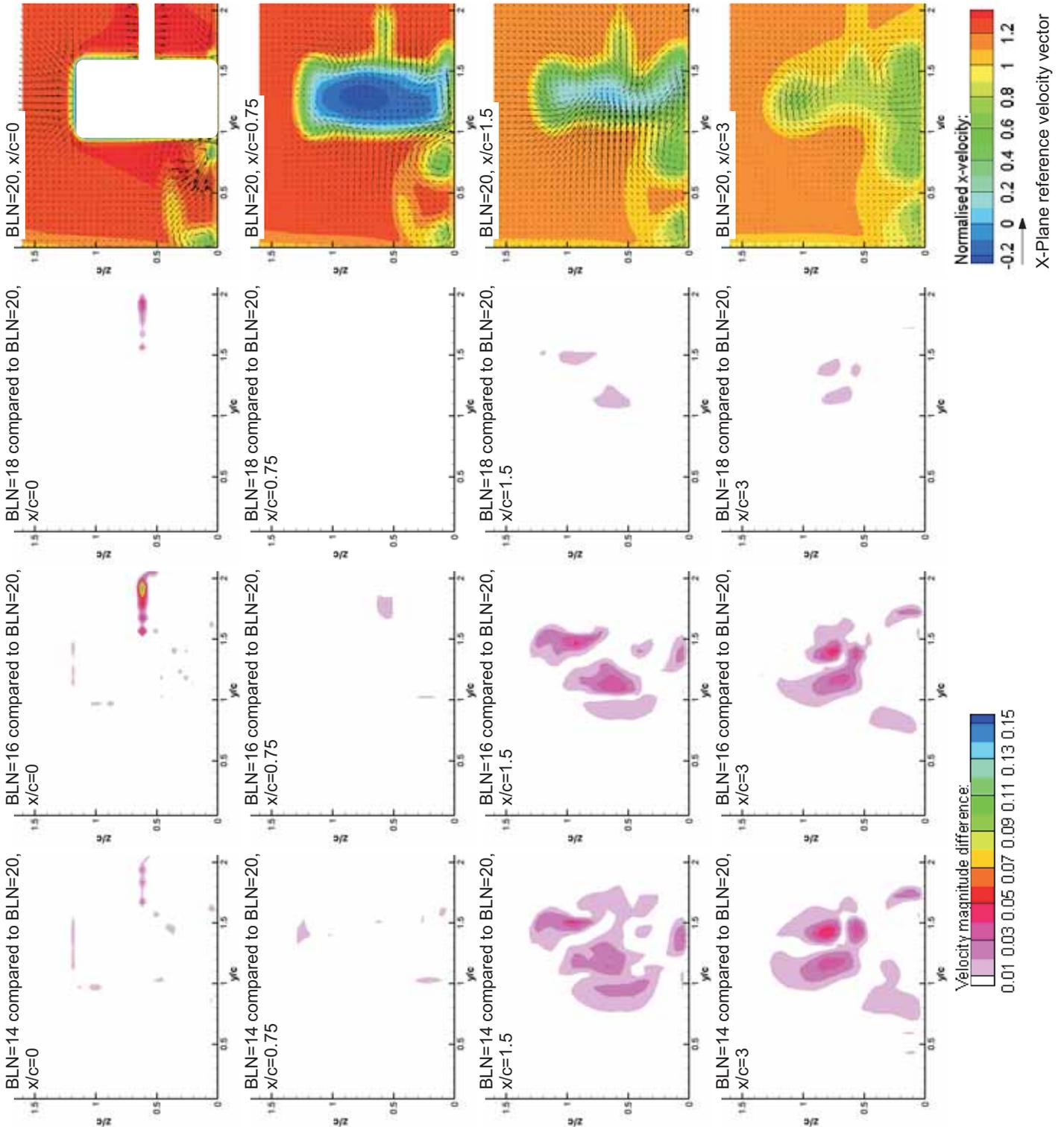


Boundary layer region depicted by green volume above. Number of control volumes perpendicular (BLN) to non-zero shear surfaces adjusted in the results shown here for the scaled computational model.



Velocity magnitude difference:
 0.01 0.03 0.05 0.07 0.09 0.11 0.13 0.15

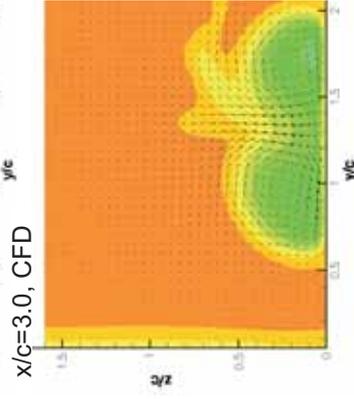
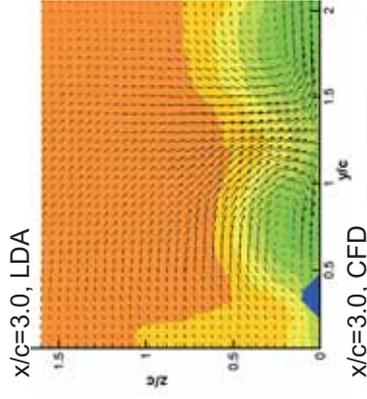
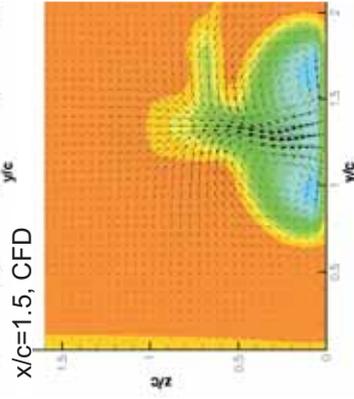
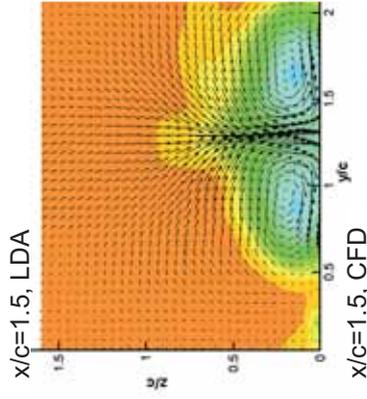
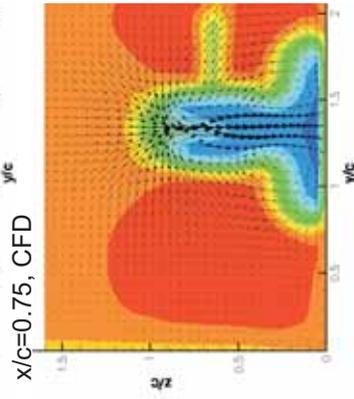
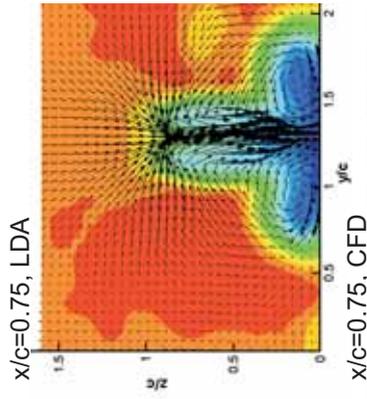
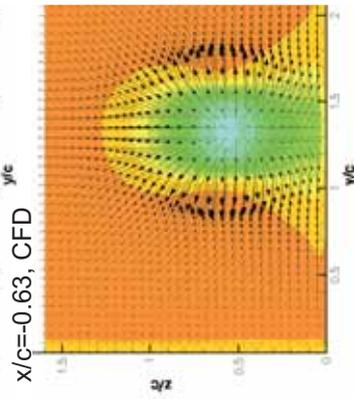
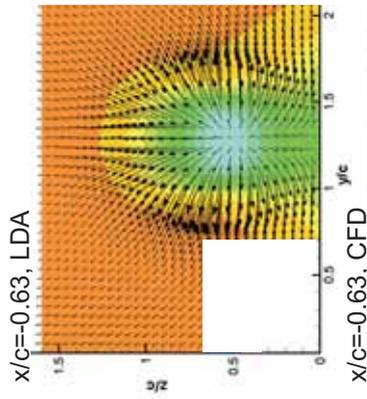
Normalised x-velocity:
 -0.2 0 0.2 0.4 0.6 0.8 1 1.2
 X-Plane reference velocity vector



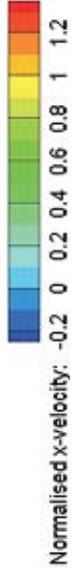
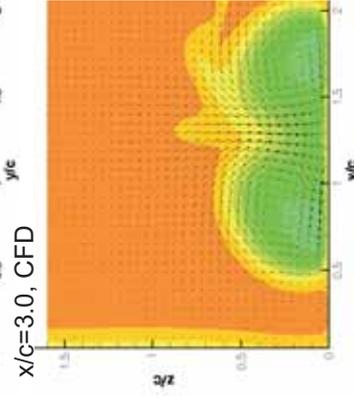
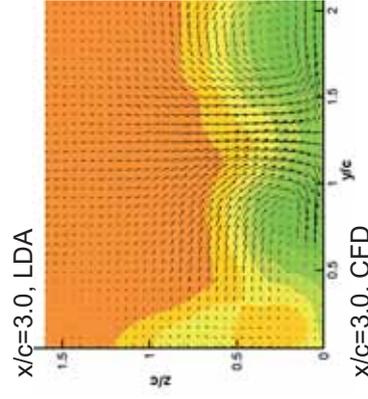
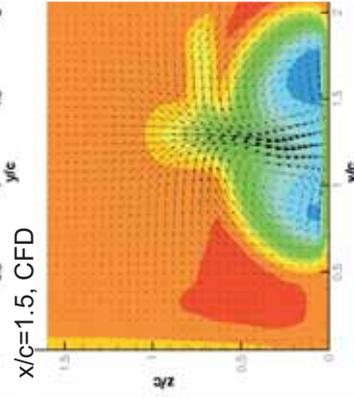
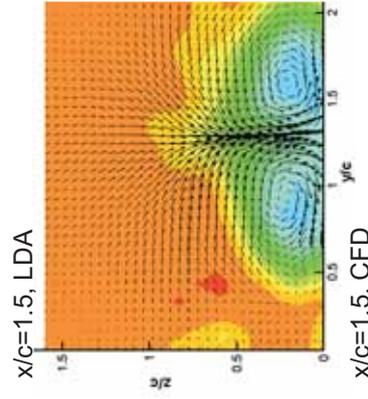
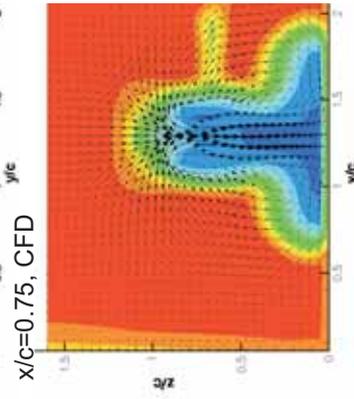
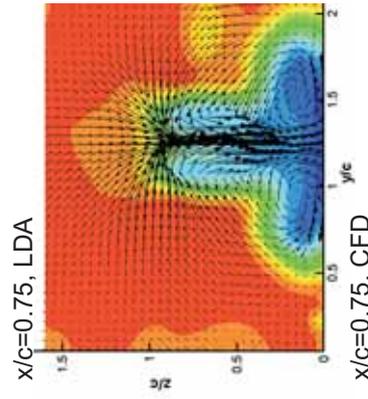
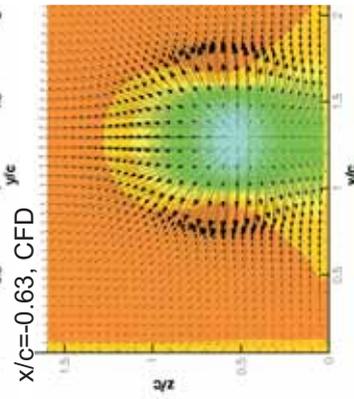
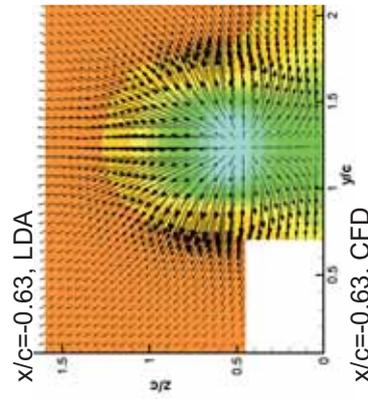
Appendix C:

Further Comparisons of LDA and computational results

Wheel only
 $T/c=1.6$
 $W/c=0.53$



Wheel only
 $T/c=1.6$
 $W/c=0.63$



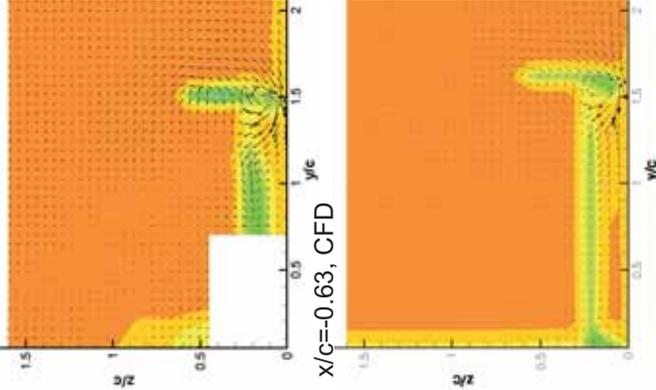
→ X-Plane reference velocity vector

Wing only

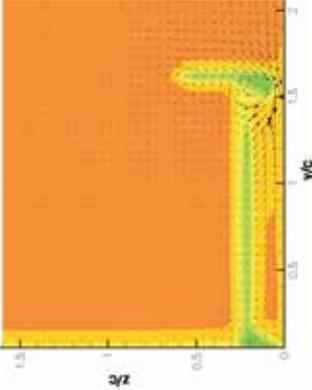
$S/c=0.97$
 $h/c=0.13$
 $AOA=0^\circ$



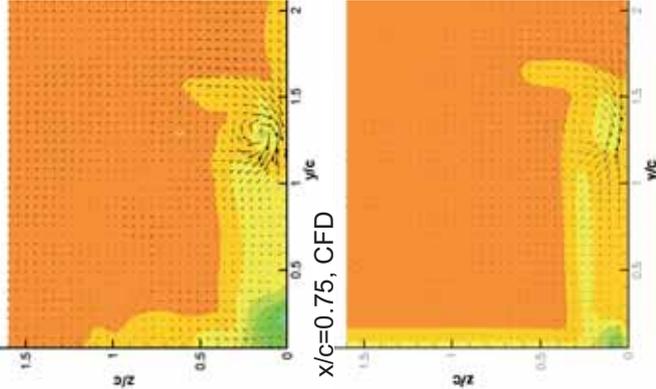
$x/c=-0.63$, LDA



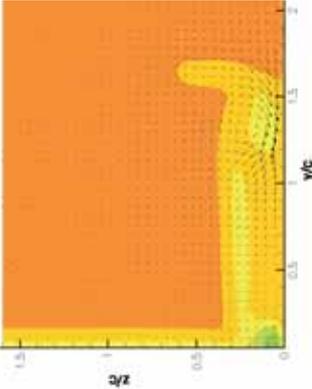
$x/c=-0.63$, CFD



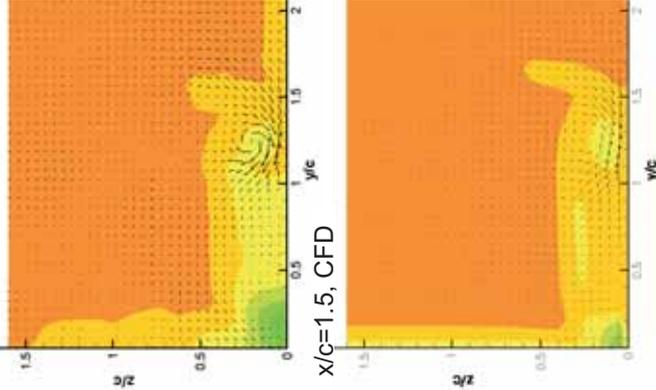
$x/c=0.75$, LDA



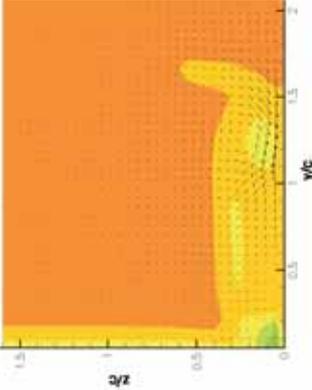
$x/c=0.75$, CFD



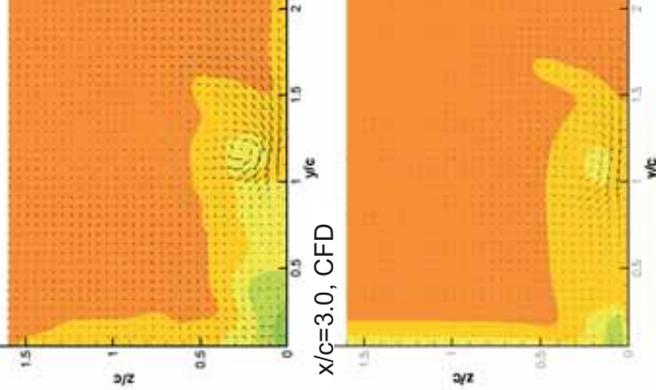
$x/c=1.5$, LDA



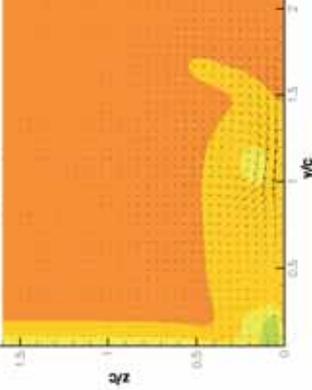
$x/c=1.5$, CFD



$x/c=3.0$, LDA



$x/c=3.0$, CFD

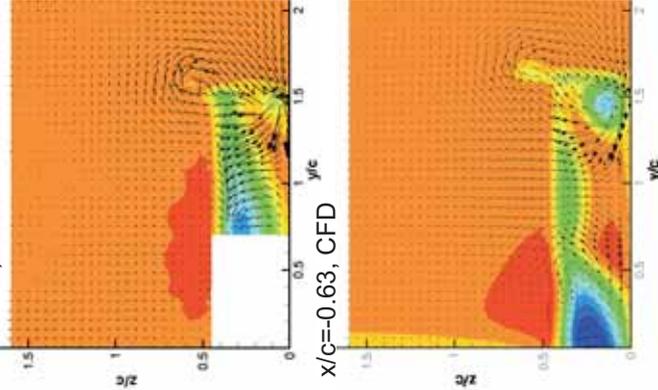


Wing only

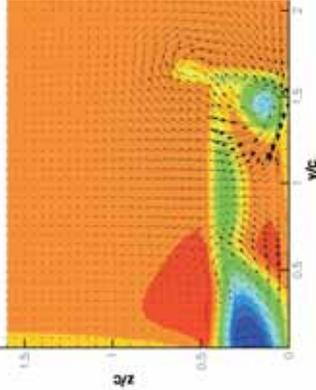
$S/c=0.97$
 $h/c=0.13$
 $AOA=12^\circ$



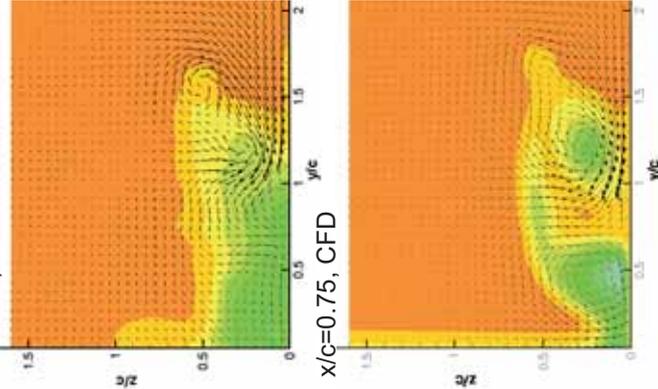
$x/c=-0.63$, LDA



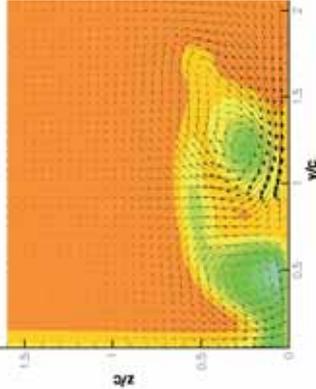
$x/c=-0.63$, CFD



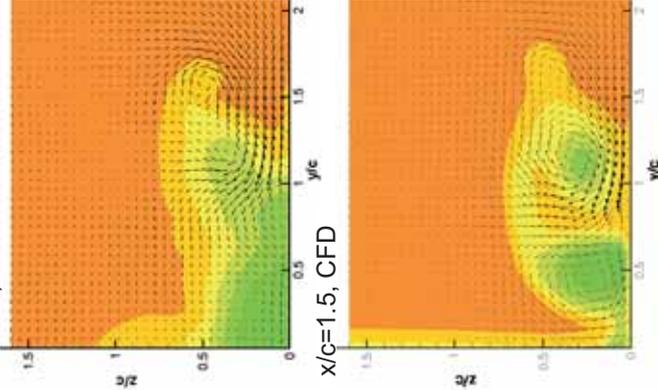
$x/c=0.75$, LDA



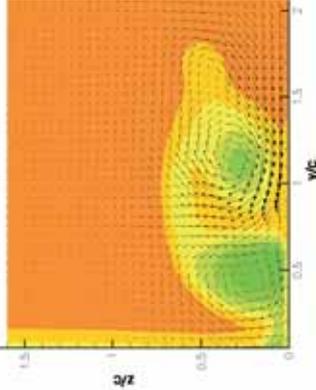
$x/c=0.75$, CFD



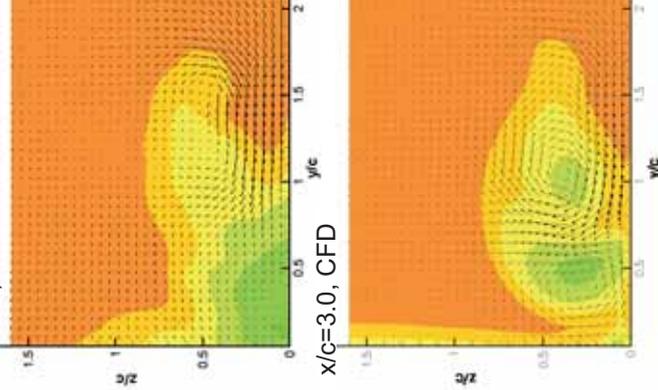
$x/c=1.5$, LDA



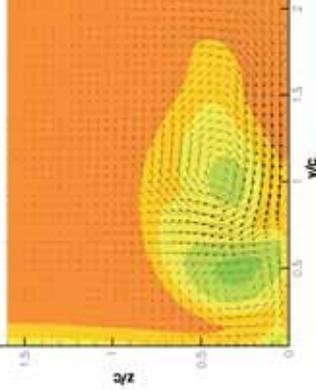
$x/c=1.5$, CFD



$x/c=3.0$, LDA



$x/c=3.0$, CFD



Normalised x-velocity: -0.2 0 0.2 0.4 0.6 0.8 1 1.2

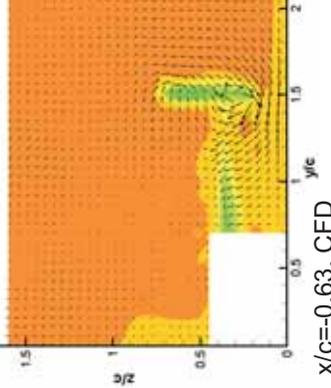
X-Plane reference velocity vector

Wing only

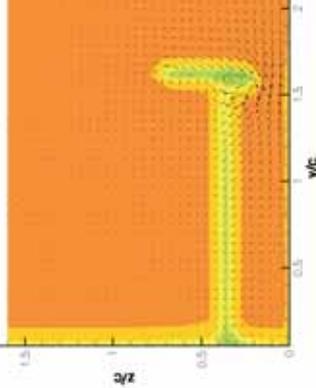
$S/c=0.97$
 $h/c=0.27$
 $AOA=0^\circ$



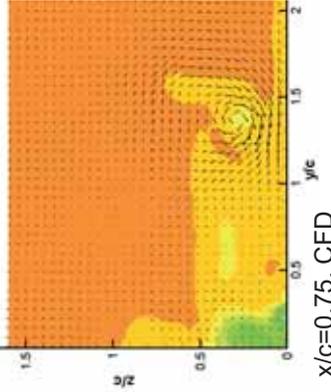
$x/c=-0.63$, LDA



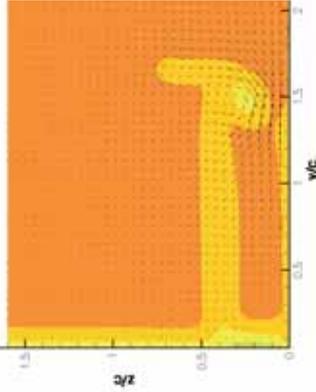
$x/c=-0.63$, CFD



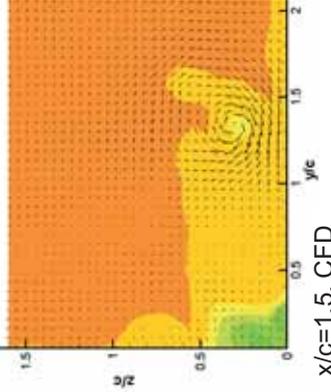
$x/c=0.75$, LDA



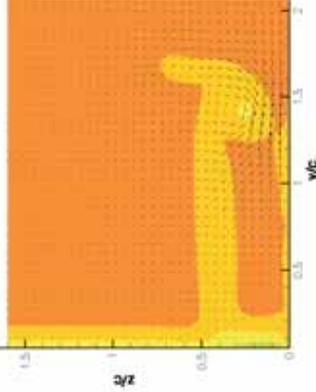
$x/c=0.75$, CFD



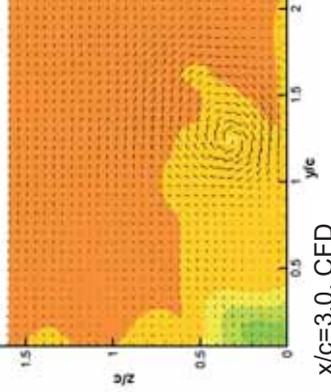
$x/c=1.5$, LDA



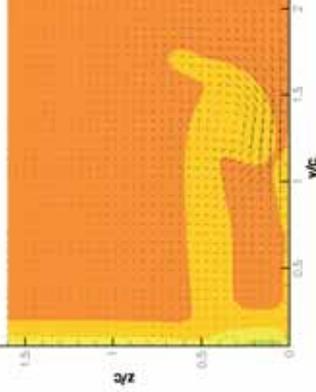
$x/c=1.5$, CFD



$x/c=3.0$, LDA



$x/c=3.0$, CFD

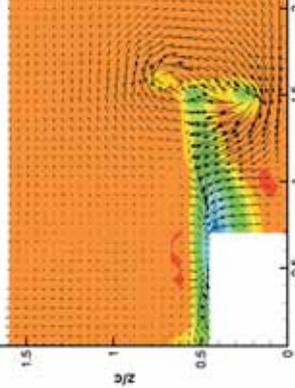


Wing only

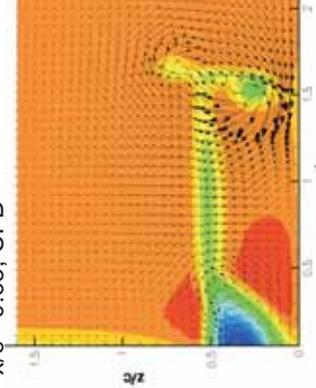
$S/c=0.97$
 $h/c=0.27$
 $AOA=12^\circ$



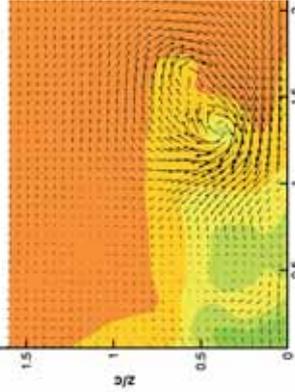
$x/c=-0.63$, LDA



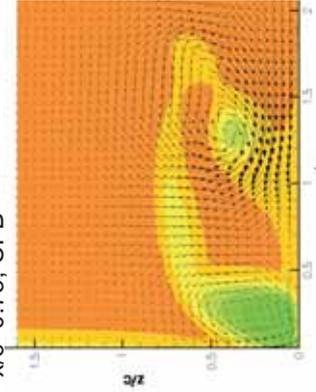
$x/c=-0.63$, CFD



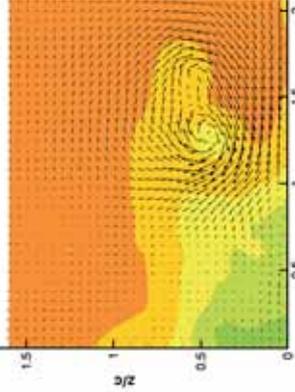
$x/c=0.75$, LDA



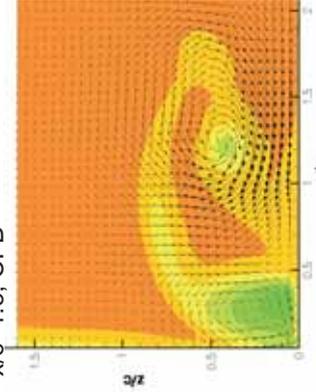
$x/c=0.75$, CFD



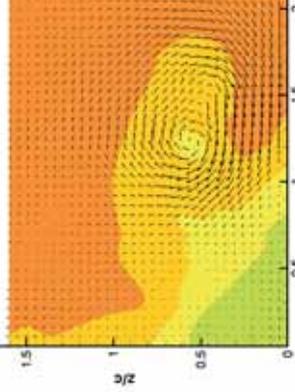
$x/c=1.5$, LDA



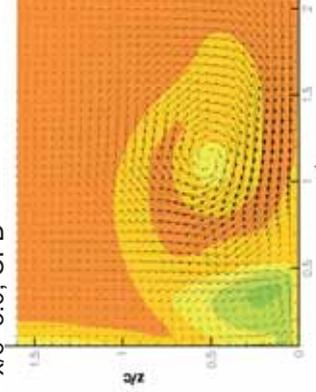
$x/c=1.5$, CFD



$x/c=3.0$, LDA



$x/c=3.0$, CFD



Normalised x-velocity: -0.2 0 0.2 0.4 0.6 0.8 1 1.2

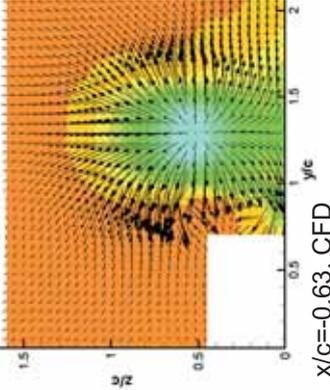
X-Plane reference velocity vector

Wing and Wheel

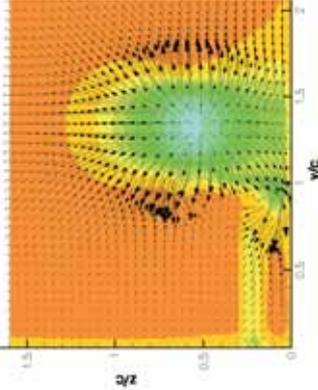
$T/c=1.6$
 $W/c=0.53$
 $S/c=1.06$
 $h/c=0.13$
 $AOA=0^\circ$



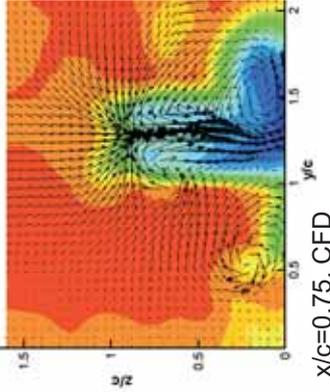
$x/c=-0.63$, LDA



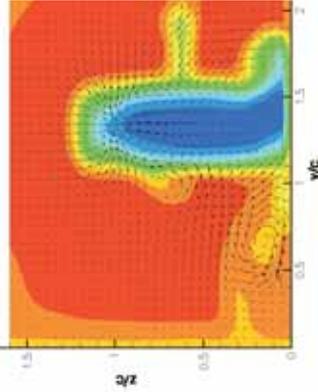
$x/c=-0.63$, CFD



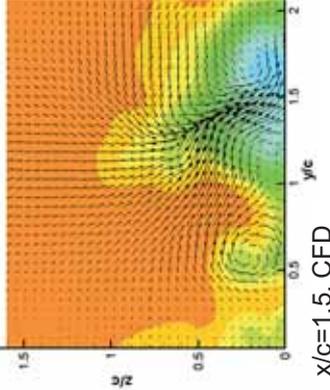
$x/c=0.75$, LDA



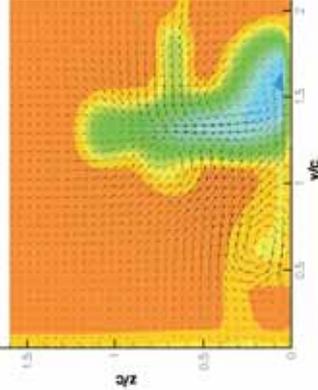
$x/c=0.75$, CFD



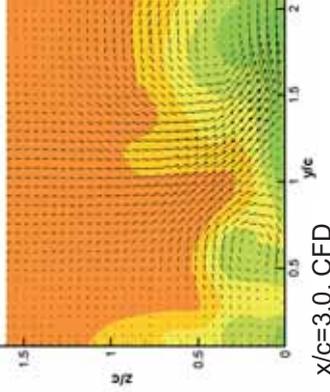
$x/c=1.5$, LDA



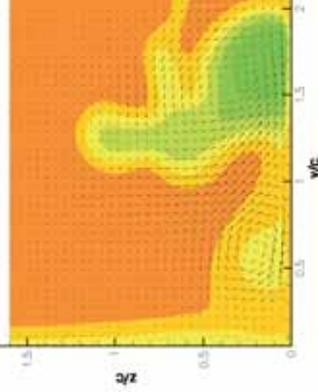
$x/c=1.5$, CFD



$x/c=3.0$, LDA



$x/c=3.0$, CFD

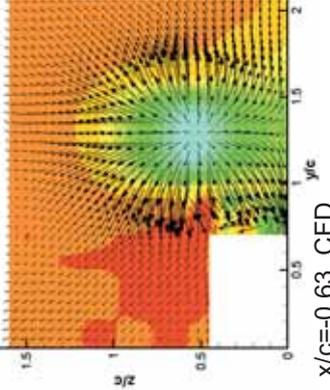


Wing and Wheel

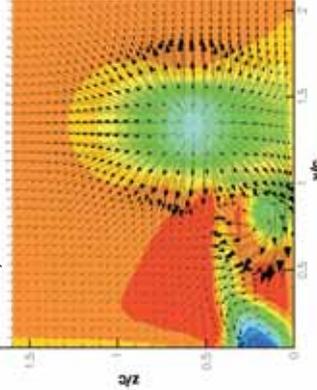
$T/c=1.6$
 $W/c=0.53$
 $S/c=1.06$
 $h/c=0.13$
 $AOA=12^\circ$



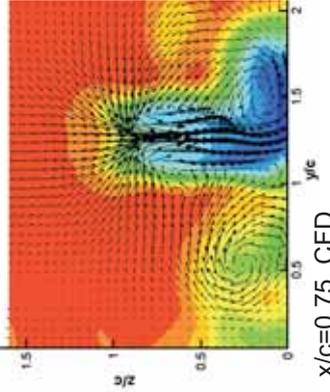
$x/c=-0.63$, LDA



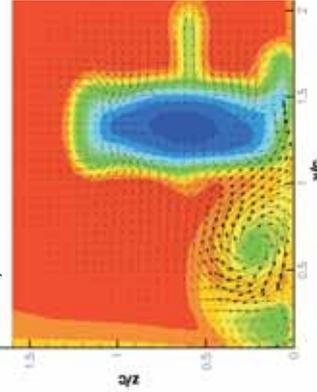
$x/c=-0.63$, CFD



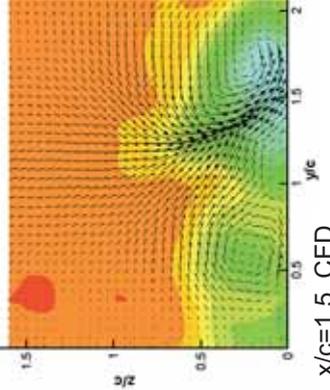
$x/c=0.75$, LDA



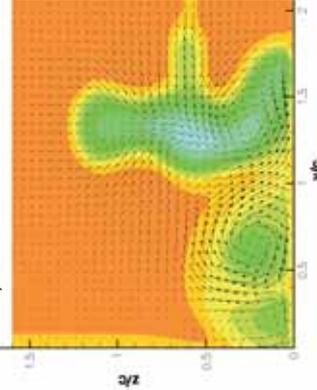
$x/c=0.75$, CFD



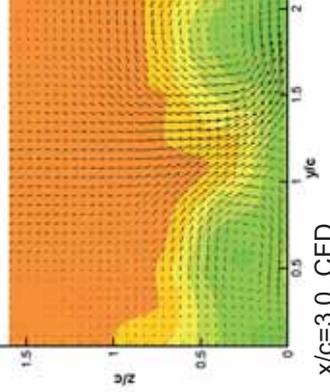
$x/c=1.5$, LDA



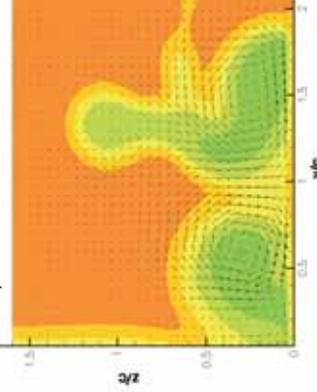
$x/c=1.5$, CFD



$x/c=3.0$, LDA



$x/c=3.0$, CFD



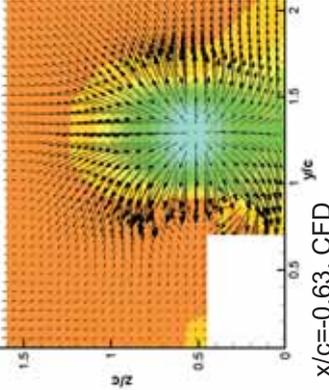
Normalised x-velocity: -0.2 0 0.2 0.4 0.6 0.8 1 1.2
 X-Plane reference velocity vector

Wing and Wheel

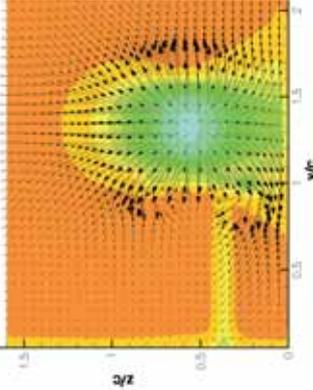
$T/c=1.6$
 $W/c=0.53$
 $S/c=1.06$
 $h/c=0.27$
 $AOA=0^\circ$



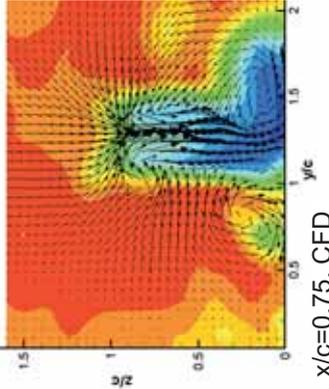
$x/c=-0.63$, LDA



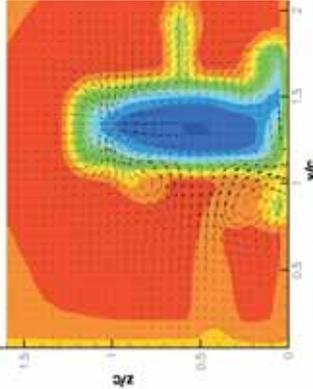
$x/c=-0.63$, CFD



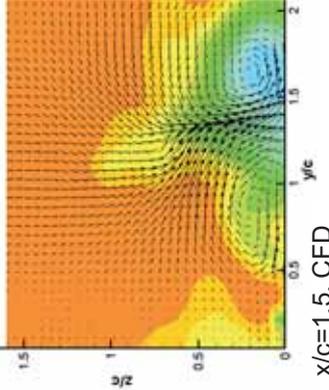
$x/c=0.75$, LDA



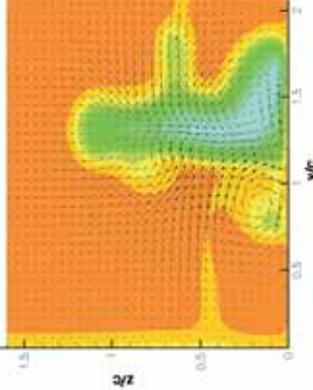
$x/c=0.75$, CFD



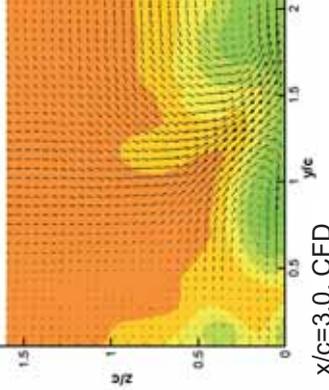
$x/c=1.5$, LDA



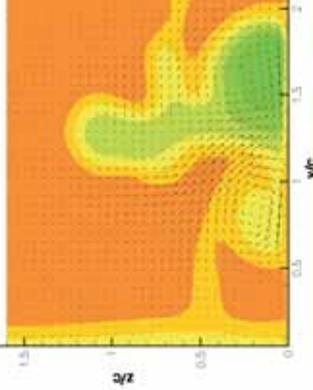
$x/c=1.5$, CFD



$x/c=3.0$, LDA



$x/c=3.0$, CFD

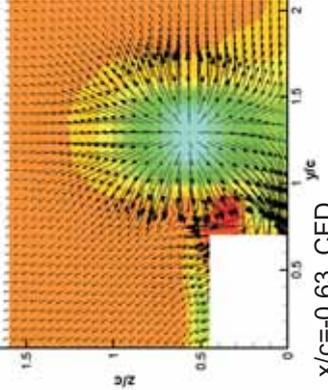


Wing and Wheel

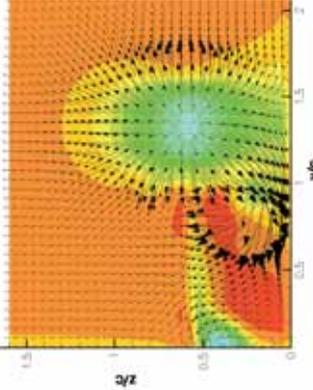
$T/c=1.6$
 $W/c=0.53$
 $S/c=1.06$
 $h/c=0.27$
 $AOA=12^\circ$



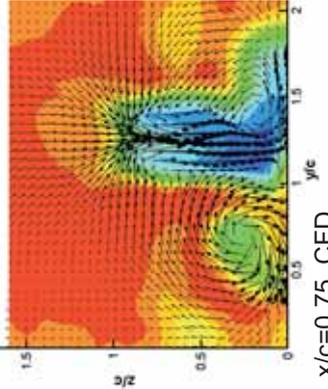
$x/c=-0.63$, LDA



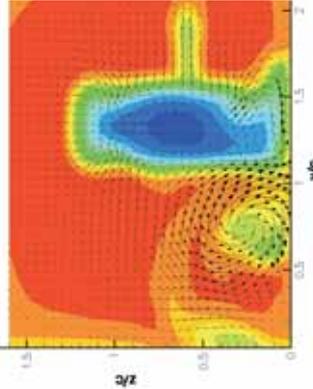
$x/c=-0.63$, CFD



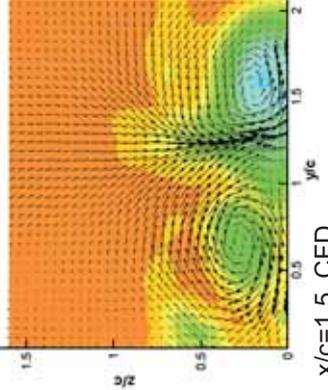
$x/c=0.75$, LDA



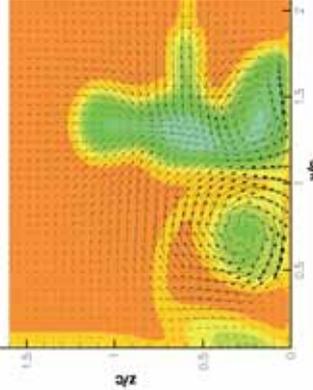
$x/c=0.75$, CFD



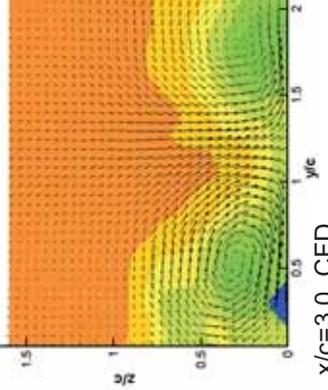
$x/c=1.5$, LDA



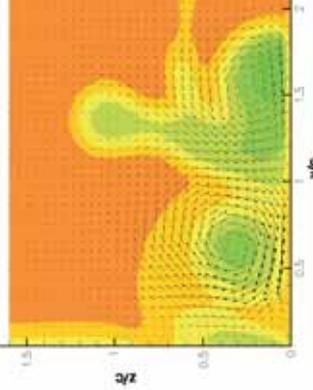
$x/c=1.5$, CFD



$x/c=3.0$, LDA



$x/c=3.0$, CFD

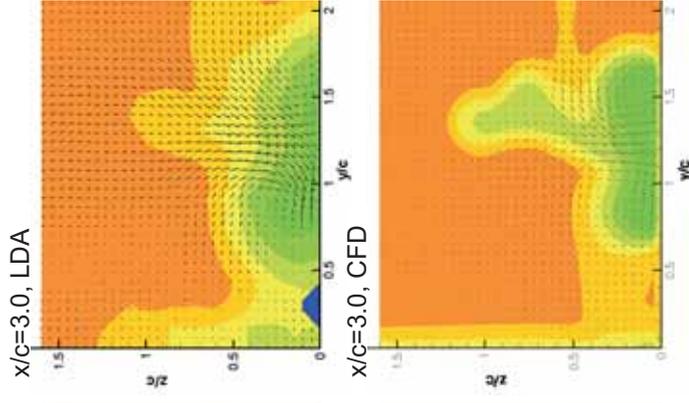
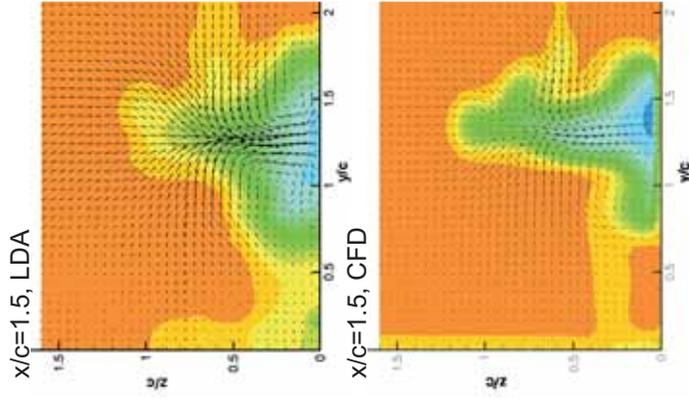
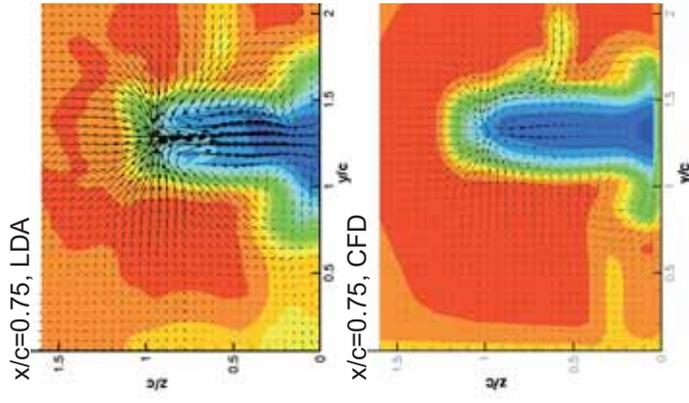
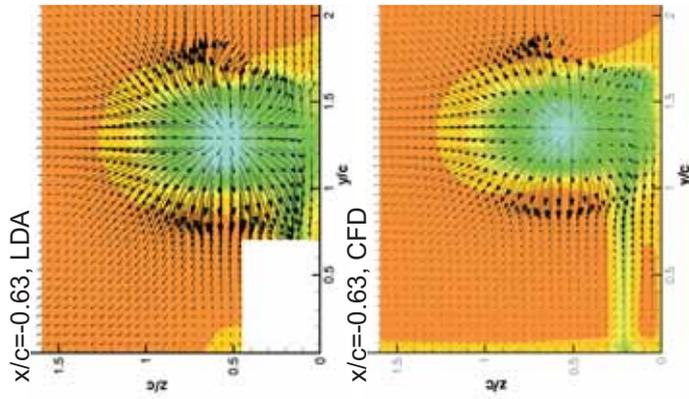


Normalised x-velocity: -0.2 0 0.2 0.4 0.6 0.8 1 1.2

X-Plane reference velocity vector

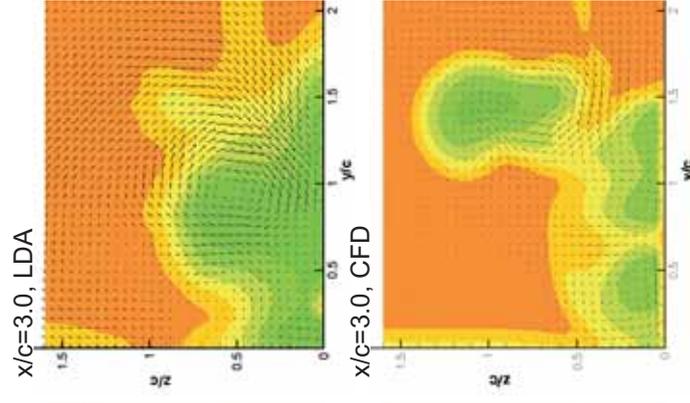
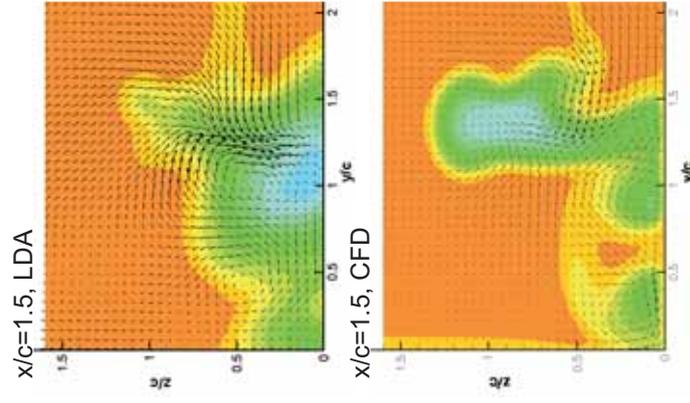
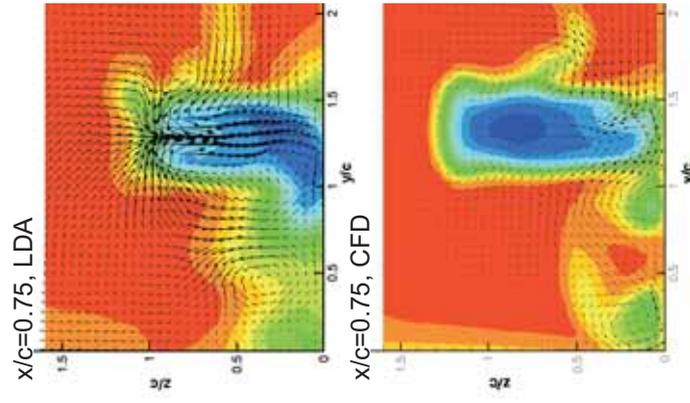
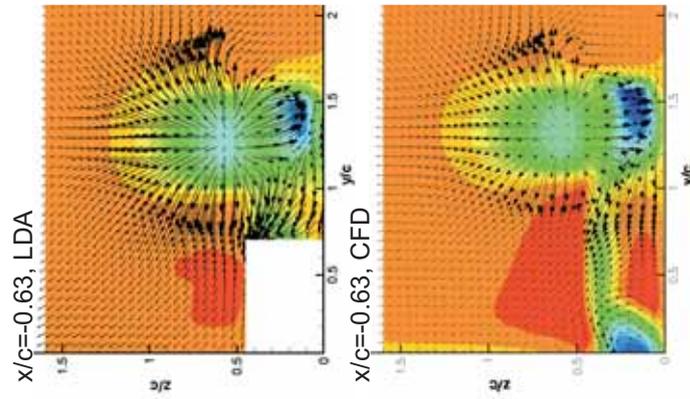
Wing and Wheel

$T/c=1.6$
 $W/c=0.53$
 $S/c=1.6$
 $h/c=0.13$
 $AOA=0^\circ$



Wing and Wheel

$T/c=1.6$
 $W/c=0.53$
 $S/c=1.6$
 $h/c=0.13$
 $AOA=12^\circ$



Normalised x-velocity: -0.2 0 0.2 0.4 0.6 0.8 1 1.2

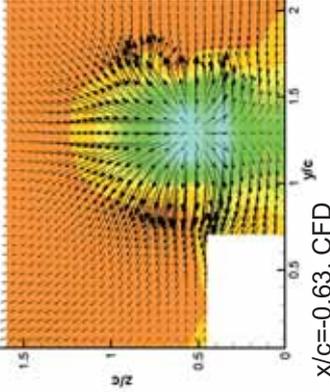
X-Plane reference velocity vector

Wing and Wheel

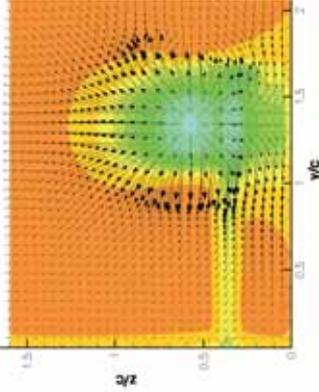
$T/c=1.6$
 $W/c=0.53$
 $S/c=1.6$
 $h/c=0.27$
 $AOA=0^\circ$



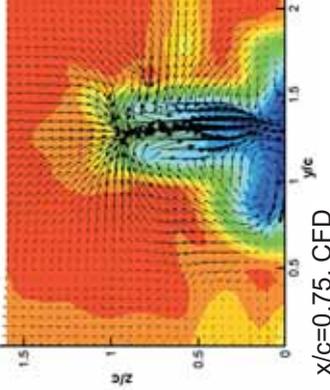
$x/c=-0.63$, LDA



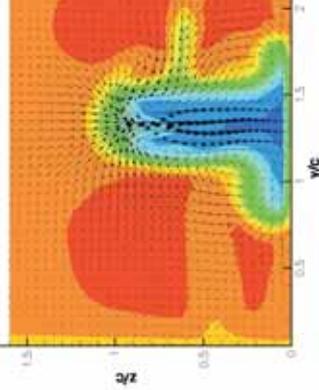
$x/c=-0.63$, CFD



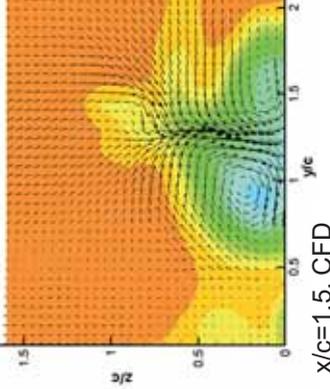
$x/c=0.75$, LDA



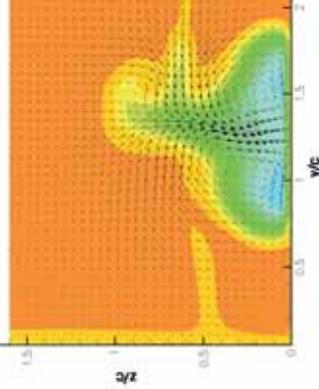
$x/c=0.75$, CFD



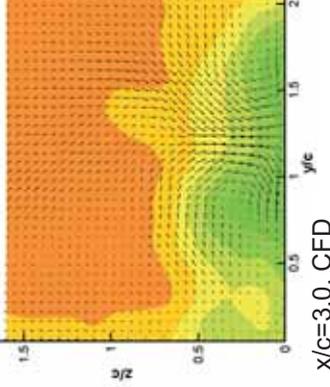
$x/c=1.5$, LDA



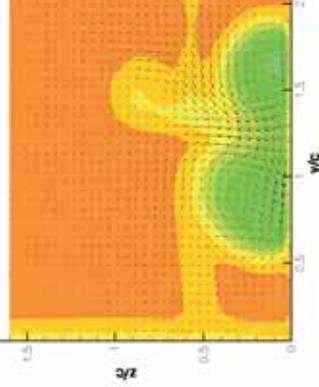
$x/c=1.5$, CFD



$x/c=3.0$, LDA



$x/c=3.0$, CFD

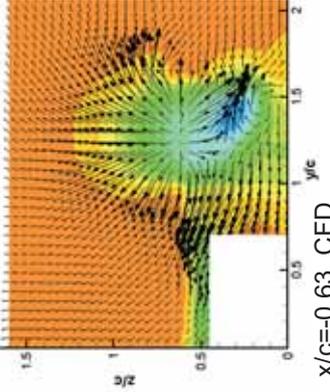


Wing and Wheel

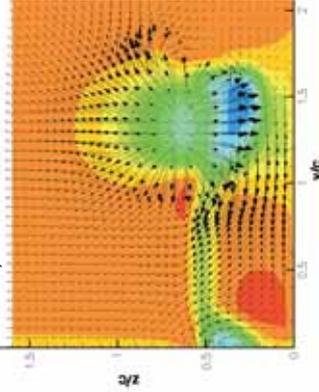
$T/c=1.6$
 $W/c=0.53$
 $S/c=1.6$
 $h/c=0.27$
 $AOA=12^\circ$



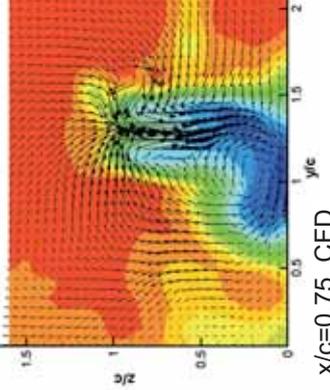
$x/c=-0.63$, LDA



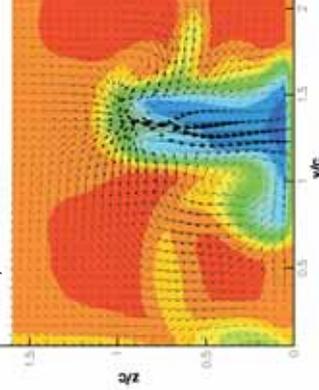
$x/c=-0.63$, CFD



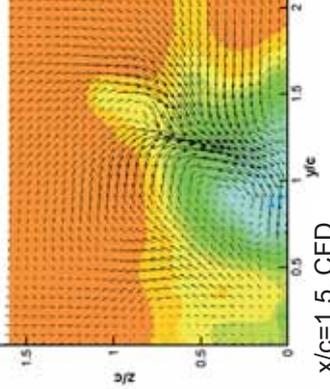
$x/c=0.75$, LDA



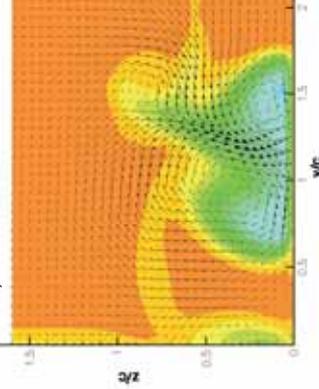
$x/c=0.75$, CFD



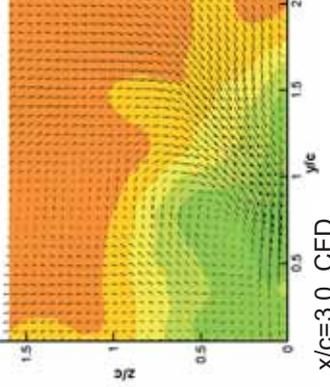
$x/c=1.5$, LDA



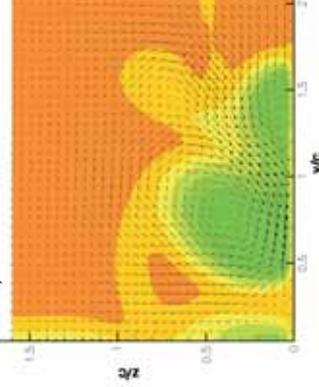
$x/c=1.5$, CFD



$x/c=3.0$, LDA



$x/c=3.0$, CFD

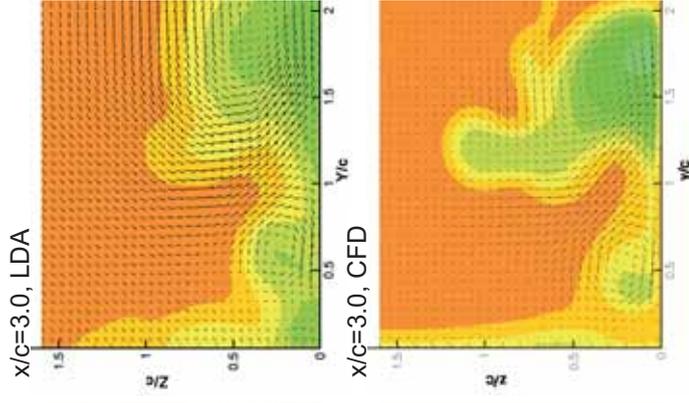
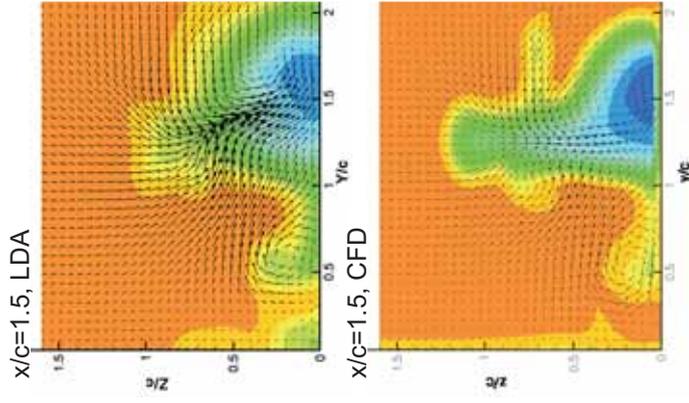
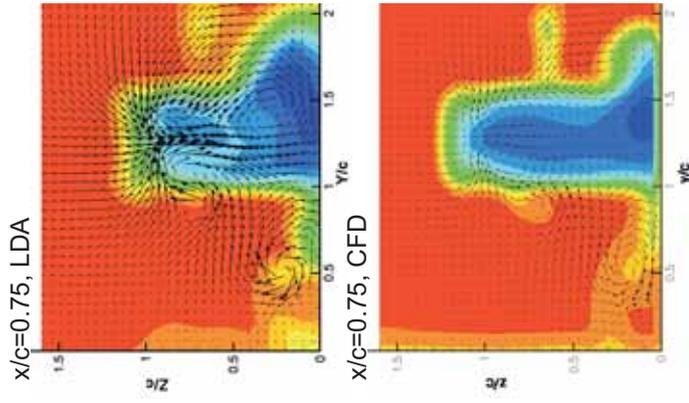
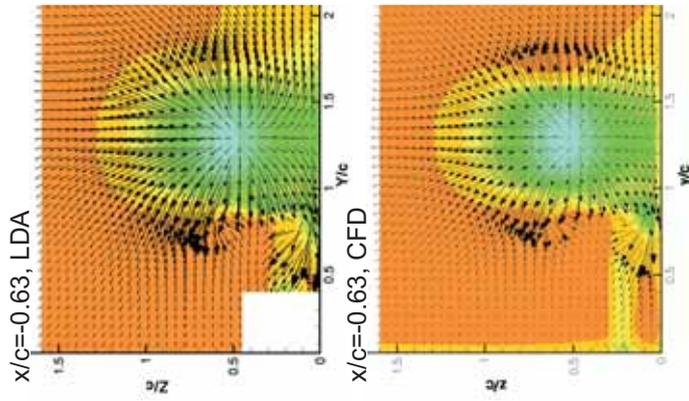


Normalised x-velocity: -0.2 0 0.2 0.4 0.6 0.8 1 1.2

X-Plane reference velocity vector

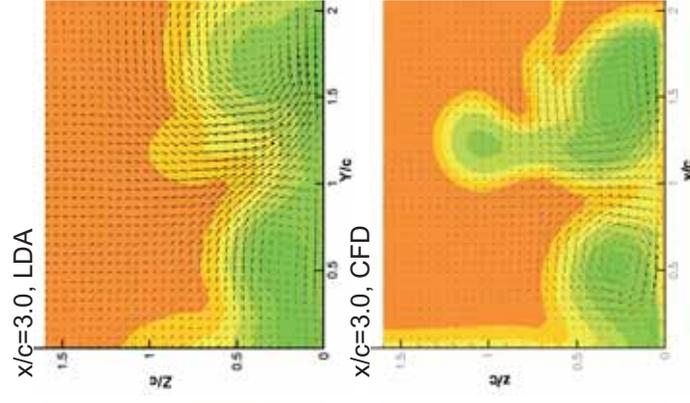
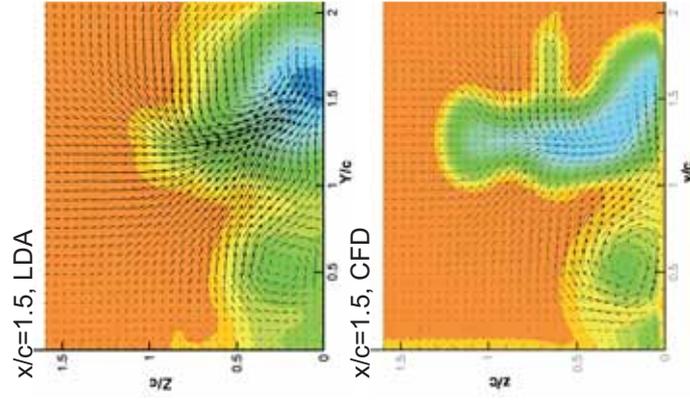
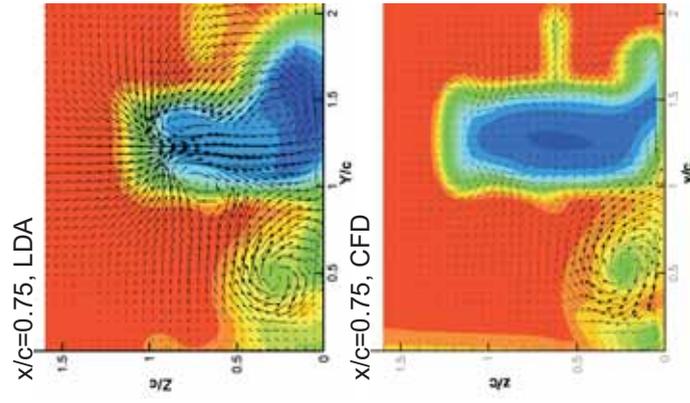
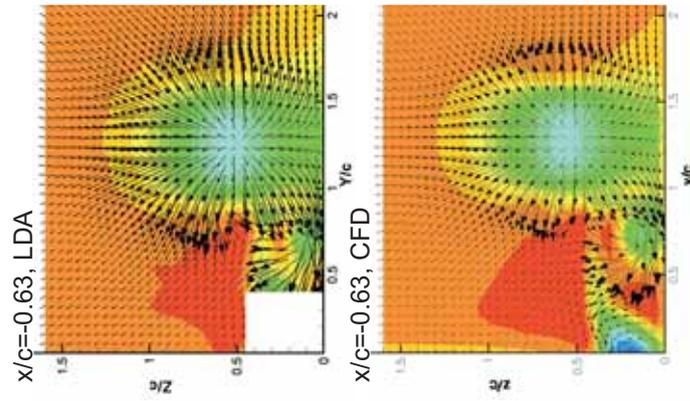
Wing and Wheel

$T/c=1.6$
 $W/c=0.63$
 $S/c=0.97$
 $h/c=0.13$
 $AOA=0^\circ$



Wing and Wheel

$T/c=1.6$
 $W/c=0.63$
 $S/c=0.97$
 $h/c=0.13$
 $AOA=12^\circ$



Normalised x-velocity: -0.2 0 0.2 0.4 0.6 0.8 1 1.2

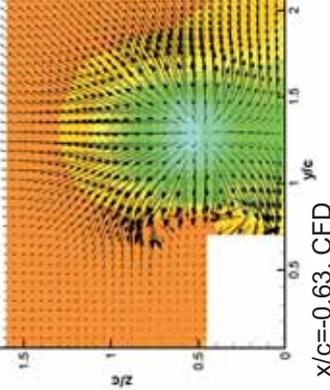
X-Plane reference velocity vector

Wing and Wheel

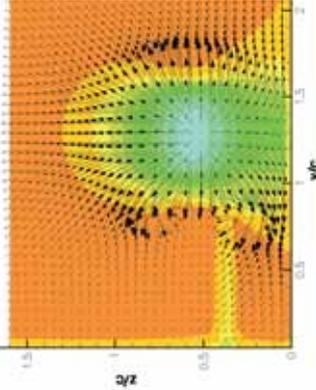
$T/c=1.6$
 $W/c=0.63$
 $S/c=0.97$
 $h/c=0.27$
 $AOA=0^\circ$



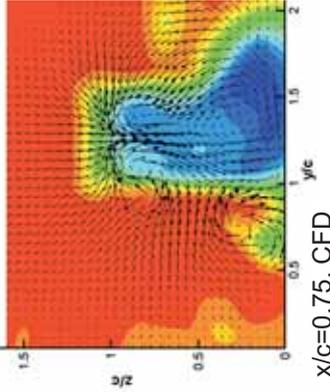
$x/c=-0.63$, LDA



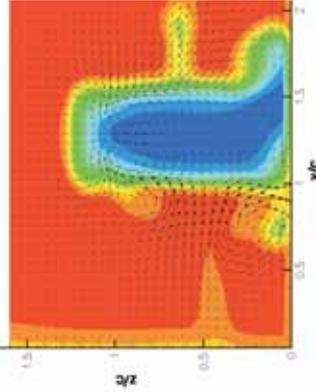
$x/c=-0.63$, CFD



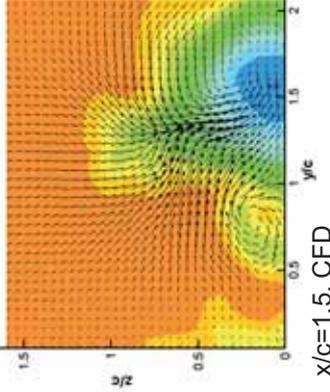
$x/c=0.75$, LDA



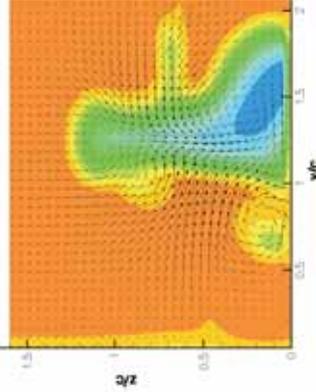
$x/c=0.75$, CFD



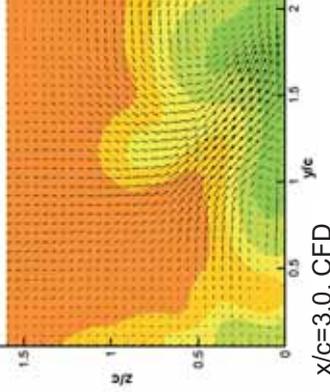
$x/c=1.5$, LDA



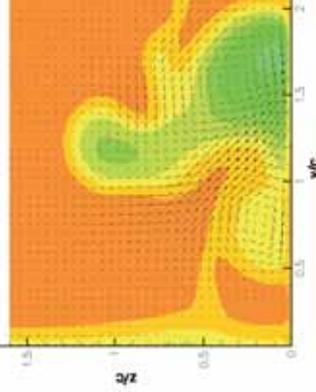
$x/c=1.5$, CFD



$x/c=3.0$, LDA



$x/c=3.0$, CFD

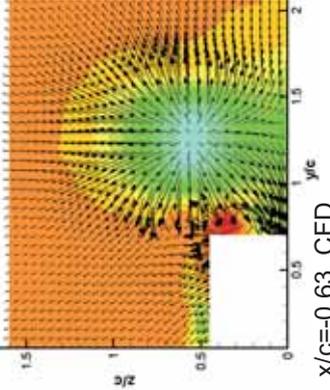


Wing and Wheel

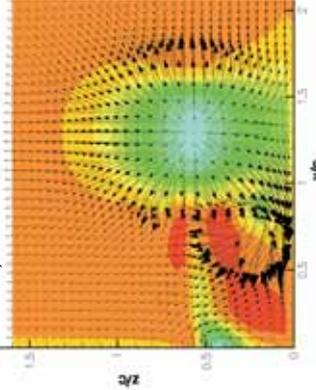
$T/c=1.6$
 $W/c=0.63$
 $S/c=0.97$
 $h/c=0.27$
 $AOA=12^\circ$



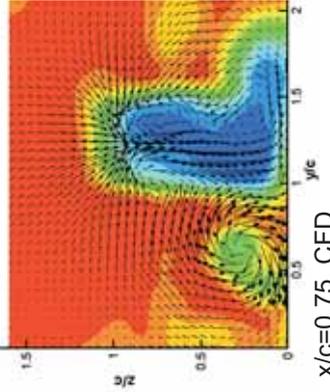
$x/c=-0.63$, LDA



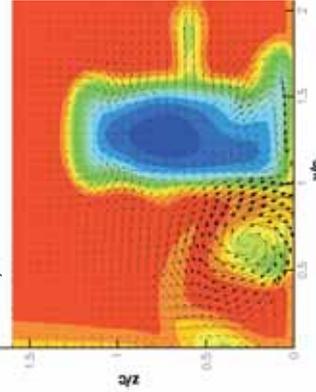
$x/c=-0.63$, CFD



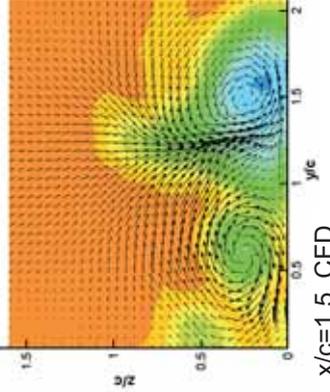
$x/c=0.75$, LDA



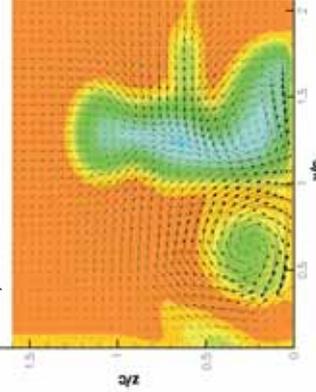
$x/c=0.75$, CFD



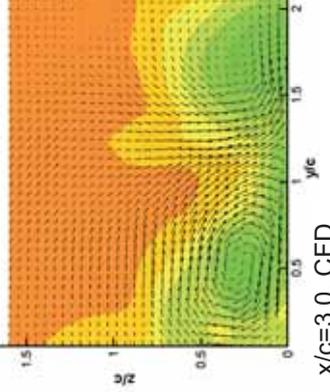
$x/c=1.5$, LDA



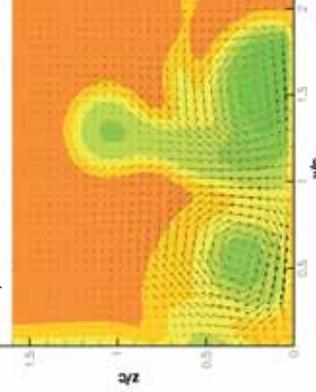
$x/c=1.5$, CFD



$x/c=3.0$, LDA



$x/c=3.0$, CFD



Normalised x-velocity: -0.2 0 0.2 0.4 0.6 0.8 1 1.2

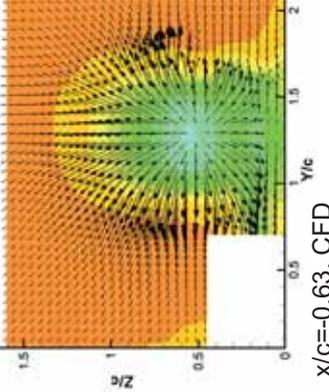
X-Plane reference velocity vector

Wing and Wheel

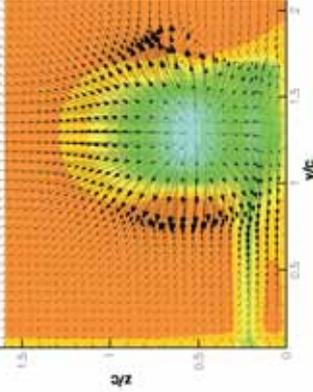
$T/c=1.6$
 $W/c=0.63$
 $S/c=1.6$
 $h/c=0.13$
 $AOA=0^\circ$



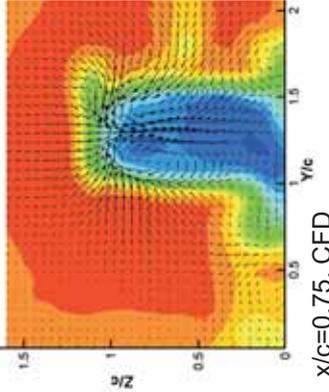
$x/c=-0.63$, LDA



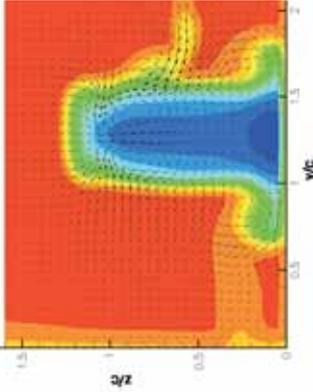
$x/c=-0.63$, CFD



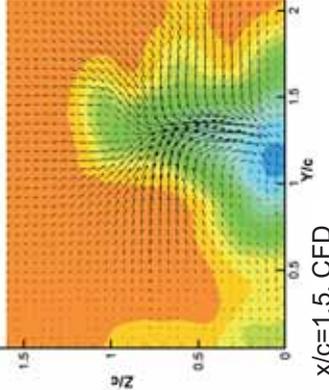
$x/c=0.75$, LDA



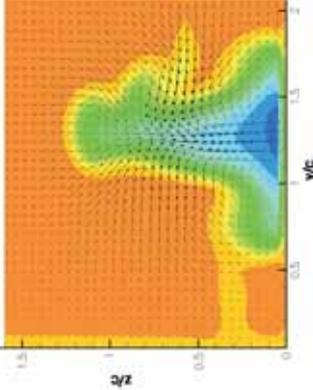
$x/c=0.75$, CFD



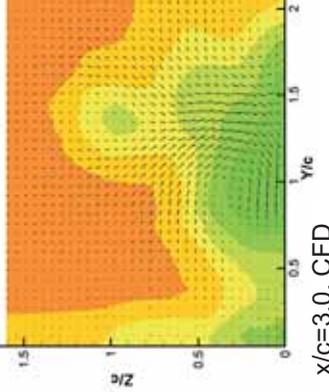
$x/c=1.5$, LDA



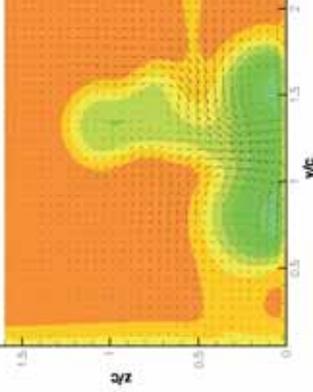
$x/c=1.5$, CFD



$x/c=3.0$, LDA



$x/c=3.0$, CFD

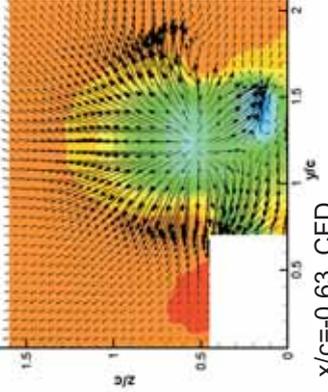


Wing and Wheel

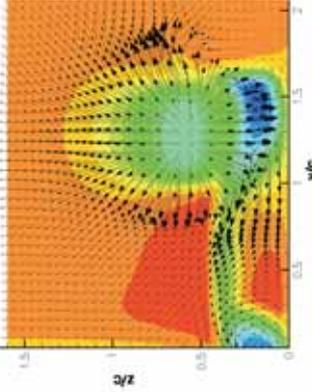
$T/c=1.6$
 $W/c=0.63$
 $S/c=1.6$
 $h/c=0.13$
 $AOA=12^\circ$



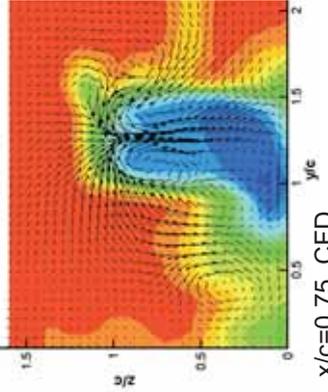
$x/c=-0.63$, LDA



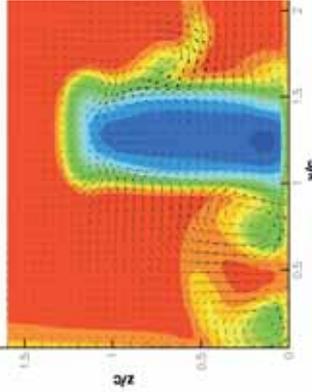
$x/c=-0.63$, CFD



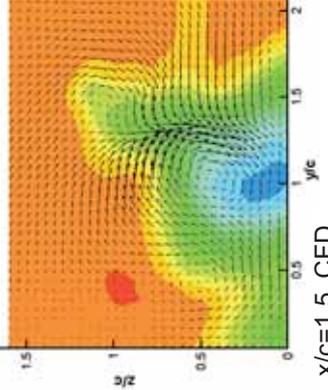
$x/c=0.75$, LDA



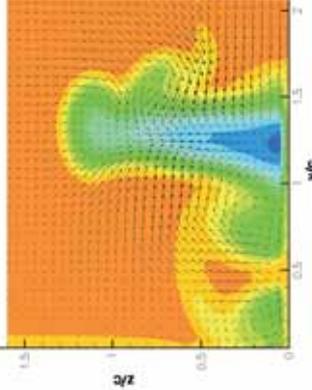
$x/c=0.75$, CFD



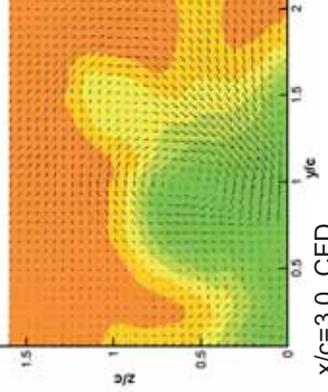
$x/c=1.5$, LDA



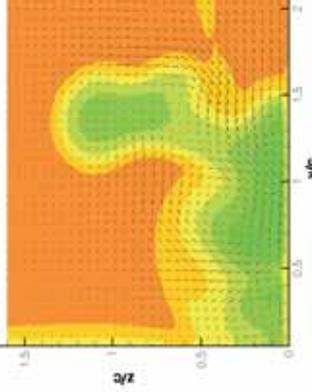
$x/c=1.5$, CFD



$x/c=3.0$, LDA



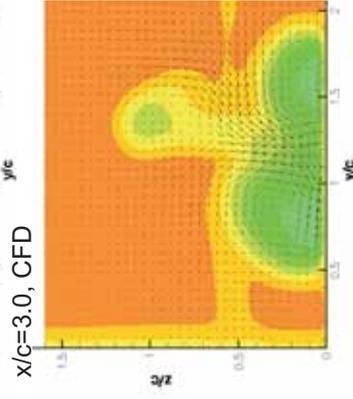
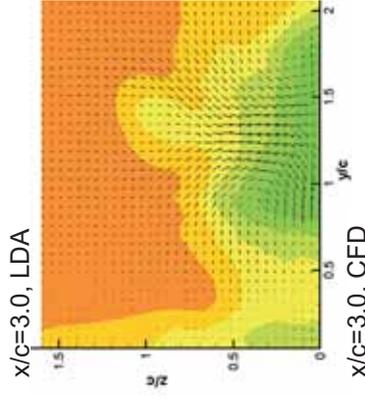
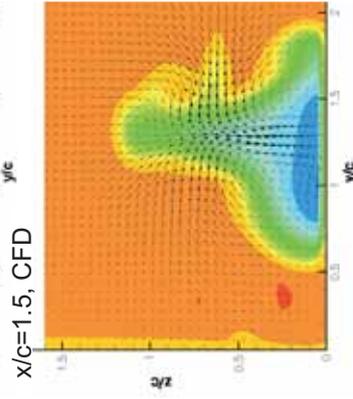
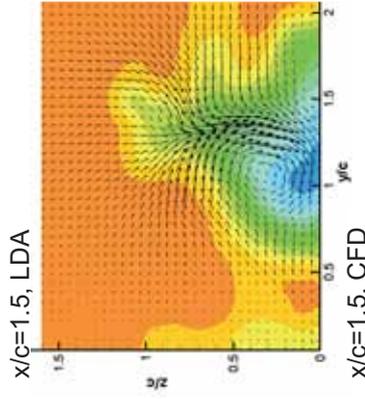
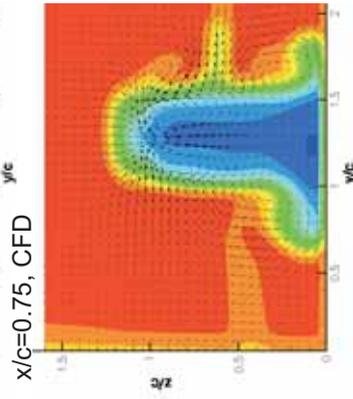
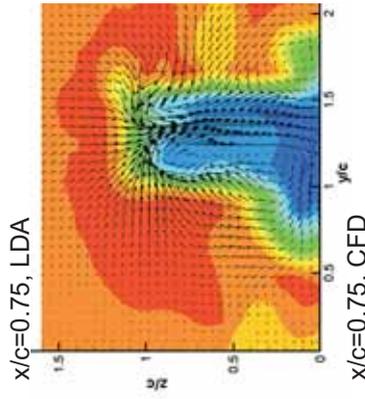
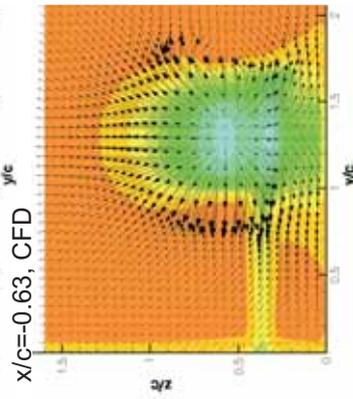
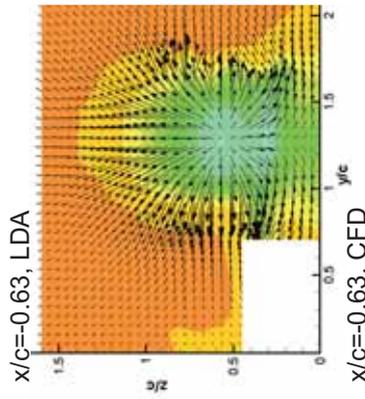
$x/c=3.0$, CFD



Normalised x-velocity: -0.2 0 0.2 0.4 0.6 0.8 1 1.2
 X-Plane reference velocity vector

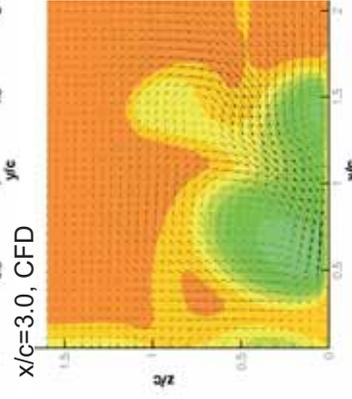
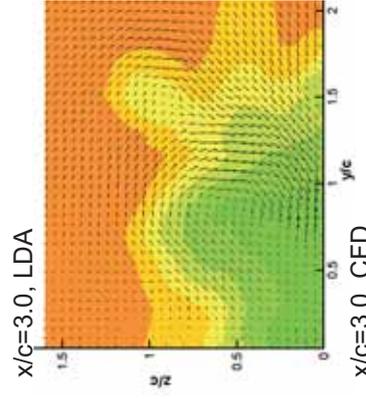
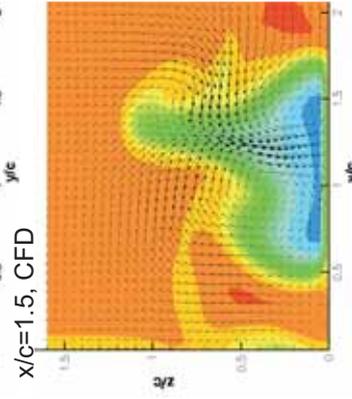
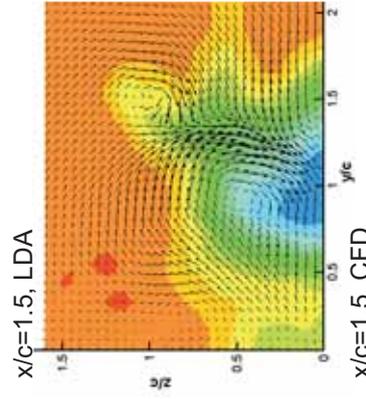
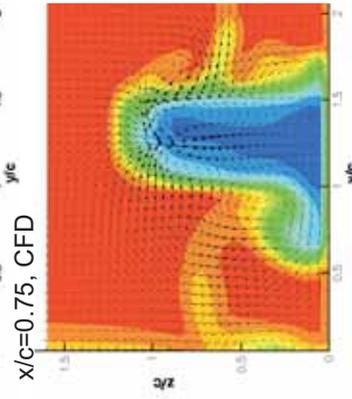
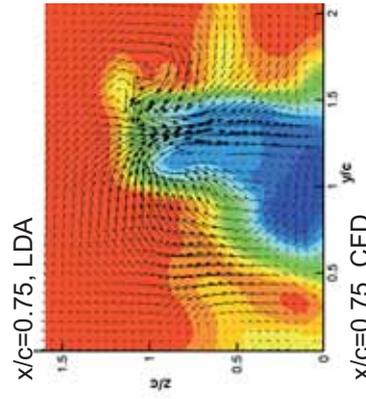
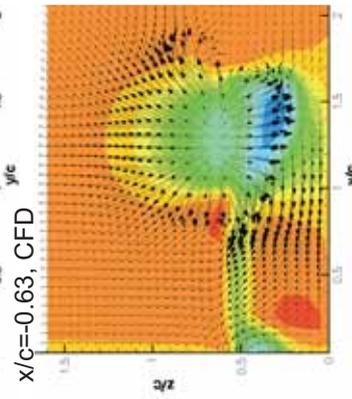
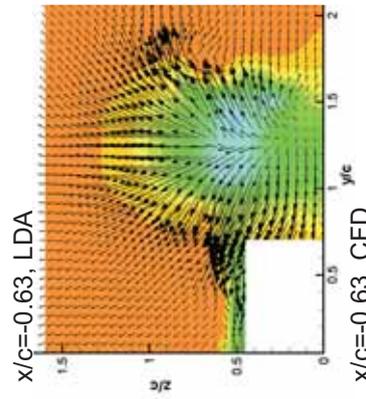
Wing and Wheel

$T/c=1.6$
 $W/c=0.63$
 $S/c=1.6$
 $h/c=0.27$
 $AOA=0^\circ$



Wing and Wheel

$T/c=1.6$
 $W/c=0.63$
 $S/c=1.6$
 $h/c=0.27$
 $AOA=12^\circ$



Normalised x-velocity: -0.2 0 0.2 0.4 0.6 0.8 1 1.2
 X-Plane reference velocity vector